Proceeding Book of First Conference for Engineering Sciences and Technology (CEST-2018)

(Part 4)

Industrial, Structural Technologies and Science Material

25-27 September 2018

Garaboulli - Libya

Table of Contents

The Effect of Usingash Residues of Olive Fruits on the Properties of Cement Mortar

Mukhtar M. Aburawi[1], Hamza Mohammed Al-Madani[2],
[1] Civil Engineering Department, El-mergib University, AlKhoms - Libya.
[2] Civil Engineering Department, Azzaytuna University, Tarhuna - Libya

ABSTRACT

This research aims at studying the effect of the use of the burnt olive oil waste ash (OWA) resulting from olive plantwastes as a partial cement replacement (5%, 7% and 10%) on the properties of cement mortar. The ash burning temperature varies as 600, 700, 800 and 900˚C, and time as 6, 7, 8 hours. The mortar cured in air and water were prepared with 0.42 w/c ratio and sand to water ratio of 1.5 by mass.

The results showed that the 600˚C was efficient in terms of contribution to strength, specific gravity while 7% cement-OWA replacement mixture was found to favour flow ability of the mortar compared to 5 and 10% substitution. Extending OWA burning time temperature to 900˚C and 8hrs increased its porosity and water absorption of the resulting mortar. The OWA slowed down the setting time which made it suitable in the hot weather concreting practice.

Keyword— cement; olive waste ash; mortar; curing; pozzolanic materials; compressive strength

1. Introduction

Large quantities of solid olive waste which contains organic minerals accumulate every year in the countries (Palestine. Tunisia and Libya) producing olive oil[1].This causes great harm to the environment due to its interaction with heat and humidity thereby resulting in chemical hazards. For instance, the carbolic acid, and other strong life-threatening smell emanates from the decomposition[1]. There is increase in such waste accumulation at an alarming rate due to the lack of waste management techniques, such as recycling or re-use in a positive or productive environmental friendly manner with a view to reducing the environmental pollution risks and problems[1].

Concrete industry has seen significant development in the utilization of waste materials as partial replacement for ordinary Portland cement[1]. This research aims at exploring the performance of olive waste as alternative materials in concrete production for structures. Therefore, it is expected that such utilization could provide additional safety and longer service life to concrete structures.

Recently, a number of researchers focused on the use of agricultural material waste, as a partial replacement for cement mixtures so as to improve several properties of concrete and cement mortar. A significant breakthrough was recorded especially on palm oil fuel ash, rice husk ash and date palm ash as regards their performances in OPC based concrete and geopolvmer or alkaline activated binder[25].In this study, the burnt out and ground waste of olive fruits will be used as a partial replacement for OPC cement to see the effect of different replacement ratios on the properties of cement mortar in terms of the workability grade, absorption and compressive strength, and setting time of cement paste.

2. Experimental program

2.1. Materials

2.1.1 Ordinary Portland Cement and sand

The ordinary Portland cement, of specific weight of 3.15 and surface area of 273 m^2/kg,in compliance with Libyan specifications No.340/1997m[2] was used in this study. The fine aggregate used was of specific weight 2.57, which is within the limit of fine aggregate in compliance with the British specifications (BS882-1992)[3].

2.1.2 Olive Oil waste treatment

The olive waste ash (OWA) was obtained through burning large quantities of olive fruit wastes at constant burning time of 6 hrs at temperatures of 600˚C, 700˚C,800˚C and 900˚C, and in different burning times,6 hrs and 8 hrs at the specific temperature of 900˚C. The rate of raising temperature inside the oven was 20˚C/Min. The a shwas left for 24 hours in the air for cooling, and then ground in the grinding machine for 10 mins before sieving through sieve No. 200 (0.075mm). The surface area of the resultant ash was measured by Blaine device in accordance with the US standards (ASTM C204-92)[4].

2.2. Mix design and sample processing

The mixture of the samples was composed of cement of 0.42:1.5:1.0 by mass of cement, sand and water, respectively while OWA was used as a partial replacement for cement with 0wt.% (control), 5wt.%, 7wt.% and 10wt.% of cement. Mixing was done with an electric mixer for 5 mins while two-layer compaction was done in metal cube mould of dimension 50×50×50 mm in size with surface dressing and leveling using 16 tamping-rod blows, according to the approved US specifications steps (ASTM C109-92)[5]. Table 1 shows the details of percentages composition of materials in the prepared mortar. For each mix 21 cubes has been treated, as 9 cubes in the air at a temperature ranging from 20 to 24˚C, and 12 cubes in Jerry water according to US specifications (ASTM C109-92)[5] at a temperature ranging from 18 to 22˚C, and to maintain the purity of the water used, the treatment water was changed every 15 days.

Table 1: Details of cement mortar mixing quantities

Batch No.	Sample code	Cement weight (gm.)	Ash percentage (%)	Ash weight (gm.)	Fine aggregate weight (gm.)	Water weight (gm.)
S1	OPC	2500	0	0	3750	1050
S2	OWA60085	2375	5	125	3750	1050
S3	OWA60087	2325	7	175	3750	1050
S4	OWA600810	2250	10	250	3750	1050
S5	OWA70085	2375	5	125	3750	1050
S6	OWA70087	2325	7	175	3750	1050
S7	OWA700810	2250	10	250	3750	1050
S8	OWA80085	2375	5	125	3750	1050
S9	OWA80087	2325	7	175	3750	1050
S10	OWA800810	2250	10	250	3750	1050
S11	OWA90085	2375	5	125	3750	1050
S12	OWA90087	2325	7	175	3750	1050
S13	OWA900810	2250	10	250	3750	1050
S14	OWA90065	2375	5	125	3750	1050
S15	OWA90067	2325	7	175	3750	1050
S16	OWA900610	2250	10	250	3570	1050

3. Results and discussion

3.1. Physical analysis of olive waste ash

With increase in burning temperature and time of olives waste, the specific weight and the surface are as of ash resulting from the burning process decreases as shown in Table 2. The decreases could be due to volatility of the amorphous fine particles like carbon or other debris there by leading volume and surface area reduction as temperature or duration increases. The physical properties and chemical composition of OWA are shown in Table 2.

Table 2: Physical properties of olive waste ash samples

Sample code	Surface area (cm^2/gm)	Specific weight
OWA6008	7461	2.28
OWA7008	5779	2.18
OWA8008	4439	2.12
OWA9006	4751	2.21
OWA9008	3310	2.09

The surface area and specific gravity (Table 2) reduced by 40.5% and 7.1%, respectively as the temperature increased from 600-800˚C whereas at 900˚C increasing the burning duration from 6-8hrs caused the reduction of 30.3% and 5.4%, respectively from original values of 4751 cm^2/gm 2.21.

3.2. Oxide composition of olive wastes ash

Through the results of the chemical composition of olive wastes ash (OWA)samples by (XRF) device, shown in Table 3, it can be seen that temperature and burning hours have impacton the oxide composition of OWA. The sample burnt at 900˚C has more calcium and alumina contents while more burning duration favours the formation of silica at the same temperature. Besides, the increase in silica content from 18.22 to 31.98% (75.5% increment) as the temperature increases from 600 to 900˚C while potassium depleted significantly at that latter temperature.

Table 3: Oxide composition of olive waste ash samples

Chemical element	Sample code				
	OWA6008	OWA7008	OWA8008	OWA9006	OWA9008
(CaO%) Calcium	21.09	19.62	20.74	23.39	20.82
(SiO2%) Silica	18.39	23.6	22.94	18.22	31.98
(Al2O3%) Aluminum	1.23	1.27	1.26	1.21	1.44
(Fe2O3%) Iron	1.88	3.01	4.32	2.21	5.90
(K2O%) Potassium	44.96	42.24	40.99	42.2	31.25
(MgO%) Magnesium	0.64	0.75	0	0.79	0.53
(SO3%) Cobalt	5.45	3.88	3.95	4.93	2.78
(P2O5%) Phosphorus	6.19	5.46	5.6	6.87	4.99
(TiO2%) Titanium	0.18	0.17	0.2	0.17	0.26
(Cl%) Chlorides	1.42	2.15	1.81	1.03	0.55

3.3. Properties of fresh mortar and cement paste

1.3.1 Flow ability and workability

From the results of the flow table for the workability values of the samples burnt at 600 deg C for 5, 7 and 10% shown in Figure 1. It is clear that 5% cement replacement percentage samples ($OWA_{60085}C$) and 10% ($OWA_{600810}C$)recorded a decline in workability values while $OWA_{60087}C$ (7%) were more homogeneous with high workability values, very close to the result of the reference sample (OWA_0C). This suggests that less the presence of CaO, SiO_2 and Al_2O_3 in the mortar with 10% OWA will definitely reduce the workability as seen in Figure 1. When the quantity of OWA was too low (5%) in concrete mixture, there could be excessive voids in the resultant mortar thereby increasing the inter particle sand grains friction which resulted in low workability as shown in the figure. The closeness of 7% OWA flow ability to the control sample indicates that effective parking that ensured the control over voids distribution. The quantity of CaO, SiO_2 and Al_2O_3 is less than that of 10%OWA thereby causing the reduction in water demand in the mixture.

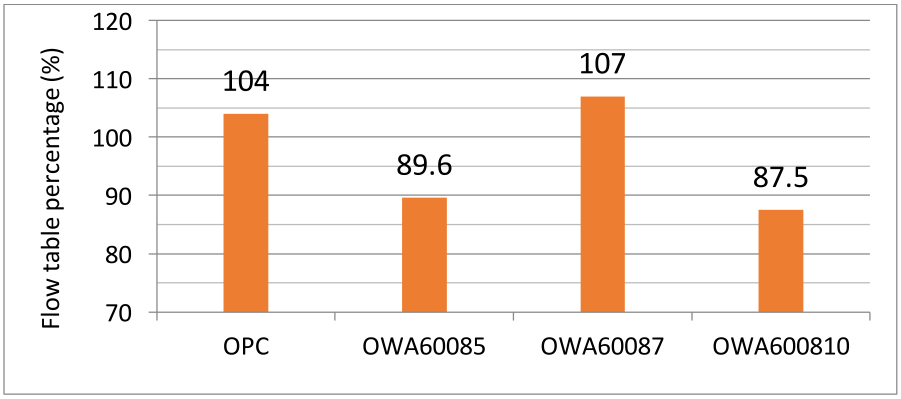

Figure 1: Effect of replacement percentage on flow

It was also observed in Figure 2 that the inclusion of OWA change the range of initial and final setting time which decreased from 135 mins of the control to 130.9 and 15 mins for 5.7 and 10% OWA additions, respectively as shown in Figure 2. This suggests that the more the quantity of OWA the more the delay of initial setting of the sample due to pozzolanic reaction and dilution of tricalcium aluminate portion of OPC that precede hydration reaction or the initial formation of forming calcium aluminium hydrate (CAH). The C_3A in the composition increases with OWA content and reacted with gypsum to from calcium-sulfo-aluminate hydrate (CSAH) – a retarding product. CSAH deposits and forms a protection film on the cement particles to hinder the hydration of C_3A and therefore delay the setting time of cement as noted in OWA 10% cement replacement. The hydration of a lite and be lite follows the initial setting spontaneously to form calcium silicate hydrate (C-S-H) in higher OWA content compared to low cement-OWA substitution.

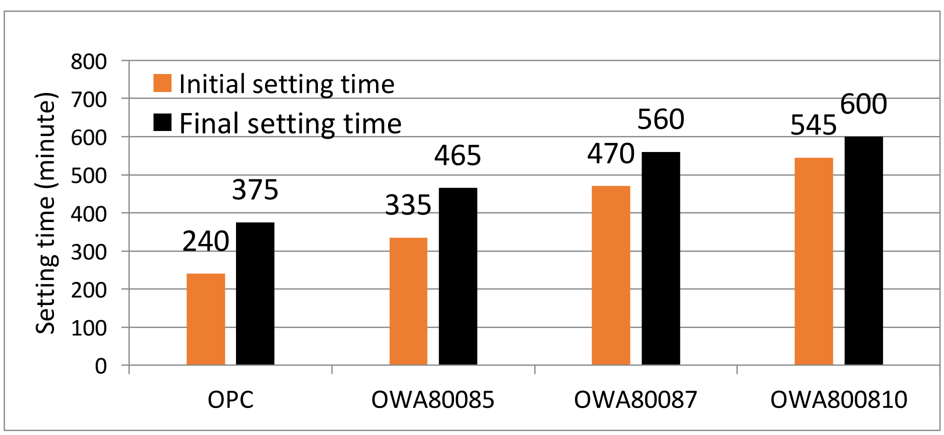

Figure 2: Effect of replacement percentage on setting time

Figure 3 shows the effect of burning time on setting time for the ash burned at temperature 900˚C and with replacement percentage 10%. The initial and final setting time of cement mortar decreased significantly, with increasing in burning time from 6 to 8 hours. The reason for this is due to increase in OWA particle surface area that resulted in more coating paste and enhanced particle reactivity as evidenced in earlier initial (485 mins) and final (540 mins) setting time in 8 hrs compared to 6 hrs of burning time of 555 and 675 mins, respectively.

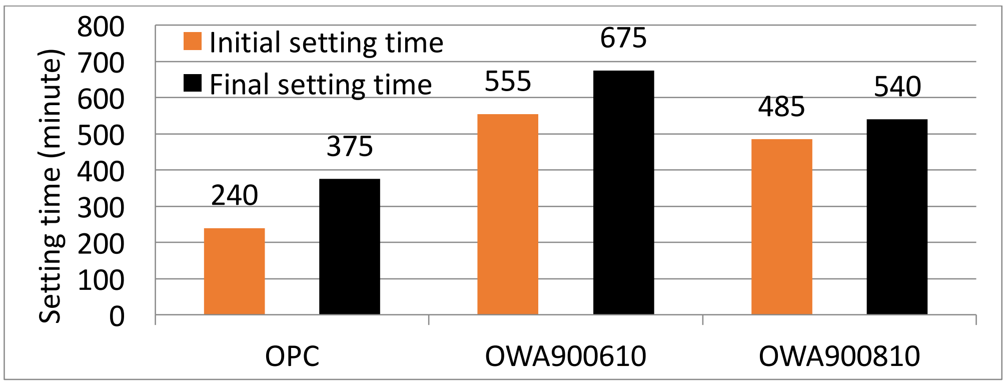

Figure 3: Effect of burning time on setting time for 10% replacement percentage

1.4 Compressive strength of mortar

Figure 4 shows the effect of burning temperature on the compressive strength for 5% cement replacement cured in the air. The OWA burnet at 600˚C appeared to perform better in compressive strength in comparison to those processed at higher temperatures. The rate of strength development was very close to the reference or control sample. However, the pozzolanic reactivity began to take effect at 28 days which indicates that about 20% of strength was gained as can be seen in Figure 4. However, there was no significant strength gained beyond 28 days in all the tested samples. This suggested that OWA underwent a limited pozzolanic reaction. This is more evident upon closely observing the OWA burnt at 700-900˚C for 8 hrs in Figure 4. Burning OWA beyond 600˚C appeared to have converted silica from amorphous phase to crystalline phase thereby affecting its reactivity.

With 100˚C margin from 600˚C, the 7, 28 and 90-day strengths were reduced by 40.1, 35.6 and 34.4%, respectively. The increment is closed to that observe at 900˚C when the difference becomes 38.5%, 26.1% and 35.1%. These values reduced to 13.9, 32 and 13.4% when the temperature margin is 200˚C that is at 800˚C, which signifies better performance compared to 700˚C and 900˚C. This suggests that the proportion of amorphous and crystalline silica at that temperature (800˚C) is at optimum and since the samples burnt at 600˚C contains more amorphous silica, the strength was noted to be the highest observed within the blended and the reference or control samples at 28 and 90 days. The burnt ash samples at 600˚C recorded 90-day compressive strength of 18.8 MPa, which was higher than the reference sample value by 27.8%.

From Table 2, the higher strength recorded in the 600˚C burnt sample could be attributed to its higher specific gravity compared to others samples whose specific gravity decreased with increasing burning temperature.

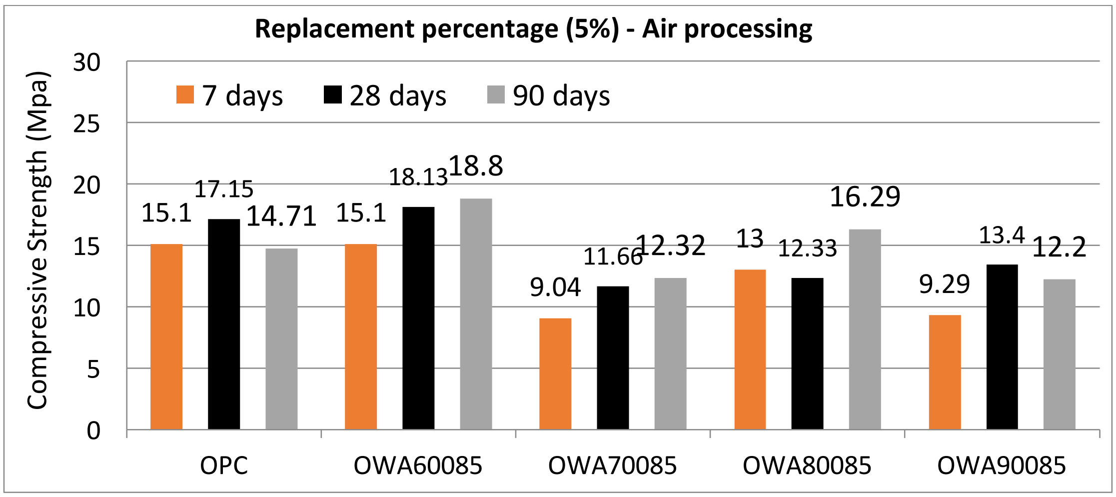

Figure 4: Effect of burning temperature on compressive strength

Figure 5 shows the effect of burning time on the absorption rate of replacement percentage of 7%. At 6 hrs duration at operating temperature of 900˚C, the absorption is found to be less than at 8 hrs by 15.4%. It implies that excessive exposure of the same leads to formation of more voids or pores with the interstices of the ash. The values recorded at 6 hrs is 4.5% higher than the control.

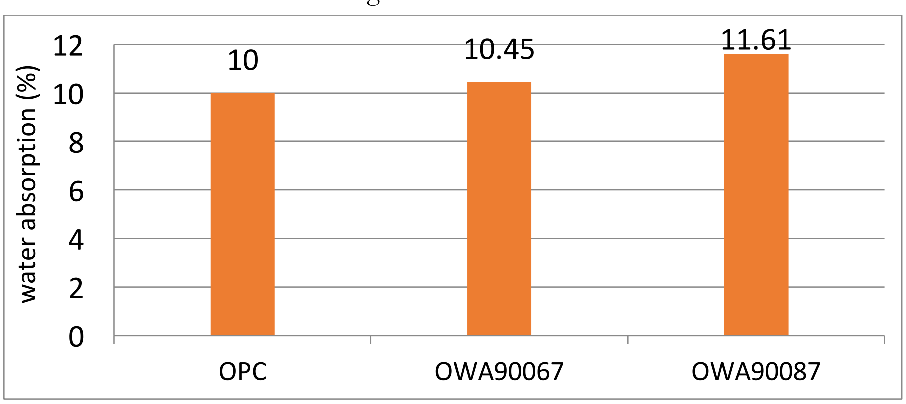

Figure 5: Effect of burning time on absorption at replacement percentage 7%

Figure 6 shows the effect of burning temperature on porosity at replacement of 10%. After 28 days of treatment in the water, it was noticed that the addition of burned ash at temperatures 600˚C, 700˚C and

800˚C led to decrease in porosity less than that of the reference sample, while adding the burnt ash at 900˚C led to increased porosity, that is increasing the proportion of air spaces inside the cement mortar, therefore leading to weakness in the compressive strength of the cement mortar.

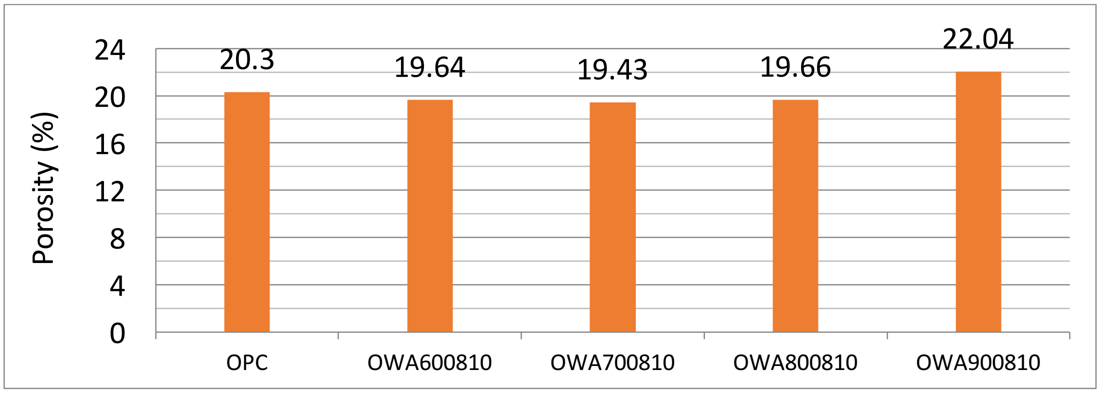

Figure 6: Effect of burning temperature on porosity at replacement percentage 10%

After 28 days of treatment in the water as shown in Figure 7, the effect of the burning temperature on the permeability at replacement percentage of 5%, was noticed to reduce at600˚C(1.26×10^{-14}m/s) and it is 37% of the control sample (2.01×10^{-14}m/s). However, increment in permeability of the ash burnt at 700˚C(2.83x10^{-14} m/s) increased by 41% compared to the control and 124% with reference to that of 600˚C. It appears the porosity of the sample treated at the temperatures of 800 and 900˚C are equally distributed.

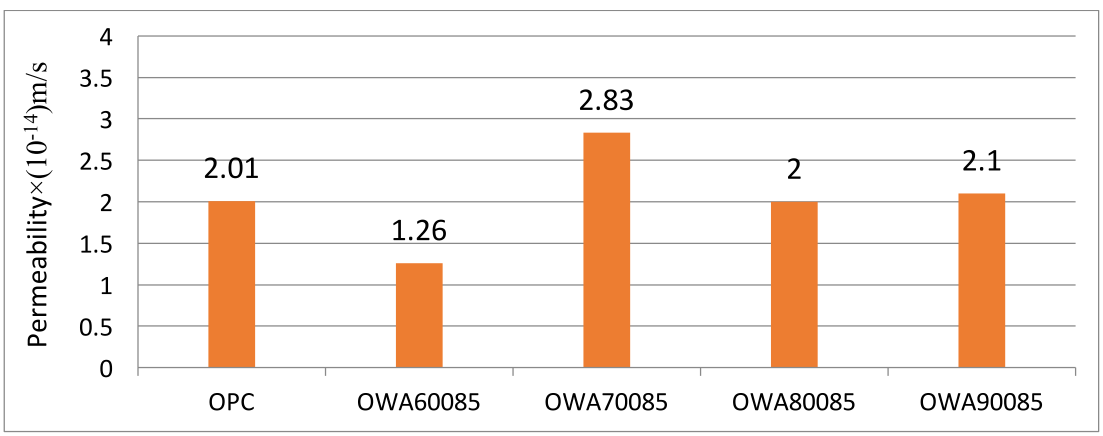

Figure 7: Effect of burning temperature on permeability coefficient at replacement percentage 5%

4. Conclusions

The following conclusions can be drawn from the results obtained from the treatment of olive waste ash (OWA) as partial cement replacement in blended mortar in terms of specific gravity, transport properties, workability and setting time:

- Burning temperature and burning time of OWA had an impact on the chemical composition and physical properties of the resulting ash most evidently, the specific gravity.
- With the increase in the replacement percentage of OWA, initial and final setting time of cement paste increased significantly due to prolonged or delayed pozzolanic reaction.
- Burning temperature had significant effect on the compressive strength of OWA blended cement mortar cured in the air. The ash was observed to perform better in terms of strength and permeability coefficient when it was treated at the 600˚C.
- Even at maximum treatment temperature of 900˚C, 6 hrs period of burning of OWA favored water absorption performance of OWA blended mortar than 8 hrs when the porosity was also noted to be worsened compared to lower treatment temperature and the control samples.

Acknowledgements

I would like to thank the personnel in the Chemistry lab, of the Industrial Research Center in Tajoura, and the personnel in the X rays and microscopic photographing labs, of the Oil Research Center in the city of Tripoli.

References

[1]. Abdulwahid, M.Y.,(2009) "Effect of Olive Waste Ash on the Mechanical Properties Of Mortar". M.Sc. Thesis, Civil Engineering Department, Jordan University of Science and Technology.

[2]. Libyan Standard Specifications No. 340 of 1997, of Portland Cement, National Center for Standard Specifications, Tripoli, Libya.

[3]. BS 882, (1992) "Specification for aggregates from natural sources for concrete". British Standards Institution, 389 Chiswik high road, London, W4 4AL, UK.

[4]. ASTM C204-92, (1992): "Standard Test Method for Fineness of Portland Cement by Air Permeability Apparatus". ASTM, 1916 Race St., Philadelphia, PA 19103, USA.

[5]. ASTM C109-92, (1992): "Standard Test Method for Compressive Strength of Hydraulic Cement Mortars (Using 2-in. Or 50-mm Cube Specimens)". ASTM, 1916 Race St., Philadelphia, PA 19103, USA.

[6]. ASTM C305-91, (1991): "Standard practice for mechanical mixing of hydraulic cement pastes and mortars of plastic consistency". ASTM, 1916 Race St., Philadelphia, PA 19103, USA.

[7]. ASTM C191-92, (1992): "Standard Test Method for Time of Setting of Hydraulic Cement by Vicat Needle". ASTM, 1916 Race St., Philadelphia, PA 19103, USA.

[8]. ASTM C642-97, (1997): "Standard Test Method for Density, Absorption, and Voids in Hardened Concrete". ASTM, 100 Barr Harbor Drive, West Conshohocken, PA 19428-2959, USA.

[9]. AT315-EN 12390-8 (2000) "Testing hardened Concrete-Part 8: Depth of Penetration of Water Under Pressure".

[10]. Haitham Abdel Hady Klob, 2009, "Study of the Impact of High Temperatures on Concrete Endurance". Master thesis, Civil Engineering Department- ElMergib University, Alkhoms-Libya.

[11]. Libyan Standard Specifications No. 294 of 1988, of Water used in Concrete, National Center for Standard Specifications, Tripoli, Libya.

[12]. Chindaprasirt, P., &Rukzon, S., (2008) " Strength, porosity and corrosion resistance of ternary blend Portland cement, rice husk ash and fly ash mortar ". Construction and Building Materials 22(2008):1601-1606.

[13]. ASTM C618 (2005) "Standard Specification for Coal Fly Ash and Raw or Calcined Natural Pozzolan for use as a Mineral Admixture in Concrete". American Society for Testing and Materials, pp.310-313, USA.

[14]. Mahmoud Imam, Mohamed Amin 2007, Materials Properties and Tests, Faculty of Engineering- El Mansoura University.

[15]. Neville, A.M., (1995), "Properties of Concrete" 4th Edition, Prentice Hall.

[16]. Rif'at Mahmoud Sallam 2004, "Causes of Concrete Damage and Methods of Repair and Protection" El Maarif Establishment, Cairo, Egypt.

[17]. Merkhoufy Abdel Malek 2004, "Contribution in the Study of Fiber Concrete Characteristics and Distortions" Faculty of Sciences and Engineering Science- University of QuasedyMerbahWarkalah, Algeria.

[18]. Ganesan, K., Rajagopal, K. & Thangavel, K. (2007) "Evaluation of bagasse ash as supplementary cementitious material". Cement and Concrete Composites, 29, 515-524.

[19]. Shvarzman, A., Kovler, K., Schamban, I., Grader, G. &Shter, G. (2002) "Influence of chemical and phase composition of mineral admixtures on their pozzolanic activity". Advances in cement research, 14, 35-41.

[20]. Bendapudi, S.C.K. &Saha, P. (2011) "Contribution of Fly ash to the properties of Mortar and Concrete". International Journal of Earth Sciences and Engineering, 4, 1017-1023.

[21]. Malhotra, V.M. & Mehta, P.K. (1996) "Pozzolanic and cementitious materials". Taylor & Francis pp. 72.

[22]. Bhatty, J.I. & Reid, K.J. (1985) "Use of thermal analysis in the hydration studies of a type 1 Portland cement produced from mineral tailings". ThermochimicaActa, 91, 95-105.

[23]. Wild, S., Khatib, J. & Jones, A. (1996) "Relative strength, pozzolanic activity and cement hydration in superplasticisedmetakaolin concrete". Cement and Concrete Research, 26, 1537-1544.

[24]. Hago, A.w., (2002) "Effect of the Fineness of Artificial Pozzolana on the Properties of Lime-Pozzolana Mix". Science and Technology, 7, pp.252-258.

[25]. Al-Akhras, N., Al-Akhras, K., &Attom, M., (2009)" Performance of olive waste ash concrete exposed to elevated temperatures". Fire Safety Journal 44(2009):370-375.

[26]. Tangchirapat, W., Jaturapitakkul, C., & Chindaprasirt, P., (2009) " Use of palm oil fuel ash as a supplementary cementitious material for producing high-strength concrete". Construction and Building Materials 23(2009):2641-2646.

[27]. Tangchirapat, W., Jaturapitakkul, C., Chindaprasirt, P., &Saeting, T., (2007) " Evaluation of the sulfate resistance of concrete containing palm oil fuel ash". Construction and Building Materials 21(2007):1399-1405.

[28]. Ayman Fathallah Mabrouk, 2014, The Impact of Burned and Ground Palm Tree Pips on the Mechanical Characteristics of Cement Mortar". Master thesis, Department of Civil and Architecture Engineering- Libyan Academy for Post Graduate Studies, Tripoli, Libya.

[29]. J MENDHAM. R C DENNY. J D BARNES. M J K THOMAS. "VOGEL'S – Textbook of Quantitative Chemical Analysis". 6th Edition, Prentice Hall.

[30]. ASTM C187-86, (1991): "Standard Test Method for Normal Consistency of Hydraulic Cement". ASTM, 1916 Race St., Philadelphia, PA 19103, USA.

Study the Performance of Solar Water Heater with Various Loads

Ghassan S. EL-MASRY[1], Mustafa EL-MUSBAHI[2], Benur MAATUG[3]
[1]gsalmasri@elmergib.edu.ly, [2]mustafa.a.elmusbahi@gmail.com, [3]saif_matug@yahoo.com
[1,2,3]Department of Mechanical Engineering, Elmergib University, Garaboulli, Libya

ABSTRACT

The performance of a certain type of solar heater was studied by install, assemble solar heater and the installation of different measuring devices, such as water flow meter and temperature meters for water inside, outside, and measuring the temperature of the atmosphere and a measure of the amount of solar radiation, all of these devices connected to a device that stores this data every 5 minutes In the form of averages or totals.

The first tests were carried out by consumption of the water in the early morning (immediately after sunrise). In the second period, the consumption of water was at the end of the day (before sunset). The third period was at noon (midday)

TRNSYS, a specialized program in simulating solar thermal processes, TRNSYS can used to connect thermal system components in any form, solving differential equations and facilitating the output of information.

TRNSYS works to compensate the practical experience with a fully simulated theory that saves time and effort and gives us the desired results of the practical experiment. The program data is the solar heater characteristics of the experiment, the period to be tested and the amount of water to be consumed.

The study explains that the best time to increase the amount of energy extracted the water must drained at the afternoon period.

Keyword— solar heater, solar energy, simulation system, consumed period, change of loads, alternative energies

1. Introduction

A field study was conducted for a complex heater at the Solar Energy Research and Studies Centre in Tajoura, where integrated measuring devices were used to study and analyse the solar thermal performance of the solar heater. The study period lasted more than two months and was divided into three stages. The water was withdrawn in the first stage in the morning, the second stage just before sunset and then in the final stage, the drawn were during the afternoon.

It will discuss the specifications of the solar heater, the measuring instruments and the methods of testing approved for the solar heater. In this study, it was based on the international standard for testing solar heaters, referred as ISO 9459-2 for the evaluation of solar heater under study, issued by the International Organization for Standardization (ISO).

2. Specifications

For data that helps to obtain the thermal performance of the heater, the solar heater is provided with measurement sensors connected to the Data Acquisition System, which can sensor data from sensors every 10 seconds and store it at the end of every five minutes in the form of cumulative or average values by The nature and characteristics of this data.

In this study, a range of variables were measured: the temperature of the water inlet to the reservoir T_i, the outlet temperature T_o, the temperature of the air surrounding the heater Tamp, the amount of hot water consumed M, and the intensity of the total solar radiation falling on the surface of the complex G_{sol}, For each five minutes throughout the day in the form of temperature averages and cumulative values of the radiation falling on the surface of the collector and water consumed. The data device calculates the amount of total thermal energy acquired for hot water Q_t.

3. Solar heaters

The heater consists of a compound with an assembly area of 3.024 m2 and a reservoir of horizontal type, with an auxiliary electric coil installed manually to meet the shortage of thermal energy resulting from the absence of the sun at night or in the days when the clouds are abundant. The collector and the reservoir are connected to each other by connecting pipes to suit the natural flow system. The system was directed to the true south at an angle of 40° from the horizontal

Table1: Specifications of solar heater

Solar heater	
Type of heater	Natural flow closed circuit
The total capacity	200 liters
The solar collector area	3.024 m2
Collector pipe	15 mm diameter copper tube
Collector glass surface	glass thermally treated thickness of 3 mm
Absorption Surface Coating	Selective Coating (Black Chrome)
Collector insulation	glass wool thickness of 30 mm
Hot water tank	horizontal ring type
Hot water tank insulator	Polyurethane foam 45 mm thick

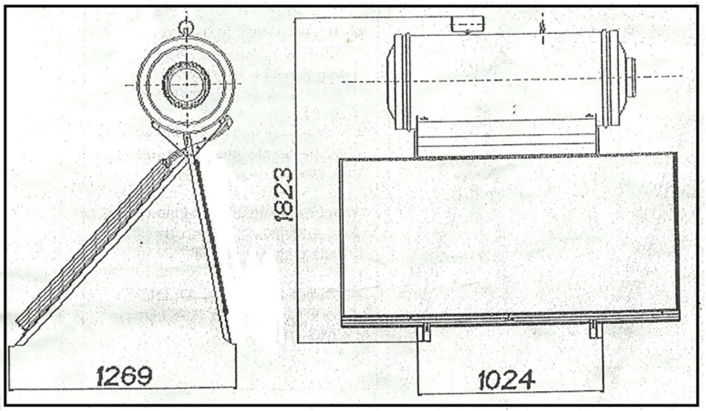

Figure 1.a: Cross section of the solar heater (from catalog)

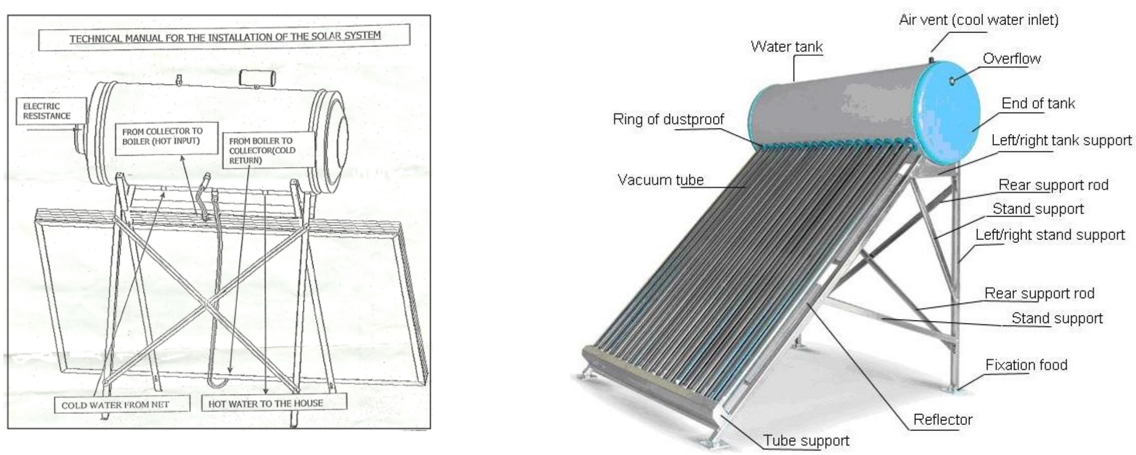

Figure 1.b: a synthesis of the solar heater(the right figure from catalog)

Figure 1 (a, b) shows the solar heater diagram used in the experiment

4. Range of test conditions

The test results are prepared in this system using a special model. The input / output graph and the temperature increase are also explained and presented.

Test results are not used to report on the performance of the heater under test. It is represented an intermediate stage in the test and is only used as entries for calculations.

Test results include daily system productivity for different values of H and ($T_{a\ (day)}$ - T_c). Therefore the performance of the solar water heating system can be represented by the following equation[2]

$Q = a_1H + a_2\ [T_{a\ (av)} - T_c] + a_3$ .... (1)

The coefficient (a_1, a_2, a_3) of the system is determined from the test results' using the linear correlation model, whereas (Q) means or refers to the net solar energy obtained by the thermal tank during the day, (Q) is calculated by total hot water drawn or extracted according to the test defined.

In addition, the results of the test containing the temperature ($T_{a\,(day)}$ - T_c) for water for different values of (H) and ($T_{a\,(day)}$ - T_c) by the following equation [2]:

$T_{d\,(max)} - T_c = b_1H + b_2\,[T_{a\,(day)} - T_c] + b_3$ .... (2)

The coefficients (b_1, b_2, b_3) are determined from the test results using the linear correlation model, while $T_{d\,(max)}$ in the equation refers to the maximum temperature of the extracted water. And the results and curves were as follows:

It was in the withdrawn curves for the morning period for three days as shown in Figure 2 (A, B, C):

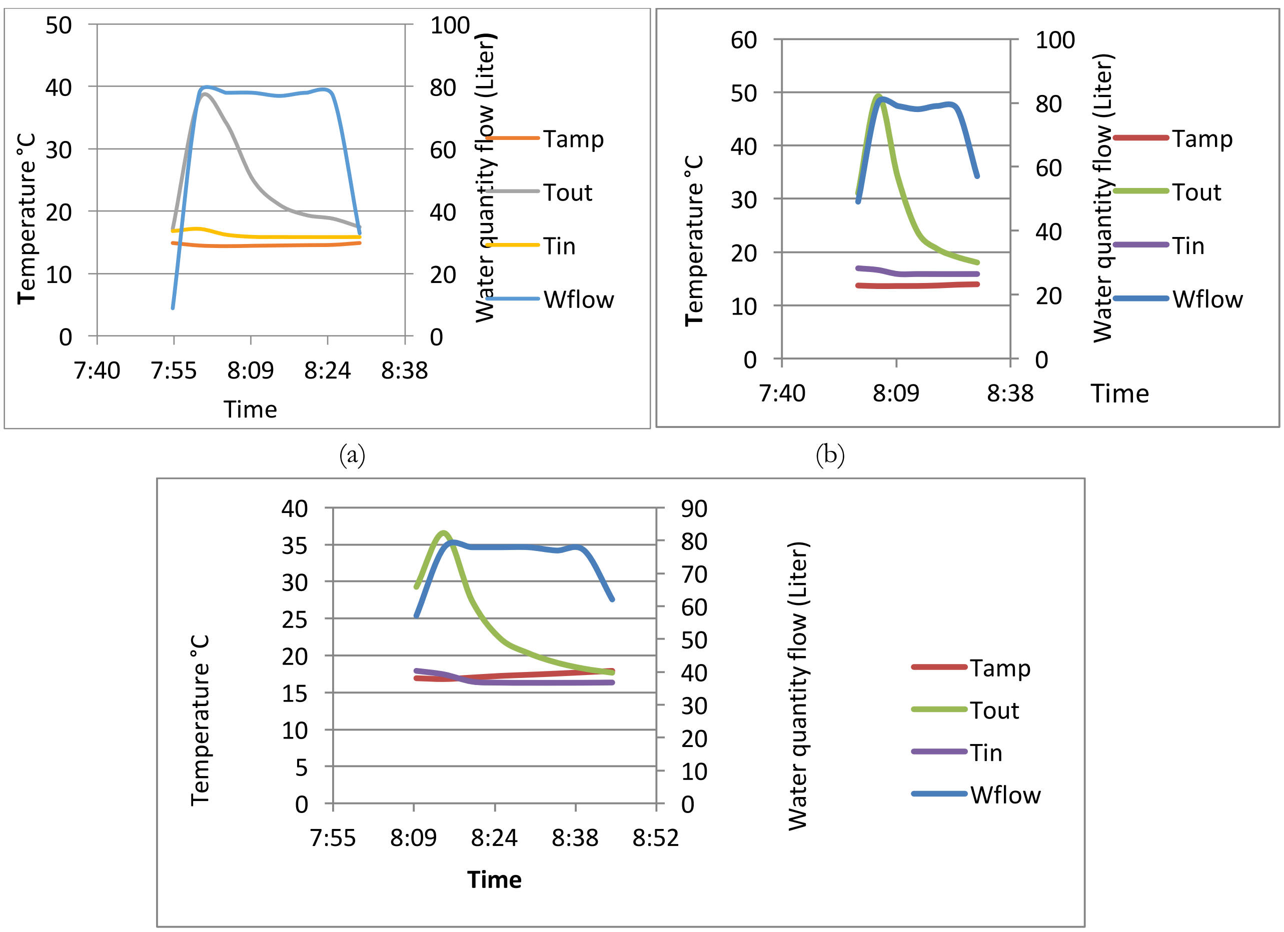

(a) (b)

(c)

Figure 2.a,b,c: withdrawn curves for the morning period

Then in the evening curves for three days as shown in Figure 3 (a, b, c):

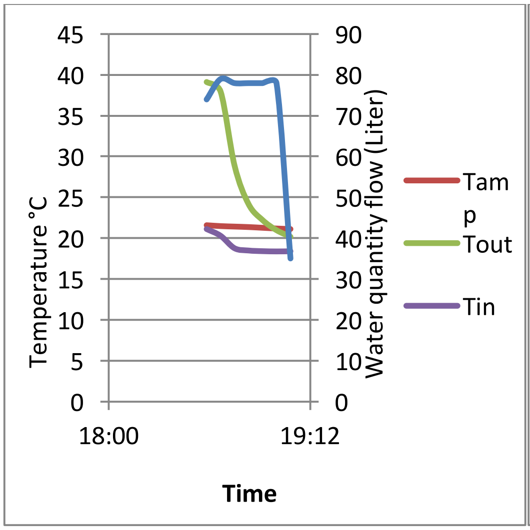

(a)

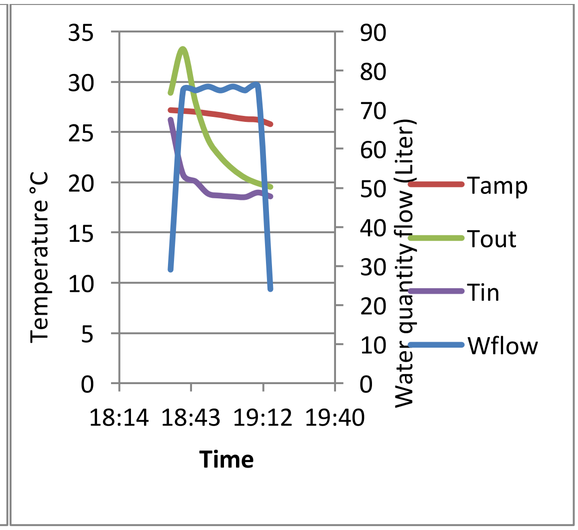

(b)

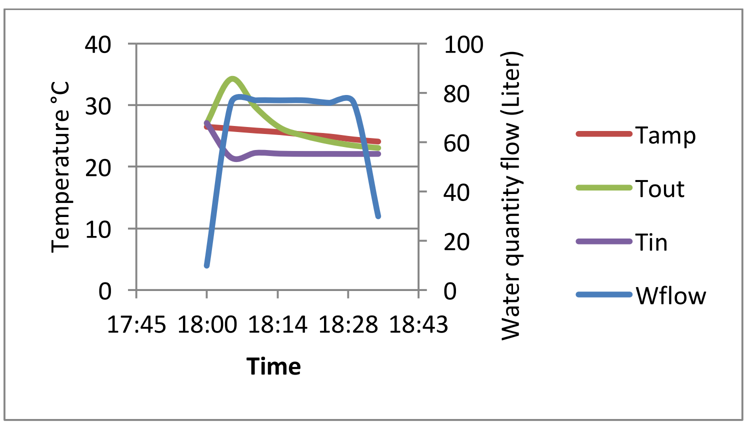

(c)

Figure 3.a,b,c: Draw curves during the evening

In the afternoon for three days , as shown in Figure 4 (a, b, c):

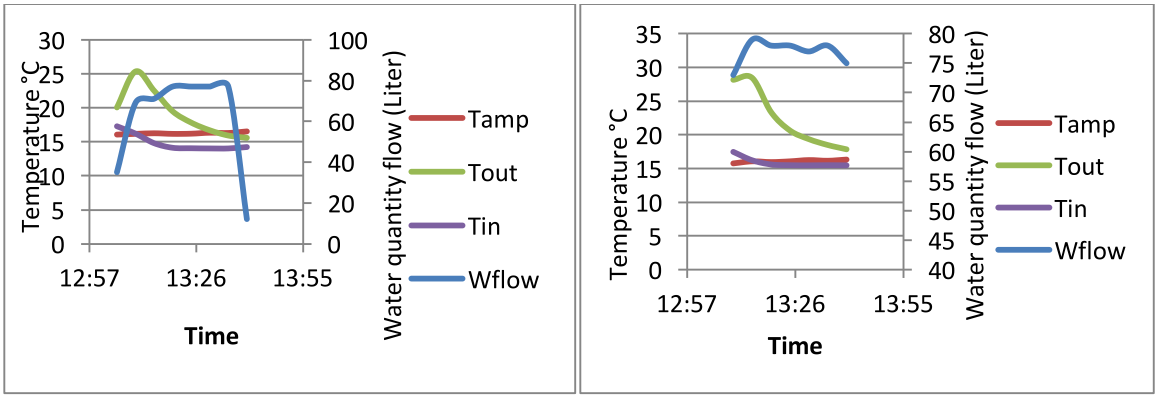

(a) (b)

Figure 4.a,b: *Draw curves during the afternoon*

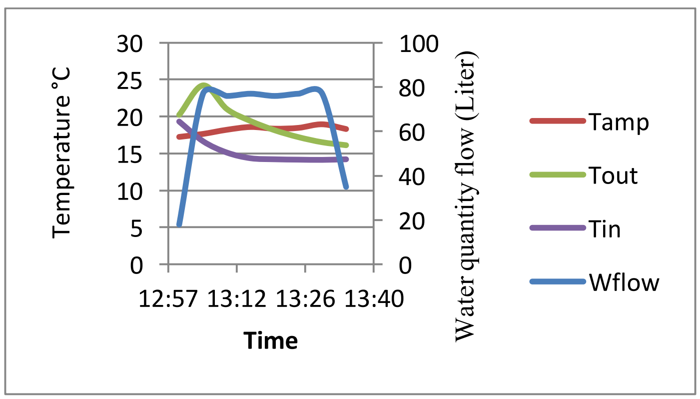

Figure 4.c: Draw curves during the afternoon

5. Representing the simulation program results

After introducing the specifications of the solar heater used in the experiment and determining the required temperature, as the temperature at which the draw water should come out, and give all the data to the program, the results are in curves as follows:

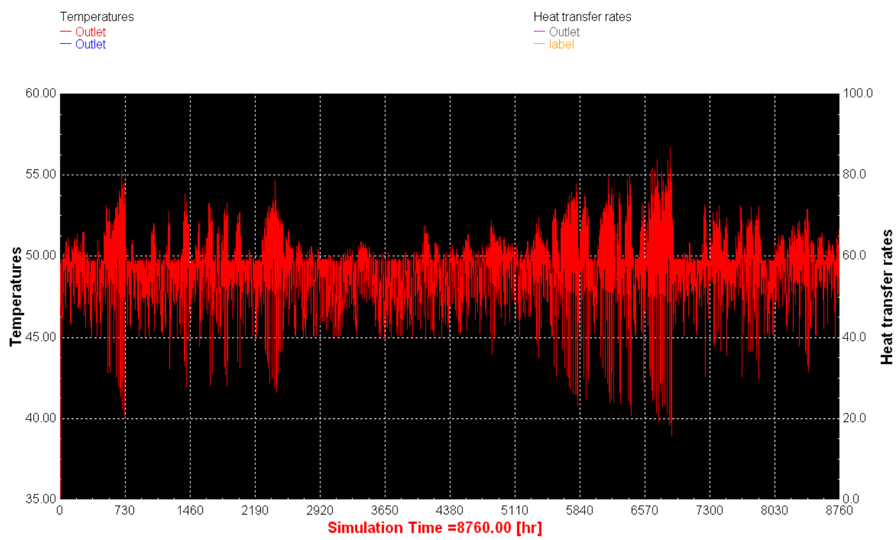

Figure 5: Comparison between the temperature of the withdrawn water and the rate of heat transfer and the simulation time over a whole year

Figure 5 shows that the higher the rate of heat transfer, the higher the temperature of the withdrawn water, that mean the relationship between the rate of heat transfer and the temperature of the withdrawn water is a direct relationship.

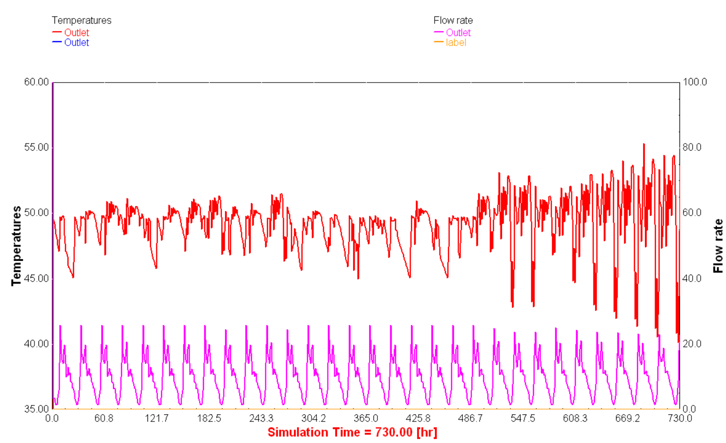

Figure 6: The relation between the draw water temperature and the water flow rate (the drag rate) and the simulation time which is a full month

In Figure (6), where the rate of drawn water was constant in the morning period over a whole month, but note that the temperature of withdrawn water increases by the end of the month, due to the fact that the solar radiation increases at the end of this month and based on the increase in The radiation increases the temperature of the drawn water.

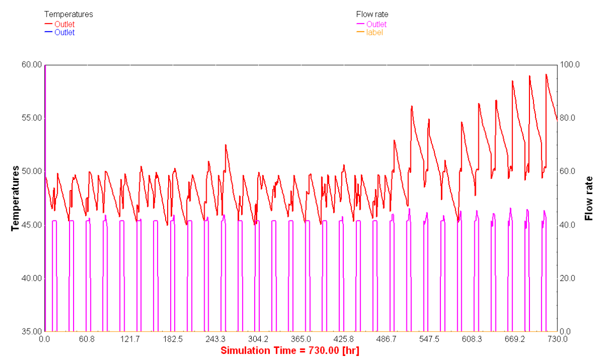

Figure 7.a: The relationship between the temperature of the withdrawn water and the drag rate and the time that represents a full month and the draw were in the evening, ie before sunset

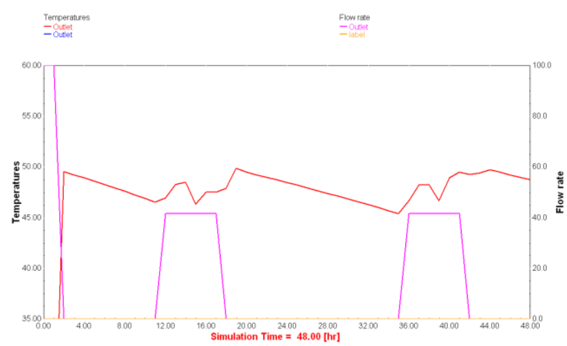

Figure 7.b: The relationship between the temperature of the drawn water and the flow rate and the simulation time, which is two full days

In Figure 7a,b, the draw here is a complete withdrawal of the load, i.e., a draw along the day from 11 am to 6 pm

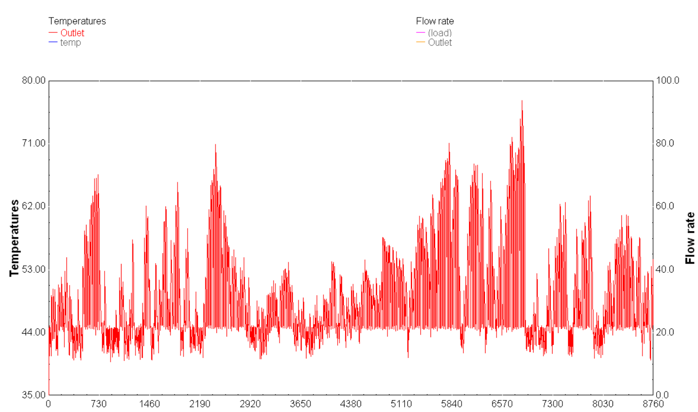

Figure 8: The relationship between the temperature of the drawn water and the flow rate at afternoon and the simulation time which is equivalent to one year

Figure 8 shows that at the afternoon there are increase of temperature of drawn water

6. Conclusion

This study explains the best time to drained the hot water from the solar collectors as shown in Figures 2,3,4 the experiment for three days for each period and the simulation program as shown in figure 7,8.This study shows the variation of results when the consumption of water is changed from morning, afternoon and evening. The best time to increase the amount of energy extracted and the temperature is at the afternoon period.

Reference

[1]. Strategical report for renewable energy-Nation board for scientific research – Libya- Nation Week For scientific and Technology 2006

[2]. ASHREA 93,77 fundamentals.

[3]. ASHRAE. 1991a. Active solar heating systems installation manual.

Built to Code Building Envelop Versus Sustainability of High-Rise Building Performance

Mohamed ali karim [1]
[1] omgaon2x@yahoo.com
[1] Department of Civil Engineering, College of Engineering, Elmergib University, Libya

ABSTRACT

Global warming and climate change are major challenges facing the nation and the world. More than two thirds of the electric energy and one third of the total energy are used to heat, cool, and operate buildings, representing majority of all CO2 emissions. A reduction in building energy consumption will help to mitigate the energy security and climate change effects on buildings. The reduction in energy consumption is accomplished through the development of new technologies (for the building's envelope, mechanical, and lighting systems) that save energy and reduce CO2 emissions. However, an alternative approach is the use of passive systems that employ renewable energy sources. Passive systems avoid the need for heating or cooling through better design, construction, and operation. They utilize solar or wind energy to heat, cool, or light buildings. This study analyzes the sensitivity of energy demanded to build to code building's envelops. In other words, investigating whether building that meets the need of enveloping code can take advantage of the weather surrounding the building, in terms of cooling, or heating (comfort) the building as needed. Four high-rise office buildings (glazed curtain wall) with four different aspect ratios (1:1, 1:2, 1:3, and 1:4) are thermally analyzed in four climate zones: cool, temperate, arid, and tropical. The envelope of these high-rise buildings is modeled to meet International Energy Conservation Code (IECC) requirements, which references several American Society of Heating, Refrigeration, and Air Conditioning Engineers (ASHRAE) standards. As a result, the energy performance of high-rise office buildings is not sensitive to the passive solar gain as long as the exterior envelopes are built to IECC 2009 requirements, which does not allow the use of the ambient climate condition of the building to get comfort. This is not appropriate from the concept of sustainability of buildings as referred to above.

Keyword— Sustainability, High-Rise Building, Energy performance, Global warming

1. Introduction

One of the criteria for the development of countries is the urban renewal, especially the high-rise buildings in their cities. Thousands of years, tall buildings and towers have fascinated human beings; they have been built primarily for defensive or religious purposes as evidenced by the Pharaonic temples (pyramids) of Giza, Egypt, the Mayan temples of Tikal, Guatemala, and the Kutub Minar of Delhi, India. In the modern era, high-rise buildings are a reality of contemporary life in cities and there are several reasons for this. Urban real estate is a premium due to the lack of available land; secondly, high-rise buildings (vertical construction) present an effective way to reduce traffic congestion in cities; thirdly, rapid population growth of urban communities, lastly, the limitations and the conditions of the terrain and topography [1, 2]. However meeting operational performance requirements and maintaining occupant comfort in high-rise buildings is a challenging design problem. The energy demands for large-scale HVAC system (Heating, Ventilating, and Air Conditioning) load is significant. Not only are the site energy costs are high, the attendant environmental consequences of using non-renewable energy sources are great. Improving the energy efficiency of high-rise buildings is a key component in increasing the sustainability of the environment. More than one-third of the world's energy consumption is attributed to the construction and building industry [3]. As a case, more than two thirds of the electric energy and one third of the total energy in the US are used to heat, cool, and operate buildings [4], representing roughly 18% of all U.S. CO2 emissions in one year. Given the current global energy crisis, there is a critical need to design and construct buildings that are more sustainable. Energy efficient buildings minimize building resource consumption, operations and life cycle costs, and can improve occupant health and comfort [5]. High-rise buildings should be designed in a manner to reduce the need for fossil fuels (oil, gas and coal) and promote greater reliance on renewable energy. This concept is reflected in what is known these days as sustainable architecture or green building. A green building is one that focuses on reducing the impact of buildings on the environment. In general, a green building is one that meets the needs of the present generation without compromising the ability of future generations to meet their needs as well [1]. For designers and architects such as William Reed, green buildings are designed, implemented, and managed in a manner that places the environment first[6]. In the state of Libya, the architectural renaissance will be an urgent necessity for the follow-up to the developed nations in this world; as the state of Libya adopts building specifications, which may not be compatible with the requirements of sustainability in terms of temperate climate. Moreover, the current standards of architectural systems do not adopt fully sustainable methods, since the concept of sustainability is a newborn concept and its implementation is economically expensive because of the cost of the techniques used. States are in a race to lay the foundations for sustainable construction. In keeping with the demand for the current architectural development, nations cannot wait for complete and integrated system to be built in sustainable ways. Thus, the idea of this research is to study if these specifications meet the requirements of sustainably performance of high building that are built according to these codes and standards (IECC code and ASHRAE standards) of the buildings envelope [7]. The study analyzes the sensitivity of energy demanded to build to code buildings envelopes. In other words, investigating whether a building that meets the need of envelop code can take advantage of the weather surrounding the building, in terms of cooling, or heating (comfort) the building as needed. Four high-rise office buildings (glazed curtain wall) with four different aspect ratios (1:1, 1:2, 1:3, and 1:4) are thermally analyzed in four climate zones: cool, temperate, arid, and tropical. Energy demand is calculated for each model with respect to two opposing orientations (Figure1). The four high-rise buildings are modeled to meet IECC 2009 code requirements, which reference several ASHRAE standards, including Std. 90.1 for commercial building construction [7, 8]. The following sections describe the analytical method and the primary variables that will be measured against energy use in the four-modeled buildings. Then summarize the results and present the conclusion.

2. Building Materials and Basic Data

Four models of high-rise office buildings are considered in this study to evaluate the sensitivity of energy demands to variations in: (1) footprint aspect ratio (1:1, 1:2, 1:3, and 1:4), and (2) building orientation. Since the goal is to isolate the influence of built to code building's on energy demand, all other buildings descriptors such as the square footage, number of stories, building height(Figure 2), and occupancy for the four buildings are held constant across all four buildings. Specifically, the thermostat range, internal design conditions, occupancy, infiltration rate, and hours of operation as fixed control variables.

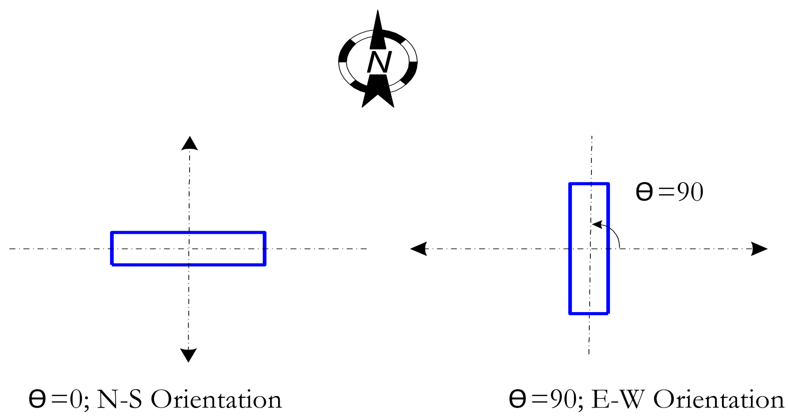

Figure 1: Building orientation considered in this study

The four buildings are 200 meters in height, 50 stories that are 4.0 m floor-to-floor height, with a total conditioned floor area of 135,000 square meters. The primary material for the meet the R-value specified for a climate according IECC 2009. To simplify the thermal analysis, the effect of surrounding buildings have been neglected assuming that the buildings were erected on flat open ground and are aligned with the cardinal directions.

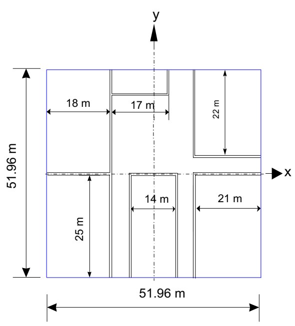

Plan view 1:1 configuration

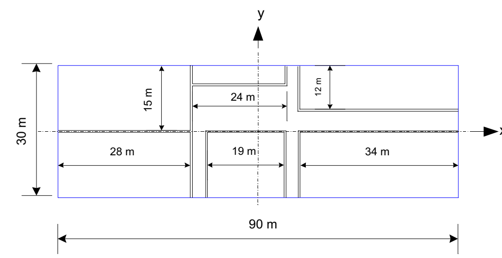

Plan view 1:3 configuration

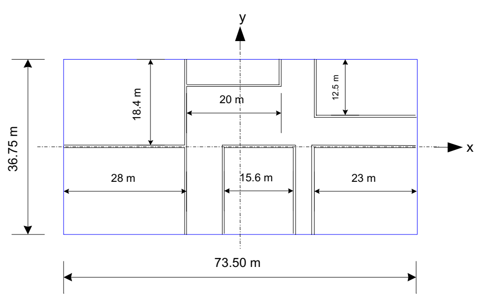

Plan view 1:2 configuration

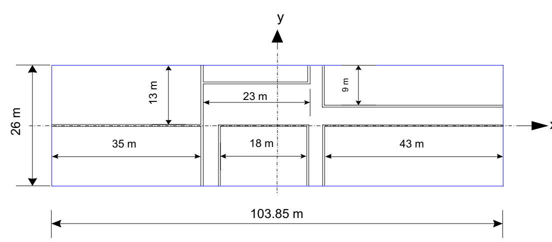

Plan view 1:4 configuration

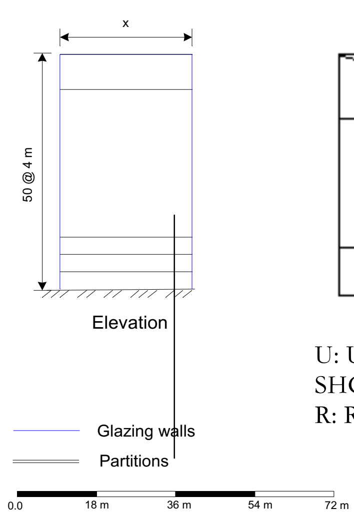

Climate / Element	Building's envelope thermal properties			
	Cool	Temperate	Arid	Tropical
Fenestration (Glazing wall with 10 % metal framing)	U=2.5	U=3.4		U=5.4
	SHGC=0.4	SHGC=0.25		
Roofs	R=3.7			R=2.7

U: U-value (W/m^{2}K)
SHGC Solar Heat Gain Coefficient
R: R-value (Km^2/W)

Figure 2: building plan view and envelope thermal properties

3. Thermal analysis

Autodesk's Ecotect energy simulation package was used for the thermal analysis. The thermal analysis involves examining each of the four models (1:1, 1:2, 1:3, and 1:4) in each of the four climatic zones (cool, temperate, arid, and tropical). That is, the only difference among the four runs for the same climate zone are the building width to length ratio (aspect ratio) for one orientation at a time. Ecotect calculates the overall heat gain/loss (Sun-path diagram Figure 3); and then with choose the way the comfort zones is calculated of each day of the year using the Flat Comfort Bands method, which sets upper and lower limits for comfort temperatures. If the internal zone temperature is either above or below the temperature limits for the prescribed comfort zone, then thermal environmental conditions are unacceptable to the majority of the occupants within that space. Factors that determine thermal environmental conditions are temperature, thermal radiation, humidity, air speed, and personal factors such as activity and clothing. Environmental factors are influenced by: (1) Direct solar gain, or radiant flow through transparent surfaces. (2) Internal (sensible) heat gain from lights, people, and equipment. (3) Conductive heat flow through opaque (envelope) elements. (4) Radiant flow through opaque (envelope) elements. (5) Ventilation and infiltration heat flow through cracks and openings. (6) Inter-zonal heat flow between adjacent zones, which for this analysis is negligible. Conductive and radiant flows through opaque elements are treated together and described as "Fabric" in Ecotect. Personal factors such as activity (metabolic rate) and clothing (insulation of clothing) are treated as constant for all building occupants.

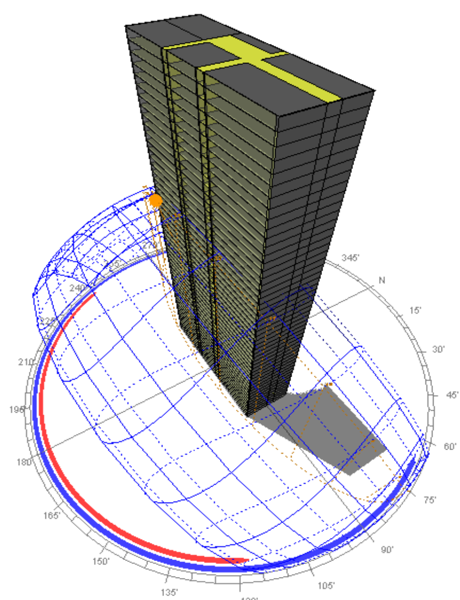

Figure 3: Sun-Path Diagram

In this study, there are two main steps of the thermal analysis. The first step is to find the sensitivity of the energy demand (heating and cooling loads) to the change of the surface area ratio (SAR), which relates to floor-plan aspect ratio:

$$SAR = \frac{(floor\ perimeter \times floor\ height)}{floor\ plan\ area} \quad (1)$$

This analysis consists of thirty-two different simulation runs (of four models in two orientations in four climate zones), where annual cool and heating loads are calculated for each model. The results corresponding to the N-S orientation are provided in Table 1; and the difference in total energy demands between the N-S and E-W orientations is not significant.

Table 1: Energy demand verses SAR (N-S orientation)

.

Width to length ratio - increase in SAR												
Climate	1:1			1:2			1:3			1:4		
	Heating	Cooling	EUI	Heating	Cooling	EUI	Heating	Cooling	EUI	Heating	Cooling	EUI
	kwh/m^2			kwh/m^2			kwh/m2			kwh/m2		
Cool	49.8	9.4	59.2	51.9	9	60.9	53.6	8.7	62.3	55.9	8.4	64.3
Temperate	7.9	30.7	38.5	8.4	30.7	39.1	8.9	30.8	39.8	9.7	31	40.6
Arid	5.8	57	62.8	6.1	57.9	64.0	6.5	59	65.5	7	60.4	67.4
Tropical	0.0	62.5	62.5	0.0	62.75	62.6	0.0	63.4	63.4	0.0	64.1	64.1

Via the model of 1:4 aspect ratio as an example, the monthly and yearly energy demand ratios (EDR) for each of the four climate zones are shown in Table 2.

$$EDR = \frac{energy\ demand\ of\ East - West\ orientation}{energy\ demand\ of\ North - South\ orientation} \quad (2)$$

In addition, the passive solar heat gains ratio (PSHGR) of the model of 1:4 aspect ratio displayed in Figure 4. Moreover, the total heat gain and heat to gain ratio (HGR) of the month of July are broken down into individual sources of direct (solar) gain, internal gain, fabric, and ventilation.

Table 2: Energy demand ratio, EDR, (model of 1:4 aspect ratio)

Months	Energy demand ratio (EDR)			
	Cool	Template	Arid	Tropical
Jan	1.01	1.01	1.03	0.96
Feb	1.01	1.02	0.97	0.99
Mar	1.01	0.99	0.99	1.05
Apr	0.99	1.02	1.04	1.07
May	0.97	1.04	1.05	1.06
Jun	0.99	1.04	1.03	1.05
Jul	**1.011**	**1.034**	**1.026**	**1.055**
Aug	1.02	1.02	1.02	1.05
Sep	1.00	0.99	1.01	1.03
Oct	1.01	0.98	0.99	1.01
Nov	1.02	1.00	0.99	0.99
Dec	1.02	1.02	1.03	0.97
yearly	**1.01**	**1.02**	**1.02**	**1.03**

Table 3, presents the percentage of each of these heat sources and how they vary by orientation. The total energy demand for each orientation is not significantly different, even though the E-W oriented models has a much higher potential for passive solar heat gain

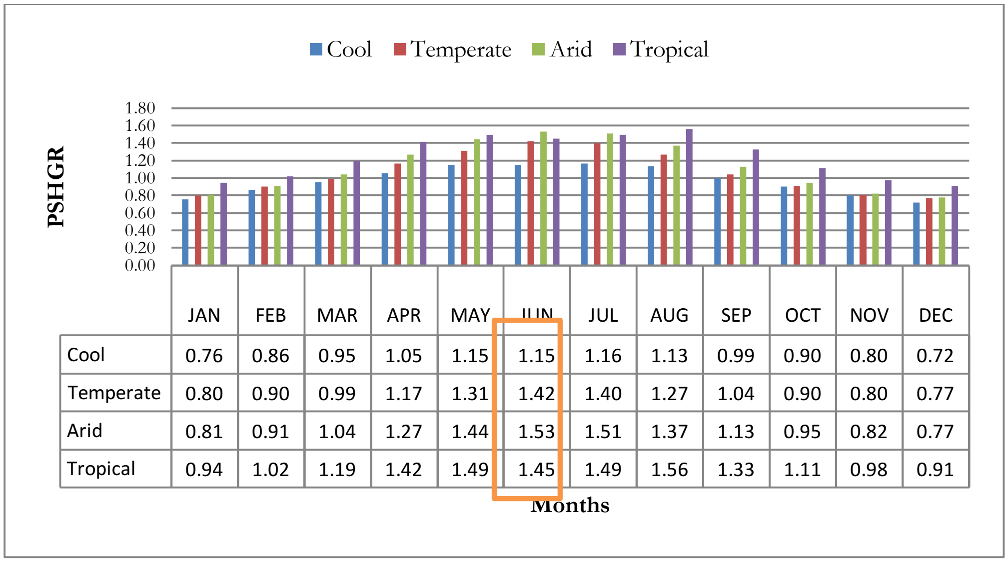

	JAN	FEB	MAR	APR	MAY	JUN	JUL	AUG	SEP	OCT	NOV	DEC
Cool	0.76	0.86	0.95	1.05	1.15	1.15	1.16	1.13	0.99	0.90	0.80	0.72
Temperate	0.80	0.90	0.99	1.17	1.31	1.42	1.40	1.27	1.04	0.90	0.80	0.77
Arid	0.81	0.91	1.04	1.27	1.44	1.53	1.51	1.37	1.13	0.95	0.82	0.77
Tropical	0.94	1.02	1.19	1.42	1.49	1.45	1.49	1.56	1.33	1.11	0.98	0.91

Figure 4: Monthly passive solar heat gain ratio (model of 1:4 aspect ratio)

The next stage of the thermal analysis investigates why the differences in the energy demand are negligible. One possible reason maybe because of the thermal properties of the IECC 2009 envelope. In the initial analysis, the glazing walls were modeled with U-factors and SHGC set according to the regional climate. These walls were subsequently modeled using single-pane glazing, which has inferior thermal properties (U=6.0 W/m²K & SHGC=0.94). The simulation was run again to evaluate the total energy demand for each of the two orientations. The results of the new simulation runs show that buildings oriented E-W require 12% more energy than those oriented N-S, and that the passive solar heat gain in July is significantly increased.

Table 3: Sources of heat gain (Wh) in July- built to code envelope (model of 1:4 aspect ratio)

Climate	**Cool**					**Temperate**				
Orientation	**Ѳ=0**		**Ѳ=90**		July HGR	**Ѳ=0**		**Ѳ=90**		July HGR
Direct	1.1E+8	17%	1.3E+8	20%	**1.16**	1.1E+8	8%	1.5E+8	11%	**1.40**
Internal	5.1E+8	78%	5.1E+8	75%	1.00	5.1E+8	40%	5.1E+8	38%	1.00
Fabric	2.1E+7	3%	2.3E+7	3%	1.11	2.8E+8	22%	2.9E+8	22%	1.02

Ventilation	1.3E+7	2%	1.3E+7	2%	1.00	3.8E+8	30%	3.8E+8	29%	1.00
Total	6.6E+8		6.8E+8		**1.032**	1.3E+9		1.3E+9		**1.038**
Climate	**Arid**					**Tropical**				
Orientation	**Ɵ=0**		**Ɵ=90**		July HGR	**Ɵ=0**		**Ɵ=90**		July HGR
Direct	1.1E+8	5%	1.6E+8	8%	**1.51**	9.9E+7	10%	1.5E+8	14%	**1.49**
Internal	5.1E+8	25%	5.1E+8	24%	1.00	5.1E+8	50%	5.1E+8	47%	1.00
Fabric	6.1E+8	30%	6.2E+8	29%	1.01	2.2E+8	21%	2.3E+8	21%	1.05
Ventilation	8.3E+8	40%	8.3E+8	39%	1.00	2.0E+8	19%	2.0E+8	18%	1.00
Total	2.1E+9		2.1E+9		**1.03**	1.1 E+9		1.1E+9		**1.057**

4. Results:

4.1. Demand sensitivity–glazing walls built to code.

For each building in the climate zones of Cool, Temperate, and Arid, the change in energy demand is slightly significant, where by increasing the surface area (up to 20%), energy demand is increased by 5.1-7.9% (Table 1) depending on the climate zone. In the tropical climate, however, the energy demands is insensitive to the variations in SAR, where the average increment percent is 0.4% and the total increase is 0.84%. Of course, an increase in the surface area (SAR) is likely to lead to an increase in the materials used, may influence construction costs and embodied energy. Furthermore, increases in the surface area may result in an increase in the area exposed to wind pressure, which might lead to the need of a larger size of structural element, which also influence construction costs and embodied energy. The differences in the total energy demand for two building orientations (N-S & E-W) in each climate zone are nearly negligible. Figure 4, demonstrating monthly breakdown solar heat gains and losses resulting from building oriented E-W are much greater than those if the building was oriented N-S. Table 3, clarifies that the influence of solar loads is small compared to internal, fabric, or ventilation loads. The amount of heat gain from passive sources represents 5-20% of the total heat gain. This is consistent for both orientations, and the effect is trivial compared to the total heat gain.

4.2. Demand sensitivity with non-code-compliant glazing on walls

The second stage of thermal analysis is an investigation of the sensitivity of built- to-code glazing systems on passive solar heat gain, compared to single-pane glazing, which has poorer thermal properties. The outcome demonstrates that code requirements for glazing systems results in reductions in direct heat gain to become to represent 5% rather than 24% of total heat gain(N-S),while become to represent 8% rather than 34% of total heat gain(E-W), (Table 3 & Table 4 for arid climate). Code-built glazing also reduces total energy demands by 12%, which also explains why there is such a small effect of varying building orientation on monthlies and yearly energy demand.

Table 4: Breakdown heat gain (Wh) in July in Arid climate – regular glass envelope (model of 1:4 aspect ratio)

	Heat gain (Wh)				July HGR
	ϴ=0		ϴ=90		
Direct	7.4E+08	24%	1.2E+09	34%	1.62
Internal	5.1E+08	16%	5.1E+08	14%	1.00
Fabric	1.0E+09	33%	1.0E+09	29%	1.01
Ventilation	8.3E+08	27%	8.3E+08	23%	1.00
Total	3.099E+09		3.564E+09		1.15

5. Conclusions

By simulating each building configuration using Autodesk's Ecotect, two major conclusions regarding building energy demand can be drawn: (1) For the buildings in Cool, Arid, and Temperate climate zones, the energy demand may be considered marginally sensitive to changes in surface area ratio (SAR). Increasing the envelope surface area by 20% leads to energy demand increases of 5.1-7.9% depending on the climate zone. The energy demand for buildings in the Tropical climate zone is insensitive to variations in SAR. (2) The energy performance of high-rise office buildings is not sensitive to the passive solar gain as long as the exterior envelopes are built to IECC 2009 requirements for thermal performance. Finally, high quality thermal properties of code-built envelope systems offer more flexibility to designers with regard to the building site planning (geometry, layout, and orientation) without creating negative impacts on total energy demand. On the other hand, this limits the possibility of maximizing the advantages of passive heat gain. In addition, because built to code buildings are not significantly sensitive to direct solar gain; it leaves little room for other passive design strategies for energy conservation such as shading devices, landscaping, and thermal mass.

References

[1]. K. Yeang, "The Green Skyscraper*," Prestel, Munich,* 1999

[2]. M. Jenks, R. Burgess, "Sustainable urban forms for developing countries," *Spon Press,* NY*,* 2004.

[3]. J. Straube*,* "Green building and sustainability," *Building science digest*, 5: 24, 2006

[4]. WBDG. "Energy Codes and Standards," May, 2011. http://www.wbdg.org

[5]. United States Green Building Council, "Green building research," June 2009. http://www.usgbc.org>

[6]. W. Reed, "The Integrative design guide to green building". *Hoboken*, N.J, 2009

[7]. The U.S. Department of Energy Building Energy Codes Program. *International Energy Conservation Code 2009*. International code council, INC., 2010

[8]. ASHRAE STANDARED. *Energy Standard for Buildings Except Low-Rise Residential Buildings*. ASHRAE, Atlanta, 2010

Simple and Sustainable Constipate to Save Cost and Time for Structure Constructions

Abdualraouf Mohamed [1*], Mohamed Ali Milad [2]
[1] raouf.amhir@gmail.com, [2] omgaon3x@gmail.com

[1, 2] Department of Civil Engineering, College of Engineering, Elmergib University, Libya

ABSTRACT

The energy required producing the structural elements such as concrete, steel; wood, etc. have serious environmental and financial consequences. The energy analysis, therefore, must take into consideration the added cost of embodied energy, which is the energy consumed by all of the processes associated with the production of a building. Generally, highly processed material, the higher embodied energy is. Hence, concrete has the lowest re-use capability that makes it a less sustainable material. Thus, wisely, use construction material leads to avoid the use of materials that are associated with high-embodied energy. Moreover, choosing the optimal construction system is one of the elementary bases of sustainability through the possibility of recycling the materials used for building construction. This study presents guidance of the sustainable constipates based on the performance of building construction using masonry barring walls system against frame concrete structure system of residential buildings, Where finite element method was used to analyze the stresses on the masonry bearing walls, and structural analysis for the frame structure. Algebra calculation of the construction materials quantities, and known sources of embodied energy estimation. As a result, this comparison turns out that the masonry barring walls system procedure is offering good distribution of stresses, more economical, require lesser time to build, and highly recyclable, which making it more contributing to sustainability.

Keyword— Embodied energy, Sustainability, Masonry, Recycling, Construction

1. Introduction

The cost of structural elements of concrete construction work and materials used in the traditional methods of construction in the State of Libya may be high; some of it is not environmentally friendly. Moreover, the lack of natural resources for these materials and the high-embodied energy in their production and taking into account the non-use of sustainability methodology in construction makes us think more careful and thoughtful about the techniques used in construction in the State of Libya. In the construction of simple residential buildings, there is known two major structural systems: concrete rigid frame structure system; and masonry wall bearing system and there is great differences in the characteristics of each system [1]. Each has its advantages and disadvantages [2, 3]. Nevertheless, the concern is the technique and performance of building that built according to these systems in the State of Libya at current era. Because of the method of implementation, where in realty construction is a mixed system between these two systems due to the embodied the concrete masonry into the rigid concrete frame. This method of construction might accidentally give very large capacity of the structural system compared to the capacity required, which leads to a non-economic building and is not sustainable for its more embodied energy and the effort of recycling materials used by the end of building's life span. On the other words, the presence and implementation of concrete masonry within the concrete rigid frame makes it an effective factor to carry forces and even change the behaviour of loads path. As result of mixing these two systems is a complex system that capable of resisting more than is required to resist. Nevertheless, unfortunately there is no need here to increase the capacity because the frame system designed to bear the whole loads alone. However, the main difference between the two systems is the mechanism of carrying loads safely through itself to the ground soil. Standers and cods commends that the characteristics of each of these structural systems individually and do not see the need to mix these two systems together because each of them is well alone [4, 5]. However, the reality of the situation in the State of Libya in the construction of simple private housing buildings, which mix these two systems made it important to know the advantages and disadvantages of this system to help the Libyan citizen to choose the optimal system to build his house in economic and sustainable way. Hence, the idea of this study evaluates the structural performance, and sustainability efficiency of each system then examines the effect mixing them [6]. Moreover, this study illustrates the behaviour of each of these known structural systems and simulate the system used extensively in the construction in the state of Libya, also compared between different systems in terms of stresses distribution, the amount of materials used, embodied energy, then evaluating these systems in terms of sustainability principle. The following sections demonstrate the method and the primary variables, then evaluates the results and present the conclusion.

2. Material and Research Methodology

The research studies a typical residential concrete building with components in line with the tradition and housing requirements of a middle-income family in Libyan society. It is single-story building of 165-square-meter footage print; Figure 1 shows the plan and 3D views of the house. 3D models of structural analysis were prepared for three structural systems. The first model is concrete rigid frame model and analyzed as line element by structural analysis method, the second model is masonry wall bearing and analyzed as surface element by finite element methods; the third is the mixed system model (concrete rigid frame and masonry wall bearing). Modeling and analysis are carried out using SAP 2000, Figure 2 shows the models as it appears on SAP 2000. Table 1 shows the characteristics of the materials used, and Table 2 shows the loads were applied [7]. Where these values simulate the properties of the materials used in practice and the application of standards and specifications in the Libyan state.

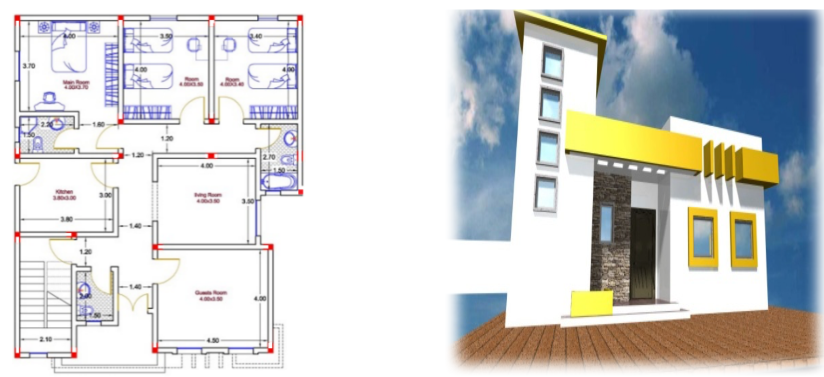

(a) (b)

Figure 1: (a) house plan view, (b) house 3D view

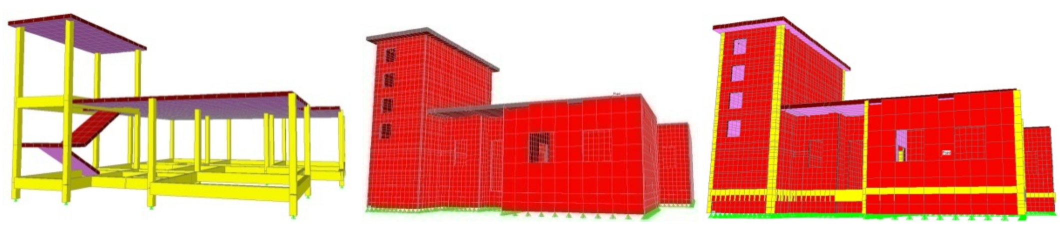

(a) (b) (c)

Figure 2: (a) Concrete rigid frame model, (b) Masonry wall bearing model, (c) Mixed model

Table 1: Characteristics of materials for analysis and design

Material property	The value
Concrete (fc')	28 MPa
Rebar (fy)	280 MPa
Reinforced concrete density	24 kn/m³
Masonry concrete density	20 kn/m³

Table 2: Applied loads, dead and live

Model / Load type	Model 1	Model 2	Model 3
Self-weight of structural elements	SAP Calculated	SAP Calculated	SAP Calculated
Finishes loads on roof	2.50 kn/m²	2.50 kn/m²	2.50 kn/m²
Wall loads	12 kn/m	SAP Calculated	SAP Calculated
Live load on roof	3 kn/m²	3 kn/m²	3 kn/m²

3. Modeling

3.1. Concrete Rigid Frame Structure System

This system is used in the design of most residential buildings, so the loads carries by the slab, which is supported by beams (or beamless) on the columns then to the foundations. Walls here are partitions to separates building's components where its weight calculated, and it is applied as a distributed load on the beams, this allows mainly concentration loads on columns, moment and shear forces on the beams. The analysis results of the axial force were varied on the columns according to their share of loads, so the columns designed to have cross section of (20 x 20 cm) with 4 Ø 12 mm. Note that, the reinforcing percentage is the minimum value allowed by the code [5]. On the other hand, the concrete required for the columns is 3.0 m^3 while all beams designed to have cross section of (40x20 cm) and required concrete is 9.2 m^3.

3.2. Masonry Wall Bearing System

In this model, no columns or beams have been modeled on the fact that the concrete masonry walls alone carry and support the roof load and other loads to the soil safely [8]. The values of the stresses on the walls have changed slightly through wall's height and the stress distribution has become more uniformly in the absence of columns and beams, where concentration of stress was occurred at interfaces between walls and columns or beams. Note that in the presence of openings, the stresses in the corners of the openings were slightly larger. Generally, concrete masonry wall bearing as structural system showed good behavior of carrying loads and stress distribution. Figure 3 illustrates the stresses in some of the selected wall's surfaces in the building.

Max stress =1.5 Mpa

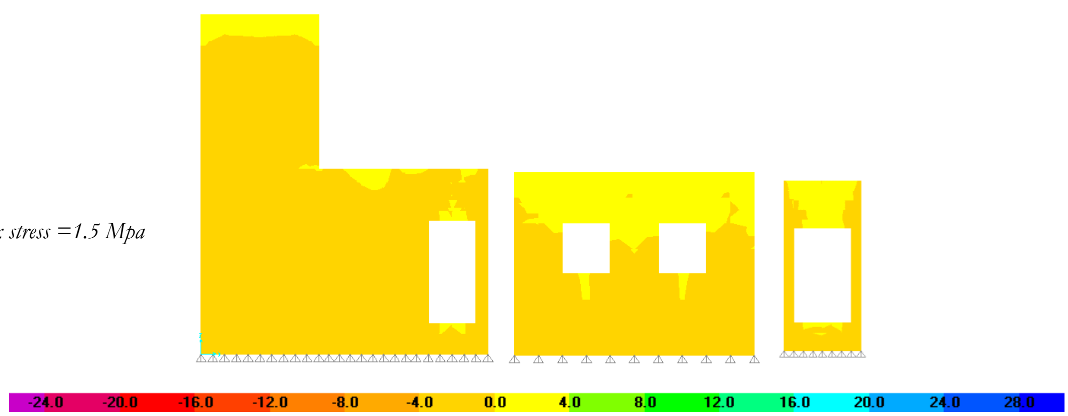

Figure 3: (a) Stresses in some of the selected wall's surfaces of the masonry wall-bearing model

3.3. Composite (Mixed) model

This model combines the first two models. The traditional way of building in the Libyan state is to embed walls in the concrete frames, where the walls are built then casting the columns and the roof. This method makes the wall an effective structural part (unintentionally) of carrying most of the load to the soil directly, resulting in a very large shortage of supporting forces through columns. As a result of the analysis, the axial force decreased from the column with the largest forces (comparing with first model) to become a load 40.58 kn which is 10% of the designed load, while the other percentages of decrease in load on the rest of the other columns depending on the place in the building. Therefore, the 20 x 20 section is used with a minimum reinforce of 4Ø12 mm, which is more than enough compared to loads on all columns. So the reinforced concrete required for the columns and beams as seam as in rigid frame structure system. Thus, masonry wall that embedded in the rigid frame carried 90% of the loads that is supposed to be carried by the columns.

4. Results and Discussion

The performance of the three systems was good for supporting and carrying the loads applied to them. The concrete rigid frame system is very effective if the implementation methodology is followed as provided for standards and codes. Nevertheless, because of the embedded of the masonry walls during the implementation made the structural elements in this system is highly inefficient and thus non-economic and non-sustainable due to waste of energy and materials in the construction and energy and the cost of recycling Table 3 summarizes the results.

Table 3: Normalized results of structural analysis and energy, cost estimations

	Concrete Rigid Frame System	Masonry Wall Bearing System	Composite System	Extreme differences (%)	
				Min	Max
cost	**1.57**	1	1.57	-	36
Stress at top of footing level	**8**	1	0.69	31	87.5
Embodied energy	**1.5**	1	1.5	-	33

The evaluations normalized with respect to the values of masonry wall bearing system

Masonry wall system is respectable from an engineering field, and because the use of masonry walls is a basic concept in the housing of the Libyan state, where these walls used as partitions in the building, thus, it can use as structural elements as well. Hence that the wall capacity well demonstrated, so that the maximum stress did not exceed at the interface with soil 1.5 MPa and gave a uniform and proportional distribution of loads to the entire building. The openings in the walls are somewhat in different form of the distribution of stress in the wall and caused a high concentration of stresses at the corners of these openings, whether for the doors or windows of the building. Concentrated stresses at the openings did not exceed 1.70 MPa. Thus, it is economy system compared to the other two systems. On the one hand, since building and construction, costs are determined mainly by the cost of materials, labor, framing, and placing or erection, and since the structural normal weight concrete cost is varying among countries and all over the world. However, for the Libya state it might be estimated 400/m^3 Libyan dinar including 100 kg rebar [9].Moreover, the embodied energy of normal-weight reinforced concrete with 100Kg rebar per cubic meter is 2.12 MJ/Kg (0.56 kwh/Kg) [10]. Therefore, using masonry wall bearing System leads to total saving resulting in cost non-use of normal-weight reinforced concrete (12.2 m$^{3)}$ is 4900 Libyan dinars, in addition to 26 Mwh of the embodied energy. These values may be small at first sight, but it is represented cost of completely house in every 100 houses and is essentially important economically and environmentally if it is taken on an international scale.

5. Conclusions

Structural analysis and design using SAP200 and embodied energy, and cost estimation are performed to investigate the structural and energy performance. The results of the structural analysis showed good and effective performance for all studied systems. However, taking into consideration the economic and environmental aspects, the masonry wall bearing system model is the best performance. Where the maximum stress at the foundation level is small 1.5 MPa, which makes it possible to build on the lowest bearing capacity of acceptable foundation soils types. In addition, uniformly distribution of the load on the walls is desirable from an engineering point of view to ensure that uniform behavior occurs because of compressing the foundation soil within the permissible limits. Furthermore, this system is economically good and can save 36% of the cost of building structural elements. This system requires less time and labor than other construction systems; also, this system is environmentally friendly. It uses as little construction material as possible. It can save 26 Mwh of the embodied energy, as well as the possibility of recycling at the end building life span, because it is made of masonry that much easier in the grinding and recycle process compared to the reinforced concrete. Finally, the adoption of this system at an international level will achieve a perfect economic and environmental return.

References

[1]. C. Russell Hibbeler. "Structural Analysis," Prentice Hall, N J, 2002.

[2]. M. Nadim, "Structural concrete: theory and design," Prentice Hall, Inc.2002

[3]. International Code Council "International Building Code" IBC code, US, 2012

[4]. American Society of Civil Engineers, "ASCE 7-10 Standard," VI, US, 2010

[5]. American concrete Institute, "Building Code Requirements for Structural Concrete," ACI Code 318-2011. American concrete Institute, MI, US. 2011

[6]. M.A. Walker, "What about House Design and Room Location," Virginia Cooperative Extension, US.2009

[7]. American Society of Civil Engineers, "Minimum Design Loads for Buildings and Other Structures,"

[8]. ASCE/SEI 7-10, NJ, US, 2010

[9]. H. Fathy, "Architecture for the poor," The University of Chicago Press.US.1973.

[10]. RC Means, "Means Cost Works," .July, 2011.http:// www.meanscostworks.com.

[11]. Council on Tall Buildings and Urban Habitat, "Tall building in numbers," CTBUH Journal, Issue III, 50-51, 2009.

[12]. Technical Manual Design for lifestyle and the future, "Australia's guide to environmentally sustainable homes". March.2010. http://www.yourhome.gov.au

[13]. Technical Manual. Embodied Energy. June 2010. http://www.yourhome.gov.au/technical/ fs52.html

[14]. AISC. "Designing for Sustainability," American Institute of Steel Construction.US, 2011 http://www.aisc.org/content.aspx?id=17560

Thermal Performance of a Heat Pipe with Different Working Fluids

Ayad Alwaer, Jasson Gryzagoridis[2]
[1] ayss732001@eamil.com , [2] GryzagoridisJ@cput.ac.za
[1]Department of Renewable Energies, Higher Institute of Science and Technology, Tarhuna, Libya
[2] Department of Mechanical Engineering, College of Engineering, Cape Peninsula University of Technology, Cape Town South Africa

ABSTRACT

The use of Heat pipes, for a variety of applications, has increased worldwide due to them achieving high thermal efficiencies. Heat pipes in evacuated tube solar collector systems, in modern domestic water heating, comprise of a sealed envelope of a copper pipe, which contain a small quantity of working fluid. The Heat pipe transfers energy by the latent heat of the evaporation of the working fluid in a heating section. This vapor travels to the cold portion of the heat pipe and condenses. The circulation is completed with the condensate flowing back through the container's inner wall to the heating section by gravity. Tests were conducted using a test apparatus specifically made for the purpose of comparing the relevant attribute of thermal performance of Heat pipes containing different working fluids. A commercially available heat pipe, with its proprietary working fluid, was used as a reference in comparing its thermal performance efficiency (57.1%) with those of identical heat pipes containing distilled water, methanol, acetone and ethanol as working fluids. The results from the experiments achieved thermal efficiencies of 63.1%, 60.5%, 57.6%, and 42.1% respectively.

Keywords: Heat pipe technology; working fluid; efficiency; solar energy; evacuated glass heat pipe collector

1. Introduction

The evacuated tube consists of an outer and inner glass tube with a vacuum trapped between these glass sections. This allows for radiation to penetrate into a centrally located heat pipe, but prevents heat loss via dissipation. The heat pipe is located centrally inside the inner tube. The heat pipe normally consists of a long copper tube containing a very small quantity of the working fluid (e.g., water, acetone, methanol, ethanol, etc.) which forms the vehicle for moving heat to the cooler section of the copper tube. Each collector is made up of a frame, a manifold and a set of tubes –either 8, 12, 18 or 24 tubes, depending upon the geyser size.

There are various forms of heat pipes, which are commercially used in the solar collector panels. As shown in Figure 1, the structure is basically very similar with variations in the shape and size of the (upper portion) condenser [1, 2].

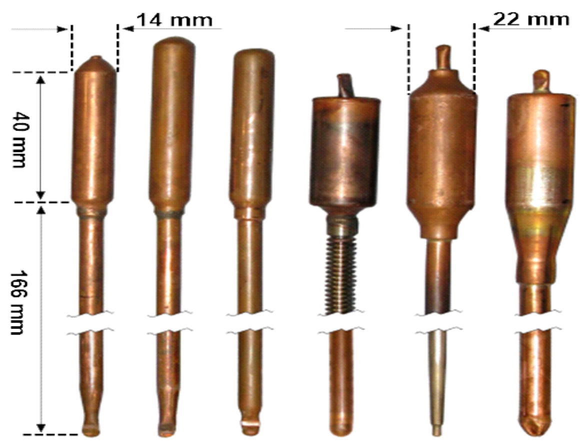

Figure 1: *Various geometrical forms of heat pipes* [1]

2. Heat Pipe Structure and Operation

The design of the heat pipe includes a long copper pipe with a larger diameter condenser at the top and welded at the other end. A small amount of working fluid is added into the heat pipe and then heated to high temperature, or a vacuum pump is used to remove the air from within the space. The result of either method is a vacuum in the copper pipe [3]. The vacuum inside the heat pipe allows the phase change of the fluid to a gas to occur at a lower temperature. The reason for this is to expedite the heat transfer process and create the continuous heat transfer cycle [4, 5&6]

The evacuated tube heat pipes typically found in solar collectors containing a small amount of working fluid have a boiling point of around 25 degrees Celsius as a result of the induced vacuum, so when heating the heat pipe above this temperature the working fluid begins to evaporate. The vapour rises to the condenser at the top of the heat pipe, where it condenses (giving off heat to the desired spot) and returns to the evaporation section at the bottom of the heat pipe. This process is repeated as a cycle [4, 5&7].

2.1 The Working Fluid

As stated before, the heat pipes can utilise various liquids as a working medium. Table 1 refers to the relevant properties of typical fluids that could be used.

Table 1: *Physical properties of Some Heat pipe working fluids* [8, 9].

Fluid	NBP (ºC)	ϱ(kg/m3)	Psat*(kPa)	μ**(kg/ms)	σ**(N/m)	λ (kJ/kg)
Water	100	1000	2.33	1.79×10^{-3}	7.56×10^{-2}	2256
Ethanol	78	789	5.95	1.77×10^{-3}	2.41×10^{-2}	846
Methanol	65	792	13.02	8.17×10^{-3}	2.45×10^{-3}	1100
Acetone	56	784	30	4.1×10^{-4}	2.4×10^{-2}	518

** The vapor pressure data are at 293 ºK., 20 ºC*
*** Surface tension and viscosity data are at 273 ºK., 0 ºC*

Some working fluids need a compatible vessel material to prevent and avoid chemical reactions or corrosion between the fluid used and the vessel. Chemical effects such as corrosion reduce the efficiency of the vessel, as a non-condensable gas can be produced by chemical reactions. For example, using ammonia as a working fluid in the heat pipe provides a temperature range from –70 to +60 ºC and is compatible with several vessel materials such as aluminum, nickel and stainless steel, but not copper [10]. In selecting a working fluid for use in a heat pipe application, the prime requirements are as follows, [11].

- Good thermal stability.
- Vapor pressures not too high or low over the operating temperature range.
- High latent heat.
- High thermal conductivity.
- Low liquid and vapor viscosities.
- Acceptable freezing or pour point.

The viscosity, sonic, capillary, entrainment and nucleate boiling limitations play important roles when selecting the working fluid [4, 5&6]. However, in the context of this research, the choice of the working fluid in the heat pipe will rest solely on the level of temperature achieved in the condenser part of the heat pipe. The reason adopted here is that this factor will govern the amount of heat that the heat pipe could transfer. In other words, the higher temperatures at the condenser will inherently be able to transfer more heat (comparatively speaking among heat pipes containing different working fluids) to the bulk of the fluid that is being heated. Therefore, internal heat pipe criteria such as the viscous limit, the sonic limit, the entrainment limit affecting the maximum heat flux, the capillary limit, etc., will be ignored and, the recommendation of which working fluid will best enhance the performance of the commercial evacuated heat pipe solar collector will depend entirely on calorific results [11, 12&13].

2.2 Energy Performance Analysis in the Heat Pipe Testing Apparatus

The energy performance indices to be obtained using a specially designed and constructed apparatus in this part of the study, will entail the energy collected from the sun simulator via the heat (using different working fluids) to equal the energy transferred by the heat pipe to the water in the apparatus's tank. In other words the efficiency of the heat pipe can be calculated in terms of heat transfer associated with the change of the internal energy of the water in the system. The heat input will be controlled using a solar simulator and the ambient temperature is not expected to change appreciably since the testing will be done in a laboratory.

2.3 Efficiency of Heat Pipe in Terms of Heat Transfer to Tank's Water

The efficiency of the heat pipe is calculated using the following formula, which involves the change of the internal energy of the water contained in the system's tank.

$$\eta_{hp} = \frac{(\Delta Q_u)/t}{I} m \times 100\%$$

Where η_{hp} is the heat pipe's efficiency (%) in terms of heat transfer to the tank's water, ΔQ_u is the change in the internal energy of the water in kJ/kg which is dependent on the temperature T and pressure P of the system, t is the solar irradiance time in hours, m is the mass in kg of water in the tank and I is the actual total solar radiation on the surface of the evacuated tube heat pipe, which is the irradiance kW/m^2 from the solar simulator multiplied by the heat pipe's actual receiving area of (0.08084 m^2).

3. A Ring for Testing the Performance of the Heat Pipe with Various Working Fluids

In order to test the performance of the heat pipe with various working fluids, an apparatus was designed and constructed consisting of a small geyser tank mounted on a frame. A heat pipe with its evacuated glass tube could easily be inserted and removed in a short turnaround time (see Figures 2 and 3). A single evacuated heat pipe assembly could be inserted in a dry bay attached to a tank which could accommodate four litters of water. Halogen floodlights mounted on a frame over the heat pipe assembly provided the heat source.

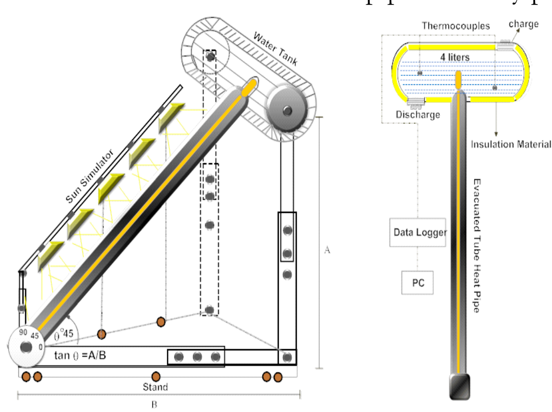

Figure 2: *Schematic diagram of the testing apparatus for the heat pipes.*

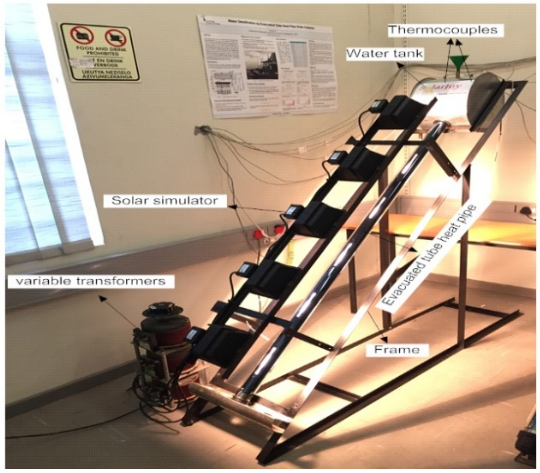

Figure 3: *The heat pipe's testing apparatus*

3.1 Tank Description

The cylindrical tank was made of 1.2 mm thick stainless steel sheet; with dimensions of 200 dia. and 150 mm long. An outer casing was built around the tank to cover the polyurethane insulation.

A brass heat pipe sleeve (14 mm internal diameter) was welded into the tank at a 45 degree angle to line up with the mounting frame of the heat pipe, tank and simulator.

In addition, two wells were built into the top of the tank to place thermo-couple sensors in order to record the temperature of the top and bottom fluid levels in the tank respectively. On the side of the tank a valve drain pipe was fitted with a 15 mm filling pipe fitted at the top. The halogen lights were controlled via a variable transformer thus regulating the simulated radiation on the heat pipe.

3.2 The Sun Simulator for the Heat Pipe Tester

The solar radiation simulator was used to heat the evacuated heat pipe. It consisted of an array of five halogen floodlights of 500 W each. The halogen lamps were distributed evenly over the length of the evacuated tube heat pipe, at a distance of 225 mm above it. The solar simulator's irradiance level was set to a level consistent with an average 800 watts per square metre, as measured over the evacuated heat pipe surface. The output of the sun simulator could be controlled by means of a variac (variable transformer) which controlled voltage supplied to the array of halogen lamps.

3.3 FRAME

The frame was built using L shape mild carbon steel sections set for testing at a fixed angle of 45 degree.

4. Instrumentation for the Heat Pipe Tests

Two J-type thermocouples, one of them at the bottom and another at the top of the "geyser", were fitted to measure the water temperature in the storage tank, and, together with the ambient temperature, were recorded during the test period. A digital display data logger (Agilent-34972A) was used to record the temperature scale. All experiments were carried out for seven hours.

5. Testing the Heat Pipe Performance with Different Working Fluids.

The relatively elevated temperatures which are obtainable when using evacuated tube heat pipes in the field of water heating is the reason for the attempt to use them in the desalination of seawater.

The method followed in testing a set of working fluids in the heat pipe is described below:

Testing of the heat pipe's performance with various working fluids required a benchmark. This benchmark was obtained by first testing the commercial heat pipe (as it came from the manufacturer) with the original working fluid. Attempts to obtain information about the constitution of the working fluid, from the manufacturer in China, were unsuccessful. It was assumed that the liquid was water, but it had an orange/yellowish colour possibly because of some kind of additive. The fluid was drained and the heat pipe was charged with new fluid, after which the performance test was undertaken over the seven-hour period. It is worth mentioning here that the quantity of working fluid encountered in the commercial heat pipes varied considerably in the range of 5 to 10 ml; however this did not seem to affect their performance.

The raw data that was collected during each heat pipe experiment with the four working fluids consisted of recording the temperatures of the water at two locations in the tank's water, the irradiance from the solar simulator and the ambient temperature Ta. The duration of the individual tests was seven consecutive hours daily. The data displayed in Appendix A is a typical sample, where T_1 & T_2 are the tank's water temperatures (in degrees centigrade) recorded every 15 minutes via two thermocouples located at the top and bottom levels in the tank's water, using a data-logger. T_{a1}, T_{a2} and T_{a3} (Ambient temperature readings): these temperature readings, represented with their average value $T_{a\,avg.}$, were also recorded each 15 minutes via three thermocouples located around the heat pipe testing apparatus.

5.1 Results of the Heat Pipe Performance with Different Working Fluids

The purpose made testing apparatus was used in testing the performance of the heat pipes with four different working fluids. As already mentioned, the results from a test using one of the commercially available heat pipes was used as a benchmark in comparing their performance. The working fluids chosen were distilled water, methanol, acetone and ethanol.

The experiments were conducted for the purpose of improving or better discovering the effect on the thermal performance and efficiency of the heat pipe, which was recharged with various working fluids at the same filling ratio by infusing always the same amount of working fluid (10 ml).

5.1.1 Results from the Experiments with the Testing Apparatus for the Heat Pipes

A summary of the results from testing the performance of the heat pipes with different working fluids appears in Table 2.

Figure 4 displays the behaviour of the temperature rise of the water in the tank of the heat pipe testing apparatus when testing each individual heat pipe, each containing a different fluid. Thus a direct comparison of their performance can be made.

Table 2: *The initial and final temperatures of the water, ambient temperature and the efficiency% of each heat pipe containing a particular working fluid*

	Description of the test	Initial& final temp. °C	Ambient temp. avg. °C	Efficiency%
1	Original heat pipe (Commercial)	16.2-71.8	21.8	57.1
2	Heat pipe with Pure water (Working fluid)	16.3-77.7	19.3	63.1
3	Heat pipe with Methanol (Working fluid)	16.4-75.3	19.3	60.5
4	Heat pipe with Acetone (Working fluid)	16.4-72.5	19.3	57.6
5	Heat pipe with Ethanol (Working fluid)	16.5-57.7	21.9	42.1

The efficiency of each heat pipe, characterised by the working fluid that it contains, is presented for comparison purposes in Figure 5. The addition of the average ambient temperature data during each test enables an enhanced or more informed comparison on the performance of the heat pipes. The ambient temperature plays a major role in the heat loss from the tank of the testing apparatus. This fact affects the heat loss from the water tank and hence affects the water's peak average temperature, reflecting in the heat pipe's efficiency calculation.

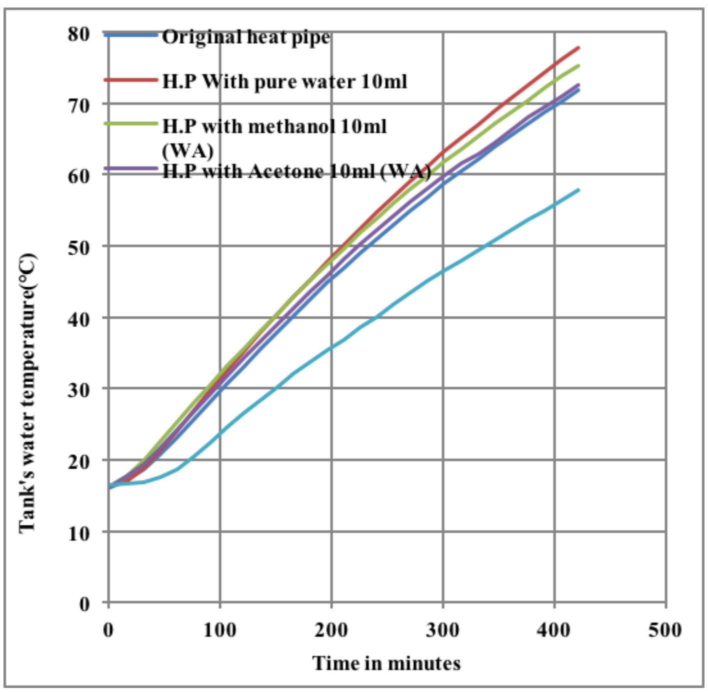

Figure 4: *Average water temperature in the tank of the testing apparatus for each heat pipe tested containing a different working fluid*

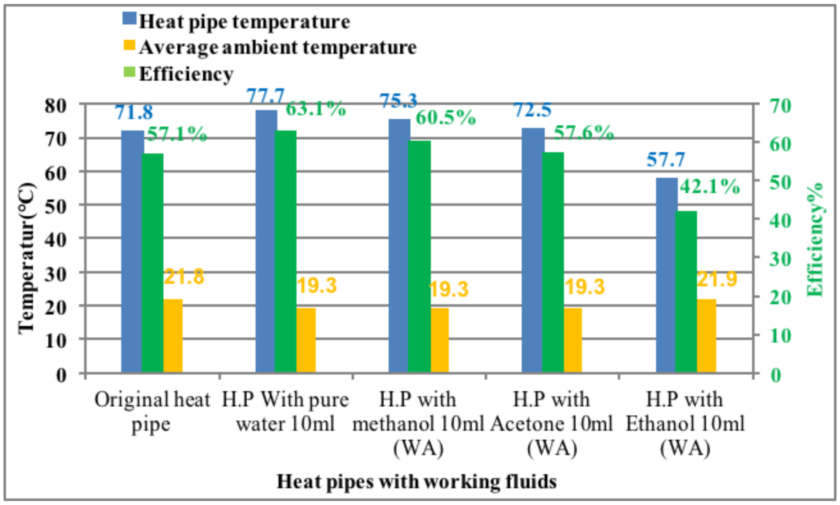

Figure 5: *Efficiencies of the heat pipe, bulk water temperatures in the heat pipe testing apparatus tank and average ambient temperatures*

5.1.2 Discussion of results with the testing apparatus for the heat pipes

The results of the experiments on different working fluids used in the evacuated tube heat pipe have shown that, of all the working fluids chosen in this study, i.e. pure water, methanol, acetone and ethanol, the former three performed well compared to the commercial working fluid.

In terms of ranking their performance, the pure water appeared superior to the others, with a thermal efficiency of 63.1%, followed by Methanol 60.5%, Acetone 57.6%, commercial working fluid 57.1% and Ethanol 42.1%. For a sample calculation of the heat pipe's efficiency in terms of heat transfer to the tank's water see Appendix B.

The averages of ambient temperatures during the tests when using methanol, water and acetone, as working fluids, were equal (19.3 ℃), which was colder/.lower than the average of ambient temperatures when testing with the commercial working fluid and ethanol in the heat pipe (21.8 ℃), as shown in figure 5.

It is not expected that such a small change in the ambient temperature would have affected the results significantly because the heat pipe's testing apparatus had a well-insulated tank. The additional heat losses to the environment (had all experiments been performed at the lower ambient temperature of 19.3 ℃), would be minimal and would have resulted in slightly lowering the efficiencies of the two heat pipes containing the commercial fluid and acetone respectively.

6. Conclusions

A totally separate, newly designed and constructed apparatus was used to test the performance of a heat pipe with various "working" fluids. The "commercial working fluid" inside the heat pipe was replaced each time with a different "working" fluid and individual experiments were performed. The results of these experiments in terms of the thermal efficiency of the heat pipe were compared as follows:

The heat pipe containing the:

- “Commercial” working fluid – thermal efficiency 57.1%
- “Pure water” – thermal efficiency 63.1%
- “Methanol” – thermal efficiency 60.5%
- “Acetone” – thermal efficiency 57.6%
- “Ethanol” – thermal efficiency 42.1%

From these experiments it is concluded that the thermal efficiency of the heat pipe was improved by 6% when distilled water was used, as opposed to the commercial working fluid. In the context of the heat pipe being used in an evacuated tube solar energy collector it is expected that such a system will improve its thermal efficiency (compared to the currently commercially available units), with heat pipes containing pure water, methanol or acetone (in this order) as working fluids.

7. References

[1] S. Jack & G. Rockendorf, “ Wärmerohre in Sonnenkollektoren– Wärmetechnische Grundlagen und Optimierung sowie neue Ansätze für die Integration,” pp.1–190, November 2013.

[2] H .Barua, M. Ali, M. Nuruzzaman, M. Quamrul Islam & C. M. Feroz, “Effect of filling ratio on heat transfer characteristics and performance of a closed loop pulsating heat pipe,” Procedia Engineering, 56, pp.88–95, 2013.

[3] F. N. Ashok & K. V. Mali, “Thermal Performance of Thermosyphon Heat Pipe Charged with Binary Mixture,” International Journal of Science, Engineering and Technology Research, 4(1), pp.92–102, January 2015.

[4] R. S. Gaugler, “Heat transfer device,” U.S., Patent No., 2350348, 6 June 1944.

[5] G. M. Grover, “Evaporation and condensation heat transfer device,” U.S., Patent No., 3229759.

[6] G.M. Grover, T.P. Cotter & G.F. Erickson, “Structures of very high thermal conductance,” J. App. Phys., Vol. 35, pp.1190-1191, 1964.

[7] R. S. Gaugler, “Heat transfer device,” U.S., Patent No., 2350348, 6 June 1944.

[8] S. M. Peyghambarzadeh, S. Shahpouri, N. Aslanzadeh, & M. Rahimnejad,“Thermal performance of different working fluids in a dual diameter circular heat pipe,” *Ain Shams Eng. J.*, Apr. 2013.

[9] E. W. Washburn,“International critical tables of numerical data, physics,” chemistry and technology. Knoven, 2003.

[10] J. P. Holman, “Heat Transfer,” Tenth Edit. USA 2010.

[11] P. Wallin, “Heat Pipe, selection of working fluid,” pp. 1–7, 2012.

[12] R. Manimaran, K. Palaniradja, N. Alagumurthi, and J. Hussain, “FACTORS AFFECTING THE THERMAL PERFORMANCE OF HEAT PIPE – A REVIEW,” *J. Eng. Res. Stud.*, III(II), pp.20–24.2012.

[13] D. A. Reay, & P.A. Kew, “Heat Pipes Theory, Design and Applications,” Fifth Edit. 2006.

Appendixes

Appendix A

Typical data collected during the heat pipe tests for the various working fluids.

Testing the heat pipe containing pure water as a working fluid

	Date &Time	T_1 at top of the tank	T_2 at Bottom of the tank	Tavg.	Ta_1	Ta_2	Ta_3	Ta avg.
		(°C)	(°C)	(°C)	(°C)	(°C)	(°C)	(°C)
1	09/09/2015 09:01:20:061	16.4	16.1	16.3	17.6	18.1	17.9	17.9
2	09/09/2015 09:16:20:046	17.9	16.2	17.1	23.4	19.7	19.0	20.7
3	09/09/2015 09:31:20:046	20.5	17.3	18.9	24.0	20.3	19.6	21.3
4	09/09/2015 09:46:20:046	23.3	19.4	21.3	24.4	20.6	19.9	21.7
5	09/09/2015 10:01:20:046	26.3	22.0	24.1	24.8	20.9	20.2	22.0
6	09/09/2015 10:16:20:046	29.1	24.8	27.0	24.9	21.1	20.4	22.1
7	09/09/2015 10:31:20:046	31.9	27.7	29.8	24.8	21.1	20.4	22.1
8	09/09/2015 10:46:20:046	34.5	30.4	32.5	24.9	21.1	20.4	22.2
9	09/09/2015 11:01:20:046	37.2	33.2	35.2	24.8	21.1	20.5	22.1
10	09/09/2015 11:16:20:046	39.8	35.9	37.8	24.8	21.2	20.4	22.2
11	09/09/2015 11:31:20:046	42.3	38.5	40.4	24.8	21.2	20.4	22.2
12	09/09/2015 11:46:20:046	44.8	41.0	42.9	24.8	21.2	20.4	22.1
13	09/09/2015 12:01:20:046	47.2	43.4	45.3	24.7	21.1	20.4	22.1
14	09/09/2015 12:16:20:046	49.7	45.9	47.8	24.7	21.1	20.3	22.1
15	09/09/2015 12:31:20:046	52.1	48.2	50.1	24.7	21.1	20.3	22.0
16	09/09/2015 12:46:20:046	54.4	50.5	52.4	24.9	21.0	20.3	22.1
17	09/09/2015 13:01:20:046	56.8	52.7	54.8	25.0	21.0	20.2	22.1
18	09/09/2015 13:16:20:046	58.8	54.9	56.9	25.0	21.0	20.2	22.1
19	09/09/2015 13:31:20:046	61.2	57.0	59.1	24.9	20.9	20.2	22.0
20	09/09/2015 13:46:20:046	63.2	59.1	61.1	25.0	20.9	20.2	22.0
21	09/09/2015 14:01:20:046	65.3	61.1	63.2	24.9	20.9	20.2	22.0
22	09/09/2015 14:16:20:046	67.2	63.1	65.2	25.0	20.9	20.2	22.1
23	09/09/2015 14:31:20:046	69.2	64.9	67.1	25.2	21.0	20.3	22.2
24	09/09/2015 14:46:20:046	71.2	66.8	69.0	25.5	21.0	20.3	22.3
25	09/09/2015 15:01:20:046	73.1	68.6	70.8	25.4	21.1	20.3	22.3
26	09/09/2015 15:16:20:046	74.9	70.4	72.6	25.4	21.1	20.4	22.3
27	09/09/2015 15:31:20:046	76.7	72.1	74.4	25.5	21.1	20.4	22.3
28	09/09/2015 15:46:20:046	78.4	73.7	76.1	25.4	21.1	20.4	22.3
29	09/09/2015 16:01:20:046	80.1	75.4	77.7	25.4	21.1	20.4	22.3

Appendix B

Sample calculation of the heat pipe efficiency in terms of heat transfer to the tank's water when the heat pipe containing pure water as the working fluid

The efficiency of the heat pipe is calculated using the following formula, which involves the change of the internal energy of the water contained in the system's tank.

$$\textbf{Efficiency} = \frac{\textbf{Output}}{\textbf{Input}}\times\mathbf{100}\%$$

$$\eta_{hp} = \frac{(\Delta Q_u)}{I\times t} m\times 100\%$$

Where η_{hp} is the heat pipe's efficiency (%) in terms of heat transfer to the tank's water.

ΔQ_u (kJ/kg), is the change in the internal energy of the water in the tester's tank that depends on the temperature *T* and pressure *P* of the system.

t is the duration of the time for the test (7 h x 3600 h/s); $m(kg)$, is the mass of the water in the tank and $I(kW)$, is the total solar radiation on the evacuated tube heat pipe, which is the irradiance R, kW/m² from the solar simulator multiplied by the heat pipe's receiving area of (0.08084 m^2).

1. Output

$$\Delta E(kJ) = \Delta Q_u \times m$$

$$\Delta E(kJ) = (Q_2\text{-}Q_1)(kj/\text{kg})\times m(kg)$$

This sample calculation refers to the case of the heat pipe containing pure water as the working fluid; the initial and final temperatures obtained were 16.3 and 77.7 $^\circ$ C respectively.

$$\Delta E = (Q_{77.7}\text{-}Q_{16.3})\times m$$

Linear interpolation was used to find the energy transferred between the temperatures from a standard table of saturated water.

$$\Delta \boldsymbol{E}(\boldsymbol{J}) = (325.3192 - 68.42258)\times 1000\times 4 = \mathbf{1027586.48}\,\boldsymbol{J}$$

2. Input

$$R = 800\, W/m^2$$

Assumed surface area of the evacuated tube heat pipe $= 1.72m\ (length)\times 0.047m\ (dia) = 0.08084\, m^2$

$$I = 800W/m^2 \times 0.068\, m^2 = \mathbf{64.672}\ \boldsymbol{W}$$

$$\boldsymbol{t} = \mathbf{7}\boldsymbol{h}\times\mathbf{3600}\boldsymbol{s} = \mathbf{25200}\ \boldsymbol{s}$$

$$\boldsymbol{I}\times\boldsymbol{t} = \mathbf{64.672}\ \boldsymbol{w}\times\mathbf{25200}\ \boldsymbol{s} = \mathbf{1629734.4}\boldsymbol{J}$$

$$\eta\% = (\mathbf{1027586.48}\,\boldsymbol{J}/\mathbf{1629734.4}\boldsymbol{J})\times 100 = \mathbf{63.1}\%$$

Effects of Reduction in Construction Temperature on Workability of Warm Mix Asphalt Incorporating Rh-wma Additive

Bashir M. Aburawi[1]
[1]Aburawi2018@gamil.com
[1] Department of Civil, College of Engineering, Elmergib University, Libya

ABSTRACT

Conventional Hot Mix Asphalt (HMA) has been the primary material used in pavement in past decades. Recently, compared to conventional HMA, Warm Mix Asphalt (WMA) has shown great potential and offers benefits not given by HMA, since the WMA can be produced at lower temperatures without affecting pavement performance. The WMA technologies allow a significant reduction in construction temperatures of asphalt mixtures through lowering the viscosity of binders. In WMA, different types of additives are added to the binder depending on the technology used and such addition of these materials brings down the viscosity drastically thus reducing the temperature to which the aggregates and binders have to be heated during mixing and compaction. This study was limited to the effects of construction temperature on the workability performance of WMA incorporating RH-WMA additive. Binder namely 80/100 was used for preparation of all asphalt mixtures and RH-WMA used as warm mix asphalt additive. Asphalt mixtures were prepared using crushed granite aggregate for AC14 wearing course and compacted by using Servopac Gyratory Compactor (SGC). The Leeds Workability Method used to determine the workability index. The results show that increase in construction temperature improves the workability of both WMA and HMA. Workability Index (WI) of mixtures incorporating 3% RH-WMA is slightly higher than mixtures incorporating 2% RH-WMA. The increase in WI is more pronounced at higher RH-WMA contents.

Keyword— Warm Mix Asphalt, RH-WMA, Servopac Gyratory Compactor, The Leeds Workability Method, Workability Index.

1. Introduction

Asphalt is a pavement material that is brittle and hard in cold environments and soft at elevated temperatures. It has been historically employed as the most popular paving material for roadways [1]. Traditionally, Hot Mix Asphalt (HMA) has been widely used for road construction. The HMA production process requires a high temperature application. This requires the aggregates to be heated to very high temperature. The major disadvantage associated with this process is that it consumes a lot of energy and discharges a large volume of toxic gasses and dust during its production and paving process. This has adverse effects on the health of the construction workers as well as the environment in particular.
Since Warm Mix Asphalt (WMA) additives can reduce the binder viscosity, the production temperatures can be lowered, compared to conventional HMA. It was reported that the mixing temperatures of WMA ranged

from 100°C to 140°C compared to the mixing temperatures of 150°C to 180°C for conventional HMA [2]. Compared with HMA, WMA technology can significantly reduce mixing temperatures of asphalt mixture by 20°C to 30°C [3]. One of the additives used to produce WMA is a type of wax named RH-WMA. The additives improved asphalt binder coating, mixture workability and compactability at lower temperatures. Hesami [4] defined the workability of asphalt as the ease of handling, paving and compacting the mixture. Asphalt mixtures with higher workability are known to have higher compactability.

1.1. Warm Mix Asphalt Technology

To overcome the disadvantages associated with HMA, the WMA technology was introduced. WMA improves the energy efficiency by reducing the construction temperature. WMA uses additives that help reduce the viscosity of the asphalt binder, which in turn causes the asphalt mixing and construction to be carried out at relatively low temperatures while maintaining its performance similar to HMA [5]. Figure 1 shows different types of WMA additives and Figure 2 shows the other advantages of using WMA.

Figure 1: Types of WMA Additives

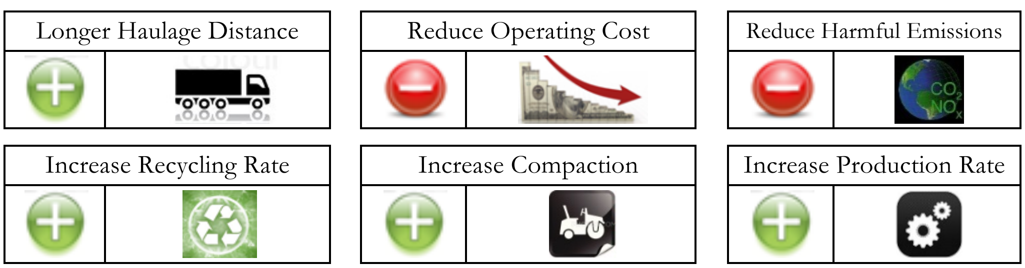

Figure 2: Advantages of WMA

One of the major advantages of WMA is the increased workability at conventional and lower compaction temperatures. Bennert. [6] defined the workability as the property of the asphalt mixture that describes the ease with which asphalt mixture can be placed and compacted to the desired mat density. Abdelgalil et al. [7] used a device that employed an electric transducer and heat regulator for evaluating mixing temperature in mixture workability and compatibility by determining the correlation between workability and compatibility. Zhao and Guo [8] developed a test instrument to measure asphalt mixture workability. From the torque, the workability of the mixture can be judged and at lower mixing temperature, WMA exhibits similar workability with HMA [9]. Foaming materials can be used to produce WMA to increase the workability and compactibility of the mixture at lower temperatures [10]. Xiao. [11] reported that chemical additives improve asphalt binder coating, mixture workability and compactibility at lower temperatures. To lower the mixing temperature, organic or wax additives are utilised for reducing the viscosity of binder [12].

2. Materials and Methods

1. Materials

The conventional virgin 80/100 asphalt binder used was obtained from Shell Bitumen Company, Singapore and used as the control binder. Granite aggregate used in the preparation of all the mixtures were supplied by Kuad Kuari in Penang. The crushed granite was used in the mix design for Asphaltic Concrete mixture AC14 wearing course mix according to the Malaysian Public Works Department local specifications [13]. Aggregates and asphalt binder with properties similar to those used by Hamzah et al. [14] were also utilized for this study.
Pavement Modifier (PMD) was the filler used in this study. The PMD modifier was supplied by NSL Chemicals Ltd, Ipoh, Perak, Malaysia [15]. Figure 3 shows the PMD filler used. The RH-WMA warm mix modification technology was used to prepare WMA. RH-WMA is an organic based additive like wax developed in China. It can be utilized as an additive to be blended with reclaimed asphalt binder [16]. Figure 4 shows the RH-WMA that exists in the form of small white particles. The mixtures were compacted using the Servopac gyratory compactor (SGC) as shown in Figure 5 at 30 gyrations per minute at a compaction angle of 1.25° for 100 gyrations.

Figure 3: PMD as Filler

Figure 4 : RH-WMA as Additive for WMA

Figure 5: Servopac Gyratory Compactor

1.2. Leeds Workability Method

Asphalt mixtures must be workable so that it can be easily handled, spread and compacted to the required density. Unworkable mixtures will be difficult to compact without tearing under the paving machine screed and hence adequate compaction will not be achieved.
The Leeds Workability Method was developed by Cabrera and Dixon [17]. It was based on the relationship between mixture porosity and the associated compaction energy input applied by the Gyratory Testing

Machine (GTM). Under the same field compaction effort, mixes with higher Workability Index (WI) shall lead to easy compaction and higher density compared to those with low workability. Mixes that achieve higher WI (workability) and lower CEI (compactability) are desirable. Higher WI is associated with easier and faster mat compaction during construction and lower CEI is associated with higher stability during trafficking. The WI can be used effectively to assess the influence of compaction temperature or mix composition, particularly binder content, coarse aggregate content, sand morphology and filler type [17]. Field experience has shown that mixes with a WI equal to or smaller than 6 are difficult to handle and compact. The mixtures were compacted at their OBC using the SGC. This compaction type is expected to realistically simulate the compaction in the field as compared to the impact compactor like Marshall compaction. Height changes and the number of its gyrations can be automatically recorded.

A high WI indicates a more workable mixture or mixture that is easier to compact. From the semi-logarithmic plot, air voids reduce with the number of gyrations. The straight line equation is defined in Equation (1).

$$Y = A - Bx \qquad (1)$$

Where:

Y = Air voids, (%)

A, B = Constant

x = Log10, number of gyration

From Equation (2), the constant A is obtained by extrapolating the straight line to intersect with the Y-axis at zero gyration. The WI is defined as in Equation (2).

$$WI = 100/A \qquad (2)$$

3. Results and Discussion

3.1. Effects of Compaction Temperature on Workability Index

The results show that increase in compaction temperature improves the workability of both WMA and HMA. This is true for all WMAs which demonstrate better workability than HMA. The compaction temperature of 125°C has a significant influence on the workability of WMA. It can be seen from Figure 7 that, as the number of gyrations increase, there is difference in the air voids of all mixtures. From Figure 7 (a) and (b), the air voids are highest for HMA and is more pronounced at 100 gyrations. This also infers that at 125°C and 110°C compaction temperatures, the increase in the number gyrations can result in lower air voids. This is not true for other temperatures as shows by no significant difference in Figure 7 (c) at 95°C compaction temperature. According to Figure 7 (c), there is no major changes in the air voids between HMA and WMA. The use of WMA additives has shown no significant benefit at 95°C compaction temperature. The WMA 2%, WMA 3% and HMA curves follow similar trend.

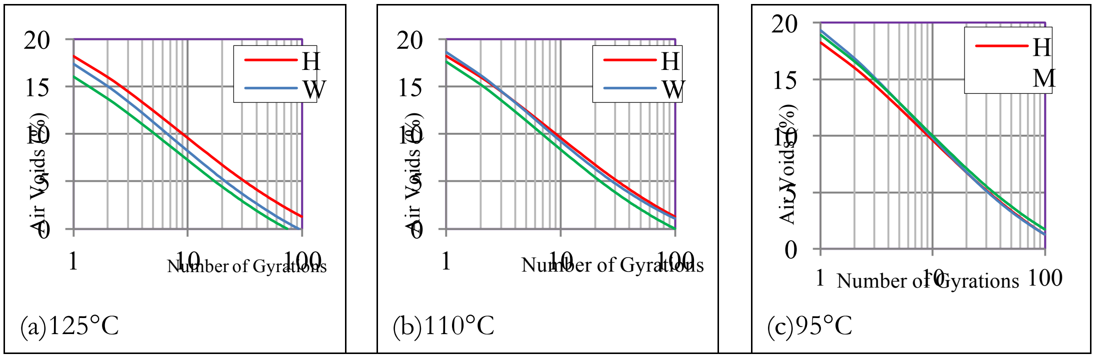

Figure 7 : Air Voids for WMA Compacted at Various Temperatures (HMA Compacted at 150°C)

All straight lines are plotted for every sample to determine the average WI. The regression value, R^2 for the straight line is above 0.90, implying good accuracy regression equations.

The effect of compaction temperature on WI can be seen by comparing WI in Figure 8. The WI increases as compaction temperature increases. The increase in WI with the increase in compaction temperature is due to the lubricating effects of asphalt mixture keeping the viscosity of the binder suitable for compaction. Higher WI values are preferred and are indicative of better mix workability.

Mixture compacted at 125°C exhibited better workability than HMA. WMA has better workability characteristics than HMA. The WI reduces by 3-16%, for mixtures incorporating 2% RH-WMA when compaction temperature reduces to 110°C and 95°C, respectively.

3-19% for mixtures incorporating 3% RH-WMA when compaction temperature reduces to 110°C and 95°C, respectively.

3.2. Effects of RH-WMA Content on Workability

From Figure 8, the average WI of mixtures incorporating 3% RH-WMA is slightly higher than mixtures incorporating 2% RH-WMA. The increase in WI is more pronounced at higher RH-WMA contents.

3.3. Correlation between CEI and WI

Figure 9 shows the relationship between CEI and WI for different mixtures. Mixtures with high WI reflects low CEI and have better workability. Figure 9 shows linear relationships between CEI and WI. The WI is inversely proportional to CEI. High WI and low CEI are desirable.

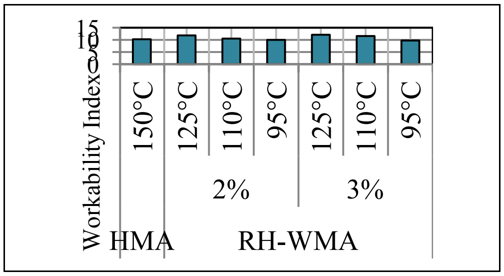

Figure 8: WI of Asphalt Mixtures Tested

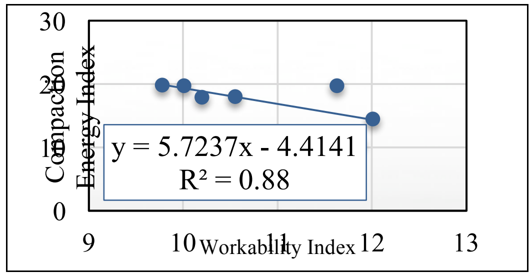

Figure 9: Correlation between CEI and WI

4. Conclusions

The RH-WMA additive would either reduce the viscosity of the binder or allow better workability of the mix at lower binder content. For this case, the OBC of WMA is slightly lower than the OBC for HMA. The WI can be used effectively to assess the influence of production temperature.

Acknowledgment

The author would like to acknowledge the Universiti Sains Malaysia that has funded this research grant through the Research University Grant Scheme which enables this paper to be written.

References

[1]. Sulyman, M., Sienkiewicz, M. and Haponiuk, J. Asphalt Pavement Material Improvement: A Review. *International Journal of Environmental Science and Development*, 5, 444-454, 2014.

[2]. Kim, Y.-R., Zhang, J. and Ban, H.Moisture Damage Characterization of Warm-Mix Asphalt Mixtures Based on Laboratory-Field Evaluation. *Construction and Building Materials*, 31, 204-211, 2012.

[3]. Wang, C., Hao, P., Ruan, F., Zhang, X. and Adhikari, S. Determination of the Production Temperature of Warm Mix Asphalt by Workability Test. *Construction and Building Materials*, 48, 1165-1170, 2013

[4]. Hesami, E., Jelagin, D., Kringos, N. and Birgisson, B. An Empirical Framework for Determining Asphalt Mastic Viscosity as A Function of Mineral Filler Concentration. *Construction and Building Materials*, 35, 23-29, 2012.

[5]. Kim, H., Jeong, K.-D., Lee, M. S. and Lee, S.-J. Performance Properties of CRM Binders with Wax Warm Additives. *Construction and Building Materials*, 66, 356-360, 2014.

[6]. Bennert, T., Reinke, G., Mogawer, W. and Mooney, K. Assessment of Workability and Compactability of Warm-Mix Asphalt. Transportation Research Record: *Journal of the Transportation Research Board*, 2180(1), 36-47, 2010.

[7]. Abdelgalil, S. M. K., Abdul Rahman, M. and Arshad, A. K. Development of Workability Measuring Device for Asphalt Mixture Using Electronic Transducer and Temperature Regulator. *Journal of Basic and Applied Scientific Research*, 1, 721-726, 2011.

[8]. Zhao, G.-J. and Guo, P. Workability of Sasobit Warm Mixture Asphalt. Energy Procedia, 16, 1230-1236, 2012.

[9]. Gudimettla, J. M., Cooley, L. A. and Brown, E. R. Workability of Hot Mix Asphalt. National Center for Asphalts Technology, Report, 03-03, 2003

[10]. Martinez-Arguelles, G., Giustozzi, F., Crispino, M. and Flintsch, G. W. (2014). Investigating Physical and Rheological Properties of Foamed Bitumen. *Construction and Building Materials*, 72, 423-433, 2014.

[11]. Xiao, F., Punith, V. S. and Amirkhanian, S. N. Effects of Non-Foaming WMA Additives on Asphalt Binders at High Performance Temperatures. *Fuel*, 94(5), 144-155, 2012.

[12]. Sheth, N. M. Evaluation of Selected Warm Mix Asphalt Additives. Master Thesis, The University of Iowa, 2010.

[13]. JKR. Standard Specification for Road Works in Malaysia, (Section 4: Flexible Pavements), Cawangan Jalan, Jabatan Kerja Raya Malaysia, Kuala Lumpur, 2008.

[14]. Hamzah, M. O., Golchin, B. and Tye, C. T. Determination of the Optimum Binder Content of Warm Mix Asphalt Incorporating Rediset Using Response Surface Method. *Construction and Building Materials*, 47, 1328-1336,2013.

[15]. Aman, M. Y. (2013). Water Sensitivity of Warm Porous Asphalt Incorporating Sasobit®. Ph.D Thesis, Universiti Sains Malaysia.

[16]. Wang, H., Dang, Z., You, Zhanping. and Cao, D. Effect of Warm Mixture Asphalt (WMA) Additives on High Failure Temperature Properties for Crumb Rubber Modified (CRM) Binders. *Construction and Building Materials*, 35, 281-288, 2012

[17]. Cabrera, J.G., Dixon, J.R. Performance and Durability of Bituminous Material, Proceeding of Symposium, University of Leeds, 1994

Effect of Corrugation Geometry And Shape On Energy Absorption of Composite Plate.

Khalid A. Elbkory[1],Fathi A.al ssahly[2]
[1] khalidattia1981@gmail.com,[2]Fathiabduallah@gmail.com,

[1]Department of Mechanical and Industrial Engineering, College of Engineering, Elmergib University, Libya
[2]Department of Marine Mechanical, College of Marine Resources Alasmarya Islamic University, Libya

ABSTRACT

It has been observed that there is a considerable interest in recent years regarding materials which have high crushing ability particularly in energy absorption in relation to car and allied industries . An important aspect of the crushing ability of materials is its specific energy absorption value which is much greater for polymer composite than conventional metallic material. In this research, series experiments were conducted including testing of the capabilities of composite material as an energy absorber with comparison to metallic materials. The method used in the current research is to fabricate and test a series of composite plate specimens with different corrugation profile, these are: sinusoidal, triangle and square. All these specimens were fabricated from glass fibers with hand layup technique. Each profile has three different types of specimens: single plate, double plates and triple plates. The corrugated plates are fixed over each other and subjected to the same kind of compression load. All these models have been exposed to lateral crushing load and then the collapse of these models have been observed and the results have been recorded. Finally; all the results obtained in this research were recorded and discussed. It is found that the highest value of specific energy absorption was (2.472Kj/Kg) recorded for level three square profile specimen. However, the lowest value (0.878Kj/Kg) was recorded for level two triangle profile specimen.

Keyword— knitted fabrics, energy absorption, crash worthiness, axial crushing

1. Introduction

The performance of composite materials that have incurred damage has long been a topic of great interest and study. Today the use of composite materials in different kinds of applications is accelerating rapidly. Composite materials have become common engineering materials and are designed and manufactured for various application including automotive components, sporting goods, aerospace parts, consumer, and in the marine and oil industries[1].

The crashworthiness performance of automobile components to perform remarkably under crash conditions is very important to vehicle occupants. As stated by Reid [2] design of crashworthy structure requires both knowledge of structural geometry and understanding of the properties and deformation mechanism of the materials and components used. Work on crushing behaviour of metal shell has advanced and well understood. Research groups have, since 1960s, carried out research, toward crashworthiness of metallic devices using empty thin-walled tube with different cross-sections[3–5]. The previous works on the axial crushing of fiber reinforced plastic composite tubes has indicated that significant specific energy absorption can be obtained from these materials, under some circumstances exceeding the ones that can be obtained from metal tubes [6-7].

In recent years there is an increasing demand in the use of composite materials for the automotive and aerospace industry. Composite material and in particular their anisotropy offers vast potential for optimally tailoring a design to meet crashworthiness performance requirements. Therefore, intensive research has been carried out to examine the failure mechanism of no hybrid and hybrid composite structure [8–13]. Looking back implementation of composite materials in the field of crashworthiness is attributed to Hull, who in 1980s and 1990s has studied extensively the crushing behaviour of fiber reinforced composite material. He found that the composite materials absorb high energy in the face of the fracture surface energy mechanism rather than plastic deformation as observed for metals[14,15]. Composite materials are playing a key role in the development of lightweight integral armor for military vehicles such as tanks or armoured personnel carriers. For future applications, revolutionary approaches are required to significantly reduce (up to 50%) the mass of these systems and improve their mobility and trans- portability without sacrificing survivability or main- trainability[16].

This paper experimentally investigating the effect of Corrugation geometry and shape on energy absorption of composite plates. Three different corrugation profile are tested which are sinusoidal, triangle and square. subjected to quasi-static compression load. All kind has three types of specimens referred to as level one, level two and level three. These tested models have been fabricated and tested under the same conditions.

2. Profiles Manufacturing

The corrugated profile are manufactured using metallic dies, Specifically iron. Hand lay-up process was used to fabricate all composite specimens. The material used for fabricating composite specimens are woven roving glass fiber and epoxy. The specification of the material used are given in table (1) the specimens were fabricated by placing the woven roving fiber glass in fabrication model as layers on each other . The woven roving fiber is passed through a resin bath, causing resin impregnation. The fabricated specimens were cured at room temperature for 24 hours to provide good hardness and shrinkage. Then the cured specimens were extracted from fabrication model to prepare them for the crushing test. Figure(1)-a shows the three metallic dies used for the fabrication of corrugated composite specimens using hand layup process and Some of tested specimens are show in figure(1) b,c, and d.

Table 1: Types of used constituents

Epoxy resin	UK Epoxy Resins UKH 137 Epoxy
Hardener	UK Epoxy Resins UKH 136 Hardener
Woven roving E-glass fiber	Synthetic fiber: 500g/m²
No. of layers of each specimens	Four layers

(a)

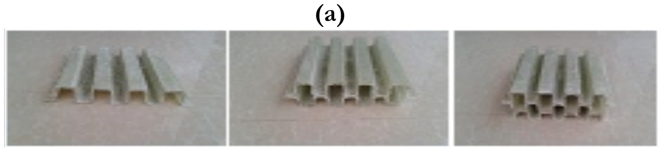

(b)

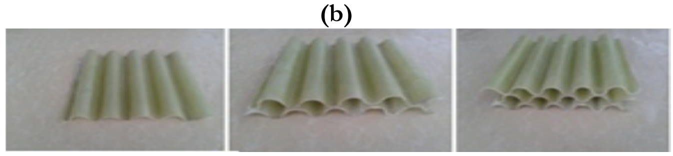

(c)

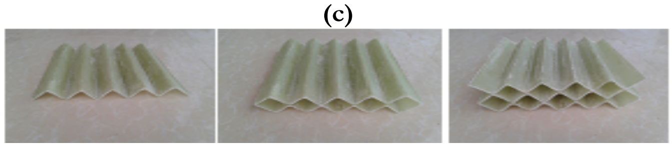

(d)

Figure1.(a) different metallic dies used for specimens fabrication(b)square specimens(c)sinusoidal specimens and(d) triangular specimens

3. Test Procedure

The specimens were tested in quasi-static axial compression between two flat plates. ASTMD1621 standards, with full-scale load range of 4000kN was used. Three replicate tests were conducted for each type of models. All models were compressed at a rate of 2.5mm/min until limited crush, which implies complete compaction of tested specimen and load records increases sharply is reached. Load and displacement were recorded by automatic data acquisition system.

4. Results and Discussion

The tested specimens collapsed following the failure mode described by Hull[15]. As illustrated in figure (2). The load-displacement curve can be divided into three distinct regions. In region I the load P increases rapidly and reaches a maximum P_{max} before dropping. In region II the load oscillates about an average $\bar{P}$ and a series of folds form successively in the corrugated plate so that a folded zone grows progressively. For the last stage (region III), the load increases rapidly representing the end of the test. The detailed discussion of the results are presented in the proceeding section ,that involves crush stages and load displacement curve of composite specimens.

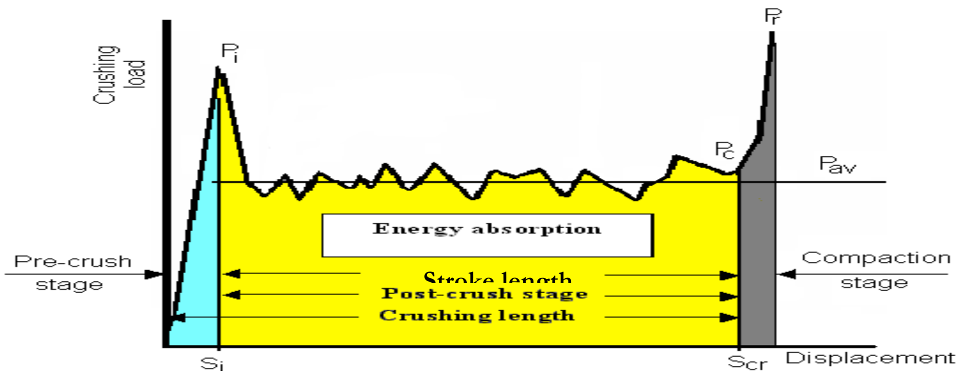

Figure 2: Schematic representation of a typical load-displacement curve of a corrugated composite with its main parameters

In this study, 27 specimens were made and tested under the same conditions. These types of specimens are divided to three levels. Level one has single corrugated plate, level two has two plates, and level three has three corrugated plates. Each level has three different profiles: Sinusoidal, triangular, and square profiles. The specimens that recorded the highest value and the lowest value of the specific energy absorption will be explained.

4.1. Three corrugated composite plate with square profile:

Typical load displacement curve for square under quasi-static compression load are shown in figure (3a). As it can be seen curve, the load increases gradually with the increase in the displacement up to initial failure where maximum load achieved 41KN at a displacement of 20 mm. Subsequently load drops down to 22KN at a displacement of 25mm. As compression load increases, it was observed that lateral split was formed (see figure 3b), and propagate causing fall down of load displacement curve. This case of crushing progress continues until the end of the test, where the specimen was completely crushed.

4.2. Two corrugated composite plate with triangular profile:

In general two triangular specimen crushed in the same manner as composed specimen except that no fracture occurred for two triangular specimen. As shown in Figure (4a) , the crushing load increases until the compression is about 14mm when full resistance is developed with 52KN load. Immediately after this stage start (plastic deformation) the load slow down until the compression is about 21mm when full resistance is developed with 16KN,after that increase resistance the loading until compression 58KN at 25mm after that droop slow until the compression 20KN. Consequently load increases during this crushing stage followed by slight fluctuation the dramatic increase at the end of crushing test (see figure (4b).

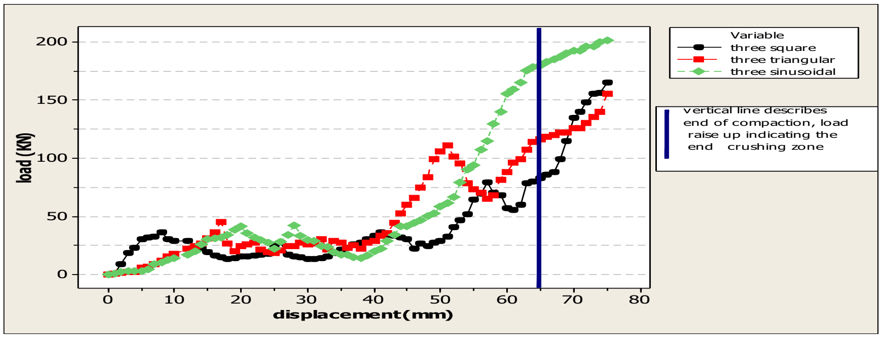

(a)

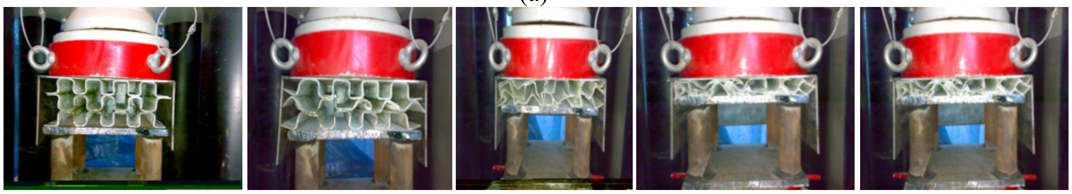

(b)

Figure3. (a) load-displacement curve of level three of composite specimens,(b)deformation history of three level plate with square profile

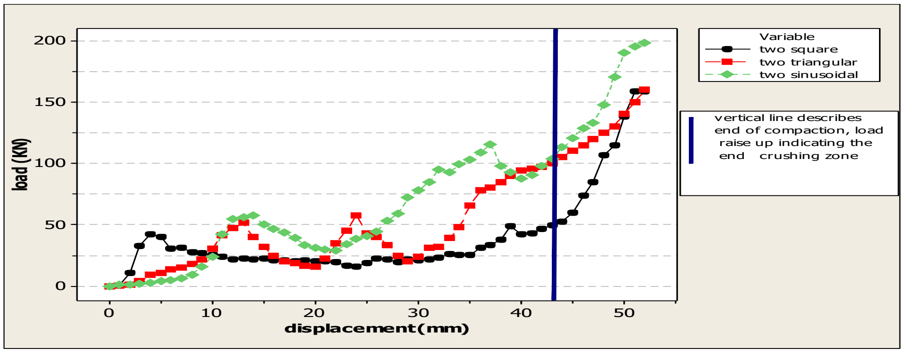

(a)

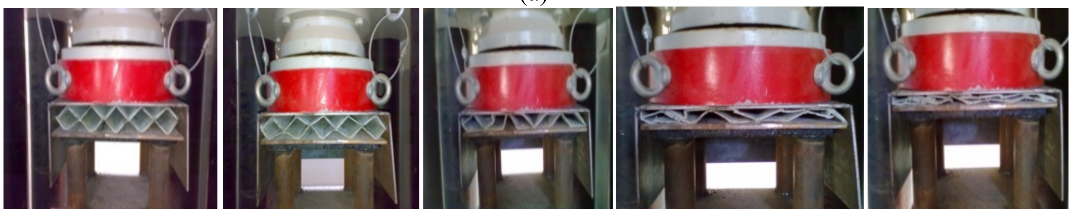

(b)

Figure4. (a) load-displacement curve of level two of composite specimens, (b)deformation history of two level plate with triangular profile

5. Crush in Energy Absorption

The energy absorption capability can be estimated by knowing different parameter. These parameters are illustrated in the following section.

5.1 Total Energy Absorption (E):

The total energy absorbed or the total work done, Wt, in crushing of composite specimens is the area under the load-displacement curve. It can be obtained by numerical integration of the load displacement curve.

$$Wt = \int_{Si}^{Scr} P_{av}\, dS = P_{av}(S_{cr} - S_i \qquad (1)$$

where, as they are indicated in figure 3, Si and Scr are the initial and final useful crush stroke and P_{av} is the mean crush load which obtained by averaging the applied loads during post crush stage. The load-deformation characteristic is a measure of the energy absorption capacity. It differs from one structure to another, and it depends on the mechanism of deformation involved and the material used.

5.2 Specific Energy Absorption (Esp):

To compare different materials or different geometry of specimens, it is necessary to consider the specific energy. The specific energy is defined as the amount of energy absorbed per unit mass crushed material (m). Therefore, the specific energy (Esp) that is dependent on the structure material was used for comparing the energy absorption of all specimen kinds. Specific energy absorption (Esp) can be calculated as;

$$Esp = \frac{W_t}{m} \qquad (2)$$

After all the lateral cracking tests are completed, the results obtained from these tests can be seen in Table 2, and represented by the curve in Figure (5). Looking carefully to the results obtained with a specific absorption from the third-level samples, the square sample still has the highest values of initial failure load of (2,472 kj/kg). From the table, it can be seen that the triangular samples recorded the lowest value of (0.878kj/kg).

Table 2: Crash worthiness parameters of lateral tests for all specimens

The level	Sp-type	P_{max}(KN)	$\overline{P}$(KN)	E_t(Kj)	W (Kg)	E_{SP}(KJ/KN)	CFE* %	SE** %
One level	sinusoidal	113	65.66	0.525	0.470	1.117	58.1	90
	triangular	89	51.79	0.725	0.400	1.812	58.19	80
	square	68	40.62	0.649	0.370	1.754	58.69	66
Two level	sinusoidal	115.6	59.62	1.304	0.940	1.387	90	73
	triangular	58	31.95	0.703	0.800	0.878	61	60
	square	49	36.23	1.304	0.740	1.762	91	73
Three level	sinusoidal	48	44.67	1.608	1.410	1.140	86	62
	triangular	111	42.49	1.827	1.200	1.522	87	66
	square	79	44.26	2.744	1.110	2.472	95	75

(CFE*) Crush Force Efficiency (SE**) Stroke Efficiency

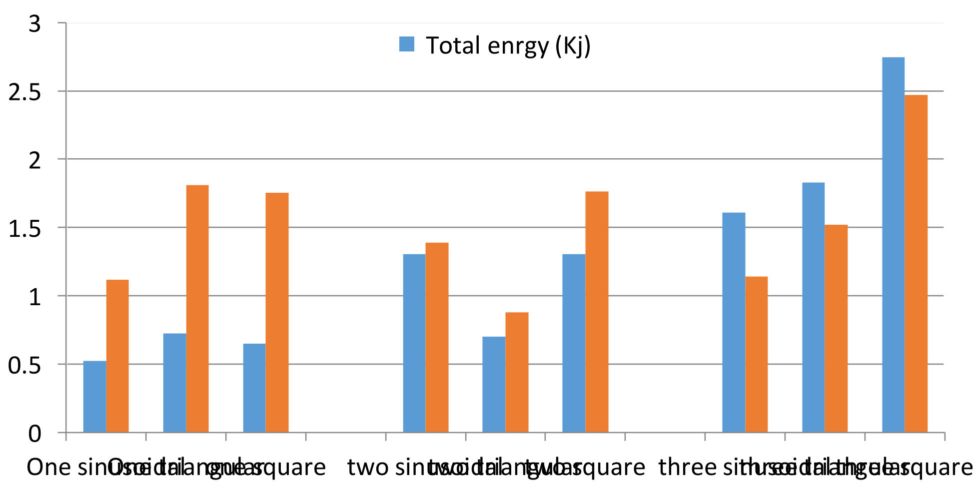

Figure 5. Total energy and specific energy of all specimens

6. Conclusion

A series of composite plates with different corrugation profile (sinusoidal, square, and triangular) has been subjected to quasi-static compression load. The difference of the specimens' shape offer a compare between them in terms of the effect of the corrugation profile in energy absorption capability. Based on the results obtained, it can be noted that, the specimen geometry has a considerable affect on energy absorption capability and load carrying capacity; it has been observed that the change in corrugation profile has important affect on energy absorption capability, where the specimens of square profile recorded the highest values of energy absorption capability comparing to specimens with sinusoidal and triangular profile; the specific energy absorption and load carrying capacity increased with the increase of the number of corrugated plates and the relationship between the two factors is directly proportional; the highest value of specific energy absorption of group A specimens has been recorded by the level three square specimens to be (2.472KJ/Kg).However, triangular specimens come second with (1.812KJ/Kg), and specimens of two triangular recorded the lowest value of (0.878 KJ/Kg).

Reference

[1]. Elfetori F. Abdewi, S. Suliman, A.M.S. Hamouda, E. Mahdi. (2006), Effect of Geometry on the Crushing Behaviour of laminated corrugated Composite Tubes.journal of Materials Processing Technology 172 394-399.

[2]. Reid SR. Plastic deformation mechanism in axially compressed metal tubes used as impact energy absorbers. Int J Mech Sci 1993;35:1035–52.

[3]. Reddy TY, Al-Hassani STS. Axial crushing of wood filled square metal tubes. Int J Mech Sci 1993;35:231–46.

[4]. Wu L, Carney JF. Experimental analysis of collapse behaviour of braced elliptical tubes under lateral compression. Int J Mech Sci1998;40(8):761–77

[5]. Beardmore P, Johnson CF. Compos Sci Technol1986;26:251–81.

[6]. Hamada H, Coppola JC, Hull D, Maekawa Z, Sato H.Composites1992;23:245–52.

[7]. Mamalis AG, Manolakos DE, Viegelahn GL. J ComposMater1990;25:72–90.

Mapping Of Sea Water Intrusion in the Western Libyan Coast Using Geo-electrical Method: Case Study

Abdel Hameed M. Salem1*,Magdi A. Mountasir2, Husam Abdussalam R. Shames3
1Hameed.ehtman@gmail.com, 2majdialmuntssir@gmail.com, 3H.Shames@aee.gov.ly

[1,3]Prospecting department, The Libyan Atomic Energy Establishment, Tripoli, Libya
[2]Scientific and technical matters department, Higher Institute for Sciences and Technology, Garaboulli, Libya

ABSTRACT

As most of the Libyan population live in the north side of the country; mainly in the western coastal zone; the sea water intrusion is a vital phenomena that need to be studied to locate, measure its diffusion rate, and take a remediation actions [1]. Conventionally, water sampling of ground water wells is used to evaluate sea water intrusion in coastal areas [2]. Nevertheless, excessive use and cost of drilling should be avoided by relaying on advanced technologies [2]. Geo-electrical methods such as electrical resistivity and electromagnetic can be used for studying sub surface geophysics from the earth surface with no need for drilling, and can give a trusted results [3]. The huge contrast in resistivity between saline and fresh water makes measurement of the resistivity in the ground a useful technique for detecting and delineate the saline interface, consequently, using the electrical resistivity method is a successful technology for studying sea water intrusion [3]. Mapping sea water intrusion in a selected area located in the western coast of Libya is reported by this study, it covers about 120 Km² from Algrabouli to Elallus by 16 profiles perpendicular to shoreline with total number of 53 vertical electric sounding (VES). This study is considered as a case study to insure the need to cover the whole Libyan coast with more detailed studies, furthermore, it concluded that the sea water intrusion in Libya is truly a serious issue that will lead to pollute the groundwater in the coastal areas with salt and costal contaminated water in the case of not correcting the situation.

Keyword— Seawater intrusion in the western Libyan coast; Geo-electrical method to study sea water intrusion; Case study of sea water intrusion by electrical resistivity method.

1. Introduction

The phenomenon of sea water Intrusion occurs in coastal areas where the different densities of both the saltwater and freshwater allow the seawater to intrude into the freshwater aquifer. Equally important to the salinization of fresh water, the intruded seawater may be contaminated with sewage water [2].

For countries like Libya, that have coasts and their main resource of freshwater is the groundwater, a high potential of seawater intrusion exist in the coastal areas threatening the freshwater aquifer with salinization and contamination [1].

Before the improvements of geophysical methods to be used for geo-environmental investigations, water sampling was the only way to locate seawater intrusion. The need for a sufficient geo-environmental investigation techniques was high for areas where no wells exist. Drilling new wells to study seawater intrusion was not always applicable, economic and friendly to the environment [3]. Today, many geophysical methods such as geo-electrical are used to investigate seawater intrusion. These techniques deals with the electrical condition of earth and it investigate electrical properties of rocks and minerals under different geological circumstances.

Many studies world wide used electrical resistivity method for mapping the seawater intrusion for coastal areas [4], some of these studies in Europe are: Oteri [5] has delineated saline water intrusion in England since 1983. Antonio Satriani et al [6] have studied on Characterization of the Coastal Saltwater Intrusion in Metapontum Reserve Forest in Southern Italy. Soldal et al [7] have done Seawater in western Norway. Nowroozi et al [8] have carried out a study on saltwater intrusion into the freshwater aquifer in the eastern shore of Virginia (USA) by electrical resistivity survey using Schlumberger configuration. Abdul Nassir et al [9] have delineated and mapped the intrusion boundary between fresh water and saline water in northwest of Malaysia by geoelectrical imaging surveys. Shaaban F.F[10] has employed Vertical electrical soundings (VES) in a coastal area of north western Egypt. Sheriff et al [11] have carried out Geoelectrical studies for delineating seawater intrusion in UAE. Abdulaziz M. et al [12] have conducted seawater intrusion in southwest of Saudi Arabia. This study aims to map the seawater intrusion in around 120 Km² area between Algarboulli and Elallus at the western Libyan coast.

2. Study Methodology

2.1. The Scientific Theory

There are a high distinguish between saline and fresh water in resistivity, this difference made the measurement of the resistivity for the ground water a useful technique for detecting and delineating the saline interface. Knowing the formation resistivity will directly lead to appoint the total dissolved salt of ground water. The relation between formation resistivity and groundwater quality is demonstrated in Table1. [2].

2.2. Data Acquisition

One of most used geophysical techniques for studying formation resistivity is the electrical resistivity method [2]. The main frequent used types of measurement are Vertical Electric Sounding (VES) and resistivity profiling [3]. A proper number of VES should be carried out in the survey area along on profiles perpendicular to shoreline. In this study, schlumberger configuration has been adapted with maximum current electrode spacing of 400 m as illustrated in Figure 1. In this technique the electrical current by two electrodes AB is stepwise made to flow through deeper and deeper parts of the ground, otherwise the distances between the potential electrodes MN almost fixed. To measure apparent resistivity to subsurface layers, a resistivity meter (Saris) is used with equation (1).

$$\rho_a = \frac{\pi(s^2 - a^2/4)}{a}\frac{\Delta V}{i} \qquad (1)$$

Where: ρa = apparent resistivity, ohm-m; a = MN distance, m; s = AB distance, m; v = Voltage, volt; i = current, amp.

Table 1: Relation between formation resistivity and groundwater quality

Ground water quality group	Total Dissolved Salt TDS (mg /L)	Formation resistivityϱ (ohm meter)
Very fresh (VF)	< 200	>200
Fresh (F)	200 - 400	200 – 100
Moderately Fresh (MF)	400 - 800	100 -50
Weakly Fresh (WF)	800 - 1600	50 – 25
Moderately Brackish (MB)	1600 -3200	25 – 12.5
Brackish (B)	3200- 6400	12.5 – 6.25
Very Brackish (VB)	6400 -12800	6.25 – 3.12
Moderately salt (MS)	12800 - 25600	3.12 – 1.56
Salt (S)	> 25600	1.56<

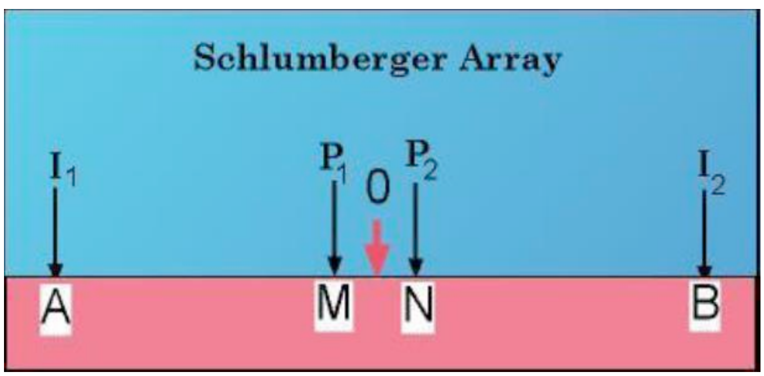

Figure 1: Schlumberger array.

2.3. Data Processing and Interpretation

The VES curves were analyzed using the available software program (IpI2Win+ip) to generate pseudo cross sections, these sections shows distribution of resistivity with the depth. A resistivity values of less than 10 Ohm meter appears as dark blue and black color in the figures which means, depending on "Tab. 1", they were affected by sea water intrusion into ground water aquifer.

Iso- apparent resistivity maps were plotted by the help of the software (Oasis Montaj). These maps indicate distribution of apparent resistivity in the area against distance of current electrodes (AB) at a fixed depth. The depth was practically almost between (AB/3, AB/4).

3. The Case Study

3.1. Location of the Study Area

The study area is located approximately 60 km East of Tripoli. The site covers an area of about 120 km². It is bounded on the north by the Mediterranean Sea, and situated between Algarboulli and Elallus Figure 2. It lies between latitudes (32°46'57.10"N, 32°43'38.99"N), and longitudes (13°41'32.70"E, 14° 0'20.17"E).

Figure 2: Location of the study area.

3.2. Distribution of the Vertical Electrical Soundings and Profiles on the Study Area

The survey was accomplished with Fifty three VES configuration with a maximum current electrode spacing (AB) of four hundred meters. A sixteen pseudo cross sections perpendicular to the shore line were selected as illustrated in Figure 3.

Figure 3: Distribution of the VES's and profiles on the study area.

4. Results and Discussions

4.1. Results Gained by (Ip I2wint +Ip) Software

As mentioned before, all sixteen pseudo cross sections have been processed using (Ip I2wint +Ip) software to show the distribution of resistivity with depth. Only three pseudo cross sections (referred to as A, B and C in Figure 3) have been selected as examples for these results in this paper. For cross section A Figure 4, the resistivity values ranged between (18 – 60 Ohm meter) at almost 75 meter depth which means there is no present of seawater intrusion according to Table 1. For resistivity obtained in Profile B, the lowest values ranged between (10 - 16 Ohm meter) at VESs (21, 22) to clearly indicate it was slightly effect by Sea water intrusion Figure 5. In cross section C, The lowest resistivity was located at VES 36 with (0-10 Ohm meter) value to declare the area as a highly effected by seawater intrusion Figure 6.

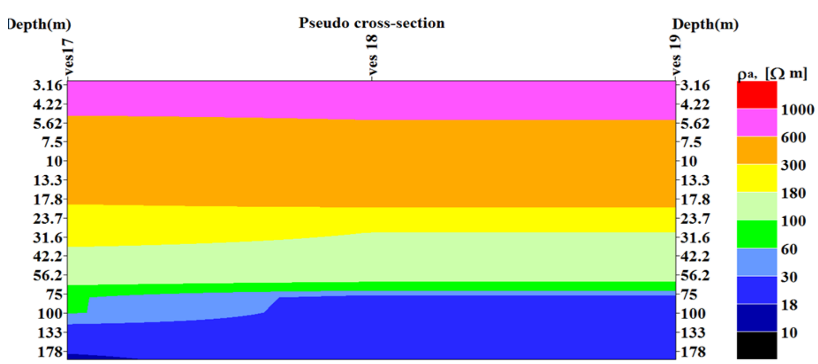

Figure 4: Profile A (VES's: 17, 18, 19).

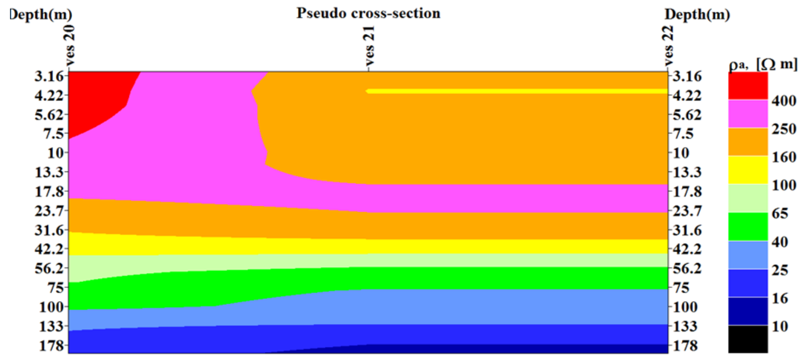

Figure 5: Profile B (VES's: 20, 21, 22)

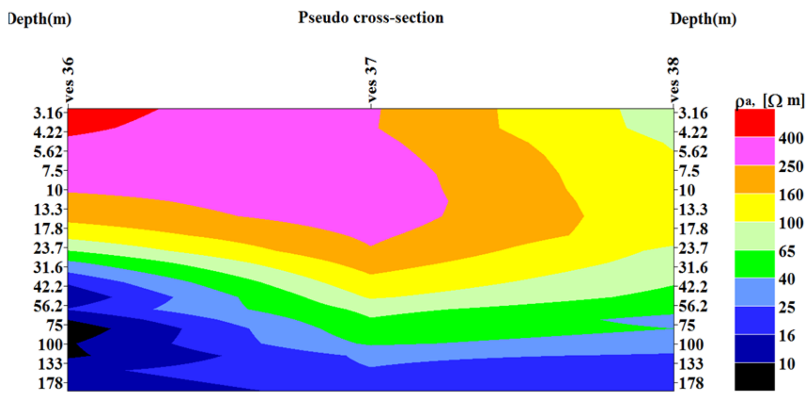

Figure 6: Profile C (VES's: 36, 37, 38)

4.2. Results Gained by Oasis Montaj Software

Three Iso-apparent resistivity maps have been generated to reflect lateral variation of apparent resistivity at a certain depth using the Universal Transverse Mercator (UTM) coordinate system, these maps indicate distribution of apparent resistivity in the area against distance of current electrodes (AB). The used AB values were: 200, 300 and 400 meters. In all three maps, the lowest resistivity values of less than (10 Ohm meter) were gained in certain VES's to specify the presence of seawater intrusion.

The iso-apparent resistivity map for AB = 200 meter at about (50 to 70 meters depth) are shown in Figure 7. , the lowest resistivity values were obtained at VESs (6, 7, 11, 30, 36, 51, 52).

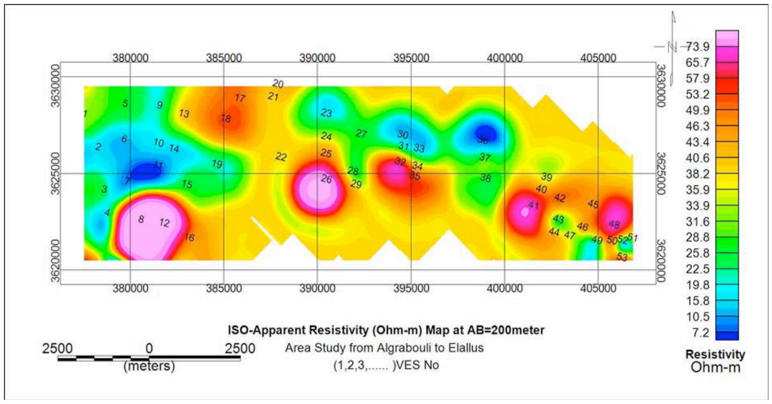

Figure 7: Iso-apparent resistivity map for AB = 200 m.

Figure 8 illustrated the iso-apparent resistivity map for AB = 300 meter at an approximate depth of (75 to 100) meters. the lowest resistivity values presented at VES's (3, 5, 6, 7, 10, 11, 14, 23, 24, 30, 31, 33, 36).

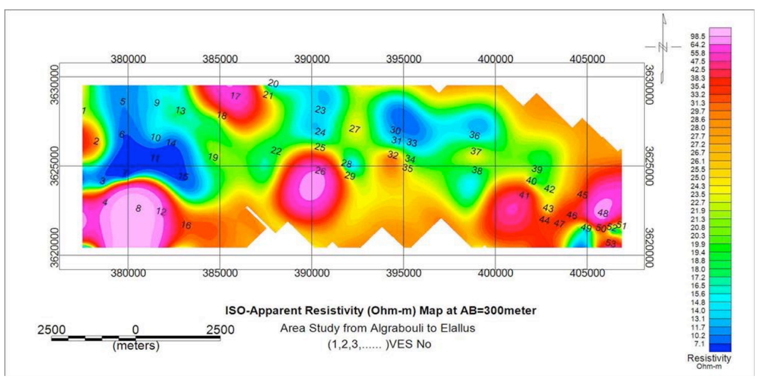

Figure 8: Iso-apparent resistivity map for AB = 300 m.

The map in Figure 9 shows iso-apparent resistivity for AB = 400 meter with almost (100 to 130) meters depth. the lowest resistivity values were considered at VES's (2, 7, 8, 11, 14, 23, 25, 27, 28, 30, 33, 34, 36, 51, 52).

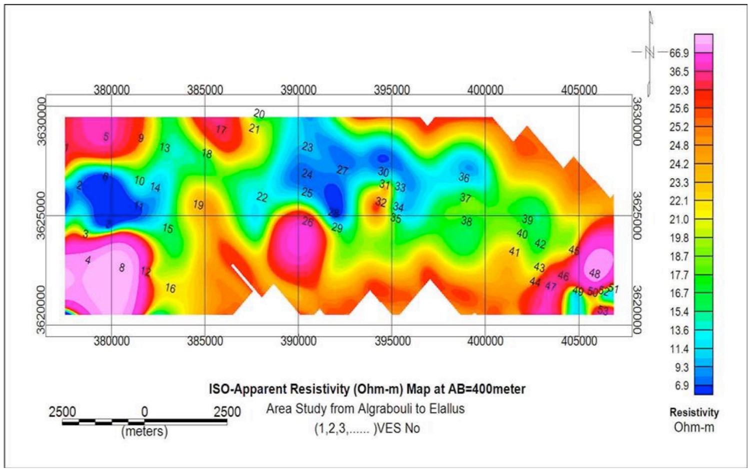

Figure 9: Iso-apparent resistivity map for AB = 400 m.

4.3. Mapping Seawater Intrusion in Western Libyan Coast

The interface between salt and fresh water is identified in the study area approximately as a red line in Figure 10. This map is evidently demonstrate and prove the occurrence of seawater intrusion in the area.

Figure 10: Mapping seawater intrusion in Western Libyan Coast.

5. Controlling and Minimizing Seawater Intrusion

Methods for controlling intrusion vary widely depending on the source of the saline water, the extent of intrusion, local geology, water use and economic factors. There are several methods for controlling seawater intrusion demonstrated with its advantages and disadvantages as follows: [13]

1- Reduction of pumping rates: needs public awareness with recycling and reuse of water. Advantages: reduction of abstraction rate. Disadvantages: private stockholders, temporary solution.
2- Relocation of pumping wells: movement of wells in more inland position. Advantages: decrease the occurrence of up coning of salt water. Disadvantages: costly, temporary solution, obstruction in relocation
3- Use of Sub surface Barriers: Reduce the permeability of aquifer; Sheet piling, Cement grout, or Chemical grout. Advantages: Reduce the intrusion of saline water. Disadvantages: Not efficient for deep aquifers, and costly.
4- Natural Recharge: Constructing dams and weirs to prevent the runoff from flowing to the sea. Advantages: Prevent the runoff to flow directly to the sea. Disadvantages: Depends on the soil properties , Take Long time, Unsuitable for confined and deep aquifers.
5- Artificial Recharge: Increase the ground water levels, using surface spread for unconfined aquifers and recharge wells for confined aquifers. Advantages: Increase the groundwater storage. Disadvantages: Ineffective in the areas where excessive ground water pumping occurs, Occupies a large area.
6- Abstraction of Saline Water: Reduce the volume of saltwater by extracting brackish water from the aquifer and returning to the sea. Advantages: Decreases the volume of saline water, Protects pumping wells from upconing. Disadvantages: private stockholders, temporary solution.

The best methodology to reduce the seawater intrusion in coastal aquifers is: Abstraction, Desalination and Recharge (ADR) [14]. This methodology aims to overcome all or at least most of the limitations of the previous methods. ADR consists of three steps; abstraction of brackish water from the saline zone, desalination of the abstracted brackish water using reverse osmosis (RO) treatment process and recharge of the treated water into the aquifer as shown in Figure 11.The reason of ranking this method as the best to control seawater intrusion is its unique ability to produce freshwater by using the saline groundwater which will directly lead to push the intrusion line back to the sea. The main disadvantage of this technique is the bad environmental effect resulted by using traditional energy sources.

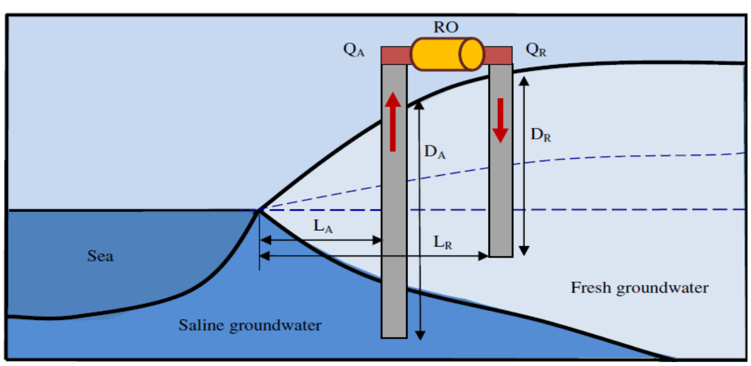

Figure 11: Diagram of the ADR Methodology.

6. Conclusion and Recommendations

- This paperwas accomplished with Fifty three VES configuration with a maximum current electrode spacing (AB) of four hundred meters and sixteen pseudo cross sections perpendicular to the shore line were selected. The study evidently indicated the existence of seawater intrusion in the study area that covers about 120 Km^2 between Algrabouli and Elallus, moreover, highly express the need to map the whole country to precisely locate this phenomena.
- Establishing a national project to map ground water contamination for the whole shore line in Libya by using the electrical resistivity method to investigate the seawater intrusion.
- Using Abstraction, Desalination and Recharge (ADR methodology) to solve the problem of seawater intrusion in Libya depending on the national map for coastal ground water contamination.
- Using clean energy in desalination plants used for ADR methodology.
- Nuclear energy should be considered as one of the best choices when selecting the most proper energy technology for ADR and seawater desalination in Libya.

Acknowledgment

The authors would like to thank The Libyan Atomic Energy Establishment for her support and permission of using the Resistivity Meter (Saris) in this paper, moreover, deep thanks also extend to Fouzie Mohamed and Osama Osman at Geophysics Department, Science Faculty, Tripoli University for their contribution in obtaining the field data.

References

[1]. O. Salem, "water resources management in Libya,"April 2007 [workshop on Integrated Water Resources Management (IWRM) in Libya. Tripoli, Libya].

[2]. Araguas, "Groundwater saline intrusion," Ed Madrid Instituto Geologic, Spain, First Edition, 2005.

[3]. Telford, "Applied Geophysics," Cambridge university press, Great Britain, First Edition, 1990.

[4]. J. Jansen, "Geophysical methods to map brackish and saline water in aquifers," April 2011 [Water Resources Conf. University of Georgia, USA].

[5]. Oteri, "Delineation of saline intrusion in the Dungeness shingle aquifer using surfacegeophysics,"1983 [Quart. J. Engg. Geol]. Volume 16, pp. 43-5.

[6]. Satriani, A. loperte, V. Imbrenda, and V. Lapenna, "GeoelectricalSurveys for Characterization of the Coastal Saltwater Intrusion in Metapontum Forest Reserve(Southern Italy),"2012 [International Journal of Geophysics]. pp. 43-5.

[7]. S. Oddmund, M. Eirik, H. Eirik, and R. Noralf, "Seawater Intrusion and Fresh Groundwater Hydraulics in Fjord Delta Aquifers Inferred from Ground Penetrating Radar and Resistivity Profiles -Sunndalsora and Esebotn, Western Norway"1994 [Journal of Applied Geophysics]. Volume 32, pp.305-319

[8]. Nowroozi, S. Horrocks, and Henderson, “Saltwater intrusion into the fresh water aquifer in the eastern shore of Virginia: a reconnaissance electrical resistivity survey”1999 [Journal of Applied Geophysics]. Volume 42, pp.1-22.

[9]. S. Abdul Nassir, M. Loke, C, Lee and M, Nawawi, “Salt-water intrusion mapping by geoelectrical imaging surveys”2000 [European Association of Geoscientists &Engineers, Geophysical prospecting]. Volume 48, pp. 647-661.

[10]. F. Shaaban, “Vertical electrical soundings or groundwater investigation in northwestern Egypt: A case study in coastal area”2001 [Journal of African Earth Sciences]. Volume 33, pp.673-686.

[11]. Sherif, El. Mahmoudi, H. Garamoon, A. Kacimov, S. Akram, A. Ebraheemand, and A. Shetty, “Geoelectrical and hydrogeochemical studies for delineating seawater intrusion in the Outlet of Wadi Ham, UAE”2006 [Environmental Geology]. Volume 49, pp.536-551.

[12]. M. Abdulaziz, M. Al-Bassam, and T. Hussein, “Combined geo-electrical and hydro-chemical methods to detect salt-water intrusion: A case study from southwest Saudi Arabia”2008 [Management of Environmental Quality: An International Journal]. Volume 19, pp.179-193.

[13]. D. Todd, and L. Mays, “Groundwater Hydrology,” Wiley, New York, USA,2005.

[14]. F. Hany, H. Abd-Elhamid, and A. Javadi, “A Cost-Effective Method to Control Seawater Intrusion in Coastal Aquifers,” J. of Water Resource Management, vol. 25, pp. 2755-2780, 2011.

Effects of Different Fluids Properties on Cavitation Performance in Centrifugal Pump

Saad Ghidhan [1], Moamar Hamed[2], Mansor Benaros[3]
[1]saadgedan@yahoo.com , [2]moamar.ehmied@gmail.com , [3]mansourbenaros@gamil.com
[1,2]Mechanical and Industrial Engineering Department, College of Engineering, Elmergib University, Libya
[3]Mechanical and Industrial Engineering Department, Alasmarya University, Libya

ABSTRACT

Cavitation, which is the formation and collapse of vaporous cavities in flowing liquids, can degrade the performance of pumps and other hydraulic equipment. The aims of the present research are to investigate the effect of different fluids properties on pump cavitation performance. Consideration is given to examine the effect of liquid viscosity and density on cavitation behavior. Experimental results are presented for a centrifugal pump operating in water, kerosene and diesel fuel with different disposal rates of flow. With references to the results, the water has affected by the cavitation at less Net Positive Suction Head (NPSH) than other liquids, also it can be conducted that the kerosene shares the closest cavitation behavior with diesel fuel. Therefore, the stress produced by cavitation bubbles decreases with increase of viscosity of the liquid.

Keyword— Water, kerosene, diesel fuel, cavitation performance, centrifugal pump, Net Positive Suction Head (NPSH)

1. Introduction

When a centrifugal pump handles liquids with different viscosity and specifications, there Net Positive Suction Head (NPSH) normally will be different. The simple definition of the NPSHA is the difference between pressure at the suction of the pump and the vapour pressure for the liquid being pumped[1]. An increase or decrease of NPSH will result in cavitation taking place in the pump. In result, the pump will be subject to abnormal operations, such as loud noise, violent vibration, performance degradation, impeller or other components damage. In fact, measuring or predicting NPSH of a centrifugal pump at various operating conditions is quite important for the hydraulic design optimization and engineering application when the pump handles different viscous liquids and it's important to know the situation of operating with this phenomena and how to avoid the problem of cavitation [2].

In almost of petroleum industries and chemical operations pumps will deal with liquids which have such different specifications, there are two sorts of liquid products, which need to be transported by centrifugal pumps. One kind of liquid is with a higher vapour pressure but with nearly the same viscosity of water, and the other kind of liquid is with a lower vapour pressure but a higher viscosity than water [3].

Many researchers [4][5] have discussed the inception of cavitation through the experiments and numerical simulations. The phenomena of cavitation are usually determined by the value of (NPSH). The physical properties of the liquid, its vapour and the flow conditions can affect the cavitation process and thus the cavitation performance of hydraulic equipment as well. The effects of the fluid properties, flow conditions, and heat transfer can improve cavitation performance for certain liquids and/or liquid temperatures, the net positive suction head (NPSH) requirements can be significantly less than that obtained for room-temperature water.

As mentioned above NPSH is defined as the total pressure above vapour pressure at the inlet to a pump This improvement (decrease) in inlet pressure requirements is attributed to the varying degrees of evaporative cooling associated with the cavitation process. Because of the evaporative cooling, the cavity pressure and the vapour pressure of the liquid adjacent to the cavity are decreased relative to the vapour pressure of the bulk liquid. This decrease in cavity pressure retards the rate of further vapour formation, thereby allowing the pump to operate at lower values of NPSH than would otherwise be possible.

The NPSH requirement for a pump operating at a given head rise and flow condition is reduced by the amount corresponding to the decrease in cavity pressure. The accurate prediction of thermodynamic effects of cavitation is therefore essential to an optimum flow system that is designed to operate with cavitation.

2. Experimental Work

To determine the effect of fluid viscosity on the performance of centrifugal pumps and the phenomenon of cavitation which usually occur and negatively affect the performance of these pumps as explained previously. Laboratory experiments were carried out on a centrifugal pump using different liquids (water, kerosene and diesel fuel)

2.1. Test Rig Facilities

There are various ways to design the test rig to study the cavitation. The most important feature of any test-rig is the means of introducing cavitation into the pump system. In this research, the closed loop configuration was chosen for this testing as indicated in a schematic diagram shown in Figure 1. The flow system consists of 1 hp centrifugal pump using DC current motor, the flow orifice meter, pressure measuring devices, suction and delivery pipelines, speed control unit, and valves. Connecting pipes and control valves are assembled with (1 in) diameter plastic connections.

The suction line consists of a tube connected to a valve that controls the flow rate and a pressure gauge connection, at the end there is a nozzle valve. The discharge line contains a valve that controls the flow rate and a connection pressure gauge and the orifice meter to measure the flow rate.

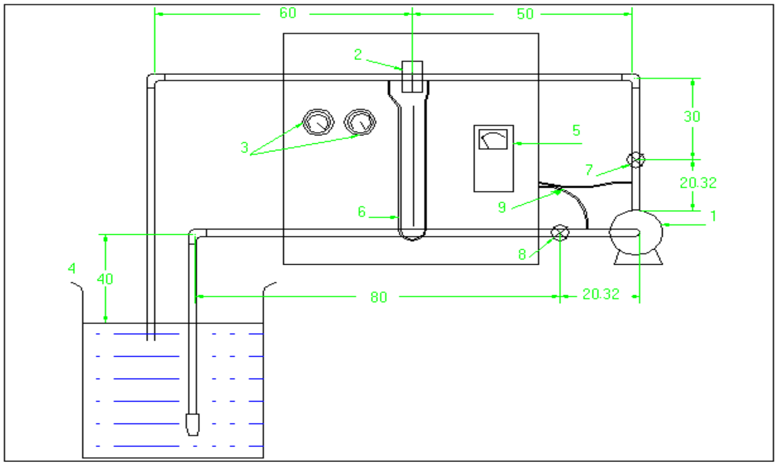

1. Pump
2. Orifice meter
3. Pressure gauges
4. Tank
5. Power gauges
6. Manometer
7. Suction valve
8. Suction valve
9. Pipes

Figure 1: Schematic diagram of test rig [6].

Measuring devices are divided into, pressure gauge for the suction line and is used to measure the pressure of the water in the suction line from the type of tube Borden range from (0 to bar1) and the rate of (0.2 bar), the pressure gauge of the discharge line is also used to calculate the pressure of the water in the line using the Borden tube, measured from (0 to 6 bar). The other measuring devices are power measuring device; the capacity of the pump can be measured by a Watt meter where it is connected to the pump. This device is read from 0 to 1000 W and is rated at 2 W.

2.2. Test Procedures

The test procedure was conducted by assembling the system and connecting all the measuring devices, the driving pump is firstly operated with the water to carry out the pump performance test and cavitation test, and then the same steps of test had repeated with the kerosene and the diesel, each test has been carried out at different values of flow rate ratios.

The cavitation test on the pump has been carried out by keeping the pump running at the required speed, and flow rate ratio, and then reducing the inlet pressure step by step until the inception condition occurred. At each step, the flow rate was adjusted through the delivery valve, then the inlet pressure further reduced until developed cavitation and fall off head and efficiency was noticed. At each setting of inlet pressure and inception condition, the measurements of suction and discharge pressures and flow rate were recorded.

The NPSH at each condition was calculated using the following equation:$NPSH = \left(\frac{P_{sg}}{\gamma} + \frac{V_s^2}{2g}\right) - \frac{P_v}{\gamma}$ also the head of the pump was calculated by the following equation: $= \left(\frac{P_d - P_s}{\gamma}\right) + 0.24$, efficiency of the pump was calculated by $\eta = \frac{\rho\, g\, Q\, H}{P}$ where ρ is density of the water, Q water flow rate, H head of the pump and P power[5].

3. Results and Discussion

In order to study the performance of the pump and also to examine the cavitation in the tested pump, three tests have been done, each test was conducted with different liquid, the first test the pump used the water and all the measurements have been taken with different flow rates, then the same procedures have been done for Kerosene and diesel.

3.1. Water Test

Firstly the performance of the pump was studied experimentally at different flow rates, the first test was conducted using the water, in this test the flow rate has been changed from 0.389 L/s to 1.4555 L/s, suction valve was totally opened and the level of the water in the tank was 40 cm from the centre of the pump.

Figure 2 presents the performance curves for the pump include power, head, efficiency and the NPSH. From Figure 2 it can be seen that the head of the pump starts decreasing with the increases of the flow rate, on the other hand the efficiency curve increase with increasing the flow rate until reached the maximum value of 26.1505 % then the efficiency start to drop, the NPSH was decreased with increasing of the flow rate and finally the power has risen with dropping the flow rate.

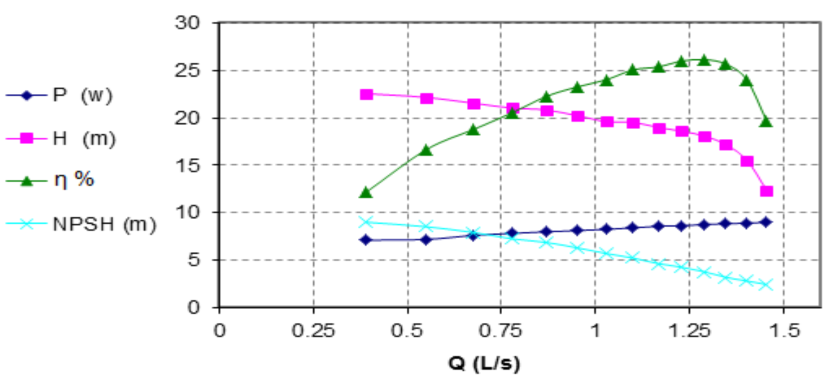

Figure 2: The performance curves for the pump for water test

Figure 3 shows the curves of NPSH at different flow rates. It can be noted that NPSH reach the collapse state, the point at which the lifting mark drops suddenly. It can be seen that, in the case of flow rate (Q = 0.30 L / s) the collapse occurs at the tenth point of the suction valve gradient when the net positive clouds (2.8693 m) and in the case of flow rate (Q = 0.60 L / s), the collapse occurs at the eighth point of the pull valve gradient when the net positive clouds (3.4282) m), as well as in the case of flow rate (Q = 0.90 L / s), these means the drops of the cavitation may occurs at different points with different flow rates.

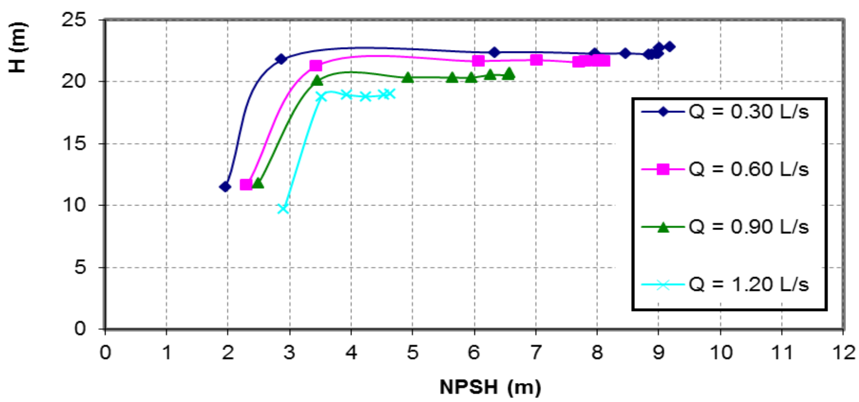

Figure 3: NPSH with different flow rate for water test

3.2. Kerosene Test

In this test the liquid in the test tank was changed to the kerosene, in order to study the performances of the pump and the cavitation. Figure 4 shows the performance curve of the centrifugal pump, it can be noted that, fluid starts to decrease as the flow rate and efficiency curve increases at a flow rate of (1.167 L / s). After that, the efficiency begins to decrease.

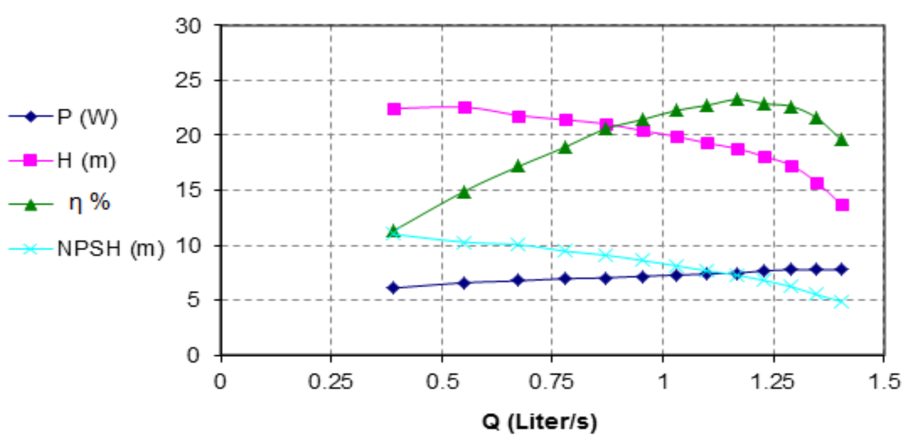

Figure 4: Performance curves for the pump for Kerosene test

Figure 5 shows the curves of NPSH at different flow rates. It can be noted that NPSH reach the collapse state, the point at which the lifting mark drops suddenly. It can be seen that, in the case of flow rate (Q = 0.30 L / s) the collapse occurs at the tenth point of the suction valve gradient when the net positive clouds (2.8693 m) and in the case of flow rate (Q = 0.60 L / s), the collapse occurs at the eighth point of the pull valve gradient when the net positive clouds (3.4282) m), as well as in the case of flow rate (Q = 0.90 L / s), these means the drops of the cavitation may occurs at different points with different flow rates.

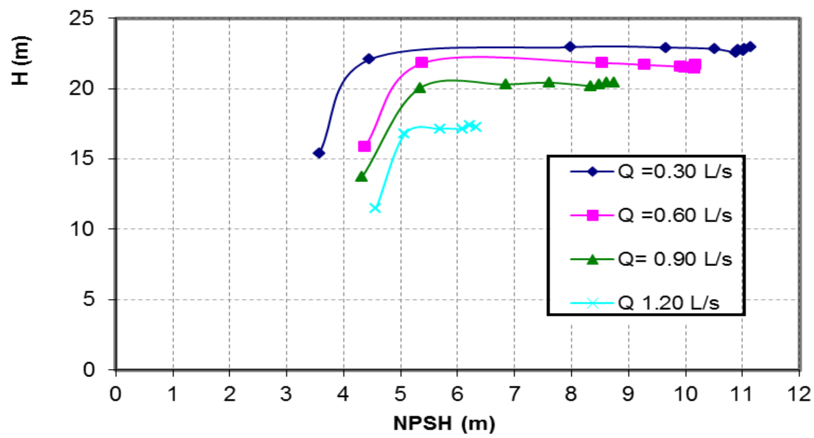

Figure 5: NPSH curves for the pump in Kerosene test

3.3. Diesel Test

In this test the liquid in the test tank was changed to diesel, in order to examine the effect of different viscosity on the pump performance and the cavitation. Figure 6 shows the performance curve of the centrifugal pump, it can be noted that the lifting properties begin to decrease as the flow rate and efficiency the higher the flow rate, the higher the flow rate, until it reaches its highest value (23.0136%) at a flow rate of 1.2301 L / s.

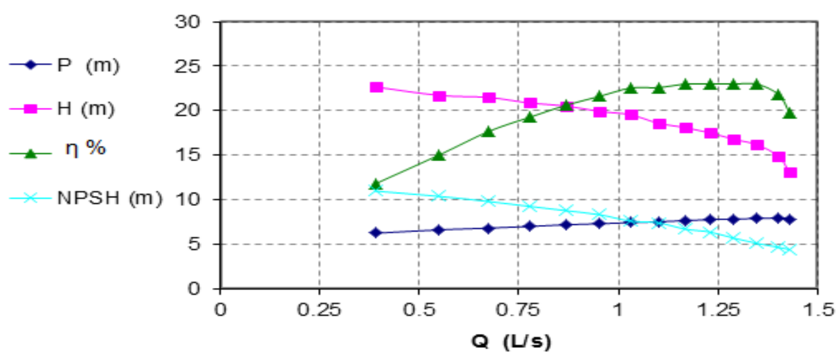

Figure 6: Performance curves of the pump for diesel with different flow rates

Figure 7 shows the curves of NPSH at different flow rates for the pump using diesel. It can be noted that NPSH reach the collapse state, the point at which the lifting mark drops suddenly. It can be seen that, in the case of flow rate (Q = 0.30 L / s) the collapse occurs at the tenth point of the suction valve gradient when the net positive clouds (2.8693 m) and in the case of flow rate (Q = 0.60 L / s), the collapse occurs at the eighth point of the pull valve gradient when the net positive clouds (3.4282) m), as well as in the case of flow rate (Q = 0.90 L / s), these means the drops of the cavitation may occurs at different points with different flow rates.

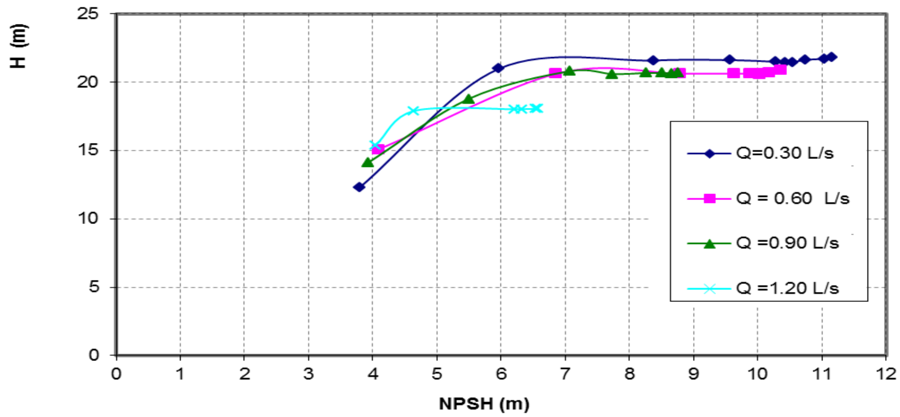

Figure 7: NPSH curves of the pump for diesel test with different flow rates

4. Comparison of the Performance of the Pump for the Liquids Used With Different Viscosity

The efficiency of the pump when operated with water is higher than its efficiency when operated with kerosene and diesel as shown in the Figure 8, so it is the highest efficiency in the case of water (26.1505%) at a flow rate equal to the maximum efficiency of kerosene (23.2624%) at a flow rate of (1.167 L / s) and the maximum efficiency of diesel (23.0136%) at a flow rate equal to 1.2301 L / s. The state of the water is different from the efficiency of the pump in the cases of kerosene and diesel where their efficiency is close to each other, and also finds that the difference between the efficiency of the pump at the small flow rates are close and increases as the flow rate is increased.

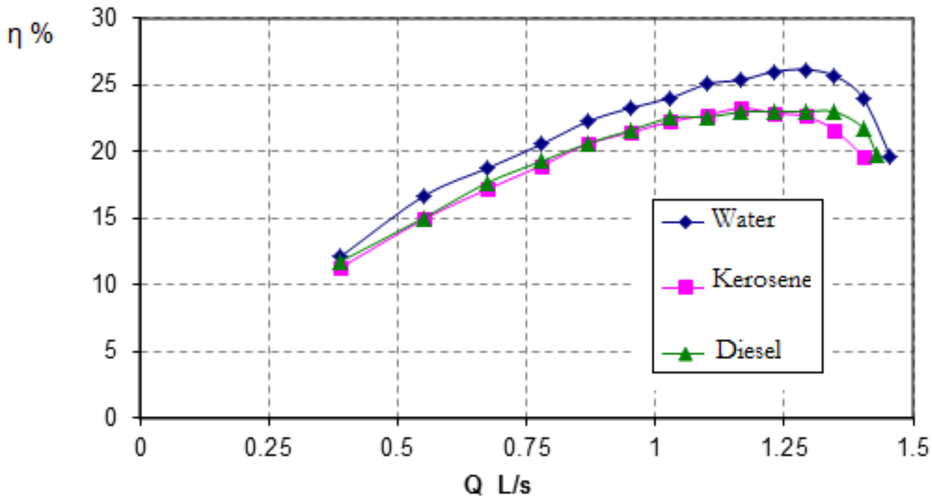

Figure 8: Efficiency curves of the pump for water, Kerosene and Diesel

Figure 9 shows the NPSH of the pump in the case of water, kerosene and diesel. It can be seen from the figure that the NPSH for the pump in the case of water is lower than in the case of kerosene and diesel to start in water from (8.9964 m) and then gradually decrease to (2.4208) m), as well as in the case of kerosene and diesel from (11,019 m), (10.9479 m) respectively, and then start to decrease to (4.9136 m), (4.3899 m), respectively.

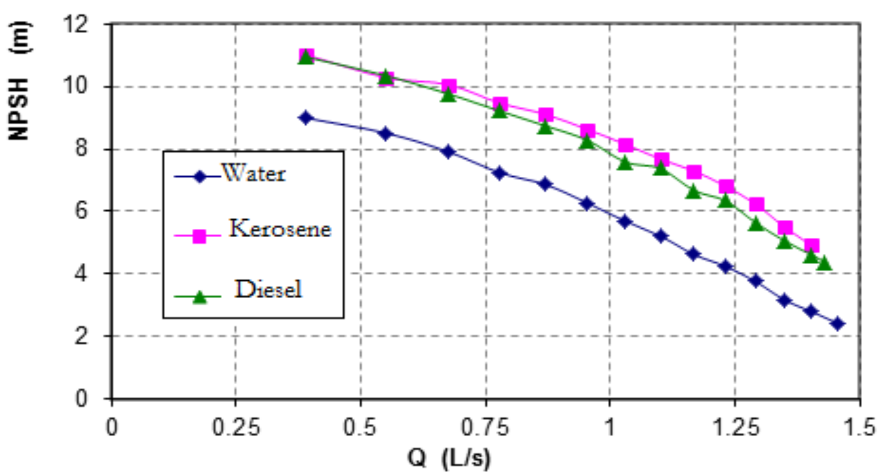

Figure 9: NPSH curves of the pump for water, Kerosene and Diesel

5. Conclusions

Experimental was conducted for different flow rates, and with different liquids, these results are presented for a centrifugal pump operating in water, kerosene and diesel fuel with different disposal rates of flow, to examine the effect of liquid viscosity and density on cavitation behaviour. Based on the experimental results, the water has affected by the cavitation at less Net Positive Suction Head (NPSH) than other liquids, also it can be conducted that the kerosene shares the closest cavitation behaviour with diesel fuel. Therefore, the stress produced by cavitation bubbles decreases with increase of viscosity of the liquid.

References

[1]. Al-Hashmi, S, Gu, F,Li, Y, Ball, A,Fen, TandLiu, "Cavitation detection of a centrifugal pump using instantaneous angular speed," ASME 7th Biennial Conference on Engineering Systems Design and Analysis, vol. 3Manchester, England, July 19–22, 2004, pp. 185-190.

[2]. Ahmed A. B. Al-Arabi andSobeih M. A. Selim, "Reality of Cavitation Inception in Centrifugal Pumps," 8th Internal Conference on Sustainable Energy Technologies; Aachen, Germany 31th August – 3rd September, 2009, pp 1-11.

[3]. Schiavello B., Visser F C, "Pump Cavitation-Various NPSHR Criteria, NPSHA Margins, and Impeller Life Expectancy," Proc. of the 25th Int. Pump Users Symp.(Houston, Tex, 23-26 Feb) 2009, pp 113-144

[4]. Spraker W. A. "The Effects of Fluid Properties on Cavitation in Centrifugal Pumps." J. Eng. Power, vol. 87, no. 3, July 1965, pp. 309-318.

[5]. Maxime Binama, Alex Muhirwa, Emmanuel Bisengimana. "Cavitation Effects in Centrifugal Pumps- A Review" Binama Maxime. Int Journal of Engineering Research and Applications, vol. 6, Issue 5, (Part-1)May 2016, pp.52-63.

[6]. M. A. Hosien,S. M. Selim., "Experimental study of cavitation criterion in centrifugal pumps". J Visual 2013; 16:99–110.

Effects of Spring Stiffness on Suspension Performances Using Full Vehicle Models

M. Hamed[1], M. Elrawemi[1], F. Gu[2], and A.D.Ball[2]
[1]moamar.ehmied@gmail.com, [2] alxme9@gmail.com , [2] f.ga@hud.ac.uk
[1] Mechanical and Industrial Engineering Department, College of Engineering, Elmergib University, Libya
[2]Centre for Efficiency and Performance Engineering, University of Huddersfield, UK

ABSTRACT

Suspension system has significant influence on the passenger safety, providing comfortable ride, stability, and handling of the vehicle. The aims of the present research are to investigate and quantify the effect of spring weakness on suspension performance. This is based on a MATLAB simulation analysis of a seven degree-of-freedom (7-DOF) model for a full vehicle. In the simulation, the suspension faults were seeded by reducing the spring stiffness by 25%, 50% and 80%. The model was validated using experimental data, collected by driving the vehicle across bumps.

The simulation results for varying degrees of spring stiffness indicated that the ride comfort was decreased as the spring stiffness was increased for excitation frequencies close to resonant frequencies of the vehicle body (approximately 1 Hz). As spring stiffness was increased at excitation frequencies below 1 Hz, the suspension travel was reduced. Within the zone of resonant frequency of sprung mass, the deformation amplitudes were increased as the spring stiffness increased. Moreover, Frequency Response Functions analysis has been used for fault detection of reduction of spring's stiffness by 25%, 50% and 80%.

Keyword— Ride comfort; Road handling; vehicle stability; Vibration measurement; spring stiffness.

1. Introduction

The main function of suspension system is to support and carry the vehicle weight, to protect drivers and passengers from vibrations, and to maintain significant contacts between the tyre and the road surface [1]. For vehicles, it is a difficult challenge to consistently maintain a high standard of ride comfort and vehicle handling under a range of driving conditions. Between October 2010 and September 2011, the Ministry of Transport (M.O.T) collected data [2] in the UK in respect of MOT tests for approximately 24.2 million vehicles. These data was illustrates that lighting and signalling problems accounted for the highest number of re-tests (19.79%), followed by suspension faults (13.18%) and 8.75% (the fourth most common fault) were tyre faults. Early detections of abnormal events in automotive suspension systems can reduce the damage caused to the vehicle in driving situations, in addition to improving passenger comfort and security. The performance of a vehicle is often downgraded due to the appearance of faults with the suspension [3]. The common faults associated with suspension components are damaged or leaking shock absorbers, spring weakness, wearing down of the pivot and bushing and damage to the main support member assembly, as shown in Figure 1.

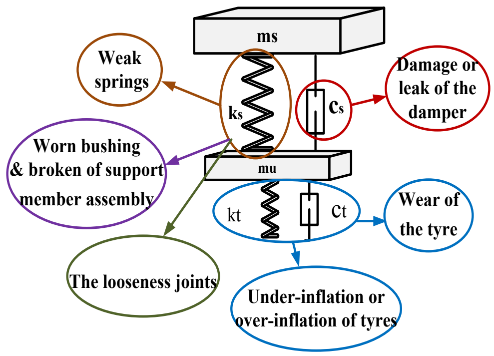

Figure 1: common faults in suspension systems

Faults occurring in the damping system can be as a result of one or more of the following factors: worn seals, a reduction in the oil volume due to leakages, broken mounts and extruded or worn bushings. All of the aforementioned causes can lead to a decline in the performance of the shock absorber, resulting in longer braking distances. This then causes the tyres to wear away reducing the car handling during cornering [4].

In order to study the performance of the suspension in terms of ride quality, handling and stability of the vehicle, some important parameters must be considered. These parameters are: wheel deflection, suspension travel and the vehicle body acceleration, with the aim of achieving a small amplitude value for each of the same [3]. Road handling is associated with the relative displacement between the suspension and the road input (Zu - Zr). This is represented as wheel deflection. Suspension travel is defined as the relative displacement between the vehicle body and the wheel (Zs – Zu). This can be used for assessing the space required to accommodate the suspension spring. Ride comfort is related to the vehicle body motion sensed by the passenger. This requires the acceleration of the vehicle body (sprung mass) to be relatively small. According to ISO: 2631-1-1997[5] proper road handling must be in the region of 0.0508 m, whilst the standard value for suspension travel must be in the region of 0.127m (as a minimum value). The passenger is thought to feel highly comfortable if the RMS acceleration is below 0.315 m/s2.

A number of researchers have investigated suspension performance using modelling/simulation and experimental investigation. Faheem [6] investigated a mathematical model for a quarter car with 2-DOF and a half car with 4-DOF. Rao[7] developed a mathematical model of a 3-DOF quarter car with a semi-active suspension system. This model was used for the testing of skyhook and other strategies involving semi active suspension systems. Esslaminasa et al [8] developed a semi-active twin-tube shock via the modelling of one and two DOF, for a quarter car design. Darus [9] adopted a state space approach in developing a mathematical model for both a quarter car and a full car using MATLAB packages. Metallidis [10], applied a statistical system identification technique to perform parametric identification and fault detection of nonlinear vehicle suspension systems. Kashi [11] applied model-based fault detection on a vehicle control system, which relied on mathematical descriptions of the system, yielding robust fault detection and an isolation of faults affecting the system. Agharkakli et al [12] presented a mathematical model for passive and active quarter car suspension systems. Ikenaga et al [13]conducted a research study to improve road handling and ride comfort. An active suspension control system was presented based on a full vehicle model which included the performance of the suspension system. Lu et al [14]discussed the effect of truck speed on shock and vibration levels indicating that the effect of truck speed on the root mean square acceleration of the vibrations, were strong at a lower speed but weak at a higher speed.

Sekulic et al[15] present a research to study the effects of spring stiffness and shock absorber damping on the vertical acceleration of the driver's body, suspension deformation and dynamic wheel load, with the purpose to define recommendations for selecting oscillation parameters while designing the suspension system of a (intercity) bus. Results of this research indicated that, the parameters which ensured good rid comfort of the driver were conflicting with the parameters which ensured the greatest stability of the bus and the corresponding wheel travel. Breytenbach [16] discussed the ride comfort versus handling argument for off-road vehicles. This research investigated a new approach of a semi-active suspension mode called "4 State Semi-active Suspensions", allowing a switch between low and high damping.

The objective of the present research is to investigate the effect of spring weakness on suspension performance, in addition to developing suspension condition monitoring based on a full vehicle mathematical model

2. Suspension System Model and Dynamics

Development of the vehicle model operates under the assumptions that the vehicle is a rigid body, represented as sprung mass (ms), and the suspension axles are represented as unsprung mass (mu) as shown in Figure 2. The suspension between the vehicle body and wheels are modelled by linear spring and damper elements and each tyre is modelled by a single linear spring and damper.

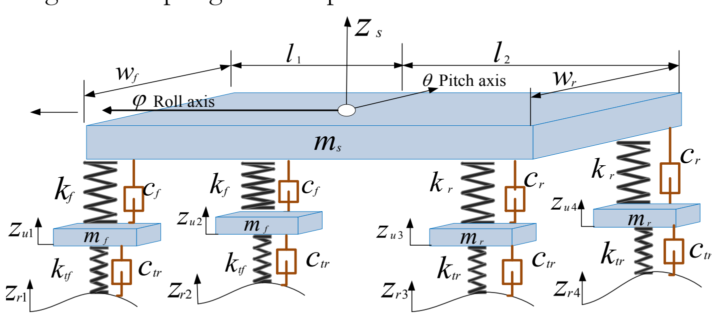

Figure 2: Full vehicle models

The equations of all motions are derived separately resulting in the equations of the body motions [8].

Equation of motion for bouncing of sprung mass:

$$ms\ddot{z}s = kf(zu1 - zs1) + kf(zu2 - zs2) + kr(zu3 - zs3) + kr(zu4 - zs4) +$$
$$cf(\dot{z}u1 - \dot{z}_{s1}) + cf(\dot{z}_{u2} - \dot{z}_{s2}) + cr(\dot{z}_{u3} - \dot{z}_{s3}) + cr(\dot{z}_{u4} - \dot{z}_{s4}) \quad (1)$$

For pitching of sprung mass

$$IP\ddot{\theta} = kfl1(zu1 - zs1) + kfl1(zu2 - zs2) - krl2(zu3 - zs3) - krl2(zu4 - zs4) + cfl1(\dot{z}u1 - \dot{z}_{s1}) +$$
$$cfl1(\dot{z}_{u2} - \dot{z}_{s2}) - crl2(\dot{z}_{u3} - \dot{z}_{s3}) - crl2(\dot{z}_{u4} - \dot{z}_{s4}) \quad (2)$$

For rolling motion of sprung mass

$$IR\ddot{\varphi} = kf\frac{wf}{2}(zu1 - zs1) - kf\frac{wf}{2}(zu2 - zs2) + kl\frac{wr}{2}(zu3 - zs3) - kr\frac{wr}{2}(zu4 - zs4) + cf\frac{wf}{2}(\dot{z}_{u1} - \dot{z}_{s1}) -$$
$$cr\frac{wf}{2}(\dot{z}_{u2} - \dot{z}_{s2}) + cr\frac{wr}{2}(\dot{z}_{u3} - \dot{z}_{s3}) - cr\frac{wr}{2}(\dot{z}_{u4} - \dot{z}_{s4}) \quad (3)$$

For each wheel motion in vertical direction

$$m_f \ddot{z}_{u1} = -k_f(z_{u1} - z_{s1}) - c_f(\dot{z}_{u1} - \dot{z}_{s1}) + k_{tf}(z_{r1} - z_{u1}) \quad (4)$$
$$+ c_{tf}(\dot{z}_{r1} - \dot{z}_{u1})$$

$$m_f \ddot{z}_{u2} = -k_f(z_{u2} - z_{s2}) - c_f(\dot{z}_{u2} - \dot{z}_{s2}) + k_{tf}(z_{r2} - z_{u2}) \quad (5)$$
$$+ c_{tf}(\dot{z}_{r2} - \dot{z}_{u2})$$

$$m_r \ddot{z}_{u3} = -k_r(z_{u3} - z_{s3}) - c_r(\dot{z}_{u3} - \dot{z}_{s3}) + k_{tr}(z_{r3} - z_{u3}) \quad (6)$$
$$+ c_{tr}(\dot{z}_{r3} - \dot{z}_{u3})$$

$$m_r \ddot{z}_{u4} = -k_r(z_{u4} - z_{s4}) - c_r(\dot{z}_{u4} - \dot{z}_{u4}) + k_{tr}(z_{r4} - z_{u4}) \quad (7)$$
$$+ c_{tr}(\dot{z}_{r4} - \dot{z}_{u4})$$

The equation variables are defined and summarized in Table 1 (adopted from [9]), along with the parameters of the suspension system. This is with the exception of the damping coefficient of the tyres for different pressures, which were adopted from [17]. Amendments were also made to some of the variables in order to meet the specifications of the vehicle used in the experiment. The road profile was calculated and created according to vehicle speeds and the height and width of the bumps by the following equation:

$$u(p) = 1/2a\sin(2\pi f_p t) \quad (8)$$

The road profile was also assumed to be a single bump with a sin wave shape. Where a is the bump height (50)

Table 1: Defines the equation variables and parameters of suspension

Variables	Definition	Units	variables	Definition	Units
ms= 1200	Sprung mass	Kg	wf=90	Front vehicle width	m
mf=90	Unsprang mass	kg	wr=1.70	Rear vehicle width	m
kf=36279	Front spring stiffness	N/m	Zs≤0.06	Displacement of the vehicle body	m
kr=19620	Rear spring stiffness	N/m	zu1-zu4≈0.0508	Displacement of each wheel	m
cf=3924	Front damper coefficient	Nm/sec	Ir=5340	Roll and pitch of moment of inertia	$Kg.m^2$
cr =2943	Rear damper coefficient	Nm/sec	Ip =6430	Pitch of moment	$Kg.m^2$

3. Experimental Set up and Test Procedure

To validate the theoretical model, a front wheel drive Vauxhall ZAFIRA (2001) car, equipped with two different sensors was used. The sensors mounted on the car include: (1) a vibration sensor with a sensitivity of (3.770 pc/ms-2) mounted on the upper mounting point of the front left shock absorber, and (2) a dynamic tyre pressure sensor (DTPS) with a sensitivity of (11.43 Pc/0.1Mpa) connected to the valve stem of the front left wheel. The pressure sensor was situated in the centre rim of the front left wheel and the vibration sensor on the inside of the car. They were placed in these positions after being assembled and connected to the wireless sensor nodes (transmitters).The gateway (receiver) was equipped with a laptop inside the car. In order to ensure a sound installation of the sensors, two different adapters were designed and manufactured at the University of Huddersfield. In addition to this, a wireless measurement system was also designed and installed on the car, to offer a complete remote measurement for the vibration and pressure data being extracted.

The most fundamental aim of the test was to obtain the acceleration (vibration) response of the suspension system to validate the model and also to enable a thorough analysis of the effects that different spring rates have on the performance of the suspension system. The test was conducted with the standard tyre pressure (2.3bar) and a vehicle speed of 8km/h.

4. Results and Discussion

The model was validated using experimental data collected when the vehicle was being driven, at a speed of 8km/h, over Bump 1 (located within the premises of The University of Huddersfield. The bump profile was 5.80 m width, 0.50 m length and 0.050 m height and this was assumed to be the input for the system.

MATLAB software was used to analyze the vehicle response. Figure 3 depicts the acceleration of the vehicle body in the time domain based on the model simulation and experiments. Upon a comparison of the experimental results, it can be noted that the model fairly predicts the suspension performance.

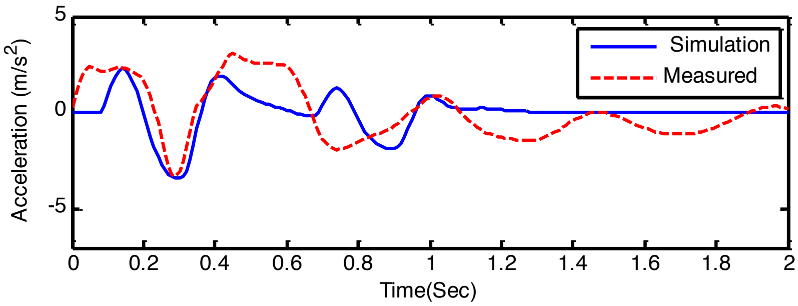

Figure 3: Vibration (acceleration) of suspension simulation and experimental

Figure 4(a) shows the plots of the road profile in the time domain for both the front and rear wheels of the vehicle. For the simulation study, road disturbance is assumed to be the input for the system. Figure 4(b) shows the effect of varying the spring rates on the vehicle body response. From these results, it was observed that decreases in spring stiffness causes a resultant decrease in the amplitude of the relative displacement of the car body. Figure 5 depicts the displacement of four wheels (unsprung mass) with different spring stiffness in the time domain. The results show that the amplitude/peak value of the wheels decreases with a corresponding decrease in the stiffness value. This indicates that the performance of the suspension may be affected by the changes made to the spring stiffness.

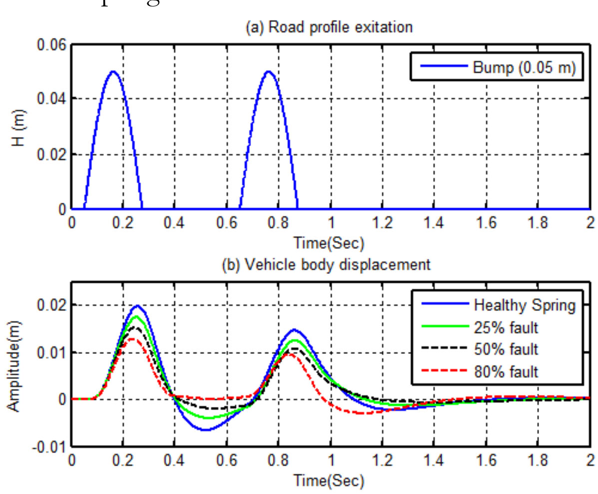

Figure 4 (a): Road profile excitation and **Figure 4 (b):** Displacement of vehicle body for different spring stiffness.

An analysis of different parameters such as: wheel deflection, suspension travel and acceleration of the vehicle body was carried out in order to consider the different effects the spring stiffness level has on the performance of the suspension, which includes, the ride quality and handling and stability of the vehicle. The road handling profile (wheel deflection) for a vehicle is associated with the contact forces between the road surface and the vehicle tyre (zu – zr).

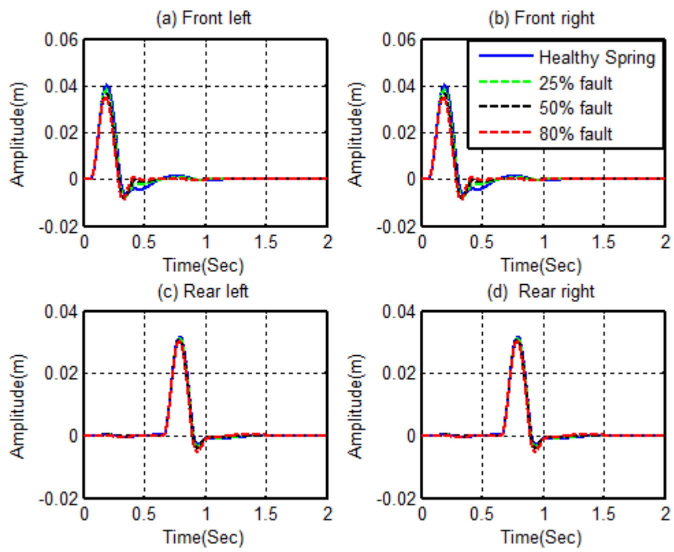

Figure 5: Vehicle wheel's displacement with different spring stiffness

For this simulation, the wheel deflections were approximately 0.015 m, 0.012 m, 0.008 m and 0.006 m for a healthy, 25%, 50%, 80% faulty spring respectively, as presented in Figure 6. From this figure, a noticeable change in the peak value of the wheel deflection can be observed. However, it can be noted that the vertical deflection does not decay quickly with the healthy spring, in particular, those with healthy and 25% faults. When compared with proper road handling as per ISO: 2631-1-1997 [4] (which must be in the range of m) this range is acceptable.

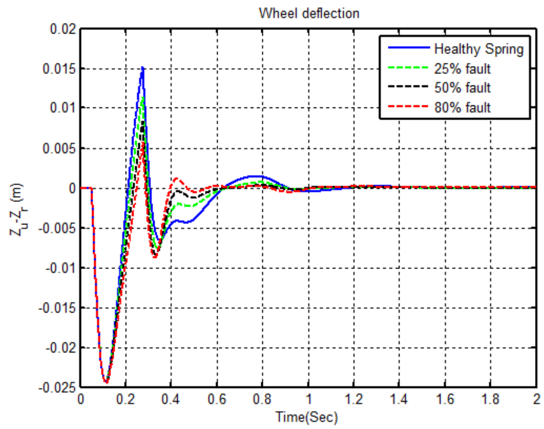

Figure 6: Wheel deflections for different spring stiffness

The suspension travel can be defined as a relative displacement between the vehicle body and the wheel (zs – zu) as shown in Figure 7. From this figure, it can be observed that lower spring stiffness provides for a lower suspension travel therefore to reduce the suspension travel a soft spring is required. In accordance with ISO: 2631-1-1997 [4] the passenger is thought to feel highly comfortable if the RMS acceleration is below 0.315 m/s^2.

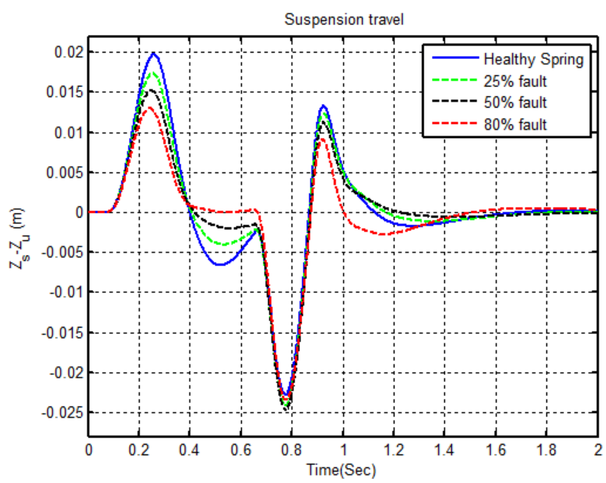

Figure 7: Suspension travel for different spring stiffness

In Figure 8 the amplitudes of the vertical acceleration were increased within the domain of the vehicle body (sprung mass) as the spring stiffness was increased. Lower values for the spring stiffness provided better oscillatory comfort for the passenger at excitation frequencies approximating the resonant frequency of the vehicle body. However, the vertical acceleration decays quickly with the reduction of the stiffness.

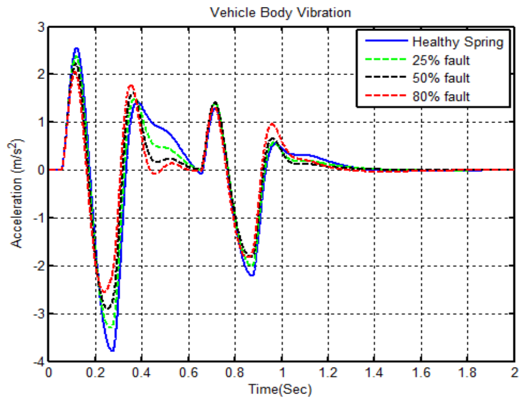

Figure 8: Acceleration of the vehicle body for different spring stiffness

To develop conditioned monitoring tools for suspension faults, detect the level of spring stiffness and also to predict potential suspension faults which may arise in the future, the Frequency Response Function (FRF) technique was used. The FRF is a fundamental measurement that isolates the inherent dynamic properties of a mechanical structure and also describes the input-output relationship between two points on a structure as a function of frequency. Figure 9 shows the amplitude-frequency characteristic curves for the changes to the spring stiffness of the suspension in four different output cases (vehicle body vertical displacement, vehicle body velocity, displacement of front and rear wheel) and the front left road input. The results show that decreasing the stiffness affects and reduces the value of the suspension displacement at the sprung mass natural frequency. A change in the amplitudes of displacement was more significant within the domain of resonant frequency of sprung mass (around 1Hz). A change of spring stiffness did not produce any effect on the change of the displacement and velocity of the vehicle body within the domain of resonant frequency of unsprang mass of the vehicle (around 10 Hz). However, the area under the curve does not necessarily decrease with a reduced peak value of the suspension displacement. From this, it can be concluded that in the frequency range close to the natural frequency of the vehicle body, a soft stiffness is required. However, lower stiffness also affects and produce vibrations in the mid- to high frequency range as shown in the front wheel responses.

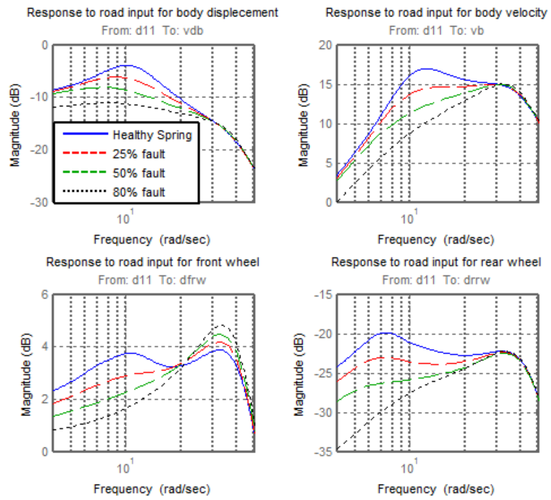

Figure 9: Transfer function response for the vehicle body and vehicle wheels

5. Conclusions

After collecting the relevant data using the full vehicle model, an analysis of the findings illustrates the effects on suspension performance when applying a range of spring stiffness. MATLAB was used to develop the full vehicle model with 7-DOF. Following this, analyses were carried out on the time and the frequency response of the vehicle. The analyses focus on the performances of the suspension in terms of ride comfort, road handling and stability of the vehicle. This study considered the faults of spring stiffness which were simulated by reducing the spring stiffness by 25%, 50% and 80%.

The simulation results indicated that the various parameters of suspension performance such as, ride comfort, road handling and vehicle stability need a design optimization due to the need to balance their conflicting requirements. For instance, the simulation results for varying of spring stiffness indicated that the ride comfort was decreased as the spring stiffness was increased for excitation frequencies close to resonant frequencies of the vehicle body (approximately 1 Hz).

FRF results show that, decreasing the stiffness affects and reduces the value of the suspension displacement at the sprung mass natural frequency. A change in the amplitudes of displacement was more significant within the domain of resonant frequency of sprung mass (around 1Hz). A change of spring stiffness did not produce any effect on the change of the displacement and velocity of the vehicle body within the domain of resonant frequency of unsprang mass of the vehicle (around 10 Hz). It can be concluded that, FRF methods can be effectively used for fault detection of suspension system.

References

[1]. B. K. N. Rao, Handbook of condition monitoring. Oxford, UK: Elsevier Advanced Technology, 1996.

[2]. H. John, "Good Garages | Honest John."

[3]. B. L. Zohir, "Ride Comfort Assessment in Off Road Vehicles using passive and semi-active suspension."

[4]. T. Weispfenning, "Fault Detection and Diagnosis of Components of the Vehicle Vertical Dynamics," Meccanica, vol. 32, no. 5, pp. 459–472, Oct. 1997.

[5]. A. Mitra, N. Benerjee, H. Khalane, M. Sonawane, D. JoshI, and G. Bagul, "Simulation and Analysis of Full Car Model for various Road profile on a analytically validated MATLAB/SIMULINK model," IOSR J. Mech. Civ. Eng. IOSR-JMCE, pp. 22–33.

[6]. Ahmad Faheem, Fairoz Alam, and V. Thomas, "The suspension dynamic analysis for a quarter car model and half car model," Dec-2006.

[7]. R. Rao, T. Ram, k Rao, and P. Rao, "Analysis of passive and semi active controlled suspension systems for ride comfort in an omnibus passing over a speed bump," Oct-2010.

[8]. N. Eslaminasab, M. Biglarbegian, W. W. Melek, and M. F. Golnaraghi, "A neural network based fuzzy control approach to improve ride comfort and road handling of heavy vehicles using semi-active dampers," Int. J. Heavy Veh. Syst., vol. 14, no. 2, pp. 135–157, Jan. 2007.

[9]. R. Darus and Y. M. Sam, "Modeling and control active suspension system for a full car model," in 5th International Colloquium on Signal Processing Its Applications, 2009. CSPA 2009, 2009, pp. 13–18.

[10]. P. Metallidis, G. Verros, S. Natsiavas, and C. Papadimitriou, "Fault Detection and Optimal Sensor Location in Vehicle Suspensions," J. Vib. Control, vol. 9, no. 3–4, pp. 337–359, Mar. 2003.

[11]. K. Kashi, D. Nissing, D. Kesselgruber, and D. Soffker, "Diagnosis of active dynamic control systems using virtual sensors and observers," in 2006 IEEE International Conference on Mechatronics, 2006, pp. 113–118.

[12]. A. Agharkakli, G. Sabet, and A. Barouz, "Simulation and Analysis of Passive and Active Suspension System Using Quarter Car Model for Different Road Profile," Int. J. Eng. Trends Technol.-, vol. 3, no. 5, 2012.

[13]. K. B. Arıkan, Y. S. Ünlüsoy, İ. Korkmaz, and A. O. Çelebi, "Identification of linear handling models for road vehicles," Veh. Syst. Dyn., vol. 46, no. 7, pp. 621–645, Jul. 2008.

[14]. F. Lu, Y. Ishikawa, H. Kitazawa, and T. Satake, "Effect of vehicle speed on shock and vibration levels in truck transport," Packag. Technol. Sci., vol. 23, no. 2, pp. 101–109, 2010.

[15]. D. Sekulic and V. Dedovic, "The Effect of Stiffness and Damping of the Suspension System Elements on the Optimisation of the Vibrational Behaviour of a Bus," Int. J. Traffic Transp. Eng., vol. 1, no. 4, Dec. 2011.

[16]. B. Breytenbach and P. S. Els, "Optimal vehicle suspension characteristics for increased structural fatigue life," Dec. 2011.

[17]. J. Y. Wong, Theory of Ground Vehicles. John Wiley & Sons, 2001.

Influence of Coolant Concentration on Surface Roughness during Turning of Steel C-60

[1]Abdulaziz Abodena, [2]Muhannad Alrzage, [3]Ibrahim K. Husain
[1]abodena65@gmail.com, [2]muhannad.alrzage@gmail.com, [3]ibrahimzg@yahoo.com
[1]Faculty of Engineering, University of Gharyan, University, Libya
[2]Faculty of Engineering, University of Gharyan, University, Libya
[3]Advanced Center of Technology, Tripoli, Libya

ABSTRACT

During recent years, considerable attention has been paid to the during turning operations, to improve forming the outer layer, such as surface cooling which enhances some of the surface characteristics and producing a good surface finish. In this experimental work, the effect of cutting fluid concentrations on surface roughness has been studied because of its importance in the cutting process. The general aim of the work in this paper was to investigate the surface roughness of the work piece when machining high carbon steel with tungsten inserts during wet machining conditions. In the experimentation, five different velocities, five feeds, five depths of cut and five coolant-oil content percentages were used to evaluate the surface roughness with these parameters. Design of experiments is a very efficient method for developing valuable research while saving time in the process. The technique used in this study for designing experiments was introduced by Box and Hunter. A rotatable factorial design of experiments with a central composite of second order can be used to enhance the reliability of investigation work. The package of design of experiments and analysis of variance used in this study has been used widely in experimentation work. The tests were performed using a traditional lathe machine. The results of this process were obtained, analyzed, and discussed using three-dimensional relationships between roughness and the cutting parameters mentioned above. The conclusions from this work show a general trend for a decrease in surface roughness as the percentage of oil in the coolant increases.

Keyword— Turning, surface roughness, cutting fluids.

1. Introduction

The nature of the surface region generated in metal machining may be quite different from that of bulk material. The surface may contain topographical features such as surface roughness. The subsurface may contain other features in the form of residual stress, plastic deformation and variation in micro structural characteristics such as hardening tempering over tempering, chemical composition and grain size [1]. Metal cutting is one of the vital processes and widely used manufacturing processes in engineering industries. Highly competitive market requires high quality products at minimum cost. Improvement of productivity with good quality of the machined parts is the main challenges of metal industry; there has been more concern about monitoring all aspects of the machining process. Surface finish is an important parameter in manufacturing engineering and it can influence the performance of mechanical parts and the production costs[2]. During recent years, considerable attention has been paid to the turning operations, to improvesforming the outer layer, such as surface cooling which enhances some of the surface characteristics and producing a good surface finish[1]. Cooling and lubrication are important in reducing the severity of the contact processes at the cutting tool-workpiece interfaces. Historically, more than 100 years ago, water was used mainly as a coolant due to its high thermal capacity and availability. Corrosion of parts and machines and poor lubrication were the drawbacks of such a coolant. Oils were also used at this time as these have much higher lubricity, but the lower cooling ability and high costs restricted this use to low cutting speed machining operations. Finally, it was found that oil added to the water gives good lubrication properties with the good cooling and these became known as the soluble oils[3, 4]. The main objective of this work is to study the effect of coolant concentration on the surface roughness of Carbon-Steel (C60) during the turning process, with other operating variables such as cutting speed, feed rate, and cutting depth, to determine the most suitable operating conditions to achieve the best surface smoothness. Even when considering the current trend towards research into minimum quantity lubrication processes, in many cases a flood of liquid is still directed over the tool with the aim of preventing the tool and workpiece from overheating, increasing tool life, and improving surface finish [5]. Selecting a suitable fluid for a particular application among the large number of commercially available fluids is an issue, and a significant challenge due to the fact it is often an empirical process.

2. Experimental work

In this study carbon steel alloy C60 was used as workpiece material. The chemical analyses, in weight percent, of this material is shown in Table (1). The material was received in the form of cylindrical bars with diameter of 60 mm and length of 70 mm.

Table 2: Chemical composition of the C60[6]

Element	Si	Mo	Cu	Mn	Ni
Weight%	max. 0.40	max. 0.10	0.61	0.75	max. 0.40

2.1. Cutting Conditions

In this work, all of cutting tests are performed under lubricated conditions on (Al-pin 180N) type model of the lathe machine. In order to study in depth the effects of each parameter on the surface characteristics of workpiece, four cutting parameters were chosen namely; oil concentration, cutting speed, feed and cutting depth. The values of the actual and coded variables of the testing condition are listed in the following table

Table 3: Coding of cutting test Parameters

Parameters	Symbol	Levels				
		-2	-1	0	1	2
Coolant composition (%)	X_1	3	6	9	12	15
Speed, (m/min)	X_2	56	120	150	412	840
Feed (mm/rev)	X_3	0.055	0.09	0.18	0.3	0.4
Depth of cut (mm)	X_4	0.2	0.6	1	1.4	1.8

2.2. Design of Experiments

Traditional experimentation involves considerable effort and time, particularly when a wide range of investigation work is needed. Design of experiments is a very efficient method for developing valuable research while saving time in the process and for achieving results in a much more economical manner. As a rule, an experiment designed to find the optimum condition of a process is described adequately by a second order polynomial. The technique used in this study for designing experiments was introduced by box and Hunter.

Experimental work involves the study of the relationships between different factors at different levels and a certain response and this is where the design of experiments technique is helpful. There is a big opportunity to study the individual effects of each parameter and their interactions using the factorial design of experiments.

The package of design of experiments and analysis of variance used in this study has been used widely in experimentation work[7, 8].The spherical variance function designs are preferable since these designs provide a constant variance for the response at all points of the experiment since they are at the same radius from the centre of the design. These kinds of designs are known as rotatable designs.

2.3. Postulation of Mathematical Model:

A functional relationship between the response surface roughness of the workpiece produced by turning process in dependent variable (oil concentration, cutting speed, cutting feed and depth of cutting) can be fitted into the following polynomial response equation of second-order.

$$Yu = b_o + b_1x_1 + b_2x_2 + b_3x_3 + b_4x_4 + b_{11\,x_1^2} + b_{22}x_2^2 + b_{33}x_3^2 + b_{44}x_4^2 + b_{12}x_1x_2 + b_{13}x_1x_3 + b_{14}x_1x_4 + b_{23}x_2x_3 + b_{24}x_2x_4 + b_{34}x_3x_4$$

where; $x_1, x_2, x_3 and\ x_4$ are the coded values of the variables. These variables are coded for convenient identification and for easy calculation.

The regression coefficients b_o,b_1, b_3, …etc can be calculated by the method of least squares using the related equations.

2.4. Analysis of Variance (ANOVA):

The relationship between the response and the cutting process parameters were quantitatively determined using empirical equations (the proposed model). The evaluation and the analysis of the experimental data were made by adopting polynomial response of second-order equations in terms of the process variables by establishing their interactions.
In the present work the variance for each of the regression coefficient is given by the related equations. The F-ratio for each term can then be determined from the variance analysis. In such an analysis, it is of interest to partition the sum of squares of the Y's into the contribution due to the first-order (Linear) term. An additional contribution due to the second-order (quadratic and interaction) terms, lack-of-fit terms (which measure the deviations of the response from the fitted surface), and the experimental error obtained from the replicated points at the center.

3. Results and Discussion

The model is developed in terms of Coolant concentration (%) cutting speed, cutting depth and cutting feed by utilizing Response Surface Methodology. As it was mentioned above, the variables are investigated using the experimental design matrix instead of the conventional one-variable at a time method. The evaluation and the analysis of the experimental data is made by adopting a polynomial response surface of second-order in terms of the process variables by establishing their interaction. The results are tested statistically using the ANOVA technique presented previously. The F-ratio test as a tool of the analysis of variance is used to check the adequacy of the model. To determine whether the final equations are a good fit to the experimental observations, the F-ratio test is carried out. The standard valued of F-ratio for the significance level a = 0.05 and degrees of freedom 4 and 6 isF0.05(4,6) = 4.53 and at degrees of freedom 10and 6 is F0.05(10,6) = 4.06.

$$\begin{aligned}\mathrm{Ra} = 0.619 + 0.708\mathrm{x}_1 - 0.882\mathrm{x}_2 + 0.98\mathrm{x}3 - 0.08\mathrm{x}4 + 2.14{\mathrm{x}_1}^2 + 2.06{\mathrm{x}_2}^2 + 0.317{\mathrm{x}_3}^2 + 0.32{\mathrm{x}_4}^2 \\ - \; 0.42\mathrm{x}_1\mathrm{x}_2 + 0.57\mathrm{x}_1\mathrm{x}_3 - 0.11\mathrm{x}_1\mathrm{x}_4 - 0.54\mathrm{x}_2\mathrm{x}_3 - 0.38\mathrm{x}_2\mathrm{x}_4 + 0.49\mathrm{x}_3\mathrm{x}_4\end{aligned}$$

3.1. Relation between roughness, oil content and speed

Cutting speed and oil content are important parameters that effect on the roughness in cutting process. The figure (1) shows the result of the effect of oil content and speed on the roughness based on the empirical equation shown up. From the figure it is noticed that there is a change in the roughness value whenever the speed and the concentration of the oil change. It was noted that when the concentration of oil and speed is at the lowest levels, the roughness is the highest levels. When the concentration of oil increased to about 9%

and the speed to about 150 m/min, it was noticed a decrease in the value of roughness until it reached its lowest value.

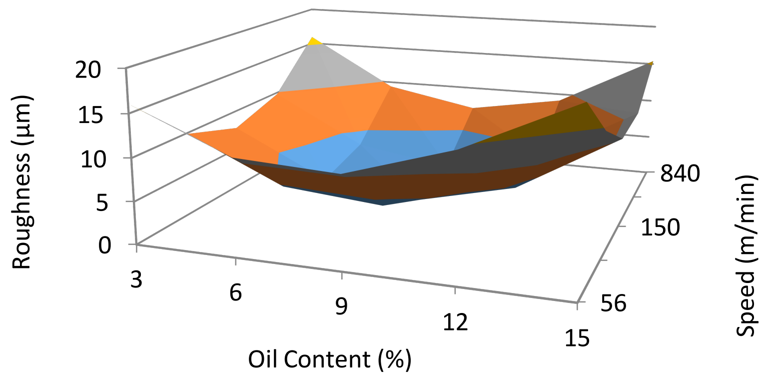

Figure 3: Relationship between roughness, oil content and cutting speed

3.2. Effect of oil content and feed on roughness

Figure (2) show the results of roughness versus different oil concentrations and cutting feed. The roughness is influenced by feed and oil concentration change. The best result of the number of smoothness is obtained at the minimum of the cutting feed and at concentration of oil about 9% used in this work.

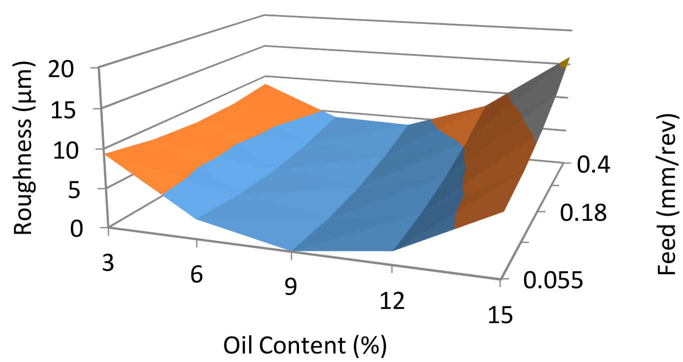

Figure 4: Relationship between roughness, oil content and cutting feed

3.3. Relationship between roughness, oil content and depth

Figure (3) shows the roughness versus different of oil content and depth of cut. The change in depth of cutting and oil content leads to change in roughness, low values of roughness is observed when oil concentrations are between 6% and 12% and the lowest value is at 9% and low depth of cut.

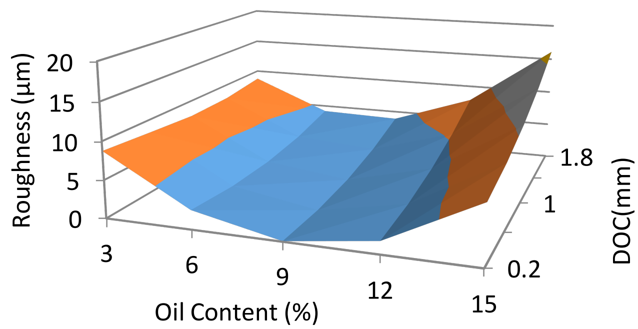

Figure 5: Relationship between roughness, oil content and depth of cutting

4. Conclusions

In this study 31 tests were made with different variables (oil concentration, cutting speed, cutting depth and feed) to reach the best value for surface smoothness. All these processes were applied to a group of samples of (C60). The following can be concluded; the results obtained from this work have shown that oil concentration has different effect on the response studied. An increase in oil concentration leads to improvement in surface finish up to a certain level. The recommended cutting feeds that result in good surface finish are from 0.055 to 0.18 mm/rev when concentration of oil is 9%.At speed of medium range 150 m/min and concentration oil of 6 to 9%, good surface finish can be obtained.

References

[1]. EL-XEER, M.E.-K.M., EFFECT OF SOME BURNISHING PARAMETERS ON RESIDUAL STRESSES AND FATIGUE LIFE 2002.

[2]. Bhavsara, H.Y.V.S.N., Experimental Investigation of Surface Roughness and Power Consumption in Turning Operation of EN 31 Alloy Steel. 2014: Elsevier Ltd.

[3]. Machado, A., The effect of extremely low lubricant volumes in machining. 1997.

[4]. McCoy, J., Tracing the historical development of metal workingfluids. 1994: New York: Marcel Dekker.

[5]. Abodena, A.M. An Investigation into the Effect of Coolants' Concentration and Cutting Conditions on the Coefficient of Friction during Turning of Aluminum 6082-T6. in 1st Conference of Industrial Technology CIT2017. 2017. Misurata.

[6]. Ravne., M. steel data. 2005; Available from: http://www.metalravne.com/selector/steels/C60.html.

[7]. Joyce, R.M., Experiment optimization in chemistry and chemical engineering, S. Akhnazarova and V. Kafarov, Mir Publishers, Moscow and Chicago, 1982, 312 pp. Price: $9.95. Journal of Polymer Science: Polymer Letters Edition, 1984. **22**(6): p. 372-372.

[8]. Allus, M.A., R.G. Brereton, and G. Nickless, The use of experimental design, multilinear regression, ANOVA, confidence bands and leverage in a study of the influence of metals on the growth of barley seedlings. Chemometrics and Intelligent Laboratory Systems, 1989. **6**(1): p. 65-80.

Seismic response of reinforced concrete buildings as predicated by the draft of Libyan standard (DSLS-1977) and (IBC-2009)

[1]Issa. A. Mohammed, [2]Suleiman. A. Khatrush
[1]eng.iessa@yahoo.com, [2]sakhatrush@gmail.com
[1]Graduate student, Department of Civil Engineering, Faculty of Engineering, Benghazi University
[2]Associate Professor, Department of Civil Engineering, Faculty of Engineering, Benghazi University

ABSTRACT

The draft of suggested Libyan Standard (DSLS-1977) is the only code of practice for designing and construction of earthquake resistant buildings in Libya, was first proposed by the Ministry of Housing in 1977, it is still used by Libyan engineers and several other foreign firms operating in Libya. The draft is suffering from many limitations and shortcomings, it has not been subjected to any development for a long period to be consistent with modern codes. DSLS-1977 divided Libya into 5 hazard zones and suggested a basic model for seismic analysis for regular buildings limited to 40 m high, suggesting linear elastic behavior of the building, and adopting the equivalent lateral force procedure associated with the fundamental mode of vibration for the determination of the resulting base shear force. The assessment and examination of the ability of DSLS-1977 for predicting an appropriate seismic forces for reinforced concrete building system was made by conducting a comparison study with the international building code IBC-2009. Special attention was made to the effect of soil structure interaction involved in the analysis when using IBC-2009 model on the resulting base shear.

Keyword— Earthquakes in Libya, seismic analysis, equivalent lateral force procedure soil structure interaction

1. Introduction

Following the earthquake of Al-Marj(1963), Dr. Minaml, the UNESCO expert in anti-seismic engineering was invited to study the damage and to submit a report on the relocation and reconstruction of the town.
In that report, Minaml also presented certain recommendations regarding the earthquake resistant regulations for design and construction of buildings and other structures in the Al-Marj region of Cyrenaica and other seismic parts of the country [1]. In 1973, a research programme was started in the civil engineering department of the faculty of engineering university of Tripoli supervised by Professor Mallick to make a seismic study of Libya and to prepare seismic zoning map. Based on the available data on the geology and tectonic structure of the country, fault location, past earthquake history and economic important of the

region, Libya has been divided into four earthquake zones, The panel of experts in the Ministry of Housing in 1977 slightly modified Mallick proposed zoning map of Libya to five zones as shown in figure.1 [2].

And producing, a first draft of a code of practice for designing and construction of earthquake resistant buildings entitled **"Criterion and practice for design and construction of earthquake resistant buildings".** denoted here as (DSLS-1977). Most of the contents of the proposed standard have been extracted from the Indian Standard Code of Practice, IS-1893-1975 [3].

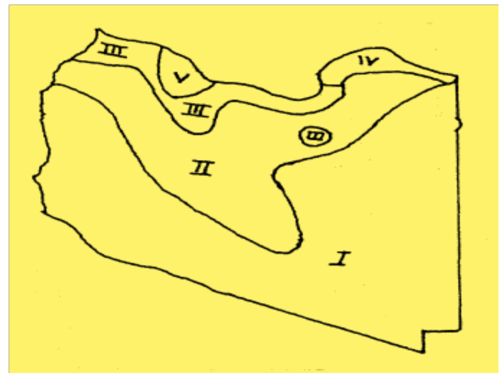

Zone	I	II	III	IV	V
Seismic coefficient	0.01	0.02	0.04	0.05	0.06

Figure.1: Seismic zoning map adopted proposed by Ministry of Housing [2].

Al-Geroushi & Ben Amir (1992) proposed a model for the development a Libyan specification for the calculation of seismic loads on the buildings named as (Garyounis model-1). They made a comparison with the proposed Libyan Specification (DSLS) , the forces obtained from the (Garyounis model-1) were found to be larger than the (DSLS) [4].

By mid -1999, a complete final first draft of IBC was assembled and ready to processed through the new procedures of the International Committee Council ICC, the first edition introduced in 2000. Subsequent IBC code editions were introduced in 2003,2006,2009 and 2012.In the IBC ,the seismic zones of the Unified Building Code UBC1997 were replaced by contour maps giving Maximum Considered Earthquake (MCE) spectral response accelerations at short period (S_s) and 1-second (S_1)for class B soil. The probabilistic MCE spectral response accelerations shall be taken as the spectral response acceleration represented by a 5% damping acceleration response spectrum having a 2% probability of ecceedance within a 50 year period.

It is aimed in this work to use the DSLS-1977 model for seismic analysis of building of reinforced concrete moment resisting frame assembly, illustrate the shortcoming in DSLS-1977 using IBC-2009 as a base code, show suitable conditions in order to use Equivalent Lateral Force Procedure of IBC-2009 applied for the Libyan case, and discuss the effect of soil condition and soil structure interaction (SSI).

2. Static analysis procedures in DSLS -1977 and IBC-2009

The several analytical methods usually adapted for earthquake analysis are mentioned in DSLS-1977, however only detailed steps of, the coefficient method employing equivalent static method ESLF is available. [2], In the IBC-2009, the American Society of Civil Engineering (ASCE7-2005) remains the primary reference for determining earthquake, snow and wind loads [5], hence the "equivalent lateral force" analysis (ELF) according to ASCE7-2005 may be applied to all structures with S_{Ds} less than 0.33g and S_{D1} less than 0.133g. as well as structures subjected to higher design Spectral response accelerations. If the structures do not meet certain requirement, more sophisticated dynamic analysis procedures must be used otherwise. Table.1 contains the required parameters to be evaluated for the application of the two codes related to the calculated steps for the evaluation of base shear in each case .

Table 1: Basic requirements of DSLS -1977 and IBC-2009 (Static Analysis)

Code	DSLS	IBC
Method	ESLF	ELF
Main equation	$V = C\,\alpha_h W$	$V = S_{DS}/(R/I)W$
Seismic Coefficient	α_0 (one value)	S_s & S_1 (contour lines)
Site class	3 Classes (TI,TII&TIII)	5 Classes (S_A, S_B, S_C, S_D & S_E)
Soil coefficient	β_0	F_a & F_v : site coefficient Table 11-4-1& Table 11-4-1
Important factor I	I	I
Time period fundamental period	$T = \frac{0.09\,H}{\sqrt{D}}$ H: height of the structure. D: dimension parallel to the applied seismic force	$T = C_t\, h_n^x$ h:height ,C_t & x: coefficient Table 12-8-2
Ductility	flexibility of the structure $C = \frac{0.50}{T^{1/3}}$	response modification factor (R) Table 12-2-1
Limitations of base shear equation	-	$Cs_{max} = S_{DS}/(R/I)$ for $T \le TL$ $Cs_{max} = S_{DS}/(R/I)$ for $T > TL$ $Cs_{min} = 0.01$
Building Height	Not exceeding 40 m	$S_{Ds} < 0.33g$ $S_{D1} < 0.133g$

Seismic weight	W: Total dead load + portion from live load to the frame defined as follow: -
	if (L.L ≤ 3 KN/m²) portion of L.L =25%
	if (L.L > 3 KN/m²) portion of L.L = 50%.
		W: Total dead load + portion from live load to the frame defined as follow: -
		in areas used for storage, a minimum of 25 % of the floor live load
		where provisions for partitions is required in the floor load design, the actual partition weight or a minimum weight of 10 psf(0.48 KN/m2) of floor area, whichever is greater

3. Application of DSLS-1977 and IBC-2009.

The assessment of Draft of Suggested Libyan Standard (DSLS-1977) is suggested to be carried out by testing its adequacy to produce comparable results with a well known code such as IBC-2009. Prior to IBC code, the Uniform Building Code (UBC 1997) was used in many countries as a code for calculating seismic forces, and Section 1653 Division III Volume II in UBC 1997 used to determine seismic zone for areas outside USA, values for seismic zone for Libya were illustrated in appendix(C) in UBC 1977 [6].

3.1. Considered spectral response acceleration

The most important factors in the use of IBC code was Ss and S_1. In this work , for the sake of comparison and since there are no mapped values available for Libya in the (IBC-2009). After searching, two methods were found to evaluate S_{Ds} and S_{D1} for the regional map of Libya [7].

Method 1

In this method the design spectral response acceleration S_{Ds} and S_{D1} can be calculated using the following equivalency relationships:-

$S_{Ds} = 2.5\ C_a$ $\quad S_{D1} = C_v$

Where : C_a and C_v = Seismic coefficients

According to appendix of chapter16 in UBC-1997 Libya and Tripoli are classified as 2A, and according to Table 16-I the seismic coefficient Z equal (0.15) from Tables 16-Q and 16-R C_a and C_v can be calculated for each soil type and then calculate S_{Ds} and S_{D1}using the equivalency relationships, the values of S_{Ds} and S_{D1} are presented in Table.2.

Table 2: Values of S_{Ds} and S_{D1} calculated by Method 1

Seismic Zone		Seismic Zone Factor Z	Soil Type	C_a	C_v	$S_{Ds} = 2.5C_a$	$S_{D1} = C_v$
TRIPOLI	2A	0.15	S_A	0.12	0.12	0.300	0.12
Section 1653 Division III Volume II UBC 1997			S_B	0.15	0.15	0.375	0.15
			S_C	0.18	0.25	0.450	0.25
			S_D	0.22	0.32	0.550	0.32
			S_E	0.30	0.50	0.750	O.50

Method 2

In this method the values of maximum considered earthquake S_s and S_1 can be obtained from those references which given values of Ss and S_1 for the location outside USA. Table G-1 in reference [8] gives values of S_s and S_1 for Tripoli illustrated in Table.3.

Table 3: Earthquake loading data at additional locations outside of the united states

Continent/Region	Country	Base/ City	Ss(%g)	S_1 (%g)	10/50* S_s(%g)	10/50* S_1(%g)
Africa	Libya	Tripoli	57.1	22.9	28.6	11.4

*10/50 it means ground motions with 10% chance of exceedance in 50 years, and the corresponding mean return period (the average number of years between events of similar severity is 500 year.

these values were used to calculate S_{Ds} and S_{D1} the results are tabulated in Table.4. The comparison between Method 1 and Method 2 are illustrated in Table .5 , it is noticed that the values calculated by method 1 are generally higher and range from 65% to 97% .

Table 4: Values of S_{Ds} and S_{D1} evaluated by method 2

10/50 S_s (%g)	10/50 S_1 (%g)	Site class	F_a	F_v	$S_{Ms}= F_vS_s$	$S_{M1}= F_vS_1$	$S_{Ds}=$ 2/3 S_{Ms}	$S_{D1}=$ 2/3 S_{M1}
		S_A	0.8	0.8	0.229	0.091	0.152	0.060
0.286	0.114	S_B	1.0	1.0	0.286	0.114	0.190	0.076
		S_C	1.2	1.69	0.343	0.192	0.228	0.128
		S_D	1.57	2.34	0.449	0.266	0.299	0.177
		S_E	2.38	2.38	0.680	0.394	0.453	0.262

Table 5: Comparison between Method 1 and Method 2 values.

	Method 1		Method 2	
Site class	S_{Ds} = 2.5 Ca	S_{D1}= Cv	$S_{Ds}=$ 2/3 S_{Ms}	$S_{D1}=$ 2/3 S_{M1}
S_A	0.300	0.12	0.152	0.060
S_B	0.375	0.15	0.190	0.076
S_C	0.450	0.25	0.228	0.128
S_D	0.550	0.32	0.299	0.177
S_E	0.750	0.50	0.453	0.262

3.2. Proposed values

In this work the values evaluated by (Method 2) are adopted. However, based on the values proposed for Tripoli and correlating them with that based on seismic zoning map adopted by Ministry of Housing 1977, using linear interpretation between the zones it became possible to propose an approximate values for the whole zones of Libya as shown in table.6.

The values proposed in this work for Libya was compatible with classification of S_s and S_1 for Region of Seismicity illustrating in reference [9] .Take into consideration Libya classifying as region of low to moderate seismic activity. Housing and Infrastructure Board and its consulting American company referred as (ACEOM) prepare a guidance document and they suggested a zoning map of Libya illustrated in figure 2., and propose a values for S_s and S_1 in each zone [10]. Table .6 showing the comparison of the proposed values in this work and those proposed (ACEOM).

Table 6: Proposed values of S_s and S_1 and comparison *with AECOM values.*

LIBYAN MAP ZONE	Values proposed in this work		Values Proposed by AECOM	
	S_s	S_1	S_s	S_1
1	0.0715	0.0285	0.06	0.02
2	0.143	0.057	0.125	0.04
3	0.286	0.114	0.25	0.08
4	0.3575	0.1425	0.31	0.09
5	0.4290	0.171	0.37	0.11

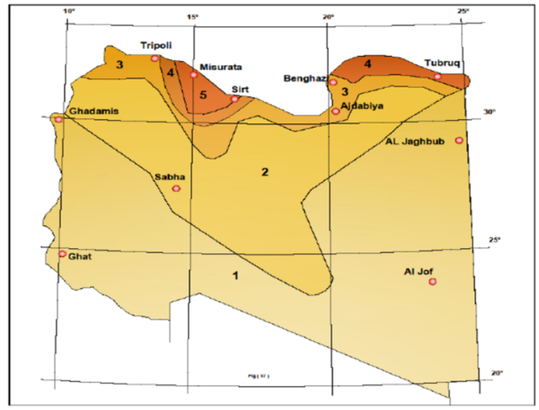

Figure 2: Libyan map and seismic zones[10].

4. Case Study

The investigated buildings are located in Tripoli and consist of a multistory reinforced concrete moment resisting frame structure, with an area 7 bays in X-direction 5m center to center and 3 bays in Y-direction 6m center to center. The plan is shown in figure. 3 and elevation heights of 5, 9 and 13 floors are shown in figure.4. The problem analyzed using both Draft of suggested Libyan standard (DSLS-1977) and the International Building Code (IBC-2009) .

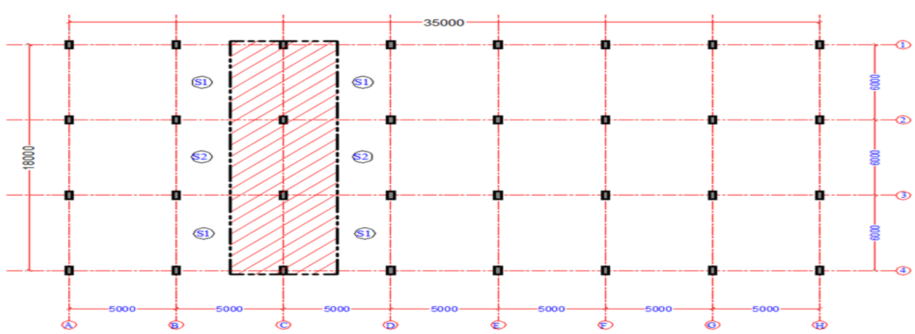

Figure. 3 : Plan configuration (all dimension in mm)

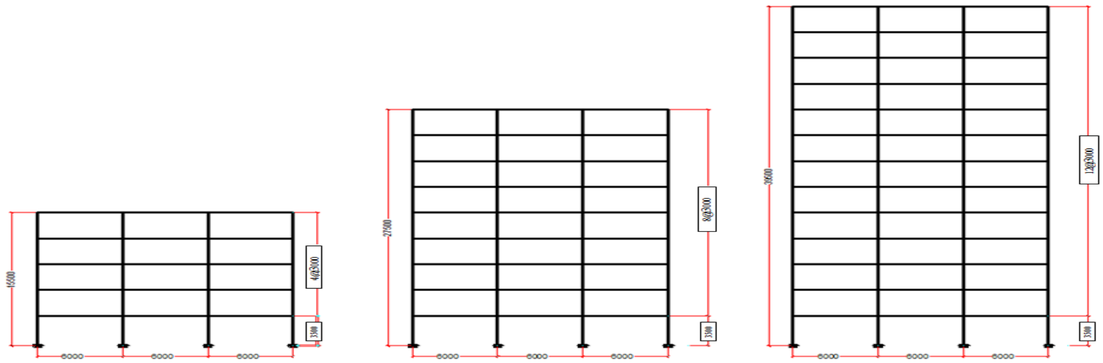

Figure .4: Elevation configuration (all dimension in mm)

4.1. Problem description

Element dimensions and planer aspect ratio are selected to satisfy the requirement of both codes for equivalent static analysis, The structures are regular in both vertical and horizontal directions consist of frame system of beams and columns supporting reinforced concrete hollow block slabs of (30 to 35cm) thick and column dimensions (25x60cm) ,(30x70cm) & (40x80cm) for 5,9 and 13 floors respectively ,the frame spacing is 5m and the type of the foundation condition adopted as raft foundation.

4.2. Site class consideration

The three types of soil in the Draft of suggested Libyan standard (DSLS- 1977), are corresponding to five types of soil in the International Building Code (IBC-2009) and presented in Table.7 and fairly matching them to allow reasonable comparison between the two codes.

Table 7: Soil type in DSLS -1977 and corresponding type in IBC-2009

DSLS- 1977		IBC -2009	
SOIL TYPE	SOIL DESCRIPTION	SOIL TYPE	SOIL DESCRIPTION
-	-	S_A	Hard rock
TYPE (I)	Rock or Hard Soils.	S_B	Rock
TYPE (I)	Rock or Hard Soils.	S_C	Very dense soil and soft rock
TYPE (II)	Medium Soils.	S_D	Stiff soil profile
TYPE (III)	Soft Soils.	S_E	Soft soil profile

5. Base shear calculations

The ground motion parameters required by the two codes for the calculation of base shear using static procedure were derived according to the governing equations previously explained. The calculations are presented in two spread sheets, Table.8 illustrating the base shear evaluated by Equivalent Static Lateral Force (ESLF) stated in (DSLS-1977), the results indicate that the resulting base shear is directly function of height of the building and no effect by the foundation soil. Table.9 illustrating the base shear evaluated by (ELF) and it can be clearly shown that the resulting base shear magnitude is a function of both building height and also significantly affected by foundation soil. A general overview of the results show that the base shear produced by IBC-2009 in all cases of greater magnitude than that predicted by DSLS-1977

Table 8: Base shear calculated by ESLF

$V_b = C\alpha hW$												
	Step 1	Step2			N	h m	Step3	Step4	Step5	Step6	Step7	Step8
CASE	α_0	Soil	Foundation system	β			T sec	C	I	$C\beta I\alpha_0$	W KN	V KN
5-Storey	0.04	T(I) Rock or Hard soils	Raft	1	5	15.5	0.5	0.6298	1.00	0.0252	34544	870
5-Storey		T(II) Meddium soils	Raft	1			0.5	0.6298	1.00	0.0252	34544	870
5-Storey		T(III) Soft soils	Raft	1			0.5	0.6298	1.00	0.0252	34544	870
9-Storey	0.04	T(I) Rock or Hard soils	Raft	1	9	27.5	0.9	0.5179	1.00	0.0207	62627	1297
9-Storey		T(II) Meddium soils	Raft	1			0.9	0.5179	1.00	0.0207	62627	1297
9-Storey		T(III) Soft soils	Raft	1			0.9	0.5179	1.00	0.0207	62627	1297
13-Storey	0.04	T(I) Rock or Hard soils	Raft	1	13	39.5	1.3	0.4582	1.00	0.0183	90710	1662
13-Storey		T(II) Meddium soils	Raft	1			1.3	0.4582	1.00	0.0183	90710	1662
13-Storey		T(III) Soft soils	Raft	1			1.3	0.4582	1.00	0.0183	90710	1662

Table 9: Base shear calculated by ELF

$V = S_{DS}/(R/I)$																							
	Step1	Step2	Step3		Step4				Step5A		Step5B		Step 6	Step 7	Step 8	Step 9						Step 10	Step 11
CASE	Occ Fac	Imp (I)	S_s	S_1	site class	Soil profil name	Fa	Fv	S_{MS}=FaSs	S_{M1}=FvS1	S_{DS}=2/3(SMS)	S_{D1}=2/3(SM1)			R	h m	Ct	x	$Tsec$	$Cs = S_{DS}/(R/I$	$Cs_{max} = S_{D1}/T(R/I)$	W KN	V KN
5-St	II	1.0	0.2860	0.1140	SA	Hard Rock	0.80	0.80	0.2288	0.0912	0.1525	0.0608	SDCB	SDCB	5	15.5	0.0466	0.90	0.5491	0.0305	0.0221	34544	765
5-St		1.0			SB	Rock	1.00	1.00	0.2860	0.1140	0.1907	0.0760								0.0381	0.0277		956
5-St		1.0			SC	Very dense soil and soft	1.20	1.69	0.3432	0.1927	0.2288	0.1284								0.0458	0.0468		1581
5-St		1.0			SD	Stiff Soil Profile	1.57	2.34	0.4490	0.2668	0.2993	0.1778								0.0599	0.0648		2068
5-St		1.0			SE	Soft Soil	2.38	3.46	0.6807	0.3944	0.4538	0.2630								0.0908	0.0958		3135
9-St		1.0			SA	Hard Rock	0.80	0.80	0.2288	0.0912	0.1525	0.0608			5	27.5			0.9200	0.0305	0.0132	62627	828
9-St		1.0			SB	Rock	1.00	1.00	0.2860	0.1140	0.1907	0.0760								0.0381	0.0165		1035
9-St		1.0			SC	Very dense soil and soft	1.20	1.69	0.3432	0.1927	0.2288	0.1284								0.0458	0.0279		1749
9-St		1.0			SD	Stiff Soil Profile	1.57	2.34	0.4490	0.2668	0.2993	0.1778								0.0599	0.0387		2421
9-St		1.0			SE	Soft Soil Profile	2.38	3.46	0.6807	0.3944	0.4538	0.2630								0.0908	0.0572		3580
13-St		1.0			SA	Hard Rock	0.80	0.80	0.2288	0.0912	0.1525	0.0608			5	39.5			1.2745	0.0305	0.0095	90710	865
13-St		1.0			SB	Rock	1.00	1.00	0.2860	0.1140	0.1907	0.0760								0.0381	0.0119		1082
13-St		1.0			SC	Very dense soil and soft	1.20	1.69	0.3432	0.1927	0.2288	0.1284								0.0458	0.0202		1828
13-St		1.0			SD	Stiff Soil Profile	1.57	2.34	0.4490	0.2668	0.2993	0.1778								0.0599	0.0279		2532
13-St		1.0			SE	Soft Soil Profile	2.38	3.46	0.6807	0.3944	0.4538	0.2630								0.0908	0.0413		3743

5.1. Consideration of soil structure interaction (SSI) by IBC code.

Buildings are subjected to different earthquake loading and behave differently with diversification in the types of soil condition. The process in which the response of the soil influences the motion of the structure and the motion of the structure influences the response of the soil is termed as SSI. In the IBC-2009, and the American Society of Civil Engineering (ASCE7-2005) a methodology for the design of building structure including the effect of soil structure interaction (SSI). The application of this methodology in sequence steps for considering the effect of SSI on base shear values using the equivalent lateral procedure (ELF), are illustrating in Table.10.

Table 10: Steps for calculating reduction in base shear

Step	Description	Formula	source
1	Previous parameters	S_{D1}, T, C_s	Table 9
2	Effective building height and weight	$\bar{h}$: the effective height 0.7 h $\bar{W}$:the effective seismic weight= 0.7 W.	Section 19.2 ASCE 7-05
3	Shear wave velocity	(Vs / Vso),	Table 19-2-1 ASCE 7-05
4	average unit weight of the soils and the average shear wave velocity	Calculated or assumed	Table 19-2-1 ASCE 7-05
5	relative weight density of the structure and soil	$\alpha = \bar{W} / (\gamma A_O h)$	Eqs 19-2-6 ASCE 7-05
6	dynamic foundation stiffness modifier for rocking	α_θ	Table 19-2-2. ASCE 7-05
7	the effective period of the structure	$\bar{T}=T\sqrt{1+\frac{25\propto r_a\bar{h}}{v_s^2T^2}(1+\frac{1.12r_a\bar{h}^2}{\propto_\theta r_m^3}}$	Eqs 19-2-5 ASCE 7-05
8	$\overline{Cs}$ using the fundamental natural period of the flexibility supported structure($\bar{T}$)	$\overline{Cs}=\frac{S_{D1}}{\bar{T}\frac{R}{I}}$	Eqs 12.8-3 ASCE 7-05
9	effective damping factor for the structure-foundation system	$\bar{\beta} = \beta_0 \frac{0.05}{(\frac{\bar{T}}{T})^3}$	Eqs 19-2-9 ASCE 7-05
10	reduction in the base shear	$\Delta V=\left[C_s-\bar{C}_s(\frac{0.05}{\bar{\beta}})^{0.4}\right]\bar{W}\leq 0.3W$	Eqs 19-2-2 ASCE 7-05
11	Reduced Base shear	$\bar{V} = V - \Delta V$	Eqs 19-2-1 ASCE 7-05

5.2. Overview of the Results and the effect of SSI.

The general overview of the resulting base shear presented in Table.11 indicate that the values of base shear calculated by IBC-2009 is mostly higher than that which is calculated by DSLS-1977. However, when SSI is considered in IBC-2009, the reduced base shear sometimes becoming lower than DSLS-1977 specifically when soil condition is hard. The values of base shear calculated by IBC-2009 increase when the type of the soil generally change from hard to soft, whereas the values of base shear calculated by DSLS-1977 are not affected by the change of ground condition, this related to the dependency only on the height of structure

(Number of floors). However, by taking the base shear values produced by DSLS-1977 as a base for comparing the difference in percent between the results of the two codes, the equation will be in the following form: -

$$\frac{\mathbf{IBC_{value}-DSLS_{value}}}{\mathbf{DSLS_{value}}}$$

The results are presented in Table 11, they indicate wider range of differences between IBC-2009 and DSLS-1977 as soil becoming weaker. The percent differences are getting lesser with increasing building height.

For 5-stories case as in **Table** 11a the percent difference is (9.89) corresponding to soil type T(I)&S_B, and gradually increases to reach (259.2) corresponding to soil type T(III)&S_E. For 9-stories case as in Table 11b the percent difference is (-19.64) corresponding to soil type T(I)&S_B and gradually increases to reach (177.95) corresponding to soil type T(III)&S_E. For 13-stories case as in Table 11c the percent difference is (-34.42) corresponding to soil type T(I)&S_B, and gradually increases to reach (126.85) corresponding to soil type T(III)&S_E. However, by considering the effect of SSI the base shear reduced by considerable amount as shown in Table.11 . For 5-storey case as in Table 11a the percent difference is (-14.88) corresponding to soil type T(I)&S_B and gradually increases to reach (152.24) corresponding to soil type T(III)&S_E. For 9-storey case as in Table 11b the percent difference is (-34.75) corresponding to soil type T(I)&S_B, and gradually increases to reach (94.57) corresponding to soil type T(III)&S_E. For 13-storey case as in Table 11c the percent difference is (-54.1) corresponding to soil type T(I)&S_B, and gradually increases to reach (58.79) corresponding to soil type T(III)&S_E, but still keeping higher values than DSLS-1977, except for hard ground condition.

Table 11a: Comparison of base shear values (DSLS-1977&IBC-2009) for 5-storey

	DSLS SOIL TYPE	BASE SHEAR DSLS-1977 (KN)	IBC SOIL TYPE	BASE SHEAR without SSI IBC-2009 (KN)	BASE SHEAR with SSI	Percent difference without	Percent difference with SSI %
			S_A HARD ROCK	765	587		
	T(I) ROCK OR HARD SOIL	870	S_B HARD ROCK	956	741	9.89	-14.88
	T(I) ROCK OR HARD SOIL	870	S_C VERY DENSE SOIL	1581	1132	81.72	30.12
	T(II) MEDIUM SOIL	870	S_D STIFF SOIL PROFIL	2068	1448	137.70	66.39
	T(III) SOFT SOIL	870	S_E SOFT SOIL PROFIL	3125	2195	259.20	152.24

Table 11b: Comparison of base shear values (DSLS-1977&IBC-2009) for 9- storey

			S_A HARD ROCK	828	580		
	T(I) ROCK OR HARD SOIL	1288	S_B HARD ROCK	1035	725	-19.64	-43.75
	T(I) ROCK OR HARD SOIL	1288	S_C VERY DENSE SOIL	1749	1224	35.79	-4.95
	T(II) MEDIUM SOIL	1288	S_D STIFF SOIL PROFIL	2421	1695	87.97	31.58
	T(III) SOFT SOIL	1288	S_E SOFT SOIL PROFIL	3580	2506	177.95	94.57

Table 11c: Comparison of base shear values (DSLS-1977&IBC-2009) for 13- storey

			S_A HARD ROCK	865	606		
	T(I) ROCK OR HARD SOIL	1650	S_B HARD ROCK	1082	757	-34.42	-54.10
	T(I) ROCK OR HARD SOIL	1650	S_C VERY DENSE SOIL	1828	1280	10.79	-22.45
	T(II) MEDIUM SOIL	1650	S_D STIFF SOIL PROFIL	2532	1772	53.45	7.42
	T(III) SOFT SOIL	1650	S_E SOFT SOIL PROFIL	3743	2620	126.85	58.79

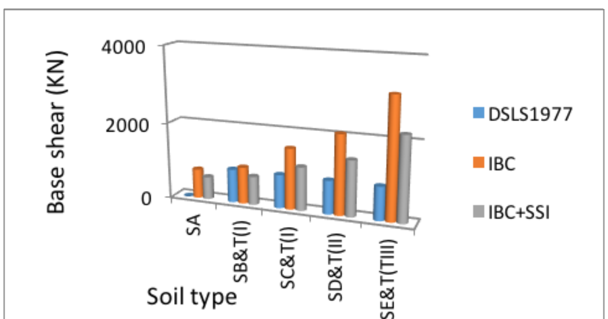

a) *Base shear by DSLS&IBC-5 storey*

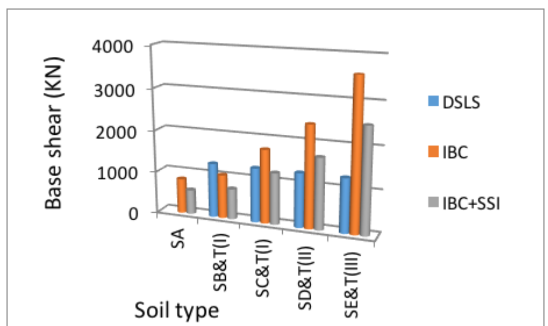

b) *Base shear by DSLS&IBC 9-storey*

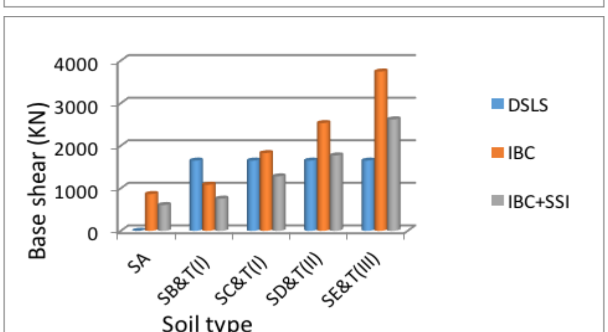

c) *Base shear by DSLS&IBC 13- storey*

Figure .5: Base shear calculation by DSLS-1977&IBC-2009 (5,9 and 13 storey)

The results are also illustrated in graphical form in figure.5 (a,b &,c). It is clearly shown that the values of base shear calculated by IBC-2009 are generally higher, and is increasing as ground condition getting softer, this is more pronounced in the cases without consideration of SSI.

6. General Discussion

The present study does not consider many factors related to structural aspects such as irregularity, ductility, structure system etc., It is essentially focused more on building height, soil condition and SSI, nevertheless, the application procedure experienced in this work for both code requirement allow us to encounter several shortcomings in DSLS-1977 that many modern codes have already overcome, such limitations could be responsible for the differences in the obtained results. The study indicate that for all the investigated cases the resulting base shear, calculated by IBC-2009 is generally higher than the values produced by DSLS-1977. Furthermore, the consideration of soil structure interaction (SSI) by the IBC-2009 has a significant effect on the reduction of base shear even though, it is limited to a maximum base shear reduction due to SSI to only 30% in order to guarantee conservative solution. Current codes and seismic provisions recognize the important rule that the soil structure interaction (SSI) can play on the seismic response of building structures [11], while in DSLS-1977 there is no addressing of SSI and the foundation soil system under the structure is rigid and hence represents a fixed base condition. The type of the soil in IBC-2009 has great influence in base shear values, while in DSLS-1977 the base shear values are not affected by the change of the soil type.

This is due to the soil condition is expressed by DSLS-1977 in terms of the factor β_o which is constant in case of raft foundation and depends only on the type of foundation rather than the type of soil.

7. Conclusion

This study investigates some aspects of the seismic response of reinforced concrete buildings, with emphasize to the effect of soil structure interaction. Special focus is made to local Libyan situation with the aim of evaluating the results obtained from the application of the proposed Libyan specification DSLS-1977, by conducting a comparison with one of the well-known specifications which widely used, specifically the International Building Code IBC-2009. The proposed Libyan specification DSLS-1977 containing many shortcomings and deficiencies, it is not considering many conditions and important factors which are necessary for conducting seismic analysis. It is not including a clear criteria of structural resisting system , structural aspect , structural configuration and soil condition. Furthermore, no consideration by DSLS-1977 for the effect of soil structure interaction SSI which regarded by the present study as very significant and having an important impact in reducing the base shear especially with low strength foundation soil.

References

[1]. Minami, Kazuo. " *Relocation and reconstruction of the town of Barce, Cyrenaica*, Libya ", damaged by the earthquake of 21 February 1963. Unesco, (1965).

[2]. Mallick, D. V., and S. Y. Barony. "*Earthquake resistant design practice in Libyan Jamahiriya*." Proceedings of the World Conference on Earthquake Engineering. Vol. 7. No. 9. publisher not identified, (1980).

[3]. Jain, Sudhir K. "*Review of Indian seismic code*, IS 1893 (Part 1): 2002." Indian concrete journal 77.11 (2003): 1414-1422.

[4]. الجروشى . رجب و بن عامر . محمد (مقترح تطوير المواصفات الليبية لحساب الأحمال الزالزالية على المبانى- نموذج قاريونس1) , المؤتمر الخامس للهندسة الانشائية , طرابلس , 27 -30 نوفمبر (1993)

[5]. Leyendecker, Edgar V., et al. "*Development of maximum considered earthquake ground motion* maps." Earthquake Spectra 16.1 (2000): 21-40.

[6]. Code, Uniform Building. "Volume 2." *Structural engineering design provisions*" (1997).

[7]. S. K. Ghosh, "Seismic ground motion values for locations outside the United States", Civil + Structural engineer. http://csengineermag.com/artic/seismic-ground-motion-values-for-locations-outside the united states.

[8]. Unified facilities criteria (UFC), "Structural Engineering", UFC 3-301-01,27 January (2010).

[9]. Department of Veterans Affairs, H-18-8, Office of Construction& Facilities Management, Strategic Management Office "Seismic design requirements." February (2011).

[10]. Guidance Document, "Design Criteria for Housing Projects, Housing and Infrastructure Board ", Program Management Department, June (2009).

[11]. Nikolettos, G. S., and C. C. Spyrakos. "*Seismic analysis and design of building structures including* SSI." WIT Transactions on The Built Environment 41 (1970).

Nonlinear Structural Dynamic Response of Multi-Story Buildings Under Seismic Loading

Awatif Othman Twil
Department of Civil and Structural, Engineering, Gharyan University, Libya
Eng_awatif@yahoo.com

ABSTRACT

A study of earthquakes in the world is performed, and also a study of methods of dynamic analysis suitable for use with linear and nonlinear systems is made with a stress on the nonlinear response of buildings due to moderate or high seismic loading.

The response of a building to a seismic load severe enough may induce inelastic deformations and the building behavior is expected to be nonlinear. Consequently, it is necessary to develop a method of analysis suitable for use with nonlinear systems. A step-by-step method is well suited to the analysis of nonlinear systems rather than using the method of superposition. The total structural response is due to each response contribution within the step. The Wilson-θ method is the step- by- step unconditionally stable method which is used for this aspect of nonlinear dynamic analysis and it is introduced in the present work.

Keyword— Large earthquake; nonlinear system; unconditionally stable.

1. Introduction

About 50,000 earthquakes occur annually over the entire earth, approximately 100 are of sufficient size to produce substantial damage if their centers are near areas of habitation. When a large earthquake occurs it may induce inelastic deformations and the building behavior is expected to be nonlinear. It is important to note that linear response analysis, whether formulated in the time domain or in the frequency domain involves the evaluation of many independent response contributions that are combined to obtain the total response. Hence, superposition technique is employed.

These methods employed only superposition method for linear systems. Neither one of them is suited for use in the analysis of nonlinear systems.

The step-by-step method is only conditionally stable and for numerical stability of the solution may require such an extremely small time step as to make the method impractical if not impossible. The Wilson-θ method serves to assure the numerical stability of the solution process regardless of the magnitude selected for the time step. For this reason, such a method is *unconditionally* stable. [1] [4] [6]

2 Linear and Nonlinear Behavior of Materials

Linear behavior is always elastic while nonlinear material behavior may be elastic or inelastic. If the spring is elastic then its force-displacement line or curve will follow the same curve, in unloading case as shown in Figures 1 and 2.

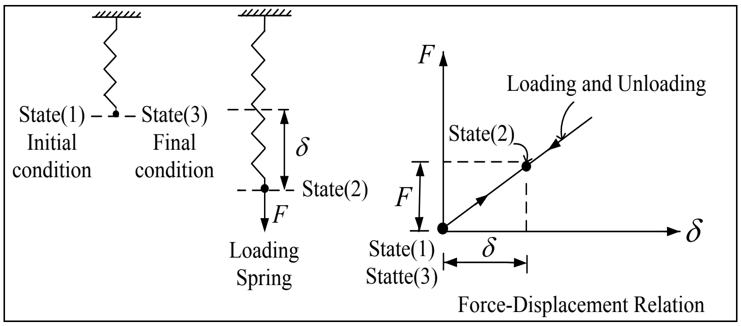

Figure 1: Linear spring: Elastic behavior

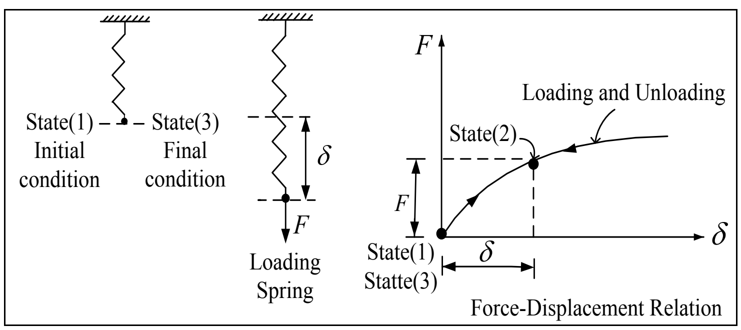

Figure 2: Nonlinear spring: Elastic behavior

If the material is inelastic and nonlinear as shown in Figure 3. Then in case of unloading, it does not follow the loading curve but follows a line parallel to the initial tangent of the loading curve. Permanent deformation δ^* will result.

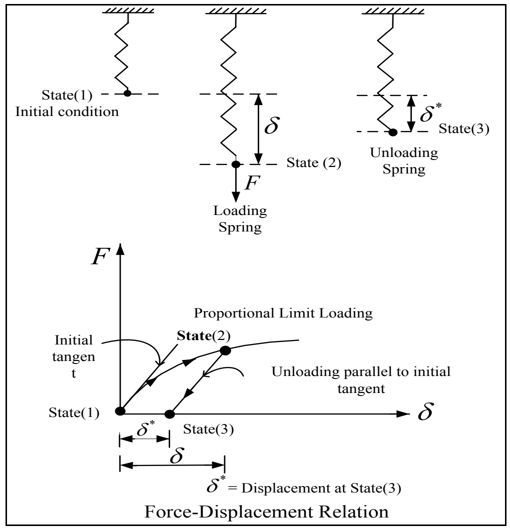

Figure 3: Nonlinear spring: Inelastic behavior

3 Linear and Nonlinear Behavior of Structures

Linear and nonlinear behavior of springs, under loading conditions are shown in the following two examples:

A. Linear Springs

Linear spring behaves linearly under loading conditions. Loading sequence is not important in case of linear material as shown in Figure 4. The resulting displacement is the same.

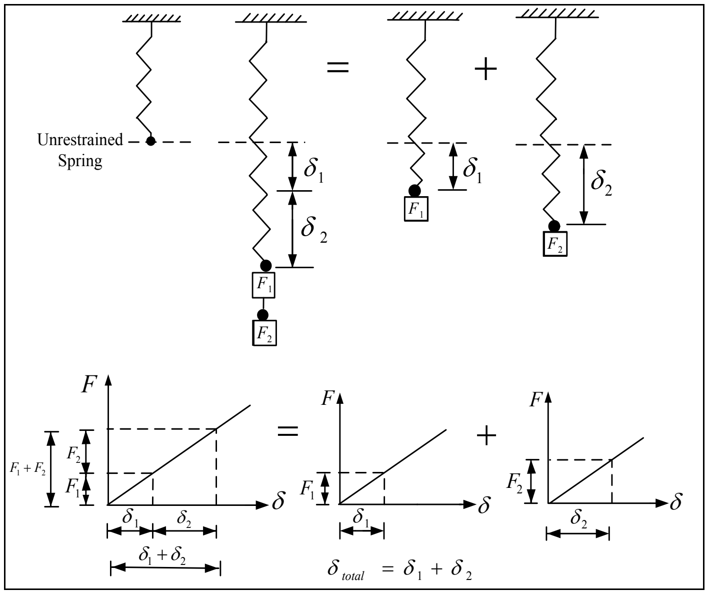

Figure 4: Superposition method applies to linear systems

Loading history is not relevant to the effect of a particular force. For example, force F_2 will always cause the same displacement δ_2 , no matter what loads are placed on the spring before it is applied.

B. Nonlinear Springs

Nonlinear spring is shown in Figure 5 the addition of loading does not result in the same effect in terms of displacements. Here, the effect of the forces F_1 and F_2 when applied together is not the same as the sum of the effects of these forces when each of them is applied separately.

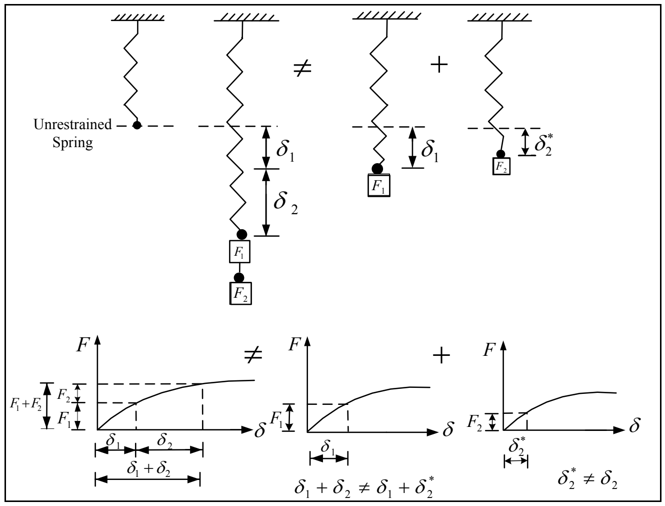

Figure 5: Superposition method does not apply for nonlinear systems

Therefore, superposition is not applicable to nonlinear springs. Loading history is relevant to the effect of a particular loading. The displacement due to a given load depends on the total force that is presently acting on a structure system or spring. Hence, superposition does not apply to nonlinear springs, which have the nonlinear force-displacement relationship.

There are many important classes of structural dynamic problems which cannot be assumed to be linear. The response of a building to a seismic load severe enough to induce inelastic deformations makes the building behavior nonlinear.

The step-by-step linear acceleration method is well suited to the analysis of nonlinear systems. The response for each time step is an independent analysis problem, and there is no need to combine response contributions within the step. This method is an explicit solution which is only *conditionally stable* and for numerical stability of the solution may require such an extremely small time step. The modification introduced to the method by Wilson serves to assure the numerical stability of the solution process regardless of the magnitude selected for the time step. For this reason, such a method is *unconditionally stable* and is suitable for this aspect for nonlinear dynamic analysis. [1] [4] [6]

4 Wilson-θ Method

The basic assumption of the Wilson-θ method is that the acceleration varies linearly over the time interval from t to $t+\theta\Delta t$ where $\theta \geq 1.0$. The value of the factor θ is determined to obtain optimum stability of the numerical process and accuracy of the solution. It has been shown by Wilson that for $\theta \geq 1.38$, the method becomes unconditionally stable. [6] [7]

Using the difference between dynamic equilibrium conditions defined at time t_i and $t_i + \tau$, where $\tau = \theta\Delta t$, we obtain the incremental equations

$$M\hat{\Delta}\ddot{u}_i + C(\dot{u})\hat{\Delta}\dot{u}_i + K(u)\hat{\Delta}u_i = \hat{\Delta}P_i \tag{1}$$

In which the circumflex over Δ indicates that the increments are associated with the extended step $\tau = \theta\Delta t$. Thus

$$\hat{\Delta}u_i = u(t_i + \tau) - u(t_i) \tag{2}$$
$$\hat{\Delta}\dot{u}_i = \dot{u}(t_i + \tau) - \dot{u}(t_i) \tag{3}$$
$$\hat{\Delta}\ddot{u}_i = \ddot{u}(t_i + \tau) - \ddot{u}(t_i) \tag{4}$$
$$\hat{\Delta}P_i = P(t_i + \tau) - P(t_i) \tag{5}$$

The stiffness coefficient and damping coefficient are obtained for each time step

$$K_{ij} = dF_{Si}/du_j \tag{6}$$
$$C_{ij} = dF_{Di}/d\dot{u}_j \tag{7}$$

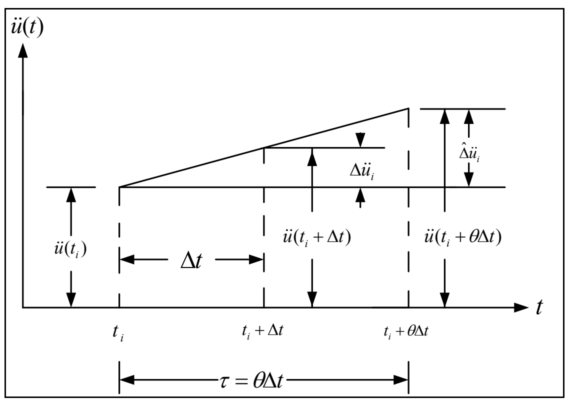

Figure 6: Linear acceleration assumption in the extended time interval.

From Figure 6, we can write the linear expression for the acceleration during the extended time step as

$$\ddot{u}(t) = \ddot{u}_i + \frac{\hat{\Delta}\ddot{u}_i}{\tau}(t - t_i) \tag{8}$$

In which $\hat{\Delta}\ddot{u}_i$ is given by (4), integrating (8) twice yields

$$\dot{u}(t) = \dot{u}_i + \ddot{u}_i(t - t_i) + \frac{1}{2}\frac{\hat{\Delta}\ddot{u}_i}{\tau}(t - t_i)^2 \tag{9}$$
$$u(t) = u_i + \dot{u}_i(t - t_i) + \frac{1}{2}\ddot{u}_i(t - t_i)^2 + \frac{1}{6}\frac{\hat{\Delta}\ddot{u}_i}{\tau}(t - t_i)^3 \tag{10}$$

Evaluation of (9) and (10) at the end of the extended interval $t = t_i + \tau$ gives

$$\hat{\Delta}\dot{u}_i = \ddot{u}_i\tau + \frac{1}{2}\hat{\Delta}\ddot{u}_i\tau \tag{11}$$

$$\hat{\Delta}u_i = \dot{u}_i\tau + \frac{1}{2}\ddot{u}_i\tau^2 + \frac{1}{6}\hat{\Delta}\ddot{u}_i\tau^2 \tag{12}$$

Equation (12) is solved for the incremental acceleration $\hat{\Delta}\ddot{u}_i$ and substituted in (11), we obtain

$$\hat{\Delta}\ddot{u}_i = \frac{6}{\tau^2}\hat{\Delta}u_i - \frac{6}{\tau}\dot{u}_i - 3\ddot{u}_i \tag{13}$$

$$\hat{\Delta}\dot{u}_i = \frac{3}{\tau}\hat{\Delta}u_i - 3\dot{u}_i - \frac{\tau}{2}\ddot{u}_i \tag{14}$$

Substituting (13) and (14) into (1), results in an equation for the incremental displacement $\hat{\Delta}u_i$ which may be conveniently written as

$$\overline{K}_i\hat{\Delta}u_i = \hat{\Delta}\overline{P}_i \tag{15}$$

where

$$\overline{K}_i = K_i + \frac{6}{\tau^2}M + \frac{3}{\tau}C_i \tag{16}$$

$$\hat{\Delta}\overline{P}_i = \hat{\Delta}P_i + M(\frac{6}{\tau}\dot{u}_i + 3\ddot{u}_i) + C_i(3\dot{u}_i + \frac{\tau}{2}\ddot{u}_i) \tag{17}$$

To obtain the incremental acceleration $\hat{\Delta}\ddot{u}_i$ for the extended interval, the value of $\hat{\Delta}u_i$ obtained from the solution of (15) is substituted into (13). The incremental acceleration $\Delta\ddot{u}_i$ for the normal time interval Δt is then obtained by a simple linear interpolation

$$\Delta\ddot{u} = \hat{\Delta}\ddot{u}/\theta \tag{18}$$

To calculate the incremental velocity $\Delta\dot{u}_i$ and incremental displacement Δu_i corresponding to the normal interval Δt use is made of (11) and (12) with the extended time interval parameter τ substituted for Δt, that is

$$\Delta\dot{u}_i = \ddot{u}_i\Delta t + \frac{1}{2}\Delta\ddot{u}_i\Delta t \tag{19}$$

$$\Delta u_i = \dot{u}_i\Delta t + \frac{1}{2}\ddot{u}_i\Delta t^2 + \frac{1}{6}\Delta\ddot{u}_i\Delta t^2 \tag{20}$$

The displacement u_{i+1} and velocity $\dot{u}_{i+1}$ at the end of the normal time interval are calculated by

$$u_{i+1} = u_i + \Delta u_i \tag{21}$$

$$\dot{u}_{i+1} = \dot{u}_i + \Delta\dot{u}_i \tag{22}$$

The initial acceleration for the next step should be calculated from the condition of dynamic equilibrium at time $t + \Delta t$, thus

$$\ddot{u}_{i+1} = M^{-1}\{P_{i+1} - C_{i+1}\dot{u}_{i+1} - K_{i+1}u_{i+1}\} \tag{23}$$

5 Earthquake Applications

El Centro of 1940 Earthquake Excitation Cases of Study

The excitation data were obtained from the acceleration original record of the first second for El Centro earthquake of 1940 shown in Table 1. And the plot of this record is shown in Figure 7. Note that the ground acceleration is varies with time in units of g, where g is the gravitational acceleration $(g = 386 in/\sec^2)$. [6]

Table 1: The acceleration record for El Centro earthquake of 1940. [6]

t, sec	$\ddot{u}_g(t), g$	t, sec	$\ddot{u}_g(t), g$	t, sec	$\ddot{u}_g(t), g$
0.000	0.1080	0.429	-0.0237	0.872	-0.0232
0.221	0.0189	0.665	0.0138	0.997	-0.0789
0.374	0.020	0.794	-0.0568	0.161	-0.0001
0.623	0.0094	0.946	-0.0603	0.332	-0.0012
0.789	-0.0387	0.097	0.0159	0.581	0.0425
0.941	-0.0402	0.291	0.0059	0.725	-0.0256
0.042	0.0010	0.471	0.0076	0.877	-0.0343
0.263	0.0001	0.72	-0.0088	1.066	-0.0666

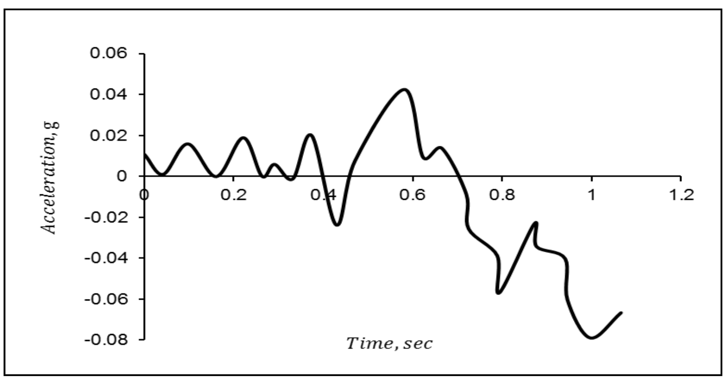

Figure 7: The acceleration record for El Centro earthquake of 1940.

Application 1: Elastic Multi Degree of Freedom System

The analysis of a two-story building system shown in Figure 8. under the effect of the same earthquake. The excitation data were scaled down from the acceleration record for El Centro earthquake of 1940 by a factor of a half, as shown in Table 1. The plastic moment for the columns on the first or second story is $M_P = 154.942 \ kip.in$.

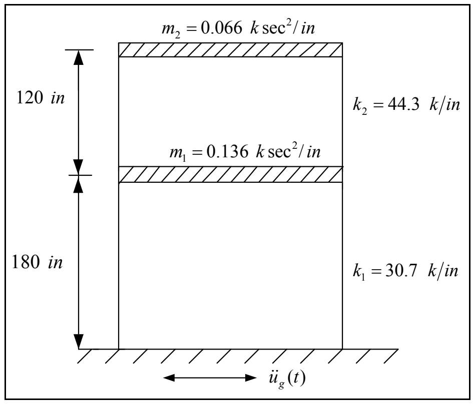

Figure 8: Two-story shear building under earthquake load.

Application 2: Elastoplastic Multi Degree of Freedom System

The analysis of a multi-story building system shown in Figure 8 with elastoplastic behavior. The input data for application (2) is the same as the input data for application (1), but the excitation data for El Centro earthquake of 1940, is used without reduction as listed in Table1.

The Wilson- θ method was used as the method of analysis for applications (1) and (2).
The results for application (1) are plotted in Figures 9 and 10 for stories (1) and (2) respectively. And for application (2) are plotted in Figures 11 and 12 for story 1 and story 2 respectively.

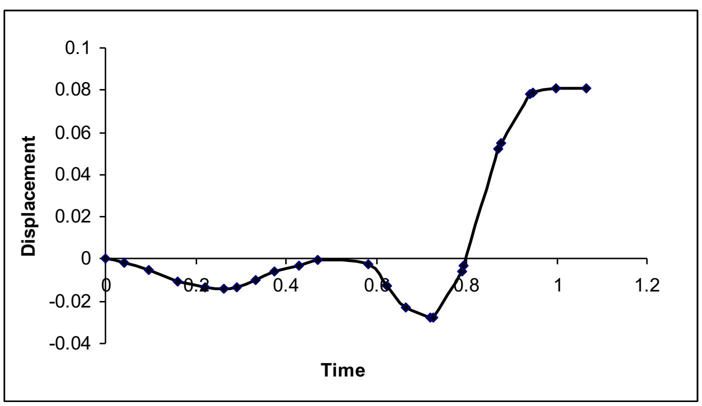

Figure 9: Displacement for earthquake application (1), elastic behavior for Story 1.

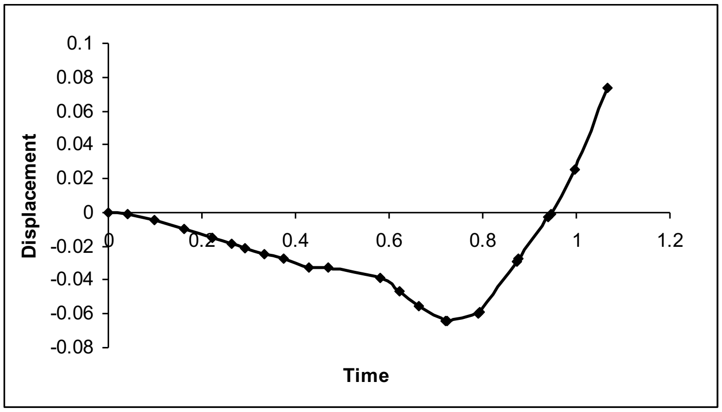

Figure 10: Displacement for earthquake application (1), elastic behavior for Story 2.

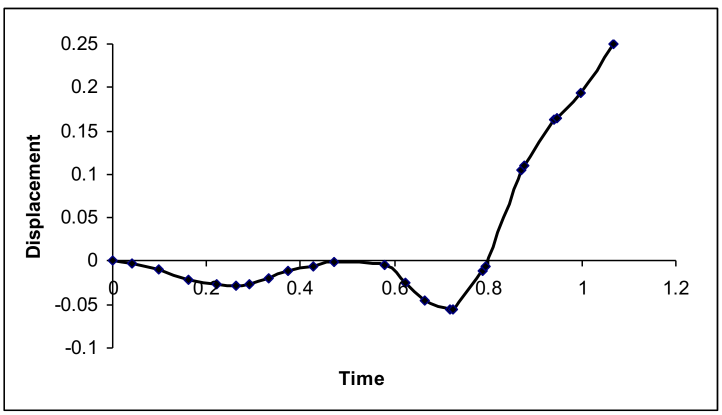

Figure 11: Displacement for earthquake application (2), elastoplastic behavior for Story 1.

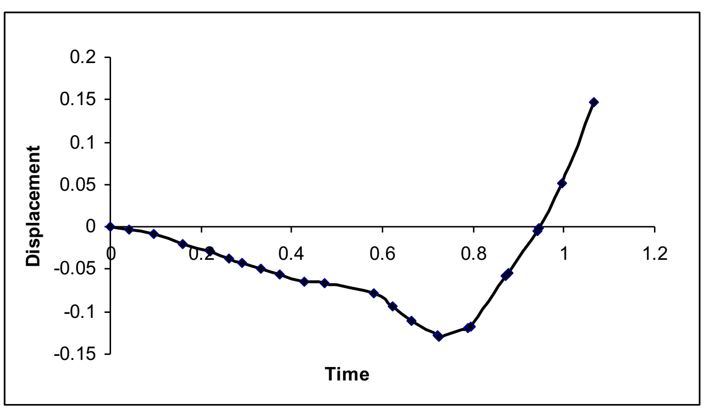

Figure 12: Displacement for earthquake application (2), elastoplastic behavior for Story 2.

Comparison between elastic and elastoplastic displacement response for story (1) and (2) are given in Figures 13 and 14 respectively.

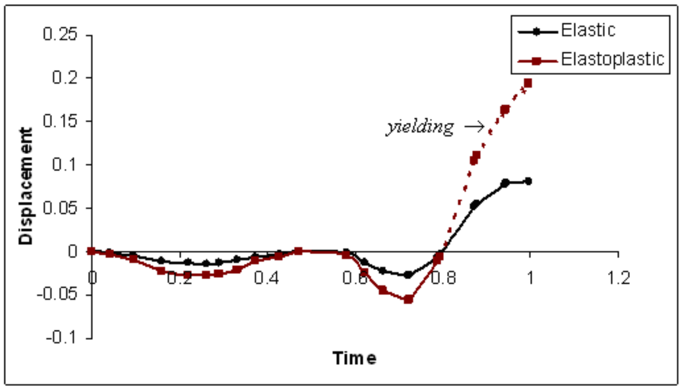

Figure 13: Comparison of elastoplastic behavior with elastic displacement response, story 1 for El Centro earthquake (applications 1 and 2).

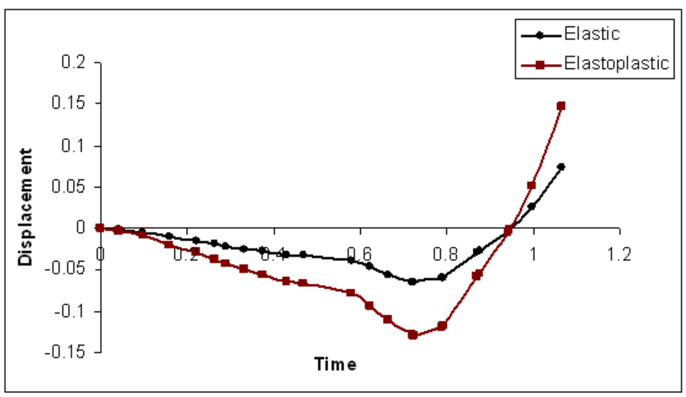

Figure 14: Comparison of elastoplastic behavior with elastic displacement response , story 2 for El Centro earthquake (application 1 and 2).

6 Conclusion

Nonlinear behavior of structures may be due to the inherent nonlinear stress-strain relationship of the material which is called material nonlinearity or due to the changes to geometry (dimensions and configuration) caused by the load, which is called geometrical nonlinearity.

The Wilson-θ method as an unconditionally stable method, serves to assure the numerical stability of the nonlinear solution process regardless of the magnitude selected for the time step. For this reason, Wilson-θ method was chosen as unconditionally stable method for this aspect of nonlinear dynamic analysis. The basic assumption of the Wilson-θ method is that the acceleration varies linearly over the extended interval $\tau = \theta\Delta t$ in which $\theta \geq 1.38$ for unconditional stability.

References

[1] Anil K. Chopra, "Dynamics of Structures ", Second Edition, Pearson Education, 2003.
[2] Alan Weary, "Designer's Guide to the Dynamic Response of Structures", 1997.
[3] Ray W. Clough and Joseph Penzien, "Dynamics of Structures ", McGraw Hill, First Edition, 1975.
[4] Ray W. Clough and Joseph Penzien "Dynamic of Structures ", Computers and Structures, Second Edition, 2003.
[5] Norman B. Green, “Earthquake Resistant Building and Construction”, Litton Educational Publishing, 1978.
[6] Mario Paz, "Structural Dynamics ", Van Nostrand Reinhold Environmental Engineering Series, 1980.
[7] Mario Paz, "Structural Dynamics ", Van Nostrand Reinhold Environmental Engineering Series, 1985.

Investigations of Kaolin Clay Collapse Behavior Using an Oedometer Apparatus

Musbah A. Hasan[1*],Gumaa Abdelazizi Hasan[2]
[1]abormila@googlemail.com, [2]gumaa.hasan@yahoo.com
[1,2]Department of Civil Engineering, College of Engineering, Sirte University, Libya

ABSTRACT

Geotechnical engineers face serious problems when construction sites contain collapsible soils, which are known by their strength when dry and experience sudden excessive settlement when inundated. Response-to-wetting oedometer tests can be used to obtain estimates of collapse settlements of structures founded on collapsible soil deposits. Generally, the collapsibility of soils is governed by the amount of water within the sample and the magnitude of the applied pressure. In this paper, an experimental study was performed, by using the one-dimensional compression test (single and double oedometer tests), to investigate the effect of the change in initial water content (IWC) and void ratio on the collapse potential of kaolin clays upon wetting. The test results confirmed that, the collapse potential value decreases with the decrease of initial void ration at a low vertical load increment. However, for the samples with different initial water content, the increase of initial water content leads to a decrease of the collapse potential values.

Keyword— Collapse potential, Kaolin clay, Water content, Void ratio, Oedometer test.

1. Introduction

When the soil has a collapsible grain structure, it can be defined as a soil that can resist moderately large applied stresses with a low value of settlement at a small amount of water content. However, a significant reduction in volume can be observed with the increase of water content, as the applied stresses remain constant. Collapsibility is limited not only to cohesive soils, but also to some cohesionless soils and constructed fills, where the collapse can occur suddenly as a result of the increase of moisture content, as the total vertical stress remains constant (M. Reznik, 2007). As is known, the density of soil plays a main role in the effect of soil collapsibility; i.e. porous fills and soils collapse once it is subjected to loads smaller than the denser fills or soils. However, in many countries, it appears, according to some official documents such as that of Rookovodstvo (1977), that the engineers and designers focus only on the effect of moisture content on soil collapsibility. The document (Rookovodstvo, 1977) designates the value of moisture content and vertical loads at which the loaded soil starts collapsing, as initial collapse moisture content and initial collapse pressure respectively. Once the applied load exceeds the initial collapsible pressure specified for particular values of water content and void ratio, the collapse of soil can be noticed. (Vilaret al., 1998) studied the collapse behaviour of a compacted lateritic soil by using the conventional loading−wetting oedometer tests and suction-controlled tests. The influence of dry unit weight, moulding water content and overburden stress on collapse strains is analyzed, and it is shown that the drier samples were the most susceptible to collapse upon wetting. The bearing capacity of collapsible soils decreased to about 50% due to soaking process, hence, the author recommends using twice the factor of safety stated in different codes to account the soaking effect in collapsible soils. The bearing capacity of collapsible soils when compacted to 95% of its dry density is larger than that of natural soil by about 24–30%. For both undisturbed and compacted soil samples, as the initial water content increases the collapse potential of soil decreases (K.E.Gaaver 2012). For the same moisture content, the collapse potential decreases when increasing the degree of compaction. Conversely, it increases in the case of soils where the percentage in fine particles is high. Also, with the same energy of compaction, the collapse decreases when increasing the moisture content and this is valid for water, and oil. Conversely, it grows in the case of soils containing more fines. The collapse by water flooding is the fastest and the most accentuated more than that oil. This is valid for all energies of compaction and moisture contents and at any moment (Rachid et al., 2010). Pre-wetting with applying the dynamic compaction at the same time will result in higher efficiency for the compaction. The determination of the most favourable moisture content is required, because the compaction of soils at upper moisture contents can lead to liquefaction, which can cause stopping of volume reduction (Kenneth et al., 1993).

2. Experimental Programe

Nine one-dimensional oedometer tests were performed on compacted soil specimens in order to study the influence of initial water content (IWC) and the initial void ratio on collapsibility of kaolin clay. In addition, specimens were saturated at different applied stresses and the amount of collapse deformation was measured.

Table 1. *Laboratory testing program*

Test type	Test Number	Initial Water Content w (%)	Saturated at	Void Ratio (e)
Double Oedometer test	1	10	-	2
	2	10	5KPa	2
	3	10	-	1.7
	4	10	5KPa	1.7
	5	20	-	2
	6	20	5KPa	2
Single Oedometer test	7	10	100KPa	2
	8	10	100KPa	1.7
	9	20	100KPa	2

2.1. Physical properties of soil

Tests were performed on specimens of kaolin clay to determine its physical properties. The kaolin clay was supplied by Whitfield & Son Ltd., England. Properties of the material were obtained according to (BS) standard. Compaction tests on the soil samples were carried out in accordance with the Standard Proctor test procedure, BS 1377. The maximum dry unit weight of kaolin clay was found to be 15.58 kN/m3 and the corresponding optimum moisture content was about 23.8%. Determination of the distribution of the silt/clay particles was achieved using a hydrometer test, BS 1377. Table 2. summarizes the recorded geotechnical properties obtained from liquid limit, plastic limit, hydrometer, specific gravity and compaction tests. Also, the tested soil sample was classified as (MH) according to the Unified Soil Classification System (USCS).

Table 2. Physical properties of kaolin clay:

31.4	2.64	58	42	MH	15.57	23.8

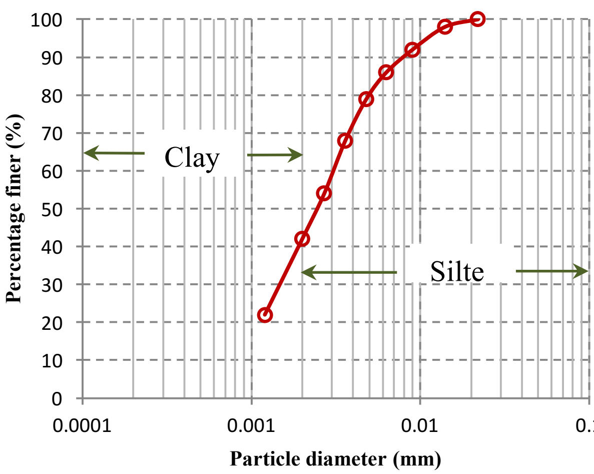

Figure 1. Kaolin clay particle size distribution curve

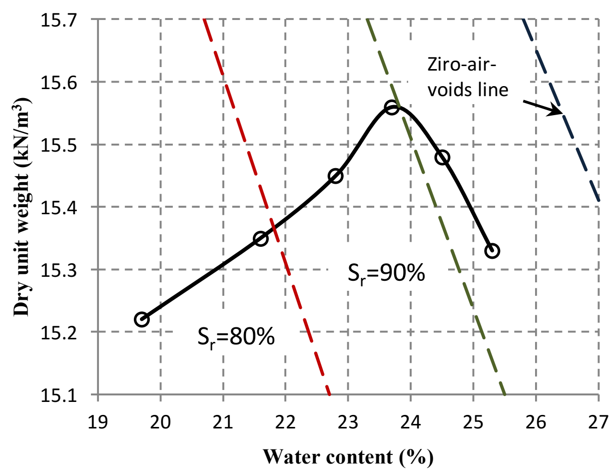

Figure 2. Standard Proctor compaction curve

2.2. Sample preparation

Soil specimens of kaolin clay were prepared by compacting moist soil, having a predetermined water content of (10 and 20 %) and an initial void ratio of (1.7 and 2), into an oedometer apparatus metal ring as shown in Figure 3. The soil was compacted into the metal ring using a small hammer. Change in the specimen initial water content, when the test is running, was prevented by cealing the odometer cell with a plastic sheet as illustrated in Figure 4. For the present investigation four groups of soil specimens were prepared, each group has a certain initial water content and void ratio. Table 1 shows the initial condition of the soil specimens.

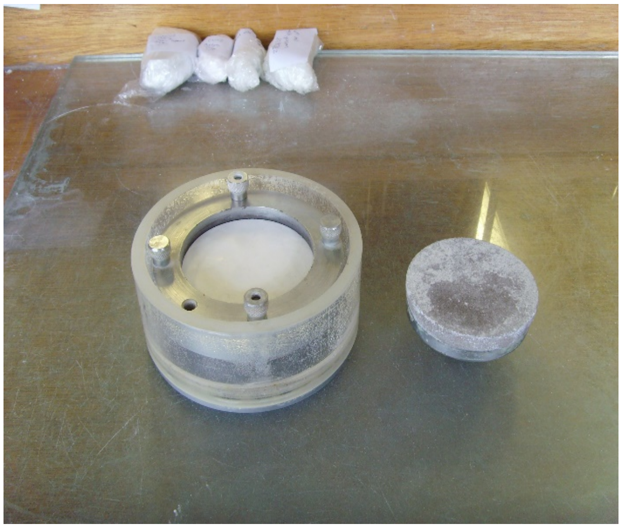

Figure 3. Soil sample placement within Oedometer

Figure 4. Isolation of sample from surrounding humidity

2.3. Oedometer Test Procedure:

A mass of kaolin clay is placed in the oedometer ring and allowed to reach equilibrium under a small hunger load. A series of load increments (5, 25, 50, 100 and 200 KPa) were applied and the dial gauge reading is recorded at the beginning and after equilibrium is reached for each loadincrement. The next load is applied and the changing of dial gauge reading is recorded once the entire consolidation is achieved. Inundation of the tested samples is taken place at 5 and 100 kPa load increment for double and single oedometer tests respectively. In this paper, the determination of collapse potential was calculated by taking the difference in volumetric strain (%) between the as-compacted and inundated specimens using Equation (1), by conducting the double and single oedometer tests considering different soil conditions in terms of the moisture content and void ratio, (BS 1377: Part 5: 1990).

$$CP = \left(\frac{e_i - e_f}{1 + e_o} \right) \tag{1}$$

Where CP = the collapse potential, e_o= the initial void ratio, e_i = the void ratio caused by the applied load at constant water content and e_f = the void ratio caused by the applied load after saturation.

3. Results and Discussion

3.1. Influence of initial water content

Figure 5 compares the compression curves of double oedometer tests at different initial water contents (IWC) of (10 and 20%). Soil specimen inundated at 5 kPa and subsequently loaded in the soaked condition up to 200 kPa. The magnitude of collapse in the specimen when (IWC = 10%) is higher than that when (IWC = 20%). Where, the reduction in void ratio at vertical stress of 100 kPa was about 39 % higher when the initial water content increases from 10 to 20%. Figure 6 shows a similar comparison between compression curves using a single oedometer test for two moist kaolin clay specimens inundated at 100 kPa. On wetting, the specimens collapse would increase approximately (28%) as the initial water content decreased from 20 to 10% at a vertical stress of 100 kPa. This could beattributed to, a portion of the fine-grained fraction of the soil exists as bonding material for the larger-grained particles. These bonds undergo local compression in the small gaps between adjacent grains. Therefore, these soils compress slightly at low moisture contents due to increase of pressures.

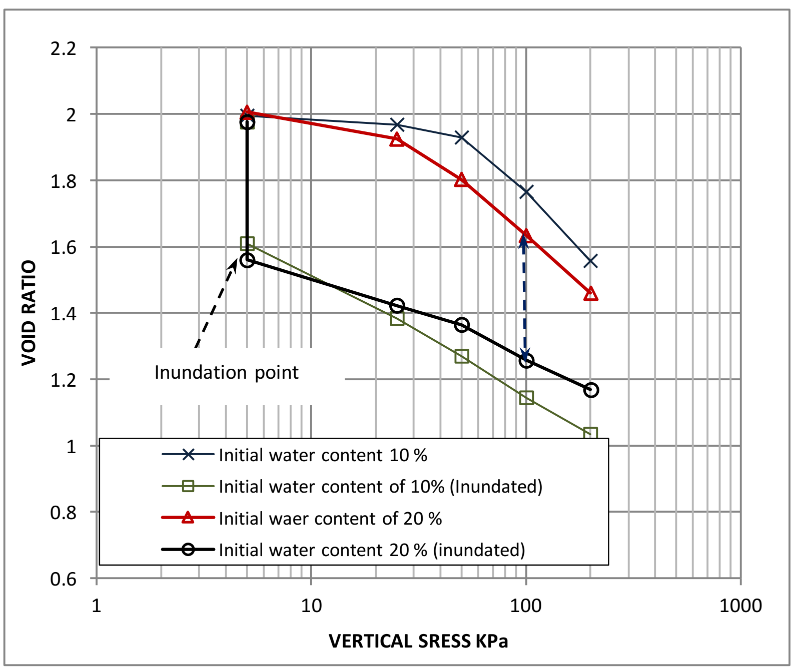

Figure 5. Void ratio versus vertical stress curves for double oedometer test with initial void ratio ($e_o = 2$)

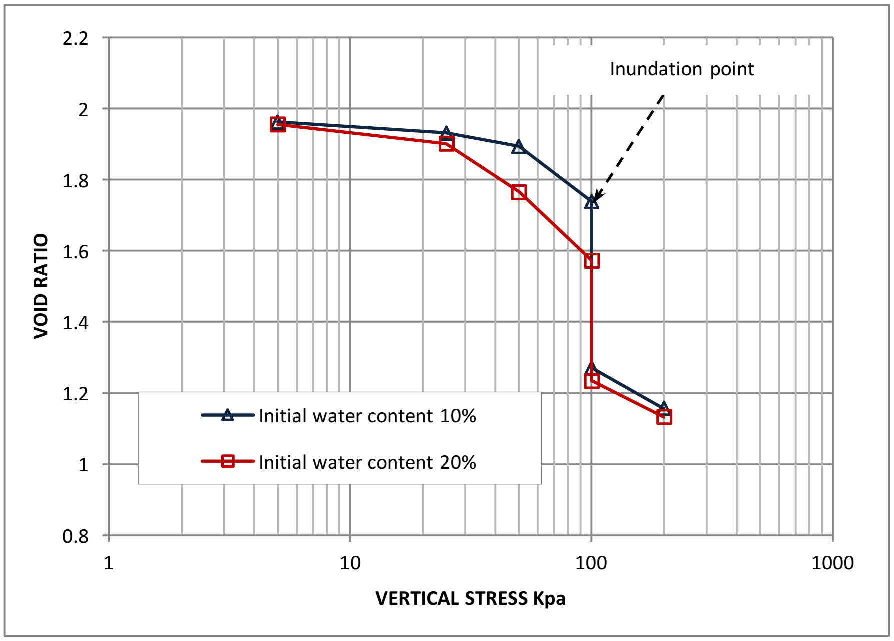

Figure 6. Void ratio versus vertical stress curves for single oedometer test with initial void ratio ($e_o = 2$)

When a collapsible soil is allowed to moisture, the fine binder that is providing the bonding mechanism between the large-grained particles will soften, weaken, and/or dissolve to some extent. Therefore, increasing the value of initial water content leads to the bonding materials start to gradually deteriorate. Consequently, a part of these bonds will undergo an earlier destruction prior to inundation. Figure 7 presents the relation between collapse potential (CP) and initial water content (IWC) of kaolin clay sample. At higher values of vertical stress, the magnitude of collapse potential, would record a significant decreasing when the initial water content is increased. Considering a double oedometer test, at a vertical stress of 100 KPa, the collapse potential decreases from20.65% to 12.47% as the initial water content increases from 10 to 20%. According to (Jennings et al 1975), the severity of the problem changes from severe trouble to very severe trouble based on the decrease in initial water content. Furthermore, results of variation of collapse potential versus vertical stress are expressed in Figure 8.

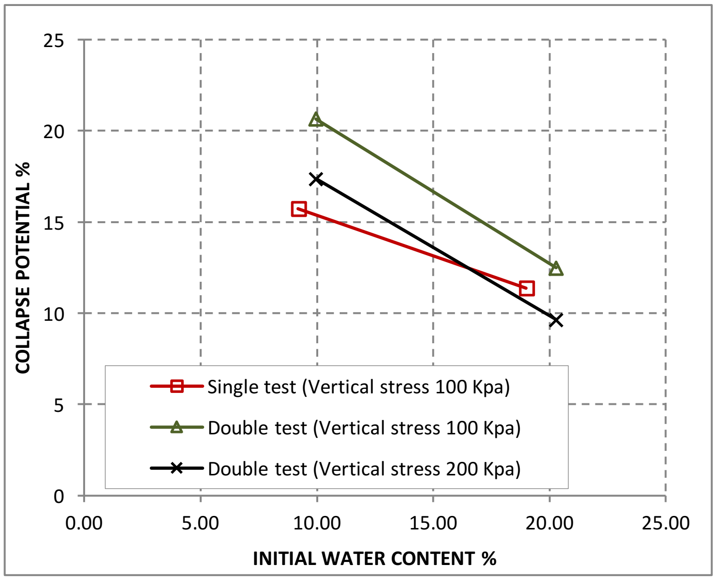

Figure 7. Initial water content versus collapse potential with constant initial void ratio of 2

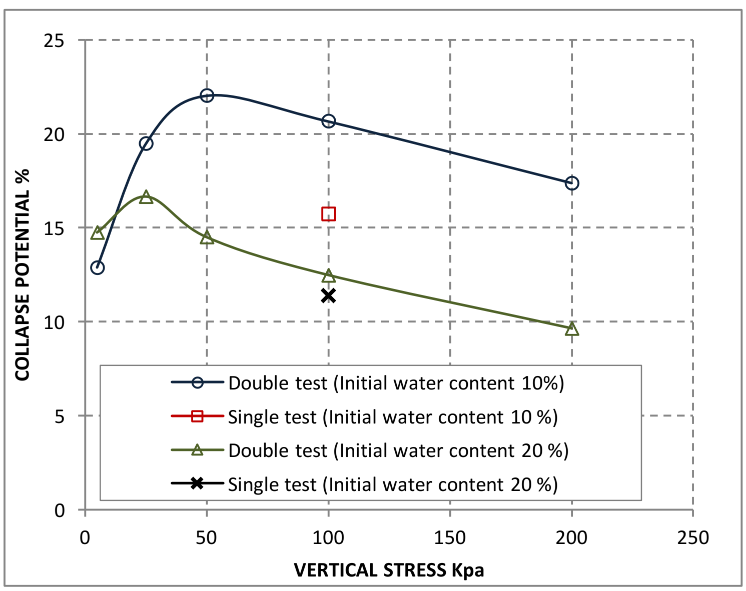

Figure 8. Collapse potential versus vertical stress with constant initial void ratio of 2

Compressing the specimens under constant initial void ratio of 2 and various initial water contents of (10 and 20%) will result in different values of (CP) as the magnitude of compression force varies.The curve representing the double oedometer test with initialwater content of 10% shows that, the highest collapsepotential value was observed at 50KPa load increment (CP=22.025). The collapse potential starts increasing with the increase of loads until it reaches its maximum value at a critical pressure (pre-consolidation pressure): "pressure at which collapse of a soil begins and the soil changes its response from low to high compressibility" (Phien-wej's et al., 1992) of 50KPa; then it begins to decrease with the increase of the loads being continued. Comparing this curve to the curve obtained from a similar test, having the value of initial water content increased to 20%, a significant reduction of collapse potential is observed. Also, the influence of test type, (single and double oedometer tests), was investigated to compare the results of collapse potential at a certain loadincrement. Figure 8 shows that, the value of collapse potential, obtained from single oedometer test, was always lower than that obtained from double oedometer test. Where, (CP = 15.73%) for single oedometer test and (CP=20.66%) for double oedometer test under the same nominal stress of 100 KPa and initial water content of 10%. This could be attributed to that, friction forces acting along the interfaces between soil specimens and oedometer ring may not decrease to the same degree during single oedometer testing as it could happen if soil specimens were inundated prior to stress application in double oedometer test. Furthermore, it is easier to inundate the unloaded soil specimens (Y.M.Reznik 2000). In addition, the difference between the results obtained from single oedometer test and double oedometer test decreases as the initial water content increases.

3.2. Influence of initial void ratio

Figures 9 and 10 show that, the decrease in void ratio upon wetting is quite small at the beginning of the loading process; however, it starts increasing rapidly with the increase of vertical loads being continued. The collapse potential values also increase with the increase of vertical loads upon wetting, where it starts from (CP=6.7%), which means trouble, at (5KPa) vertical stress, to end up with (CP=27.10%) which means a very severe trouble, at (200KPa) vertical stress as shown in Figure 11. Also the single oedometer test results show that, the value of collapse potential, at a certain point of a 100 KPa load increment, increases from (CP=15.73%) to (CP=18.89%) by reducing the value of void ratio from 2 to 1.7. This proves the fact that, the collapse potential, for kaolin clay soil, increases with the decrease of the initial void ratio at later stages of load increment.Thiswas observed when the same sample subjected to a double oedometer test show in Table (1) [tests (1 and 2) and (3 and 4)], where (CP=20.65%) from tests (1 and 2) at 100KPa vertical stress and (CP=25.91%) from tests(3 and 4) at the same vertical stress.

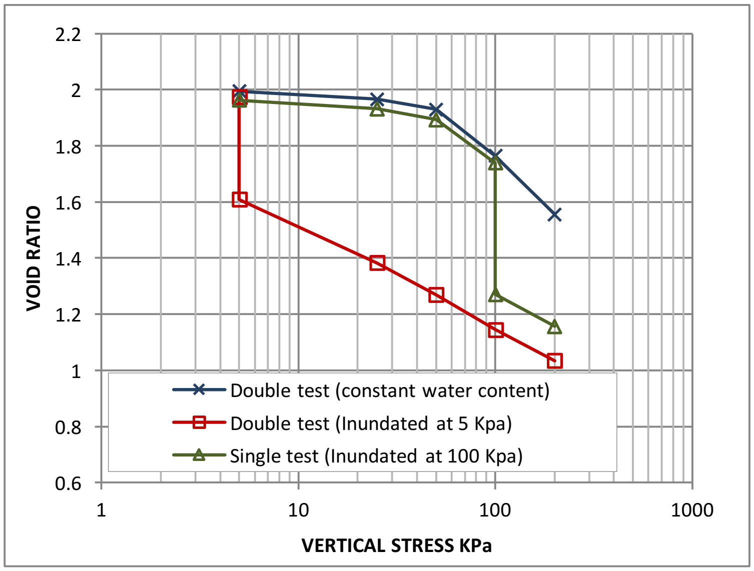

Figure 9. Void ratio versus vertical stress curves with initial water content of (10%) and initial void ratio ($e_o = 1.7$)

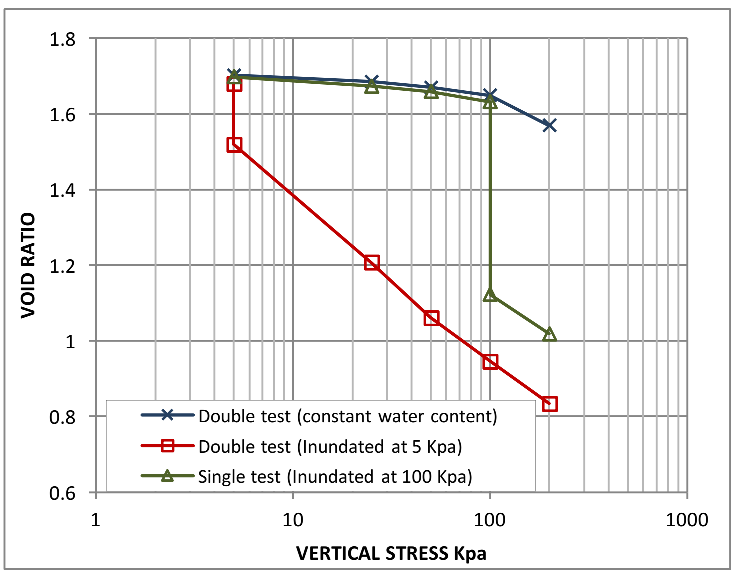

Figure 10. Void ratio versus vertical stress curves with initial water content of (10%) and initial void ratio (e∘=2)

In Figure 11 and 12, a comparison, between the results obtained from double and single oedometer tests, is drawn in order to investigate the effect of the change in void ratio, from 2 to 1.7 with constant initial moisture content of about 10%, on the collapse potential of kaolin clay. It is observed that, the collapse potential values obtained when considering a void ratio of 2 are higher than those obtained using a void ratio of 1.7 at vertical loads of (5 and 25KPa) and constant water content of 10%. However, a further increase in the vertical stress results in the opposite of that, where the values of collapse, potentialobtained from both tests, become bigger for higher vertical stresses of (50, 100, and 200KPa) as shown in Figure 12. The reason for that might be that the rearrangement of kaolin clay particles for a specimen with a high initial void ratio is fasterthan a specimen with lower initial void ratio, under loads being increasingly added, for the same specimen volume and initial water content. Therefore, from Figure 11, the sample with an initial void ratio of (2) becomes more compacted and stable than the sample with an initial void ratio of (1.7) after load increment of (50KPa). This leads to the collapse potential for the sample with an initial void ratio of (2), starting to decrease after exceeding this point, because a high percentage of compaction occurred in earlier stages of load increment as shown in Figure 10. Whereas, the other sample, a low percentage of compaction has occurred in earlier stages of load increment Figure 9, so that the (CP) value keeps increasing after exceeding the point of 50KPa vertical load. Accordingly, the outcome of this comparison is that the collapse potential value decreasing with the decrease of theinitial void ratio under low values of vertical stress (earlier stages of load increment).

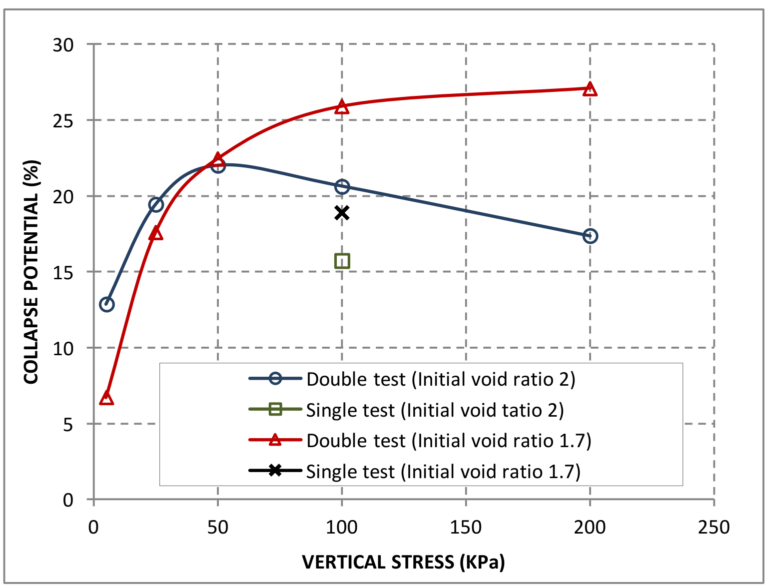

Figure 11. Collapse potential versus vertical stress with constant initial water content of 10 %

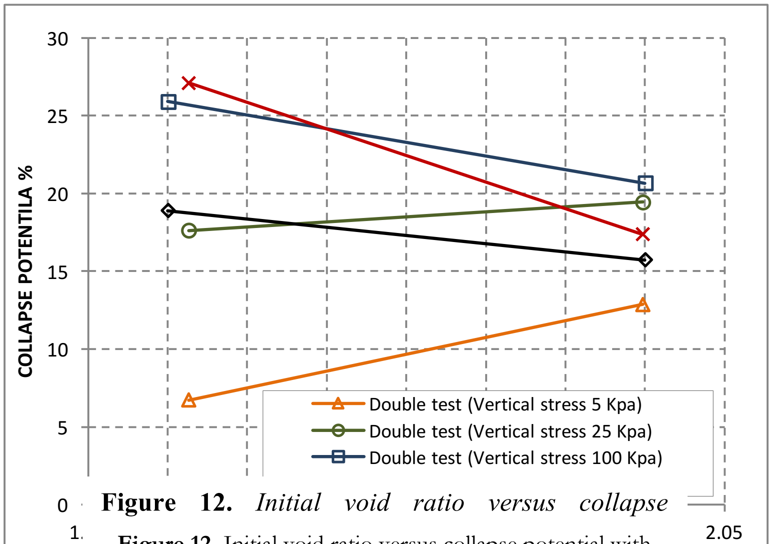

Figure 12. *Initial void ratio versus collapse*

Figure 12. Initial void ratio versus collapse potential with constant initial water content of 10 %

4. Conclusions

1. Under a low in situ water content (w.c. =10%) and void ratio of 2 the kaolin clay soil will pose a very severe trouble upon wetting (the collapse potential index at 50 kPa is as high as 22.03%). However, rising the initial water content (IWC) as high as 20%, resulting in a reduction in the collapse potential index to 14.49%.
2. At an initial water content of 10% and constant void ratio of 2, a considerable difference between the collapse potential index obtained from double and single oedometer tests is observed when subjected to a vertical load increment of 100 KPa. However, this difference will decrease as the initial water content increases at the same vertical load increment and void ratio.
3. the collapse potential values obtained when considering a void ratio of 2 are higher than those obtained using a void ratio of 1.7 at vertical loads of (5 and 25KPa) and constant water content of 10%. However, a further increase in the vertical stress results in the opposite of that, where the values of collapse potential index obtained from both tests, become bigger for higher vertical stresses of (50, 100, and 200KPa).

References

[1]. British Standards Institution. Methods of Test for Soils for Civil Engineering Purposes.

[2]. J.E. Jennings, K. Knight, A guide to construction on or with materials exhibiting additional settlements due to collapse of grain structure, in: Proceedings, Sixth Regional Conference for Africa on Soil Mechanics and Foundation Engineering, Johannesburg, 1975, pp. 99–105.

[3]. Jennings, J.E. and Knight, K. (1975) "A guide to construction on or with materials exhibiting additional settlement due to collapse of grain structure". Proceedings 6th African Conference on Soil Mechanics and Foundation Engineering. 99 – 105.

[4]. Kenneth D. Walsh, William N. Houston, and Sandra L. Houston. Evaluation of in-place wetting using soil suction measurements. J. Geotech. Engrg. 119, 862 (1993).

[5]. Khaled E. Gaaver. Geotechnical properties of Egyptian collapsible soils. Alexandria Engineering Journal (2012).

[6]. Phien-wej, N., Pientong, T., Balasubramaniam, A.S. In: collapse and strength in characteristics of loess in Thailand, Engineering Geology vol. 32. Elsevier Science, Amsterdam, pp. 59-72. 1992.

[7]. Rachid Benkadja, Brahim Belouahri. Influence of Oil on the Magnitude and Rate of Collapsible Soils. Journal of Civil Engineering Research and Practice, Vol. 7 No.1, April 2010, pp. 1 - 12

[8]. Reznik, Y.M. Engineering approach to interpretation of oedometer tests performed on collapsible soils. Engineering Geology Vol 57, Issues 3–4, Pages 205-213 (July 2000)

[9]. Reznik, Y.M., 1994a. Evaluation of collapse potential using single oedometer test results. Bulletin of the Association of EngineeringGeologists XXXI (2), 255–261.

[10]. Reznik, Y.M., 1994b. Comment: Evaluation of collapse potential using single oedometer test results. Bulletin of the Association of Engineering Geologists XXXI (3), 279.

[11]. Vilar, O.M., Machado, S.L. and Bueno, B.D.S. Collapse Behavior of a Compacted Lateritic Soil; 1998.

[12]. Yakov M. Reznik, influence of physical properties on deformation characteristics of collapsible soils. Engineering Geology, vol. 92, pp 27-37, (2007).

[13]. Lawton, E. C., Fragaszy, R. J., and Hetherington, M. D. (1992). "Review of wetting-induced collapse in compacted soil." J. Geotech. Eng., 118(9), 1376–1394

Modeling effects of outlet nozzle geometry on swirling flows in gas turbine

Hesham Baej [1], Adel Akair[2] ,Adel Diyaf [3], Salem Adeilla [4] Abdurahman Kraiem [5]

[1]heshamttt@gmail.com, [2]adel_akker@scitechgh.edu.ly, [3]adeldiyaf@yahoo.com, [4]salem_279@yahoo.com, [5]akme.glassgo@gmail.com
[1,2,4]Department of mechanical engineering ,College of Engineering, Higher institute of science and technology, Gharyan-Libya

ABSTRACT

Swirl stabilised combustion is one of the most successful technologies for flame stabilisation in gas turbine combustors. Lean premixed combustion systems allow the reduction of NOx coupled with fair flame stability. The swirl mechanism produces an aerodynamic region known as central recirculation zone (CRZ) providing a low velocity region where the flame speed matches the flow velocity, thus anchoring the flame whilst serving to recycle heat and active chemical species to the root of the former. Another beneficial feature of the CRZ is the enhancement of the mixing in and around this region. However, the mixing and stabilisation processes inside of this zone have shown to be extremely complex. The level of swirl, burner outlet configuration and combustor expansion are very important variables that define the features of the CRZ. The complex fluid dynamics and lean conditions pose a problem for stabilization of the flame. The problem is even more acute when alternative fuels are used for flexible operation.

Therefore, in this paper swirling flame dynamics are investigated using computational fluid dynamics (CFD) with commercial software (ANSYS). A new generic swirl burner operated under lean-premixed conditions was modelled. A variety of nozzles were analysed using isothermal case to recognize the behavers of swirl . The investigation was based on recognising the size and strength of the central recirculation zones. The dimensions and turbulence of the Central Recirculation Zone were measured and correlated to previous experiments. The results show how the strength and size of the recirculation zone are highly influenced by both the shear layer surrounding the Central Recirculation Zones (CRZ) and outlet configurations

Keyword— Central Recirculation Zone, swirling flow, CFD, turbulent.

1. Introduction

A proved technology to reduce the impact of NOx is the use of lean premixing with swirl-stabilized combustion. Swirling flow technologies have shown to give high flame stability taking advantage of coherent structures such as corner and central recirculation zones which anchor the flame, recirculating hot products and active chemical species whilst also increasing their residence time, allowing the use of low equivalence ratios thus giving lower flame temperatures and NOx emissions [1].

However, premixed combustion is not perfect because fuel and air mix just before entering the combustion chamber, thus leading to a significant degree of un-mixedness. These create complex instabilities that would feedback into the mixing-reaction combustion process. Combustion instabilities remain a critical issue limiting the development of low emission, lean premixed gas turbine combustion systems. Strong efforts are currently undertaken for the numerical simulation of swirl-stabilized flames with the intention of designing improved gas turbine combustors [2-3]. The biggest challenge to fuel-flexibility of most combustors is the

large differences between natural gas and the proposed replacement fuels. Moreover, gas turbines must meet the current emissions regulations, which often mean running very near lean blowoff. However, blowoff continues to be a phenomenon that is difficult to predict across reactor types and fuel compositions. To describe the lean blowoffbehaviour of swirl combustors under various fuel compositions, correlations have to be determined and simplified models developed to allow the implementation of fuel flexible technologies [4].
The crucial feature of swirl burners is the formation of a central recirculation zone (CRZ) which extends blow off limits by recycling heat and active chemical species to the root of the flame in the burner exit [5-6]. Thus, the CRZ is one of the mechanisms for flame stabilization that through an aerodynamically decelerated region creates a point where the local flame speed and flow velocity match [7]. A vast amount of literature exists on measuring, correlating and predicting blow off limits for bluff body and swirl stabilized combustors. There are three basic characterizations of the physical phenomena responsible for blow off. Long well et al. [8] suggested that blow off occurs when it is not possible to balance the rate of entrainment of reactants into the recirculation zone, viewed as a well stirred reactor, and the rate of burning of these gases. A different view is that the contact time between the combustible mixture and hot gases in the shear layer must exceed a chemical ignition time. This leads to scaling the characteristic dimension by the recirculation zone length, leading to a similar Da criterion [9]. Current theories are based on a flamelet based description upon local extinction by excessive flame stretch [10]. Flame stretching starts blow off with the initiation of holes in the flame, that are healed by the same flame creating stretching in areas that otherwise would have been unaffected. Flame will extinguish when flame stretch rate exceeds a critical value. However, it is also recognized that this mechanism is not the one causing the final blow off, as it is clear from data that the flame can withstand some extinction [11]. Therefore, it is considered that the "critical extinction level" must be somehow influenced by other mechanisms [8-9]. Regarding the central recirculation zone, the use of different configurations has demonstrated that the shape and strength of the CRZ can change drastically depending on these alterations [12-13]. Valera-Medina et al. [13] have observed how the change of the combustor nozzle can produce different central recirculation zones under the same injection conditions.

2. Numerical Methodology

CFD modelling was used to simulate the isothermal of swirl burner. A 100kW swirl burner constructed from stainless steel was used to examine the flow behave limits at atmospheric conditions (1 bar, 293 K) based to the previous experiments conducted at Cardiff University's Gas Turbine Research Centre (GTRC). Different nozzles were used with various angles: 15°, 25°, 35°, 45°, with swirl numbers of 1.05 . A single tangential inlet (a) feeds the premixed air and fuel to an outer plenum chamber (b) which uniformly distributes the gas to the slot type radial tangential inlets (c). Swirling unburned fuel then passes into the burner body (d), then into the burner exhaust (e) where the gases pass around the flame stabilizing central recirculation zone. The central diffusion fuel injector (f) (which was not used for fuel during the course of this study) extends centrally through the combustor body to the exhaust, Figure1.

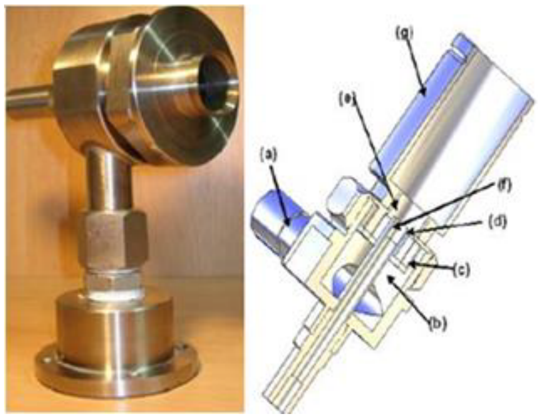

Figure 1: Swirl burner and schematic diagram, respectively.

CFD modelling is initially performed to simulate at the isothermal and atmospheric pressures conditions with 300 K . Isothermal conditions with no combustion were used to calibrate the system and indicate the flow pattern, although it is well known that there are also 3D time, dependant coherent structures, thus the results are of an indicative nature. During the simulation, various types of solvers were investigated and conclusions drawn as to which were the most effective. Based on the experimental results obtained the best turbulent option for the present work was the ϰ-ω SST model [11, 14-16].

Swirl combustor and burners are usually characterized by the degree of swirl, via a swirl number (S). For this particular project, the swirl element of 1.05 has four tangential inlets symmetrically distributed. The swirl burner produces a CRZ that extends back over the central fuel injector, allowing the flame to propagate into this region. This effect can be reduced by fitting a divergent of the exhaust nozzle of the burner, as shown in Figure 2, producing a different CRZ.

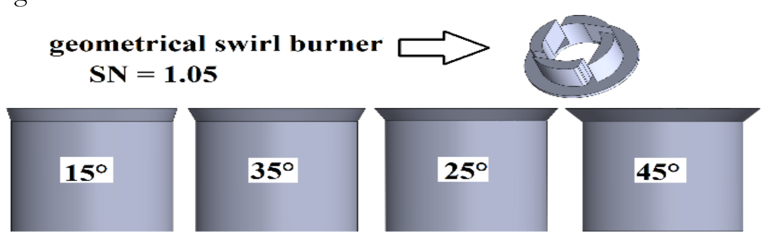

Figure 2: Geometrical swirl number 1.05 and various divergent angles nozzles, respectively.

3. Turbulence modelling

The turbulence model used was the shear-stress transport (SST) k-ωmodel, so named because the definition of the turbulent viscosity is modified to account for transport of the principal turbulent shear stress. It has features that give the SST k- ωmodel an advantage in terms of performance over both the standard K-ωmodel and standard k-ϵ model. Other modifications include the addition of a cross-diffusion term in the ωequation and a blending function to ensure that the model equations behave appropriately in both the near-wall and far field zones. The turbulence kinetic energy, k, and the specific dissipation rate, ω, are obtained from the following transport equations:

$$\frac{\partial}{\partial t}(\rho k)+\frac{\partial}{\partial_{xi}}(\rho k u_i)=\frac{\partial}{\partial x_i}\left(\Gamma_k\frac{\partial}{\partial x_j}\right)+G_k-Y_K+S_K$$

$$\frac{\partial}{\partial t}(\rho\omega)+\frac{\partial}{\partial x_i}(\rho\omega u_i)=\frac{\partial}{\partial x_i}\left(\Gamma_\omega\frac{\partial\omega}{\partial x_j}\right)+G_\omega-Y_{K\omega}+D_\omega+S_\omega$$

Calculations for all previous terms have been fully described in [17].

4. Mesh distribution and Boundary Conditions

A fresh air at normal conditions was used to simulate the behaviours of the flow pattern based on previous works [18-19]. The air flow mass flow rate and the operating conditions of the burner are given in Table 1,

Table 1: Inlet boundary conditions forall nozzles.

Test	Pressure	Temperature	Inlet velocity
1	1 bar	300K	2.5 m/s
2	1 bar	300K	5 m/s

FLUENT 15.0 was used to achieve the modelling and simulation [20]. The pre-processor used to construct the model grid was ICEM 15.0The computational mesh consists of 1700162 elements, with a structured grid created with a higher density of nodes in areas where the fluid flow was expected to considerably change and where a finer grid resolution was assumed to be beneficial for achieving an accurate resolution.
This was essentially done close to the burner exit and around the fuel nozzles, Figure 3.

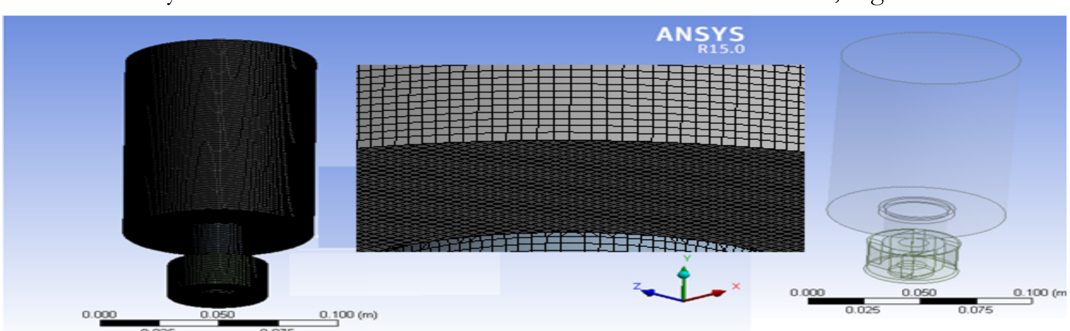

Figure 3. Mesh distribution swirl numbers 1.05 and 1.50, respectively

5. Results and Discussions

The comparison of the CFD simulation presented in Figure 4(a) and (b) reveals the effects of outlet configurations on the flow pattern. The predicted and measured boundaries of the CRZ for isothermal flows show a longer CRZ extending up to the combustor exit, as expected. However, the usage of different nozzles showed the reduction of both the size and the strength of the CRZ, Table 2.

Table 2. Comparison of isothermal patters of the CRZ using different nozzle angles.

Inlet velocity		15°	25°	35°	45°
2.5 m/s	Width	1.15 D	1.20 D	1.26 D	1.31 D
	length	2.58 D	2.60 D	2.63 D	2.80 D
5 m/s	Width	1.37 D	1.38 D	1.40D	1.37 D
	length	3.24 D	3.24 D	3.29 D	3.62 D

The flow rate increases with the intensity of the shear layer. This will converge into a new structure called High Momentum Flow Region (HMFR), highly correlated to the CRZ [19]. This will increase the strength of the CRZ but reduce its dimensions, as observed in table 2. The changing of nozzle angles affects the velocity of the flow, thus showing slower profiles than with nozzle 45°. At the same time, it seems that the dimensions of the CRZ with 45° angle have increased to a width of 1.37D and height of 3.62D, compared to a width of 1.15D and a height of 2.58D with nozzles of 15°, 45° under similar conditions, Figure 5. show the progression of the CRZ and its boundaries, defined as a region of greater turbulence compared to the low velocity case. It is clear that the CRZ using high velocity has increased the turbulent intensity with both nozzles 35° , 45° while the observed reduction with the 25° nozzles at the same conditions as shown in table 3 .

Table 3: Comparison of turbulent intensity of all cases.

Turbulent intenisity	15°	25°	35°	45°
2.5 m/s	60.3%	61.8%	63.5%	63.8%
5 m/s	129%	66%	135%	135%

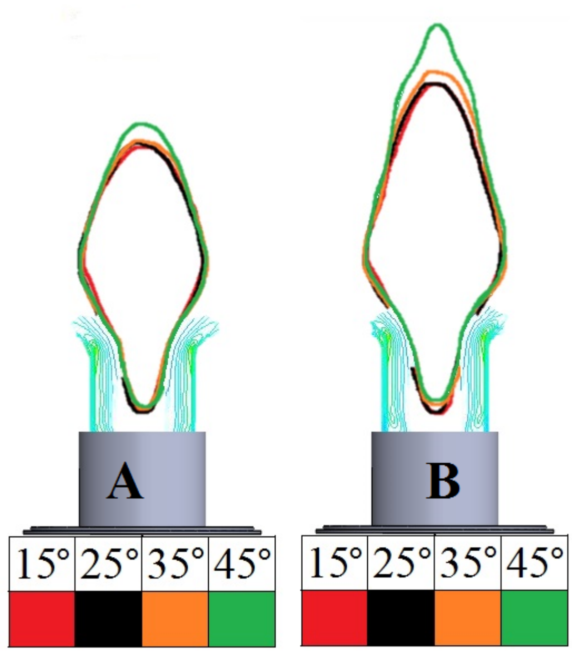

Figure 4. Comparison *of CRZ size of all nozzles A at 2.5 m/s and B at 5 m/s*

The usage of deferent nozzles alters the size and inner turbulence of the structure; in Table 3 and Figures 5 it is clear that the turbulence intensity inside the CRZ with high velocity blends is higher than with low velocity . The increase of the nozzle divergence from the 15 degree up to 45 degree will increases in almost 7-10% the turbulence of the structure, whilst augmenting its width and length in ~10% for all cases, Figure 4. The length of the recirculation zone increases due to the reduced reaction time of the blend and the higher turbulence inside of the structure.

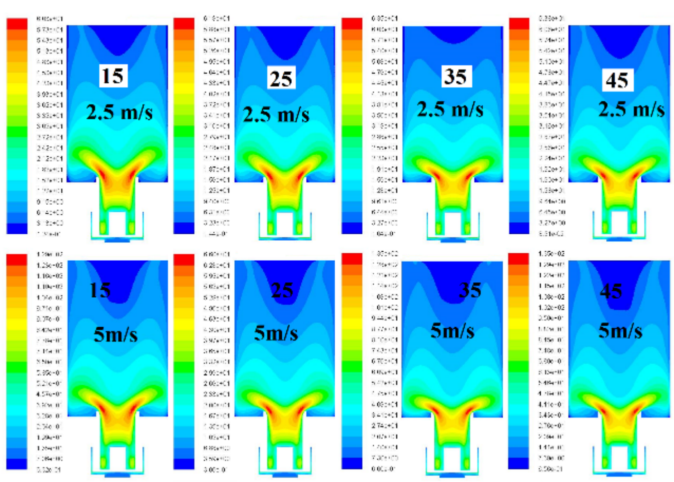

Figure 5: Comparison of turbulence intensity of different velocity 2.5m/s and 5 m/s.

The flow rate increases with the intensity of the shear layer. This will converge into a new structure called High Momentum Flow Region (HMFR), highly correlated to the CRZ [19]. This will increase the strength of the CRZ but reduce its dimensions, as observed in table 2. At the same time, it seems that the dimensions of the CRZ with 35° have increased to a width of 1.40D and height of 3.29D, compared to a width of 1.37D and a height of 3.62D with 45° nozzle under similar conditions, Figure 4-5. show the progression of the CRZ and its boundaries, defined as a region of greater turbulence compared to the low flow rate.
Figure 6 illustrates the axial velocity using different nozzle angles at a constant mass flow rate. The smallest CRZ width size was observed using the 15^0geometry, as expected. Also the 45^0nozzle produces higher outlet velocities than the 25° and 35° divergent angles due to the sharp sudden expansion. The 45° nozzle generates axial velocities 25% slower than the straight 15° geometry, thus allowing a better recuperation of the CRZ. This causes an increase in size of CRZ, Figure 6.

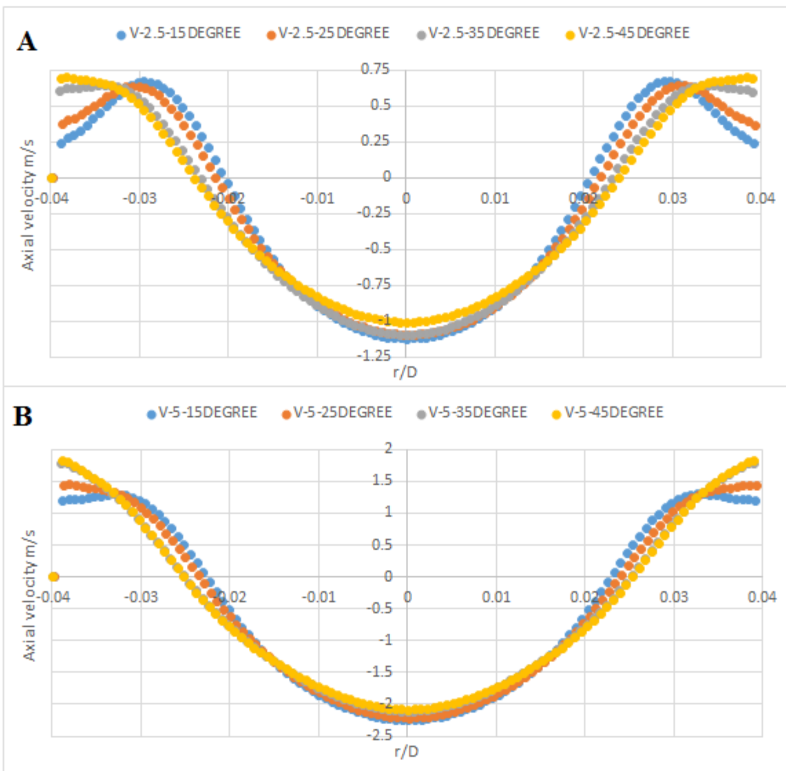

Figure 6: comparison of two velocities A 2.5 m/s and B 5 m/s

The high momentum shearing flow region illustrated in Figure 7 with swirl numbers of 1.05 shows the divergence of the flow at the outlet of the nozzle. It is clear that the increase in the velocity will produce higher stretch in the radial and tangential direction with a faster decay of velocity in a zimuthal direction and wider CRZs.

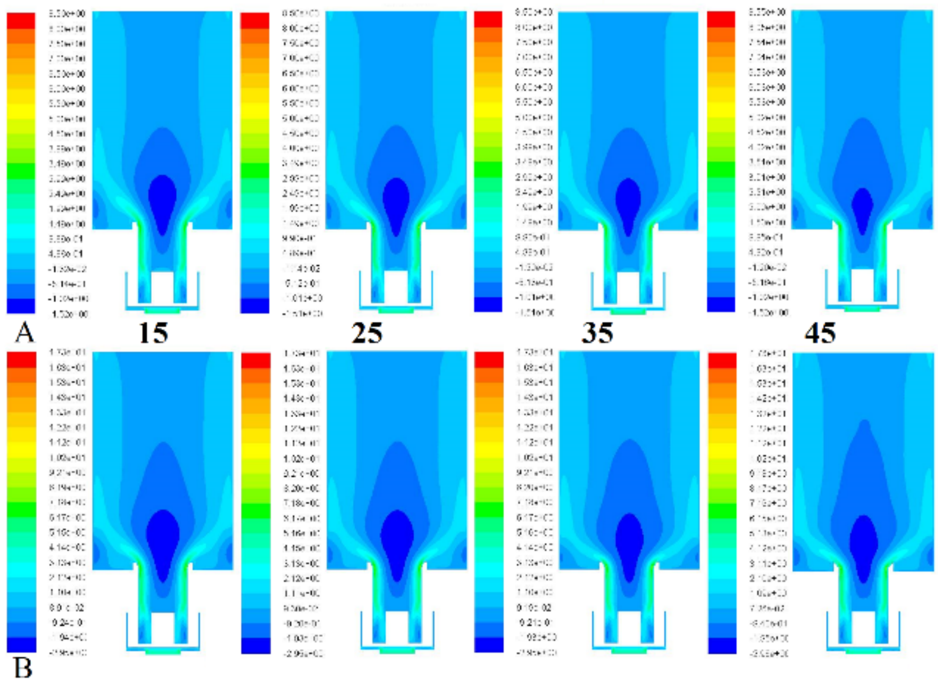

Figure 7: comparison of HMFR using all nozzles

6. Conclusion

The CFD predictions of swirl burner aerodynamics show how variable outlet configurations change the CRZ patterns. The changing of the geometry could be have the important factor of great importance to the change of the CRZ. It is clear that the CRZ is increased with the usage of 45° compared with another outlet nozzles angles. Changing the angle of the nozzle will control the direction of shear layer. This in return could be beneficial for new blends and the increase of the residence time of the products/reactants of the fuels/diluent compositions.

The results showed that for all nozzles produced different central recirculation zones under the same power loads. Measurements indicate that the 45° nozzle produced the largest, and shorter CRZ structure, while the nozzle with the 25° nozzle produced the narrowest CRZ.

Acknowledgment

I am gratefully acknowledges the support of the Cardiff university and Libyan Embassy and the Libyan Cultural and Education Bureau in London during my research.

References

[1]. Sadanandan R., Stohr M., Meier W: “Simultaneous OH-PLIF and PIV measurements in a gas Turbine model Combustor”,*Applied Physics B*, vol. 90, 609-618 (2008).

[2]. Huang, Y., and Yang, V: "Dynamics and stability of lean-premixed swirl stabilized combustion," Progress in Energy and Combustion Science, 35(4), 293-364 (2009).

[3]. Syred N,: A review of oscillation mechanisms and the role of the PVC in swirl combustion systems, Prog Energy Combust Sci 32 (2), 93-161(2006).

[4]. Megan Karalus: An Investigation of Lean Blowout of Gaseous Fuel Alternatives to Natural Gas, PhD Thesis, University of Washington,(2013).

[5]. Lieuwen T, Yang V: Combustion Instabilities in Gas Turbine Engines, Prog. In Astronautics Aeronautics, AIAA, U.S.A., vol. 210, 213-276 (2005).

[6]. Tuttle SG, Chaudhuri S, Kotska S, Koop-Vaughan KM, Jensen TR, Cetegen BM, Renfro MW: Time-resolved blowoff transition measurements for two-dimensional bluff body-stabilized flames in vitiated flow. Combust Flame 159, 291-305(2012).

[7]. Lieuwen T: Unsteady Combustor Physics, Cambridge Press, U.S.A., pp. 430(2012).

[8]. Longwell JP, Frost EE, Weiss MA: Flame stability in bluff body recirculation zones. IndustEngChem 8, 1629-1633 (1953).

[9]. Shanbhogue SJ, Husain S, Lieuwen T: Lean blowoff of bluff body stabilized flames: Scaling and dynamics, Prog Energy Combust Sci, 35, 98-120 (2009).

[10]. Driscoll J: Turbulent premixed combustion: flamelet structure and its effect on turbulent burning velocities, Progress in Energy and Combustion Science 34 (1), 91-134(2008).

[11]. Poinsot T, Veynante D: Theoretical and Numerical Combustion, R.T. Edwards, U.S.A., pp. 522(2005).

[12]. Valera-Medina A, Syred N, Bowen P :Central Recirculation Zone Analysis using a Confined Swirl Burner for Terrestrial Energy, J AIAA Propulsion and Power 29 (1), 195-204 (2013).

[13]. Valera-Medina A, Syred N, Griffiths A Visualization of Coherent Structures in a Swirl Burner under Isothermal Conditions. Combustion and Flame 159,1723-1734 (2009).

[14]. Versteeg HK and Malalasekera W, An Introduction to Computational Fluid Dynamics – The Finite Volume Method, Longman Group Ltd (1995).

[15]. Date A W: Introduction to Computational Fluid Dynamics, Cambridge University Press (2005).

[16]. Syred, N.J M.Beer: Combustion in swirling flows: A review combustion and flame 23,143-201(1974)

[17]. ANSYS FLUENT 12.0 Theory Guide 2009 [Online]. Available:atwww.scribd.com/doc/191713736/Ansys-Fluent-12-0-Theory-Guidem

[18]. Baej H., Valera-Medina A., Bowen P., Syred N., O’Doherty T., Marsh R ., Impacts on Blowoff by a variety of CRZs using various gases for Gas Turbines

[19]. Vigueras-Zuniga MO, Valera-Medina A, Syred N, Bowen P: High Momentum Flow Region and Central Recirculation Zone Interaction in Swirling Flows, SOMIM. Approved

[20]. Zimont V, Gas Premixed Combustion at High Turbulence. Turbulent Flame Closure Model Combustion Model. Exp Thermal Fluid Sci 21:179– 186 (2000).

Aerodynamic Effects of Blade Positive Sweep in Axial Flow Cascades

Ali R. kwedikha [1*], Abdul Azeam A. Elgayed[2], Abelmalek N. Algaaoud[3]
[1] ali.kwedikha@zu.edu.ly, [2] Abdoelgayed@gmail.com, [3]malk.algaaoud@gmail.com
[1, 2, 3] Department of Mechanical Eng., College of Engineering, University of Zawia, Libya

ABSTRACT

In this work, the effects of sweep applied to rotor of axial flow turbomachines were investigated by means of applying computational fluid dynamics (CFD) tools. Low-aspect-ratio rotors of positive sweep (**PSW**) have been studied and compared to unswept datum (**USW**) rotors, at one flow rate and different span wise locations.

Comparative studies have been carried out on positive sweep and upswept rotors at the design flow rate, by means of developing structured fully hexahedral mesh of the entire computational domain. The structured meshing technique offers the moderation of cell number and skewness, and makes possible cost-effective CFD investigations. Investigations of inlet and outlet flows field were carried out at the design flow rate.

It was pointed out that the efficiency for the positive sweep rotor is deteriorated near the tip and near the hub at the design point.

Keyword— Three-dimensional turbomachinery flow, blade sweep, structure meshing.

1. Introduction

In the turbomachinery manner, blade positive sweep may possibly give opportunity to control the flow and to demonstrate the impact of blade positivity on rotor aerodynamics, thus contributing to a more comprehensive understanding of the effects of consequences. This paper presents an investigation using computer codes for studying the blade sweep positivity effects on the Three-Dimensional (3-D) flow of axial fan.

A comparative investigation using a computational Fluid Dynamics (CFD) tool for Positive Sweep (**PSW**) and Unswept (**USW**) blades is carried out. **Figure 1** shows the front views of these blades.

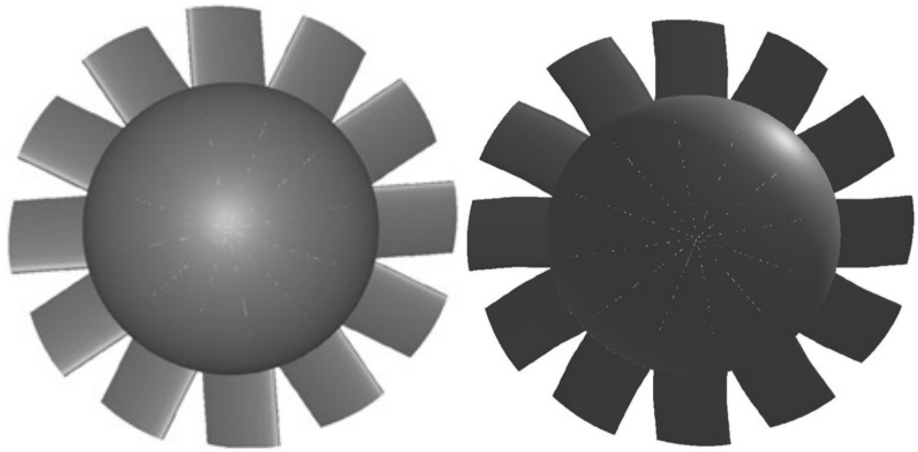

USW rotor PSW rotor

Fig. 1. Front views of USWand PSW rotors

Low-aspect-ratio rotor of **PSW** sweep has been studied and compared to unswept datum rotor, at the design flow rate and different spanwise locations.

Sweep is a non-radial blade stacking technique. Sweep is forward or backward if a blade section at a given radius is upstream or downstream of the adjacent blade section at lower radius respectively, and termed positive or negative if a blade section under consideration is upstream or downstream of the adjacent inboard blade section, respectively [1].

In the literature, several studies have been carried out for axial flow turbo machinery in order to investigate the effect of backward or forward sweep on the 3-D flow of axial fan. These studies have focused on the inter blade and downstream flow phenomena e. g. Yamaguchi et al. [2]. Others report negligible effects of pure positive sweep on the upstream flow field, as in Clemen et al. [3]. Few researches focused on the pure positive sweep of the turbo machinery rotors. Therefore, lack of information appears in the literature concerning positive sweep rotor designs. This has made some difficulty to compare with the results of other research projects. According to Braembussche and Vad [1], no generally valid concept for aerodynamically optimum prescription of blade sweep angle along the span has been published in the open literature.

The study presented here contributes to a more comprehensive understanding of the positive sweep effects. The aim is to provide some answers not presented by the available literature. This study provides a comparative study between **USW** and **PSW** rotors using CFD tools. The numerical simulation was carried out using ANSYS Student Release 17.2, the code is a state-of-the-art computer programs for modelling fluid flow in complex geometries, using Finite Volume Method (FVM).

Some$\varphi = \frac{\nu_x}{u_{ref}} = \frac{\nu_x}{u_t}$ assumption used in this work such as: the flow is considered steady state, incompressible, with swirl-free inlet, no entrance guide vane and negligible heat transfer.

2. Blade positive sweep geometry

The stacking line (SL) is the line passing through the centres of gravity of the blade airfoil sections enclosed in cylindrical stream tubes. The chord line is the straight line connecting the two points of leading edge (LE) and trailing edge (TE) of each blade section. Blade sweep is known as technique of non-radial blade stacking. Sweep can be provided if the blade sections of a datum blade of radial stacking line (RS) are displaced parallel to the chord [4] as sketched in **Figure 2a.** A blade is swept forward (FSW) or backward (BSW) at a given radius if the blade sections of a radially stacked datum blade are shifted parallel to their chord in such a way that a blade section under consideration is upstream or downstream of the neighbouring blade section at lower radius, respectively [5], Sweep is said to be positive near an endwall when a blade section under consideration is upstream of the adjacent inboard section, as shown in **Figure2**.

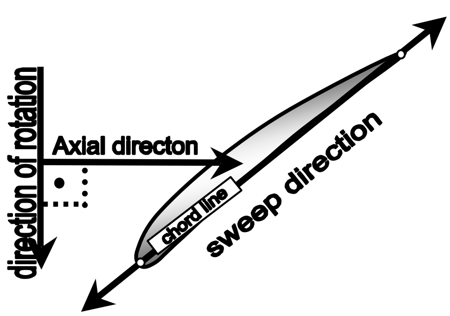

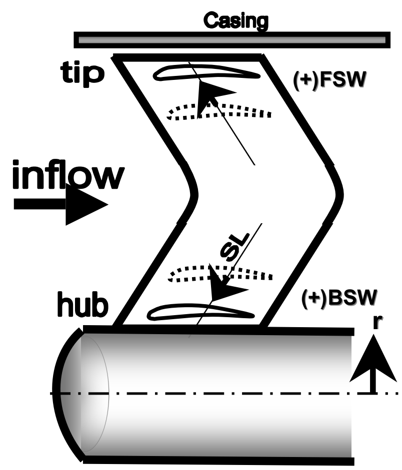

a) Direction of sweep b) Schematic drawing for PSW

Fig. 2. Sweep direction and schematic drawing for PSW

In this case study, reference [**6**] is taking as preliminary reference. The rotor blade sections has C4 (10%) profile along the entire span, with circular arc camber lines. The Reynolds number (*Re*) determined using speed of blade tip, characteristic length of chord tip and the kinematical viscosity of air at 20 $°C$ is approx. $1.074x10^6$.

Taking the reference velocity (u_{ref}) as the tangential velocity of the blade tip (u_t), the global flow coefficient (Φ_D) is defined as the area-averaged axial velocity in the annulus divided by u_{ref}. Hub-to-tip ratio (ν) is defined as the ratio of blade hub diameter to the blade tip diameter, while the tip clearance (τ) is defined as the ratio of rotor tip clearance to the blade span. The main fan characteristics are summarised in **Table 1.**

Table 1. Main fan characteristics[6]

Casing diameter	2000 mm
Hub-to-tip ratio ν	0.6
Rotor blade count N	12
tip clearance τ τ(%span)	5
flow coefficient Φ_D	0.33

The rotor blades are arranged in such a way that, the blades are assembled in an annular cascade with cylindrical and part of spherical as well as cylindrical casing, as shown in **Figure3.**

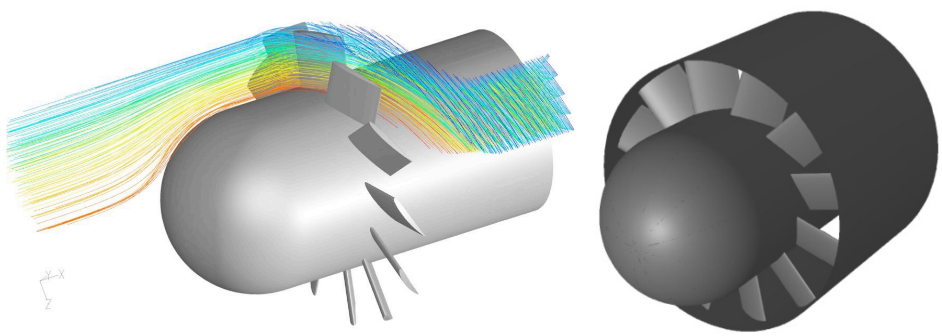

Fig. 3. Virtual isometric of USW rotor

In this study, to create positive sweep the blade sections are swept upstreamlly from the middle of the blade span to the both end walls by 3.5 degree.

3. CFD technique

The CFD investigations were carried out by using the commercial available finite-volume ANSYS-17.2 code. 3-D geometry was constructed by split volumes and meshed using multi blocks structured grids. This technique used to provide hexahedral meshes for the whole geometry of both rotors. It must be noted as Wenneker stated that, discretization of the flow equations on unstructured grids is considered to be more difficult than on structured grids [7]. 2-D structured meshes take place in two essential forms H-grids and C-grids. With consideration of periodicity, one computation domain instead of all geometry has been created to avoid the mesh size and time consuming. Typical computational domain for **USW** rotor is presented in **Figure 4.**

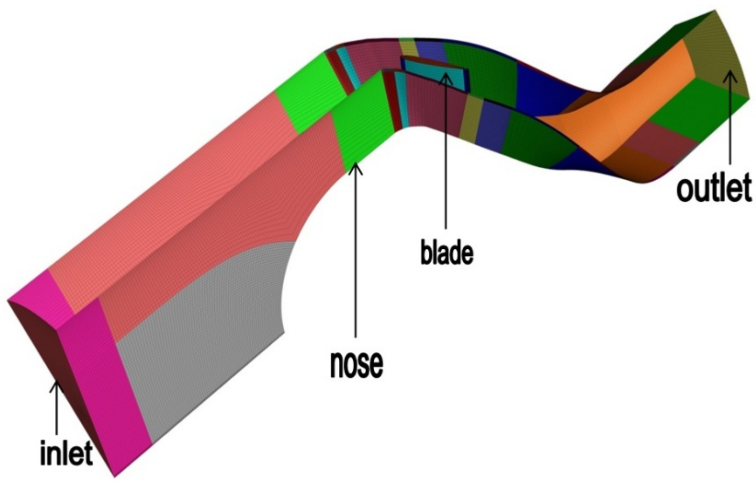

Fig. 4. Typical computational domain for USW rotor

The domains extend to approx. 7 and 4 midspan axial chord lengths in the axial direction upstream and downstream of the rotor blading, respectively. The coordinates of domain in x-axis started from (-X= -1750 to 2000 mm). Sector shape is inlet face with 30 degree central angle. Cone and hub sectors with one blade in the middle of the domain are provided next to the downstream of inlet face.

3.1. Boundary Conditions

- **Inlet boundary condition**: the inlet is set as a velocity inlet with magnitude of 9.2 [m/s]. The flow direction is parallel to the rotational x-axis.
- **Wall boundary condition**: the blade, hub and outer cassing have been defined as wall.
- **Outlet boundary condition**: outflow is used for the condition of outlet boundary.
- **Interior boundary condition**: the remaining part of the domain is set as default interior and the air fluid is applied with density of 1.225 kg/m^3.
- **Periodic condition**: all the side surfaces of the domain are defined as rotational periodic.

The standard k-ε model with enhanced wall treatment has been used as the turbulence model. The non dimensional wall normal cell size y+ values mostly fell within the range of 30 to 100, which agreeable with the requirements of the applied law of the wall. The discretisation of the convective momentum and turbulent quantity fluxes were carried out for both rotors by the second Order Upwind method. Typical computations required approximately 5000 iterations. The solutions were considered converged when the scaled residuals reached to 10^{-8} .

3.2. Meshing

To provide hexahedral meshes, the domain has been spitted to 31 volumes for both rotors and meshed using multiblocks structured grids. Biswas and Strawn stated that, hexahedral meshes provide a more accurate solution than their tetrahedral counterparts for the same number of edges [8], in this work; all the volumes have been meshed by the method of "Cooper". The most of the domain was meshed with "Hexahedral" structured meshing. Before starting with 3-D meshing, two types of grid meshing are applied in 2-D topology, C- type meshing applied for the vicinity of blade LE and TE, whereas H-type applied in most of the left. Dense meshing near the blade LE and TE as well as near the hub and tip is applied as in work of Kamenik et al [9]. The structured grid is usually applied to a relatively simple configuration. However, the swept blade geometry is being considered as a relatively complex design, in which a result of applying 3-D annular cascade instead of linear cascade. The total number of cells for **USW** and **PSW** rotor are 498889 and 469410 hexahedral cells, respectively. To develop annular cascade configuration and to take advantages of the periodicity, boundary condition of periodicity for one domain was applied, so that each meshing points and arrangement of each periodic face were created just identical with corresponding matching face.
Acceptable equiangle skewness of cell volume was achieved; the maximum skewness values are 0.82 and 0.75 for **USW** and **PSW** rotors, respectively.

4. Results and Discussion

4.1. Comparative flow survey of PSW and USW rotors at design flow rate

Results of valuable analysis by means of CFD technique for a comparison between **PSW** and **USW** rotors can be achieved, which is the purpose of this section.

Pitchwise averaged data

The inlet and outlet planes have positioned closely to the blade at the axial direction of -20% and 113% midspan axial chord, respectively, where the zero axial position indicates the LE at midspan as shown in **Figure 5a**. Another investigations located at the spanwise locations of 20%, 50% and 90% measured from the hub are shown in **Figure 5b**. The flow field will be surveyed at these five locations where significant 3-D results of the fluid mechanical behaviour can be achieved.

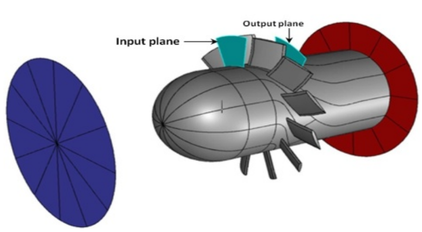

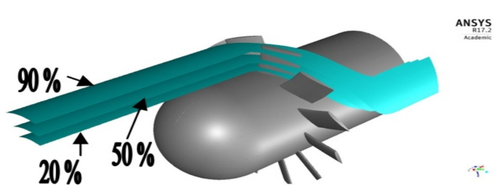

a) input and output planes b) 20% ,50% and 90 % span

Fig. 5. Location of results

The reference velocity (u_{ref}) or (u_t) in [m/s] can be defined as blade tip speed = ($d_t\,\pi\;\; n$) where, d_t is the blade tip diameter and n is the rotor speed (in revolutions per second). The definition of local flow coefficient (φ) is the ratio of axial velocity (v_x) to u_t

Figure 6a shows the distribution of local inlet axial velocity at the inlet plane and **Figure 6b** presents the spanwise distribution of pitchwise-averaged values for outlet axial velocity. **Figure 6b** indicates the two rotors having nearly similar pitch-averaged outlet axial velocity performance; which is possibly due to the small sweep angle. It was observed, that in **Figure 6a, PSW** decreases inlet axial velocity near the tip at **PS**, this acts to reduce the axial velocity downstream of the inlet especially at pressure side (**PS**) and blade LE as it is visible on the **Figure 7.**

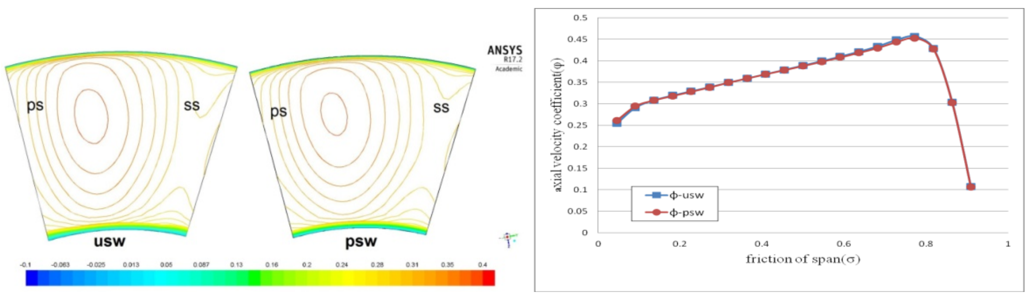

a) distribution of inlet φ b) pitchwise-averaged outlet φ

Fig. 6. Inlet and outlet of axial velocity coefficients.

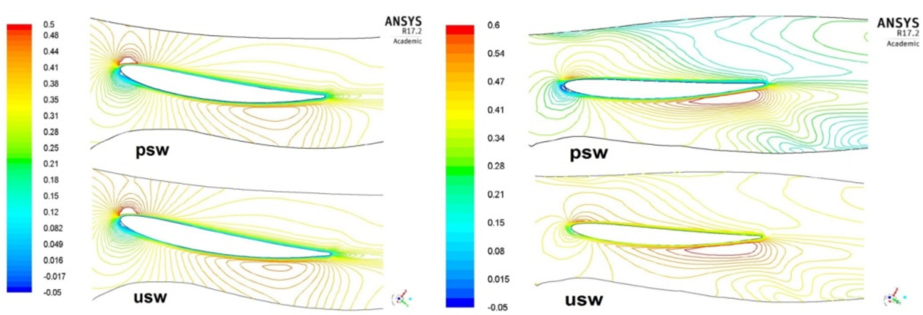

at 20% span at 90% span

Fig. 7. Distribution of local axial velocity coefficient

The definition of ideal total pressure rise coefficient (ψ_{id}) is $\psi_{id} = \Delta p_{t\,id} \,/\, (\rho\; u_{ref}{}^{2}/2)$. Where, $\Delta p_{t\,id} = \rho\, r\, \omega\; v_{u2}$, v_{u2} is the tangential pitchwise mass-averaged tangential velocity, r is radial coordinate, ω is rotor angular speed and ρ is the air density. For inviscid flow, the ideal total pressure rise (ψ_{id}) of turbomachines is assumed swirl-free inlet flow according to the Euler equation. Also according to effects of the so called "controlled vortex design (**CVD**)" in both rotors, the ideal total pressure rises gradually increased along the blade spanwise especially above midspan, the ideal total pressure rise increases significantly at TE of the **PSW** which is due to the blade positivity, as visibly shown in **Figure 8a**. As zhang et al.[10] concluded that, the pressure fluctuation of forward sweep blade is decreased while the pressure fluctuation of backward sweep blade is increased, likewise to our case that, **PSW** blade tip acts to increase ideal total pressure rise near the cassing compared to **USW** as shown in **Figure 8b**, this is due to decreasing the axial velocity at higher radii especially at the blade pressure side. However, **PSW** reduces ideal total pressure compared to **USW** along the spanwise except near the blade tip.

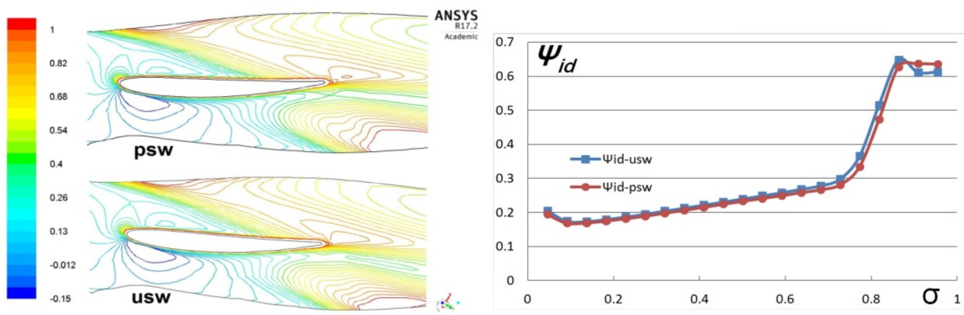

a) at 90% span b) at span wise distributions

Fig. 8. Ideal total pressure rise coefficient

The definition of the local total pressure rise coefficient (ψ) is Δp_t / (ρ u_{ref} ^{2}/2), where Δp_t is the pitchwise mass-averaged local total pressure rise. The local total efficiency (η) and total pressure loss coefficient (ω) can be defined as $\eta = \psi / \psi_{id}$ and $\omega = \psi_{id} - \psi$, respectively. **Figure 9b** shows the local total efficiency (η) profiles along the span. By employing the positivity of sweep, the total local efficiency is observed to be decreased compared to the unswept rotor. **PSW** blade sweep showed reduced local efficiency especially at lower the midspan and close to the blade tip, this is due to the increased ideal total pressure rise and increased losses where the aerodynamic benefits of blade positivity would be expected on the basis of Clemen and Stark[4]. Furthermore, the local total efficiency is found almost similar to **USW** within the range of 70% to 85% of the spanwise otherwise. **PSW** exhibits the worst local total efficiency, especially at the part of the blade tip in suction side (**SS**) as shown in **Figure9a**.

It is pointed out that the local efficiency for **PSW** rotor is deteriorated near the tip which considered as a disadvantage of applying positive blade rotor at the case of design flow rate.

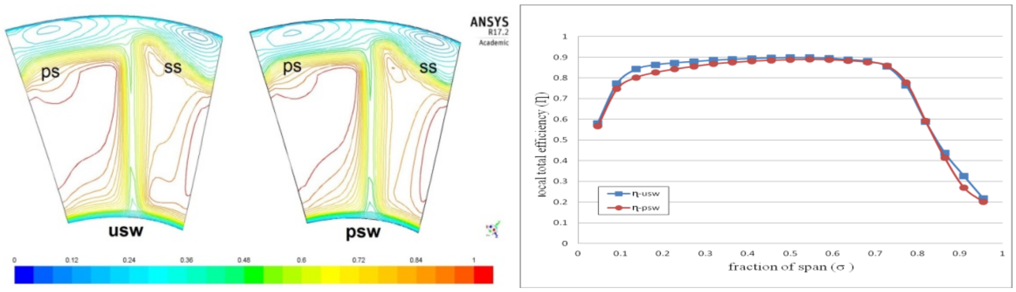

a) at outlet plane b) at span wise distributions

Fig. 9. Local total efficiency.

Increased total pressure loss for both rotors was found for both rotors above 80 percent span due to the existing tip clearance. At the blade tip, developing the local losses can be exist, the reason is that due to the combined effects of endwall tip-clearance, re-arrangement of the axial velocity and increased ideal total pressure rise, and can further increase by existing of positive sweep near the endwalls especially at SS, as shown in **Figure 10**. Clemen and Stark mentioned that, increased losses can be expected near the endwall in the case of negative sweep, due to opposite tendencies. By this means negative sweep and positive sweep can cause the shift of blade load toward the **LE** and toward the **TE** near the endwall, respectively [4]. By applying the positivity of sweep, the local total pressure loss observed to be increased at the blade tip, this causes to increase losses and decrease local total efficiency at the endwall.

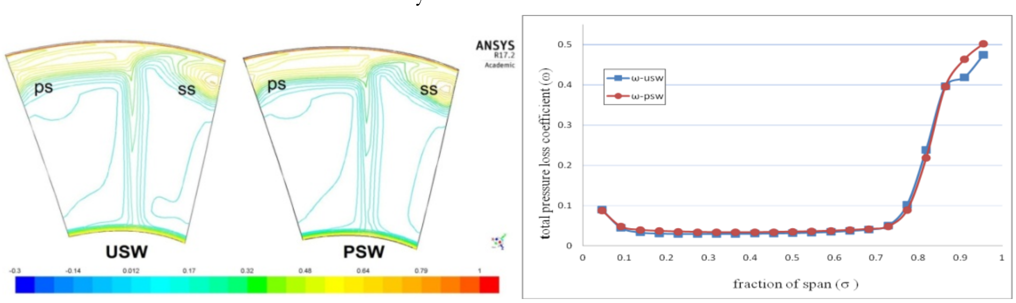

a) at outlet plane b) at span wise distributions

Fig. 10. Total pressure loss coefficient

5. Conclusions

The aim of this study was to investigate the effects of positive sweep applied to rotor of axial flow turbomachines using CFD tools. In this work, it is concluded that, the **PSW** rotor exhibits the lowest local total efficiency along the entire span, especially near the blade tip and near the hub at the design point, where as **USW** exhibits the highest local total efficiency along the entire span. It is pointed out generally that positive sweep gives a potential near-tip to increase of losses.

These results, therefore, demonstrate that the **PSW** rotor is considered as a disadvantage of applying positive blade rotor at the design flow rate.

Since, there is a deterioration of efficiency by using positive sweep near the tip and near the hub. It is recommended that, other investigations on a negative sweep should be carried out.

References

[1]. Van Den Braembussche, R. A. and Vad, J. "Challenges in optimisation of axial flow turbomachinery blades for 3D flow, including sweep and dihedral effects. In Modelling Fluid Flow", Springer Verlag Heidelberg, 2004, pp. 99-103.

[2]. Yamaguchi, N., Tominaga, T., Hattori, S., and Mitsuhashi, T., *"Secondary-Loss Reduction by Forward-Skewing of Axial Compressor Rotor Blading,"* Proceedings Yokohama International Gas Turbine Congress, Yokohama, Japan, 1991,pp. II.61-II.68.

[3]. Clemen, C., Gümmer, V., Goller, M., Rohkamm, H., Stark, U. and Saathoff, H., *"Tip-aerodynamics of forward-swept rotor blades in a highly-loaded single-stage axial-flow low-speed compressor."* 10th International Symposium on Transport Phenomena and Dynamics of Rotating Machinery (ISROMAC10), Honolulu, 2004, Paper No. 027. (CD-ROM Proceedings)

[4]. https://www.researchgate.net/publication/274636618_Tip aerodynamics_of_forward_swept_rotor_blades_in_a_highly-loaded_single-stage_axial-flow_low-speed_compressor

[5]. Clemen, C. and Stark, U. *"Compressor blades with sweep and dihedral: a parameter study"*. 5th European Conference on Turbomachinery Fluid Dynamics and Thermodynamics, Prague, 2003, Proceedings pp. 151-161.

[6]. Corsini, A. and Rispoli, F., *"Using Sweep to Extend the Stall-Free Operational Range in Axial Fan Rotors",* Proc. Instn Mech. Engrs, Part A, J Power and Energy, 2004, Vol. 218, pp. 129-139.

[7]. Vad, J., Kwedikha, A. R. A., Horváth, Cs., Balczó, M., Lohász, M. M., and Régert, T., *"Combined Aerodynamic Effects of Controlled Vortex Design and Forward Blade Skew in Axial Flow Rotors"*. Proceedings of the Institution of Mechanical Engineers – Part A: Journal of Power and Energy, 2007, Vol. 221, pp. 1011-1023.

[8]. Wenneker, Ivo, *" Computation of flows using unstructured staggered grids"* Dissertation at Delft University of Technology. 2002, Delft, the Netherlands.

[9]. Rupak Biswas, Roger C. Strawn, *"A dynamic mesh adaption procedure for unstructured hexahedral grids."* Paper 96-0027, 34th AIAA Aerospace Sciences Meeting, Reno, NV, 1996.

[10]. Kamenik, Jan, Keane, Andrew, Toal, David and Bates, Ron, *"Application of sweep to transonic compressor rotor blades for low-order statistical moment averaging in robust design"*. In Proceedings of the 1st Global Power and Propulsion Forum: GPPF, 2017, 7 pp. https://eprints.soton.ac.uk/406744/

[11]. Di Zhang, Jiao-Bin MA, and Qi Jing , *"Numerical Study Of Unsteady Flow And Exciting Force For Swept Turbomachinery Blades"*. Thermal Science, year 2016, vol. 20, suppl. 3, pp. s669-s676.

[12]. http://thermalscience.vinca.rs/pdfs/papers-2016/tsci160205199z.pdf

Theoretical Investigation of an Indirect Evaporative Air Cooling System

Mohamed I. Alowa[1], Gassem A. Azzain[2]
[1]moh.alowa@sebhau.edu.ly, [2]g_azzain@yahoo.com
[1,2] Department of Renewable Energies Faculty of Energy and Mining Engineering, Sebha University, Libya

ABSTRACT

In this paper an indirect evaporative cooler theoretically investigated. Because of its low cost and low environment pollution, the indirect evaporative coolers have great potential as an alternative to conventional air conditioning in an arid hot climates such as southern of Libya where the temperature and relative humidity reach 45°C and 20 % respectively. The present investigated system consists of cooling tower, cross unmixed heat exchanger, air blower, circulating pump, air filter, humidifier, and air duct. The main factors that affect on the temperature output of the system are presented. The affect of air conditions input to the cooling tower and air duct were clarified by solving the control equations using Matlab program. The results show that the air dry bulb temperature directly proportion to the outlet dry bulb temperature, and air input relative humidity notable proportion to the outlet dry bulb temperature. The water flow rate in the cooling tower affect on the outlet air temperature, were as it increases the outlet air temperature decreases. Also the air flow rate through the cooling tower contributes in the outlet air temperature, while the increasing in the air flow rate leads to decreasing in the outlet air temperature. Furthermore as the flow rate of the air inside the air duct increases, the outlet temperature decreases. Moreover investigation proves that the indirect evaporative cooling successfully can be used in the southern of Libya.

Keyword— Indirect evaporative cooling, Cooling tower, Arid hot climates

1. Introduction

An indirect evaporative air cooler (IEC) is one of the promising solution for air conditioning specially in the arid hot climates, which encouraging the researchers to taken up different studies concerning of this subject. The analysis for theoretical and experimental works takes place over a wide world locations even in the cold weather State, such as European countries where the experimental analysis of (IEC) system studied [1]. The components of the (IEC) have factors effecting on the system performance, [2] investigated the conductivity of metal, fibers, ceramics and how they impact on the (IEC) system. The (IEC) acts as an energy recovery device in air conditioning systems which called a semi-indirect evaporative cooler [3]. The outdoor conditions have a most effect on the (IEC) availability applications that provide a comfort conditions, [4]. The review of (IEC) [5] technology was undertaken from a variety of aspects including background, history, current status, concept, standardization, system configuration, operational mode, research and industrialization, market prospect and barriers, as well as the future focuses on commercialization indicated that (IEC) technology has potential to take up the air conditioning duty for buildings. The (IEC) systems has been modified to increase its cooling performance one of modification is an effectiveness- number of transfer unit (Ɛ-NTU) method analysis using an indirectly pre-cooling the working air before it inters the wet passage that could be based on (Ɛ-NTU) heat exchanger by redefining the potential gradients, transfer coefficient, heat capacity rate parameters[6]. The thermodynamic characteristics of (IEC) experimentally and theoretically research works on feasibility studies, performance test and optimization as well as transfer analysis reviewed [7]. The advantages of the (IEC) is the low energy consumption and the environmental friendly and very low warming impact, the disadvantage is the water consumption [8]. For the (IEC) system, the main equipment is the cooling tower where the cold water produced. The principle of the cooling tower is the process of heat and mass transfer by direct contact between air and water in the tower packed by means of the coefficient of both heat and mass transfer. The simultaneous heat and mass transfer between water and air experimentally investigated [9] where the effect of air and water flow rates on the global heat and mass transfer coefficient clarified. In this paper the effect of the air conditions and the flow rates of both air and water on the air out of (IEC) that mainly consists of cooling tower, cross unmixed heat exchanger, air blower, circulating pump, humidifier, and air duct is investigated by solving the control equations using Matlab computer program.

2. System Description

The investigated (IEC) system is shown in Figure 1,and it can be described as following.

Air Blower: It is a centrifugal fan type that supply the air from an ambient air to the conditioning duct where the processing equipments of the system assembled.

Heat Exchanger : The heat exchanger is the equipment where heat transfer between the water from the cooling tower and the air inlet to the system is taken place. The heat exchanger type is staggered order find tube unmixed cross flow and its effectiveness is 75%.

Humidifier : The humidifier is a bank of atomizer nozzles that spry the cooled water from the cooling tower into the stream of the cooled air that is outlet from the heat exchanger.

Duct System: Duct is a passage where the ambient air flows onto the equipments of blower, filter, heat exchanger, humidifier, and eliminator. Duct cross section area, and length are 64×64 cm^2, and 1.3 m respectively.

Cooling Tower : The cooling tower is the equipment where the heat and mass transfer occurring by direct contacting between the air and to produce the cold water. The cooling tower type is the forced counter flow. The tower consists of a draft axial fan mounted at the top of the tower. The nozzles spray water on the dick for enlarging the contacting area between the air and water to maximize the heat and mass transfer rate. The bottom of the tower body is a water sump which collects the cold water. The tower height is 2 m, cross section is area, 1×1 m^2.

Cooling Water Circulating System : The cooling water is circulated by means of a centrifugal pump and water flow rate is controlled by three valves.

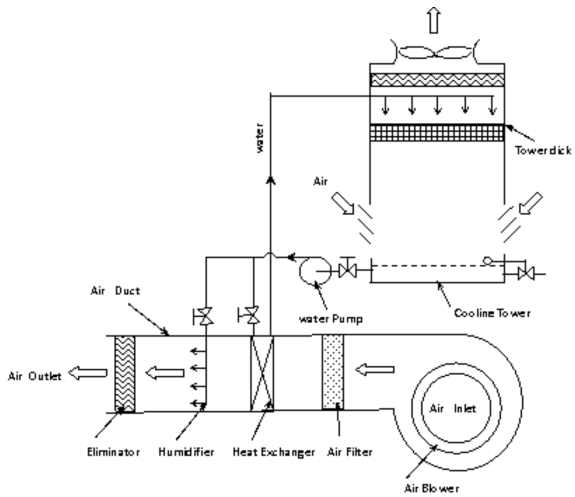

Figure1: Indirect evaporative air cooler system.

3. Theory

The main processes are occurred first in the cooling tower where the mass and heat transfer takes place to produce the cold water, next the heat transfer between the air and cold water through the heat exchanger for air cooling, then the air humidified by the cold water. For the cooling tower, from Figure 2, ignore water loosing and heat transfer through the tower walls, the energy balance equation for the process of direct contact of heat and mass transfer in cooling tower is[10]

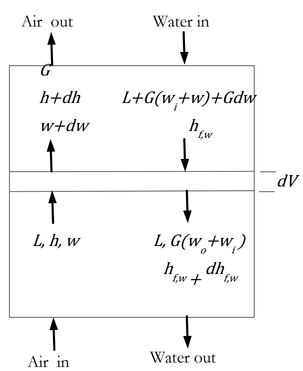

Figure2: Counter flow cooling tower diagram.

$$Gdh = -[L - G(w_2 - w)]dh_{f,w} + Gdwdh_{f,w} \tag{1}$$

Where G is the air flow rate, (kg/s), h is the moist air enthalpy, (kJ/kg),L is the water flow rate, (kg/s), w, is humidity ratio of moist air, (kg_w/kg_a), $h_{f,w}$ is water enthalpy at its temperature, (kJ/kg).

(w_2-w) is small and it can be ignored so,

$$Gdh = -Ldh_{f,w} + Gdwdh_{f,w} \tag{2}$$

For water energy balance in terms of the heat and mass transfer coefficients, K_C(kw/m^{2o}C) and, K_D(kg/s.m^2) respectively

$$-Ldh_{f,w} = K_C A_V dV(t_w - t) + K_D A_V dV(w_{s,w} - w)h_{fg,w} \tag{3}$$

where, A_V, is water surface area per unit volume, (m^2/m^3), t_w , water temperature (ºC), t, moist air dry-bulb temperature, (ºC), $w_{s,w}$, humidity ratio of saturated air at t_w, (kg_w/kg_a), $h_{fg,w} = h_{g,w} - h_{f,w}$.

$h_{g,w}$, is the enthalpy of saturated water vapor at t_w(kJ/kg).

The air side water vapor mass balance is

$$-Gdw = K_D A_V dV(w_{s,w} - w) \tag{4}$$

Introducing Lewis number $Le = \frac{K_C}{K_D c_{pa}}$in equation (3) gives,

$$-Ldh_{f,w} = K_D A_V dV[Lec_{pa}(t_w - t) + (w_{s,w} - w)h_{fg,w}] \tag{5}$$

Combining equs. (2), (4),and (5)

$$\frac{dh}{dw} = Lec_{pa}\frac{t_w - t}{w_{s,w} - w} + h_{g,w} \tag{6}$$

The enthalpy of moist air for constant C_{pa},

$$h = c_{pa}dt + wh_g$$

$$dh = c_{pa}dt + dwh_g$$

$$h_{s,w} - h = c_{pa}(t_w - t) + h_g^o(w_{s,w} - w)$$

Where $h_{s,w}$, is the enthalpy of saturated air at t_w, h_g^o is the enthalpy of saturated water vapor at0^{o}C.

From equ. (6)

$$\frac{dh}{dw} = Le\frac{h_{s,w} - h}{w_{s,w} - w} + (h_{g,w} - h_g^o Le) \tag{7}$$

For$Ldh_{f,w} = LC_w dt_w$ so by equs. (5)and (7), we have

$$-\frac{dt_w}{h_{s,w} - h} = \frac{G}{LC_w}\left[Le + \frac{h_{fg,w} - h_g^o Le}{(h_{s,w} - h)/(w_{s,w} - w)}\right]\frac{dw}{(w_{s,w} - w)} \tag{8}$$

For the Heat exchanger the effectiveness is$\varepsilon = \frac{\acute{t}_o - t_i}{t_i - t_{w,i}}$ (9)

The humidifier control equations are.

$$h_{ih} = \acute{t}_o + w_i(2501 - 1.805t_{ih}) \tag{10}$$

$$h_{f,w} = 0.204266 + 4.18609t_w \quad (11)$$
$$l = g(w_o - w_i) \quad (12)$$
$$h_o = \frac{l}{g+l} \times h_{f,w} + \frac{g}{g+l} \times h_{ih} \quad (13)$$
$$t_o = \frac{h_o - 2501w_o}{1+1.805w_o} \quad (14)$$

h_{ih}, t_{ih}, w_i, enthalpy, temperature, and humidity ratio of air input to the humidifier respectively, $\acute{t}_o$, isthe air temperature out of the heat exchanger, l,g, water, and air flow rates through the humidifier respectively (kg/s), t_o,w_o , temperature, and humidity ratio of the air output.

4. Results and Discussion

The above control equations (8) through (14) solved using Matlab computer program for steady state and assuming no heat and water loss from the cooling tower and air duct. Input the system specifications, and G, L, input t_w, for Le =1, the solution is starting with the initial conditions and applying trial and error procedure to get the air outlet conditions. The process bath of the air through the air duct is shown in Figure 3where, the air sensible temperature dropping in heat exchanger by the cold water from the cooling tower. The temperature dropping takes place as a result of the operation conditions. Finally the cold air is humidified by the humidifier which increases the air humidity as well as slightly deceases its temperature.

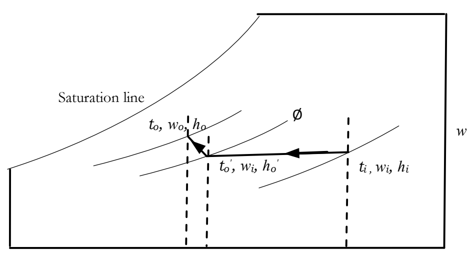

Figure 3: Processes bath of the air through the air duct.

The effect of the conditions of the inlet air to the system for a constant air relative humidity(RH)Ø, and water, air flow rates in the cooling tower are L= 0.65 kg/s, G= 2.6, respectively, and air flow in condition duct g=1.5 kg/s is shown in Figure 4 which reveals that as inlet dry bulb air temperature t increases, its outlet temperature increases t_o. But as (RH) decreases for constant air dry bulb temperature, the outlet air temperature deceases, that because, for the low (RH)which means low wet bulb temperature more amount of water evaporated in the cooling tower due to the high mass an heat transfer coefficient and as a result the water heat capacity between inlet and out let lowered hence, the water temperature from the cooling tower that flow to the heat exchanger and the humidifier causing air temperature drop.

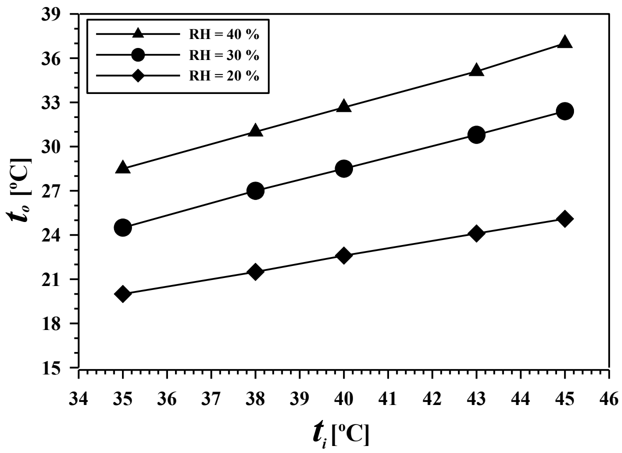

Figure 4: Effect of inlet air conditions on the outlet air at *L*= 0.65 kg/s, G=2.6kg/s, and *g*=1.5kg/s.

The water flow rate plays noticeable effect on the water temperature outlet from the cooling tower which then supplied to the heat exchanger. The effect of cold water flow rate from the cooling tower on the air temperature exit from the duct is shown in Figure 5 which illustrates that as the flow rate of water increases, the exit temperature from the duct decreases that because higher water flow rate enables heat and mass transfer between the air and water to increase as well as the increasing of the water flow rate into the heat exchanger, increases the heat transfer rate.

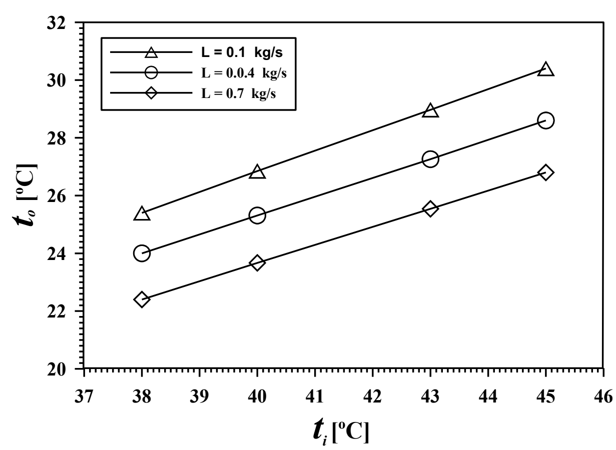

Figure 5: Effect of the water flow rate in the cooling tower on the outlet air at G= 2.6kg/s,*g*=1.5kg/s, and Ø=25%.

From Figure 6, it's clear that when the air flow rate increases into the cooling tower the air out let of the duct decreases due to water temperature drop in the tower and consequently in the heat exchanger as a result of enlargement of heat and mass transfer area between air and water that gives big chance of the transferring process to take place.

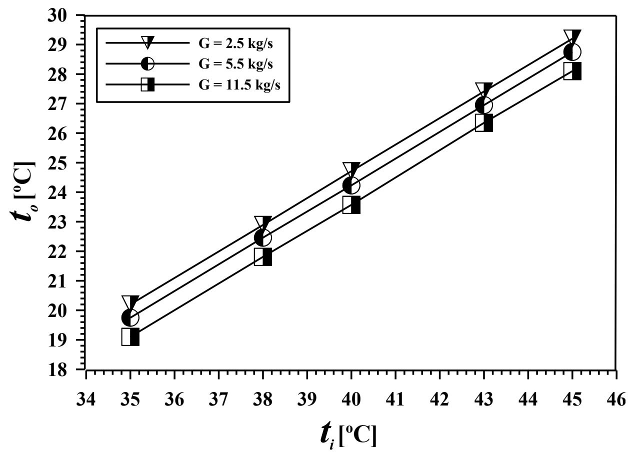

Figure 6: Effect of the air flow rate in the cooling tower on the outlet air at *L*= 0.65 kg/s, *g*=1.5 kg/s, and Ø=25%.

The air velocity in the air duct has a manifest effect on the outlet air temperature as shown in Figure 7, from which it can be deduced that as the air velocity increases the air temperature outlet decreases due to the increasing in the NTU of the air-water heat exchanger.

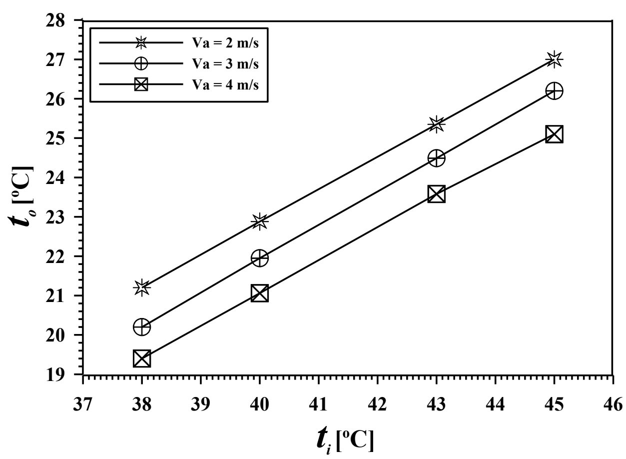

Figure 7: Effect of the air velocity in the air duct on the outlet air at *L*= 0.65 kg/s, G= 2.6kg/s, and Ø=25%.

5. Conclusion

The (IEC) system have been investigated which reveals that the main principles of the (IEC) system depends on the direct contact between the air and water where both heat and mass transfer between the air and water takes place in the cooling tower. The factors that effect on the performance of the (IEC) system are the inlet air conditions mainly inlet air wet bulb temperature or (air relative humidity) as its decreases the air temperature outlet decreases for constant water and air flow rates, also the flow rates of both the air and water in the cooling tower have highly impact on the (IEC) system and whenever these flows increases the air temperature out of the system decreases due the simultaneous of heat and mass transfer raising up. Likewise as air velocity in the duct increases the outlet of air temperature decreases due the heat exchanger effectiveness improvement. The (IEC) systems may successfully used as air cold conditioners at the arid climates such as Libya particularly southern regions. more studies on the (IEC) systems required to be done to improve their performance.

References

[1]. B. Costelloe, D. Finn, "Indirect Evaporative Cooling Potential in Air - Water Systems in Temperate Climates", *Energy and Buildings* Vol. 35 (2003) 573-591.

[2]. X. Zhao, Shuli Liu, S. B. Riffat, "Comparative Study of Heat and Mass Exchanging Materials for Indirect Evaporative Cooling Systems", *Building and Environment* Vol. 43, Issue 11, Nov. 2008, Pag. 1902-1911

[3]. R. Herrero Martin, "Numerical Simulation of a-Semi-Indirect Evaporative Cooler", *Energy and Buildings* Vol. 41, Issue 11 Nov. 2009, Pag. 1205-1214.

[4]. G. Heidarinejad, M. Bozorgmehr, S. Delfani, J. Esmaeelian, "Experimentally Investigation of Two-Stage Indirect/Direct evaporative Cooling System in Various Climatic Conditions", *Building and Environment* Vol. 44, Issue 10, Oct. 2009, Pag. 2073-2079.

[5]. Z. Duan,et al., "Indirect Evaporative Cooling: Past, Present and Future Potentials", *Renewable and Sustainable Energy Reviews",* Vol. 16, Issue 9, Dec. 2012, Pag. 6823-6850.

[6]. Ala Hasan, "Going Below the Wet-Bulb Temperature by Indirect Evaporative Cooling: Analysis Using a Modified Ɛ-NTU Method", *Applied Energy*, Vol. 89, Issue 1, Jan. 2012, Pag. 237-245.

[7]. Y.M. Xuan, et al., "Research and application of Evaporative Cooling in China: a Review (1)-Research", *Renewable and Sustainable Energy Reviews*", Vol. 16, Issue 5, Jun. 2012, Pag. 3535-3546.

[8]. Bogdari Porumb, et al., "A Review of Indirect Evaporative Cooling Technology", *Energy Procedia* , Vol. 85, Jan. 2016, Pag. 461-471.

[9]. M. Lemouari, M. Boumaza, and A. Kaabi, "Experimental Analysis of Heat and Mass Transfer Phenomena in a Direct Evaporative Cooling Tower", *Energy Conversion and Management*, Vol. 50, Issue 6, Jun. 2009, Pag. 1610-1617.

[10]. T. Kuehen, J. Ramsey, and J. Threlkeld, "Thermal Environmental Engineering", *Prentice Hall,* 1998.

Monitoring Mis-Operating Conditions of Journal Bearings based on Modulation Signal Bispectrum Analysis of Vibration Signals

Osama Hassin[1], Usama Haba1,[2], Fengshou Gu[2], Andrew Ball[2]
[1]osamingo@yahoo.com, [2] usama.haba@hud.ac.uk, [3] f.gu@hud.ac.uk,[4] a.ball@hud.ac.uk
[1]Department of mechanical, College of Engineering, University of Gharyan, Gharyan, Libya
[2]School of Computing and Engineering, University of Huddersfield, Huddersfield, UK

ABSTRACT

Journal bearings are widely used to undertake a wide range of operating conditions. Under high radial load, low rotating speed and thin lubrication films, asperity collisions between the journal and the bearing surfaces may occur. These self-excitations can create wideband random vibrations due to asperity contact and asperity churn. On the other hand, under low radial load and high rotating speed they can have instable operations due to oil whirls and shaft fluctuations. In addition, because of high lubricant viscosity, fluid shearing forces can be dominant, which may also result in wideband vibrations. These types of excitations together with structural responses can be coupled to produce nonlinear modulation phenomena. In this paper, modulation signal bispectrum (MSB) is used to analyses the vibration responses in order to identify the vibration signals values under different operating conditions and hence achieve condition monitoring of journal bearings. Furthermore, MSB coherences display clear regular modulating components in the high carrying frequency range due to coupling between shaft frequencies and the wideband compounds. In associating MSB-Coh. with normalising of MSB magnitude makes possibility to differentiate responses between asperity collision vibration and instability vibration. Thereby, it is possible to identify optimal operating conditions and detect abnormal operations caused by degraded lubrications or worn surfaces.

Keyword— Journal bearings, vibration condition monitoring, MSB, optimal operating conditions.

1. Introduction

A self-aligning spherical journal bearing has been designed for applications such as high speed fans and other similar applications. One usage of the journal bearing is to support radial load under high speed. It also designed to work at hydrodynamic lubricant regime in which thick oil film formed between the shaft and the bearing. Because of lubricant stiffness and damping coefficients, journal bearings are considered the best element for absorbing vibration, resisting shock, quietness and long life. In contrast, high radial load, low rotating speed, and weak of oil film may lead the journal bearing to work at boundary lubricant regime which causes metal-to-metal contact.

The idea of condition monitoring is monitoring the asset behaviour to detect, diagnose and prognoses faults and mis-operating conditions that have reached a certain symptomatic level to provide system breakdown. Vibration monitoring analysis is one of the main techniques used to diagnose and predict various defects [1]. Vibration monitoring is to break down a composite signal which generated from different vibration sources in which each source has a unique signal characteristic. Therefore, when the analyses of the journal bearing vibration signals carried out, many different sources of vibrations should be considered. The most well know external excited vibration sources of journal bearing are mechanical unbalance and misalignment. Furthermore, oil coefficients and asperity collisions also causes self-excited vibrations of journal bearing [2]. In this paper, vibration monitoring analysis is used to detect mis-operating conditions. When the machine operating conditions changes, the vibration signal changes accordingly. Modulation Signal Bispectrum (MSB) is a technique used to analyse the vibration of the composite signal which is a combination of the information and the carrier signals. This research found that MSB magnitude and MSB coherence are useful to identify vibration caused by internal and external excitations. MSB magnitude directed to vibration caused by self-excitation forces, in contrast, MSB coherence indicated to vibration caused by external-excitation forces. Finally, optimal operating conditions have been identified by coupling mean values of both MSB-Mag. and MSB-Coh. spectrums. Because the journal bearing does not contain any rotating element as a rolling bearing, vibration signals correlated to shaft rational speed and random asperity collisions.

2. The Lubrication Regimes

In 1846, Stribeck reported that the friction coefficient was inversely proportional to speed. Thus, he presented the characteristic curve of the coefficient of friction versus speed. Figure 6 illustrates the Stribeck curve, this shows the relationship between the coefficient of friction and bearing parameter or modulus $\eta N/p$, where η is the absolute viscosity of the lubricant in kg/m.s, N is the shaft speed in rpm and p is the pressure on the projected area in Pa. The Stribeck curve shows how the coefficient of friction changes with lubrication regime: boundary lubrication, mixed-film lubrication and hydrodynamic lubrication. The optimum point of the curve is when the coefficient of friction passed through a minimum point from mixed to hydrodynamic lubrication [4]. Many parameters influence the friction coefficient such as the operating condition (speed and pressure), the material properties (roughness of surface) and the viscosity of the lubricant. Later, the Stribeck curve application extended to a number of tribology component besides journal bearing. For example, ball bearing, seals and wet clutches have applied the Stribeck curve idea.

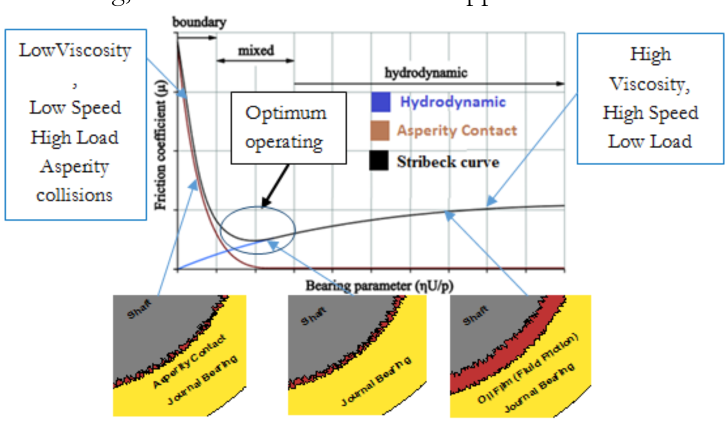

Figure 6: Lubrication regimes of a journal bearing [3]

3. Vibration of Journal Bearing

Vibration responses of a self-aligning journal bearing directly linked to the radial load, rotating speed, lubricant viscosity, oil film thickness, eccentricity, surface asperity characteristics and material of the bearing. Different forces placed on journal bearing affect the vibration responses and produce both low and high frequency vibrations. For example, the low journal whirling frequency is influenced by shaft fluctuating. Likewise, high random frequency bands of the vibration signals are occurred by asperity collisions and churns [5]. At hydrodynamic regime, journal bearing vibration sources often are generated by mechanical contact between the rotating shaft and stationary bearing [6]. High clearance causes looseness of bearing which generates more of a square wave than a sinusoid wave [7] and, many harmonics are generated from these signals. In the case of severe looseness, it is stretched all the way across the spectrum and half-harmonics are even generated in extreme cases (one time, double times, three times, four times, five times, six times, etc.) rpm [7]. Another type of excitations is mechanical unbalance which causes a pure sinusoid and therefore generates a peak at one time rpm [8]. Journal bearing is often generate vibration peaks at frequencies lower than one time rpm. Another problem of the journal bearing is oil whirl. In which oil whirl is a phenomenon that vibrations are excited by oil film between frequency from 0.38 time rpm to 0.48 time rpm. Changes in viscosity and pressure of the oil and related loads can affect oil whirl [9]. Asperity collisions and churns interactions are sources of self-excitation, which result in high responses at structure resonances. The random high frequency of vibration responses is mainly related to two frictional effects. High frequency bands around 10kHz of the bearing are related with both asperity contacts and fluid friction through the method of clustering spectrum of vibration signals, [10]. The response frequency of self-excited vibration is very close to one of the system's natural frequencies [11]. Finally, the interaction between periodic responses and resonant responses produce modulation signals. The equation bellow presents different sources of vibration in a journal bearing [12].

$$m_s x + \overset{\text{Hydrodynamic}}{k[p(x),\omega,\mu]x} + \overset{\text{Asperity churns}}{\sum_{\mathrm{i}=1}^{n} k_{\mathrm{i}}\Gamma[p(x),\omega,\mu]x} + \overset{\text{Asperity collisions}}{\sum_{\mathrm{i}=1}^{n} k_i\Psi[p(x),\omega,\mu]x}$$

$$= \overset{\text{Static radial load}}{F_r} + \overset{\text{Unbalance+misalignment}}{\sum_{\mathrm{i}}^{n} \mathrm{A_i}\cos(i\omega t + \alpha_{\mathrm{i}})} \qquad (1)$$

where m_s is the mass of the shaft; k_{i} denotes the bending stiffness of an arbitrary micro asperity; k is the stiffness coefficients due to hydrodynamic pressure effect which includes inherent surface defects and journal elastic deformations of micro asperities and main load zones.

4. Modulation Signal Bispectrum

Understandably, high forces of external and internal excitation will generate massive vibration responses. Any mechanical problem will produce vibration with low frequency correlated to shaft rotational speed. Contrast, random asperity collisions will produce high band frequency. Due to a low frequency (information signal) is superimposed on a high frequency (carrier signal) modulation signal of vibration will be generated in journal bearing. Bispectrum is a non-linearity signal generated by interact two waves. MSB is used to detect coupling signal between shaft frequencies and the wideband compounds. The modulation signal of vibration is formed by nonlinear of two components, periodic and random signal. Thus, it is anticipated that bispectrum can give a more accurate representation of the vibration signal for mis-operating diagnosis [13]. The Discrete Fourier Transform (DFT) $X(f)$ of a vibration signal $x(t)$ is defined in the form of Modulation Signal Bispectrum (MSB),

$$B_{MS}(f_x, f_c) = E\left\langle X(f_c + f_x) X(f_c - f_x) X^*(f_c) X^*(f_c) \right\rangle \quad (2)$$

The phase relationship of MSB is

$$\begin{aligned} \varphi_{MS}(f_x, f_c) &= \varphi(f_c + f_x) + \varphi(f_c - f_x) - \varphi(f_c) - \varphi(f_c) \\ &= \varphi(f_x) + \varphi(-f_x) \end{aligned} \quad (3)$$

where f_x is information frequency; f_c is the carrier frequency, $f_c + f_x$ and $f_c - f_x$ are the higher and lower sideband frequencies respectively. It takes into account both $f_c + f_x$ and $f_c - f_x$ simultaneously in Equation above for quantifying the nonlinear effects of modulation signals. If they are due to the modulation effect between f_c and f_x, a bispectral peak will be at bifrequency $B_{MS}(f_x, f_c)$. On the other hand, if these components such as various noises are not coupled but have random distribution, their magnitude of MSB will be close to zeros. In this way, the wideband noise and aperiodic components of vibration signals can be suppressed effectively so that the discrete components relating modulation effects can be represented sparsely and characterised more accurately.

A normalized form of MSB, also named as modulated signal bicoherence, is introduced as,

$$b^2{}_{MS}(f_x, f_c) = \frac{|B_{MS}(f_x, f_c)|^2}{E\left\langle |X(f_c) X(f_c) X^*(f_c) X^*(f_c)|^2 \right\rangle E\left\langle |X(f_c + f_x) X(f_c - f_x)|^2 \right\rangle} \quad (4)$$

It is to measure the degree of coupling between three components against noise influences, in the same way as the conventional bicoherence [14, 15].

5. Experimental Procedure

A self-aligning spherical journal bearing, SA35M shown in Figure 7, has been tested. In this experimental, three types of lubrication are used to generate different operating conditions denoted as lube 22, 37 and 46

VG. Also, three different speed 1500, 1200 and 900 rpm are used. Furthermore, four different radial loads 1, 5, 10 and 20 bar are exerted on the shaft supported between two bearings. These different viscosities, rotation speed and radial load will lead journal bearing to work under different lubricant regimes. Figure 7 shows the journal bearing test rig. An accelerometer sensor is fixed horizontally to collect the vibration signals. Also, an encoder and a pressure sensor are placed to measure the output rotating speed and radial load, respectively.

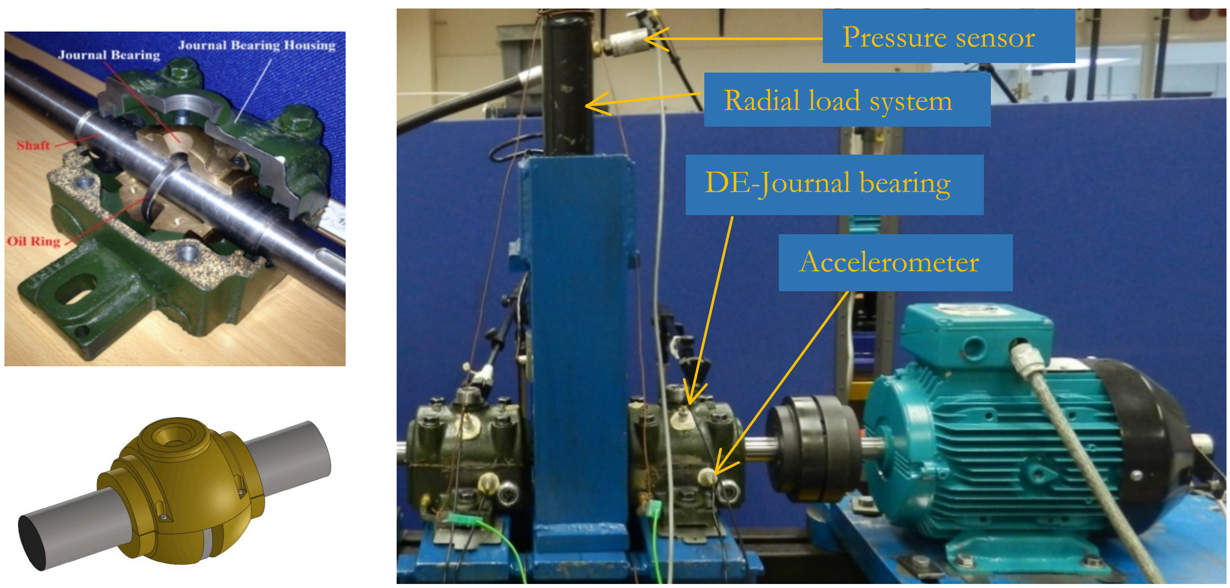

Figure 7: Self-aligning journal bearing components and test rig [12]

6. Experimental Results

RMS values are proportional to speeds, loads but do not show any significant difference between lubrication types because of instability distribution of the oil by oil ring and non-linearity distribution of the temperature. In theory, low speed causes more friction especially at high load but in the RMS results,
Figure 8, show that the high speed always has high vibration and high load conditions generate high vibration energy. Also, different viscosities generate nonlinear RMS values of the vibration signals Thus in this study; the RMS values do not provide any good indication to present the bearing condition at different lubricant regimes. Therefore, these values do not consider to be a good indicator to obtain optimum operating conditions because they are always proportional to loads and speeds.

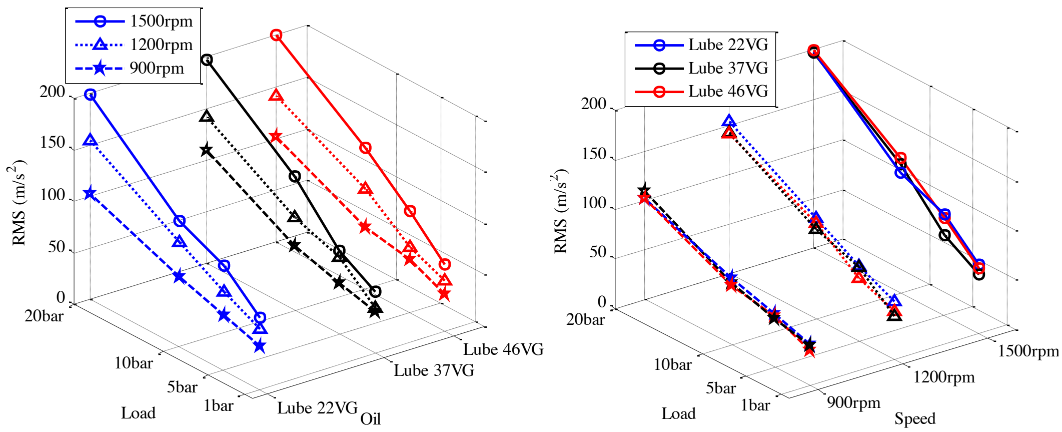

Figure 8: RMS values of vibration signals under different operating conditions

6.1. MSB Magnitude and MSB Coherence Results

Modulation signal bispectrum is dealing with coupled signals. In this manner, the wideband noise and periodic components of vibration signals can be suppressed effectively so that the discrete components relating modulation effects can be represented sparsely and characterised more accurately. MSB-Mag. and MSB-Coh. can provide a more clear representation of the journal bearing operation under different operating conditions. From Figure 10, it can be found that there is a high frequency band sensitive to changing radial load in MSB-Mag. These bands might be correlated with the friction of asperity collision caused by increasing the radial loads, which decrease the contact point at hmin and leads to metal-to-metal contact. In MSB-Coh. Figure 12, there is clear frequency band related to shaft speed. As a result of that, the small wedge may decrease fluctuating of the shaft and make it rotates more stable. High viscosity lubricant has high damper coefficient to absorb more vibration than low viscosity, but it loses its ability to move easily into the gap between surfaces. Moreover, high viscosity might cause asperity churns at high radial clearance in load zone.

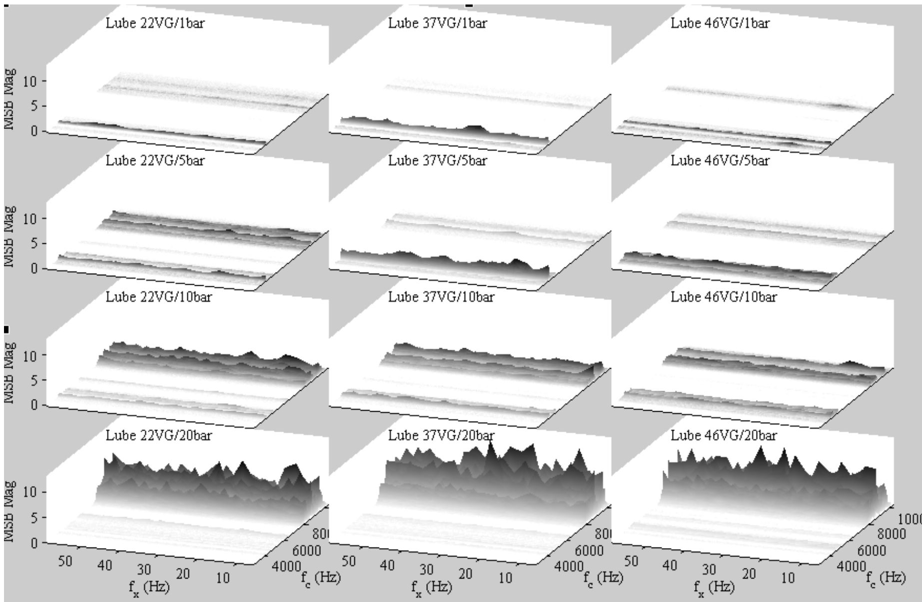

Figure 9: MSB-Mag. at 900rpm under different loads and viscosities

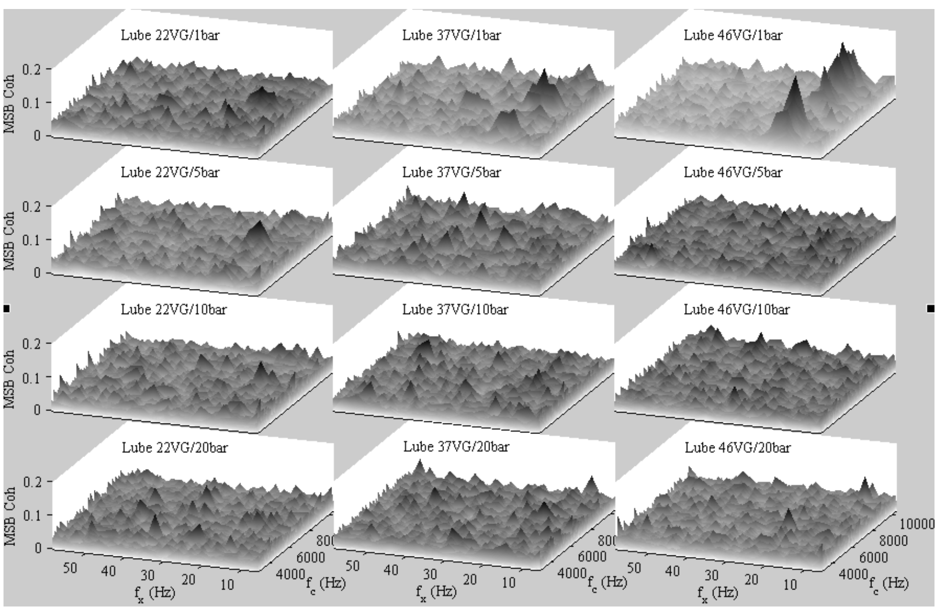

Figure 10: MSB-Coh. at 900rpm under different loads and viscosities

6.2. Mean Values of MSB Magnitude and MSB Coherence Results

MSB-Mag. manly presents asperity collision. In contrast, MSB-Coh. presents stability of the shaft. By calculating mean values of both MSB-Mag. and Coh. It can be found that the low load has the lowest mean of MSB-Mag., and at the same time has a higher mean value of MSB-Coh. In contrast, high load has less value of MSB-Coh. and high value of MSB Mag. as can be seen in Figure 11 That means, high load makes shaft more stable but causes asperity collision.

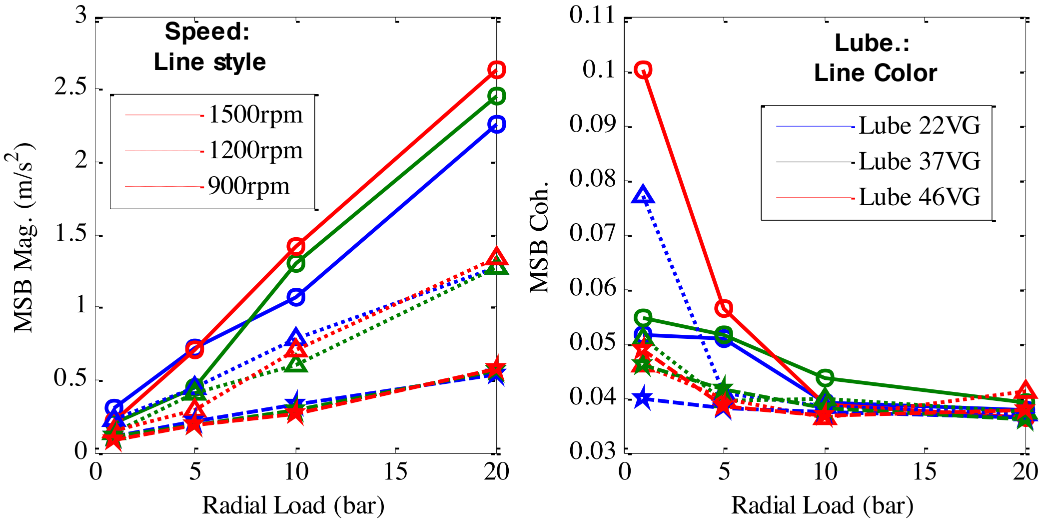

Figure 11: Mean values of MSB-Mag. and MSB-Coh.

Figure 12 shows gathering results of mean values of normalized MSB-Mag. and mean values of MSB-Coh. Examine the Figure representation; this operating condition could be considered as an acceptable operating conditions of the journal bearing compared with Stribeck curve in Figure 6. So, less mean value of MSB-Mag. and less value of MSB-Coh can be identified as an optimum operating condition.

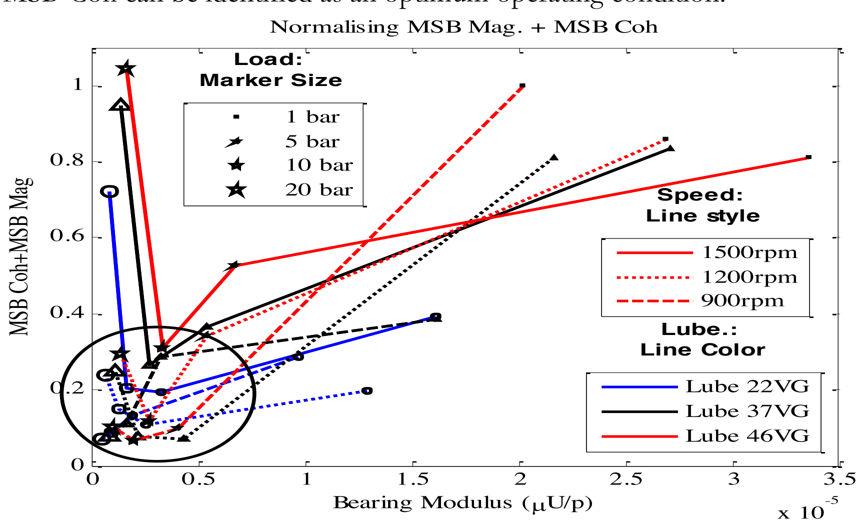

Figure 12: Representative Stribeck curve by coupling MSB-Mag. and MSB-Coh.

The optimum operating conditions in this experiment is at speed 1200 rpm and under 5 bar load of oil 37. The worst operating condition at hydrodynamic regime is at speed 1500rpm under load 1 bar and oil 46. The worst operating condition at boundary regime is at speed 900 rpm under load 20 bar and oil 22. These results prove the theory of Stribeck curve.

7. Conclusion

When the shaft rotates under a different operating condition, vibration signals manifests rich frequency components due to various vibration excitations such as mechanical problem, asperity collisions and asperity-fluid interactions. The mechanical problem, unbalance, occurs when the radial clearance is too large. To avoid this instability, a small radial load should be applied, or radial clearance should be decreased. However, if the radial load exceeds a certain level, metal-to-metal contacts will occur and generate more unneeded frictions, so the radial load should be carefully chosen.

RMS values of raw data are not convenient to obtain optimum operating conditions and do not differentiate between speeds and oil viscosities under different loads. On the other hand, mean values of MSB-Mag. and MSB-Coh. are found to be effective to determine the optimum operating condition. Abnormal conditions such as high loads, low viscosities and low speeds have high mean values of MSB-Mag. In the meantime, un-wanted operating conditions such as low load, high viscosity and high speed have high means value of MSB-Coh. Finally the mis-operating conditions have been found by analysing vibration signals based on coupling MSB-Mag. and MSB-Coh.

References

[1]. Sethiya, S., Condition Based Maintenance (CBM). Secy. to CME/WCR/JBP, 2006.

[2]. Raharjo, P., An Investigation of Surface Vibration, Airbourne Sound and Acoustic Emission Characteristics of a Journal Bearing for Early Fault Detection and Diagnosis. University of Huddersfield, May 2013.

[3]. Tomanik, E. and A. Ferrarese. Low friction ring pack for gasoline engines. in ASME 2006 Internal Combustion Engine Division Fall Technical Conference. 2006. American Society of Mechanical Engineers.

[4]. Frene, J., et al., Hydrodynamic lubrication: bearings and thrust bearings. Vol. 33. 1997: Elsevier.

[5]. Raharjo, P., et al., Vibro-Acoustic Characteristic of A Self Aligning Spherical Journal Bearing due to Eccentric Bore Fault. 2012.

[6]. Kim, M., et al., Experimental identification of abnormal noise and vibration in a high-speed polygon mirror scanner motor due to mechanical contact of plain journal bearing. Microsystem technologies, 2010. **16**(1-2): p. 3-8.

[7]. Looseness - Bearing - VibrationSchool.com. 17 Nov 2015

[8]. Unbalance - Single Plane - VibrationSchool.com. 11 Nov 2015.

[9]. Journal bearing problem . VibrationSchool.com. 27 Nov 2015

[10]. Osama Hassin, et al., Journal bearing lubrication monitoring based on spectrum cluster analysis of vibration signals in CMADEM 2015. 2015.

[11]. Muszynska, A., Free, forced, and self-excited vibration. December 1997.

[12]. Osama Hassin, Condition Monitoring of Journal Bearings for Predictive Maintenance Management Based on High Frequency Vibration Analysis**,** PhD thesis**,** May 2017.

[13]. Gu, F., et al., Electrical motor current signal analysis using a modified bispectrum for fault diagnosis of downstream mechanical equipment. Mechanical Systems and Signal Processing, 2011. **25**(1): p. 360-372.

[14]. Gu, F., et al., A new method of accurate broken rotor bar diagnosis based on modulation signal bispectrum analysis of motor current signals. Mechanical Systems and Signal Processing, 2015. **50**: p. 400-413.

[15]. Gu, F., et al., A Novel Method for the Fault Diagnosis of a Planetary Gearbox based on Residual Sidebands from Modulation Signal Bispectrum Analysis. COMADEM 2014 16th-18th Sep. Brisbane, Australia., 2014.

Design Of Reinforced Concrete Beams Using Two different Specification

Gumaa A. Hasan[1],Mohammed A. Elsageer[2], Musbah A. Hasan[3]
[1]Gumaa.hasan@yahoo.com, [2]drmohammedalsger@gmail.com, [3]abormila@googlemail.com
[1, 2, 3]Department of Civil Engineering, College of Engineering, Sirte University, Libya

ABSTRACT

Nowadays, reinforced concrete beams are designed using traditional specification, such as BS8110 and Eurocode2 based on truss action. In this research BS8110 and Eurocode2 specification of designing a beam for flexure and shear are studied and compared with each other, to provide an in depth understanding of the two approaches. Two beams are designed, the first beam using BS8110 and the second beam using Eurocode2. The designs based on BS8110 and Eurocode2 at the ultimate and serviceability limit states are discussed and the approach used to predict deflections is described and checked using standard relationship based on statics. Secondly the BS8110 and Eurocode2 approaches to designing a beam for shear and deflection are compared with each other. the two test beams are tested and the test results are compared with predicted results. The results from the laboratory tests have shown that the Eurocode2 beam carried a higher load and gave a higher central deflection compared to BS8110.

Keyword— Reinforced Concrete, Beam analysis, shear and deflection.

1. Introduction

Concrete is the most important construction material in the construction industry [1, 2]. There are approximately 2,000,000 billion tonnes of concrete being produced yearly [2]. Although concrete is good in compression and a durable material, it is weak in tension, where its tensile strength is approximately 10% of its compressive strength [3]. Concrete fails in tension when it is exposed to tensile stresses that are greater than its tensile strength capacity. So concrete on its own cannot resist these tensile stresses and it needs to be reinforced with another material that is good in tension, such as steel bars, to prevent failure of concrete in tensile region.

Current design approaches for structural concrete beams are based on truss action [4]. In these design approaches the beam is designed firstly for flexure and then for shear independently of each other.

2. Comparison Between Provisions for Shear in BS8110 And Eurocode2

2.1 Shear:

In the design for shear the basic principles behind the approaches in BS8110 and Eurocode2 are the same [5], and they are as follows

If the applied shear is less than the shear resistance of the concrete, minimum shear reinforcement should be provided, If the applied shear is higher than the concrete shear strength and less than the maximum design shear, designed shear reinforcement should be provided and if the applied shear is higher than the maximum design shear then a larger section must be chosen.

2.1.1 Shear Strength of Concrete

vc in BS8110 is equivalent to $\frac{VRd}{bd}$ in Eurocode2, where vc is design shear stress for concrete, VRd is the shear stress in concrete, b is the width of the section, and d is the effective depth of tension reinforcement

In BS8110 and Eurocode2 the strength of the concrete without shear links is dependent on the percentage of tensile reinforcement steel, the concrete grade and the effective depth of section and any axial forces are ignored [5, 6, 7].

Expression In BS8110

$$\mathrm{vc} = \frac{0.79[\left(100\frac{\mathrm{As}}{\mathrm{b.d}}\right)^{\frac{1}{3}} \times \left(\frac{400}{\mathrm{d}}\right)^{\frac{1}{4}} \times \left(\frac{\mathrm{fcu}}{25}\right)^{\frac{1}{3}}]}{\gamma_\mathrm{m}}$$

(1)

where vc is Shear stress in concrete, As is Area of tensile reinforcement, fcu is Characteristic strength of concrete, and γ_m is Factor of safety

Expression In Eurocode2

$$v_{Rd,c} = 0.18 \times \left(1 + \sqrt{200/d}\right) \times (100\rho_1 \times fck)^{1/3}/\gamma_m \quad (2)$$

where ρ_1 is Longitudinal reinforcement ratio, and fckis Characteristic of concrete

The limitations associated with each of these equations are as follows:

Expression In BS8110:

The percentage of tensile reinforcement should not be greater than 3% [BS8110]

The effective depth d should not be greater than 400 mm [8]. According to BS8110 the concrete shear capacity increase with depth less than 400 mm.

The ultimate concrete strength f_{cu}should not be greater than $40N/mm^2$[BS8110, 8]

The factor of safety is 1.25 [BS8110, 8]

Expression In Eurocode2:

The percentage of tensile reinforcement should not be greater than 2% [7, 8]

The effective depth d should not be greater than 600 mm

There is no limit placed on the concrete strength (f_{ck}) [8]

The factor of safety is 1.5 [7, 8]

Tables 1 and 2 show the shear stresses for a concrete with a cube strength of $30\ N/mm^2$using BS8110 and Eurocode2

Table 1: Shear Strength of Concrete BS8110 [8]

	d (mm)				
100As/bd	150	250	300	400	600
0.15%	0.46	0.4	0.38	0.36	0.36
0.3%	0.57	0.51	0.48	0.45	0.45
1%	0.86	0.76	0.72	0.67	0.67
3%	1.24	1.09	1.04	0.97	0.97

Table 2: Shear Strength of Concrete Eurocode2 [8]

	d (mm)				
100As/bd	150	250	300	400	600
0.15%	0.40	0.35	0.34	0.32	0.29
0.3%	0.51	0.44	0.43	0.40	0.37
1%	0.75	0.66	0.63	0.60	0.55
3%	1.09	0.96	0.92	0.86	0.80

2.1.2 Strength of Concrete Section With Shear Links

Designing concrete beam in shear using Eurocode2 can lead to significant economies in shear links compared to a beam designed using BS8110 [5, 7]

BS8110 – Assumptions:

- The angle between the notional compressive struts and the axis of the beam is constant and fixed at an angle $45°$ [5]
- The lever arm is assumed to be equal to the effective depth of the section [5]

Eurocode2 – Assumptions:

- The angle $\theta°$ between the notional compressive struts and the axis of the beam has a value within the range of 22° to 45° [5, 7].
- The lever arm is assumed to be equal to $0.9d$ [5, 7].

The resulting equations are as follows:

BS8110

$$\frac{\mathrm{Asv}}{\mathrm{b\times Sv}} = \frac{(\mathrm{v-vc})}{\mathrm{fyv}/\gamma_{\mathrm{m}}} \tag{3}$$

where Asv is the area of shear reinforcement, v is the Shear stress, Sv is the Spacing between links and fyv is Characteristic strength of links

Eurocode2

$\frac{\mathrm{Asw}}{\mathrm{b \times S}} = \frac{\gamma_m \times v_{Ed}}{0.9.\mathrm{fyk}.\cot\theta}$ where $v_{Ed} = \frac{V_{Ed}}{b.d}$

(4)

where v_{Ed} is the Shear forces at the ultimate limit state, fyk is the Characteristic strength of reinforcement and S is the Spacing between links

it should be noted that in BS8110 the shear reinforcement does not resist the total applied shear but only resists the shear in excess of that which can be resisted by the concrete $(v - vc)$ [7], where v is the design shear stress and vc is the design concrete shear stress. In Eurocode2 all the shear must be carried by the shear links, when shear links are required [5, 7]

2.1.3 Maximum Shear Strength of Section

The maximum allowable shear force is limited by placing a limit on the crushing strength of the diagonal compression member to prevent excessive stress from occurring in the diagonal compressive strut and hence prevent compressive strut failure of the concrete.

In BS8110 the maximum allowable shear is dependent on the strut angle and concrete strength, and since the angle of inclination of the strut has a constant value, the maximum shear is dependent only on the concrete strength [7].

$v_{max} = 0.8\sqrt{fc} \quad \leq 5N/mm^2[BS8110]$. where fc is the Compression stress of concrete (5)

In Eurocode2 the angle $\theta°$ has a value within the range of 22° to 45° , and hence the maximum shear is a function of the angle $\theta°$ and the concrete strength [7].

$v_{Rd,max} = \frac{0.36(1-{fck}/{250})\times fck}{\cot\theta - \tan\theta}[7]$ (6)

A comparison of the maximum shear stress permitted within BS8110 and Eurocode2 is shown in Table 3.

Table 3: Maximum Shear Stress Limitation in BS8110 and Eurocode2 [5].

Cube strength (N/mm^2)	Eurocode2		BS8110
	$\theta°$		
	27°	35°	
25	2.91	3.38	4
30	3.38	3.92	4.38
40	4.19	4.87	5
50	4.85	5.64	5
60	5.36	6.22	5

2.1.4 Enhanced Shear Near Supports

BS8110 and Eurocode2 allow greater shears to be resisted by a concrete section which is close to the supports of a beam. The enhancement is a function of the av/d ratio where d is the effective depth of the section and av is the distance from the section considered to the face of the beam support. In BS8110, the design concrete shear stress vc, can be enhanced by $2d/av$ where $2d$ is greater than av. In Eurocode2 the shear which can be resisted by the concrete without shear links, can be enhanced by $2.5d/av$ where $2.5d$ is greater than av[5, 6]. Eurocode2 allows a slightly higher enhancement of the shear capacity than BS8110 , so benefits are less in the case of BS8110 compared to Eurocode2 [8]

2.1.5 Spacing Of Links

BS8110

"The spacing of links in the direction of the span should not exceed 0.75d. At right-angles to the span, the horizontal spacing should be such that no longitudinal tension reinforcing bar is more than 150 mm from a vertical leg; this spacing should in any case not exceed d"[9]

Eurocode2

In Eurocode2 the spacing is a function of the applied shear. The rules are shown in Table 4.

Table 4: Spacing between Links [5, 6]

Applied Shear	Spacing (mm)	
	Lateral Spacing	Longitudinal Spacing
$v < v_{max}\times 1/5$	$d \leq 800$	$0.8d \leq 300$
$v_{max}\times 1/5 < v < v_{max}\times 2/3$	$0.6d \leq 300$	$0.6d \leq 300$
$v > v_{max}\times 2/3$	$0.3d \leq 200$	$0.3d \leq 200$

2.1.6 Additional Tensile Forces

In Eurocode2 the tensile force in the bottom tension member is given by:

$$Fs = M/Z + 1/2 \times V_{Ed} \times \cos\theta \tag{7}$$

where Fs is the Tensile stress of reinforcement, M is the Design ultimate moment, and Z is the Lever arm. The second term in this equation is related to the shear forces in the links, so Eurocode2 takes into account the tensile forces which are caused by the bending and shear force in the links.

BS8110 takes into account only the first term in this equation (the bending term) and ignores the tensile force which is caused by shear force (second term in this equation).

2.2 Deflection

1- The assumptions which are required to define the behavior of a section under any loading condition are as follows:

BS8110

In an un-cracked section the reinforcement and the concrete in tension and compression are assumed to behave elastically. The modulus of elasticity of the reinforcement may be taken as 200 kN/mm^2 and for the concrete may be taken from BS8110-2:1985, Section 3.5

In a cracked section the reinforcement in tension and compression is assumed to behave elastically and the concrete in compression is also assumed to behave elastically but in the tension region the concrete is assumed to behave linearly from zero stress at the neutral axis to a limiting stress of $1\ N/mm^2$ at the centroid of the tensile reinforcement for short term loading and $0.5\ N/mm^2$ for long term loading. [9].

Eurocode2

In an un-cracked section the reinforcement and concrete in tension and compression are assumed to behave elastically [5]. The modulus of elasticity for the reinforcement can assumed to be $200kN/mm^2$.

In a cracked section the reinforcement in tension and compression is assumed to behave elastically and the concrete in compression is assumed to behave elastically but in tension the concrete stress is ignored. [7].

Where BS8110 assumes that the tensile strength of concrete is approximately 1 N/mm^2 and Eurocode2 uses a significantly higher value than BS8110 [5].

2- Curvature

According to Narayanan [18], see Figure 1 (a parameterized moment-curvature diagram), when M/bd^2 is in between 0.3 and 0.6, BS8110 gives higher curvature values than Eurocode2. This is because BS8110 uses a value for the tensile strength of concrete of approximately 1 N/mm^2 and Eurocode2 uses a much higher value. In general terms BS8110 and Eurocode2 are more or less equivalent.

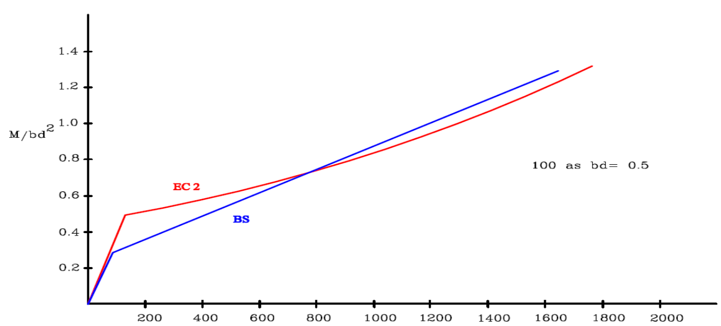

Figure 1: Comparison of Curvatures Predicted by BS8110 and Eurocode2 [18]

2.3 Economic Study

The Table 5 shows that the traditionally designed beams, which have been designed using BS8110 and Eurocode2, the weights of the reinforcement are 38.48 kg and 39.78 kg respectively.

Table 5: Weight and Cost of Reinforcing Bars in Beam

	Size of bar	No. Of bars	Length of bar (m)	Total length of bars (m)	Density of bar	Weight of bar (kg/m)	Total weight of bars (kg)	Weight of beam (kg)
Beam (1) BS8110	6	23	1.178	27.094	7.8	0.220	5.97	38.48
	10	2	3.45	6.9	7.8	0.612	4.225	
	20	3	3.85	11.55	7.8	2.45	28.297	
Beam (2) Eurocode2	6	28	1.178	32.984	7.8	0.220	7.27	39.78
	10	2	3.45	6.9	7.8	0.612	4.225	
	20	3	3.85	11.55	7.8	2.45	28.297	

3. Details of Materials And Test Procedure

3.1. Description Of Beams And Loading Arrangement

Two beams were prepared for the laboratory based test programme with a rectangular cross-section of $200mm\times300mm$, an overall length of 3500 mm, an effective span of 3000 mm and a minimum cover of 25 mm.

The two beams were tested using a four point loading arrangement the loading points were located at distance equal to 662.5 mm from the center line of each support, see Figure 2, the spacing was based on Kani's Valley.

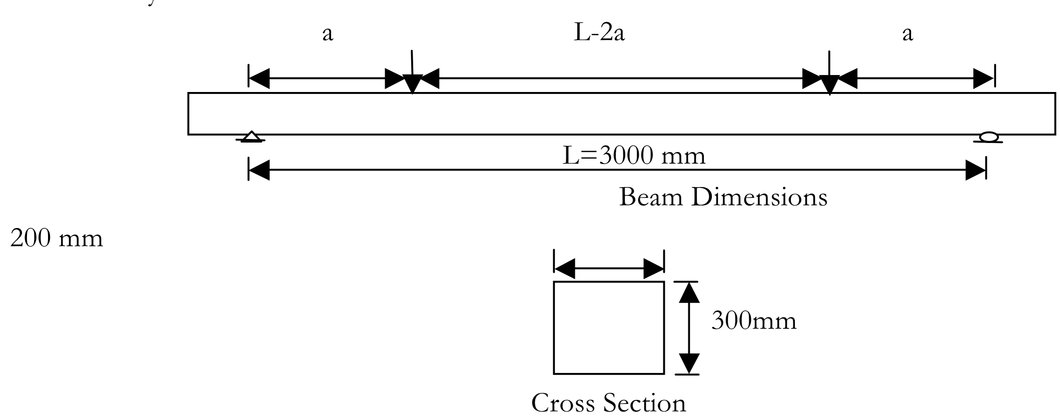

Figure 2: Details of Beam and Loading Arrangement

3.2. Design Of Test Beams

The beams were designed using two design approaches i.e. BS8110 Part 1 [1] and Eurocode2 [7]. The first beam was designed using the approach described in BS8110 and the secondbeam was designed using the approach in Eurocode2. Table 6 provides details of the three beams.

Table 6: Beam Specifications

Beam	Cross-section (mm^2)	Tensile bars (mm^2)	Spacing of links (mm)
BS8110	(200×300)	$3T20$	$T6\ at\ 150$
Eurocode2	(200×300)	$3T20$	$T6\ at\ 100$

3.3. Details Of Reinforcement

Three sizes of reinforcing bars were used and they are as follows:

- 6mm diameter reinforcing bars were used as shear reinforcement in all three beams.
- 10mm diameter reinforcing bars were used as hanger bars for the links in all three beams.
- 20mm diameter reinforcing bars were used as tensile reinforcement in all three beams.

The three bar sizes were tested to obtain the mechanical properties using of the steel. Tables 7, 8 and 9 show the tensile test results. All reinforcing bars were high yield steel.

Table 7: Tensile Test Results for 6mm Diameter Reinforcing Bars

Test	Maximum load (kN)	Tensile strength (N/mm^2)	Young's modulus (N/mm^2)
Test 1	16.61	588	196
Test 2	16.51	584.1	194
average	16.015	567	195

Table 8: Tensile Test Results for 10mm Diameter Reinforcing Bars

Test	Maximum load (kN)	Tensile strength (N/mm^2)	Young's modulus (N/mm^2)
Test 1	49	624	197
Test 2	47.98	611	202
average	48.49	617.5	199.5

Table 9: Tensile Test Results for 20mm Diameter Reinforcing Bars

Test	Maximum load (kN)	Tensile strength (N/mm^2)	Young's modulus (N/mm^2)
Test 1	203.2	647	211
Test 2	199.47	635.25	205
average	201.33	641.13	208

3.4. Details Of The Concrete

Six cubes and six cylinders were taken from the concrete mix in order to obtain the concrete crushing strengths at the time the beams were tested. These results were used to obtain the best estimate of the flexural/shear capacities of the beams and also the deflection values for the beams i.e. two sets of calculation were prepared one set assuming the concrete strength to be 30 N/mm^2 and the second set using actual concrete strength obtained from the cubes and cylinders. The material and load safety factors were moved from all the calculations used to predict the flexural and shear carrying capacities and the deflections of the beams. Tables 10 and 11 show the results obtained from the cube and cylinder tests carried out at the time the beams were tested.

Table 7: Concrete Cube Crushing Test Results

Ten day strength	Weight of cube (g)	H_1 (mm)	H_2 (mm)	H_3 (mm)	Applied loading (kN)	f_{cu} (N/mm^2)
Cube 1	2417	100	100	100	182	18.2
Cube 2	2518	100	100	100	200.4	20.04
Cube 3	2442	100	100	100	195.3	19.53
Cube 4	2421	100	100	100	211	21.1
Cube 5	2420	100	100	100	180.7	18.07
Cube 6	2400	100	100	100	203.4	20.34

Table 8: Concrete Cylinder Crushing Test Results

Ten day strength	Weight of cube (kg)	Diameter (mm)	high (mm)	Applied loading (kN)	f_{cK} (N/mm^2)
Cylinder 1		150	300	214.5	12.4

Average cube strength = $19.54 \quad N/mm^2$
Average cylinder strength = $12.4 \quad N/mm^2$

4. Results From Laboratory Based Test Programme

4.1. BS8110 Beam

According to the results from the laboratory based test, the maximum failure load was 80kN and the maximum deflection at mid span was 11.64 mm. Figure 3 shows the relationship between the applied load and central deflection of the beam.

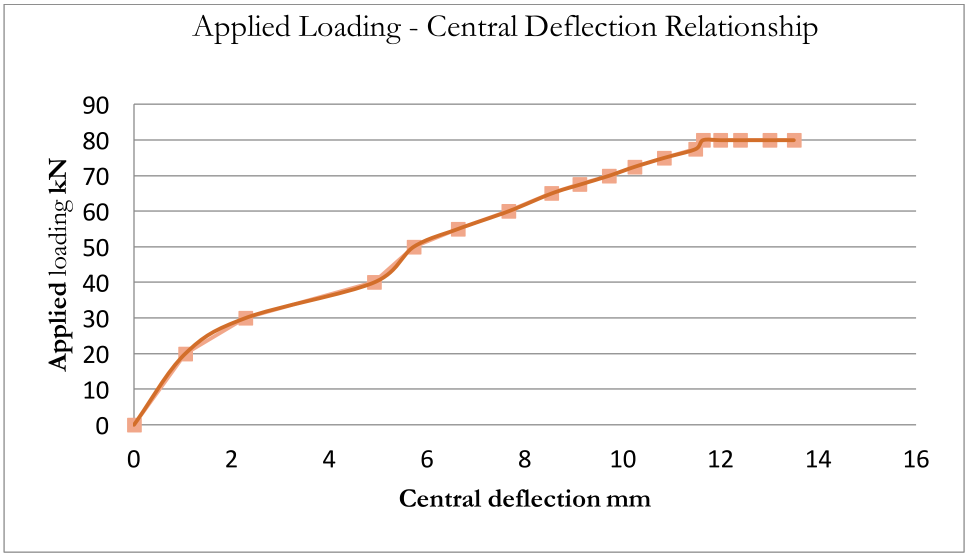

Figure 3: Applied Load- Central Deflection Relationship

4.2. Eurocode2 Beam

The maximum applied load at failure for the Eurocode2 Beam was 95kN and the maximum deflection at mid span at failure was 24 mm. Figure 4 shows the corresponding applied load - deflection relationship.

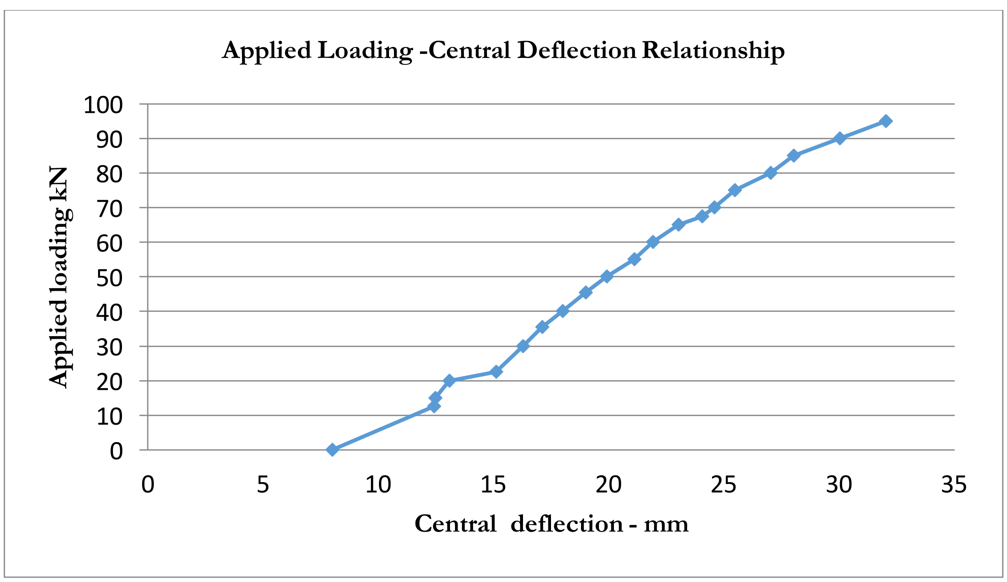

Figure 4: Applied Loading-Central Deflection Relationship

5. Conclusion

1. The BS8110 and Eurocode2 beams failed in shear before reaching their ultimate flexural capacity.
2. The Eurocode2 specification is much easier to follow than the specification detailed in BS8110
3. The Eurocode2 specification requires less shear reinforcement than the BS8110 specification
4. BS8110 and Eurocode2 are similar in that
   - The shear stress depends on the effective depth and tensile reinforcement ratio and the concrete strength
   - There is a shear stress below which only minimum shear reinforcement need be provided
5. BS8110 and Eurocde2 are different in that
   - In BS8110 the shear reinforcement does not resist all the applied shear but resists only the shear in excess of that which can be resisted by the concrete $(v - vc)$ [18], where v is the design shear stress and vc is the design concrete shear stress. In Eurocode2 the shear must be carried by the shear links, when the shear links are required
   - The BS8110 specification gives a higher value of $v_c$than is obtained from Eurocode2 for C30 concrete
   - Eurocode2 permits significantly higher shears to be resisted by a section than does BS8110
   - The scope of the approach in Eurocode2 is more extensive than the specification used in BS8110 for instance in Eurocode2 there is no limit placed on the concrete strength and designer is free to chosen any angle of inclination of the compression strut between 22° and 45° [8].
   - In Eurocode2 the designer can seek out economies in the provision of shear reinforcement.
6. The results from the laboratory tests have shown that the Eurocode2 beam carried a higher load (95kN) and gave a higher central deflection (24mm) compared to BS8110 beam which failed under a load of 80 $kN$and a maximum central deflection of 13.5mm.

References

[1] MacGinley T J, Choo B S, Reinforced concrete, design theory and examples. Second edition, 1990.

[2] Royal Society of Chemistry, The Concrete conundrum. Available on: http://www.rec.org/chemistryworld/restricted/2008/Msrch/TheConcreteConundrum. asp.

[3] Gambhir M L, Concrete Technology, 2004.

[4] Kuttab, A S and Haldane, Detailing for shear with the compressive force path concept. Proceeding of the IABSE Colloquium. Structural Concrete, Vol 69 No: 6, pp74-150, 1991.

[5] Narayanan R S, Concrete structures: Eurocode EC2 & BS8110 Compared, 1994.

[6] Hulse R, Monypenny P C, An instruction to EC2 and comparison with BS8110, 1993.

[7] Mosley W, Bungey J, and Hulse R, Reinforced concrete design to Eurocode2. Sixth Edition, 2007.

[8] Moss, R. EN1992-Eurocode and BS8110 Compared. Proceedings of the Institution of Civil Engineers - Civil Engineering, Volume: 156 Issue: 3, Aug 2003.

[9] British Standard BS8110, Structural use of concrete of concrete – Part 1: Code of practice for design and construction, 1997.

High Density Polyethylene/Libyan Kaolin Clay Nanocomposites: Effect of Clay Particle Size on Rheological, Surface and Mechanical Properties

Anour Shebani[1], Wael Elhrari[2*], Abdalah Klash[3], Abdelkader Aswei[4], Khalid Omran[5], Abdalbary Rhab[6]

1 g.manger@prc.ly, 2 wael@prc.ly, 3 aklashsa@gmail.com, 4khalidomran4@gmail.com, 5abd.swie@yahoo.com, 6abdoorhabb@gmail.com

[1,2,3,6] Polymer Research Center, Tripoli, Libya

[4, 5] Higher Institute for Comprehensive professions Al garaboulli, Libya

ABSTRACT

This research work focuses on the effect of Libyan Kaolin clay particle size on the reheological, surface and mechanical properties of high density polyethylene (HDPE)/clay nanocomposites. Three polymer clay nanocomposites (PCNs) using 2 wt.% clay with different particle size (< 75, 75-150 and 150-300 μm) and 2 wt.% polyethylene grafted maleic anhydride (PE-g-MA) were prepared by melt processing method. The rheological (viscosity and melt flow rate), surface (wettability/hydrophilicity), and mechanical properties (tensile strength, elongation at break, Young's modulus, hardness and impact strength) were investigated. The obtained properties of PCNs were compared with HDPE. A better enhancement in the rheological properties properties was observed when clay particle size of < 75 μm was used. It was exhibited lower viscosity and higher MFR value, which provide better processing properties in comparison to HDPE and other PCNs. PCN with clay particle size of (75-150 μm) had more wettability and/or hydrophilicity than HDPE and other PCNs. Mechanical properties results showed significant improvement only in the impact properties as compared to HDPE. In short, PCN made with Libyan kaolin clay with particle size 75-150 μm appears to has comparatively better overall properties in comparison to other PCNs.

Keyword— polyethylene/clay nanocomposites, particle size, rheological properties, mechanical properties, Surface properties

1. Introduction

Polymer nanocomposites (PNs) are termed as multiphase systems in which the nanofillers with at least one dimension in the nanoscale regime are dispersed in the polymer matrix [1]. One of the most promising PNs is the nanocomposites based on polymers and clay or clay minerals. This a special class of composites known as polymer/clay nanocomposite (PCN). PCNs have attracted great interest, because they exhibit significant improvement in polymers properties when compared with virgin polymer or conventional micro- and macro-composites [2]. Superior mechanical, thermal, electrical, rheological, barrier and optical properties are achievable with these nanocomposites [3-5]. PNCs are very promising materials for various applications and their demand increases in modern material industries such as aerospace, automobile, barrier materials, construction, and biomedical [6-7]. It is noteworthy, that the most important polymers that are employed in the PCNs are polyethylene, polypropylene, polyvinyl chloride, polyamide, polysulfone, polycarbonate, polyaniline, and poly(ethylene oxide). On the other hand, number of clay types have been used in PCNs include Kaolinite, Illite, Bentobite, Chlorite, and Montmonillonte.

Although, Libya rich in clay, there is no attention has been paid to use local clay as reinforcing filler for PNCs. In our previous work [8], the influence of Libyan Kaolin clay on the impact strength properties of high density polyethylene (HDPE)/clay nanocomposites was investigated. In that study, the effect of clay loading, compatibilization, and clay particle size on impact properties of HDPE/clay nanocomposites was studied. We found that the addition of Libyan Kaolin filler has resulted in an improvement in the impact strength properties of HDPE. Maximum improvement in the impact strength properties was obtained at low clay loading (2 wt.%) using clay with particle size 75-150 μm and 2 wt.% PE grafted maleic anhydride (PE-g-MA) as a compatibilizer. To gain more understanding about the influence of Libyan Kaolin clay on PCNs properties, this study aims to investigate the effect of clay particle size on rheological, surface and other mechanical properties (e.g. tensile strength, elongation at break, Young's modulus, and hardness) using HDPE/clay nanocomposites with 2 wt.% clay with different clay particle size and 2 wt.% PE-g-MA. As it was declared in our previous work [8], we hope that the obtained results will encourage Libyan scientists to start using of Libyan kaolin clay and other clays in the field of PCNs.

2. Materials and Methods

2.1. Materials

HDPE was used as the matrix polymer (SABIC Saudi Arabia, HDPE F00952, melt flow index 0.05 g/10 min and density 952 g/cm^3). PE-g-MA prepared in our lab according to reference [9], was used as a compatibilizer. Kaolin is supplied by Industrial Research Center Tripoli (collected from Jarmah Member, Sabha city in Libya). Kaolin was sieved to remove impurities and then passed through different sieves size to get particle size of (< 75, 75-150 and 150-300 μm). The plate thickness of this type of kaolin ranges from 26.5 to 40.5 nm [11]. *p*-Xylene (Alfa Aesar 99%) was used to melt HDPE before compounded process.

2.2. Composite Preparation

HDPE was used as received. kaolin was dried in an air circulating oven at 85 °C for 24 hr. The HDPE of desire amount was melt in small amount of xylene and then mixed with 2 wt.% kaolin and 2% PE-g-MA in a separate bowl. The mixture then dried in an air circulating oven at 85°C for 24hr. Then the final mixing was carried out using twin screw extruder (Brabender) (L/D ratio 48) with screw speed of 70 r.p.m. at temperature from 140-190 °C (140 °C for zone1, 160 °C for zone 2, 170 °C for zone 3, 180 °C for zone 4, and 190 °C for zone 5 and zone 6). The extruded composites were cooled in air and then granules to small pieces. Specimens for impact strength were prepared in an injection molding (Xplore 12ml) at temperature 230 °C, and injection pressure of 14 bar. Details of the composites and codes are reported in Table 1.

Table 1: Composites composition and codes

No	Composite name	HDPE, wt. %	Clay, wt. %	Compatibilizer wt.%	Clay's particle size μm
1	HDPE	100	0	0	---
2	Composite 1	98	2	2	< 75
3	Composite 2	98	2	2	75-150
4	Composite 3	98	2	2	150-300

3. Characterization

3.1. Rheological properties

Examples of desirable rheological properties may include: viscosity and melt flow rate (MFR). Thus, MFR and viscosity of the melt were studied using CEAST modular line melt flow models 7024 according to ASTM D 1238P. The tests were carried out at 190 °C under specified load of 5.0 kg.

3.2. Wetting properties and surface characteristics

The measurement were carried out using Contact angle ramè-hart instrument co. model 200-F4 at room temperature. 3 μl volume drops of water were deposited on the surface of the HDPE and the three PCNs with a syringe. Pictures of the water drops were acquired through a digital camera positioned on a static contact angle analyzer. The θ of the contact angle was measured automatically from the image setup. Each contact angel value is an average of 5 measurements.

3.3. Mechanical properties

The tensile strength, elongation at break and young modulus were determined using SATRA tensile tester for HDPE and the three PCNs. Tensile test were performed at room temperature. Four specimens (73mm-4mm-2mm) were tested for each sample under speed test (100mm/min). The hardness of molded HDPE and all composite materials were determined using a Shore D durometer RayRan in accordance with ISO 868:2003. Hardness value for each sample is an average of 8 measurements. The charpy impact test was carried out to determine the impact strength of the HDPE, and all composite materials using (CEAST Resil Impactor tester), with impact energy of 15 J. The specimens for impact test were prepared and notched according to ASTM (D256-87). Four specimens were tested for HDPE and each composite.

4. Results and Discussion

4.1. Rheological properties

Results of rheological properties of HDPE and the three PCNs are presented in Figures 1 (a,b). The obtained results indicate that the particle size of Libyan Kaolin clay clearly affects the rheological properties of PCNs. Generally, the PCNs performance depends on a number of nanoparticles features such as the size, aspect ratio, specific surface area, volume fraction used, compatibility with the matrix and dispersion [12]. As shown in Figures 1 (a,b), it is apparent that the addition of Libyan Kaolin to HDPE caused decrease of the viscosity and thus an increase of the MFR in comparison to HDPE. It is known from the literature [12] that the organically clay can undergo degradation, which cause radicals formation and result chain scission. This normally reduces the molecular weight and viscosity and increases the MFR. On the other hand, the decrease viscosity of PCNs in comparison to neat polymer can be due to the reorientation of the nanoclay [13]. It is important to know that the high viscosity means a high molecular weight polymer with low MFR. Low viscosity offers better processing properties, while high viscosity is recommended for better mechanical properties. It has been reported that the addition of small amounts of nanofiller can enhance the composite properties and reduce the processing problems [14]. Kerstin et. al. [11] declared that introducing nanoparticles into the polymer might be a solution to fulfill both requirements: mechanical stability and simple processability. Therefore, it is important to describe PCNs, not only mechanically and morphologically but also rheologically as well.

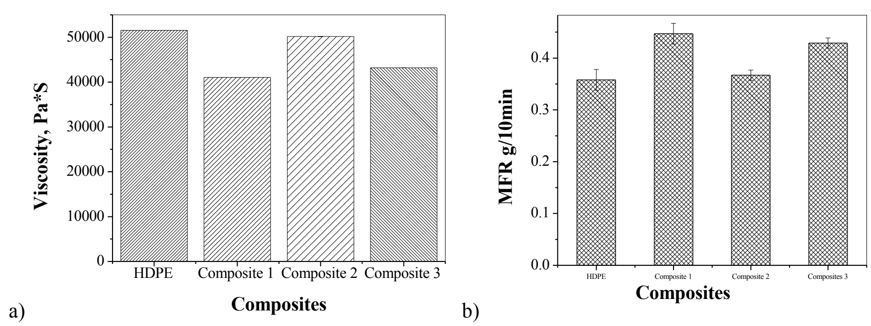

Figure 1: a) Viscosity for HDPE and the three PCNs, b) MFR for HDPE and the three PCNs.

As illustrated in Figures 1 (a,b) HDPE showed to has the highest viscosity and the lowest MFR values in comparison to the three PCNs. PCN with clay particle size of (< 75 μm) exhibited lower viscosity and higher MFR, which provide better processing properties in comparison to HDPE and other PCNs. Whereas PCN with clay particle size of (75-150 μm) showed higher viscosity and lower MFR in comparison to other PCNs. Strong interaction between filler particles and the polymer results in immobilized polymer chains on the surface of the filler, which leads to an increase in viscosity [15]. It seems that PCN with clay particle size of (75-150 μm) may have the strongest interaction between the clay and HDPE in comparison to other PCNs. Additionally, PCN with clay particle size of (150-300 μm) displayed viscosity and MFR values which are intermediate between the values of the other PCNs. These results are in fair agreement with literature because MFR showed to be inversely proportional to viscosity [16]. However, such a behaviour is explained by an increase in polymer chain mobility and more free volume obtained in the nanocomposites samples [17]. According to Agboola [18], rheological behaviors of PCNs are strongly influenced by the material structure and the interfacial characteristics. Mackay et al. [19], suggested that the decrease in viscosity can be related to the free volume introduced by the clay nanoparticles. The effect of the nanoclay particles on the free volume depends on the clay/polymer interactions [9]. According to Gholizadeh et al. [20], the addition of nanoclay decreases the free volume, while opposite tendency was observed by Yu et.al. [21]. To clear this contradiction further investigations on the effect of the addition of nanoclays to polymer matrices are required.

4.2. Wetting properties and surface characteristics

Wetting properties and surface characteristics of HDPE and the three PCNs were studied using contact angle measurements (CAMs). CAMs are often used as an empirical indicator of wettability and interfacial tension. For polymer production where particulates or fibers are used for reinforcement, colorant, flame retardancy or stability, understanding the wetting phenomena has considerable value in relation to the material performance [22]. In practical, wettability and hydrophilicity are closely related phenomena. More wettability means more hydrophilicity. The results of the CAMs in Figure 2 revealed some information on the wettability of the HDPE and the three PCNs. Wettability and contact angle are inversely related: the lower the contact angle, the greater the wettability. The contact angle depends on several factors, such as surface energy, wettability of the surfaces, viscosity of the liquid, roughness, the manner of surface preparation, and surface cleanliness [23,24].

The HDPE represented more hydrophobicity behavior, which means less wettability property than the three PCNs because its contact angle above 90° and the water droplet was tended to ball up and run off the HDPE surface. HDPE is basically a hydrophobic polymer and thus the high value of contact angle is justifiable. A surface is hydrophilic if the value of the contact angle is less than 90°, whereas the surface is hydrophobic if the value of the contact angle is greater than 90° [30]. The contact angle of HDPE was decreased by the addition of Libyan kaolin clay in the three PCNs. This means that the wettability and/or hydrophilicity is increased for the HDPE. This is because the surface of each PCN contains some of the nanoclays [25].

The clay particle size has apparent effect on the contact angle. It decreased from 91.4 (for neat HDPE) to around 88.3 when clay with particle size of (< 75 μm) was added to the HDPE, while it decreased to about 85.2 when clay with particle size of (75-150 μm) was added to the HDPE. It decreased finally to approximately 85.9 when clay with particle size of (150-300 μm) was added to the HDPE. This indicates that PCN with clay particle size of (75-150 μm) had more wettability and/or hydrophilicity than other PCNs. On the other hand, PCN with clay particle size (< 75 μm) was exhibited lower wettability and/or hydrophilicity than other PCNs. In short, the ultimate enhancement in the wettability and/or hydrophilicity which observed when clay with particle size of (75-150 μm) means that the surface of HDPE became more polar in comparison to the other PCNs. This enhances the above finding and explanation. As declared above, strong interaction between filler particles and the polymer results in immobilized polymer chains on the surface of the filler, which leads to an increase in viscosity. Hence, the improvement in wettability and/or hydrophilicity of PCNs's surface can be attributed to the enrichment of the HDPE surface with nanoclays. Good wettability is often a predictor of high quality adhesive bonding. Indeed, wettability is of importance in adhesion, surface coating, water repellency, and waterproofing [26]. To our knowledge, the effect of clay's particle size on the wettability and/or hydrophilicity properties of PCNs has so far not been extensively studied.

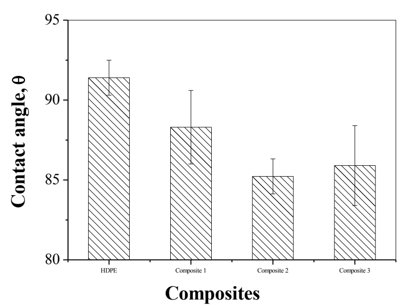

Figure 2: Contact angle for HDPE and the three PCNs.

4.3. Mechanical properties

Table 2 shows experimental data obtained for some mechanical properties of the HDPE and the three PCNs. It is important to note that the standard deviations are given in parentheses next to the values of the mechanical properties. Experimental results in Table 2 proved that clay particle size can notably affect the mechanical behavior of HDPE matrix. It was found that tensile strength, elongation at break, Young's modulus and hardness decreased, whilst impact strength increased with the addition of clay in all cases.

Table 2: Mechanical properties of HDPE and the three PCNs.

Sample	Tensile strength, MPa	Elongation at break, %	Young's modulus, MPa	Hardness	Impact strength, $KJ.m^{-2}$
HDPE	29.68 (3.13)	2.39 (0.16)	794.23 (2.40)	60.4 (1.34)	12.18 (1.57)
Composite 1	19.45 (1.06)	2.30 (0.16)	734.21 (1.91)	58.20 (20.20)	25.03 (4.10)
Composite 2	19.86 (1.03)	2.20 (0.05)	760.15 (1.17)	57.70 (0.28)	39.13 (5.34)
Composite 3	22.11 (1.31)	2.28 (0.08)	599.79 (5.17)	52.70 (0.28)	38.85 (4.36)

The tensile strength of HDPE decreased approximately 34% when clay with particle size of (< 75 μm) was used (composite 1), while it decreased about 33% when clay with particle size of (75-150 μm) was used (composite 2). The lowest decrease (about 25%) in the tensile strength of HDPE was observed when clay with particle size of (150-300 μm) was used (composite 3). In the case of PNs, most studies report the tensile properties as a function of clay content [27]. This is because the degree of crystallinity is dependent of the clay content [28]. This is important since the tensile properties are mainly dependent on the crystallinity of the polymer. Also, composite strength is very much dependent on the interface adhesion quality between the clay and polymer matrix [29].

Addition of Libyan kaolin clay caused a little reduction in the elongation at break of HDPE. The elongation at break for HDPE decreased approximately 4%, 8%, and 5% when clay with particle size of (< 75 μm), (75-150 μm) and (150-300 μm) were used, respectively. This is because nanoclay particles are stiff materials with no elongation properties; therefore, their addition can lower composites elongation [30]. Similar findings were reported by many studies [31,32]. According to Ahmadi et. al. [32], the reduction in the elongation at break may be attributed to the fact that ductility decreases when stiffness is increased by reinforcement.

The experimental measurements of Young's modulus (also known as the elastic modulus) of the three PCNs in Table 2 illustrates that the addition of Libyan kaolin clay caused a reduction in the stiffness of HDPE matrix. This is because Young's modulus is a measure of the stiffness of a solid material. Particularly, a stiff material has a high Young's modulus and changes its shape only slightly under loads. The decrease in the Young's modulus in composite 1 and composite 2 was approximately 7.6% and 4.3%, respectively. More reduction in the Young's modulus (about 24.5%) was observed when clay with particle size of 150-300 μm was used. It is well known that the elastic modulus "Young's modulus" is a stiffness parameter which governs by the size and amount of the dispersed phase [25].

Table 2 represents also the Shore D hardness results of pure HDPE and its nanocomposites. The hardness of HDPE decreases with incorporation of nanoclay. The average value of the Shore D hardness is observed to be ~ 60, 58, 57 and 52 for pure HDPE, composite 1, composite 2 and composite 3, respectively. This means that the hardness was deceased by 3.6 % for composite 1, 4.5% for composite 2 and 12.7% for composite 3 as compared to pure HDPE. This indicates that the hardness showed to decrease with increasing the clay particle size. Hardness is found to be based on the clay loading [33].

Impact strength properties in Table 2 was published and discussed elsewhere [8]. The results show that particle size has considerable effect on the impact strength properties of HDPE/clay nanocomposite. The three PCNs showed better impact strength properties than pure HDPE. Maximum impact strength value (39.125 KJm^{-2}) for the composites was obtained at particle size of 75-150 μm (composites 2). Composite with particle size of 150-300 μm (composites 3) exhibited impact strength value (38.851 KJm^{-2}) close to that of composites 2. Proper particle size of kaolin at given filler content probably decreases the level of stress concentration in the composites with the resultant increase in impact strength. However, the proper particle size cannot be predicted, it depends on the particle shape, matrix and particle/matrix adhesion [25]. However, quality dispersion of nanoparticles in matrix plays key role for an improvement of impact properties of nanocomposites [34].

As shown in Figure 3, PCN made with Libyan kaolin clay with particle size 75-150 μm appears to has comparatively better overall mechanical properties in comparison to other PCNs. It can be noted from the above results that the addition of 2% of Libyan kaolin clay with different particle sizes to HDPE did not cause improvement in the mechanical properties, such as strength, elongation at break, Young's modulus and hardness. On the other hand, it has resulted in an improvement in the impact strength properties of HDPE. The properties of PCNs not only depends on the adhesion and compatibility of the organoclay with the matrix, but also on other factors such as processing conditions and clay loading. For example, George et. al. [35] studied the effect of kaolin clay particles on the mechanical, morphological and processing features of kaolin clay reinforced PS/HDPE blends and found that the tensile strength and tensile modulus of PCNs was increased with 2% clay loading, while the impact strength was increased at 3 % of clay loading.

Generally, better interfacial bonding imparts better properties to a PCN, such as tensile strength, hardness and high modulus, as well as resistance to fatigue, tear, corrosion and cracking. Since, the mechanical properties of PCNs can be altered by various factors: properties of the polymer matrix, clay particle size and morphology, particle loading and distribution, interfacial adhesion between clay and matrix, etc.. According to this it seems that the addition of 2% of Libyan kaolin clay seems to be not enough to produce the expected reinforcement in the PCNs. For example, in the case of biodegradable PCNs, most studies report the tensile properties as a function of clay loading, as mentioned above. This is because clay content effects the crystallinity which have an effect on the tensile properties. Moreover, Libyan kaolin clay appears to need special treatment to obtain clay in nanometer dimensions with narrowed particle size distribution. It is important to reveal here that nanoclays with smaller particle size distributions exhibit better dispersion in the polymer matrix. This because smaller particles have a higher surface area for a given particle loading. High surface area means more contact area available, and therefore have a higher potential to reinforce the polymer matrix. Therefore, the preparation of PCNs by using clay with smaller and more uniform particle sizes can lead to nanocomposites with better properties.

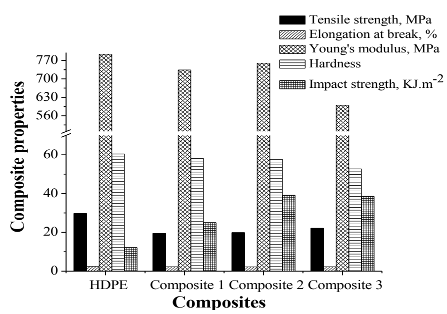

Figure 3: Comparison between the mechanical properties of HDPE and the three PCNs.

5. Conclusions

PCNs were produced using HDPE, 2% Libyan kaolin clays with different particle sizes (< 75, 75-150 and 150-300 μm) and 2% PE-g-MA as a compatibilizer. PCNs were prepared by melt-mixing technique using mini-twin-extruder. The effects of the kaolin clay particle size on the rheological, wetting and mechanical properties PCNs were studied. PCN made with Libyan kaolin clay with particle size 75-150 μm appears to has comparatively better overall properties in comparison to other PCNs. The effects of the kaolin clay particle size on some desirable rheological properties such as viscosity and MFR was studied. HDPE showed to has the highest viscosity and the lowest MFR values in comparison to the three PCNs. PCN with clay particle size of (< 75 μm) exhibited lower viscosity and higher MFR value, which provide better processing properties in comparison to HDPE and other PCNs. Whereas PCN with clay particle size of (75-150 μm) showed higher viscosity and lower MFR in comparison to other PCNs. Additionally, PCN with clay particle size of (150-300 μm) displayed viscosity and MFR values which are intermediate between the values of the other PCNs.

Wetting properties and surface characteristics of HDPE and the three PCNs were studied using CAMs. The contact angle of HDPE decreased by the addition of Libyan kaolin clay in the three PCNs, which resulted in an improvements in the wettability and/or hydrophilicity. PCN with clay particle size of (75-150 μm) had more wettability and/or hydrophilicity than other PCNs. On the other hand, PCN with clay particle size (< 75 μm) exhibited lower wettability and/or hydrophilicity than other PCNs. the improvement in wettability and/or hydrophilicity of PCNs's surface could be attributed to the enrichment of the HDPE surface with nanoclays.

Mechanical characterization tests including tensile strength, hardness and impact strength tests have been performed. The results showed that the addition of 2% of Libyan kaolin clay with different particle sizes to HDPE did not cause improvement in the mechanical properties, such as strength, elongation at break, Young's modulus and hardness. On the other hand, it has resulted in an improvement in the impact strength properties of HDPE. According to these results, it seems that the addition of 2% of Libyan kaolin clay not enough to produce the expected reinforcement in the PCNs. Moreover, Libyan kaolin clay appears to need special treatment to obtain clay in nanometer dimensions with narrowed particle size distribution. In this regard, more attention will be given to study the effect of clay loading and optimizing the clay particle size and distribution on the properties of HDPE/clay made by Libyan kaolin clay in future.

Acknowledgment

The authors would like to thank Industrial Research Centre who performed the tensile strength test.

References

[1]. Tatyana, S. Ilya, K. József, "Polymers and related composites via anionic ring-opening polymerization of lactams: recent developments and future trends: review", *Polymers*, vol. 10, no. 4, pp. 357-404, 2018.

[2]. K. Behzad, "Nanofiller reinforcement effects on the thermal dynamic mechanical, and morphological behavior of HDPE/rice husk flour composites", *Bioresources*, vol. 6, no. 2, pp. 1351-1358, 2011.

[3]. M. A. Rajan, A. Ramasubbu, A. Thaddeus, V. F. Latha, T. S. Vivekanandam, S. Umapathy, "Thermal properties of PMMA/Montmorillonite clay nanocomposites", *Journal of Nanoscience and Nanotechnology*, vol. 6, no. 12, pp. 3993-3996, 2006

[4]. Xu, W. M. Huang, Y. T. Pei, Z. G. Chen, A. Kraft, R. Reuben, J. M. Hosson, Y. Q. Fu, "Mechanical properties of attapulgite clay reinforced polyurethane shape-memory nanocomposites", *European Polymer Journal*, vol. 45, no. 7, pp. 1904-1911, 2009.

[5]. R. Sudip, Y. Q. Siew, E. Allan, D. C. Xiao, "The potential use of polymer-clay nanocomposites in food packaging", *International Journal of Food Engineering*, vol. 2, no. 4, pp. 1-11, 2006.

[6]. R Paul., L. M Robeson., "Polymer nanotechnology: nanocomposites", *Polymer*, vol. 49, no. 15, pp. 3187-3204, 2008.

[7]. G. Sagheer, K. Ayesha, M. Bakhtiar J. Saira, "Research Progress on Properties and Applications of Polymer/Clay Nanocomposite", *Polymer-Plastics Technology and Engineering*, vol. 55, no. 7, pp. 684-703, 2015

[8]. Shebani, W. Elhrari, A. Klash, A. Aswei, O. Khalid, R. Abdalbary, "Effects of Libyan kaolin clay on the impact strength properties of high density polyethylene/clay nanocomposites", *International Journal of Composite Materials*, vol. 6, no. 5, pp. 152-158, 2016.

[9]. M. Ghaemy, S. Roohina, "Grafting of maleic anhydride on polyethylene in a homogeneous medium in the presence of radical initiators", *Iranian Polymer Journal*, vol. 12, no. 1, pp. 21-29, 2013.

[10]. M. A. Shiwa, A. Hussin, "Sabha clay deposit, Libya: its mineralogy and impending industrial significance", *Electronic Journal of Geotechnical Engineering*, vol. 18, pp. 3803-3811, 2013.

[11]. M. Kerstin, B. Elodie, L. Marcos, J. Maria, E. S. Yolanda, M. José, M. Oliver, B. Alvise, H. Steve, B. Uwe, P. Germán, J. Marius, L. Martina, S. Zuzana, C. Sara, S. Markus, "The Influence of New Hydrophobic Silica Nanoparticles on the Surface Properties of the Films Obtained from Bilayer Hybrids", *Nanomaterials*, vol. 7, no. 2, pp. 1-10, 2017

[12]. Sahar, S. Husam, "An overview of the oxidation and stabilization of polymer nanocomposites", *Nanocomposites MoDeSt Workshop*, Warsaw-Poland, 2013.

[13]. Farida, K. Nadir, B., Catherine, T. Francois, E. Ruiz, "A comparative study of dispersion techniques for nanocomposite made with nanoclays and an unsaturated polyester resin", *Journal of Nanomaterials*, vol. 2011, pp. 1-12, Article ID 406087, 2011.

[14]. M. Joshi, B. S. Butola, G. Simon, N. Kukaleva, 'Rheological and viscoelastic behavior of HDPE/octamethyl-POSS nanocomposites", *Macromolecules*, vol. 39, no. 5, pp. 1839-1849, 2006.

[15]. J. Sapkota, "Influence of clay modification on curing kinetics of natural rubber nanocomposites", Master of Science Thesis, Tampere University of Technology, Finland, 2011

[16]. Y. Basel, "Simple rheological analysis method of spinnable-polymer flow properties using MFI tester", *Indian Journal of Materials Science*, vol. 2015, Article ID 790107, pp. 1-8, 2015.

[17]. S. H. Jin, D. K. Choi, D. S. Lee, "Electrical and rheological properties of polycarbonate/multiwalled carbon nanotube nanocomposites", *Colloids and Surfaces A*: *Physicochemical and Engineering Aspects*, vol. 313-314, pp. 242-245, 2008.

[18]. O. S. Agboola, E. R. Sadiku, A. T. Adegbola, O. F. Biotidara, "Rheological properties of polymers: structure and morphology of molten polymer blends", *Materials Sciences and Applications*, vol. 2, no. 1, pp. 30-41, 2011

[19]. M. E. Mackay, T. T. Dao, A. Tuteja, D.L. Ho, B. V. Horn, H. Kim, and C. J. Hawker, "Nanoscale effects leading to non-einstein-like decrease in viscosity", Nature Materials. vol. 2, pp. 762-766, 2003

[20]. Gholizadeh, Arefazar A., and Barzin J., "Polycarbonate/polyamide 6/nanoclay ternary nanocomposite membranes: preparation, characterisation, and gas separation properties", Polymers and Polymer Composites, vol. 17, no. 3, pp. 181-187, 2009

[21]. Yu, H. Wang, Y. Feng, and Z. P. Fang, "Investigation of free volume, interfacial, and toughening behavior for cyanate ester/bentonite nanocomposites by positron annihilation", Journal of Applied Polymer Science, vol. 102, no. 2, pp. 1509-1515, 2006.

[22]. S. P. Thomas, S. Thomas, R. Abraham, and S. Bandyopadhyay, "Polystyrene/calcium phosphate nanocomposites: Contact angle studies based on water and methylene iodide", eXPRESS Polymer Letters, vol. 2, no. 7, pp. 528-538, 200

[23]. W. Adamson, and A. P. Gast, "Physical chemistry of surfaces", John Wiley & Sons, Inc., USA, 1990.

[24]. J. N. Israelachvili, 'Intermolecular and surface forces", 2ed, Academic Press, UK, 1992

i. Alateyah, H. N. Dhakal, and Z. Y. Zhang, "Contact angle measurement of the vinyl ester matrix nanocomposites based on layered silicate", International Journal of Materials and Metallurgical Engineering, vol. 7, no. 12, pp. 976-981, 2013

[25]. Piao, J. E. Winandy, and T. F. Shupe, "From hydrophilicity to hydrophobicity: a critical review: part 1. wettability and surface behavior", Wood and Fiber Science, vol. 42, no. 4, pp. 490-510, 2010.

[26]. W. M. Yiu, and Z. Y. Zhong, "Polymer nanocomposites", Woodhead Publishing and Maney Publishing, England, 2006.

[27]. R.K. Gupta, and S.N. Bhattacharya, "Polymer-clay nanocomposites: current status and challenges", Indian Chemical Engineer, vol. 50, no. 3, pp. 242-267, 2008.

[28]. S. Y. Fu, X. Feng, B. Lauke, Y. Mai, "Effects of particle size, particle/matrix interface adhesion and particle loading on mechanical properties of particulate-polymer composites", Composites: Part B, vol. 39, 933-961, 2008

[29]. Selver, and S. Adanur, "Processing and property relationship of polypropylene monofilaments containing nanoclay", Journal of Industrial Textiles, vol. 40, no. 2, pp. 123-137, 2010

[30]. Pegoretti, A. Dorigato, and A. Penati, "Tensile mechanical response of polyethylene-clay nanocomposites", eXPRESS Polymer Letters, vol. 1, no. 3, pp. 123-131, 2007.

[31]. S. J. Ahmadi, H. Yudong, and W. Li, "Synthesis of EPDM/organoclay nanocomposites: effect of the clay exfoliation on structure and physical properties", Iranian Polymer Journal, vol. 13, no. 5, pp. 415-422, 2004.

[32]. B. Sharma, S. Mahajan, R. Chhibber, and R. Mehta, "Glass fiber reinforced polymer-clay nanocomposites: processing, structure and hygrothermal effects on mechanical properties", Procedia Chemistry, vol. 4, pp. 39-46, 2012.

[33]. R. Valek, and H. Jaroslav, "Impact properties of polymeric nanocomposites with different shape of nanoparticles", 1st Nano conference, Brno-Czech Republic, 2011

[34]. T. S. George, K. K. Asha, R. Anjana, and K. E. George, "Studies on nano kaolin clay reinforced PS-HDPE nanocomposites", Indian Journal of Advances in Chemical Science, vol. 1, no. 4, pp. 201-206, 2013.

Particle Size Dependence of MnO Reduction for Fabrication of Al-MnO_X Composite vir Stir Casting

Khalid Almadhoni[1], Sabah Khan[2]
[1]K_almadhoni@yahoo.com, [2] Skhan2@jmi.ac.in
[1]Dr. Engineer, Department of Mechanical Engineering, Faculty of Engineering, Sabratha University, Sabratha, (Libya)
[2] Dr. Assistant Prof., Department of Mechanical Engineering, Faculty of Engineering and Technology, JMI, Jamia Nagar, New Delhi-110025 (India)

ABSTRACT

In the present work, a composite of Al matrix reinforced with 10% MnO particles has been developed using stir casting technique. MnO with particles size of range of 53 to 90 μm for composite (A) and 188 to 250 μm for composite (B) as reinforcement and pure Mg powder as wetting agent to improve the wettability of MnO particulates with molten Al were used for production of Al-MnO composites having 10 wt.% of MnO. The pouring temperature and stirring speed have been set to 750 ℃ and 900 RPM, respectively. The main purpose of this work is to study the dependence of MnO reduction on particle size for fabrication of Al matrix composite via stir casting route. For structural analysis, fundamental material characterization like SEM, EDX, XRD and OM was carried out for developed composite samples. The results reveal that an in-situ formed finer alumina (Al_2O_3) particles and an intermetallic precipitate of Al-Mn as a result of chemical reaction between molten Al and MnO particles have been observed using SEM with EDX of both developed composite samples. SEM with EDX analysis has detected that the composition of reinforcement particles of composite sample of A contains Al and O, which indicates presence of in-situ generated Al_2O_3. While the composition of reinforcement particles of composite samples of B contains high percentage of Mn, high percentage of O and low percentage of Al, which indicates presence of unreacted MnO and generated in-situ Al_2O_3 to form in-situ ($AlMnO_x$) intermediate compound. This has been also confirmed by elemental mapping SEM analysis. SEM analysis of in-situ $AlMnO_x$ particles at high magnification has detected that their structure is porous. Optical micrographs have shown that a good bonding between particles and the matrix in both developed composite samples with presence some aggregations of particles and pores. For both developed composite samples, the amount of (Al-Mn) phases formed in the specimens may be too little to be detected directly from the bulk specimens by XRD. Phase identification by X-ray diffraction technique verifies of presence Al and Al_2O_3 phases in composite sample of A, while it verifies of presence Al and MnO phases in composite sample of B.

Keyword— Al, MnO, Morphology, microstructure, $AlMnO_x$, Al-Matrix Composite.

1. Introduction

The low density, environment resistance and adequate mechanical and physical properties of Al metal matrix composites (AMMC's) make them one of the most interesting material alternatives for the manufacture of lightweight parts for many types of modern engineering equipments.. Composites are classified by matrix into metal matrix composites (MMC's), ceramic matrix composites (MMC's) and polymer matrix composites (MMC's) while by filler type are classified into particle reinforced composite, fiber reinforced composites and structural composites [1-2], Figure 1.1.

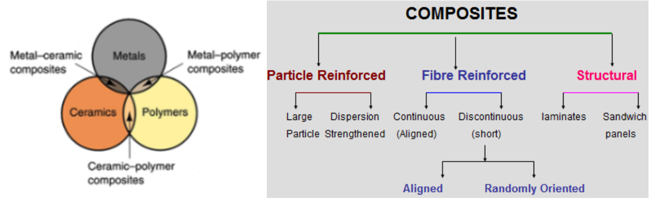

(a) (b)

Figure 1.1: Classification of composites (a): by matrix type and (b): by filler type (1-2)

Al and its alloy are the most commonly used metal matrix materials in the production of MMC's because of their preferred properties such as lightness, corrosion resistance and ductility and easy availability. Reinforcing of AMC with whiskers, short fibers or particulates of various kinds of ceramic materials such as SiC, SiO_2, Al_2O_3, MgO, ZnO, BeO, MnO_2, TiO_2, TiC, etc., provide properties compared to monolithic base alloy [3]. MMC's as compared to other MMCs have superior values of refractoriness, compressive strength, hardness and show excellent wear resistance [2-4-5]. Thermal characterization is one of the prime physical characterization of composites, which also include electrical, magnetic and optical properties. Heat is transferred at a higher rate across materials of high thermal conductivity than across materials of low thermal conductivity [6]. Melt stir casting has a good potential in all-purpose applications as it is a low cost MMC's production method. Its advantages lie in its simplicity, flexibility and applicability to large quantity production. This route is also attractive because, in principle, it allows a conventional metal processing method to be used, and hence reduces the final cost of the product [7-8]. The particle size and orientation have greater effect on the properties of the composite. Zhou et al. [9] used Al_2O_3 with different size to fill silicone rubber, and reported that nano-sized Al2O3 composite exhibited higher thermal conductivity and mechanical properties than the micro-sized one. Many researchers have reported that at the same percentage of reinforcement, smaller particle size leads to lower inter-particle distance and more chances for the formation of thermal conductive 'pathway' [10]. When the average inter-particle distance is in a suitable range, extensive plastic deformation in the matrix can be easily induced [11–12]. Operating temperature should be kept at semisolid stage to improve the wettability of reinforcements with the matrix, this is attributed to interactions among the particles themselves, between solid Al and particles and between remaining liquid phases of Al with particles [13]. Manganese has been known as an alloying element of Al alloys which contributes to uniform deformation. The effect of Mn on the mechanical behavior of Al alloys is investigated by S. W. Nam and D. H. Lee. It was found that as the Mn content increases over 0.5 wt% in Al alloys, both yield and ultimate tensile strength increased significantly without reduction of ductility. Adding Mn to aluminum alloys also improves both low-cycle fatigue resistance and corrosion resistance [14]. Release of manganese (Mn) in the matrix, intermetallic compound of Al-Mn precipitated in the matrix in different phases. Results showed that the porosity was evident in the micrographs and with increase in Al_2O_3-MnO_2wt%, the strength improved and the ductility decreased [15]. Adding Mg improves the wettability of MnO_2 with molten Al and thus increases the amount of reinforcing phase in the composite material [16]. A. Agarwal, S. Singh and others prepared hybrid composites using both in-situ and ex-situ approaches together by dispersing powder mixture of alumina (Al_2O_3) and manganese dioxide (MnO_2) in a ratio of 1:1 but with different sizes, by stir casting method in Al matrix. They investigated and compared the microstructures and mechanical properties of Al-Al_2O_3, Al-$MnO_2$and Al-Al_2O_3(MnO_2) composites. Results showed that fine Al_2O_3 particles were formed as result of reduction of MnO_2 by Al and Mn was released in the matrix, which combined with Al to form intermetallic compounds of Al-Mn precipitate in the matrix in different phases of Al-Mn and reinforce it. It was also found that with increase in wt.% of Al_2O_3-MnO_2, mechanical properties of the composite enhanced with decrease in ductility, however they reported evidence of porosity in the micrographs [17].

2. Manganese Oxide Mesoporous Solids (MOMS)

As we know mesoporous material contain pores with diameters between 2 and 50 nm. These materials are classified into according to their size by IUPAC. The microporous materials have pore diameters of less than 2 nm and macroporous materials have pore diameters of greater than 50 nm; the mesoporous category thus lies in the middle. Manganese oxide mesoporous solids (MOMS) are gaining popularity and are characterized by a high surface area mesoporous and /or microporous mixed oxidic solid [16]. Researchers have found that the surface area of $AlxMnO_2$ is 711 m^2/g, while the mean pore diameter was 3.6 nm. Results showed that the extreme surface area value of $AlxMnO_2$ is attributed to the existence of an open network interconnected particles forming features medium height with no preferential orientation [18].

3. Material Selection

The composite of Al-AlMnOX was fabricated by stir casting method. Pure aluminum (AA-1070) with 99.77% purity is used as the matrix for fabrication of the composite. Table 3.1 gives the chemical composition of the matrix

Table 3.1: Chemical composition of MatrixAl (wt %)

Si%	Cu%	Mg%	Fe%	Zn%	Ni%	Mn%
0.0637	0.0152	0.0017	0.0874	0.0130	0.0056	0.0026
Cr%	V%	Ti%	Sn%	Bi%	Pb%	Al%
0.0024	0.0105	0.0071	0.0033	0.0023	0.0040	99.77

Manganese(II) oxide, also called Manganese monoxide, is used as reinforced material, in the particle size range of 53 to 90 µm for composite (A) and 188 to 250 µm for composite (B) and with 10% RVR.The purity of the powder, its density and the size of the particles selected for the present l study is given in the Table 3.2.

Table 3.2: Specifications of MnO powder selected for present study

Purity %	Density (g/mL) at 25 °C(lit.)	Size of particles selected
99	5.45	(188-250) microns
99	5.45	(53-90) microns

Additive material:
Pure Mg powder was used 1% by weight as wetting agent to increase the wettability of MnO particulates with molten Al. Mg is added to in order to help wetting of particles in molten Al and to retain the particles inside the melt [19-20].

4. Experimental Setup and Fabrication of Composite

The experimental setup consist of conical shaped silicon carbide (SiC) crucible for melting of Al, as it withstands high temperature up to [1700°C]. The crucible is placed in electric melting furnace made up of high ceramic alumina around which heating element is wound. The coil which acts as heating element is K thermocouple (Nickel-Chromium / Nickel-Alumel). Due to the high affinity of Al at liquid stage to react with atmospheric oxygen, the process of stirring is carried out in closed chamber with an inert gas such as nitrogen or argon. Closed chamber is formed. Due to corrosion resistance to atmosphere, silver steel is selected as stirrer shaft material. One end of shaft is connected to 0.05 HP motor, while at the other end blades are welded. Four blades are welded to the shaft at 90°C. The speed can be varied from (0 - 4000) RPM. A permanent mould made of cast iron used to pour the fabricated composite. Figure 4.1 shows a setup of stir casting apparatus developed in the lab.

Figure 4.1: Stir-Casting-Apparatus Set-up

The impurities and thick oxide layers on the surface are removed by mechanical cleaning by grinding on grinding belt machine, polishing on polishing machine followed by chemical etching by immersing the part in 50% nitric acid aqueous solution at room temperature for 15 min. The part is then rinsed in cold water, followed by hot water and blow dried, as suggested by R. Gadag, 2010 and G. Totten, 2003 [21-22] .The procedure of preparing the composite was carried out by initially setting the temperature at 500°C and then gradually increasing up to 850°C. The pure Al (purity 99.77 %) matrix was cleaned to remove impurities, weighed and then kept in the crucible for melting. Nitrogen gas was used as inert gas to avoid oxidation. Required quantities of 1% pure Mg powder as wetting agent and 10% MnO as reinforcement particles in the size of range of 53 to 90 μm for composite (A) and 188 to 250 μm for composite (B) are weighed to be added. In order to remove any gases and moisture present in reinforcing material, MnO is preheated for half an hour at temperature of 200°C [19-20]. After the matrix completely melts, it was stirred for one minute for homogeneity. Temperature is set to 630°C which is below the melting temperature of the matrix. While stirring semisolid Al, a preheated the wetting agent Mg is added followed by preheated particulate MnO. Dispersion of preheated reinforcements at the semisolid stage of the matrix enhances the wettability of the reinforcement, thus preventing the particles from settling at the bottom of the crucible [23].Measured flow rate of reinforcements was about 0.2 gm/s. Dispersion time was taken as 4 minutes. Stirrer rpm is gradually increased from 0 to 900 RPM with the help of speed controller. Immediately, after completion of dispersion of particles with continued stirring at semisolid stage, slurry was reheated up to 750°C to make sure slurry is fully liquid. Total stirring time was 8 minutes. Composite slurry was poured in a cast iron preheated mold. Preheating of mold at 500°C was done to remove the entrapped gases from the mold which could reduce the porosity and improve the mechanical properties of composite [20].

5. Results

The specimen were removed from the mold and taken for morphological characterization. The morphological studies of the composite were carried out using the following techniques:

5.1. Scanning Electron Microscopy (SEM/EDX)

The morphology of the composite was observed by scanning electron microscopy (SEM),using a SEM-EDX Oxford INCA 400 model at an acceleration voltage 10 kv. The micrographs were taken at a magnification of 1000.

Composite A:

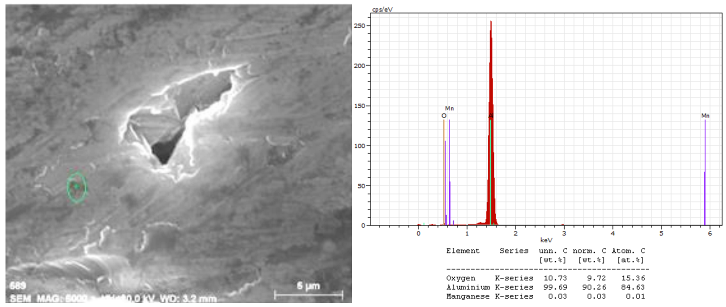

(a) (b)

Figure 5.1: (a) Un-etched SEM micrograph of Al-10wt.%MnO composite A at 600X and (b) composition of encircled spot by EDX

Figure 5.1 (a) shows un-etched SEM micrograph of Al-10wt.%MnO compositeA at 600X and its chemical composition of entire area is given in Figure 5.1 (b) at an encircled spot by EDX analysis. Figure 5.1 (a) indicates white string phase. It also shows dark gray phase. These phases are identified as Al and O, as well as a virtually non-existent ratio of Mn by EDX in Figure 5.1 (b). Presence of Mn traces in the Al-matrix is attributed to the result of the reduction of MnO with Al melt. Mn released in the matrix reacts with Al-rich matrix to make Al_2O_3 and an intermetallic precipitate of Al-Mn as is suggested by the following chemical reaction taking place in the (Al-MnO) composite system:

$2Al + 3MnO = 3Mn + Al_2O_3$ (1),

Al+Mn = AL(Mn) ppt. (2).

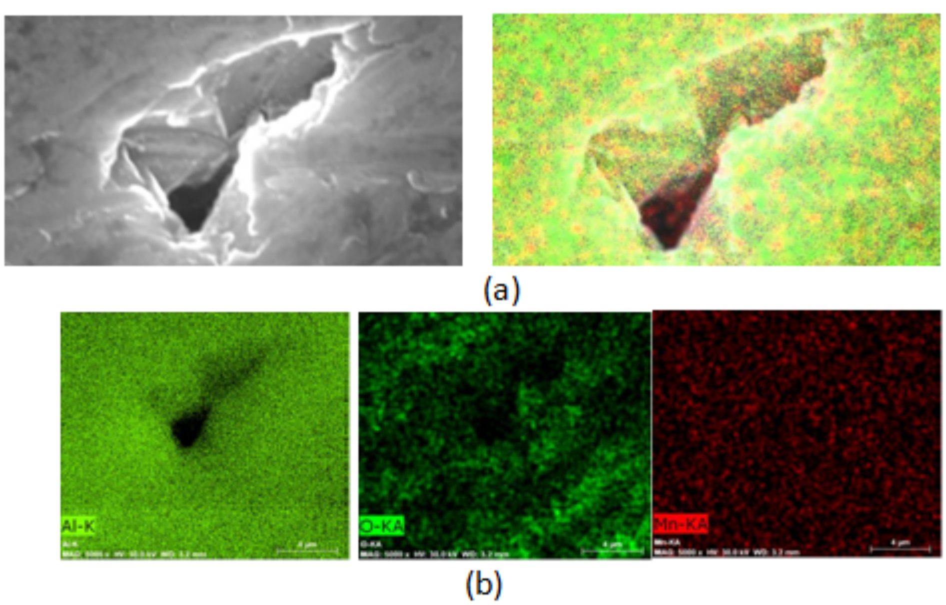

Figure 5.2: Un-etched elemental mapping SEM micrograph (Al, O and Mn) of Al-10wt.%- MnO composite A at 5000X. at 300X, (a) Collectively and (b) Separately

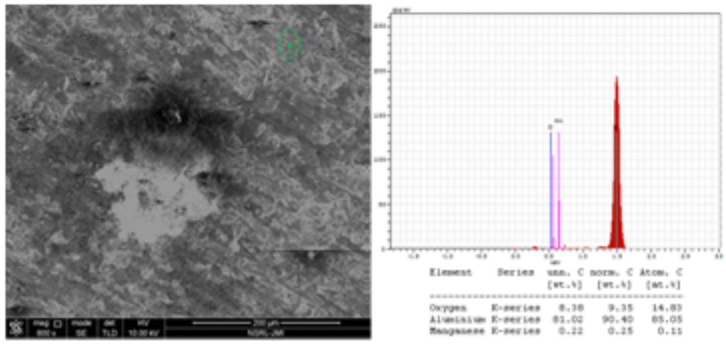

(a) (b)

Figure 5.3: (a) Un-etched SEM micrograph of Al-10wt.%MnO composite B at 600X and (b) composition of encircled spot by EDX.

Figure 5.3 (a) indicates SEM micrograph of the Al-10wt.%MnO composite B at 600X and its chemical composition is given in Figure 5.3(b) at a encircled spot by EDX analysis. Figure 5.3 (a) indicates fine bright particles in the Al matrix identified as Al_2O_3 particles by EDX in Figure 5.3 (b) and traces of Mn is detected by EDX which indicates presence of Mn in the Al matrix to make an intermetallic precipitate of Al-Mn. Presence of Al_2O_3 and Al-Mn is attributed to the result of the chemical reaction between Mn released in matrix by reduction of MnO with molten Al and Al-rich matrix itself in the composite system as is suggested by the reactions referred to in equations (1) and (2).

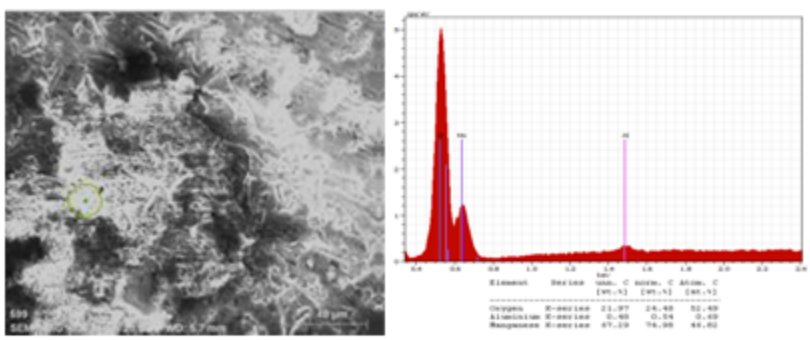

Figure 5.4: (a) Un-etched SEM micrograph of Al-10wt.%MnO composite B at 600X and (b) composition of encircled spot by EDX

Figure 5.4 (a) shows un-etched SEM micrograph of the reinforcement particle in the matrix of composite B at 600X and its chemical composition is recorded by EDX in Figure 5.4 (b). EDX analysis indicates presence of Mn in the Al matrix to make an intermetallic precipitate of Al-Mn.

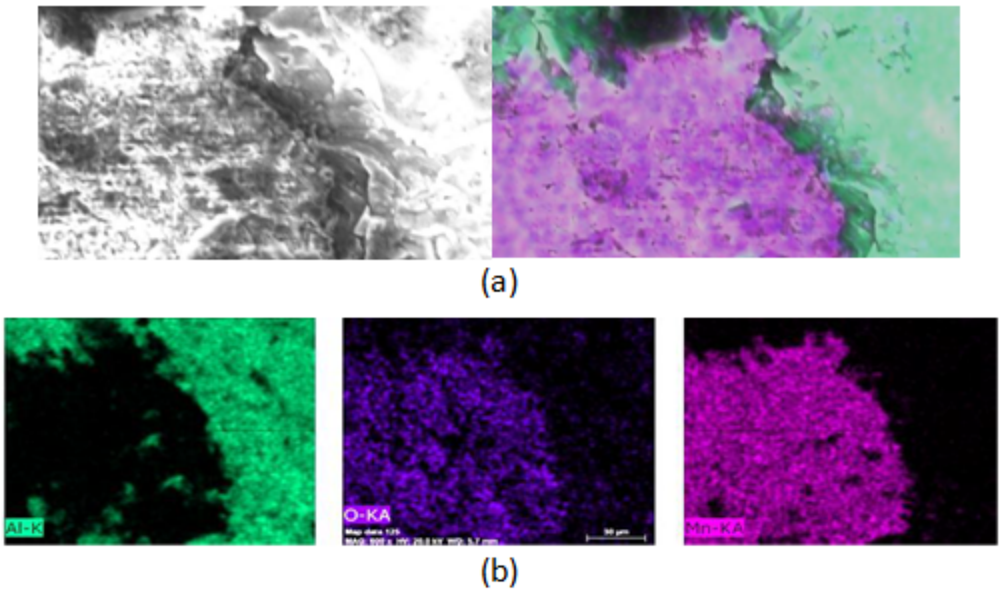

Figure 5.5: Un-etched elemental mapping SEM micrograph (Al,O and Mn) of Al-10wt.%-MnO composite B at 600X, (a) Collectively and (b) Separately

Figure 5.5 illustrates un-etched elemental mapping SEM micrograph (Al, O and Mn) of composite B at 600X. Figure 5.9 (a) illustrates presence of Al (green), O (cyan) and Mn (Pink) collectively in the matrix. More O and Mn with little Al are seen to form porous AlMnOx particle, thus confirming Al_2O_3 (light green) embedded in an unreacted MnO particle (light pink) in the Al-matrix (green). More O at the matrix-reinforcement boundary is clearly visible to appear as dark green Al_2O_3 layer from matrix side and dark pink MnO layer from reinforcement side. Distribution of Al, O and Mn is shown in Figure 5.5 (b) separately, thereby confirming what has been indicated in Figure 5.5 (a).

5.2. Optical Microscopy

Optical microscopic technique was applied for the analysis of microstructure of the composite samples. The magnified images of the samples were obtained using a microscope digital camera Leica DM 2500 M. Optical images of composites were taken at different points of the samples surfaces. All of the analyses were carried out at room temperature. The maximum magnification obtained with the optical microscope was about 500X.

(a) b) (c)

Figure 5.6: Un-etched OM of Al-10wt.%MnO composite A at (a): 25X, (b): 100X and (c): 500X

On macroscopic scale at low magnification, at 25X in Figure 5.6 (a), un-etched optical micrograph of Al-10wt.%MnO composite A is shown. The density of small dark spots in the matrix is less than those observed in composite samples of A. In Figure 5.6 (b) at higher magnification of 100X, few small light spots are inside the bigger particles. Figure 5.6 (c) at higher magnification of 500X indicates big reinforcement particle containing more small light spots than those indicated in composite samples of A1, which may indicate formation of porous alumina (Al_2O_3) particle or agglomerated cluster of alumina particles. It also shows a good bonding between the particles and matrix.

(b) b) (c)

Figure 5.7: Un-etched OM of Al-10wt.%MnO composite B at (a): 25X, (b): 100X and (c): 500X.

Figure 5.7 (a) shows un-etched optical micrograph of Al-10wt.%MnO composite B at 25X. It indicates reinforcement particles surrounded by small dark spots in the matrix. Small light and dark spots are inside the bigger particles are visible in Figure 5.7 (b) at higher magnification of 100X, which could be pores and in-situ formed Al_2O_3 particles embedded in MnO particles. It also shows an aggregation of the particles. On microscopic scale, at magnification of 500X in Figure 5.7 (c), big aggregated reinforcement particles containing small light and dark spots is shown. This could be indication of in-situ formed alumina particles embedded in MnO particles to form porous in-situ generated intermediate compound (AlMnOX) particle. It also shows a good bonding between the particle and matrix.

5.3. X-ray diffraction (XRD)

XRD analysis is based on constructive interference of monochromatic X-rays and a material sample. The characteristic x-ray diffraction pattern generated in the XRD analysis provides a unique "fingerprint" of the crystals present in the sample. In the present analysis as part of morphological characterization, a comparative XRD analysis is carried out between the Matrix Al and the developed composite.

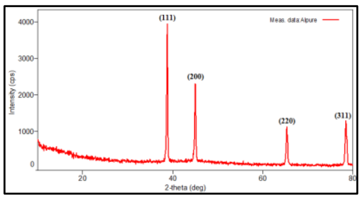

Figure 5.8: XRD analysis of pure Al

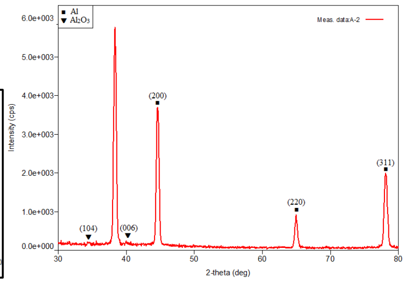

Figure 5.9: XRD analysis of composite A

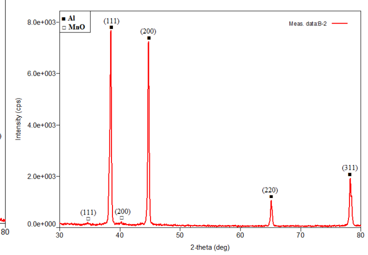

Figure 5.10: XRD analysis of composite B

The Figure5.8 illustrates the XRD result of the matrix (Al). The result reveals that the main phases present belong to Al, which is present in the form of phases e.g.,Al(111), Al(200), Al(220) and Al(311).The Figure 5.9 illustrates the XRD result of developed Al-10%MnO composite A. The result shows that the main phases present belong to Al (largest peaks) and Al_2O_3 (lower peaks). The Al is present in the form of phases i.e. Al (111), Al (200), Al (220) and Al (311), while Al_2O_3 is present only in the form of phases i.e. Al_2O_3 (104) and Al_2O_3 (006) phases. Peaks are identified by using JCPDS software. The peak intensities of Al in the manufactured composite are changed. There is a significant increase in peak intensities of Al (111) and Al (200) phases, and slight increase in peak intensity of Al (311) phase. However, the peaks are of only of Al and Al_2O_3phases, which confirms that MnO particles have been completely reduced with molten Al forming in-situ Al_2O_3 particles and little amount of an intermetallic (Al-Mn) compound phases that can be detected directly from the bulk specimen as indicated by XRD.The Figure 5.10 illustrates the XRD result of developed Al-10%MnO composite B. The result shows that the main phases present are Al (largest peaks) and MnO (lower peaks). The Al is present in the form of phases i.e. Al(111), Al(200), Al(220) and Al(311). MnO is present in the form MnO(111) and MnO(200). Peaks are identified by using JCPDS software. The peak intensities of Al in the manufactured composite are changed. There is a significant increase in peak intensities of Al(111) and Al(200) phases, and moderate increase in peak intensity of Al(331). Manganese oxide was indicated in low intensities of MnO(111) and MnO(200) phases. However, there are peaks corresponding to Al and MnO phases. This confirms that MnO particles have been partially reduced with molten Al forming little amount of in-situ Al_2O_3 particles and an intermetallic (Al-Mn) compound phases to be detected directly from the bulk specimen as indicated by XRD.

6. Conclusion

Results show that the use of manganese oxide (MnO) as reinforcing ceramic particles in pure aluminum can produce (Al-Al_2O_3) or (Al-$AlMnO_X$) in-situ particulate composite via stir casting method. The composite can be developed by controlling the particle size.There is appreciable reaction between MnO particles and melted Al matrix, producing in-situ finer Al_2O_3 particles and an intermetallic precipitate of Al-Mn compound, which could be in various phases with uniform distribution in Al to make Al-alloy as matrix.Some portion of Al diffuses into MnO particles to react with oxygen and generate Al_2O_3 particles forming MnO porous intermediate compound ($AlMnO_X$).Fine alumina (Al_2O_3) particles and an intermetallic precipitate of Al-Mn as a result of chemical reaction between molten Al and manganese oxide (MnO) particles have been observed using scanning electron microscopy (SEM) with energy dispersive X-ray analysis (EDX) of entire area of both developed composite samples. EDX analysis of the reinforcement particles of developed composite sample B has detected that their composition contains high percentage of Manganese (Mn) and Oxygen (O) with low percentage of Al, which indicates presence of unreacted MnO and generated Al_2O_3 particles. SEM analysis of in-situ formed $AlMnO_X$ particles at high magnification has detected a characterized porous structure.EDX Analysis of the reinforcement particles of composite sample of A has detected that their composition contains high percentage of (Al) and (O) without presence of (Mn), which indicates presence of generated Al_2O_3 only. This has been also confirmed by elemental mapping SEM analysis.

Optical micrographs have indicated presence of porosities in the both composite samples, but their density varies from A to B, depending on the reinforcement particles size.Optical micrographs have shown that a good bonding between particles and the matrix of both developed composite samples.

XRD analysis has indicated that the main phases present in both developed composite samples are Al (largest peaks). It is present in the form of phases Al(111), Al(200), Al(220) and Al(311), but with various intensities. Al_2O_3 (lower peaks) has only been indicated in composite sample of A. It is present in the form of phases Al_2O_3(104) and Al_2O_3(006).MnO (lower peaks) has been indicated in composite sample B,. It is present in the form of phases MnO(111) and MnO(200) of composite sample B.MnO phases of composite sample B have shown low intensity peaks, which indicates that less amount of unreacted MnO particles. Amount of intermetallic compound (Al-Mn) phases formed in the specimens of both developed composites may be too little to be detected directly from the bulk specimen by XRD.

Thus, the morphological structure analysis using XRD of developed composite samples indicates the presence of a porous $AlMnO_X$ embedded in pure Al matrix in developed composite sample B only.

References

[1]. ASM International Handbook Committee: "Composite, Engineered Materials Handbook," Volume 1, Third Printing, August 1989.

[2]. K. Surappa, "Aluminium matrix composites: Challenges and opportunities". Sadhana. 28: 319-334, 2003.

[3]. Sabah Khan, "Analysis of Wear Rate and Tribological Behavior of Aluminum Cast Alloy A356 and Granite Composite at Different Speeds", (IJEAT), Volume-5, Issue-3, February 2016, Pp 128 – 131.

[4]. Khedera, G. Marahleh and D. Al-Jameaa, "Strengthening of Aluminum by SiC, Al2O3 and MgO". Jordan Journal of Mechanical and Industrial Engineering. Volume 5, Number 6, Dec. 2011.

[5]. D. Ramesh, R. Swamy and T. Chandrashekar, "Effect of weight percentage on mechanical properties of frit particulate reinforced Al6061 composite". ARPN Journal of Engineering and Applied Sciences. Vol. 5, No. 1, January 2010.

[6]. K. Almadhoni and S. Khan," Evaluation of the effective thermal properties of aluminum metal matrix composites reinforced by ceramic particles", International journal of current engineering and technology, E-ISSN 2277 – 4106, P-ISSN 2347 – 5161, Vol.5, No.4, 2015.

[7]. R. Calin, M. Pul and Z. Pehlivanli, "The Effect of Reinforcement Volume Ratio on Porosity", Materials Research, 15(6): 1057-1063, 2012.

[8]. [8] N. Jit, A. Tyagi and N. Singh, Al-Cu-Si - (Al_2O_3)p composites using A 384.1 Al Alloys.. Vol. 21, No. 10, S066-071, 2009.

[9]. Zhou W. Y., Qi S. H., Tu C. C., Zhao H. Z., Wang C. F., Kou J, "Effect of the particle size of Al_2O_3 on the properties of filled heat-conductive silicone rubber" Journal of Applied Polymer Science, 104, 1312–1318 (2007).

[10]. Ling W., Gu A. J., Liang G. Z., Yuan L." New composites with high thermal conductivity and low dielectric constant for microelectronic packaging", Polymer Composites, 31, 307–313 (2010).

[11]. R. Gadag and A. Shetty, Handbook of engineering chemistry, Department of chemistry, National institute of technology, Karnataka, Shurathkal, 2010.

[12]. J. Hashim, L. Looney and M. Hashmi, "The wettability of SiC particles by molten aluminum alloy", Journal of Materials Processing Technology, 119(1-3):324-328, 2001.

[13]. K. Almadhoni and S. Khan, "Review of effective parameters of stir casting process on metallurgical properties of ceramics particulate Al composites", Journal of mechanical and civil engineering (IOSR-JMCE), Vol. 12, Issue 6, Ver. IV, PP 22-40, 2015.

[14]. S. Nam and D. Lee, "The effect of Mn on the Mechanical Behavior of Al Alloys, Metals and materials", Vol. 6, No. 1, pp. 13-16, 2000.

[15]. V. Tirth, "Process parameters and improvements in properties of metals and alloys by squeeze casting", IJNSTEEES, International Science Press 2, pp 26- 61, 2009.

[16]. C. Singh and K. Mer, "Wear characterization of Al- Al_2O_3 in-situ particulate composite synthesized in open hearth furnace with manually controlled stirring method", Proceedings of international conference on innovation & research in technology for sustainable development (ICIRT), 2012.

[17]. Agarwal, S. Singh and others, "Development of Al- $Al_2O_3(MnO_2)$ hybrid MMCs and their characterization for mechanical properties", MIT international journal of mechanical engineering, Vol. 2, No. 1, pp. 62-69, 2012.

[18]. G. Kreysa, J. Baselt and K. Unger, Novel Mn-based Mesoporous mixed oxidic solids, Technology & Engineering, Elsevier, 2000.

[19]. D Saheb, "Aluminum silicon carbide and aluminum graphite particulate composites", ARPN, Journal of engineering and applied sciences, Vol. 6, No. 10, ISSN 1819-6608, 2011.

[20]. P. Sharma, "Production of AMC by stir casting – An overview", International journal of contemporary practices, ISSN: 2231-5608, Vol.2, Issue 1, 2013.

[21]. R. Gadag and A. Shetty, Handbook of engineering chemistry, Department of chemistry, National institute of technology, Karnataka, Shurathkal, 2010.

[22]. G. Totten and D. Scott, Handbook of aluminum, Physical metallurgy and processes, Vol. 1, 2003.

[23]. J. Hashim, L. Looney and M. Hashmi, "The wettability of SiC particles by molten aluminum alloy", Journal of Materials Processing Technology, 119(1-3):324-328, 2001.

كيفية الاستفادة من مخلفات الخرسانة في حالتها الطازجة

م. محمد ميلاد الأشتر [1] ، م. علي عثمان مسعود [2]
[2]aothmanem@gmail.com, [1]mohammedmtaz@gmail.com
[1]مدير عام، شركة معايير الاستدامة، الجبل الغربي، ليبيا
[2]مساعد مدير مكتب ضمان وضبط الجودة، شركة الاتحاد العربي للمقاولات، طرابلس، ليبيا

الملخص

جزء كبير من الخرسانة في حالتها الطازجة والزائدة عن الكميات الفعلية المراد صبها تتحول إلى مخلفات صلدة مما يترتب عليه تكلفة عالية لإعادة تدويرها في هذه الحالة، وإذ تعتبر الخرسانة ثاني أكثر مادة استهلاكاً بعد الماء عليه فمن المهم الاستفادة منها قبل تصلدها أو إعادة تدويرها وهي في حالتها الطازجة. حيث تشير اغلب الدراسات إلى ضرورة الاستفادة من مخلفات الخرسانة سواء كانت في حالتها الطازجة أو حالتها المتصلدة، ولكن اغلب مصانع الخرسانة الجاهزة في مدينة طرابلس لا يقومون بالاستفادة من هذه المخلفات أو إعادة تدوير نتيجة لعدم درايتهم دراية كافية بتقنيات إعادة تدوير الخرسانة في حالتها الطازجة أو عدم اقتناعهم بها، بل يتم وضعها في الأماكن المخصصة للمخلفات ومن تم التخلص منها بنقلها إلى المقالب العمومية، مما يترتب عليه إهدار في الموارد وزيادة في تكاليف التشغيل ناهيك عن الأضرار البيئية الناجمة عن ذالك.

عليه فإن الهدف من هذه الورقة هو تحديد أفضل الأساليب للاستفادة من مخلفات الخرسانة في حالتها الطازجة سواء استخدامها مباشرة أو في إنتاج بعض المنتجات الخرسانية الأخرى أو إعادة تدويرها لإنتاج ركام خشن واستخدامه فيما بعد في إنتاج الخرسانة، وتشمل الورقة دراسة الجدوى الاقتصادية من إعادة استخدام مخلفات الخرسانة في حالتها الطازجة ومقارنتها بطرق التخلص من هذه المخلفات. وبناءً عل ذلك فإن إعادة تدوير أو استخدام مخلفات الخرسانة في حالتها الطازجة قد يوفر في تكاليف إنتاج الخرسانة الجاهزة وكذلك الحفاظ على الموارد الطبيعية والتقليل من الإضرار بالبيئة.

الكلمات الدالة: الخرسانة في حالتها الطازجة، مخلفات، إعادة تدوير، أساليب الاستفادة.

1 المقدمة

تعتبر الخرسانة من المنتجات الأساسية التي تستخدم في قطاع الإنشاءات حول العالم حيث يتم إنتاجها بكميات كبيرة سنوياً تصل إلى 3.8 مليار متر مكعب [1]. وحيث أن نسبة المخلفات تقدر بـ 1.5% من إجمالي الإنتاج حسب ما تشير له بعض الدراسات [3]، وأن كمية مخلفات الخرسانة وهي في حالتها الطازجة تصل إلى 253 مليون متر مكعب سنوياً. وبالنظر إلى هذه الكمية فانه يجب الاستفادة من مخلفات الخرسانة وهي في حالتها الطازجة أو إعادة تدويرها لما لها من نتائج ايجابية تساهم في خفض مستوى التلوث البيئي والحفاظ على الموارد الطبيعية وغيرها. إن اغلب الدراسات السابقة والمتعلقة بموضع الدارسة تشير إلى ضرورة الاستفادة أو التقليل من المخلفات، وحيت أن أغلب مصانع الخرسانة في مدينة طرابلس لا يقومون بالاستفادة من هذه المخلفات أو إعادة تدويرها، وأن اغلبهم لا يستفيدون الاستفادة المثلى من مخلفات الخرسانة في حالتها الطازجة نتيجة لعدم درايتهم دراية كافية بطرق الاستفادة أو عدم اقتناعهم بها أو لعدم وجود الجدية للتقليل من التأثيرات البيئية. إن كل مصانع الخرسانة الجاهزة داخل نطاق الدراسة يتخلصوا من المخلفات إما مباشرة بمواقع الصب في حال الكميات الصغيرة أو بوضعها في الأماكن المخصصة للمخلفات داخل المصانع ومن تم التخلص منها بنقلها إلى المقالب العمومية في حال الكميات الكبيرة، مما يترتب عليه تكاليف تشغيل زائدة وتأثيرات سلبية وإهدار للموارد المحلية غير المتجددة (اسمنت، ركام خشن،ركام ناعم، ماء) ناهيك عن التلوث البيئي. عليه فإن الهدف من هذه الورقة تحديد أفضل الأساليب للاستفادة من مخلفات الخرسانة في حالتها الطازجة سواء استخدامها مباشرة في بعض الأعمال أو المنتجات الخرسانية أو تدويرها لإنتاج ركام خشن واستخدامه بعد ذلك في إنتاج الخرسانة، والجدوى من إعادة استخدام مخلفات الخرسانة في حالتها الطازجة ومقارنتها بالأساليب الحالية المستخدمة للتخلص من هذه المخلفات، وقد قمنا بإجراء مسح لمواقع مصانع إنتاج الخرسانة الجاهزة، والشكل (1) يوضح صورة جوية لعدد وأماكن مصانع إنتاج الخرسانة بمدينة طرابلس.

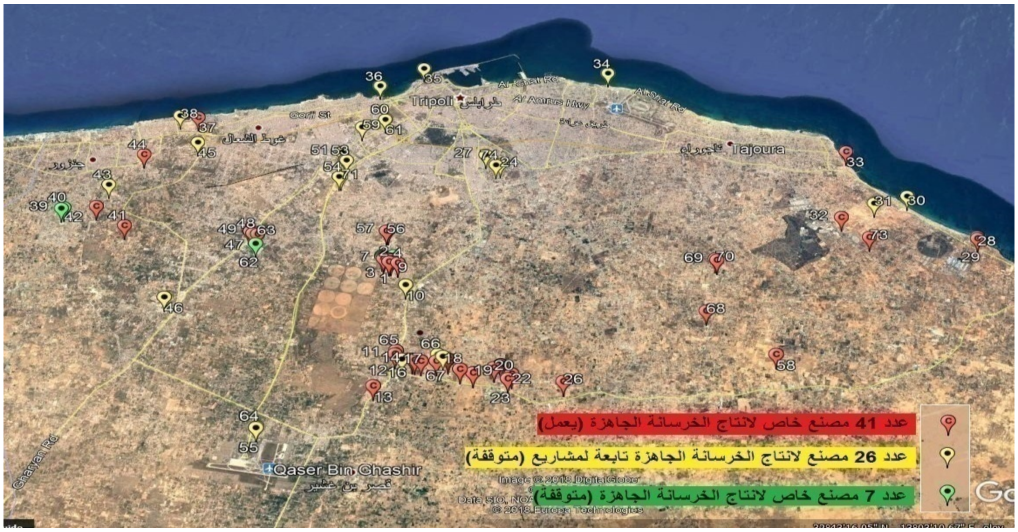

شكل (1) صورة جوية توضح عدد وأماكن مصانع إنتاج الخرسانة بمدينة طرابلس

2 منهجية البحث

تم تقسيم هذا البحث إلى خمسة مراحل:

المرحلة الأولى: زيارة ميدانية لمصانع إنتاج الخرسانة لحصرها وجمع المعلومات والبيانات.

المرحلة الثانية: دراسة المعلومات والبيانات المتحصل عليها وتحليلها ومقارنتها بالدراسات السابقة.

المرحلة الثالثة: حصر الأساليب المثلى للاستفادة من مخلفات الخرسانة في حالتها الطازجة.

المرحلة الرابعة: الجدوى الاقتصادية من الدراسة ومقارنة الأساليب المتبعة.

المرحلة الخامسة: الخلاصة والتوصيات.

3 مصادر مخلفات الخرسانة في حالتها الطازجة بمدينة طرابلس

للخرسانة مخلفات تنتج عند كل عملية إنتاج، ابتداء من عملية الخلط ثم النقل وانتهاء بعملية الصب، ففي كل مرحلة من هذه المراحل قد ينتج بعض المخلفات للأسباب التالية:

1.3 كميات الخرسانة المرفوضة من الزبائن:

نتيجة لعدم مطابقة الخرسانة الموردة للزبون للمواصفات المطلوبة أو المتفق عليها ي تم رفض الشحنة وإعادتها إلى المصنع، وهذه الكمية تمثل نسبة صغيرة من إجمالي كمية المخلفات الطازجة في هذه الفترة باعتبار أن اغلب كميات الخرسانة تورد للمواطنين حيث أن اغلبهم لا يقومون بإجراء الاختبارات عليها، وان جل المشاريع الإسكانية والخدمية وغيرها متوقفة، إذ أن اغلب الخرسانة الموردة لهذه المشاريع تخضع للاختبار قبل صبها من قبل المهندسين.

2.3 كميات الخرسانة التي زادت عن الكمية الفعلية المراد صبها للزبون:

اغلب هذه الكميات ناتجة إما لصعوبة تقدير الكمية المطلوبة أو لطلب كمية اكبر من الكمية الفعلية عن قصد، نتيجة لبعد المسافة وخوفاً من تأخر الشحنات الأخيرة وحدوث فواصل في الصب، وتمثل هذه الكميات النسبة الأكبر إذ تحدث عند كل عملية صب تقريباً مع التفاوت في الكمية من عملية إلى أخرى.

3.3 إرسال الخرسانة إلى موقع الصب لسوء التنسيق مع الزبون:

تنتج كميات من المخلفات لعدم جاهزية العناصر المراد صبها أو إرسال مضخة خرسانة لا تصل إلى العناصر المراد صبها وكذلك نتيجة عدم صلاحية موقع الصب أو عوارض أخرى وهذا السبب يعزى لعدم التنسيق الجيد.

4.3 أعطال ميكانيكية وحوادث مرورية عارضة:

للأعطال الميكانيكية والحوادث المرورية نصيب في التسبب بوجود كميات من مخلفات الخرسانة في حالتها الطازجة، تحدث هذه الأعطال والحوادث بشكل قليل جداً، إذ قد تحدث مرة أو مرتين في العام الواحد إلا أن حدوتها يتسبب في إنتاج كمية كبيرة من مخلفات الخرسانة وهي في حالتها الطازجة، وقد يتسبب حدوثها في تلف حلة الشاحنات الناقلة للخرسانة.

5.3 كميات متبقية في حوض مضخة الخرسانة:

في جميع الحالات التي تتطلب استخدام مضخة الخرسانة لعملية الصب يتبقى جزء صغير من الخرسانة في حوض المضخة تتراوح كميته من 0.1 إلى 0.125 م^3 على حسب حجم الحوض وطول خرطوم المضخة.

6.3 كميات ناتجة عن أخذ عينات الاختبارات:

للتأكد من جودة الخرسانة يتم اخذ عينات منها لإجراء الاختبارات عليها وهي في حالتها الطازجة ومن تم التخلص منها كمخلفات.

7.3 مصادر أخرى:

قد تنتج مخلفات لعدة أسباب أخرى كالأسباب الأمنية والاجتماعية وجراء العوامل الطبيعية كالأمطار الغزيرة وغيرها.

4 الأساليب الحالية المستخدمة للتخلص من مخلفات الخرسانة في حالتها الطازجة بمدينة طرابلس

1.4 الاستفادة المباشرة:

1.1.4 إعادة توجيهها لمواقع أو عناصر أو أصناف أخرى:

جزء صغير من الكميات الراجعة إلى المصانع يتم إعادة توجيهها إلى مواقع أخرى قريبة من موقع الصب، إذ لا يوجد تواصل وتنسيق كافي مع مصانع الخرسانة بعضها البعض. وإن أغلب مصانع الخرسانة لا يقومون بعمليتي صب في وقت واحد، نظراً لأن أغلب المصانع لا تمتلك إلا مضخة واحدة. حيث يتم الاستفادة من هذا الأسلوب جزئياً نوعاً ما لحل مشكلة المخلفات إذ لم يتم استغلاله بالصورة الصحيحة التي تضمن عدم تكون المخلفات.

2.1.4 تصنيع بعض المنتجات الخرسانية:

القليل من المصانع التي تمت زيارتهم يقومون بتصنيع بعض المنتجات الخرسانية مثل بردورات الطرق وبردورات الحدائق وبلاطات تغطية القبور وحواجز خرسانية كما هو موضح بالشكل (2). إلا أن هذه المنتجات لم ترتقي للمستوى المطلوب الذي يغطي كميات كبيرة من المخلفات الزائدة عن الحاجة، إذ يلجأ اغلبهم لعمل قوالب صغيرة الحجم كمحاولات خجولة من بعض المهندسين أو المشرفين القائمين على التشغيل. إلا أن هذه القوالب لا تكفي ولا تلبي المتطلبات أو لا ترتقي للمستوى المطلوب من حيث الجودة. إذ أن المخلفات الصلدة بالمصانع تكاد تكون هي نفسها عند الذين يتبعون هذا الأسلوب أو الذين لا يتبعونه.

استخدام الخرسانة في تصنيع بردورات الطرق والحدائق

استخدام الخرسانة في تصنيع بلاطات تغطية القبور

استخدام الخرسانة في تصنيع حواجز خرسانية

شكل (2) استخدام الخرسانة في تصنيع بعض المنتجات الخرسانية

2.4 الاستفادة غير المباشرة "إعادة التدوير بالطرق الميكانيكية":

من خلال زيارة مصانع الخرسانة الجاهزة تبين استخدام مصنعين للطرق الميكانيكية لإعادة تدوير الخرسانة في حالتها الطازجة كما هو موضح بالشكل (3)، حيث أن محطات التدوير المستخدمة تنتج ركام خليط بين الخشن والناعم ولا يمكن استخدامه إلا في الخرسانات العادية، وهي شبه متوقفة عن العمل أو تعمل بنصف طاقتها لعدم وجود الصيانة والمتابعة الدورية.

شكل (3) محطة تدوير الخرسانة الطازجة بالطريقة الميكانيكية في احد المصانع

3.4 التخلص من مخلفات الخرسانة الطازجة

كل مصانع إنتاج الخرسانة الجاهزة بما فيهم المصانع التي تستفيد جزئياً من المخلفات الطازجة تقوم بالتخلص منها بنقلها بعد تصلدها إلى المقالب العمومية كما هو موضح بالشكل (4)، وبالنظر إلى هذه العملية ودراسة نتائجها على الجانب الاقتصادي والبيئي والاجتماعي يتضح أن لها تأثيرات سلبية كبيرة من جميع النواحي، حيث أثبتت بعض الدراسات أن تكلفة التخلص من مخلفات الخرسانة بنقلها إلى المقالب العمومية ضعف تكلفة إعادة استخدامها أو تدويرها [3].

شكل (4) التخلص من مخلفات الخرسانة الطازجة وذلك بوضعها على الأرض حتى تصلدها ومن ثم نقلها إلى المقالب العمومية

5 نتائج المسح لكميات مخلفات الخرسانة في حالتها الطازجة في مدينة طرابلس:

تم حصر مصانع إنتاج الخرسانة الجاهزة في مدينة طرابلس حيث يوجد عدد حوالي 74 مصنع لإنتاج الخرسانة الجاهزة، وبناء على المسح الميداني (الاستبيان والمقابلة الشخصية) الذي تم إجراءه على عشرين مصنع لإنتاج الخرسانة الجاهزة تم حصر كل من كميات الإنتاج وكميات مخلفات الخرسانة الطازجة حسب مصدرها لعدد 20 مصنع كما هو موضح بالجدول رقم (1). وتم تقدير كميات مخلفات الخرسانة الطازجة في مدينة طرابلس وفق المصادر المشار إليها سابقاً لعدد 74 مصنع كما هو موضح بالجدول رقم (2).

الجدول رقم (1) كميات مخلفات الخرسانة في حالتها الطازجة لعدد 20 مصنع بمدينة طرابلس

ر.م	الموقع	متوسط كمية إنتاج الخرسانة	كميات الخرسانة المرفوضة من الزبائن	كميات الخرسانة التي زادت عن الكمية الفعلية	كميات ناتجة عن إرسال الخرسانة إلى موقع الصب لسوء التنسيق	كميات ناتجة عن أعطال ميكانيكية وحوادث مرورية	كميات متبقية في حوض المضخة	كميات ناتجة عن أخذ عينات الاختبارات	إجمالي كمية المخلفات لكل مصنع	نسبة المخلفات من إجمالي الإنتاج
		م^3/سنوياً	م^3/سنوياً	م^3/سنوياً	م^3/سنوياً	م^3/سنوياً	م^3/سنوياً	م^3/سنوياً	م^3/سنوياً	%
1	طريق الكريمية - السواني	78000	67.5	936	15	22.5	130	58	1229	1.6
2		54000	0	360	7	8	90	38	503	0.9
3		42000	7	96	3	9	70	9	194	0.5
4		24000	0	180	4	9	40	9	242	1.0
5	مشروع الهضبة - شارع الخلاطات	54000	15	624	16	16	90	26	787	1.5
6		48000	0	312	8	7	80	9	416	0.9
7		27000	0	720	3	4	45	9	781	2.9
8		30000	0	156	4	7	50	9	226	0.8
9		39000	8	360	3	8	65	9	453	1.2
10	سوق الأحد	45000	16	312	3	3	75	9	418	0.9
11	طريق وادي الربيع	21000	0	156	3	8	35	9	211	1.0
12		36000	0	720	7	9	60	15	811	2.3
13		24000	0	312	3	4	40	9	368	1.5
14		46200	9	120	16	16	77	19	257	0.6
15		36000	9	360	4	7	60	2	442	1.2
16	عين زارة	24000	108	120	7	8	40	19	302	1.3
17	الغيران - جنزور - النجيلة	28800	0	312	4	8	48	9	381	1.3
18		42000	0	360	4	8	70	9	451	1.1
19		36000	0	180	3	9	60	9	261	0.7
20		60000	0	360	4	8	100	25	497	0.8
الإجمالي (م^3/سنويا)		795000	239.5	7056	121	178.5	1325	315	9235	%1.2
المتوسط (م^3/سنويا)		39750	12.0	352.8	6.1	8.9	66.3	15.7	461.7	

الجدول رقم (2) تقدير كميات مخلفات الخرسانة الطازجة في مدينة طرابلس لعدد 74 مصنع

مصادر مخلفات الخرسانة في حالتها الطازجة	عدد مصانع إنتاج الخرسانة الجاهزة في مدينة طرابلس	متوسط كمية مخلفات الخرسانة الطازجة سنوياً لمصنع واحد من واقع الدراسة	إجمالي الكمية التقديرية لمخلفات الخرسانة الطازجة السنوية في مدينة طرابلس
		$م^3$ / سنوي	$م^3$ / سنوي
كميات الخرسانة المرفوضة من الزبائن	74	12.0	886.2
كميات الخرسانة التي زادت عن الكمية الفعلية المراد صبها		352.8	26107.2
كميات ناتجة عن إرسال الخرسانة إلى موقع الصب لسوء التنسيق مع الزبون		6.1	447.7
كميات ناتجة عن أعطال ميكانيكية وحوادث مرورية عارضة		8.9	660.5
كميات متبقية في حوض مضخة الخرسانة		66.3	4902.5
كميات ناتجة من أخذ عينات الاختبارات		15.7	1164.5
الكمية التقديرية لمخلفات الخرسانة في حالتها الطازجة في مدينة طرابلس ($م^3$/سنوي)		461.7	34169

تشير الدراسات إلى أن نسبة مخلفات الخرسانة في حالتها الطازجة حوالي 1.5 % من نسبة الإنتاج [3]، وفي بعض الدراسات الأخرى 0.4-0.5 % [5] من إجمالي إنتاج الخرسانة. ومن خلال هذه الدراسة تبين أن متوسط نسبة مخلفات الخرسانة في حالتها الطازجة في مدينة طرابلس بلغت 1.2 % من إجمالي إنتاج الخرسانة، والشكل (7) يوضح نسبة كمية مخلفات الخرسانة الطازجة من إجمالي إنتاج الخرسانة، كما يوضح الشكل (8) نسب كميات مخلفات الخرسانة الطازجة حسب مصدرها من إجمالي المخلفات.

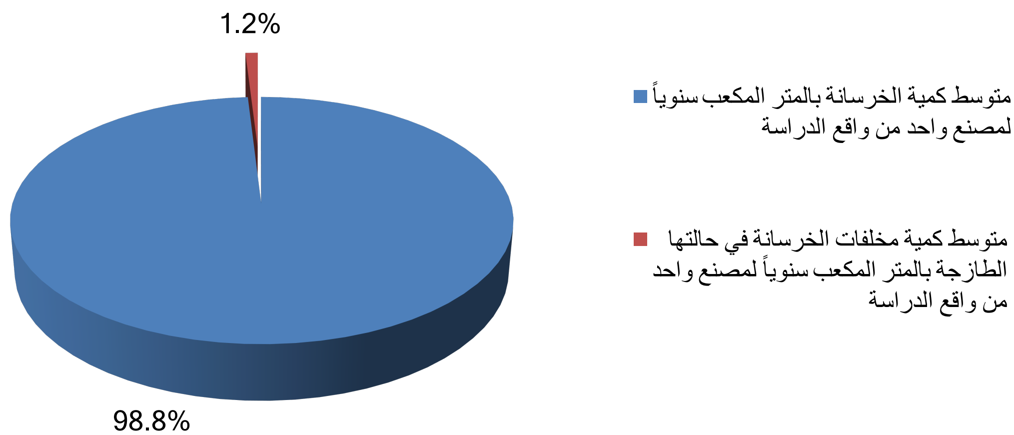

شكل (7) نسبة كمية مخلفات الخرسانة الطازجة من إجمالي انتاج الخرسانة

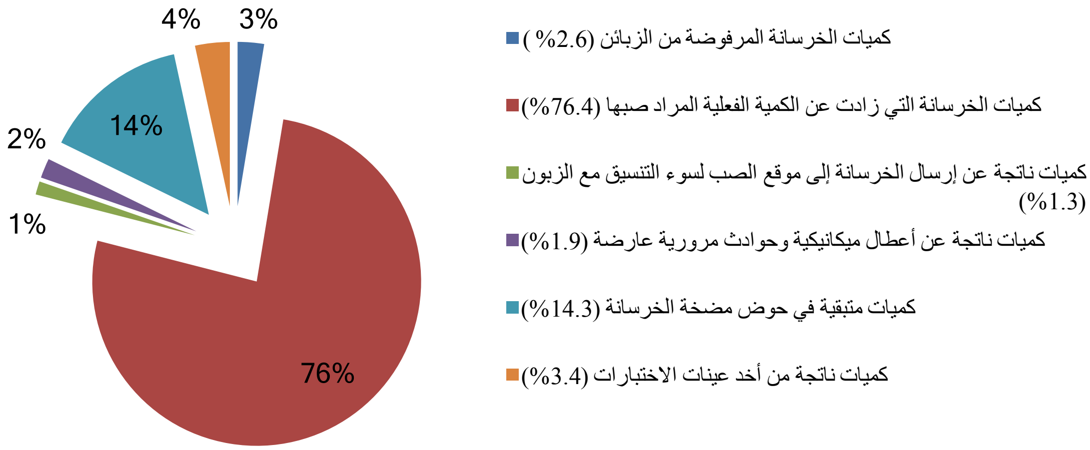

شكل (8) نسب كميات مخلفات الخرسانة الطازجة حسب مصدرها من إجمالي المخلفات

6 الأساليب الواجب إتباعها للاستفادة من مخلفات الخرسانة في حالتها الطازجة

1.6 إعادة توجيه الخرسانة لمواقع أو عناصر أو أصناف أخرى:

يجب الاستفادة من هذه الكميات إما بإعادة توجيهها إلى عناصر أخرى في نفس الموقع أو إلى مواقع أخرى قريبة إن أمكن، فهذا الأسلوب لا يحتاج إلا لإدارة منظمة تتبع أساليب الإدارة الحديثة للتواصل، باستغلال جميع وسائل الاتصال المتاحة للحد من المخلفات قدر الإمكان، وإنشاء الخطط البديلة للمخاطر بالاستعانة بأحد الأساليب المشار إليها أدناه كخطط بديلة.

2.6 تصنيع بعض المنتجات الخرسانية:

على مصانع الخرسانة تجهيز قوالب لبعض المنتجات الخرسانية ذات أحجام مختلفة لاستخدامها في تصنيع بعض المنتجات الخرسانية مثل المقاعد الخرسانية والطاولات وبردورات الطرق والحدائق وممرات المشاة والحواجز الخرسانية وأغطية غرف التفتيش وغيرها. وعدم الاقتصار على المنتجات الصغيرة فقط، وزيادة الاهتمام بالقوالب والاستعانة بالمهندسين المعماريين لخلق أشكال ونماذج ترتقي للمستوى العالمي. إذ أن سعر تكلفة طاولة القهوة المصنوعة من الخرسانة حسب موقع الأمازون يقدر بـ 880 دولار أمريكي [4]، إذ لا تستهلك أكثر من 0.125 م^3 من الخرسانة لتصنيعها.

3.6 استخدام الإضافات الكيميائية لضبط عملية التميوء:

تطورت صناعة الإضافات الكيميائية المحسنة لخواص الخرسانة والتي من بينها إضافات تستخدم لإعادة الاستفادة من الخرسانة الزائدة عن الحاجة بتبطئة زمن الشك لفترة تصل إلى 72 ساعة [5]، لاستخدامها فيما بعد بخلطها مع كميات من الخرسانة المنتجة حديثاً، وهذه الإضافات لا تؤثر سلباً على الخواص الميكانيكية للخرسانة وتعطي زمن شك أطول ومقاومة أعلى [7,6,5]. قد تحدث هذه الإضافات فارق كبير في كمية المخلفات إذا ما تم أخذها بعين الاعتبار واستغلالها الاستغلال الأمثل.

4.6 استخدام الإضافات الكيميائية لإنهاء عملية التميوء:

احد الأساليب الواجب إتباعها لإعادة التدوير للاستفادة من المخلفات، بعمليات رطبة حيث يتم إضافة المواد الكيميائية إلى شاحنات نقل الخرسانة بدون الحاجة إلى أي معدات أخرى، وتخلط لزمن محدد حسب نوع المادة المضافة ومن تم تفريغ الشحنة ومعالجتها، حيث تقوم هذه المواد بإيقاف التفاعل بين الاسمنت والماء وتحويل 1 م^3 من الخرسانة إلى 2400 كجم من الركام الجاف [8,5]، وهذا الركام يمكن

استخدامه بنسبة 100% في الخرسانة غير الإنشائية وبنسب أقل في الخرسانة المسلحة، حسب درجة الخرسانة بدون تأثيرات سلبية على خواص الخرسانة [8] كما هو موضح بالشكل (5).

شكل (5) استخدام الإضافات الكيميائية لإنهاء عملية التميوء لإنتاج ركام خشن

5.6 إعادة التدوير بالطرق الميكانيكية:

هذا الأسلوب احد الأساليب المهمة للحد من تكون المخلفات الخرسانية، فإذا لم يتم الاستفادة من المخلفات بتطبيق الأساليب المشار إليها أنفاً فإنه لا خيار إلا اللجوء إلى الأسلوب الميكانيكي لفصل مكونات الخلطة إما كلي وإما جزئي، لاستخدام ما قد تم فصله من ركام خشن لإنتاج خرسانات جديدة وبنفس كفاءة الركام العادي وإما الاستفادة من الركام الناعم في إنتاج خرسانات ذات جودة منخفضة، أو الاستفادة من الماء مباشرة للخلط أو بخلطه بكميات أخرى. ومن خلال الدراسة يتضح أن عملية التدوير الميكانيكية مكلفة ولكنها أقل تكلفة من التخلص من مخلفات الخرسانة بنقلها إلى المقالب العمومية. والشكل (6) يوضح بعض محطات تدوير الخرسانة في حالتها الطازجة.

شكل (6) إعادة تدوير الخرسانة في حالتها الطازجة بالطرق الميكانيكية

7 الخلاصة:

كما اشرنا سابقاً أن اغلب مصانع الخرسانة الجاهزة تتخلص من مخلفات الخرسانة في حالتها الطازجة بنقلها بعد تصلدها إلى المقالب العمومية مما يترتب عليه مجموعة من التأثيرات الاقتصادية والبيئية والاجتماعية، حيث أن متوسط التكلفة التقديرية لنقل مخلفات الخرسانة إلى المقالب العمومية حوالي 5,550 د.ل/سنوي لكل مصنع كما هو موضح بالجدول (3)، وبالرغم من أن هذه القيمة ليست كبيرة إلا أن الاستفادة من المخلفات في حالتها الطازجة بأحد الأساليب المشار إليها ينتج عنه أرباح إضافية كبيرة كما هو موضح بالجداول (4،5،6،7،8).

الجدول رقم (3) تكلفة نقل مخلفات الخرسانة بعد حالة تصلدها إلى المقالب العمومية في مدينة طرابلس

مصادر مخلفات الخرسانة في حالتها الطازجة	كمية مخلفات الخرسانة الطازجة في مدينة طرابلس	متوسط تكلفة تشوين المخلفات	متوسط تكلفة نقل المخلفات الخرسانة الطازجة من المصنع إلى المقالب العمومية	ضريبة المقالب العمومية	إجمالي التخلص من المخلفات	إجمالي تكلفة نقل المتر المكعب من المخلفات الخرسانة الطازجة من المصنع إلى المقالب العمومية
	$م^3$	$د.ل / م^3$	$د.ل / م^3$	$د.ل / م^3$	$د.ل / م^3$	د.ل
كميات الخرسانة المرفوضة من الزبائن	12					143.942
كميات الخرسانة التي زادت عن الكمية الفعلية المراد صبها	353					4240.727
كميات ناتجة عن إرسال الخرسانة إلى موقع الصب لسوء التنسيق مع الزبون	6	0.455	11.111	0.455	12.020	72.722
كميات ناتجة عن أعطال ميكانيكية وحوادث مرورية عارضة	9					107.280
كميات متبقية في حوض مضخة الخرسانة	66					796.338
كميات ناتجة من أخذ عينات الاختبارات	16					189.159
التكلفة التقديرية لنقل مخلفات الخرسانة في حالتها الطازجة إلى المقالب العامة						**5,550.169**

الجدول رقم (4) قيمة الأرباح من إعادة توجيه الخرسانة كأحد أساليب الاستفادة من مخلفات الخرسانة الطازجة

كمية الخرسانة	سعر البيع	صافي التوفير *
$م^3$	$د.ل/م^3$	د.ل/سنوي
371	150	60,081

* صافي التوفير عبارة عن إجمالي قيمة بيع الخرسانة المعاد توجيهها بالإضافة إلى توفير تكلفة نقل المخلفات إلى المقالب.

الجدول رقم (5) قيمة الأرباح من تصنيع المنتجات الخرسانية كأحد أساليب الاستفادة من مخلفات الخرسانة الطازجة

كمية الخرسانة	تكلفة تصنيع المنتج	سعر البيع	عدد البردورات المنتجة	صافي التوفير *
$م^3$/سنوي	د.ل/قطعة	د.ل/قطعة	قطعة/سنوي	د.ل/سنوي
462	1.813	6	8795	42,378

* صافي التوفير عبارة عن إجمالي قيمة بيع المنتجات الخرسانية بالإضافة إلى توفير تكلفة نقل المخلفات إلى المقالب.

الجدول رقم (6) قيمة الأرباح من استخدام الإضافات الكيميائية لضبط عملية التميوء كأحد أساليب الاستفادة من مخلفات الخرسانة الطازجة

كمية الخرسانة	تكلفة الإضافات الكيميائية	سعر البيع	صافي التوفير *
$م^3$/سنوي	د.ل/سنوي	$د.ل/م^3$	د.ل/سنوي
380	4,747	150	56,780

* صافي التوفير عبارة عن إجمالي قيمة إعادة بيع الخرسانة بالإضافة إلى توفير تكلفة نقل المخلفات إلى المقالب.

الجدول رقم (7) قيمة الأرباح من استخدام الإضافات الكيميائية لإنهاء عملية التميوء كأحد أساليب الاستفادة من مخلفات الخرسانة الطازجة

كمية الخرسانة	تكلفة الإضافات الكيميائية	كمية الركام المتحصل عليه	قيمة المتر المكعب من الركام الخشن المعاد تدويره	صافي التوفير *
م^3/سنوي	د.ل/سنوي	م^3/سنوي	د.ل/م^3	د.ل/سنوي
380	1,899	380	20	10,261

* صافي التوفير عبارة عن إجمالي قيمة الركام الخشن الناتج من إعادة تدوير الخرسانة بالإضافة إلى توفير تكلفة نقل المخلفات إلى المقالب.

الجدول رقم (8) قيمة الأرباح من إعادة التدوير بالطرق الميكانيكية كأحد أساليب الاستفادة من مخلفات الخرسانة الطازجة

كمية الخرسانة	تكلفة الاستثمار	مصاريف الصيانة	كمية الركام المعاد تدويره		قيمة الركام المعاد تدويره		صافي التوفير *
			الركام الخشن	الركام الناعم	الركام الخشن	الركام الناعم	
م^3/سنوي	د.ل/سنوي	د.ل/سنوي	م^3/سنوي		د.ل/م^3		د.ل/سنوي
453	8,000	800	362	181	25	12	7,980

* صافي التوفير عبارة عن إجمالي قيمة الركام الخشن والناعم الناتج من إعادة تدوير الخرسانة بالإضافة إلى توفير تكلفة نقل المخلفات إلى المقالب.

8 الاستنتاجات والتوصيات:

تبين من خلال الدراسة أن الاستفادة من مخلفات الخرسانة وهي في حالتها الطازجة سواء باستخدامها مباشرة أو استخدامها في تصنيع المنتجات الخرسانية الأخرى أو بتدويرها له العديد من النتائج الايجابية التي يمكن تضمينها في النقاط التالية:

- المحافظة على الموارد الطبيعية غير المتجددة عن طريق الحد من الحاجة إلى إنتاج الاسمنت واستخراج الركام.
- خلق المزيد من فرص العمل.
- التقليل من تكلفة شراء المواد الخام، وبذلك التقليل من تكلفة نقل المخلفات إلى المقالب العمومية، مما يترتب عليه توفير في المصروفات.
- المحافظة على البيئة بالتقليل من مساحة الأراضي المستخدمة لدفن المخلفات.
- التقليل من الغبار الناتج عن تدوير مخلفات الخرسانة المتصلدة.
- بالاستفادة من 1 متر مكعب من مخلفات الخرسانة في حالتها الطازجة ينقذ حوالي 200 لتر من الماء.

المراجع:

[1]. http:// training.ce.washington.edu/wsdot/Modules/03-4 body.htm.

[2]. Aynur K, Serdar U, Bayram Er, Volkan A, Murat A, Ahmet A, Fresh Ready Mixed Concrete Waste in Construction Projects: A Planning Approach, Resources, organization, technology and management in construction· an international journal, 2015.

[3]. Tam, V.W.Y., Tam, C.M. Economic comparison of recycling over-ordered fresh concrete: a case study approach, Resources, Conservation and Recycling, 2007.

[4]. https://www.amazon.com/Lyon-Beton-Rectangular-Coffee-Table/dp/B01M659LKS/ref=sr_1_34?ie=UTF8&qid=1525037788&sr=8-34&keywords=concrete%20table%20coffee https://www.amazon.com/Lyon-Beton-Rectangular-Coffee-Table/db/B01M659LKS/ref=sr_1_34?ie=UTF8&qid

[5]. Aynur Kazaz, Serdar Ulubeyli, Current Methods for the Utilization of the Fresh Concrete Waste Returned to Batching Plants, Resources, World Multidisciplinary Civil Engineering-Architecture-Urban Planning Symposium, 2016, WMCAUS, 2016.

[6]. M. Paolini, R. Khurana, Admixtures for recycling of waste concrete, Cem. Conc. Comp. 20 (1998) 221-229.

[7]. C. Lobo, W.F. Guthrie, R. Kacker, A study on the reuse of plastic concrete using extended set-retarding admixtures, J. Res. Nat. Inst. Stand.Tech. 100 (1995).

[8]. G. Ferrari, M. Miyamoto, A. Ferrari, New sustainable technology for recycling returned concrete, Const. Build. Mater. 67 (2014).

Nanotechnology: Concepts, Importance and the Current State of Scientific Research

Samieh Abu Saad[1],Amani Elmahjub[2]
[1]samieh7@yahoo.com, [2]amanielmahjubi@gmail.com
[1]Head of Engineering Department, Industrial Research Centre Tajoura, Libya
[2] Head of Chemicals& Glassware Storage Unit, Industrial Research Centre Tajoura, Libya

ABSTRACT

In nowadays, research in nanoscale science has been greatly developing and obtaining more interests. Numerous research activities in the last two decades focus on exploring nanoscience, understanding the fundamentals, and developing technical solutions. Materials in nanoscale showed remarkable and superb properties that are completely different from those when the material in the bulk condition. This makes nanotechnology to hold a great promise in effecting profound scientific, medical, energy, economic and even cultural change on society. Almost all countries are placed long and short term strategic plans as to obtain more experience and carefully examine the potential implications of nanotechnology and its strategic benefits. Consequently, research indicators on this technology indicate that some developing countries compete with the world's largest countries in the control of this technology. This paper, however, provides an introduction to the nanotechnology, and also discovers the current status of the research on this particular field globally and in the Arabic region. The real status of the scientific research on the nanotechnology in Libya correspondingly is realised. Steps required by the Libyan authorities and research principles to fill in the gape in this area are also expressed.

Keyword— Nanotechnology; Nanoscience; Research in Nanotechnology; Nanotechnology Applications.

1. Introduction

Nanotechnology has become a competitive scientific technology that most of developed countries competed to control. The research and development in this particular field of technology has impacted every aspect of modern human life. More and divers areas of research have been continuously increasing and gaining the interest of researchers and scientists to apply this kind of technology and benefit from [1]; e.g. energy; agriculture; petroleum industry; food industry; and probably the strongest field is medicine and healthcare. Nanotechnology refers to the science and technology of which a matter is controlled in a nanoscale. It is commonly attributed for the technologies leading to produce nanoscale materials at nanometre dimension (10-9 m) [2, 3]. The nanoscale is consensually considered to cover the range of 1 to 100nm. According to the US National Nontechnology Initiative (NNI), the nanotechnology is '*the understanding and control of matter at dimensions between approximately 1 and 100 nanometres, where unique phenomena enable novel applications. Encompassing nanoscale science, engineering, and technology, nanotechnology involves imaging, measuring, modelling, and manipulating matter at this length scale*'. Yet, numerous definitions of nanotechnology have migrated and expanded with the passage

of time. For instance, in [4], the definition is expressed as '*nanotechnology is the design, characterization, production and application of materials, devices and systems by controlling shape and size of the nanoscale*'. While in [5], a slightly different nuance is given by '*the deliberate manipulation, precision placement, measurement, modelling and production of matter at the nanoscale in order to create materials, devices and systems with fundamentally new properties and functions*'. Another different definition, though floating around, is introduced in [6] that is '*the design, synthesis, characterization and application of materials, devices and systems that have functional organization at least one dimension on the nanometre scale*'. Obviously, the definitions, however, should provide some form of proactive engineering to the term nanotechnology. Nevertheless, to avoid the debate about the definition as it is not the particular scope of this paper, it would be better to suggest that a certain technology can be considered nanotechnology only if it involves all of the following three attributes: first, research and technology development at the atomic, molecular or macromolecular levels, in the scale of approximately 1–100 nm range; second, creation and use of structures, devices and systems that have novel properties and functions because of their small and/or intermediate size; and finally, an ability to control or manipulate on the atomic or the nanoscale [7].
This paper provides an introduction to the basic principles and applications of nanotechnology. It also discovers the current status of research on this particular field globally and in Arabic countries. The real situation of the scientific research on nanotechnology in Libya is finally concluded, and steps required by authorities and research principles to motivate the research in this area are expressed.

2. Importance of Nanotechnology

Nanotechnology is considered as a powerful tool and technique in medical technology as well as almost every filed life. This kind of technology develops so fast; while its applications diverse to touch all branches of science, engineering and industries. The momentum of nanostructures stems from the fact that new materials with absolutely new properties can be developed. Properties of a matter depend strongly on how atoms are arranged in space; e.g. if atoms in coal (Carbon) is rearranged, it could make diamond. Therefore, nanotechnology holds great opportunities for innovation in, virtually, every industry and application. New materials and advanced devices of a desirable properties and functions can be developed for numerous applications using this technology. The main aspects that make nanotechnology attractive to researchers are the fact that it is relatively cheap, can be manufactured in bulk with lower energy; the ability to control the material's properties by controlling its particles size and structural form as well as controlling the conditions and methods of preparation; and relatively safe in terms of use for people and environment [8]

3. Influence of Size on the Materials' Properties

Owing to the small size of the building blocks (particle, grain, or phase) nanomaterials demonstrate unique mechanical, optical, electronical, and magnetic properties [3]. Properties of nanomaterials depend on [9]: fine grain size and size distribution (<100 nm); the chemical composition of the constituent phases; the presence of interfaces, more specifically, grain boundaries, hetero-phase interfaces, or the free surface; and lastly interactions between the constituent domains.

Changes in the size-dependent properties of a matter are observed due to the fact that wave-like properties of electrons inside the matter and atomic interactions are influenced by the size of materials at the nanometre scale. Confinement of the DeBroglie wavelength of charge carriers inside nanomaterials could also lead to quantization effect [3]. As the size decreases, the ratio of atoms on the surface increases. Such atoms are high energy surface atoms and very reactive. This also creates a high surface to volume ratio leading to a tremendous improvement in chemical properties. Platinum nano particles, for example, are efficient catalysts for many reactions whereas platinum bulk sheets are sufficiently inert [8, 9]. Large surface to volume ratio means subtle changes to the surface due to addition of numerous atoms or molecules leading to dramatic alterations of physical properties. Number of fields,including magnetism, luminescence and renewable/alternative energy to sensors as well as photo-catalysis, will benefit from capitalizing on the surface–volume relationship. The possible enhancement of physical properties is therefore due to quantum size and clustering interface effects [10]. Figure 1 shows how surface volume ratio changes with particle size.

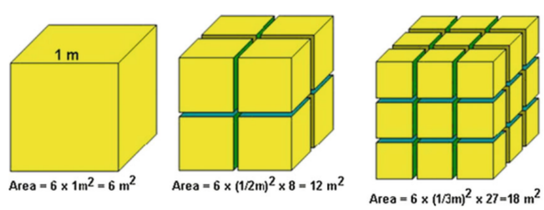

Figure 1: The surface volume ratio changes with particle size.

4. Nanofacture

There is a wide variety of technologies that have the potential to produce nanomaterials with different degrees of quality, speed and cost. Yet, grain size, shape and structure of the required nanomaterials are the main factors restrict the selection of the technology [11]. Almost all of these techniques fall into the main categories described in Figure 2. The top-down methods mostly require large (and also expensive, needs considerable concentrations of capital) installations [11]. Traditionally, scaling-down processes are based on process that include grinding or etching and utilise an ultraprecision engineering. Mechanical stiff parts are used to ultra-precisely shape objects. While on the other hand, for semiconductor processing a very high-quality thin films are deposited, either physical vapour deposition (PVD) or chemical vapour deposition

(CVD), with nanometre control, perpendicular to the plane of a substratum [11, 12]. Sophisticated technologies, e.g. exposure to a plasma, or ions implantation, are employed to modify existing surfaces of materials [12].

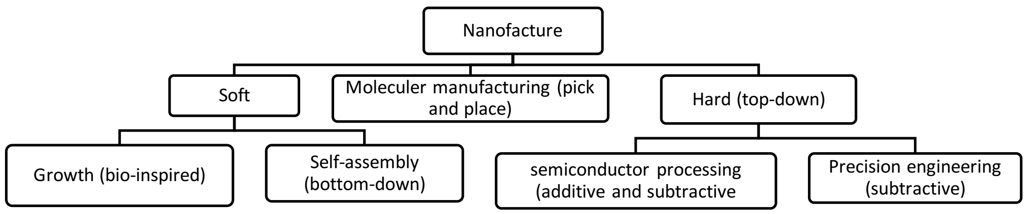

Figure 2: Different modes of nano-manufacture (nanofacture).

The other approach is known as molecular manufacturing; also known as "pick and place" or bottom-to-bottom methods, literally construct things atom-by-atom [11, 12].
The third approaches, known as bottom-up or self-assembly, are based on creating objects that capable of spontaneously assembling into useful structures. Precursors are gathered in random positions and orientations, and supply energy to allow them to sample configuration space. Once the precursors are in position, the bonds connecting them are strengthened and the final object is fixed permanently [11, 12].

5. The Current Situation of Research in Nanotechnology

To study the development trends of the research in nanotechnology, the outcomes of nanotechnology related research is examined. Indicators; namely, funding, publications and patents are presented, investigated and analysed. The results of such studies would also help policymakers in assessing their past policies, forecasting future trends based on the previous and contemporary trends[14], and take new valuable actions to succeed.

5.1. Globally

Governmental funding plays a critical role in establishing and stimulating nanotechnology research and development (R&D). Based on the Global Funding of Nanotechnologies & its Impact report [15], since 1997 the United States (US), followed by most countries in the European Union (EU), and other countries have announced series of policies and heavy funding to support academia for the field of nano-innovation R&D. Since then, as denoted in Figure 3, this budged was gradually increasing. Remarkably, the US outspends every country else. Yet Japan and Russia have managed to take a temporary lead in 2000-2003 before fall back. Also, it points out that the funding trend in EU grows gradually; while on the other hand faster growth rates are observed in Asia.

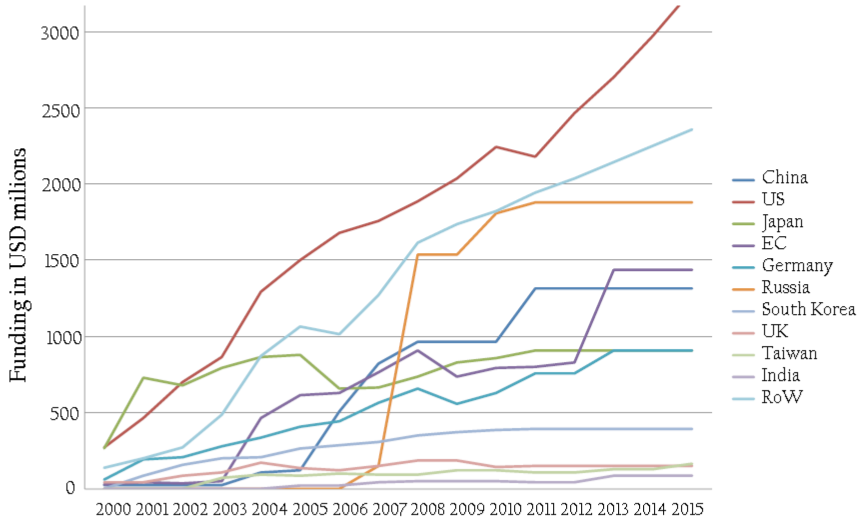

Figure 3: Funding of nanotechnologies by country [15]

Such funding is expected to positively reflect on the nanotechnology related R&D activities. This can be observed in the number of nanotechnology related articles and the number of granted patents annually. These two figures are mainly considered when examining the outcomes of R&D activities [14]. Visibly, scientific articles are the major source of knowledge production and transfer from academic research to industrial applications and developing innovations [14].

In this work, statistics of published scientific articles are obtained from the Thomson Reuters Web of Science (WoS) which are usually used for retrieving and analyzing academic research outputs [15]. Additionally, to avoid confusion and for better understanding only the top 5 countries are considered for the period of 2010-2017 as represented in Figure 4. It reveals that China possesses the highest rate of growth with about 47% while the US comes second with mostly half growth rate. Remarkably, India, South Korea and Iran rank in the list with growth rate of about 24%.

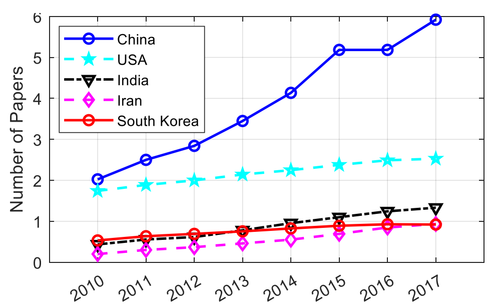

Figure 4: The number of nanotechnology article in 2010-2017

Nevertheless, number of articles need to be carefully analysed when used as an indicator for nanotechnology developing. Obviously, it is related to other figures such as population, stage of development, percentage of R&D expenditures, and some other important factors. Therefore, to reliably analyse data, another index is deployed to study the growth of nanotechnology research globally; i.e. the local share of nano-articles to total articles published by each country. Figure 5 shows the top 5 shares (%) in 2010-2017. It represents that Asian countries have the highest share in this indicator, and almost all of them have shares higher than the world average (9.5%). Iran and Saudi Arabia have consistincreasing share and achieved their highest shares in 2017. Both have experienced huge growth in the published nano-articles by giving propriety to nanotechnology research. Noticeably, Bahrain is in this particular list indicating the level of interest paid to this technology.

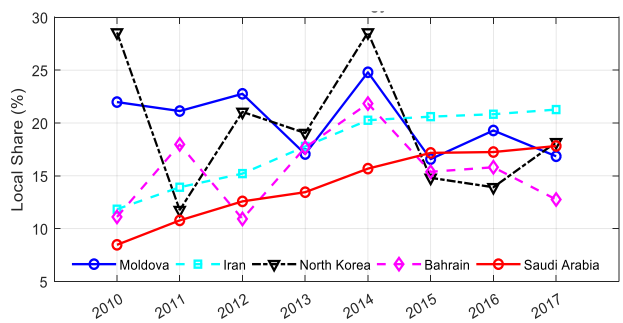

Figure 5: The local share in nanotechnology articles in 2010-2017

It is worth mentioning that although US is ranked2ndin published nano-articles, it possesses an average share of around 6 % in 2010-2017. While India ranked 6thin this list explaining the reason they both are not appearing in Figure 5.To further analyse the global development in nanotechnology, patents number is employed as a technology and innovation indicator. Patent data were retrieved from the United States Patent and Trademarks Office (USPTO) and European Patent Organisation (EPO). Figure 6 represents the nanotechnology patents granted in the USPTO in 2010-2017. It shows that US ranks 1stby possessing 60% of all nanotechnology patents. Noticeably, South Korea has consistent increasing patents and ranked 2ndin 2017 moving Japan 3rdwith a gap of 500 patents.

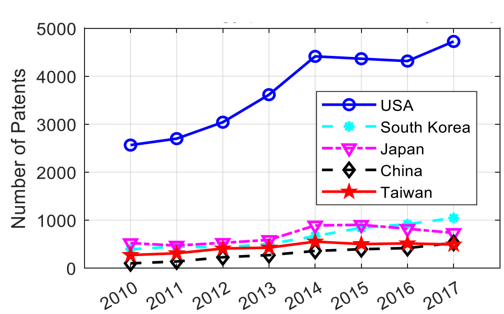

Figure 6: Nanotechnology related patents in USPTO

The EPO also shows that US possesses the highest patents granted in 2010-2017 as denoted in Figure 7. Apart from France and Japan, the gap between each country and other is visible.

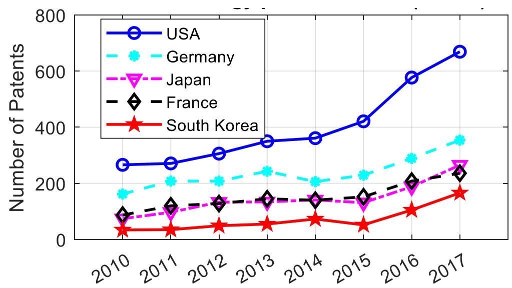

Figure 7: Nanotechnology *related patents in EPO*

5.2. The Arabic countries

Similarly, the current situation of research in the field of nanotechnology in Arabic countries is explored using both the number of publications and corresponding local share. It is worth mentioning that trusted resources about the exact funding spend on nanotechnology related R&D by most Arabic governments is not available. Hence only publications number and local share are explored. Additionally, due to the fact that published articles are very small in contrast to that published globally, the accumulative number in 2000-2017 is used instead, as denoted in Figure 8. Saudi Arabia has the highest accumulative number with more than 8000 articles, followed by Egypt with about 7750 articles. The rest are all either around 1500articles or reasonably lower; whereas Libya stands in the back with less than 100 articles.

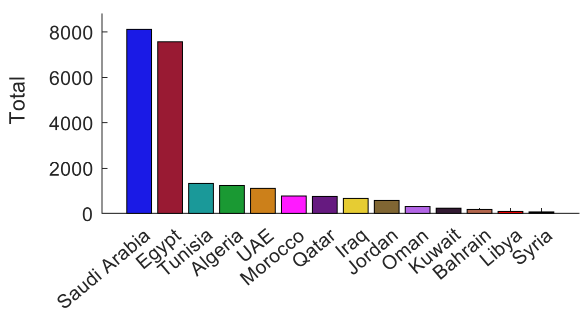

Figure8: Published nanoarticles in Arabic countries, total in 2000-2017

The local share is also calculated for every single Arabic country and represented in Figure 9. It appears that Saudi Arabia leads the list with about 8% share; Qatar comes 2nd with 6%. UAE, Iraq, Bahrain, Kuwait and Egypt have close shares of about 5%. Libya has no share calculated as a trusted total number of articles is not available.

More, apart from Saudi Arabia patents granted in USTPO by Arabic countries is as small as less than 8, see Figure 10. In fact Saudi Arabia has been ranked 12th globally in USPTO.

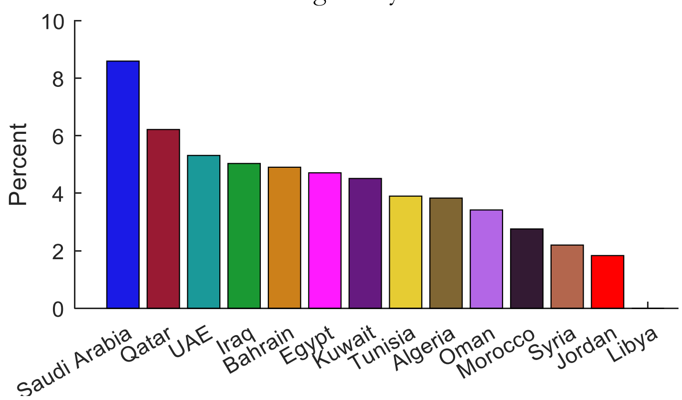

Figure 9 Local share of nano articles in the Arabic countries

Statistics from EPO showed similar results to that of the USPTO indicating that research activities in nanotechnology is still in early stages in Arabic countries. However; Saudi Arabia represents the best performance and possesses advanced position globally.

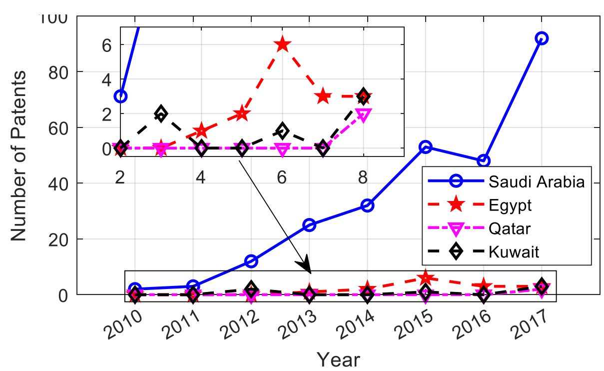

Figure10: Arabic nanotechnology related patents in USPTO

To further analyse the current situation in Arabic countries, the Global Innovation Index (GII) [16] in 2013-2017 is discovered. This would also provide detailed metrics about the innovation performance in Arabic countries. Table 1 represents the ranking of GII of top 10 Arabic countries. It illustrates that UAE ranks first mostly in 2013-2017. Particularly it possesses the 35thglobally in 2017. Qatar also showed good performance in that it moved from the 50thglobally in 2016 to 49thSaudi Arabia also develops gradually, although its rank decayed from 49thin 2016 to 55thin 2017 globally moving to 3rdin the Arabic GII list. Kuwait, Bahrain and Morocco have systematic improvement in the GII globally. The table indicates that the some Arabic countries keen interest in innovation. In fact, innovation is the main pillars for a high-productivity knowledge economy. It is worth mentioning that these countries have made important progress by localization of nanotechnology research in universities and research bodies as well as establishing specialized research centres in the field of nanotechnology. For instance, Saudi Arabia established 6 institutes specialised in nanotechnology and at least three companies in the field of Nanotechnology industries; while almost all universities have departments educate nanoscience and nanotechnology. Egypt also possesses the highest number of specialized organizations, institutions and research centres in Arabic countries; i.e. more than 10[17].

Table 1: Global rankings of Arabic countries in GII.

Country	Arabic countries GII ranking				
	2013	2014	2015	2016	2017
UAE	38	36	47	41	35
Qatar	43	47	50	50	49
Saudi Arabia	42	38	43	49	55
Kuwait	50	69	77	67	56
Bahrain	67	62	59	57	66
Morocco	92	84	78	72	72
Tunisia	70	78	76	77	74
Oman	80	75	69	73	77
Lebanon	75	77	74	70	81
Jordan	61	64	75	82	83

6. Development of Nanotechnologyin Libya

Pessimistically, the concern for this technology in Libya, formally, is not yet clear. Despite the attempts from scholars, research centres and universities to concretize it; yet these efforts are solitary and not comprehensive. Figure 8 showed that only around 85 articles were published globally. Governmental actions are urged to initiate programs that involve different institutions, focuses on the R&D, the creation of human capacity, the provision of infrastructure. Steps need to be taken may include but not limited to:

- Establish clear and objective policies as well as national initiative with obvious objectives and visions for excellence in this particular field to create a favorable investment environment;
- Establish and implement an objective plan for scientific and technological research and innovation in the field of nanoscience and technology. The plan should include the foundations of joint cooperation to maximize the benefit from the scientific and human resources available in R&D centres, institutes and universities;

- Provide the necessary long term resources for the constitution of capacities; and suitable funds toward R&D to motivate the development in this field;
- Encourage (i.e. by funds, special policies and targeted intermediaries) to involve scientists, researchers, and scholars in the nanotechnology field, and establish clusters or networks to adapt and develop rapidly;
- Promote management in mediators to focus on linking academic and industrial organisations together, in order to motivate collaborative research and innovation;

7. Conclusions

This work has provided a brief introduction to the nanotechnology, including definition, the basic principles, applications, and manufacturing methods. It is also expanded to identify the global pattern of nanotechnology related indicators, i.e. articles number, patents number and GII, in a developmental context in 2010-2017. Based on the analysis, the results reveal that the most of developed countries have made a considerable funding to support and encourage academia for the R&D in the field of nanotechnology. The USA and china have the highest indicators; while countries in Asia, generally, have showed the fastest growing rate. The study also showed that some Arabic countries have dramatically improved nanotechnology indicators. Namely, Saudi Arabia has identified increasing trend and systematic development in most indicators studied. Qatar, UAE, Kuwait, Bahrain and Egypt have also experienced developing trends. On the other hand Libya stands back in almost all indicators. Libyan policy makers must take serious actions to initiate strategies, make funds available and initiative programs that involve institutions focus on R&D, creation of human capacity, and the provision of infrastructure to encourage scientists and researchers to develop their related nano-activities.

References

[1]. Carolina Fracalossi Rediguieri, "Study on the development of nanotechnology in advanced countries and in Brazil," *Brazilian Journal of Pharmaceutical Sciences* vol. 45, n. 2, abr.jun. 2009

[2]. Kannaparthy R., Kanaparthy A. "The changing face of dentistry: nanotechnology". *Int J Nanomedicine* 6: 2799-804.2011

[3]. Iadiz MAR, Bamedi M, Fakour SR "Periodontal Diseases and Recently Applied Nano-Technology: A Review Article." *Health* 9: 345-51.2017

[4]. E. Abad et al "Nano Dictionary. Basel: Collegium Basilea" 119-146, 2005

[5]. Jeremy Ramsden "Essentials of Nanotechnology".*Ventus Publishing ApS,*SBN-13: 9788776814182, 2009

[6]. Lubick N; Betts ‘Kellyn "Silver socks have cloudy lining"*Environ Sci Technol.* 42 (11): 3910, 2008.

[7]. RocoMC "Building foundational knowledge and infrastructure for nanotechnology: 2000-2030". Chapter 4. In: Cheng et al (eds) '*anotechnology: delivering the promise'*, vol 1. ACS, Washington, DC, pp 39–52, 2016

[8]. Liming Dai (Ed.) "Carbon Nanotechnology: Recent Developments in Chemistry, Physics, Materials Science and Device Applications", *Elsevier: Amsterdam*, 2006.

[9]. Hari Singh Nalwa, "Nanostructured Materials and Nanotechnology", *Elsevier,* ISBN: 0080537278, 2001

[10]. Günter Schmid "Nanotechnology. Volume 1: Principles and Fundamentals"*WILEY-VCH Verlag GmbH & Co. K GaA, Weinheim*I SBN: 978-3-527-31732-5. 2008

[11]. Jeremy R. Ramsden, "Applied Nanotechnology", *Elsevier Inc*, ISBN: 978-0-8155-2023-8, 2009

[12]. Jeremy R. Ramsden, "Nanotechnology: An Introduction", *ElsevierInc*, ISBN: 978-0-08-096447-8, 2011

[13]. Wang J, Shapira P "Funding acknowledgement analysis:an enhanced tool to investigate research sponsorshipimpacts: the case of nanotechnology". *Scientometrics87*(3):563–586, 2011

[14]. Gorjiara T, Baldock C "Nanoscience and nanotechnologyresearch publications: a comparison between Australia andthe rest of the world". *Scientometrics* 100(1):121–148, 2014

[15]. http://cientifica.com/wp-content/uploads/downloads/2011/07/Global-Nanotechnology-Funding-Report-2011.pdf; accessed on 14/06/2018 @ 12:01PM

[16]. https://www.globalinnovationindex.org/

[17]. ALECSO "A diagnostic study to survey the possibilities in the field of nanoscience and technology in the Arabic world",A study launched by the *Arab Organization for Industrial Development and Mining*, 2017.

The Effect of Adding Steel Slag and Lime on The Engineering Properties of a Sandy Soil

[1]Ayad Abdelmoula Mohammed, [2]Mohammed Ali Abdalla Elsageer

aermila@yahoo.com, drmohammedalsger@gmail.com
[1,2]Department of Civil Engineering, Faculty of Engineering, Sirte University, Libya

ABSTRACT

Compaction is the process of mechanically densifying a soil which increase its density to meet engineering requirements. Unstable soils can create significant problems for pavements or structures ,therefore soil stabilization techniques are necessary to ensure the good stability of soil so that it can successfully sustain the load of the superstructure especially in case of soil which are highly active, also it saves a lot of time and millions of money when compared to the method of cutting out and replacing the unstable soil. This research describes a study of the effect of adding steel slag and lime on the engineering properties of a sandy soil. A series of laboratory experiments have been implemented and varieties of samples were made by mixing steel slag and lime with soil. different percentages of steel slag and lime were used as stabilization materials. Test results show that adding steel slag and lime can improve the properties of compacted sandy soil, and has a great effect on the behavior of compaction of stabilized soil, the maximum dry unit weight increased gradually at the low addition ratios and the maximum increase occurred at steel slag and lime content equals to 25% and 15% respectively.

Keyword— Steel Slag, Compaction, Sandy Soil

1. Introduction

The availability of build able land is fast drifting away each day due to scarcity of lands with good natural bearing capacity. This leads to construction of building on poor soils which eventually lead to structural foundation failures. It has become very imperative to improve soil or the quality of grounds by the adoption of suitable improvement methods depending on the materials available . however, during soil or ground improvement, cost effectiveness is one of the major factors. Consequent upon this, there is paramount need to adopt the use of admixture during steel slag/soil improvement or stabilization. However, steel slag which is a waste product from steel production could replace some proportions of sand/soil. This admixture not only replaces some proportions of soil for cost effective soil improvement. this review work exposes those qualities and applications that make steel slag a good replacement or not during mixing with soil, to find out how improvement and for a more economic approach for stabilization soil. The present review also gives researchers and geotechnical engineering a clue on the application of steel slag and the limit for its usage. Different methods can be used to improve and treat the geotechnical properties of the problematic soils (such as strength and the stiffness) by treating it in situ , these methods include dandifying treatments (such as compaction or preloading). The chemical stabilization of the soils (soft fine-grained soils) is very important for many of the geotechnical engineering applications such as pavement structures, roadways, building foundation, channel and reservoir linings, to avoid the settlement of soft soil.

Many materials and items discarded by organizations, companies and people have the potential to be reused for their original purposes or for new ones. Reuse discarded materials and items allows companies to get the most out of it. Additionally, reusing products conserves natural resources and saves valuable landfill space. Use of environment friendly materials in any industry is of paramount importance. limited waste landfill space, increasing cost of waste disposal in combustion facilities and landfills, depletion of the natural resources, and the need for sustainable development have all amplified the need to reuse the materials that were once regarded as wastes as substitutes for natural resources. In 2002, 50 million metric tons of steel slag was estimated to be produced worldwide [1] and 12 million tons was estimated to be produced in Europe [2]. Currently, the world annual production of steel slag is estimated to range between 90-135 million metric tons. Approximately 15 to 40% of the 10-15 million metric tons of steel slag generated in the United States in 2006 was not utilized [3] and a larger percentage of the 0.35-0.45 million metric tons of steel slag estimated by Akinwumi et al. [4].

GGBS or GGBFS (Ground Granulated Blast Furnace Slag) is a waste product drawn by the rapid cooling of molten iron slag. It is obtained from steel manufacturing process. In order to make use of GGBS, an attempt has been made for adopting it in soil stabilization. From the previous studies, it is clear that the GGBS induces the strength of cement and is extensively used as cement additives. This can be implemented in the soil for stabilization.

Addition of these wastes in stabilization technique makes proper utilization of these wastes and solves the problem of disposal. Steel slag is a by-product produced during the conversion of iron ore or scrap iron to steel.

Numerous studies have been conducted by various researchers for the use of steel slag to improve the engineering properties of weak soils .

The use of steel slag has been established in a number of applications in the construction industry. Slag can be applied as a material in cement, as road base course material due to large bearing capacity and excellent in wear resistance [5] as aggregate material for the asphalt concrete mixture [6] as fine and coarse aggregates in cement concrete mixture [7] and as improvement weak soil due to high angle of internal friction and high particle density.

Osinubi, et al. [8] studied the effect of using Blast Furnace Slag (BFS) to stabilize a lateritic soil to be used as hydraulic barrier. It was observed that inclusion of BFS increased the CBR value to 10% of the soil treated with 9% BFS and it became suitable for the use as hydraulic barrier.

Oormila and Preethi [9] examined the properties of black cotton soil stabilized using fly ash (FA) and Ground Granulated Blast Furnace Slag (GGBFS).Different percentages of FA and GGBFS were added. They found that the stabilizers have significantly improved the index properties of the soil and to achieve the maximum CBR value, the soil was blended with 20% GGBFS.

Golakiya and Savani [10] investigated the effect of Electric Arc Furnace Dust (EAFD) and Dolime fine addition on black cotton soil to improve geotechnical properties. Electric arc furnace dust generated during steel production and considered as hazardous waste. Dolomite stone is a type of lime stone and additive for slag formation. During the crushing process of Dolomite stone, fine particle is generated known as Dolime fine and regarded as industrial waste. They found that addition of 30% EAF dust and 12% Dolime to the black cotton soil had shown a good result.

Akinwumi [11] who studied soil improvement using electric arc furnace (EAF) steel slag. Various percentages of pulverized steel slag were applied to the soil. It was observed that pulverized steel slag improved the plasticity, uncured strength and drainage characteristics of the soil at the optimum percent of slag 6%.

Biradar, et al. [12] investigated the effect of using Fly ash and Steel slag to stabilize clay soils. Fly ash and Steel slag were mixed at different percentages 0, 10, 20, 30, 40 and 50% by weight of the soil to obtain the optimum percentage of admixture required. The study results showed that addition of steel slag and fly ash decreased the consistency limits and increased the CBR value of the soil.

2. Objective

The objective of the study is to improve the proctor compaction test properties of the soil, through the addition of steel slag and lime as stabilizers to become able to withstand the loads located

3. Experimental Work

Proctor compaction tests are conducted using equipment and procedures. The soil is brought to a desired moisture content and compacted in layers in the selected mold. After compaction, the moist unit weight and moisture content are determined and the dry unit weight calculated. These procedures are repeated at a sufficient number of moisture contents to establish a relationship between dry unit weight and moisture content at compaction. This data, when plotted, represents a curvilinear relationship known as the compaction curve or moisture-density curve. The values of maximum laboratory dry unit weight (ϒd-max) and optimum moisture content are determined from the compaction curve.

3.1. Materials

- **Water**

Tap water was used for mixing and increase moisture content.

- **Soil**

Soil was collected from Sirte and used in this research. The soil was stored in dry place and passed through U.S. sieves and the results of sieve analysis (D 6913) test are shown in Figure 1.

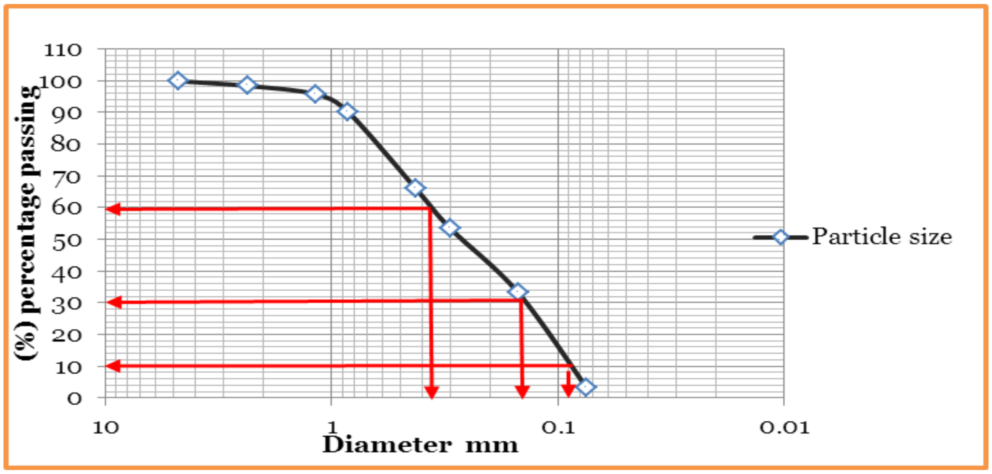

Figure 1: Particle Size Distribution of Tested Soil

According to the sieve analysis results and Unified Soil Classification System soil experimented in this work is classified as granular materials , and the type of soil is **SP** : sand poorly graded.

- **Steel Slag – Blast Furnace Slag (GGBS) :-**

Steel slag was collected from Libyan iron and steel company (Misurata) and used in this research. Six ratio 5, 10, 15, 20, 25 and 30%, by weight of the soil used. The steel slag samples were crushed to reduce its particle size down to less than 0.425 mm.

- **Lime**

Commercially available lime which was used in this study, passed through sieve No 200 and mixed with soil in varying percentages 5, 10, 15, 20, 25 and 30%.

3.2. Sample Preparation

To prepare sand soil . it was first oven –dried at 105ºC approximately 24 hours. Then , it was taken out of the oven and compacted. After that, 5000 gm of these soil were taken and mixed with lime, steel slag in varying percentage 5, 10, 15, 20, 25 and 30%. The lime and steel slag were passed through sieve No 200 before to be mixed with soil.

4. Results and Discussion

4.1. Compaction Test on Non-Treated Soil

Figure 2 shows the results of standard proctor test on the natural soil , which shows a typically shaped curve with a single peak, with maximum dry density of 1.95 g/cm^{3}cm^{3}at optimum moisture content of 11%.

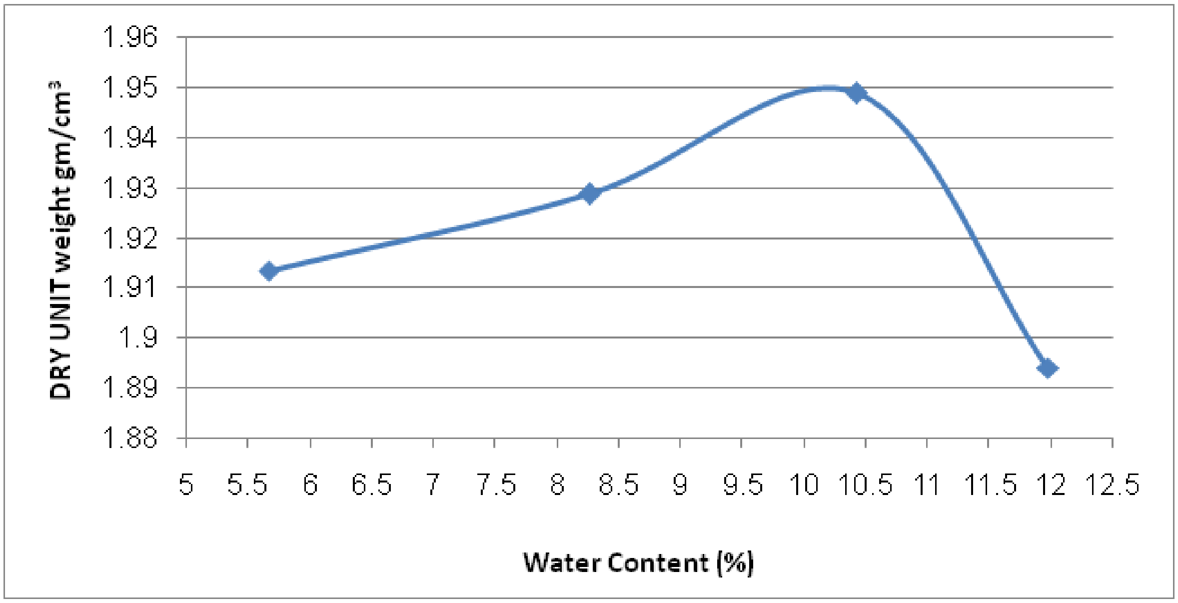

Figure 2: Standard Proctor Test Results on Natural Soil

4.2. Standard Proctor Test on GGBS Treated Soil

In order to investigate the effect of addition of steel slag on optimum water content and maximum dry unit weight of the selected soils, a series of standard proctor tests on GGBS treated soils 5, 10, 15, 20, 25 and 30% GGBS content by weight of selected soil were conducted according to ASTM D(698). Selected soil was dried in a oven and mixed until uniform color was observed before compaction. Figure 3 shows the effect of replacing GGBS on the soil with the investigated percentages, which shows that at the beginning of GGBS replacement, the maximum dry unit weight increased gradually. The highest value of dry unit weight was obtained at GGBS content equal 25%. On the contrary, increasing the GGBS content more than 25% (GGBS>25%) decreased the maximum dry unit weight of stabilized soil.

It is clear also from the figure that the optimum water content varied with GGBS content. The optimum water content fluctuated with the increase of GGBS content. This can be attributed to the change of surface area of treated soil than that in natural sandy soil.

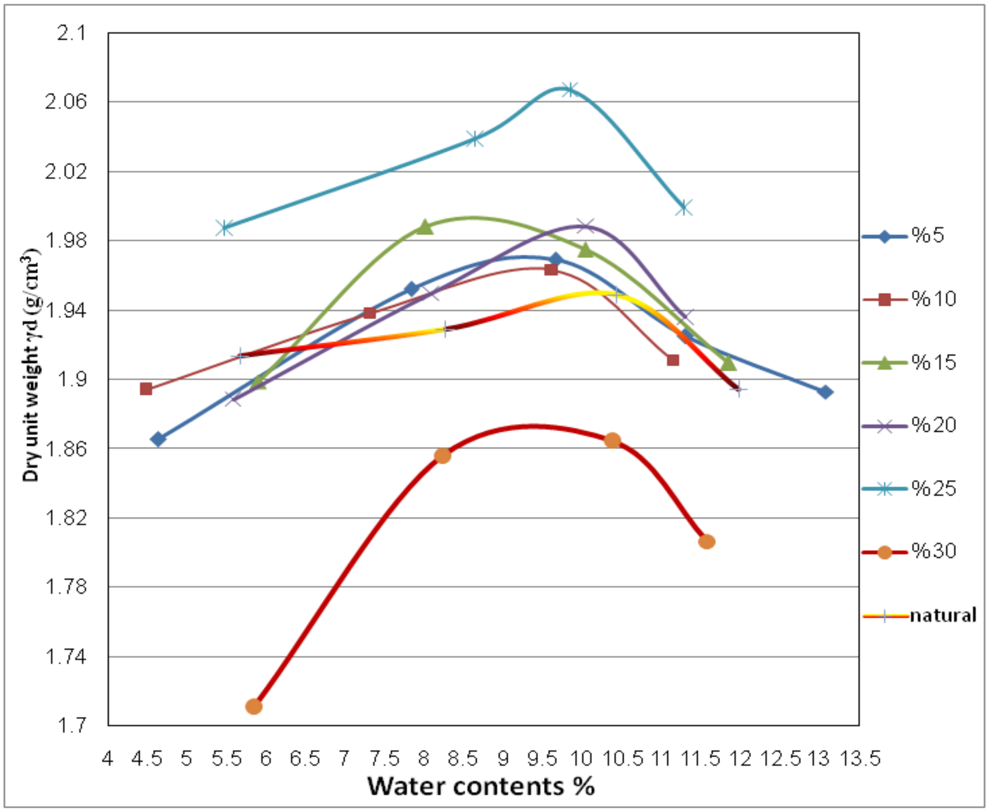

Figure 3: Standard Proctor Test Results on Soil With Various GGBS Content

4.3. Standard Proctor Test on Lime Treated Soil

Figure 4 shows the effect of adding Lime on compaction characteristics of the tested soil samples. it is clear that the effect of replacing five different percentage of lime to soil had nearly similar results, However, the replacement of lime to sandy soil was important to develop the behavior of stabilized soil. It also shows that at the beginning of replacing lime the maximum dry unit weight is almost stay the same, then the maximum dry unit weight was achieved at lime content equal 15% dry unit weight of stabilized soil then decreased by replacing more lime.

It is also from the below result that the optimum water content varied with lime content. The optimum water content fluctuated with increasing of lime content.

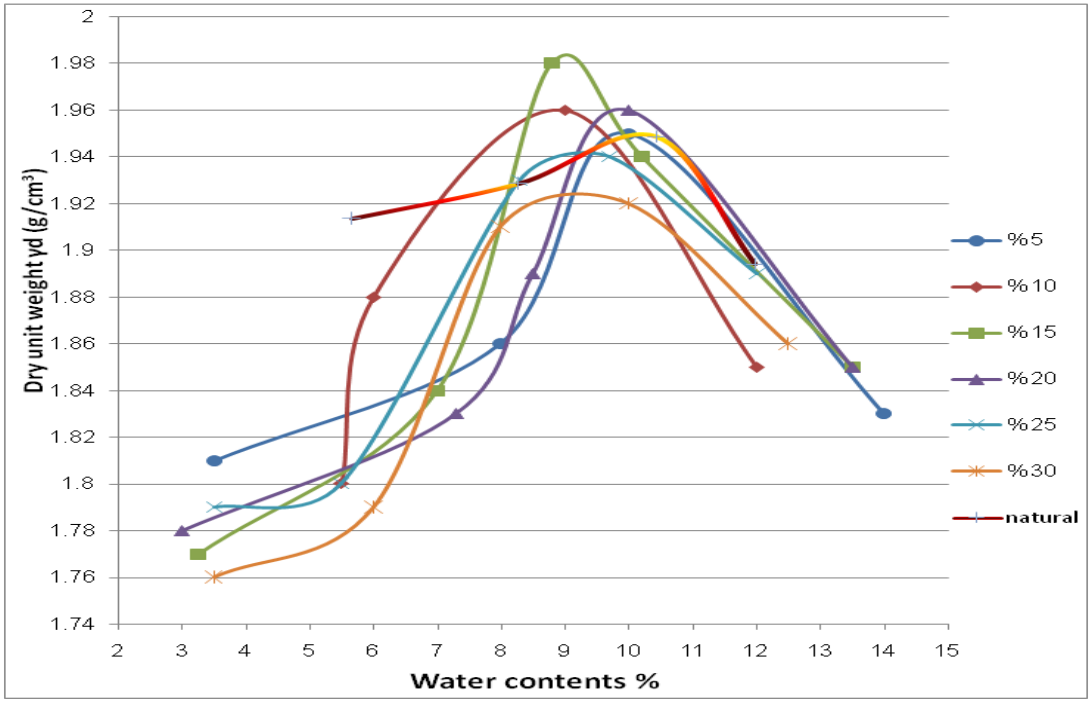

Figure 4: Standard Proctor Test Results on Soil With Various Lime Contents

Figure 5 shows that the values of the max dry unit weight of soil increase with the increase of the both additives (GGBS and lime) and the highest values of dry unit weight (γdmax) is obtained at GGBS content equal to 25% and 15%for lime. Furthermore the replacement of GGBS has a marked effect on the increase of max dry unit weight of soil comparing with the replacement of lime at the different tested percentages.

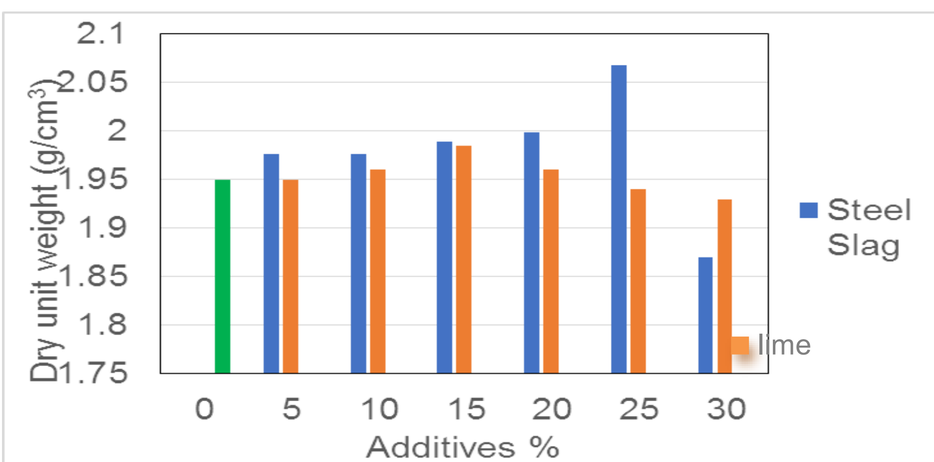

Figure 5: Comparison Between The Effect of Percentage of Additives on Maximum Dry Unit Weight

From Figure 6 it is obvious that the highest value of the optimum moisture content is obtained at natural soil , and the lowest at GGBS ratio (15%).

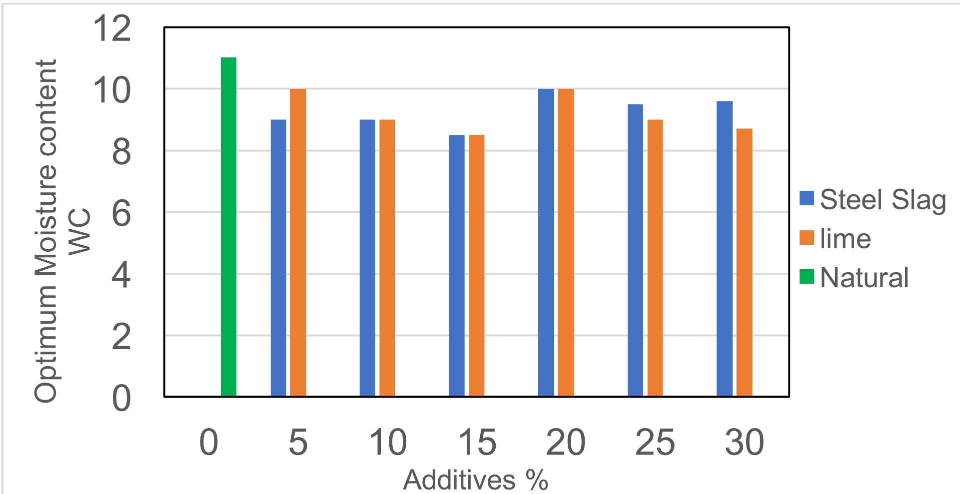

Figure 6: Comparison between the effect of percentage of additives on optimum moisture content

5. Conclusions

An extensive laboratory testing program was carried out to investigate the effect of addition of the steel slag and lime on the compaction characteristics of a sandy soil. The obtained results from both additives and were compared the following conclusions are made. The replacement of steel slag to sandy soil has a marked effect on the behavior of compaction of stabilized soil. The maximum dry unit weight increased gradually at the beginning of replacement of steel slag and the maximum dry unit weight increased by about 4.655% when the steel slag content increased from 5% to 25%. Increasing the steel slag content more than 25% (GGBS>25%) decreased the maximum dry unit weight, where steel slag content equal to 30% the maximum dry unit weight of treated soil decreased significantly by about 9.57% than that at 25%. The optimum water content varied with steel slag content. the optimum water content fluctuated with the increase of steel content. The comparison between the effect of both replacement shows that steel slag is more effective than lime on the improvement of the max dry unit of the soil, while the effect of the both replacement on the OMC is almost the same at different used percentages. In addition of that steel slag has advantage of its low cost and easy availability in large quantities.

Acknowledgment

First and foremost, we thank Allah. This paper based on undergraduate project during the Academic year 2017/2018 done by the students, Abdelkader Hatim Abdelkader, Awad Zhran Awad and Abdalslam Musbah Alsdaiunder under the supervision of MSc. Ayad Abdelmoula Mohammed.

The authors are gratefully and sincerely thank the students for their hard work on the experimental and theoretical parts of the project. Special thanks are due to Mr. Suliman Ahmed the technicians in the Soil Mechanics lab for his assistance with the laboratory work.

References

[1]. Altun A, Yilmaz I, Study on steel furnace slags with high MgO as additive in Portland cement, Cement and Concrete Research, 32(8), (2002), 1247–1249, DOI 10.1016/S0008-8846(02)00763-9.

[2]. Motz H, Geiseler J, Products of steel slags an opportunity to save natural resources, Waste Management, 21(3), (2001), 285–293, DOI 10.1016/S0956- 053X(00)00102-1.

[3]. Yildirim IZ, Prezzi M, Chemical, Mineralogical, and Morphological Properties of Steel Slag, Advances in Civil Engineering, 2011(2011), (2011), 1–13, DOI 10.1155/2011/463638.

[4]. Akinwumi II, Adeyeri JB, Ejohwomu OA, Ee cts of Steel Slag Addition on the Plasticity, Strength, and Permeability of Lateritic Soil, International Conference of Sustainable Design, Engineering and Construction 2012, In: Chong WKO, Gong J, Chang J, Siddiqui MK (eds.), ICSDEC 2012, ICSDEC Conference Proceedings, American Society of Civil Engineers; Texas, United States, 2013, pp. 457–464, DOI 10.1061/9780784412688.055.

[5]. K. Horii, T. Kato, K. Sugahara, N. Tsutsumi, and Y. Kitano, "Overview of iron and steel slag application and development of new utilization technologies," Nippon Steel and Sumitomo Metal Technical Report No. 1092015.

[6]. J. Emery, "Steel slag utilization in asphalt mixes. National Slag Association, MF 186-1." Retrieved from www.nationalslagassoc.org, 1984.

[7]. G. Singh, S. Sangwan, and M. Usman, "Experimental study of blast furnace slag concrete," International Journal of Engineering Sciences and Research Technology Experimental, vol. 9655, pp. 475–480, 2015.

[8]. K. J. Osinubi, A. O. Eberemu, and A. A. Amadi, "Compacted lateritic soil treated with blast furnace slag as hydraulic barriers in waste containment systems," International Journal of Risk Assessment and Management, vol. 13, pp. 171-189, 2009. View at Google Scholar | View at Publisher

[9]. R. Oormila and T. V. Preethi, "Effect of stabilization using fly ash and GGBS in soil characteristics," International Journal of Engineering Trends and Technology, vol.11,pp.284-289,2014.

[10]. H. D. Golakiya and C. D. Savani, "Studies on geotechnical properties of black cotton soil stabilized with furnace dust and dolomitic lime," International Research Journal of Engineering and Technology, vol. 2, pp. 810-823, 2015.

[11]. Akinwumi, "Soil modification by the application of steel slag," Rperiodica Polytechnica Civil Engineering, vol. 58, pp. 371–377, 2014. View at Google Scholar | View at Publisher.

[12]. K. B. Biradar, U. Arun, and P. V. V. Satyanarayana, "Influence of steel slag and fly ash on strength properties of clayey soil : A comparative study," International Journal of Engineering Trends and Technology, vol. 14, pp. 61–64, 2014. View at Google Scholar | View at Publisher.

Analysis of the Failure of Cylindrical Pressure Vessels

Osama A. Terfas[1], Arwa M. Elambrouk[2], Ahlam Y. Elraqiq[3]
[1]o.terfas@uot.edu.ly, [2]arwashalali@gmail.com, [3]ahlamyousef583@gmail.com
Department of marine and offshore engineering, University of Tripoli, Libya

ABSTRACT

This study investigates the failure of cylindrical pressure vessels and examines their integrity in the presence of cracks using von-Mises (Distortion Energy) yielding criterion and fracture mechanics methodology. The design Code of ASME-VIII section-2 was used to determine safe thickness and maximum allowable working pressure. The fracture stress, the critical stress intensity factor, the critical crack length and maximum pressure were determined. The results showed that yielding criterion with factor of safety of "2" for materials proposed in this study are applicable to design and construct pressure vessels under considered internal pressure and vessel size. The study revealed that cracked pressure vessels can be fit for service under some conditions of crack size and internal pressure. It can be concluded that pressure vessels that are safe under yielding theories could be safe as well where the crack exists under restricted conditions of the applied internal pressure, shell thickness, and material property.

Keyword— Fracture mechanics, pressure vessels, structural integrity, yielding criterion.

1. Introduction

The continued and prolonged use of pressure vessels for power plants, nuclear reactor vessels, storage vessels for liquefied gases such as LPG or chemical reactions, industrial processing, and oil refineries storage tanks requires them to withstand severe conditions of pressure, temperature, and other environments. Such environmental conditions include corrosion, neutron irradiation, and hydrogen embrittlement. Pressure vessels are required to operate at a temperature as high as 600 C to as low as -20C, with design pressures as low as 0.1MPa to as high as 15MPa [1]. To ensure safe design, installation, operation, and maintenance, the pressure vessels must be in accordance with codes such as American Society of Mechanical Engineers (ASME) Boiler and Pressure Vessel code. Therefore, great emphasis should be placed on analytical and experimental methods for determining their operating stresses [2]. When the pressure vessel is exposed to internal pressure, the material comprising the vessel is subjected to stresses acting in all directions. The normal stresses resulting from this pressure are functions of the radius and the shape of the pressure vessel, open ended cylinder, closed end cylinder as well as the applied pressure [3].

Furthermore it also needs to understand the significance of these stresses on the structural integrity of the pressure vessel by considering the material properties of the vessel [4]. In this context a major achievement in the theoretical foundation of the linear fracture mechanics was the introduction of the stress intensity factor (SIF) as a parameter for the intensity of stresses close to the crack tip. The stress intensity factor (K_a) is compared with the critical stress intensity factor K_{IC} (material fracture toughness) to determine whether or not the crack will propagate. This fracture parameter depends on size, shape and location of the defect; the applied load and geometry of the structure [5]. The presence of cracks on the walls of a pressure vessel can severely reduce the strength of the vessel and can cause sudden failure at nominal tensile stresses less than the material's yield strength [6]. Therefore, to ensure the integrity of a structure when a crack is present, the designer should understand and adequately apply the mechanics of fracture, particularly the relation between applied stress, the flaw size and the fracture toughness.

For the purpose of developing the design philosophy and the related operational limitations of various approaches, the yielding strength of the vessel is used as the criterion of failure [7]. In this context, failure theories of Von-Mises, Tresca, and maximum principle stress in conjunction with software and finite element method are widely adopted to design pressure vessels [8]. In addition, the numerical analysis of thin walled pressure vessel design parameters, material properties and temperature are found effective tools, and the maximum stress criteria is in good agreement with Von-Mises criteria for the failure of pressure vessels [9]. The analysis method applied in this work is the thin-walled pressure vessels theory for a ratio of inner radius to wall thickness r/t>10.

2. Materials

The materials selected for pressure vessels for the present work are shown in Table 1[10-11].

Table 1. Mechanical properties and chemical composition of materials used.

Material	σ_{uts} MPa	σ_y MPa	C %	Cr %	Ni %	Cu %	Mn %	Mo %	Si %
SS 316L	482	172	0.03	16	14	-	2	2.5	0.75
A 283-GR.C	455	207	0.24	-	-	0.2	0.9	-	0.4
SS 304N	551	241	0.03	18	8	-	2	-	0.75
A106-GR.C	485	276	0.30	0.4	0.4	0.4	0.67	0.15	0.1

3. Pressure Vessel Design Procedure

3.1. Stresses Developed in Thin-Walled Pressure Vessels

Thin-walled pressure vessels provide an application of the analysis of plane stress condition. The stresses developed due to the hydrostatic pressure are longitudinal stress (axial) σ_L and hoop stress σ_h in the circumference direction. The analysis of stresses in thin-walled pressure vessels will be limited to cylindrical pressure vessels as these are used widely and easy to manufacture in contrast to spherical vessels. For a cylindrical pressure vessel shown in Figure 1 with length "L", radius "r" and thickness "t", the stress σ_L in the axial direction of a cylindrical vessel with closed ends is[12]:

$$\sigma_L = \frac{p.r}{2.t} \tag{1}$$

The hoop stress σ_H, acts in the vessel wall in the circumferential direction can be written as:

$$\sigma_H = \frac{p.r}{t} \tag{2}$$

Note that the hoop stress is twice the axial stress.

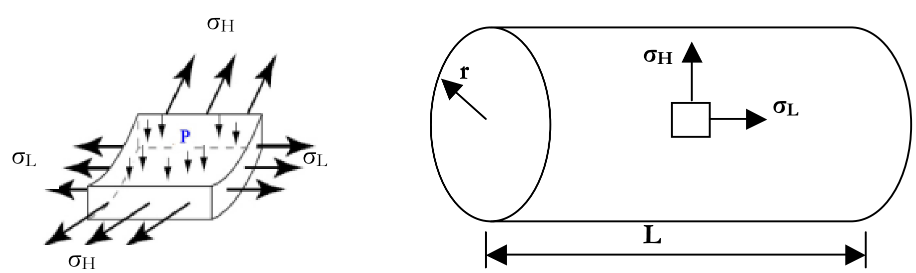

Figure 1: Longitudinal and hoop stresses in a cylindrical closed-end vessel.

3.2. Code Selection

There are many engineering standards which give information on the design. It is emphasized that any standard selected for manufacture of the pressure vessels must be followed and complied with in entirety and the design must not be based on provisions from different standards [13]. The ASME is normally followed cross the world, but other national or international standards may also be used. For this design, ASME VIII (division 2) "Construction of Pressure vessel Codes" are selected.

3.3. Implementation of ASME Code (section VIII-division 2)

The minimum thickness or maximum allowable working pressure of cylindrical shells shall be the greater thickness or lesser pressure as given by (3) or (4).

1. ***Circumferential Stress (Longitudinal joints)***

When the thickness does not exceed one-half of the inside radius, or P does not exceed 0.385SE, the following formulas shall apply [14]:

$$t = \frac{PR}{SE-0.6P} \quad \text{or} \quad P = \frac{SEt}{R+0.6t} \tag{3}$$

Where R is the inside radius, t is the shell thickness, E is the welded joint efficiency, S is the material strength, P is internal pressure.

2. Longitudinal Stress (Circumferential joints)

When the thickness does not exceed one-half of the inside radius, or P does not exceed 1.25SE, the following formulas shall apply[14]:

$$t = \frac{PR}{2SE+0.4P} \quad \text{or} \quad P = \frac{2SEt}{R-0.4t} \tag{4}$$

4. Failure Assessment Analysis

4.1. Yielding Criterion

Yielding criterion of Von-Mises is applied in order to assess the integrity of the pressure vessels considered in this study. In von-Mises theory of failure, the yielding occurs when the von-Mises stress σ_v is equal to the yielding stress [15]:

$$\sigma_v = \sqrt{\sigma_1{}^2 - \sigma_1.\sigma_2 + \sigma_2{}^2} = \sigma_y \tag{5}$$

Where, $\sigma_1=\sigma_H$ is hoop stress, and $\sigma_2=\sigma_L$ is longitudinal stress, and σ_y is yielding strength.

4.2. Fracture Mechanics Criterion

The cracked cylindrical pressure vessel subjected to a longitudinal crack considered for the present work is shown in Figure 2.

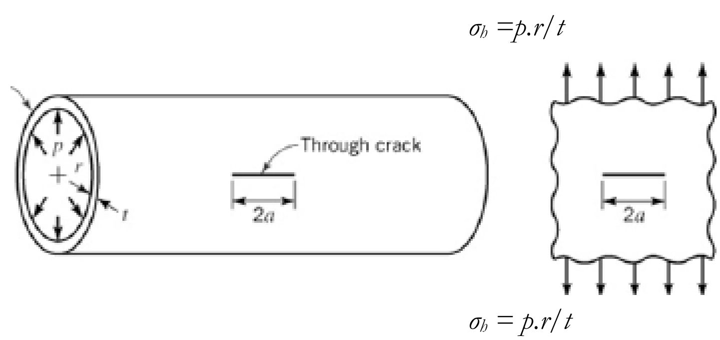

Figure 2: A cylindrical pressure vessel with a longitudinal crack.

The corresponding fracture stress σ_f (MPa) required propagating the crack is [16]:

$$\sigma f = \frac{K_{Ic}}{\sqrt{\pi . a_c}} \quad (6)$$

Where, K_{Ic} (MPa.√m) is the material fracture toughness, and "a" is the crack length. This can also be re-written in terms of the applied stress intensity factor (K_a), and the crack propagates when:

$$K_a = \frac{p.r}{t} . \sqrt{\pi . a} \geq K_{Ic} \quad (7)$$

4.3. Software Developed

A computer program has been constructed and used to assess the integrity of cracked and uncracked pressure vessels. The program is based on the von-Mises theory and fracture mechanics method by considering the von-Mises stress, yielding strength, critical fracture toughness and critical crack depths. Figure 3 shows the front window of the program where the input data are: crack depth (a), internal pressure (p), shell thickness (t), vessel radius (r), and (K_{Ic}). The output results are the von-Mises stress (σ_v) which is compared with the yielding strength, and fracture stress (σ_f) as a function of the fracture toughness and crack depth, and applied stress intensity factor (K_a).

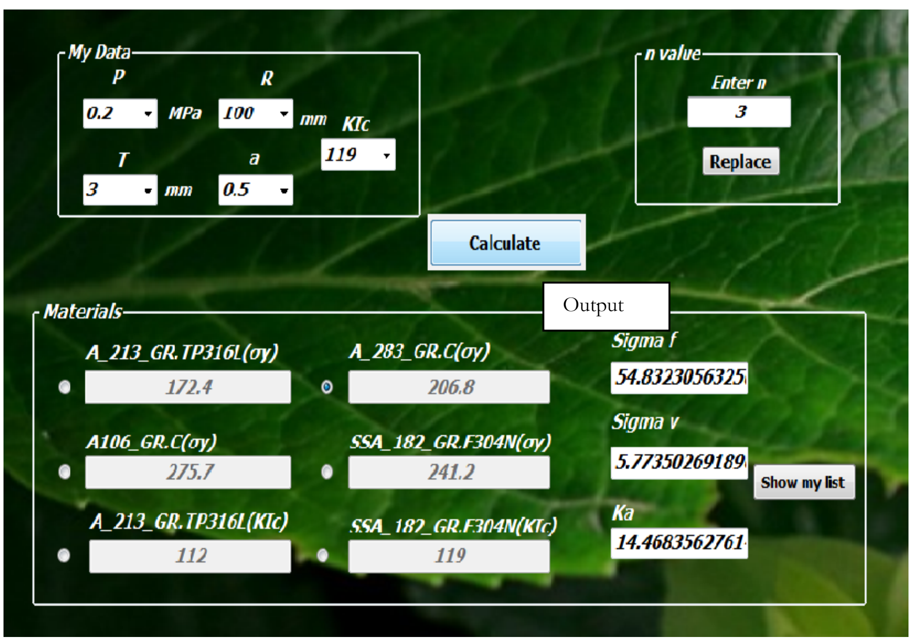

Figure 3: A view for the input and output data of the program.

5. Results and Discussion

Figure 4 shows the von-Mises stress (σ_v) as a function of vessel diameter for different shell thicknesses. The figure shows very conservative results with factor of safety greater than one ($\sigma_y > \sigma_v$). It is shown that the yielding does not occur for all materials considered in this study for vessels diameters of 200 to 1000 for shell thickness 3mm to 20mm under designed pressure varies between (14.5psi-130.5psi) 100 to 900KPa.

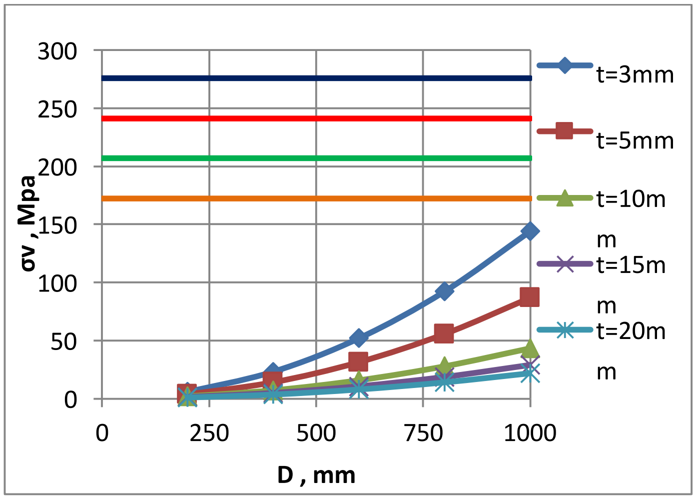

Figure 4: The von-Mises stress (σ_v) as a function of vessel diameter and thickness.

Figure 5 shows pressure vessels yield criterion using factor of safety of 2. For shell thickness of 5mm or greater, all used materials are safe for diameters from 200mm to 1000mm, while vessels with shell thickness of 3 mm are safe as long as the diameter less than 800mm.

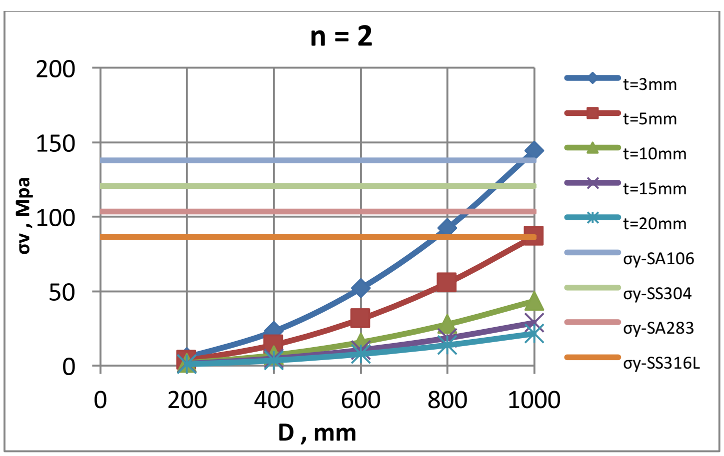

Figure 5: Pressure vessels yield criterion using factor of safety of 2.

Figure 6 shows the assessment of the pressure vessel in terms of applied stress intensity factor (K_a) and the material fracture toughness (K_{Ic}) of SS A-F304N with material strength of 241.2MPa and fracture toughness of K_{Ic}=119MPa.√m, for a crack length (a = 0.5 t). It is shown that thin pressure vessels with 3 and 5 mm thickness can be run safely under a considered pressure of (1 to 9 bar) for vessel diameters less than 600mm for a crack depth less than 0.5t. For thicker vessels, bigger vessels can be made from this type of material.

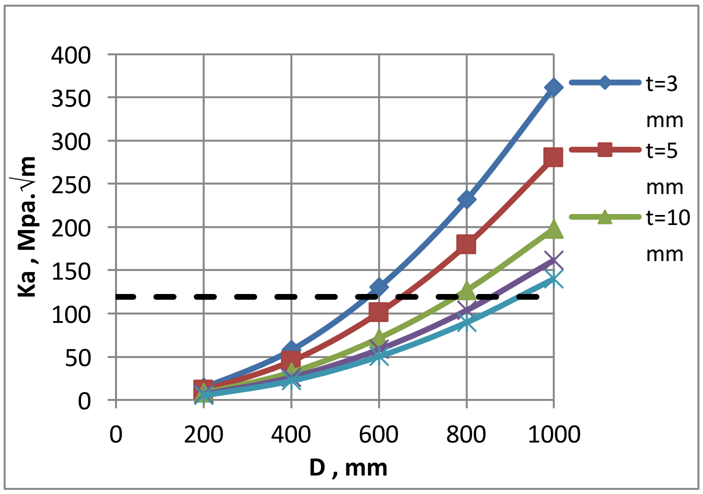

Figure 6: The applied stress intensity factor as a function of vessel diameter for a=0.5t.

Figure 7 shows the assessment of the cracked pressure vessel made of SS F304N of material strength of 241.2MPa and k_{Ic}=119MPa.√m, based on a crack depth (a=0.2t). The assessment is considered safe when values of the applied stress intensity factor (K_a) are less than the fracture toughness of the material (k_{Ic}). Therefore, vessels with diameters ranges from 200mm to 1000mm are safe as long as their thickness is greater than 10mm. However, thinner vessels having 3 and 5 mm thickness can be operated safely under a pressure considered for vessel diameters less than 720mm for a crack depth less than 0.2t.

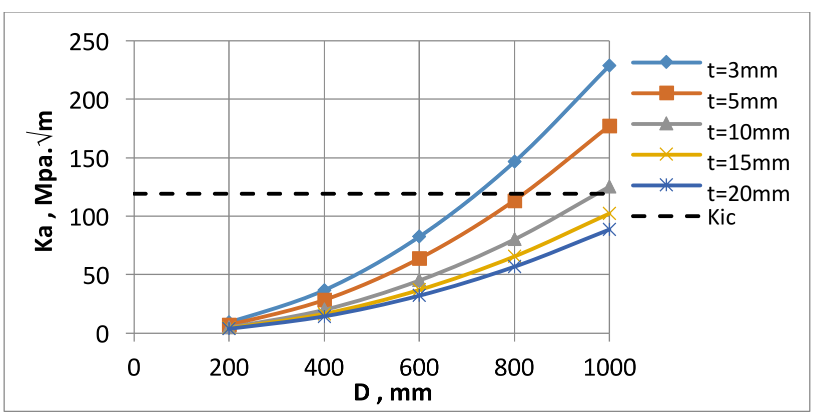

Figure 7: Applied stress intensity factor as a function of vessel diameter for a=0.2t.

Figure 8 shows the applied stress intensity factor for cracked pressure vessels of (a = 0.5 t), made of SS316L of k_{Ic}=112 MPa.√m. It is shown that cracked vessels are safe as long as the crack depth is less than 0.5t for specific vessel diameter and thickness. For example, cracked vessels with diameters of 600mm are safe with thickness greater than 5mm.

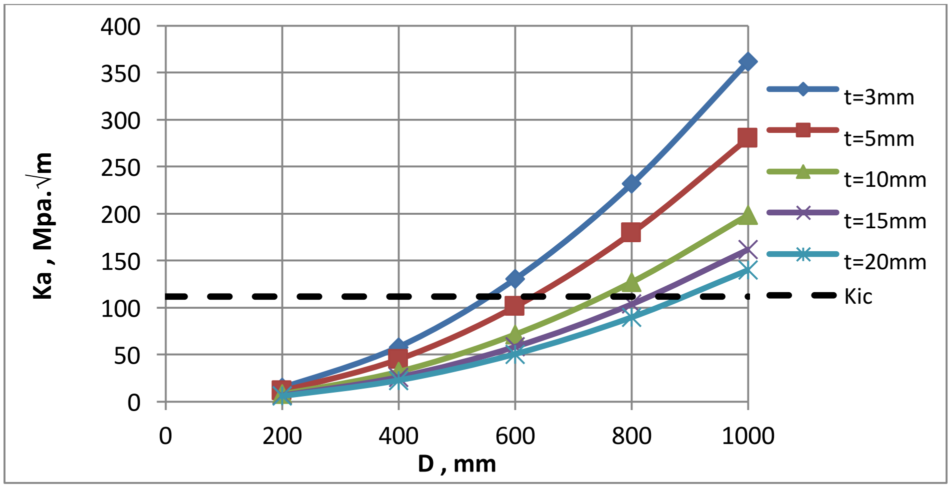

Figure 8: Applied stress intensity factor as a function of vessel diameter for a=0.5t.

Figure 9 shows the applied stress intensity factor for cracked pressure vessels of (a=0.2t), made of SS316L with K_{Ic}=112MPa.√m. It is obvious that the majority of K_a values are below the horizontal line of K_{Ic} which means these vessel sizes are safe except for thin vessels (t=3, 5mm) with large vessel diameter (D=700, 1000mm).

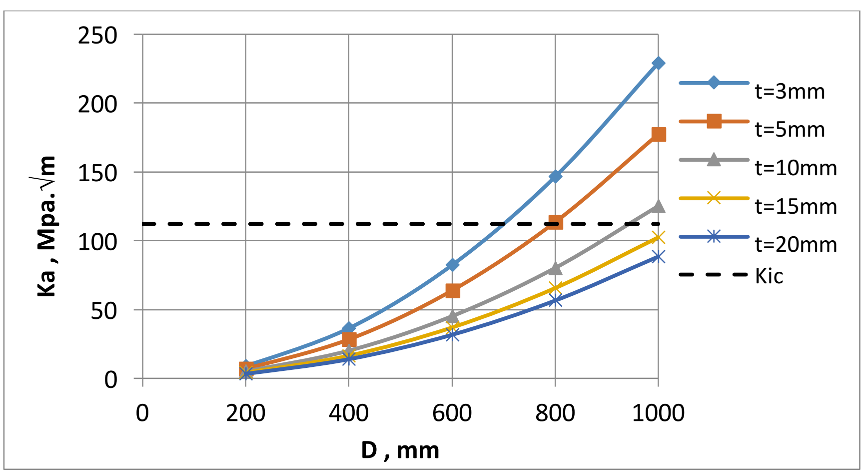

Figure 9: Applied stress intensity factor as a function of vessel diameter for a=0.2t.

Figure 10 shows the fracture stress as a function of crack length. This figure is used in conjunction with Figures 11 and 12 to determine the fracture stress required to propagate the crack, critical crack length and maximum pressure. The SS304 steel vessel having diameter of 1000mm, shell thickness of 15mm and 20mm is safe under maximum pressure of 9bar when the crack length is less than 6mm. For vessels of 10mm thickness, the largest acceptable crack length is 3mm. However, vessels with shell thickness of 5mm are not safe under a pressure of 9bar, unless the pressure is reduced below 5bar for (a<2mm). For vessel diameters of 500, the shell thickness of 5mm is safe as long as the crack length is less than 3mm at the maximum pressure used.

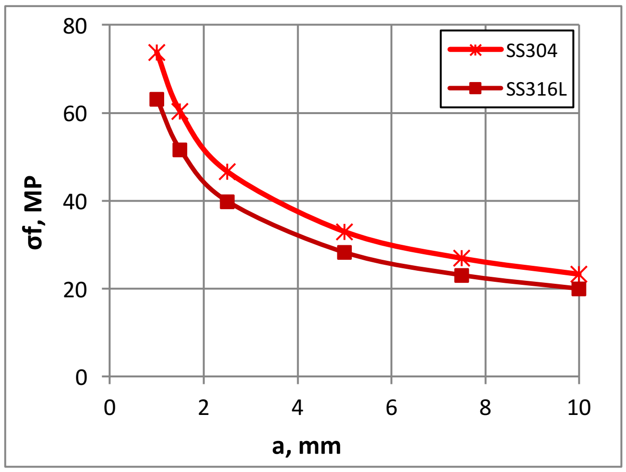

Figure 10: Fracture stress as a function of crack length for steel used.

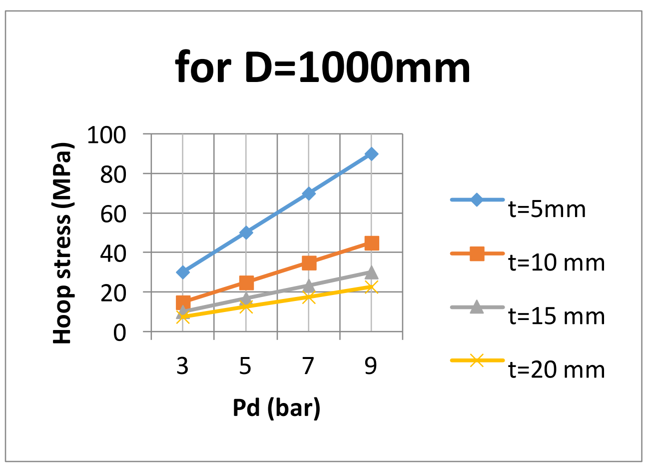

Figure 11: Hoop stress as a function in design pressure for vessel diameter of 1000mm.

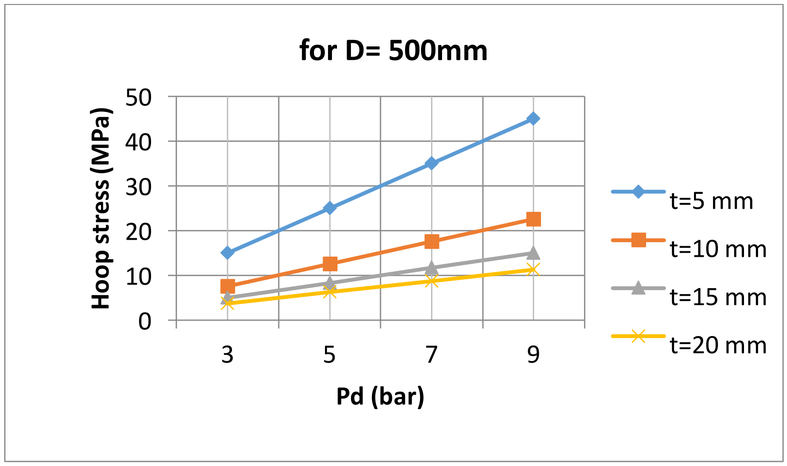

Figure 12: Hoop stress as a function in design pressure for vessel diameter of 500mm.

For SS316L, a vessel with diameter of 1000mm and the shell thickness of 5mm is safe if pressure reduced below 6bar and the crack length is less than 1.5mm. For 10mm thickness the largest acceptable crack length is 2mm under pressure of 9bar. However, for pressure less than 6bar cracked pressure vessels with diameter of 1000mm and shell thickness of 15mm and 20mm are safe as long as crack length is shorter than 7.5mm and 10mm respectively. For vessel diameters of 500 with shell thickness of 5mm is safe as long as the crack length is less than 2mm at the maximum pressure. While for 10mm thickness the vessel is safe as long as the crack length is less than 5mm.

6. Conclusions

This research investigated the effects of design parameters in terms of material strength and internal pressure on the integrity of pressure vessels. Both yielding criterion of von-Mises, and fracture stress theory were used to assess the integrity of pressure vessels. The von-Mises stress (σ_v) method showed that all materials used in this study are safe for dimensions and thicknesses considered and ensures factor of safety greater than one. However, for factor of safety of 2 only a very thin vessel with t=3mm and D>800mm is subjected to yielding. In the presence of a crack with the length of (0.2t) vessels with diameters greater than 700mm associated with thickness less than 10mm become unsafe. However, vessels with diameters ranges from 200mm to 1000mm with thickness of 15mm and 20mm are safe under considered conditions.

References

[1]. Somnath Chattopadhyay, Pressure Vessels: Design and Practice, CRC press, 2005.

[2]. Ahmed Ibrahim, Yeong Ryu, Mir Saidpour, Stress Analysis of Thin Walled Pressure Vessels, Modern Mechanical Engineering, Scintific Research Publishing, V5, 01-09, 2015.

[3]. Busuioceanu Paraschiva, Stefanescu Florentinab, Ghencea Adrianc, Study of Stresses and Stress Concentrations in Pressure Vessels, Journal of Bussiness economics and Information Technology, V3, 2016.

[4]. Dennis H. Moss, Pressure Vessel Design Manual. 3rd edition, Elsevier, 2004.

[5]. Kuna, M. Finite Elements in Fracture Mechanics: Theory - Numerics - Applications (Solid Mechanics and Its Applications, 2013.

[6]. S. Kotrechko,Yu. Meshkov, A new approach to estimate irradiation embrittlement of pressure vessel steels, pressure vessel and piping, 2007.

[7]. Analysis of a thick and thin walled pressure vessel for different materials. Qayssar S. Masikh, Mohammad Tariq, Prabhat K. Sinha. International Journal of Mechanical Engineering and Technology, V5, 09-19, 2014.

[8]. Thin Z. Hlaing, Htay H. Win, Failure Analysis of A Thin-walled CNG Cylindrical Pressure vessel, International Journal of Scientific Engineering and Technology Research, V3, 1874-1879, 2014.

[9]. Özmen S. Eruslu, Sencer S. Karabeyodlu, Failure Analysis of thin Walled Pressure Vessels, International Scientific Conference, Gabrovo, 22-24 Nov. 2007.

[10]. Carbon Steel Handbook, Electric Power Research Institute (EPRI), Palo Alto, CA: 2007.

[11]. Stainless Steel Grade Datasheet, Atlas Steel Technical Department, 2013.

[12]. Apurva P., Mahesh G., Nitin D., Rajkumar P., Design and analysis of pressure vessel, International Journal of Innovative Research in Technology & Science(IJIRTS), V2, 28-34, 2013.

[13]. B. S. Thakkar, S.A.Thakkar, Design of pressure vessel using ASME code Section VIII, Division-1, International Journal of Advanced Engineering Research and Studies, 2012.

[14]. ASME-VIII Code, Division 2, Boiler and Pressure Vessel, Alternative Rules for Construction Pressure Vessels, 2010.

[15]. Hibbeler, C., Mechanics of materials, 8th edition, prentice hall (pearson), 2011.

[16]. Anderson, T. L. Fracture Mechanics: Fundamentals and Applications, Third Edition. CRC Press, 2012.

Influence of Surface Roughness on Adhesion Between the Existing and New Plain Concretes

Nurdeen Mohamed Altwair [1], Saad Jaber Abu Jarir [2]
[1]nmaltwair@elmergib.edu.ly, [2]saadabougarir@gmail.com,
[1,2] Civil Engineering Department, College of Engineering, Elmergib University, Libya

ABSTRACT

The bonding that exists between the old concrete and the new concrete depends largely on the quality of substrate surface preparation. The accurate representation of substrate surface roughness can help determine very precisely the correct bonding behavior. In this work, the experimental program aimed to investigate the bond strength between two plain concretes, the first one is a concrete substrate as existing concrete, the second one is a new concrete overlay. Four types of original concrete substrate surface preparation were used: as-cast (without surface preparation) as a reference, wire-brushed, grooves and drilled holes. Adhesion strength is quantified at 30 days based on the results of the slant shear test and splitting cylinder tensile test, as well as shrinkage test which was made after 56 days of casting the new overlay concrete. The results generally indicate that the surface roughness of the concrete substrate is very much required to obtain superior mechanical bond of the composites; whereby the concrete with grooves and drilled holes substrate providing the most superior mechanical bond.

Keyword— Bond strength; New concrete overlay; Original concrete substrate; Slant shear test; Splitting tensile test; Surface roughness; Shrinkage.

1. Introduction

Developed infrastructure is a vital factor of economic growth and the prosperity of human life in many countries around the world. Many structures which make up the entire infrastructure and especially those made of reinforced concrete, such as buildings, bridges and pavements, etc. be suffered from severe deterioration. In the structural elements, these problems lead to cracks and breakdown in the concrete elements due to aggressive environmental impact such as exposing to different types of salts, freeze-thaw cycles and increase in unexpected live loads, etc. [1].

Nowadays, the most important and main challenges facing civil engineers are saving and rehabilitation of degraded constructions, as well as, developing and enhancing the durability and efficiency of these constructions. Furthermore, rehabilitation and repairing methods of the concrete are beneficial to the owner as compared to rebuilding [2]. The idea of rehabilitating and strengthening of the concrete structures is to apply a new concrete layer over an existing concrete to increase the resistance of the structural component and thereby increase the durability over time [3]. The linkage between the existing and new concrete layers is often weak [3,4]. Bonding quality of these layers is the main successful objective of the restructuring process being repaired. Furthermore, the successful development and performance of the structure directly depend on the roughness of the surfaces [5,6].

It has been recently observed that a numerous number of concrete structures existing in some regions around the world which had been repaired are still facing the risks of collapse and failure. It has been observed that the main reasons for this failure are the chemical bonding and interaction between the two layers materials. In addition, the physical and mechanical bonding depends on the porosity and roughness of the surfaces, as well as the shear and tensile strengths between two surfaces [7].

The problem of study lies in the inefficiency of bonding between the existing and new concrete layers at the maintenance of concrete structures, as a result of the surrounding environmental conditions, such as the difference in temperature as well as excessive loads. For this reason, many researchers interested in the repair of concrete structures have conducted several experiments to bond the existing and new concrete layers. The results were varied due to the difference in the use of bonding material, the method of bonding the existing concrete, the smoothness of the surface to be repaired, environmental effects and differences of expansion and shrinkage between both concretes. Therefore, the study will seek to increase the bond between the existing and new concrete when changing the roughness of existing concrete. Thus, reducing the use of chemical additives which are used to improve adhesion between existing and new concrete, especially since the use of such materials are considered a high cost. In addition, identifying the best mechanical methods that improve adhesion, will reduce the cost of repair, strengthening the structural elements and extending the age of the concrete members.

2. Materials and Methods

2.1. Materials

Ordinary Portland cement (OPC) that complies with the requirements of BS EN 197-1:2011 was used. The physical properties and chemical compositions of OPC is provided in Table 1.

Table 1. Chemical compositions and physical properties OPC.

Chemical composition (mass %)		Physical properties	
Items	Value	Items	Value
Silicon dioxide (SiO_2)	20.14	Specific gravity	3.15
Aluminum oxide (Al_2O_3)	5.91	Specific surface area(m^2/g)	2977
Ferric Oxide (Fe_2O_3)	2.99	Strength activity index at 3 days (MPa)	26
Calcium oxide (CaO)	62.9	Strength activity index at 28 days MPa	44
Magnesium Oxide (MgO)	1.59		
Sodium oxide (Na_2O)	0.18		
Potassium oxide (K_2O)	0.88		
Sulfur oxide (SO_3)	2.11		
Phosphorus oxide (P_2O_2)	0.9		
LOI	0.4		

Coarse aggregate of different maximum size viz; 19 mm, 14 mm was obtained from the quarries of Al-Alus in Al-Kums area. The coarse aggregate has a specific gravity of 2.72, water absorption of 0.41 % and bulk density of 1530 kg/m^3. Natural sand with maximum size of 1.2 mm, used as a fine aggregate was collected from Zlitan area. The fine sand has a fineness modulus of 2.7, specific gravity of 2.66 and water absorption of 0. 85 %.

2.2. Mix Proportion

Each of the composite specimens consists of the same material, i.e existing (concrete substrate) and new concrete overlay were designed as normal concrete. The design method used for normal concrete mixtures is based on absolute volume method, and the target strength of the normal concrete used was approximately 30 MPa. Samples representing the existing and new concrete were prepared using the mix proportions shown in Table 2.

Table 2. Mix proportions for plain concrete.

Items	Cement	Water	Fine aggregate	Coarse aggregate
Quantity (kg/m^3)	396	185	425	1344

2.3. Preparation and Processing of Samples

In order to gain proper bond strength the surface must be prepared prior to performing the overlay. In this study, each test specimen consisted of two equal layers of thickness; normal strength concrete (plain concrete substrate) will be used as original substrate material which represents the existing concrete, the other layer is also composed of the same type of concrete (the difference in casting time) which represents the new concrete (plain strength concrete overlay). Original concrete substrate specimens are placed in lubricated half piece of specimen mold. After casting, the fresh specimens were left at room temperature in their molds for 24 hours. After one day, the specimens were demoulded, cleaned from suspended parts of concrete or oil or any particles and dust, and cured for 28 days in a water curing tank. At 28 days of casting and curing in the water, specimens were taken out from the water tank for surface preparation. Four types of concrete substrate surface preparation were used: as-cast (without surface preparation) (CS) as a reference, wire-brushed (WS), grooves (GS), and drilled holes (DS), as shown in Figure 1. After surface preparation, all the concrete substrate specimens were left to dry for 1 month. Thus, the total period applied to the concrete substrate specimens before casting the new concrete as a repair material was 58 days. Before casting the new concrete overlay, the concrete substrate specimens were saturated in the water for one day, followed by 25 minutes of drying. The concrete substrate specimens were then placed into their moulds; in the case of the slant shear and shrinkage samples, the slanting side was facing upward to be overlaid with the new concrete overlay. For the tensile splitting samples, the substrate halves with different surface roughness were placed vertically at one side of the cylindrical moulds, and the moulds were then filled with new concrete (Figure 2). The composite specimens were left at room temperature in their molds for 24 hours. After 24 hours, the specimens were demoulded, and cured in water (for slant shear and tensile splitting samples) for 30 days. The specimens for the shrinkage test were left at room temperature until the testing days.

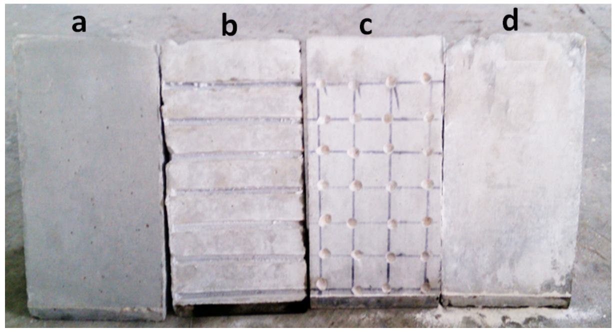

Figure 1: Different surface roughness of concrete substrate specimens. (a) as-cast (b) grooves (c) drilled holes (d) wire-brushed.

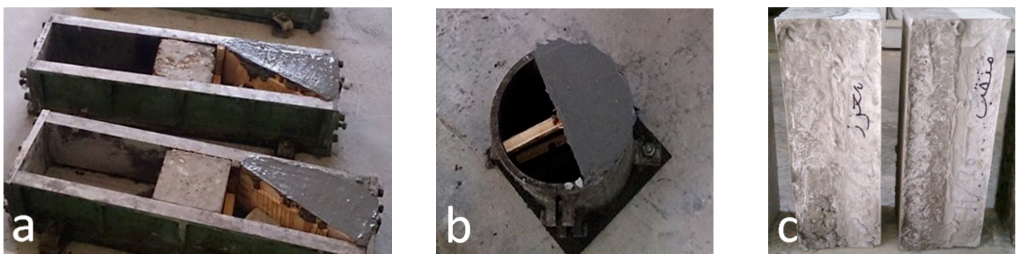

Figure 2: Specimens preparation. (a) Slant shear test specimen (b) Splitting tensile test specimen (c) shrinkage test specimen.

2.4. Testing of Specimens

The study of the surface quality is quantified by slant shear test, splitting cylinder tensile test and shrinkage test.

Slant shear test has been selected for being sensitive to roughness. The adopted geometry for the slant shear specimens was a 15 cm x15 cm x 30 cm prism with the interface line of 30° to the vertical (Figure 3). The specimens were tested under compression using the standard procedure for the testing of cubes of compressive strength according to ASTM C 882 standard [8].

The nominal shear strength between the concrete over layer can be calculated as follows.

$$\text{Slant shear strength (MPa)} = \frac{F}{A} \qquad (1)$$

Where:

F is the maximum force recorded (in N), and A is the area of the slant surface (in mm^2). The slant surface area can be taken as a nominal value of 150 x 150/sin 30°.

The splitting tensile test was conducted to determine the bond strength between two layers of concrete, according to ASTM C496 [9]. In the present study, new concrete overlay was cast and bonded with the concrete substrate specimens to form a cylindrical composite cylinder (300 mm height x 150 mm diameter) as shown in Figure 4. The splitting tensile strength was calculated using the following equation:

Splitting tensile strength (MPa) $= \frac{2F}{\pi A}$ (2) $= \frac{2F}{\pi A}$

Where:

F is the maximum force recorded (in N), and A is the area of the bond plane (in mm^2). The bonded area can be taken as a nominal value of 300 *150 = 45,000 mm^2.

As for shrinkage test, three composite specimens with dimensions of 12 cm×12 cm×35 cm were prepared. After casting the new concrete overlay as shown in paragraph no 2.3, approximately 24 hours after shrinkage test composite specimens cured at room temperature in their molds, they were demolded as ASTM C596 [9]. After composite specimens removed from the mold, using a super glue, stainless steel discs were adhered onto all four surfaces of each composite specimen centred about the length and width, where the measurement direction was perpendicular to the specimen composite specimen axis as shown in Figure 5.

Figure 3: Slant shear test set-up.

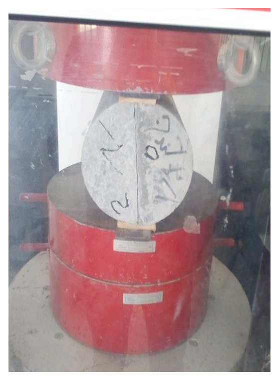

Figure 4: Splitting tensile test set-up.

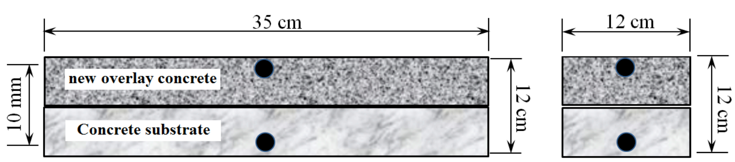

Figure 5: The shape and dimensions of the shrinkage test sample**.**

The initial shrinkage reading was taking after 6 days of curing in the air. All specimens were exposed to drying conditions up to 56 days. Initial shrinkage reading was taking using stain gauge and length comparator complying with ASTM C596 (the gauge length is 100 mm). The drying shrinkage measurements were taken at the periods of exposure of 3, 5, 10, 15, 20, 25, 30, 35, 40, 45, 50 and 56 days, and the results of average for each of two opposite surfaces reading of three specimens were taken.

3. Results and Discussions

3.1. Slant Shear Test Properties

Over the year, slant shear test is the most common type of tests to determine the bonding strength under combined state of compression and shear stresses. This test has become the most acceptable method and has been officially adopted in many international standards.

The experimental slant shear strength test results were shown in Table 3. As demonstrated in Table 3, the average slant shear bond strength was the highest in the grooved surface (12.26 MPa) and then wire brush and drill holes surfaces which were 7.79 MPa, 7.15 MPa respectively. Compared with the control specimen which represented by CS, the slant bond strength increases in the order of as cast surface (CS), drilled holes (DS), wire-brushed (WS) and finally grooved (GS) as shown in Figure 6. The relative percentage increases in bond strength were found to be around 81.9 % for DS, 95.9 % for WS and 210.4 % for GS.

Table 3. Slant shear strength and failure modes for different types of surface treatment.

Surface preparation	Sample No.	Max. force F (kN)	Comp. stress (MPa)	Shear Stress τ (MPa)	τ Average (MPa)	S.D.	C.V.	Failure mode
As-cast	CS1	155.6	6.92	3.46	3.99	2.9	0.75	A
	CS2	59.7	2.65	1.33				
	CS3	323.3	14.4	7.18				
Wire brush	WS1	461.3	20.5	10.3	7.79	2.17	0.28	A
	WS2	275.3	12.2	6.12				
	WS3	312.6	13.9	6.95				
Drill holes	DS1	156.9	6.97	6.97	7.15	2.17	0.28	A
	DS2	199.6	8.87	8.87				
	DS3	126.3	5.61	5.61				
Grooves	GS1	482.7	21.5	10.7	12.26	2.02	0.17	B
	GS2	656.8	29.2	14.6				
	GS3	516.5	23	11.5				

τ = Slant shear bond strength; S.D. = standard deviation C.V.= Coefficient of variation.
A = Interface failure; B = Interface failure with partially substrate failure.

Thus, the different roughness surfaces improve the slant bond strength by between 81.9 and 210.4 %, with the grooved surface presenting the highest value of increase; i.e. the most efficient. Hence, this confirms that the surfaces with different roughness provide significant improvement in slant bond strength of the composites in comparison to the control. The minimum acceptable slant bond strength which set out in the ACI Concrete Repair Guide in the range of 6.9–12 MPa [10]. Thus, the results obtained show that the surfaces treated in this study are actually required in order to fulfill the minimum prescribed slant bond strength of the composite. In conducting the slant shear test on the studied specimens, the failure modes can be classified into two types, type (A) is the interface failure; type (B) is the interface failure with partially substrate failure. The observations refer that the control specimen, drilled holes and wire-brushed exhibit type A failure; i.e. a total interfacial failure or complete de-bonding of the composite, while the grooved surface reveals a type (B) failure mode which is interface failure with partially new concrete overlay failure. Hence, low slant bond strength shown in the specimens with different roughness mentioned is compatible with failure mode of these specimens. However, the highest slant bond strength shown by the grooved surface is compatible with the observed failure mode; i.e. Interface failure with partially substrate failure.

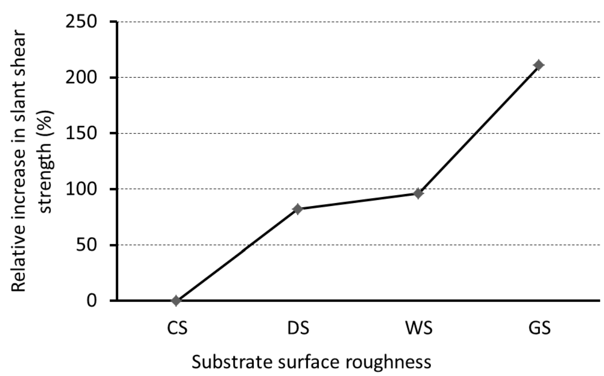

Figure 6. Relative increase in slant shear bond strength for the different types of surface treatment.

3.2. Splitting Tensile Test Properties

The splitting tensile test supplies measure of the indirect tensile capacity of the composite interface. The splitting tensile test results are shown in Table 4, whereas the percentage increase in the splitting tensile strength of the different types of surface treatment relative to that of the reference composite is shown in Figure 7. The results show that different types of surface treatment were able to significantly increase the splitting tensile strength of the composites when compared to the control composite (SC). Compared with the control composite, with the use of rough interface surface, the splitting tensile strength significantly increased for example, with about 1.44 %, 4.02 % and 7.62 % for WC, DC and GS, respectively. Hence, the grooved surface was the most efficient types of surface treatment, as it gave the highest increase in the splitting tensile strength among the composites in comparison with the reference composite, which indeed agree with the trend for slant bond strength results given and explained previously. Two types of failure modes of the splitting tensile test can be spotted, namely A = pure interface failure; B = interface failure with partially substrate failure. Obviously, the results reveal the relationship between the types of surface treatment and splitting bond tensile strength and the failure mode in the splitting tensile test. The observation show that the control composite (as-cast) and wire-brushed surfaces exhibit type (A) failure; i.e. a pure interface failure, while both the grooved and drilled holes surfaces reveal a type (B) failure mode which is interface failure with partially new concrete overlay failure. Based on the ACI concrete repair guide [10], which shows the classification of minimum acceptable bond tensile strength, whereby all of the results obtained in this study were excellent, since the splitting bond tensile strength was higher than 2.1 MPa.

Table 4. Splitting tensile strength and failure modes for different types of surface treatment.

Surface preparation	Sample No.	Max. force F (kN)	Ten. strength T (MPa)	T Average (MPa)	S.D.	C.V.	Failure mode
As-cast	CS1	447	9.5	9.71	0.28	0.029	A
	CS2	473	10.03				
	CS3	452.7	9.6				
Wire brush	WS1	451	9.57	9.85	0.3	0.03	A
	WS2	480	10.18				
	WS3	462	9.8				
Drill holes	DS1	488.8	10.37	10.1	0.21	0.021	B
	DS2	475.6	10.1				
	DS3	469.5	9.96				
Grooves	GS1	477	10.2	10.45	0.35	0.034	B
	GS2	481	10.4				
	GS3	510	10.8				

T = Splitting tensile strength; S.D. = standard deviation C.V.= Coefficient of variation.
A = Pure interface failure; B = Interface failure with partially substrate failure.

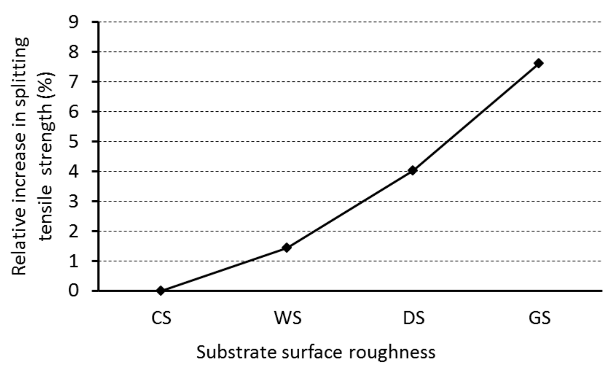

Figure 7. Relative increase in splitting tensile strength for the different types of surface treatment.

3.3. Shrinkage (Volume Changes)

When shrinkage is restrained, permanent tensile stresses develop in the new concrete that result in the formation of tensile cracks in the new concrete material itself, or in splitting at the interface of the new concrete overlay and the concrete substrate. Since most of the repair materials, including new concrete are applied to an older concrete substrate that has negligible shrinkage, new concrete overlay with very low shrinkage potential should be chosen to minimize the compatibility problems between concrete overlay and substrate concrete. Shrinkage values for the different types of surface treatment whether the direction of the measurement is perpendicular to the long axis or short axis of specimen, are shown in Figure 8 and Figure 9. In both cases and at all measurement durations (i.e. at 3, 5, 10, 15, 20, 25, 30, 35, 40, 45, 50 and 56 days), it can be observed that the composite specimens with grooved and drilled holes surfaces showed low shrinkage compared with the control and wire-brushed surfaces composites. The significant reduction in shrinkage values for composite specimens with grooved and drilled holes surfaces could be attributed to the strong overlap between old concrete substrate and new concrete overlay (penetration of the concrete material into the grooves and holes) leading to prevents the new concrete overlay from the movement. Shrinkage values for the different types of surface treatment at 56 days are demonstrated in Figure 10. Compared with the control composite, with the use of rough interface surface, shrinkage values significantly decreased for example, with about 48 % and 24 % and for DC and GS, respectively, and when calculating the shrinkage values with the direction of the long axis, about 53 %, and 43 % and 32 % for DC, GS and WS, respectively with the direction of the short axis of composite specimen. However, according to Emmons et al. [11], shrinkage values of repair materials in excess of 0.05%, and 0.1% at 30 days are considered to represent moderate and high levels of drying shrinkage, respectively, that can potentially result in premature failures, whereby all of the shrinkage values obtained in this study were less than the mentioned values.

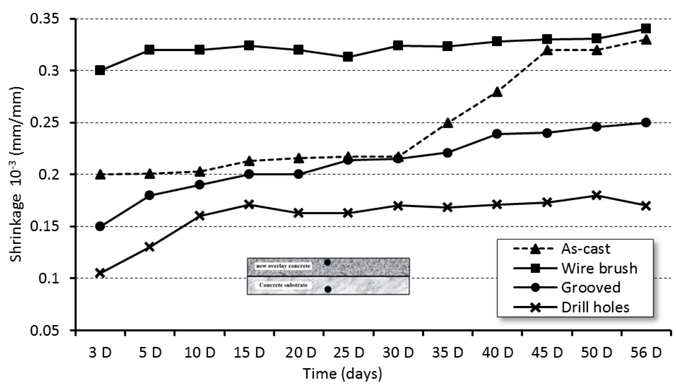

Figure 8. Shrinkage values for the different types of surface treatment; The direction of the measurement is perpendicular to the long axis.

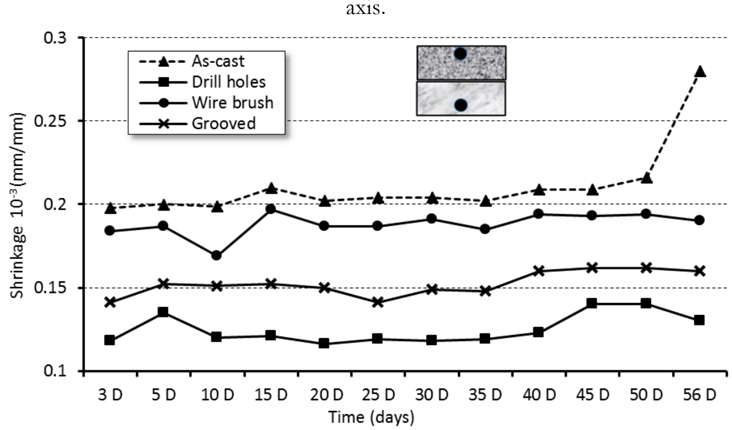

Figure 9. Shrinkage values for the different types of surface treatment; The direction of the measurement is perpendicular to the short axis.

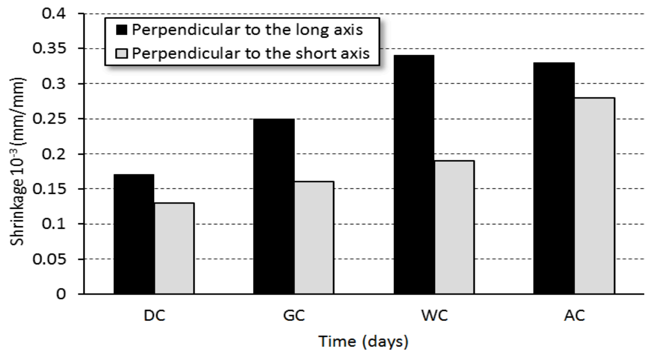

Figure 10. Shrinkage values for the different types of surface treatment at 56 days.

4. Conclusions

Based on the results and observations, the following conclusions can be drawn:

- The surface roughness suggested in this study; i.e. wire-brushed, grooves and drilled holes significantly affect adhesion with new concrete overlay, since all concrete substrate surface preparation methods revealed higher bond strengths compared with that of the as-cast (control specimen).
- Grooved and drilled holes surfaces were the preparation method of the substrate surface that presented the highest values of bond strength in shear and in tension, from all the considered techniques.
- Based on ACI Concrete Repair Guide, the results obtained show that the surfaces treated in this study are indeed required in order to achieve the minimum prescribed slant bond strength of the composite.
- All the results obtained from the split tensile strength test shows that new plain concrete overlays have excellent bond quality, since the splitting bond tensile strength was higher than 2.1 MPa.
- The observations of failure mode in the slant shear test show that the control specimen, drilled holes and wire-brushed exhibit a total interfacial failure, while the grooved surface reveal interface failure with partially new concrete failure. In addition, the failure mode in the split cylinder tensile strength test show that the control composite (as-cast) and wire-brushed surfaces exhibit a pure interface failure, while both the grooved and drilled holes surfaces reveal interface failure with partially new concrete overlay failure.
- The composite specimens with grooved and drilled holes surfaces showed low shrinkage compared with the control and wire-brushed surface composites. However, all the shrinkage values obtained in this study were less than the permissible limit according to Emmons et al. (0.1% at 30 days).

References

[1]. B. A. Tayeh, B.H. Abu Bakar, M. A. Megat Johari, "Characterization of the interfacial bond between old concrete substrate and ultra-high performance fiber concrete repair composite", *Materials and Structures*, vol. 46, no 5, pp. 743-753, 2014.

[2]. B. A. Tayeh, B.H. Abu Bakar, M. A. Megat Johari, "Assessment of adhesion between RPC overlay and existing concrete substrate", *Applied Mechanics and Materials*, vol. 802, pp. 95-100, 2015.

[3]. Momayez, M.R. Ehsani, A.A. Ramezanianpour, H. Rajaie "Comparison of methods for evaluating bond strength between concrete substrate and repair materials", *Cement and Concrete research*, vol. 35, no. 4, pp.748-757, 2005.

[4]. S. Wall, N. G. Shrive, "Factors affecting bond between new and old concrete,, *Materials Journal*, vo. 85, no. 2, pp. 117-125,1998.

[5]. Y. A. Ali, R. Ambalavanan, "Flexural behavior of reinforced concrete beams repaired with styrene–butadiene rubber latex, silica fume and methylcellulose repair formulations", *Magazine of Concrete Research*, vol. 51, no. 2, pp.113-120, 1999.

[6]. N. Gorst, L. Clark, "Effects of thaumasite on bond strength of reinforcement in concrete", *Cement and Concrete Composite*, vol. 25, no. 8, pp.1089–1094, 2003.

[7]. Rahman, A. Changfa, " State-of-the-art review of interface bond testing devices for pavement layers: toward the standardization procedure", J*ournal of Adhesion Science and Technology*, vol. 31, no 2, pp. 109 -126, 2016.

[8]. ASTM-C882, "Standard test method for bond strength of epoxy-resin systems used with concrete by slant shear", *West Conshohocken*, American Society for Testing and Materials, 1999.

[9]. ASTM-C496, "Standard test method for splitting tensile strength of cylindrical concrete". *West Conshohocken*, American Society for Testing and Materials, 1996.

[10]. G. Chynoweth, R.R. Stankie, W.L. Allen, R.R. Anderson, W.N. Babcock, P. Barlow, J.J. Bartholomew, G.O. Bergemann, R.E. Bullock, F.J. Constantino, "Concrete repair guide", ACI committee, concrete repair manual, vol. 546, ACI, Farmington Hills, pp 287–327, 1996.

[11]. P.H. Emmons, A.M. Vaysburd, J.E. Mcdonald, "A Rational Approach to durable concrete repairs", *Concrete International*, vol.15, no. 9, pp. 40-45,1993.

Static and Dynamic Analysis of Multistory RC Building with Various Heights in High Seismic Zone

Ghusen Al-Kafri1,Md. Shahnewaz Sarkar[2], Md. Shaizuddin Sarkar[3]
[1]galinak66@yahoo.com, [2]shahnewaz2020@gmail.com, [3]mdshaizuddin@gmail.com
[1]Department of Civil Engineering, College of Engineering, Sirte University, Libya
[2, 3]Department of Civil & Architecture Engineering, College of Engineering and Applied Science, Libyan Academy, Libya

ABSTRACT

The earthquake ranks as one of the most destructive natural disasters recorded all over the world. It has taken millions of lives and caused vast damages to infrastructures through the ages. Since the earthquake forces are random in nature and unpredictable, the engineering tools are needed to be sharpened for analyzing structures under the action of these forces. This paper deals with the comparison of static and dynamic analysis of four RC multistory building models with different height in high seismic zone. The considered structure is modeled as 5, 10, 15 & 20 story structure and analyzed by commercial software Autodesk ROBOT Structural Analysis 2018. Equivalent Lateral Force (ELF) Procedure is used for static analysis and Response Spectrum (RS) Procedure is used for dynamic analysis. All the analyses are conducted according to ASCE7-10. Then results are compared based on different parameters such as: Displacement, Story Drift, Base Shear, Story Shear and Story Moment. Finally, a comparative study has been carried out between static and dynamic analysis. It was found that ELF procedure provides higher displacement, story drift and base shear compared to RS procedure. Based on the findings of the study it is recommended to use dynamic analysis (RS) instead of static analysis (ELF) specially in high rise building.

Keyword— Equivalent lateral force; response spectrum; static analysis; dynamic analysis; displacement; story drift; base shear.

1. Introduction

Nowadays, it is very popular for constructing low to high-rise buildings in the world due to increasing population that is required to resist the lateral dynamic loads caused by earthquake. Earthquake effects are more intense than wind effects. From past intense disaster, it can be proved that many structures are totally damaged because of earthquakes, that is natural and unpredictable, which gives intense ground shaking. Therefore, earthquake analysis and design are very important in today's world. There are various types of structural analysis used to analyse high-rise buildings subjected to seismic load such as Equivalent Lateral Force (ELF) procedure, Response Spectrum (RS) procedure, Time History Analysis etc. In the present study, ELF & RS procedures have been carried out according to ASCE7-10.

A research work was carried out on two methods of seismic analysis namely static and dynamic for14 story RC building under Equivalent static and dynamic loads according to Egyptian code 2012. (Mahmoud and Abdallah, 2014). Another study (Tafheem *et al.*, 2016) investigated the seismic performance of a 10 story reinforced concrete moment resisting framed building under static and dynamic loading as per Bangladesh National Building Code (BNBC 2006). Furthermore, a study was carried out on the seismic analysis of two reinforced concrete moment resisting frame buildings (G+10 and G+25) using ELF and RS (Kakpure and Mundhada, 2017).

The objective of this study is to make a comparative study between static (ELF) and dynamic (RS) analysis by investigating a reinforced concrete multi story building with different heights located in high seismic zone according to ASCE7-10.For this purpose, four models with different heights are modelled and analysed using ROBOT 2018 and the results are compared together based on five parameters: Displacement, Story Drift, Base Shear, Story Shear and Story Moment.

2. Project Description

For this study, a regular reinforced concrete building is considered as shown in Figure 1. The floor area of the structure is 625 sqm (25m x 25m) with 5 bays along each side (each span 5m). The structure is modelled four times as 5, 10, 15&20 storied structure. Height of each story is 3m.

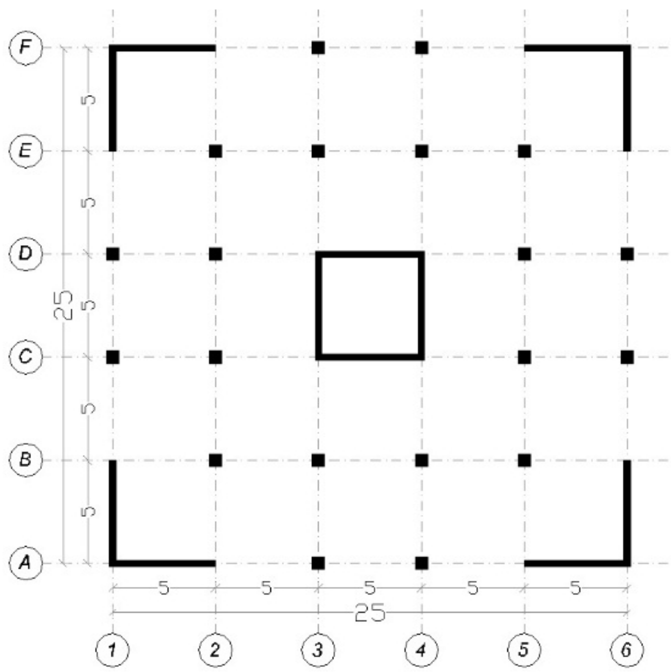

Figure 1: Plan view of considered structure

For the structures with different height, different dimensions are taken for structural elements. Table 1 shows the dimensions taken for different structural elements in this study.

Table 1: Dimension of structural elements

Structure	Story	Column		Shear Wall Thickness (cm)	Slab Thickness (cm)
		b (cm)	h (cm)		
5 Story	1 to 5	40	40	30	17
10 Story	1 to 5	50	50	35	17
	6 to 10	40	40	30	17
15 Story	1 to 5	60	60	40	17
	6 to 10	50	50	35	17
	11 to 15	40	40	30	17
20 Story	1 to 5	70	70	45	17
	6 to 10	60	60	40	17
	11 to 15	50	50	35	17
	16 to 20	40	40	30	17

While designing any building, different loads acting on it play a major role. An error in estimation of these loads can lead to the failure of the structure. Therefore, a careful study of loads that are acting on the structure becomes necessary. The loads in particular area must be selected properly and the worst combination of these loads must be evaluated.

The dead load in a building should be comprised of the weight of all walls, partitions, floors, roof and should include the weight of all other permanent constructions in that building. Based on the materials used in the building, the dead load (DL) is calculated as 2.96 KN/m². Live Load (LL) is taken 1.92 KN/m² according to ASCE 7-10. The structure is assumed to be located in high seismic area, Los Angeles, USA. The seismic parameters used in this study are taken according to ASCE 7-10 and are shown in Table 2.

Table 2: Seismic parameters

Site Class	D
Acceleration Parameter for 1-sec Period, S_1	0.857g
Acceleration Parameter for short Period, S_s	2.442g
Risk Category	III
Importance Factor, I	1.25
Long-Period Transition Period, T_L	8s
Response Modification Factor, R	4.5

3. Modeling and Analysis

All the structures with different heights are modeled and analyzed by ROBOT 2018 using Equivalent Lateral Force Procedure (ELF) as static analysis and Response Spectrum Procedure (RS) as dynamic analysis according to ASCE7-10. Figure 2 shows the modelling of different structure in software.

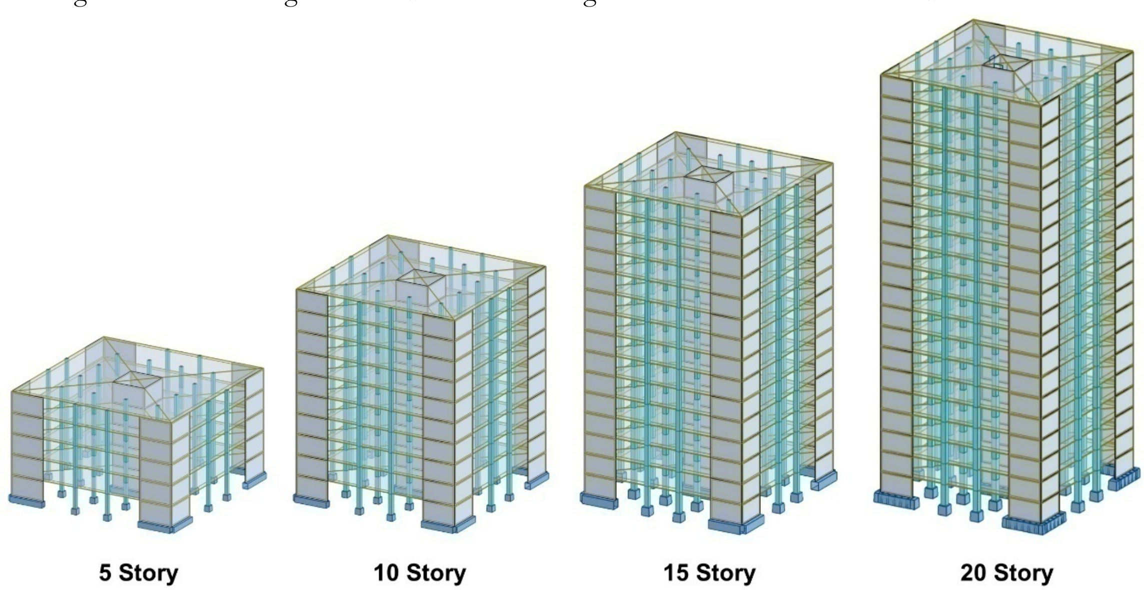

Figure 2: Modelling of different structures in ROBOT

4. Results and Discussion

After performing static and dynamic analysis for all the structures with different height, the obtained results were compared based on five factors i.e. Displacement, Story Drift, Base Shear, Story Shear and Story Moment as shown in Table 3, 4 and 5.

Table 3: Comparison of static and dynamic analysis results for structures with different height

Analysis Type	Story	Displacement		Story Drift		Base Shear (KN)
		X (mm)	Y (mm)	X (mm)	Y (mm)	
Static (ELF)	20	626.1	626.9	41.8	41.9	28,955.96
	15	278.0	278.3	24.3	24.4	26,146.06
	10	88.3	88.4	11.2	11.2	22,929.92
	5	9.8	9.8	2.3	2.3	13,249.58
Dynamic (RS)	20	230.2	233.0	21.6	21.6	24,612.55
	15	136.1	137.3	16.7	16.7	22,224.15
	10	54.1	54.4	9.6	9.6	19,490.45
	5	6.2	6.2	2.0	2.0	11,262.14

Table 4: Comparison of story shear by static and dynamic analysis

Story	Story Shear (KN)							
	5 Story		10 Story		15 Story		20 Story	
	Static (ELF)	Dynamic (RS)	Static (ELF)	Dynamic (RS)	Static (ELF)	Dynamic (RS)	Static (ELF)	Dynamic (RS)
20							2,974.31	4,210.68
19							5,760.18	7,362.71
18							8,360.33	9,394.46
17							10,777.60	10,564.48
16							13,014.92	11,127.95
15					3,423.83	4,252.66	15,194.91	11,323.35
14					6,581.28	7,399.56	17,191.20	11,361.80
13					9,475.63	9,451.15	19,007.36	11,432.03
12					12,110.39	10,761.86	20,647.19	11,705.20
11					14,489.29	11,679.13	22,114.70	12,298.83
10			4,221.94	4,407.09	16,739.76	12,518.70	23,491.35	13,293.21
9			7,996.56	7,983.76	18,728.39	13,459.21	24,694.82	14,649.53
8			11,326.96	10,705.45	20,460.20	14,558.22	25,730.36	16,228.88
7			14,216.65	12,836.90	21,940.73	15,813.74	26,603.67	17,900.87
6			16,669.60	14,588.58	23,176.18	17,174.57	27,321.05	19,549.00
5	4,416.53	4,169.75	18,807.60	16,140.21	24,232.81	18,614.09	27,923.85	21,137.28

4	7,949.75	7,323.97	20,494.13	17,477.58	25,045.93	19,990.81	28,377.28	22,538.90
3	10,599.66	9,448.09	21,736.31	18,523.31	25,625.99	21,130.25	28,691.40	23,627.42
2	12,366.27	10,729.12	22,543.54	19,205.56	25,986.35	21,897.39	28,878.64	24,326.07
1	13,249.58	11,262.14	22,929.92	19,490.45	26,146.06	22,224.15	28,955.96	24,612.55

Table 5: Comparison of story moment by static and dynamic analysis

Story	Story Moment (KN.m)							
	5 Story		10 Story		15 Story		20 Story	
	Static (ELF)	Dynamic (RS)	Static (ELF)	Dynamic (RS)	Static (ELF)	Dynamic (RS)	Static (ELF)	Dynamic (RS)
20							1,143.16	791.00
19							1,1136.82	14,077.26
18							29,416.71	36,541.46
17							55,426.77	64,715.80
16							88,619.46	95,841.93
15					1,315.93	806.09	129,431.64	128,513.13
14					12,800.99	14,219.26	175,905.76	159,936.16
13					33,657.25	36,764.99	228,288.50	189,837.86
12					63,096.80	65,007.07	286,041.15	217,799.96
11					100,342.28	96,465.39	348,636.52	243,860.43
10			1,622.68	803.25	145,699.15	130,303.77	416,982.90	268,966.56
9			15,739.27	14,722.66	196,804.40	164,477.01	488,064.27	292,969.36
8			41,008.96	39,114.70	253,761.11	199,630.81	562,671.32	317,602.45
7			76,100.49	71,297.33	315,801.32	236,174.80	640,303.13	344,371.08
6			119,693.23	109,344.04	382,173.93	274,740.72	720,476.17	374,719.91
5	1,697.47	782.95	171,674.31	152,899.15	453,606.01	316,857.23	804,326.29	410,516.61
4	16,305.02	13,937.24	228,848.50	199,482.62	526,714.78	361,504.58	888,352.36	451,154.66
3	41,172.74	36,257.31	290,884.32	249,383.45	602,145.28	409,858.20	973,660.53	497,472.17
2	73,650.71	64,569.95	356,452.89	301,995.35	679,205.10	461,923.30	1,059,839.85	549,152.21
1	111,089.01	96,363.00	424,255.66	356,609.80	757,244.76	517,266.35	1,146,519.18	605,417.63

Figure 3 & Figure 4 show the displacement for different structures by static and dynamic analysis. From the figures it can be observed that the displacement obtained by static analysis (ELF) is higher than that obtained by dynamic analysis (RS) for all structures. Static analysis gives 58.1% to 172% higher displacement than dynamic analysis. It can be also noticed that the difference in displacement calculated by static and dynamic analysis increases with the increase of height of the structure.

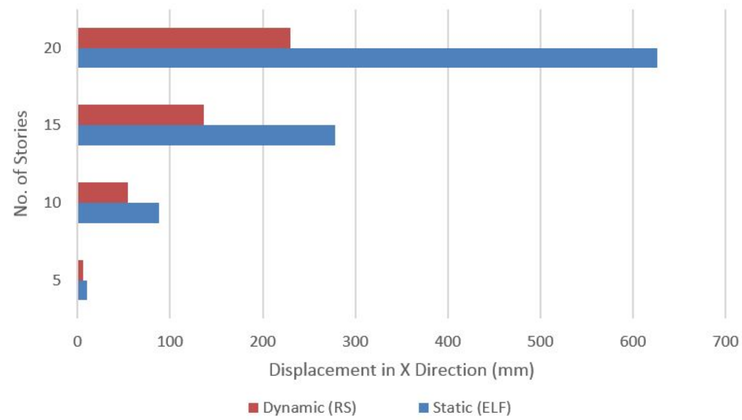

Figure 3: Displacement in X Direction by Static and Dynamic Analysis

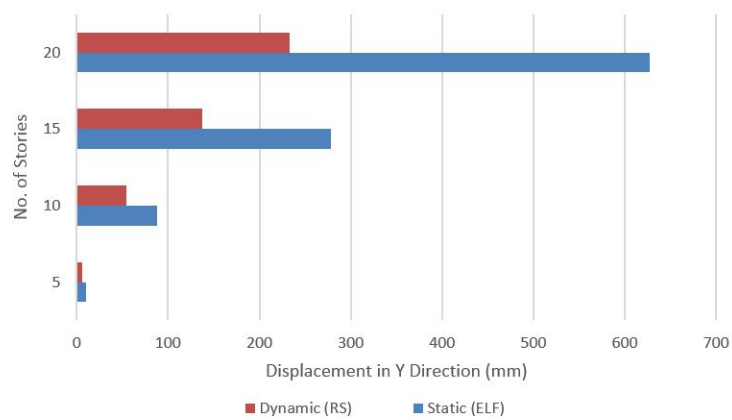

Figure 4: Displacement in Y Direction by Static and Dynamic Analysis

Figure 5& Figure 6show the story drift for different structures by static and dynamic analysis. According to the code ASCE 7-10 the story drift for this study is limited to 45 mm. It can be noticed that the story drift for all structures is within permissible limit. The figures show that the story drift calculated by dynamic analysis is lower than static analysis, where it gives 15% to 94% less drift. It can be noticed that the difference increases gradually with the height of the structure. This indicates that static analysis may lead to uneconomical design as it gives higher drifts.

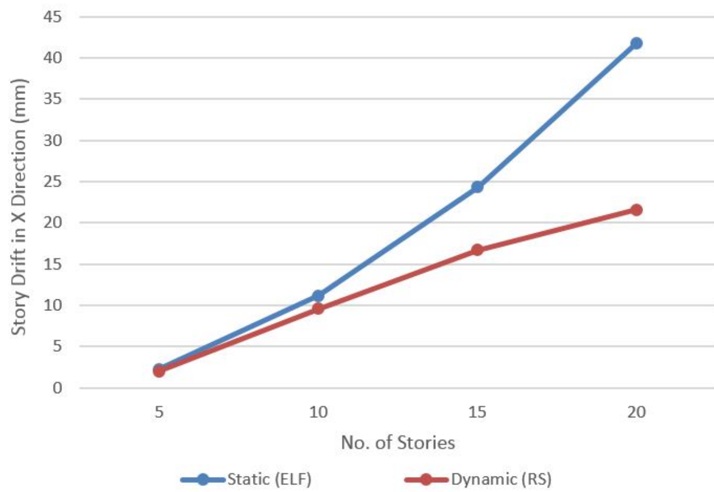

Figure 5: Drift in X Direction by Static and Dynamic Analysis

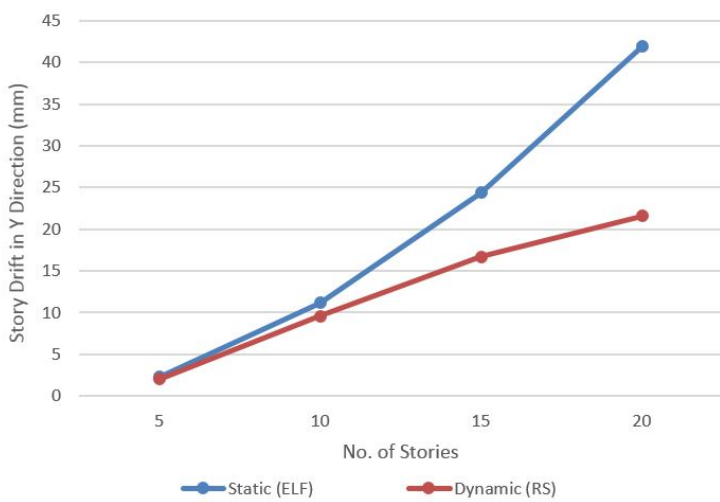

Figure 6: Drift in Y Direction by Static and Dynamic Analysis

Figure 7 indicates the base shear for different structures by static and dynamic analysis. From this figure along with Table 3 it can be noticed that the base shear obtained from dynamic analysis is about 85% of static analysis. A study (Mahmoud and Abdallah, 2014) showed that the total base shear obtained from static analysis is about 8% higher than that of dynamic analysis. On the other hand, another study (Tafheem *et al.*, 2016) found that the total base shear obtained from static analysis is about 17% higher than that of dynamic analysis. Similarly, in the present study, it has been found that in case of static analysis, the base shear is 17.6% higher than that of dynamic analysis.

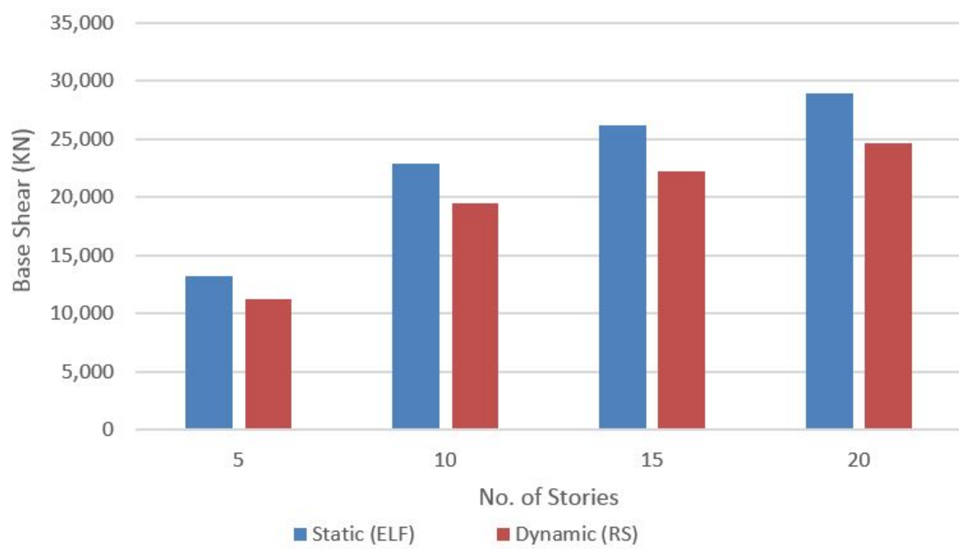

Figure 7: Base Shear by Static and Dynamic Analysis

Figure 8 shows the story shear for different structures by static and dynamic analysis. From the figure it can be observed that the story shear obtained by static analysis (ELF) is higher than dynamic analysis (RS) for all stories of all structures except for top stories of 10, 15 & 20 storied structure, where dynamic analysis gives slightly higher story shear compared to static analysis. It can also be noticed that the difference in story shear obtained by static and dynamic analysis gradually decreases with the increase of height for 5 and 10 storied structure, while for 15 and 20 storied structure the difference in story shear is high in middle stories and decreases in upper& lower stories. Maximum difference in story shear is 17.6% for 5 & 10 storied structure while the difference is 40.5% & 79.8% for 15 & 20 storied structure respectively.

Figure 9 shows the story moment for different structures by static and dynamic analysis. From the figure it can be clearly noticed that the difference in story moment obtained by static and dynamic analysis gradually decreases with the increase of height of the structure. It can also be observed that the story moment obtained by static analysis (ELF) is higher (upto 116.8%) than dynamic analysis (RS) for all structures except for some top stories of 15 & 20 storied structure, where dynamic analysis gives higher story moment (upto 26.4%).

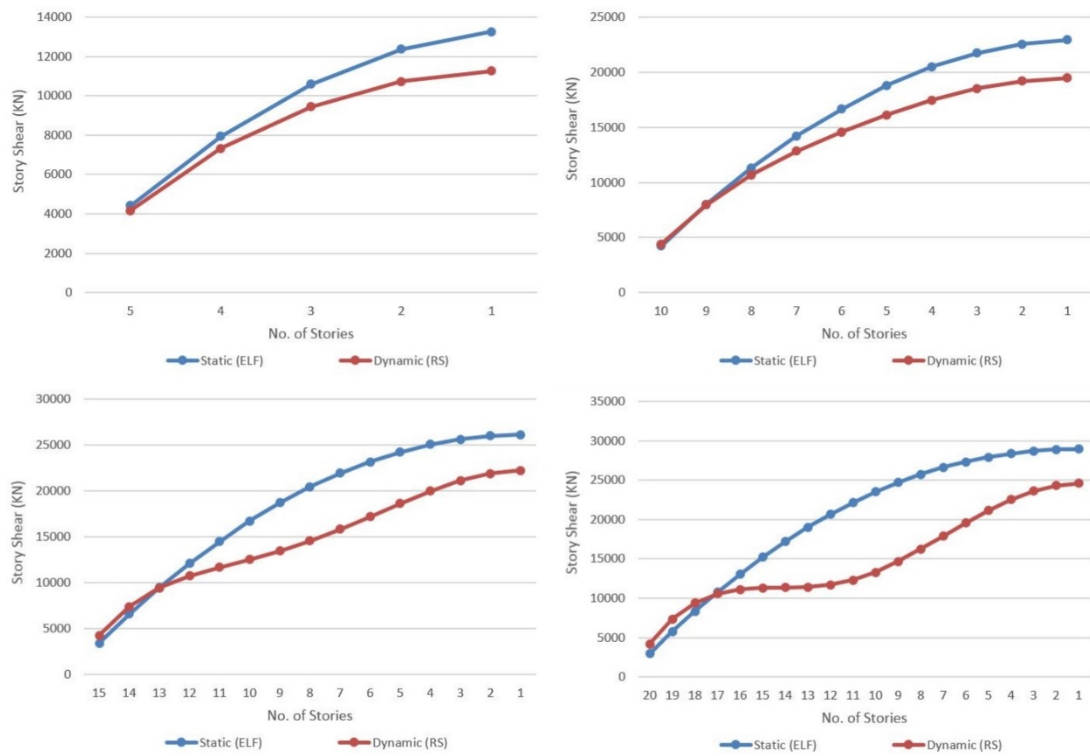

Figure 8: Story Shear for5, 10, 15 & 20 storied structure by Static and Dynamic Analysis

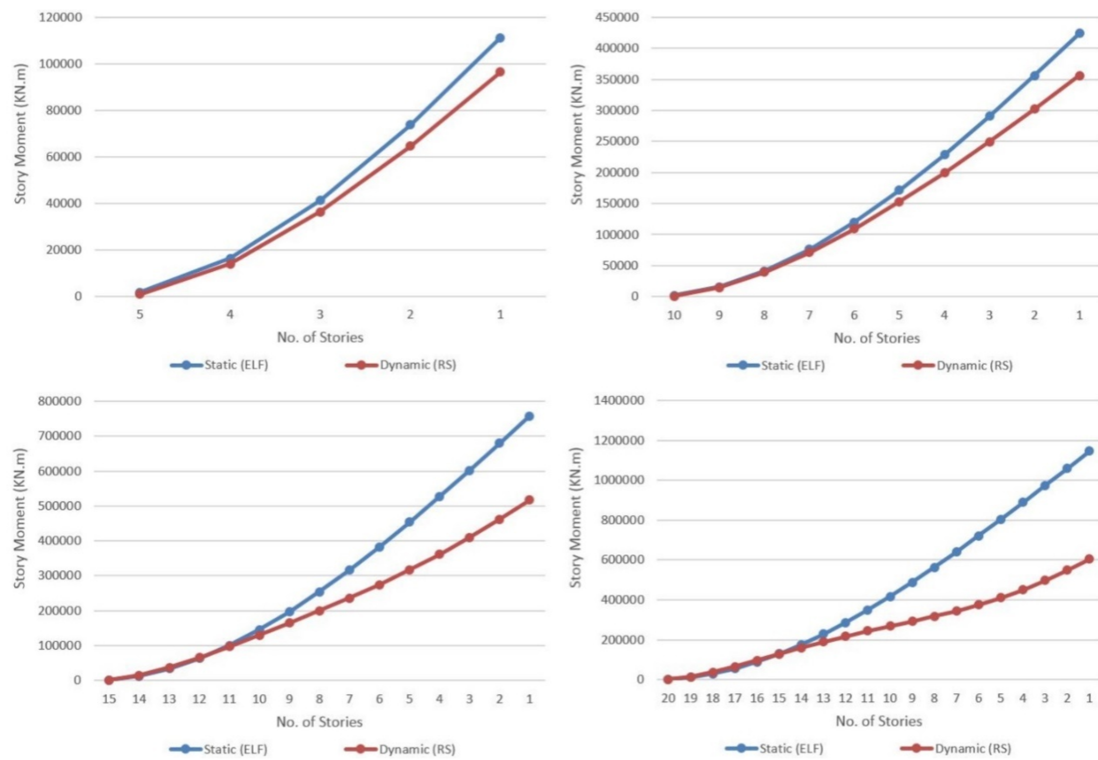

Figure 9: Story Moment for5, 10, 15 & 20 storied structure by Static and Dynamic Analysis

5. Conclusions

From the results of the study it is found that Response Spectrum Analysis is an important dynamic analysis tool and it does not require high level of modelling and in the same time it provide better results compared to static analysis. Although Response Spectrum Analysis (dynamic)preferred over Equivalent Lateral Force Procedure (Static), it is very important to engineers and researchers to understand that the RS analysis is an approximate method and has limitations, as it is restricted to linear elastic analysis only. For more accurate and exact results, other advanced dynamic analysis tool such as Non-linear time history analysis can be used, but this method is more complex and time consuming. Finally, in terms of practical application, it is recommended to use dynamic analysis (RS) instead of static analysis (ELF) specially in high rise building, as it requires less computational efforts while it gives reasonably better results, leading to more economic and safe design.

References

[1]. Autodesk, Robot Structural Analysis 2018, Structural Analysis Software, version 2018.

[2]. B. S. Taranath, "Reinforced Concrete Design of Tall Buildings", CRC Press, New York, USA, 2010.

[3]. G. G. Kakpure and A. R. Mundhada, "Comparative Study of Static and Dynamic Seismic Analysis of Multistoried RCC Buildings by ETABS," *International Journal of Engineering Research and Applications*, vol. 7, Issue 5, pp. 06-10, 2017. DOI: 10.9790/9622-0705050610.

[4]. "Minimum Design Loads for Buildings and Other Structures" (ASCE/SEI 7-10), American Society of Civil Engineers, USA.

[5]. Seismic Design Tool. Access online on 10 June 2018 at https://earthquake.usgs.gov/designmaps/us/application.php

[6]. S. Mahmoud and W. Abdallah, "Response Analysis of Multi-Storey RC Buildings under Equivalent Static and Dynamic Loads According to Egyptian Code," International Journal of Civil and Structural Engineering Research, vol. 2, Issue 1, pp. 79-88, 2014.

[7]. Z. Tafheem, J.I. Jihan, T. Samdanee, M.Z. Islam and A.S.M. Tarin, "Earthquake Response Analysis of a Multistoried RC Building Under Equivalent Static and Dynamic Loading as per BNBC 2006," *Malaysian Journal of Civil Engineering*, vol. 28, Issue 1, pp. 108-123, 2016.

Capability of Designing a Novel Fluid Damper Using a McKibben Actuator

Haithem Elderrat1, Elganidi Elsaghier2
1 h.elderrat@eng.misuratau.edu.ly , 2 e.elsaghier@eng.misuratau.edu.ly
[1] Department of Mechanical Engineering, Faculty of Engineering, Misurata University, Libya
[2] Department of Industrial Engineering, Faculty of Engineering, Misurata University, Libya

ABSTRACT

Flow fluid between moving parts is providing the damping force. Such characteristic can be utilized to build fluid dampers for a wide variety of vibration control systems. Most previous works have studied the application of fluids damper in pistons/cylinders actuator, where the kinetic energy of a vibrating structure can be dissipated in a controllable fashion. The reduction of the friction can cause a sudden jump in the velocity of the movement. Stick-slip friction is present to some degree in almost all actuators and mechanisms and is often responsible for performance limitations. To overcome this problem, this report investigates the capability of designing a fluid damper that seeks to reduce the friction in the device by integrating it with a McKibben actuator. It is also reduced the total weight of such damper. In this paper, the concept of McKibben actuator has been reviewed, the modelling of device made is also presented. Also, the model has been validated experimentally. It is founded that the model predicts the behavior of the test rig with accuracy 85%. Also, the total weight could be reduced to 50% from the original weight.

Keyword— Viscus fluid, Stick-slip friction, McKibben actuator.

1. Introduction

A vibration isolator is a device inserted between the source of vibration and the primary device to reduce unwanted vibration [1]. The basic constituents of anti-vibration devices are the resilient load-supporting means and the energy dissipation means or the damping elements. Damping force exists if there is a relative velocity between two ends of the damper, and it refers to three types which are coulomb, viscus and material damping. In a coulomb damping, energy is absorbed via sliding friction (friction between rubbing surfaces that are either dry or have insufficient lubrication) [2]. Viscous damping is an energy loss occurs in liquid lubrication between moving parts or in a fluid forced through a small opening by a piston [3, 4]. A material damping where the material is deformed due to an applied force, and some energy is absorbed and dissipated by the material due to the friction between the its internal planes [5].

The majority of anti-vibration devices have studied the application of fluids damper in piston and cylinder actuator, where the kinetic energy of a vibrating structure can be dissipated in a controllable fashion. Although the friction has a positive effect in the damping devices, the dry sealing friction makes a vibration transmission to the equipment; this tiny vibration may cause poor accuracy for sensitive devices [6]. Friction could have a bad effect on the system when applied force is close to overcoming the static friction. The behaviour is called stick-slip motion. Stick-slip motion occurs at close to zero velocity and is in the form of a sudden jerking motion. Typically, the static friction coefficient between two surfaces is larger than the kinetic friction coefficient. If an applied force is large enough to overcome the static friction, the friction reduces from static to dynamic friction. The reduction of the friction can cause a sudden jump in the velocity of the movement. Stick-slip friction is present to some degree in almost all actuators and mechanisms and is often responsible for performance limitations [7]. Using a McKibben actuator instead of a hydraulic actuator could reduce the friction in the device. Such actuator has advantages over cylinder and piston dampers for instance: high power/weight ratio and low cost, also there is no stick-slip phenomena in such actuator [8]. This report investigates the possibility of designing a fluid damper by using a McKibben actuator instead of piston and cylinder actuator.

2. McKibben Actuators

The McKibben actuator is a device that converts fluid pressure to force; it consists of an internal rubber tube inside a braided mesh shell. When the inner tube is pressurized, the internal volume of the actuator changes causing the actuator to expand or contract axially as shown in Figure 1. The McKibben actuator is usually used to mimic the behaviour of skeletal muscle [9]. It is also used in medical equipment [10] and industrial applications [11]. Although the working fluid in a McKibben actuator is usually air, there are some applications using water as a working fluid, especially in exoskeleton devices and devices working in a water medium, such as an actuator for an underwater robot introduced by Kenneth et al. [12]. Shan et al. developed a variable stiffness adaptive structure based upon fluidic flexible matrix composites (F2MC) and water as the working fluid [13]. The fibres in an F2MC actuator can be placed at any one angle or combination of angles. This material can be designed to bend and it also provides a greater axial force.

The advantages of the McKibben structure tubes are that it uses inexpensive and readily available materials, and it can easily be integrated into a structure. A McKibben actuator also offers others advantages such as being light weight and with low maintenance costs when compared to traditional cylinder actuators [13]. A comparison of the force output of a pneumatic McKibben actuator and a pneumatic cylinder was made, and the result shows that the McKibben actuator produces a higher ratio of power to weight than the pneumatic cylinder actuator [8].

Figure 1: Concept of McKibben actuator.

3. Modelling of McKibben Actuator

To predict the behaviour of the test rig under static load, there is no effect of viscous damping of the valve, and the test rig could be modelled similar to a McKibben actuator. The variable parameters of this device are: a force applied to the test rig, internal pressure of the McKibben tube, type of internal material, and length of the McKibben tube. There are several techniques used for predicting the behaviour of this actuator and to provide a relationship between variable parameters. The technique of energy analysis, where input work (W_{in}) is equal to the output work (W_{out}), will be used in this research. It is assumed the shape of the McKibben tube is cylindrical. By neglecting the effect of the inner tube at this stage, the input work is done on this actuator by applying compressed air; this air moves the inner rubber surface, so the work is:

$$dW_{in} = P'dV \quad (1)$$

Where: dV volume change, and P' gauge pressure. The output work from this pressure is tension in the actuator, which leads to a decrease in the length of the tube:

$$dW_{out} = -FdL \quad (2)$$

Where: F axial force, and dL axial displacement. From the principle of virtual work, we could reach to the next expression [13]

$$F = P'\left(\frac{3L^2 - b^2}{4\pi n^2}\right) \quad (3)$$

Where: n number of turn, and b uncoiled length of fibre. Now, the effect of elastic energy of inner tube will be accounted. So,

$$dW_{in} = dW_{out} + V_r dW \quad (4)$$

Where: Vr the volume is occupied by the inner tube, and W is the strain energy density function. From the previous analysis of input work and output work:

$$P^{'}dV = -FdL + V_r dW \quad (5)$$

To determine the strain energy density of the inner tube, the rubber tube will be assumed to behave as a Neo–Hookean solid. The strain energy function of the actuator W could be expressed as a function of the first invariant of strain [14].

$$W = \frac{\mu_r}{2}[I_1 - 3] \quad (6)$$

μ_r is the shear modulus for infinitesimal deformations [14], and I_1 strain invariants which could be expressed:

$$I_1 = \lambda_1^2 + \lambda_2^2 + \lambda_3^2 \quad (7)$$

λ_i (i=1,2,3) are the principle stretches. $\lambda_1 = \frac{L}{L_0}$, $\lambda_2 = \frac{D}{D_0}$ and $\lambda_3 = \frac{1}{\lambda_1 \lambda_2}$.

Where L and D, are instantaneous length and diameter, while L_0 and D_0, are initial length and diameter of the tube, respectively. The diameter of the tube could be expressed in terms of length of tube [12]:

$$D^2 = \frac{b^2 - L^2}{\pi^2 n^2} \quad (8)$$

Therefore, strain energy density of inner tube W is determined by using the equation:

$$W = \frac{\mu_r}{2}\left[\frac{L^2}{L_0^2} + \frac{b^2 - L^2}{D_0^2 \pi^2 n^2} + \frac{D_0^2 L_0^2 \pi^2 n^2}{L^2 (b^2 - L^2)} - 3\right] \quad (9)$$

The derivative strain energy density regarding the length:

$$\frac{dW}{dL} = \frac{\mu_r}{2}\left[\frac{2L}{L_0^2} + \frac{-2L}{D_0^2 \pi^2 n^2} + \frac{-2 D_0^2 L_0^2 \pi^2 n^2 (b^2 - 2L^2)}{L^3 (b^2 - L^2)^2}\right] \quad (10)$$

Therefore, the force output of the actuator could be expressed:

$$F = P'\left(\frac{3L^2 - b^2}{4\pi n^2}\right) + \frac{V_r \mu_r}{2}\left[\frac{2L}{L_0^2} + \frac{-2L}{D_0^2 \pi^2 n^2} + \frac{-2 D_0^2 L_0^2 \pi^2 n^2 (b^2 - 2L^2)}{L^3 (b^2 - L^2)^2}\right] \quad (11)$$

The equation illustrates that there are four variable parameters of this device: an applied force, internal pressure, and the length of the tube and type of internal material.

4. Experimental Work

The rig used in this research is shown in Figure 2; it consists of a McKibben tube, valve and accumulator.

The McKibben tube is sealed at one end, and it is able to carry load at this tip, while the tube is attached to an accumulator via a valve at another end. Pressurizing the McKibben tube could be achieved at the top of the accumulator. By applying force to the end of the volume of actuator is changed, consequently the pressure inside tube is increased. Then, the fluid is able to flow in and out of the tube, and energy is eliminated through the viscous effect of the controlled valve. The total weight of such device is less than the half weight of similar piston/cylinder damper, the same results were found in previous researches [12-13].

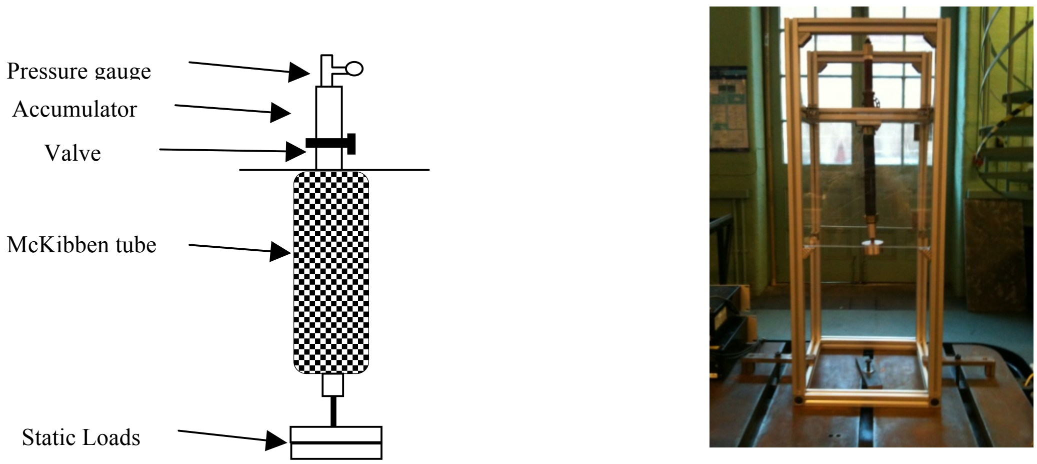

Figure 2: Test rig.

To validating of the model, the isotonic test was carried out in this report. The actuator was loaded to known load, then internal pressure was increased 0.5 bar increments, and the internal pressure P, length of tube L are recorded. Changing in the pressure is causing to chaining length of the actuator. So, these parameters are governed by equation 11.

The length of McKibben actuator was 0.12m with diameter 0.011m. when uncoiled fibre the Length was 0.138m. Such actuator has 2.15 turns. The inner tube was made by rubber with thickness is 0.0003m and Shear modulus is 0. 6MPa.The procedures were examined at two constant loads which are 25N and 50N. Figure 3 shows the experimental results which are compared with the modelling results at a constant load. The figures show the model gives acceptable results in comparison with experimental data. Although there are differences between the modelling results and experimental results, the accuracy of this model is above 85%.

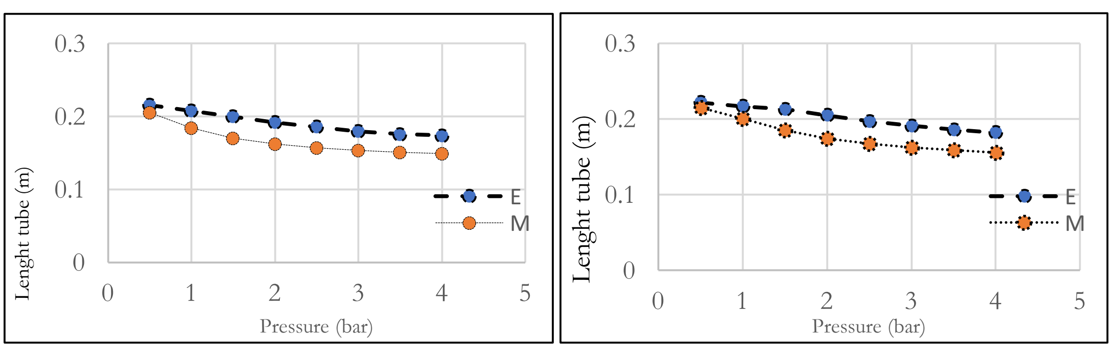

a b

Figure 3: Model and experimental result of rig: a) force is 25N; b) force is 50N.

To minimize these differences, it is important to consider the realistic shape rather than ideal cylindrical shape, also to account the force losses in the system due to friction between fibres and friction between the inner tube and outer tube.

Moreover, it is noticed, the model is shown to have less accuracy at low pressure, and the error is bigger when applying higher loads. To minimize such error, the end effects of the tube should be captured. The end effects changes in the output of the force at the length limits. When the actuator is reaching the length saturation L_s (length saturation), the stretching will be occurring in the fibres; therefore, the output force will be dependent on stiffness of the fibre material. While the force is zero if the length of actuator is less than minimum length L_m, this model is shown in next equations [15].

$$F = \begin{cases} P'\left(\frac{3L^2-b^2}{4\pi n^2}\right) + \frac{V_r\mu_r}{2}\left[\frac{2L}{L_0^2} + \frac{-2L}{D_0^2\pi^2 n^2} + \frac{-2D_0^2L_0^2\pi^2n^2(b^2-2L^2)}{L^3(b^2-L^2)^2}\right] + K_{\mathrm{f}}(L-L_s) & L > L_{\mathrm{m}} \\ 0 & L < L_{\mathrm{m}} \end{cases} \quad (12)$$

Where: K_f stiffness of fibre material.

5. Conclusions

Flow fluid is considered as one of the most superior means of control of vibration, and there are many of applications which profit from the characteristics of viscus fluid, which have been employed successfully. However, a conventional fluid damper has dry sealing frictions which cause a vibration transmission to the equipment. To reduce the friction in a device, a McKibben actuator could be used instead of a hydraulic actuator. Also, using such actuator could be reduced more than half of total weight of devices. A model of a McKibben actuator has been developed and then, it is validated experimentally. The model predicts the behaviour of the test rig with accuracy about 85%.

References

[1]. R.A. Ibrahim, "Recent advances in nonlinear passive vibration isolators". *Journal of Sound and Vibration*, 2008. 314(3-5): p. 371-452.

[2]. D.J. Mead, "Passive vibration control," 2000: John Wiley and Sons Ltd.

[3]. M.R. Jolly, J.W. Bender, and J.D. Carlson, "Properties and Applications of Commercial Magnetorheological Fluids," . *Journal of Intelligent Material Systems and Structure*, 1999. 10(1): p. 5-13.

[4]. D. H. Wang,. and W.H. Liao, "Magnetorheological fluid dampers: a review of parametric modelling". *Smart Materials and Structures*, 2011.

[5]. Y. A. Yu, et al., "Automotive vehicle engine mounting systems: A survey". *Journal of Dynamic Systems, Measurement and Control, Transactions of the ASME*, 2001. 123(2): p. 186-194.

[6]. M.S. Seong, S.-B. Choi, and C.-H. Kim, "Design and Performance Evaluation of MR Damper for Integrated Isolation Mount". *Journal of Intelligent Material Systems and Structures*, 2011. 22(15): p. 1729-1738.

[7]. Karnopp, D., "Computer Simulation of Stick-slip Friction in Mechanical Systems". Journal of Dynamic Systems, Measurement and Control, *Transactions of the ASME*, 1985. 107(1): p. 100-103.

[8]. K.L.Hall, "Dynamic Control For a Pneumatic Muscle Actuator to Achieve Isokinetic Muscle Strengthening" 2011, Wright State University.

[9]. E. J. Koeneman, et al. "A pneumatic muscle hand therapy device. in Engineering in Medicine and Biology Society*", 26th Annual International Conference of the IEEE*. 2004.

[10]. D. G.Caldwell., et al., "A pneumatic muscle actuator driven manipulator for nuclear waste retrieval". *Control Engineering Practice*, 2001. 9(1): p. 23-36.

[11]. K. K. Kenneth, and R. Bradbeer, "Static Model of the Shadow Muscle under Pneumatic Testing". Department of Electronic Engineering, City University of Hong Kong, Kowloon, Hong Kong, 2006.

[12]. Y. Shan et al., "Variable Stiffness Structures Utilizing Fluidic Flexible Matrix Composites". *Journal of intelligent material system and structures* 2009. 20: p. 443.

[13]. S, Lightner, "The Fluidic Muscle: A 'New' Development". *The International Journal of Modern Engineering*, 2002. 2.

[14]. M.S. Chou-Wang, and C.O. Horgan, "Cavitation in nonlinear elastodynamics for neo-Hookean materials". *International Journal of Engineering Science*, 1989. 27(8): p. 967-973.

[15]. R.W. Colbrunn, G.M. Nelson, and R.D. Quinn. "Modeling of braided pneumatic actuators for robotic control ". *Intelligent Robots and Systems*, 2001.

Investigation Into Accuracy Of LGD2006 For Medium-Elevation Areas

Adel Alkilani[1], Ahmed Hamruni[2]
[1]adelalkilani91@gmail.com, [2]elhamrouni@hotmail.com
[1]Faculty of engineering technology, Misallata, Libya
[2]Department of Civil Engineering, Faculty of Engineering, Elmergib University, Libya

ABSTRACT

This paper presents a study about the Libyan Geodetic Datum 2006 (LGD2006) where a triangulation network has been established in a medium-elevation area in Libya. The network is consisted of braced quadrilaterals of 45 km lines in direction of meridians and 7 km lines in direction of parallels. The network distances and angles were accurately measured and then the coordinates were computed. In addition, coordinates of the major traverses points were measured using static GPS observation technique for several hours to ensure the maximum accuracy. GPS measurements were conducted using the World Geodetic System of 1984 (WGS84). Inverse geodetic methods were used to compare the achieved results with those of the Libyan ordinance survey. The results show that the best fit datum for medium-elevation areas (300-500m) in Libya is LGD2006 whereas WGS84 is best for low-elevation areas.

Keyword— :LGD2006, triangulation, static GPS, accuracy, inverse geodetic problems.

1. Introduction

1.1. Background

As the surface of the earth is irregular and complex, for many centuries geodesists tried to determine the shape of the earth. They found that the most complex model of the earth is the geoid and the simplest model is the ellipsoid. This has led to many different reference ellipsoids around the world. Each country takes the newest reference ellipsoid as its reference datum for surveying purposes. Using an incorrect datum to express coordinates can result in position errors of hundreds of meters. As a result, countries modify the global datums to best fit their topographic relief by minimising the geoid undulations. The resulted new datum is known as the local datum [7].

European datum of 1950 (ED1950) had been used in Libya in late fifties and early sixties of last century. This datum best fits Europe not North Africa. European-Libyan datum of 1979 (ELD1979) is another datum that has been used in Libya. Nowadays the Libyan Geodetic Datum of 2006 (LGD2006), which is based on the international ellipsoid of 1924, is the most used datum for surveying applications in Libya [5].

Several researches found that the used ellipsoid for Libya fits only the northern part of the country because of deformations in the datum and that the used ground control points had been established by different companies using different measuring methods.

1.2. Aim and Objectives

The overall aim of this paper is to investigate the accuracy of using the LGD2006 for the medium-elevation areas in Libya. This aim will be assessed through investigating the following objectives:

- Choosing study area where ordinance survey ground control points are available.
- Establishment of a triangulation network of braced quadrilaterals of 45 km lines in direction of meridians and 7 km lines in direction of parallels.
- Using static GPS to measure the coordinates of Laplace station.
- Using geodetic formulas to compute distances and comparing results with those obtained by field observations.
- Establishment of new accurate ground control points to be used in other surveying applications.

2. Test site and Apparatus Used

2.1. Test Site

The test site is located in a medium-elevation area (300 to 400m above mean sea level) close to the city of Tarhuna. The site is between longitudes of 13° 30′ E and 13° 54′ E and latitudes of 31° 21′ N and 31° 52′ N. The test site is shown in Figure 1 while Figure 2 illustrates the topography of the site.

This site was chosen according to its elevation and to availability of two ground control points from the ordinance survey of Libya. These control points are called GPS 12-3 and GPS 12-4 and are located close to the site. Their coordinates are in LGD2006.

2.2. Apparatus Used

The instruments used in this research are:

- 1″ Total station from Trimple
- Prism
- Leica dual frequency GPS receiver
- Communication equipment

3. Trials, Results and Analysis

3.1. Observation Techniques

A total number of two accurate ground control points were available from the ordinance

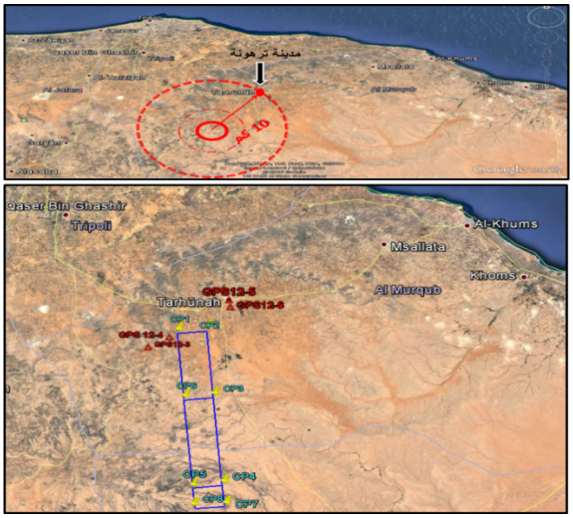

Figure 1: Test site (source: Google earth)

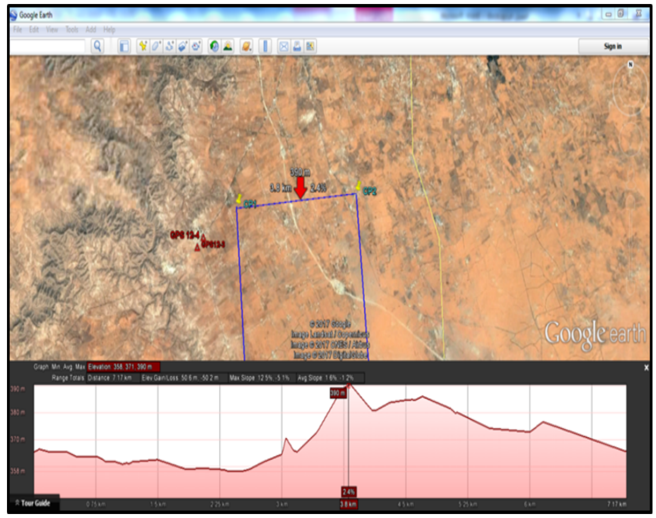

Figure 2: Topography of the test site

survey of Libya. These points were collected using static GPS with an estimated accuracy of 0.0068 m. These points were used as starting points to establish the network's other points. The number of established control points is 8 and were called CP_1 to CP_8 . In-between, points were called X_1, X_2, ……………., X_n . Figure 3 depicts the established control points.

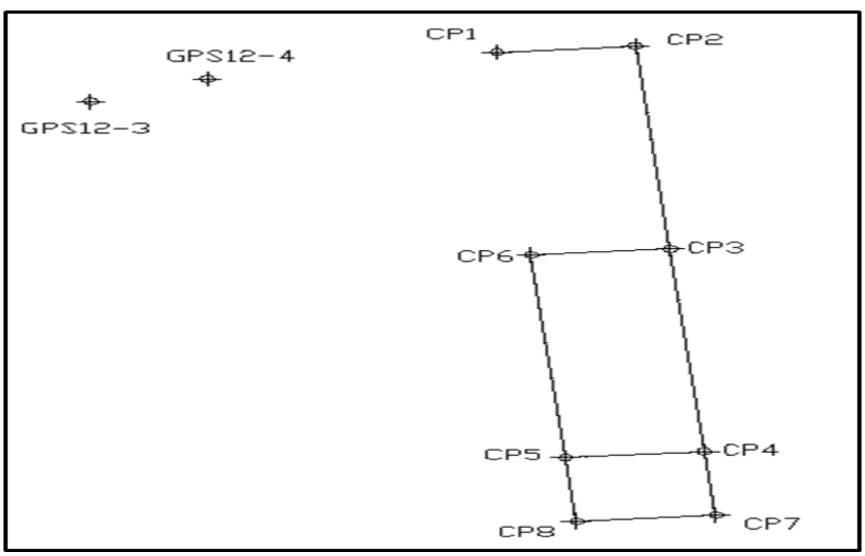

Figure 3: Established control points

The lines' length of the established triangulation network is 45km in the direction of meridians and 7km in the direction of parallels. These lengths were chosen so that the curvature of the earth will be taken into account. The chosen shape of the network is the braced quadrilateral. The control point GPS 12-4 was occupied by the total station and back sight was taken on GPS 12-3 to determine the true north. Then using the total station, the coordinates of all points, azimuths of lines and lengths of network lines were computed. In addition, static GPS observation technique, for several hours, was used to get the coordinates of the control points in WGS84.

3.2. Results and Discussion

The obtained coordinates for the control points in LGD2006 (UTM6º) and in WGS84 are shownin Table 1.

Table 1: coordinates of control points

Coordinates of network points in LGD2006 (UTM6º)			Coordinates of network points in WGS84		
point Id	Easting (m)	Northing (m)	Latitude (φ)	Longitude (λ)	Ellip. Hgt (m)
GPS12-3	356678.648	3578390.064	32° 19' 57.82" N	13° 28' 38.18" E	410.66
GPS12-4	357214.163	3578344.043	32° 19' 56.58" N	13° 28' 58.68" E	402.41
CP1	359198.744	3579582.980	32° 20' 38.92" N	13° 30' 11.68" E	400.12
CP2	366328.401	3580205.442	32° 21' 02.28" N	13° 34' 44.03" E	402.12
CP3	368067.873	3560281.212	32° 10' 16.13" N	13° 36' 00.50" E	418.49
CP4	369830.714	3540088.677	31° 59' 21.40" N	13° 37' 17.63" E	468.53
CP5	362699.684	3539466.102	31° 58' 58.15" N	13° 32' 46.33" E	541.94
CP6	360936.841	3559658.352	32° 09' 52.84" N	13° 31' 28.68" E	488.91
CP7	370308.386	3534617.252	31° 56' 22.78" N	13° 37' 40.67" E	492.14
CP8	363177.398	3533994.688	31° 55' 59.56" N	13° 33' 9.52" E	489.86

3.2.1 Transformation of Cartesian coordinates to geodetic coordinates

As the used coordinate system in the network is the Cartesian system and the ellipsoid represents the geodetic coordinate system, it's necessary to represent the relationship between the two systems mathematically according to the theory of cylindrical conformal projection as follows [6]:

$$\varphi = f(X, \mathrm{Y}) \quad , \quad \lambda = f(X, \mathrm{Y}), X = f(\varphi, \lambda) \quad , \quad Y = f(\varphi, \lambda)$$

Conformal projection has two projection parameters, forward and reverse.

1- Forward (direct) parameters to get Cartesian coordinates

The assumptions put by Kruger to solve the projection equation are to keep the longitudes constant function and to make latitudes variable function as follows:

$$X = X_0 + C_2\lambda^2 + C_4\lambda^4 + C_6\lambda^6 + C_8\lambda^8 + C_{10}\lambda^{10} + \cdots$$
$$y = C_1\lambda + C_3\lambda^3 + C_5\lambda^5 + C_7\lambda^7 + C_9\lambda^9 + C_{11}\lambda^{11} + \cdots$$

2- Reverse (inverse) parameters to get geodetic coordinates

$$\varphi = B_x + C'_2 y^2 + C'_4 y^4 + C'_6 y^6 + C'_8 y^8 + \cdots$$
$$\lambda = C'_1 y + C'_3 y^3 + C'_5 y^5 + C'_7 y^7 + C'_9 y^9 + \cdots$$

where $C_1, C_2, C_3, C_4, C_5, \ldots$ are the forward parameters and
$C'_1, C'_2, C_{\prime 3}, C'_4, C'_5, \ldots$ are the reverse parameters
In addition, Bidshivalf theory was used to get the reverse parameters as following [4]:

$P'_0 = 1 \quad , \quad Q'_0 = 0$
$P'_1 = dx \quad , \quad Q'_1 = y$
$P'_2 = P'^2_1 - Q'^2_1 \quad , \quad Q'_2 = 2P'_1 Q'_1$
$P'_3 = P'_1 P'_2 - Q'_1 Q'_2 \quad , \quad Q'_3 = P'_1 Q'_2 + Q'_1 P'_2$
$P'_n = P'_1 P'_{n-1} - Q'_1 Q'_{n-1} \quad , \quad Q'_n = P'_1 Q'_{n-1} + Q'_1 P'_{n-1}$

The values of $P'_1, P'_2, P'_3, \ldots P'_n$ are substituted back into the following formula to transform Cartesian coordinates to geodetic ones:

$$q = q_0 + \sum_{j=1}^{n} C'_j P'_j \quad \rightarrow \quad q = q_0 + C'_1 P'_1 + C'_2 P'_2 + C'_3 P'_3 + \cdots$$

$$L = L_0 + \sum_{j=1}^{n} C'_j Q'_j \quad \rightarrow \quad L = l_0 + C'_1 Q'_1 + C'_2 Q'_2 + C'_3 Q'_3 + \cdots$$

$$q_0 = ln \sqrt{\left[\frac{1 + sin\varphi}{1 - sin\varphi}\right]\left[\frac{1 - e * sin\varphi}{1 + e * sin\varphi}\right]^e}$$

Latitude can be obtained from the following new formula developed by the geodesist Bidshivalf

$$B = 2\, arctan\left[\sqrt{\left[\frac{1 - esinB_0}{1 + esinB_0}\right]^e} . Exp(q)\right] - \frac{\pi}{2}$$

Where C' represents the reverse parameters, L represents the longitude, B is the latitude and B_0 is the central latitude.

The process is iterative so a Matlab program was developed to perform the conversion of coordinates from Cartesian to geodetic and the reverse process with the possibility to change datums as required. The program has been tested using the ordinance survey control point (GPS 12-3), the discrepancies in coordinates were close to zero and they were as a result of using 8 parameters in the program while the ordinance survey used only 5 parameters.

The Matlab program was used to convert the LGD2006 (UTM6º, International Hayford1924) network coordinates to geodetic coordinates, the results are shown in Table 2.

Table 2: Network Cartesian and geodetic coordinates in LGD2006 (UTN6º)

point Id	Longitude (λ)	Latitude (φ)	Easting (m)	Northing (m)
GPS12-3	13.47727320 º	32.33272965 º	356678.648	3578390.064
GPS12-4	13.48296802 º	32.33238317 º	357214.163	3578344.043
Control Point 1	13.50386317 º	32.34380816 º	359198.782	3579582.981
Control Point 2	13.57951374 º	32.35029741 º	366328.427	3580205.404
Control Point 3	13.60075344 º	32.17081670 º	368067.856	3560281.184
Control Point 4	13.62217705 º	31.98894569 º	369830.460	3540092.809
Control Point 5	13.54681925 º	31.98249019 º	362700.774	3539470.353
Control Point 6	13.52524994 º	32.16434433 º	360938.280	3559658.728
Control Point 7	13.55264639 º	31.93321194 º	370307.987	3534622.442
Control Point 8	13.62796417 º	31.93966278 º	363178.325	3533999.995

3.2.2 comparing obtained results and ordinance survey results using geodetic formulas

The reverse geodetic formulas were used to compute the lengths of network lines to compare them to those of the ordinance survey to determine the accuracy of LGD2006 in medium-elevation areas.
To compute the distance between two points, first a number of parameters has to be calculated as following [6]:

$$e' = \sqrt{\frac{a^2 - b^2}{b^2}} \quad , \quad e = \sqrt{\frac{a^2 - b^2}{a^2}} \quad , \quad C = \frac{a^2}{b} \quad , \quad \rho = \frac{pi}{180} \quad , \quad fm = \frac{\varphi_1 + \varphi_2}{2 * \rho} \quad ,$$

$$ff = \frac{\varphi_2 - \varphi_1}{\rho}, \qquad Lm = \frac{\lambda_2 - \lambda_1}{\rho}$$

$$W_1 = \sqrt{(1 - e^2 \sin^2 \varphi_1)} \quad , \quad W_2 = \sqrt{(1 - e^2 \sin^2 \varphi_2)} \quad , \quad N = \frac{C}{\sqrt{(1 + H)}} \quad ,$$

$$M = \frac{N}{1 + H} \quad , \quad H = e'^2 * COS^2(fm)$$

$$\sin u_1 = \frac{\sin \varphi_1 . \sqrt{1 - e^2}}{W_1} \quad , \quad \sin u_2 = \frac{\sin \varphi_2 \sqrt{1 - e^2}}{W_2} \cos u_1 = \frac{\cos \varphi_1}{W_1} \quad ,$$

$$\cos u_2 = \frac{\cos \varphi_2}{W_2}$$

$$P = \cos u_2 . \sin w \quad , \quad q = \cos u_1 . \sin u_2 - \sin u_1 . \cos u_2 \cos w$$

$$\cot x_1 = \cot u_2 . \cos \Delta w \quad , \quad \cot x_2 = \cot u_1 . \cos \Delta w$$

$$\tan \Delta\beta_{12} = \frac{\tan q}{\tan p} = \frac{\cos x_1 . \tan \Delta w}{\sin(x_1 - u_1)} \; , \beta_{21} = \frac{\tan q_1}{\tan p_1} = -\frac{\cos x_2 . \tan \Delta w}{\sin (x_2 - u_2)}$$

$$\beta_{21} = \beta_{12} \pm 180 + \Delta\beta$$

Using the above parameters, distances can be computed using two methods, one for short distances and the other is for long ones.

1- Geodetic formulas for short distances

$$Z = Lm\,.\,N\,.\,COS(fm)\left(1 + (1 - 9.\,e'^2 + 8.\,H^2).\frac{ff^2}{24} - \frac{(Lm\,.\,Sin(fm))^2}{24}\right)$$

$$Q = ff.\,M\left(1 - \left(e'^2 - 2H^2\right).\frac{b^2}{8} - \frac{(1 + H^2)(Lm.\,COS(fm))^2}{12} - \frac{(Lm.\,COS(fm))^2}{8}\right)$$

$$S = \sqrt{Z^2 + Q^2}$$

2- Geodetic formulas for long distances

If the azimuth is less than 45º, the formula used is: $\tan\sigma = \frac{\tan p}{\cos\beta_{12}}$

If the azimuth is more than 45º, the formula is: $\sin\sigma = \frac{\sin q_2}{\sin\beta_{12}} = \frac{\cos u_2.\sin\Delta w}{\sin\beta_{12}}$

Where:

e, e': first and second eccentricity *M*: meridional radius of curvature

u_1, u_2: reduced latitude of the point *N*: radius of curvature in the prime vertical

β_{12}, β_{21}: forward and back azimuth$\Delta\beta$: convergence of meridians

Δw: difference between longitudes*p , q*: lines lengths from spherical triangle

S: measured short distance on ellipsoid$\boldsymbol{\sigma}$: measured long distance on ellipsoid

Another Matlab program was developed using the above formulas to solve the reverse geodetic problems of short and long distances using LGD2006. The results are presented in Table3.

Table 3: Distances between network points using LGD2006

Distance	points	$\boldsymbol{\varphi}$	$\boldsymbol{\lambda}$	Distance measured by total station	Reverse formulas for short distances	Reverse formulas for long distances
S_{6-3}	Point(cp6)	32.16434433	13.525249944	7158.019	7157.938	7157.939
	Point(cp3)	32.17081670	13.600753444			
S_{3-4}	Point(cp3)	32.17081670	13.600753444	20269.338	20268.990	20268.991
	Point(cp4)	31.98894569	13.622177055			
S_{4-5}	Point(cp4)	31.98894569	13.622177055	7158.155	7158.091	7158.092
	Point(cp5)	31.98249019	13.546819250			
S_{5-6}	Point(cp5)	31.98249019	13.546819250	20269.055	20268.500	20268.502
	Point(cp6)	32.16434433	13.525249944			
S_{4-7}	Point(cp4)	31.98894569	13.622177055	5492.236	5492.220	5492.220

	Point(cp7)	31.93966292	13.627964358			
S_{7-8}	Point(cp7)	31.93966292	13.627964358	7158.112	7158.076	7158.077
	Point(cp8)	31.93321203	13.552646394			
S_{8-5}	Point(cp8)	31.93321203	13.552646394	5492.129	5492.086	5492.086
	Point(cp5)	31.98249019	13.546819250			

Using the same Matlab program the distances were computed using the WGS84 datum, the results are shown in Table 4.

Table 4: Distances between network points using WGS84

Distance	points	$\boldsymbol{\varphi}$	$\boldsymbol{\lambda}$	Distance measured by total station	Reverse formulas for short distances	Reverse formulas for long distances
S_{6-3}	Point(cp6)	32.16467923	13.52463410	7158.019	7157.908	7157.909
	Point(cp3)	32.17115206	13.60014078			
S_{3-4}	Point(cp3)	32.17115206	13.60014078	20269.338	20268.888	20268.889
	Point(cp4)	31.98927792	13.62156647			
S_{4-5}	Point(cp4)	31.98927792	13.62156647	7158.155	7158.056	7158.057
	Point(cp5)	31.98282194	13.54620554			
S_{5-6}	Point(cp5)	31.98282194	13.54620554	20269.055	20268.401	20268.402
	Point(cp6)	32.16467923	13.52463410			
S_{4-7}	Point(cp4)	31.98927792	13.62156647	5492.236	5492.195	5492.195
	Point(cp7)	31.93999427	13.62735433			
S_{7-8}	Point(cp7)	31.93999427	13.62735433	7158.112	7158.042	7158.043
	Point(cp8)	31.93354290	13.55203324			
S_{8-5}	Point(cp8)	31.93354290	13.55203324	5492.129	5492.062	5492.062
	Point(cp5)	31.98282194	13.54620554			

3.3 Discussion of results

The field measurements by the total station is considered as a reference for the purpose of comparison. Comparing the field observations by the total station using the reverse geodetic problems, ordinance survey measurements using LGD2006, and GPS measurements using WGS84, it's clear from Table 3 and Table 4 that there are some differences between the above mentioned measurements. The distances using LGD2006 are closer to reference distances. From Table 3, the biggest difference between reference distances and short distances computed by reverse geodetic problems is 55cm which is between control points 5 and 6 and the smallest difference for short distances is 16mm which is between control points 4 and 7.For long distances using LGD2006, the results are almost the same for short distances. When WGS84 datum was used to compute the distances, either short or long, using geodetic problems (Table 4), the differences between the resulted distances and the reference ones are bigger than those obtained when using LGD2006 datum. The biggest difference is 65cm between control points 5 and 6 and the smallest difference is 41mm between control points 4 and 7.

4. Conclusion and recommendations

A triangulation network was established on a large lot of medium-elevation land using UTM6º (zone 33) and a number of field and office trials and tests were conducted to check the accuracy of LGD2006 in medium-elevation areas. The results show that the best fit datum for areas of elevations 300 to 500m is the LGD2006 and WGS84 is best for areas of low elevations.
Based on the research findings, the following recommendations are being made for possible future work.

- Another study should be made on high-elevation areas to check the suitability of LGD2006 in those areas.
- Continuing studies on the ellipsoid used in Libyan datum and its conformance with the geoid.
- Using static GPS to establish high accuracy first class ground control point in all regions of Libya.

References

[1]. Edward M.Mikhail, Analysis and adjustment of survey measurements, School of Civil Engineering Purdue University-1981.
[2]. Paul R.Wolf ,Elementary Surveying Ninth Edition, Civil and Environmental
[3]. Saudi authority of geological survey, 1994, geodetic datum for maps and ground data systems, Saudi Arabia
[4]. Bidshivalf, 2004, principles of coordinate transformation in new techniques, university of boltsk, Belorussia
[5]. Ordinance survey of Libya,2006, geodetic project and map projection systems, Libyan datum, Libya.
[6]. Ikreesh, Mohamed, 2012, Advanced geodetic surveying and new mapping for GIS, Libya.
[7]. Dawod, Gomaa, 2012, geodetic surveying, Saudi Arabia.

A Review Study of The Effect Of Air Voids on Asphalt Pavement Life

Ali Mohamed Zaltuom
amzaltuom@elmergib.edu.ly
Department of Civil Engineering, College of Engineering, Elmergib University, Libya

ABSTRACT

Roadways play a main role in the development of the countries and societies by providing the essential links between the different parts of the country, to facilitate the transport of goods and movement of people. Compaction is one of the most critical factors associated with the performance of asphalt pavements. When the asphalt content is too high, the compact of mixture might too easily, moreover resulting in low air voids. When the asphalt content is too low, the compact of mixture may be stiff and difficult to the specified density .Asphalt pavements are constructed with initial air voids of 6-8 % depending on the type of mixture and pavement layer. Asphalt mixtures has high air voids content during constructed, it is expected to reduce and this densification can be considered as a predominant cause of rutting during initial periods of traffic. Due to air voids reduction, the material becomes stiffer leading to increase rut resistance. Such increase could also be contributed due to age hardening of the material. Inadequate compaction is one of the leading causes of early deterioration and failure of these pavements. The purpose of this paper is to review the importance and the effect of air voids on asphalt pavement lifespan. The result indicated poor compaction of the mix will leave a high percentage of air voids making it susceptible to moisture infiltration and cracking. Conversely, over compaction may cause mixes to have very low air voids making it subject to asphalt bleeding in hot weather environments.

Keyword— Asphalt Pavements, Air Voids, Fatigue , Rut Resistance.

1. Introduction

Road pavements are one of the largest infrastructure components in most of the developed nations of the world and vitally important to a country's economic development. The construction of a high quality road network directly increases a country's economic output. Roads are constructed to provide fast and safe access between important cities, the construction process will have the added effect of stimulating the construction market[1]. Everything in the life has limited age. For road pavements, wearing surfaces have a life expectancy of between 10-20 years [2]. Asphalt concrete pavements have a short life cycle [3].

Fatigue damage is one of the primary distresses in asphalt concrete pavements besides thermal cracking and rutting [4].Asphalt consists of four main materials: bitumen, aggregate, fillers (fine particles) and air. Asphalt without sufficient air entrapped in the layer will deform under traffic and result in a rutted and rough surface. Field air voids represent the amount of entrapped air in an asphalt layer that has been placed on-site. The objective of asphalt mix design is to achieve an asphalt mix with the lowest practicable air voids without compromising long term performance. Too many air voids and the asphalt becomes permeable to water and air, which causes reduced service life. Too few air voids and the asphalt becomes rutted and deformed under trafficking [5].

Porous asphalt is designed to provide the optimum functional and structural performance particularly the mixture's permeability, modulus and durability. However, these properties are not proportional. High air void content provided in the mixture will improve the permeability but reduces its modulus and durability [6].

2. Compaction Importance and Pavement Performance

Construction of high quality roads can help minimize pavement distresses such as rutting, cracking, and other forms of distresses, and improve the long-term performance of the pavement [7].Compaction is one of the most important factors affecting the performance of asphalt pavements. The asphaltic layer is the most susceptible layer as it is in direct contact with the environment and traffic [8].The volume of air in a pavement is important because it has a profound effect on long-term pavement performance [9]. Compaction is the process by which the asphalt and aggregate are compressed into a reduced volume. It is generally conceded that the compaction of asphalt concrete is one of the most critical factors associated with the performance of flexible pavements [10].

2.1. Stability

Stability can be defined as the resistance to deformation of an asphalt concrete pavement when subjected to traffic loadings under a variety of environmental conditions.A stable pavement maintains its shape and smoothness under repeated loading. In general, the stability increases as density increases with air voids decrease [13]. In this case stability is reduced by five or more points for each percent decrease in air voids [10].

2.2. Durability

The durability of asphaltic concrete has been defined as the resistance to weathering and the abrasive action of traffic (These factors can be the result of weather, traffic or a combination of the two). Good durability can be described as the ability to provide long-term performance without premature cracking or ravelling [10] [13]. The durability of asphalt concrete is largely a matter of the durability of the asphalt cement. Reduction in penetration or increase in viscosity with time. Research has shown that for a given asphalt the rate at which an asphalt hardens is related to the total air voids in the asphalt concrete. If the volume and interconnection of voids in a pavement is such that water is transmitted to the base course, the pavement may fail due to loss of strength in the base material [13].

2.3. Rutting

Figure 1 shown that at low air voids (less than 2%) the binder almost totally fills the void space between the aggregate particles, so that the mix acts as a fluid and is less resistant to rutting when subjected to heavy traffic. Poorly compacted mixes also have less resistance to rutting due to a weaker structure under traffic.

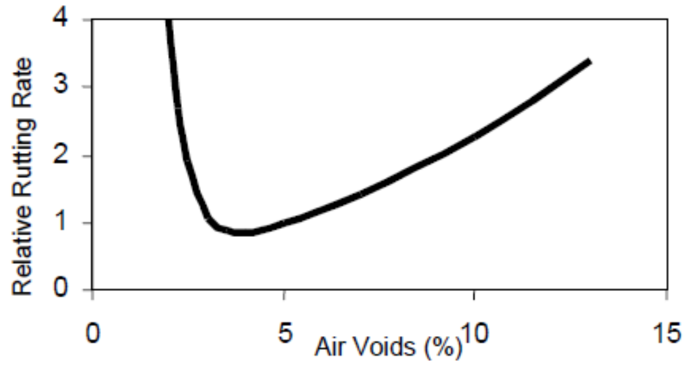

Figure 1: Relative Rutting Rate vs Air Voids

2.4. Fatigue Life

The air void content is important on the fatigue behaviour of asphalt concrete. Previous studies results show that high air void contents produce mixes with comparably short fatigue lives. These data suggest that variations in air void content create greater changes in fatigue life [13].Laboratory investigations indicate that the fatigue life of asphalt concrete could be reduced by 35 percent (or more) for each one percent increase in air voids [10].Fatigue life or resistance to cracking under repeated load, is directly proportional to the compaction level, Figure 2 shows results of fatigue testing. In this case an increase of air voids from 5% to 8% has resulted in a 50% reduction in fatigue life[15].

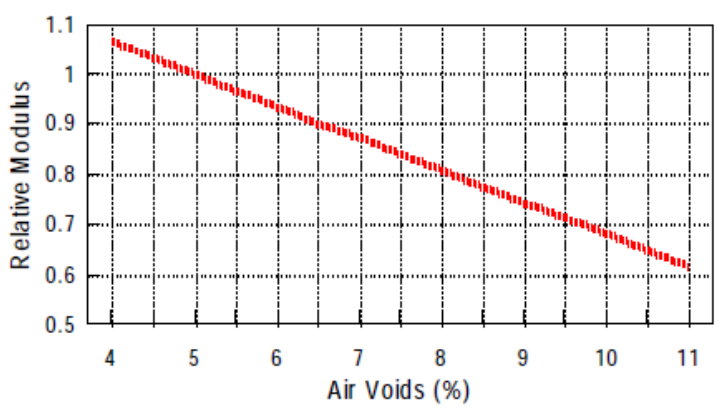

Figure 2: Relative Fatigue Life vs Air Voids

2.5. Strength or Stiffness

Stiffness has been shown to be dependent upon density. The investigators presented the stiffness increases with density suggesting that a more dense mixture results in greater load supporting capabilities of the material [13]. The structural strength of an asphalt mix as measured by its stiffness or modulus, is also related to compaction level. Figure 3 shows strength relative to 5% air void. In this case an increase in voids from 5% to 8% has resulted in a 20% reduction in stiffness or load carrying capacity [15].

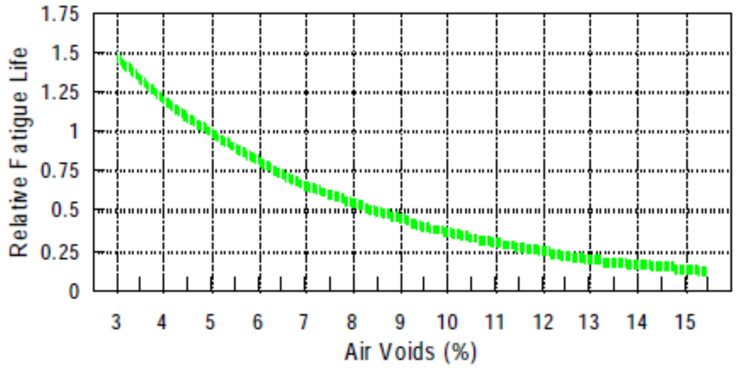

Figure 3: Relative Strength vs. Air Voids

2.6. Flexibility

The flexibility of an asphalt paving mixture is defined as the ability of an asphalt pavement to adjust or the ability of the mixture to conform to long-term variations in base and sub grade elevations. In general, those mixtures of acceptable stabilities with high asphalt contents and high air voids will produce mixtures with the greatest flexibility without cracking [13].

Sometimes the need for flexibility conflicts with stability requirements. For example, an open-graded mixture, which is generally more flexible, is designed to be water permeable. A dense graded mix is relatively impermeable, but is less flexible. Both can affect stability.

3. Factors effecting compaction

The purpose of compacting asphalt pavements is to density the asphalt concrete and thereby improve its mechanical properties as well as to provide a watertight segment for the underlying materials in the pavement structure [13].

Asphalt compaction is a densification process during which air voids are reduced and compaction in the field is commonly performed using vibratory compactors through the application of combined static and dynamic forces. It is necessary to reduce the air void content of asphalt as the properties of the pavement depends on its density [14].

Impact compaction relies on a high impact force. Most premature failures of asphalt pavement are concerned with poor compaction [12].

4. Design air voids

Air voids are small airspaces or pockets of air that occur between the coated aggregate particles in the final compacted mix. A certain percentage of air voids is necessary in asphalt mixes to allow for some additional pavement compaction under traffic and to provide spaces into which small amounts of asphalt can flow during this compaction [15].Air-voids have significant influence on the properties of asphalt pavement, they causes the fatigue damage under repeated load and aggravates the strength of asphalt mixture, causing the macro crack appears in asphalt pavement [16].

Porous asphalt mixture is an open graded gradation that consists of low composition of fine aggregates to allow the mixture to have large quantity of interconnected air voids. These interconnected voids forms capillary channels for the water to flow through and reduce the water runoff from the pavement surface. This shows that the presence of air voids (interconnected and isolated voids) within the mixture is the most significant factor that influences its permeability [17].

Too much air voids also can cause the mixture having excessive aging and stripping problems , that submergence of flexible pavement in moisture over a period of time can damage the fatigue life considerably before design life is achieved [18]. On the other hand, inadequacy of air void within the mixture will lead to the loss in permeability and clogging problem [6].

Least fine materials mixture has caused the mixture to become sensitive towards the changes in voids content as shown by the sudden drop in resilient modulus and large increase in permeability and abrasion loss at high voids content. fine aggregate mixture indicates it is more durable and resilient to deformation but produces low coefficient of permeability. Therefore, any combination of materials (aggregate composition and binder) used should possess strong cohesion and adhesion properties so that a stabilized mixture can be achieved but simultaneously maintaining an open structure of the porous mixture [6].

The range of design air void values in laboratory compacted asphalt mixes is included in asphalt mix design standards. Different types of asphalt include different design air voids as shown in Table 1.

Table 1: Design air voids [9]

Mix Type	Marshal Method Mix Design
	Air Voids range %
L	3.8 - 4.2
H	4.9 - 5.3
V	5.9 - 6.3

Asphalt with high design air voids (H) is used for locations with heavy traffic volumes where there is potential for further compaction of the asphalt mix after placing. (V)asphalt has higher design air voids and is used for heavily trafficked intersections where there is significant potential for further compaction of the asphalt mix after placing. As a result of the higher air voids.

Asphalt with lower design air voids (L) is used for locations with light traffic volumes where there is very little further compaction of the asphalt mix after placing. This type of asphalt achieves high levels of durability and fatigue resistance as a result of the lower air voids and provides long service life. That air void content was the most significant factor affecting on pavement performance [19]. Clearly, the in-place air voids and therefore the in-place density have a significant impact on the pavement life [20].

5. Importance of Air Voids

The asphalt should be flexible enough to resist distress. Also, compaction locks the asphalt-coated aggregate particles together to achieve stability and provide resistance to different types of deformation while simultaneously reducing the permeability of the mixture and improving its durability [14].

Previous research has shown that air-voids have significant influence on the strength and durability of asphalt mixture [16].There is considerable evidence that dense graded mixes should not exceed 8 percent nor fall below 3 percent air voids during their service life. This is because high air void content (above 8 percent) or low air void content (below 3 percent) can cause the following pavement distresses [9].

It was also observed that the frequency of loading inversely affected the fatigue life of the asphalt concrete mixture. In other words as the rate of loading was increased the life of the pavement was decreased [18].Reducing in density could result in reduced the air voids for asphalt mixture ,therefore could have the opposite effect leads to a loss of fatigue life and serviceability of the pavement [19].

Achieving good density of the hot mix asphalt optimizes all desirable mix properties. The result showed that as the percent of air voids increased the number of load cycles to failure representing fatigue life decreased. Thus fatigue decreases with increasing air voids.

6. Conclusions

The quality of compaction is important to the performance of asphalt pavement . Air voids are generally described as the most effective parameter to explain the behavior of the mix. High level of air voids always results in a high expectations of moisture flow within mixtures.

Most premature failures of asphalt pavement are concerned with poor compaction. Increase of air voids in asphalt mixture by 1% than that of design may cause 35% decrease of pavement fatigue life and double the permeability [12].

Previous study showed that a 1% increase in air voids (above the base air void level of 7%) tends to produce about a 10% loss in pavement life [21]. The results clearly reflect the importance of air voids when drilling in the AC layer. From the figures we can see that looking at the 4% central air voids can reduce the gradual response of the material [22].

References

[1]. R. Martin, "Highway Engineering," Blackwell Publishing, 2003.

[2]. Australian Capital Territory, "Transport Canberra and City Services" Access online on April 2018 at https://www.tccs.act.gov.au/roads-paths/Road_Infrastucture_and_Maintenance/roadpavement.

[3]. F. Onyango, Salim R. Wanjala, M. Ndege and L. Masu, "Effect of Rubber Tyre and Plastic Wastes Use in Asphalt Concrete Pavement" International Journal of Civil and Environmental Engineering, vol. 9, no. 11, pp. 1395-1399, sep, 2015. Access online on April 2018 at https://waset.org/publications/10002602/effect-of-rubber-tyre-and-plastic-wastes-use-in-asphalt-concrete-pavement.

[4]. W.A. Zeiada, K.E. Kaloush, B.S. Underwood and M.S. Mamlouk, "Effect of Air Voids and Asphalt Content on Fatigue Damage Using the Viscoelastic Continuum Damage Analysis," *Conference: Airfield and Highway Pavement*, vol. pp. 1122-1133,2013. Access online on 20 May 2018 at https://www.researchgate.net/publication/261635455_Effect_of_Air_Voids_and_Asphalt_Content_on_Fatigue_Damage_Using_the_Viscoelastic_Continuum_Damage_Analysis?enrichId=rgreq-66454f7fd59a7b9c6301de2f33375701-XXX&enrichSource=Y292ZXJQYWdlOzI2MTYzNTQ1NTtBUzozMjU3NjQ1NjMxMjgzMzlAMTQ1NDY3OTczMjg4Mg%3D%3D&el=1_x_2&_esc=publicationCoverPdf

[5]. Papacostas and C. Simpson, "Air voids in asphalt," PAVERTREND, 2016. Access online on MaY 2018 athttp://www.pavertrend.com.au/index.php/asphalt/air-voids-in-asphalt?showall=&limitstart=

[6]. Abdul Hassan, M. Mahmud, N. Adi, N. Rahmat, M. Hainin and R. P. Jaya, "Effects of Air Voids Contenton The Performance of Porous Asphalt Mixture," Journal of Engineering and Applied Sciences, vol. 11, no. 20, pp. .11884-11887, ARPN. October 2016.

[7]. Chadbourn, E. L. Skok, B.L. Crow, D. E. Newcomb and S. Spindler "The Effect of Voids in Mineral Aggregate (VMA) on Hot-Mix Asphalt pavements," Final report, March, 2000. Minnesota Department of Transportation Office of Research Serices, Ireland, Boulevard.

[8]. S. Badeli, A. Carter and G. Doré, "Importance of Asphalt Mixture Air Voids on the Damage Evolution During Freeze-Thaw Cycles," *Conference: Canadian Technical Asphalt Association*, November, 2016. Access online on March 2018 at https://www.researchgate.net/publication/308890481_The_Importance_of_Asphalt_Mixture_Air_Voids_on_the_Damage_Evolution_During_Freeze-Thaw_Cycles

[9]. Pavement Interactive, "Compaction Importance," 2012. Access online on March 2018 athttp://www.pavementinteractive.org/compaction-importance/

[10]. F. N. Finn and J. A. Epps, "Compaction of Hot Mix Asphalt Concrete," Research Report 214-21, Texas Transportation Institute, The Texas A&M University System College Station, August 1980.

[11]. Behl, and S. Chandra and , "Compaction Characteristics and Performance of Warm mix Asphalt"8th International Conference on maintenance and Rehabilitation of Pavements. July, 2016. Access online on 5 March 2018 at http://rpsonline.com.sg/proceedings/9789811104497/html/037.xml

[12]. G. Ying , H. Xiaoming and Y. Wenbin, "The compaction characteristics of hot mixed asphalt mixtures," Journal of Wuhan University of Technology-Mater. Sci. Ed, vol. 29, no. 5, pp. 956-959, GAO. October, 2014. Access online on March 2018 at https://link.springer.com/article/10.1007/s11595-014-1027-z.

[13]. J. A. Epps, B. M. Gallaway, W. J. Harper, W. W. Scott and J. W. Seay "Compaction of Asphalt Concrete Pavements," *Research Report 90-2F*, Texas Transportation Institute, Texas A&M University College Station, Texas. July 1969.

[14]. F. Beainy, S. Commuri and M. Zaman, "Asphalt compaction quality control using Artificial Neural Network," 49th *IEEE Conference on Decision and Control*, CDC. 2010.

[15]. AUSTROADS in conjunction with AAPA, "Pavement Work Tips," no.17, pp. June, 1999. Access online on April 2018 at http://www.pavementengineering.com.au/wp-content/uploads/2015/12/Pavement-Work-Tips.pdf

[16]. H. Jing, L. Pengfeiand S. Bernhard "A study on fatigue damage of asphalt mixture under different compaction using 3D-microstructural characteristics," *Frontiers of Structural and Civil Engineerring*, vol. 11, no. 3, pp. 329-337. September, 2017. Access online on 5 March 2018 at https://link.springer.com/article/10.1007/s11709-017-0407-9

[17]. N. Abdul Hassan, M. Z. H. Mahmud, N. Adi, N. Rahmat, M. R. Hainin and R. P. Jaya "Effects of Air Voids Content on the Performance of Porous Asphalt Mixtures," *Engineering and Applied Sciences*, vol. 11, no. 20, pp. 11884-11887, ARPN. October, 2016. Access online on 5 March 2018 athttp://www.arpnjournals.org/jeas/research_papers/rp_2016/jeas_1016_5163.pdf

[18]. E. A. Igwe and K. I. Amadi-oparaeli "A Proof of Moisture Damage on Fatigue Life of Flexible Pavement Submerged in Water ," *Journal of Scientific and Engineering Research*, vol. 4, no. 9, pp. 210-216, JSERBR.2017. Access online on 5 March 2018 athttp://jsaer.com/download/vol-4-iss-9-2017/JSAER2017-04-09-210-216.pdf

[19]. H. Y. Ahmed, "Methodology for Determining Most Suitable Compaction Temperatures for hot Mix Asphalt," *Journal of Engineering Sciences*, vol. 33, no. 4, pp. 1235-1253. July, 2005. Access online on 5 June 2018 at http://www.aun.edu.eg/journal_files/181_J_9085.pdf

[20]. Transportation Research Circular, "Factors Affecting Compaction of Asphalt Pavements," General Issues in Asphalt Technology Committee, Number E-C105.WashingtonSeptember, 2006. Access online on 5 May 2018 at http://onlinepubs.trb.org/onlinepubs/circulars/ec105.pdf

[21]. L. N. Robert, M. P. Joe,and J. C. Newton "Effect of compaction on asphalt concrete performance," *Transportation Research Record*, no. 1217, pp. 20-28, Abbrev. March, 1990. Access online on March 2018 athttp://onlinepubs.trb.org/Onlinepubs/trr/1989/1217/1217-003.pdf

[22]. R. Neethu, A. Veeraragavan and J. M. Krishnan "Influence of Air Voids of Hot Mix Asphalt on Rutting Within the Framework of Mechanistic-Empirical Pavement Design," *2nd Conference of Transportation Research Group of India*, Procedia - Social and Behavioral Sciences 104, pp. 99-108, 2nd CTRG.2013. Access online on May 2018 athttps://www.sciencedirect.com/science/article/pii/S1877042813044935.

Modeling and Finite Element Analysis of Leaf Spring Using Pro-Engineer and ANSYS Softwares

Salem Elsheltat[1],Abdulbaset Alshara [2], Walid Elshara [3]

[1]salem.sheltat@eng.misuratau.edu.ly, [2]baset.a.a@gmail.com, [3]walidelshara@yahoo.com
[1]Department of Mechanical Engineering, College of Engineering, Misurata University, Libya
[2,3]Department of Medical &Electromechanical Engineering, College of Medical Technology-Misurata, National Board for Technical and Vocational Education, Libya

ABSTRACT

Leaf spring is an important mechanism of suspension system in vehicles that is still widely used. In automotive industry, the motivation is to increase the capability to produce vehicles of inordinate quality at best prices. For saving the natural resources, reducing the weight of vehicle is constantly the priority of car manufacturing. While decreasing the weight of an automobile, engineering designers should consider the strength of materials and the size of components. This deigned leaf spring is built up of several plates with steel material, but the steel leaf spring has an excessive weight .The weight of leaf spring may perhaps be reduced by using strength materials, and reducing the thickness of leafs. The purpose of this paper is to study the deformations and stresses of the current design of leaf spring under static and dynamic loading conditions. The system of this leaf spring is designed to minimize the vibration forces that a vehicle confronts when moving on a surface. This leaf spring has been sketched via Pro-Engineer software, and analyzed through ANSYS. As a result of the conducted stress study, the deformations due to the static and dynamic loading are determined along the leaf spring. The main point of the analysis study is to improve the quality of this design for a leaf spring with a longer life, and achieve a big reduction in vibration forces; for the cost reduction, modification is carried out by varying the thickness of spring leaves; and an optimization study is accompanied to satisfy the allowable values of deformation and the factor of safety by changing the size of meshing elements. Altogether analytically calculated values of deformations and stresses are someway comparable to the values obtained from ANSYS.

Keyword— Leaf spring, Modeling, FEA, Deformation, Safety factor.

1. Introduction

When an engineering designer desires stiffness, negligible deflection is an adequate approach, as long as it does not destruct function. Elasticity is often required and is regularly provided by solid bodies with specific geometries. These bodies can give flexibility to the degree the designer strives for. This flexibility varies linearly or nonlinearly with applied loads. For the significance of machinery to engineering designers, springs have been comprehensively investigated. Furthermore, there are world-wide rapid developments of mass-production techniques for making low cost ingenious springs .Mostly, springs areassorted as flat springs, wire springs, or special designed springs. Flat springs are compartmentalized into cantilever and elliptical shapes [1]. Leaf springs are widely used for the suspension system in cars and commercial vehicles to absorb vibrations and shocks. The spring is made of multi leaves with different lengths. The spring leaf is designed of an arc-shape. The inner leaf is the tallest blade and bent from both ends to form two holes where the spring should be attached to the frame of the vehicle. The outer blades are shorter than the inner blades, and those blades are all held up using bolts and rebound clips. The spring is attached from its centre to the axle of the vehicle. Importantly, the spring should be fixed from the front eye of the master blade to the vehicle's frame and freely in vertical motion from the rear [2]. For simplicity of the calculations, the bending stresses and deformations in laminated leaf springs are determined from formatted standard equations for simply supported beams. The main components (master leaf, graduated leaf, eye, camber, span, central clamp, rebound clips) of a semi-elliptic leaf spring are shown in figure 1.

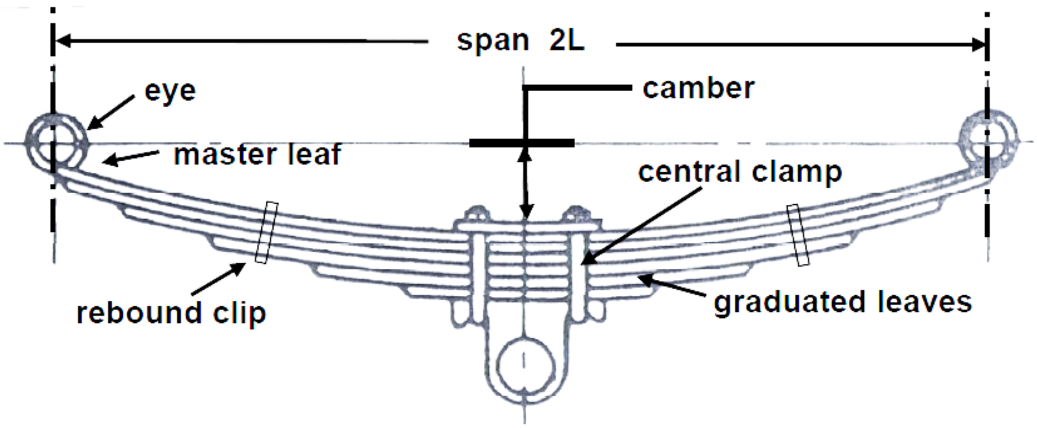

Figure 13 Semi-elliptic leaf spring [2].

1.1. Literature Survey

Some of the pervious studying papers that have done an excellent contribution are mentioned in this paragraph. Sarika Yede and Sheikh [3] modelled and finite element analysed a leaf spring made of different materials. The study concluded that from the comparison of different materials that glass fibre is better than composite material and EN-45 Steel. Amitkumar Magdum [4] analysed leaf springs using finite element methods considering the dynamic effect on stability of vehicle. The work concluded that the best harmonic response of a spring depends on the different materials and loads. The capacity to absorb energy is more in composite materials and less in steels. Shiva Shankar and Vijayarangan [5] designed and fabricated a composite mono leaf spring and tested it under loading conditions, and compare edit to the steel spring. They concluded that more stresses are occurred in the steel spring than they are in the composite spring when subjected to the same loading condition. Also, they found out that the natural frequency is higher in the composite spring. Mahesh Khot and Sameer Shaikh [6] carried out a FEA analysis and did an experimental study on a leaf spring made of a composite material and found out that this material can offer advantages in strength, light weight relative to conventional metallic materials. Trivedi Achyut andBhoraniya [7] performed static and dynamic analysis on leaf Springs, the research concluded that with respect to conventional steel leaf spring composites having high strength to weight ration. Also, composites have less weight than conventional steel leaf spring. G Harinath Gowd and E Venugopal Goud [8] modelled a leaf spring and carried out a static analysis using ANSYS software and they concluded that the maximum stress is developed at the inner side of the eye sections. They recommended that the selected material must have good ductility, resilience and toughness to avoid sudden fracture for providing safety and comfort to the occupants. S. Karditsas, and others [9] have shown design process using finite element method (FEM) and simulation and tested a parabolic 2-leaf-spring for front axles of heavy duty under operating conditions. The stress limitations were exceeded and approximately uniform stress distribution was achieved along the length of the two leaves.

1.2. Problem Statement

This deigned leaf spring is built up of several plates with steel material, but the steel leaf spring has an excessive weight. The weight of leaf spring may perhaps be reduced by using strength materials, and reducing the leaf thickness. Another worry, due to the concentration of stresses at the sudden change of cross sections of the spring geometry, failure might occur at the eyes of the spring and at the portions around the central hole of the spring. Hence, stress analysis study is needed to be carried out on the entire geometry of the leaf spring.

1.3. Objectives of This Work

Firstly, a mathematical model will be developed for studying the deformations and stresses of the current design of leaf spring under loading conditions**.** Secondly, this leaf spring will be sketched via Pro-Engineer software, and analysed through ANSYS. The main point of the stress investigation is to improve the quality of this design for a leaf spring with a longer life, and achieve a big reduction in vibration forces. Thirdly, for the cost reduction, modification swill be carried out by varying the thickness of spring leaves. Fourthly, an optimization study will be accompanied to satisfy the allowable values of deformation and factor of safety by changing the size of meshing elements. Lastly, the results will be verified by comparison of the solution of analytical analysis and FEA.

2. Materials and Methods

The most common material that has been used widely in the world for the leaf spring industry is conventional steel. The advantages of using Steel are local availability, low cost, high strength. The selected material for the designed laminated leaf spring has mechanical properties such as Young's modulus of 200GPa, tensile strength of 880MPa,yield strength of 600MPa, Fatigue of 275MPa, and Poisson's ratio of 0.3 [10].

2.1. CAD Modelling via Pro/Engineer

Pro/E is a suite of programs that are used in the design, analysis, and manufacturing of a virtually unlimited range of products. Its field of application is generally mechanical engineering design, although recent additions to the program are targets at ship building and structural steel framework as well [11]. In this current paper, a computer model creation using the powerful design tool (Pro/Engineer) is to be carried out for a laminated leaf spring. The geometry of the spring has dimensions of (number of spring leaf(n=4), Length of span of the spring (2L=1000 mm), thickness of leaf (t = 10mm), width of leaf (b = 220mm)). Assuming that the total load of 140 KN is applied on the spring, and the material assigned to the leaf spring has an allowable deflection of (49.72mm). Figure 2 shows the 3D solid model of the leaf spring that sketched via Pro/Engineer, this model is to be exported for a simulation via ANSYS software.

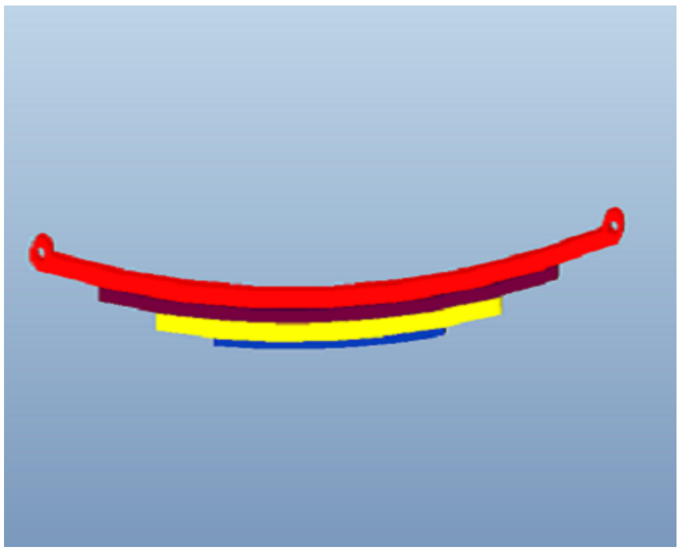

Figure 2: Pro-E model of the designed leaf spring

2.2. Finite Element Analysis via ANSYS

Finite element method (FEM) is a numerical method for solving differential equations that describe many engineering problems. One of the reasons for FEM's popularity is that the method results in computer programs versatile in nature that can solve many practical problems with a small amount of training. Capitalizing on an engineer knowledge of mechanics, reinforcing an engineer knowledge, and solving problems that can only be tackled numerically on the computer, using software tools like ANSYS, Pro/E, Solid Works [12]. The goal of numerical simulation is to make predictions concerning the response of physical systems to various kinds of excitation and, based on those predictions, make informed decisions. To achieve this goal, mathematical models are defined and corresponding numerical solutions are computed. The main elements of numerical simulation and associated errors are summarized among these five stages: physical reality, mathematical model, numerical solutions, predictions and decision [13].

2.3. Simulation Steps in ANSYS

All real-life structures are three-dimensional. It is engineers who make the approximation as a one-dimensional (e.g., beam) or a two-dimensional (e.g., plane or plane solid) structure. When the stresses on a plane normal to one of the axes are approximately zero, then the solid is assumed in the state of plane stress. Similarly, when the corresponding strains are zero, the solid is in the state of plane strain [11].
In this current work, the leaf spring can be assumed to be solved as a beam element, using different sizes of elements. A static structure study is to be carried out using ANSYS 15 beginning with assigning the engineering data of the material used in this design, and going through the following steps.

2.3.1 Geometry and Boundary Conditions

When starting a static structure study in ANSYS, geometry has to be defined. The Pro-E model of a leaf spring is imported to ANSYS. The boundary conditions are to be specified. Figure 3 shows the static structure of the spring, where fixed supports are applied at both eyes and load (F= 7868.3 Ibf) is vertically applied as shown in figure 3.

2.3.2 Finite Element Discretization

We can discretize the geometry of the domain, depending on its shape, into a mesh of more than one type of element (by shape or order). For example, in the approximation of an irregular domain, we can use a combination of rectangles and triangles. However, the element interfaces must be compatible in the sense that solution is continuous [14]. For this case of study, the geometry of the leaf spring can be meshed by creating rectangle meshing type with element size of 0.3 in, 44950 elements, and 221503 nodes. . Figure 4 shows the finite element discretization of the laminated leaf spring.

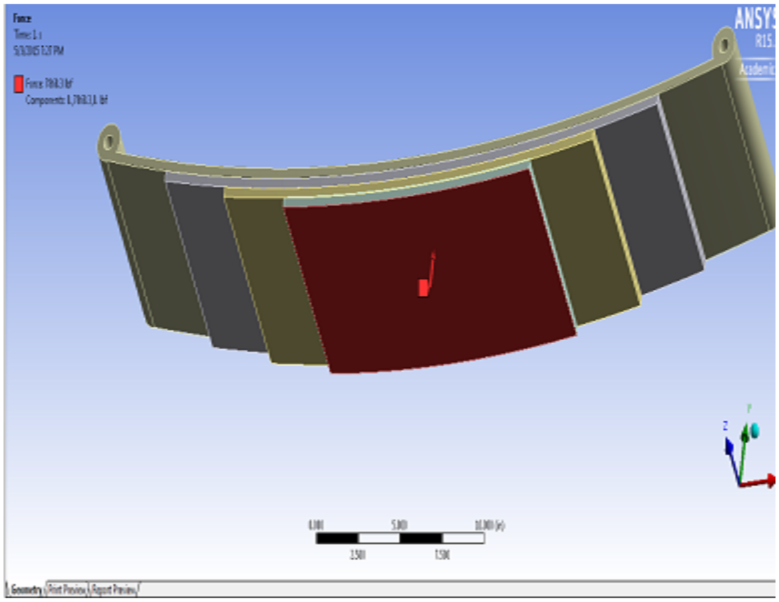

Figure 3: Static structure of laminated leaf spring

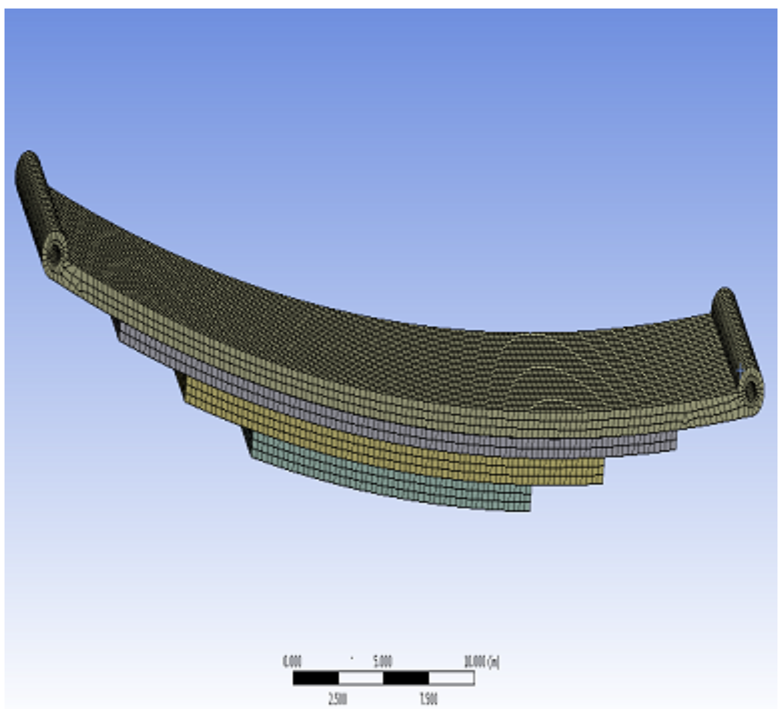

Figure 4: Finite element discretization of the leaf spring

3. Theory and Calculation

Laminated leaf spring can be assumed to be a beam of layers, which is fixed from one end and loaded from the other end. Figure 5shows a simple cantilever type leaf spring. Considering a cantilever beam with the same length of span (2L), width (b),and thickness (t) of the designed leaf spring and subjected to the load (F)[2].

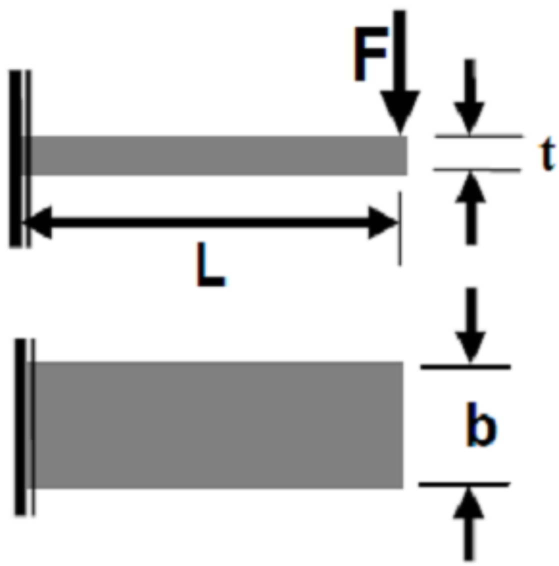

Figure 5: Simple cantilever type leaf spring [2]

3.1. Stresses and Deformation Equations

From the basic equations of bending stress and deflection of beam, the maximum bending stress(σ_{max}),maximum deflection (δ_{max}),Von Mises stress (σ_v), and factorof safety (F.S) can be calculated from the followingformulas [1], [2].

.

$$\sigma_{max} = \frac{6\,F\,L}{n\,b\,t^2} \tag{1}$$

$$\delta_{max} = \frac{4\,F\,L^3}{n\,Y_a b\,t^3} \tag{2}$$

$$\sigma_v = \sqrt{{\sigma_{max}}^2 + 3\tau_{max}^2} \tag{3}$$

$$f.s = \frac{\sigma_y}{\sigma_v} \quad (4)$$

Where: maximum shear stress in the beam ($\tau_{max} = F/A$), A is the cross section of the beam (A= b*t), σ_y is the yield stress,and Y_a isYoung's modulusfor the material as previously specified.

4. Results and Discussion

From the beam equations that introduced in the previous section, the applied load is varied by an increment of 500 N, the corresponding maximum stresses, Von Misses Stresses and deformations are determined; the maximum load that this current leaf spring can bear without failing based on safety factor is 17500 N. Those equations are coded to the equations window of the Engineering Equation Solver (EES) software, and then solved. Table 1 shows the relations among the applied load (F),the maximum stress(σ_{max}), Von Mises stress (σ_v), maximum deflection (δ_{max}), and factor of safety o (F.S) for the leafspring.

Table 1: Variation stresses and deformations with load

F (N)	σ_{max} (Pa)	δ_{max} (m)	σ_v (Pa)	F.S
7000	2.386E+08	0.01989	2.387E+08	2.514
9500	3.239E+08	0.02699	3.239E+08	1.852
10500	3.580E+08	0.02983	3.580E+08	1.676
11500	3.920E+08	0.03267	3.921E+08	1.53
12500	4.261E+08	0.03551	4.262E+08	1.408
13500	4.602E+08	0.03835	4.603E+08	1.303
14500	4.943E+08	0.04119	4.944E+08	1.213
15500	5.284E+08	0.04403	5.285E+08	1.135
16500	5.625E+08	0.04688	5.626E+08	1.066
17500	5.966E+08	0.04972	5.967E+08	1.005

4.1. ANSYS Simulation Solution

Based on the design parameters that have been specified for the leaf spring and from table 1 the critical applied load can be assumed to be 17500 N.

4.1.1 Distribution of Stresses, Deformations, and Factor of Safety

For thickness of 10 mm with mesh size of 0.3in, the stresses are calculated using the tool of beam results in ANSYS, all analysis results are illustrated in the following figures. Figure 6, shows the variation of Von Mises stresses caused to the leaf spring, and figure 7 is shown the corresponding total deformation in the leaves of the spring. For verification of this numerical results, firstly the maximum deformation and stress occurred at the areas around the force's applied point, which is the centre of the leaf, secondly the concentration of the stress accumulated at the eyes of the leaf spring.

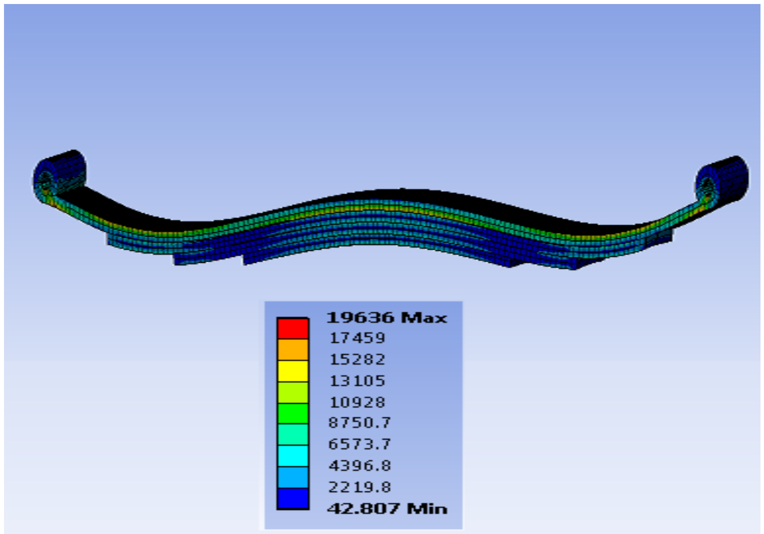

Figure 6: Von-Mises stress distribution (unites in psi)

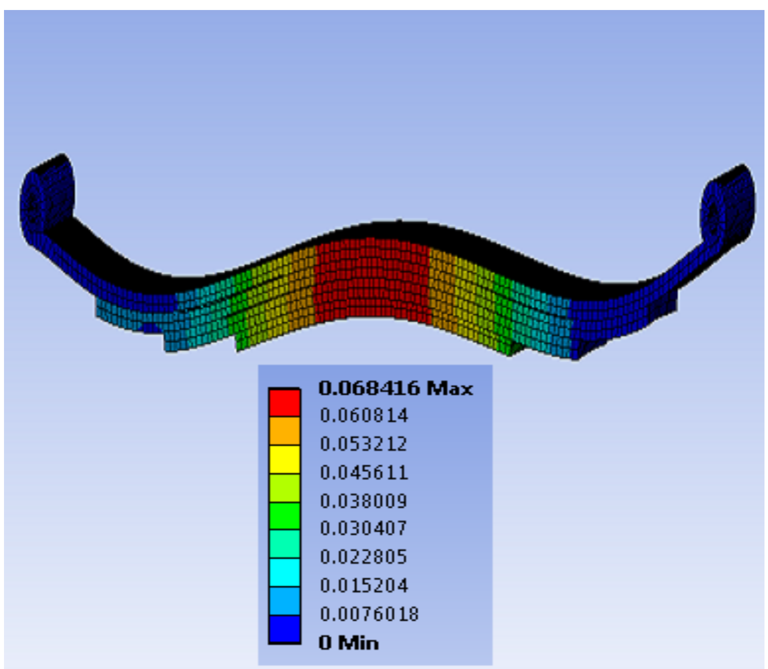

Figure 7: Total deformation distribution (unites in inches)

The safety factor for each element of this design is plotted in figure 8, since the safety factor is affected directly by the maximum stress, the minimum factor of safety occurred at the stress concentration areas of the spring. The numerical solution supports the design of the spring proposed in this work with safety factor of 1.8, which is good enough to be used in the car applications, with a convincing lifespan.

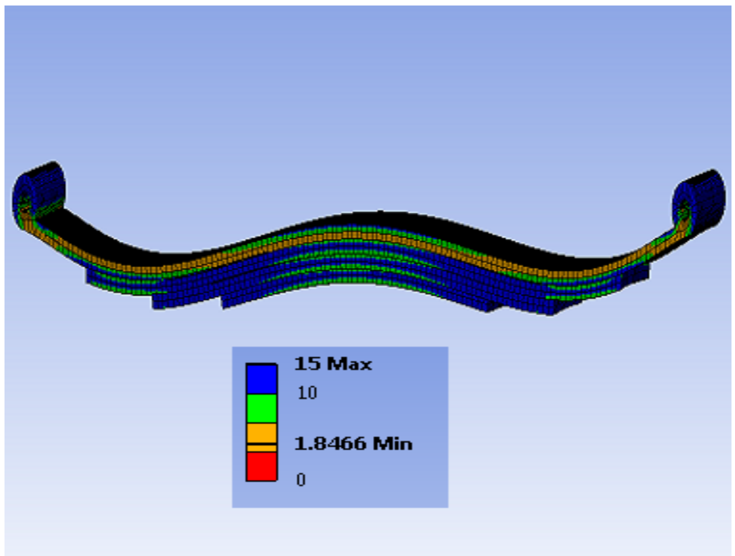

Figure 8: Safety factor distribution for the leaf spring

4.1.2 Design Parameter Variation

The leaf thickness is one of the important design parameter that should be varied in favour of reducing weight. ANSYS has a powerful simulation tool for changing the parameters, and the corresponding solutions can provide such a great visualization that helps the engineers for making their decisions. In this work as it's shown in table 2, stresses, deformations, safety factors are determined for each different value of the leaf thickness. From the table 2, its noticeable that as the thickness is increased, the better safety factor is achieved .However, engineers, should be worried about the weight and cost of the product.

Table 2: Variation thickness with stress, deformations, and Safety factors

Thickness (mm)	Mesh Element size(in)	Von-Mises Stress (psi)	Deformation (in)	Safety Factor
10	0.3	19636	0.068416	1.8466
15	0.3	9406	0.02281	3.8549
25	0.3	6876.6	0.015006	5.2729

4.1.3 Convergence Study

A convergence study is performed by varying the size of mesh element. Increasing the size of meshing element will reduce the number of equations that ANSYS solve. Therefore, the computer with higher specifications is required for less running waiting time. The disadvantage of increasing element meshing size is that it is not possible to create a mesh that precisely covers the entire area for a complicated geometry. This approximated solution will lead to deviations from the exact solutions. At the moment, the version of the simulator used in this work is academic and not able to perform a concise advanced study, but the principle of the converge study is applied by increasing the size of element for meshing the entire geometry of the leaf spring. The stresses and deformations are determined as it's shown in table 3. The mesh size of 0.3 with 44950 elements and 221503 nodes is the optimal meshing size among the options stated in this particular work in table 3.

In future studies, the mesh size should be reduced to its minimum to find the exact solutions, and to obtain a better decision for competitive design. The recommendedanalysis to complete this convergence study for obtaining more satisfying results is to reduce the element size of meshing by 0.1 in. Thiswould increase the number of elements and nodes.In each step, run the solve tool to collect the results, and repeat this step until a no change in results is noticed. Consider the last mesh to be optical for your design andadvanced studies. The numbers of elements and nodes might exceed millions, so keep in mind that high computer specifications are needed.

Table 3: Convergence study

Meshing Size (in)	Stress (Psi)	Deformation (in)
0.5	16146	0.0080364
1	14600	0.0079407
2	17108	0.0079639

5. Conclusions

In leaf spring world industry, reducing weight, and increasing strength are always the main matter in order to yield a competitive product. For that reason, the weight of leaf spring was reduced by using strength steal material, and reducing the thickness of leaves of the desired laminated spring. The geometry of spring was modelled using Pro/E and statically structurally analyzed using ANSYS. The Finite element analysis was the selected method for stress and deformation distributions. The thickness of the spring was varied with stresses and deformations. Based on a convergence study for the accuracy of the results obtained from FEM, the meshing element size is selected to be 0.3 inches for this current condition.

The theoretical results and finite element method solutions are somehow deviated, so an experimental solution is recommended for future studies. Finally, the optimal design steel leaf spring was made up of four plates with thickness of 10 mm, span of 1000 mm, and width of 220 mm. The steel material that is used in this spring should have a yield stress of 600Mpa and subjected to a load less than 17500 N. If heavier loads are desired, we recommend using a composite material that is lighter and has a better stiffness, though the cost reduction should be questioned.

References

[1]. Richard Gordon, Keith Nisbett, "Shigly's Mechanical Engineering Design, " The McGraw-Hill Companies, Ninth Edition, ISBN. 978–0–07–352928–8, 2009.

[2]. R.S. Khurmi, J.K. Gupta,, "A textbook of Machine Design," Eurasia Publishing, year 2005.

[3]. Sarika S. Yede, M. J. Sheikh, "Modeling and Finite Element Analysis of Leaf Spring," International Journal of Computer Applications, Proceedings on ICQUEST, no. 2, pp. 24-26, IJCA.2014,. Access online on 02April 2018 at https://www.ijcaonline.org/proceedings/icquest/number2/18697-1548

[4]. Amitkumar Magdum, "Dynamic Analysis of Leaf Spring Using ANSYS," International Journal of modern Trends in Engineering and Research, vol. 3, Issue. 10, pp. 51-59, IJMTER.. October, 2016. Access online on 10April 2018 athttps://www.ijmter.com/past-issues/

[5]. G.S .Shiva Shankar, Sambagam Vijayarangan, "Mono Composite Leaf Spring for Light Weight Vehicle – Design, End Joint Analysis and Testing," Materials Science (MEDŽIAGOTYRA), vol.12, No.3, pp. 220-225, MSM.. 2006. Received 20 June 2005; accepted 07 April 2006.

[6]. Mahesh A. Khot , Sameer M. Shaikh, "Finite Element Analysis and Experimental Study of Composite Leaf Spring," International Journal of Innovations in Engineering Research and Technology, vol.3, Issue.1, pp. 01-09, IJIERT. January, 2016. Access online on 15 April 2018 at http://www.ijiert.org/vol_iss.php?id=17

[7]. Trivedi Achyut V, R.M. Bhoraniya, "Static and Dynamic Analysis of Automobile Leaf Spring (TATA ACE)," International Journal of Science Technology & Engineering, vol.1, Issue.11, pp. 151-156, IJSTE. May, 2015. Access online on 10May 2018 at http://ijste.org/index.php?p=Archieve&v=1&i=11.

[8]. G Harinath Gowd, E Venugopal Goud, "StaticAnalysis of Leaf Spring," International Journal of Engineering Science and Technology, vol.4, No.8, pp. 3794-3803, IJEST. August, 2012.

[9]. S. Karditsas, G. Savaidis, A. Mihailidis, "Leaf springs – Design, calculation and testing requirements," 35th International Conference on Mechanics and Materials, At Faliraki, Greece, pp. 117-126, ICMMFG. June, 2014.

[10]. Sushil B. Chopade, Prof. K. M. Narkar, Pratik K Satav, "Design and Analysis of E-Glass/Epoxy Composite Monoleaf Spring for Light Vehicle," International Journal of Innovative Research in Science Engineering and Technology, vol..4, Issue.1, pp. 18801-18808, IJIRSET. January, 2015.

[11]. Roger Toogood, "Pro/Engineer Wildfire 3.0 Tutorial and Multimedia CD," SDC Publications Schroff Development Corporation, ISBN.978-1-58503-307-2, 2006.

[12]. Nam-Ho Kim, Bhavani V. Sankar, "Introduction to Finite Element Analysis and Design," John Wiley and Sons,Inc, ISBN.978-0-470-12539-7, 2009.

[13]. Barna Szabo, Ivo Babuska, "Introduction to Finite Element Analysis Formulations, Verification and Validation ," John Wiley and Sons, Inc, First Edition, ISBN.978-0-470-97728-6, 2011.

[14]. J. N. Reddy, "An Introduction to the Finite Element Method Formulations, Verification and Validation," The McGraw-Hill Companies, Third Edition, ISBN.13-978-0-07-060741-5.

Influence of Plastic Bottles Fibre on Self Compacting Concrete

Abdelhamed Ganaw[1], Basel Meghari[2], Abdulnasir Alkoum[3], Mohammed Alawig[4]
[1]engnaw12@gmail.com,[2]bfmbfm95@gmail.com,[3]nasealkoom@gmail.com,
[4]Mohammed15502070@gmail.com
[1,2,3,4] Department of Civil, College of Engineering, Elmergib University, Libya

ABSTRACT

It is well known to all of us that water plastic bottles waste has become a major problem to the environment. At the same time, incorporating the fibres in concrete like polypropylene is advantageous as they improve its properties. Nowadays self compacting concrete (SCC) has become very common in casting concrete due to its high flow properties and attained the required strength.

The aim of this research is to study the effect of addition of shredded waste water plastic bottles to the constituents of SCC and comparing the results with those resulted from employing polypropylene fibre available in the market to the mix.

In the study, SCC was produced at constant water content of 0.4 with the addition of constant super-plasticizer of 2% of cement weight, four fibre contents of 0.05, 0.075, 0.1 and 0.125 of the cement weight were employed to the mix, and then fresh and hardened properties of concrete were measured. From the results obtained, it was clearly observed that fresh and hardened properties of SCC can be obtained by using fibres produced from recycled water plastic bottles, and that off course will help in minimizing the pollution of environment.

Keyword— Self compacting concrete, polypropylene, plastic bottles and super-plasticizer

1. Introduction

Fibre has been used in concrete for many years because of their advantages; they increase concrete strength and sometimes prevent sudden failure in concrete. Natural and manufactured fibres are used in concrete to improve its properties [1]. Natural fibre of plants like Bamboo was added to concrete and resulted in little increase of its compressive strength and higher modulus of elasticity compared with reference concrete [2]. Manufactured fibres have been also used in concrete like, steel, glass, carbon, and Petrochemicals products fibres like polypropylene (PP), polyethylene (PET), polyester and nylon are also used in concrete production industry, and they improve its properties. Steel fibres are the most common fibres used in concrete they are available in the market with different lengths and shapes [3]. For instant, increase of steel fibres addition in concrete from 0.5% to 2% by volume resulted in an increase of concrete strength [4]. Moreover, flexure strength of concrete beams was increased by using steel fibres at percentages of 0.75 % and 1.5% by volume at 7, 14 and 28 days [5]. Fibre glass was also employed in concrete production at 0.03% by volume and resulted in an increase of concrete compressive and flexure strength up to 30% [6]. Polyethylene fibre was used in Indonesia in the production of self compacting concrete (SCC), percentages of up to 0.15 % of mix volume were used in concrete, however flow of concrete was decreased but still in the range and hardened concrete compressive and impact strength were good when fibre added in the range of 0.05 to 0.1%[7]. Polyethylene shredded fibres from water drinking bottles at slices of 2*10 mm are added to the concrete at 0.16 and 0.325 % of concrete volume, the results of hard concrete showed that compressive and flexure strength have been increased compared with reference concrete[8]. It is obviously that using fibres in concrete generally improves its properties which leads to the need to study both natural and manufactured fibres, moreover study of using of waste materials like drinking water bottles showed good results in concrete production but still a lack of such study on its effect on self compacting concrete, in this research the effect of such fibres on concrete will be done.

2. Materials Used

Port land cement used in concrete production was imported from Albourg Factory - Zliten, cement fineness of 3100 cm^2/g, soundness of 1.5mm and specific gravity of 3.15. Its properties were satisfied by British specifications [9]. Water used in this work was drinkable and satisfied by Libyan specifications [10]. Superplasticizer(SP)(Degasetpc7070) from (Yapichem) company was added to concrete mix at 2% of the cement weight, and its properties are accepted by European specification [11]. The used fine aggregate in the study was also imported From Zliten quarries, its gradation is accepted by the British standards BS 882:1992 [12], and has specific gravity of 2.65 and absorption of 0.0124. Coarse aggregate was imported from local quarry to produce SCC, it was passed from 20mm sieve and retained on 14, 10 and 5 mm sieves, and it was comply to the British standards BS 882:1992 [12]. Coarse aggregate has specific gravity of 2.67 and absorption of 0.0136. Aggregate gradations, specific gravity and absorption tests were carried out at the Alkhums School of engineering concrete lab. PP fibres (Monofilament Fibres, Sika) are available in the market were used in the study [13], PET fibres were produced from shredding of drinking water bottle, Figures 1 and compared with PP, Figure 2 (They are PET and PP from left to right).

3. Methodology of the research

Nine different mix proportions were designed in the study after defining the required water cement ratio (w/c=0.4) ratio and SP required to give high workability for SCC without segregation and that was obtained from experimental work of trial mixes in the lab. The first mix did not contain any fibre, and then PP and PET fibres were employed each at 0.05, 0.075, 0.1 and 0.125 %. Fresh concrete first produced by normal mixer in the concrete lab, slump flow test for SCC and J ring tests were carried out according to the British specifications [14, 15], all fresh concrete mixes were able to pass through the bars of J-Ring and gave the required workability for Self compacting concrete. After that concrete was casted in three 100 mm cubes and three prisms of 400*100*100 mm and left in their moulds, no vibration was employed for SCC. After 24 hours concrete samples were extracted from their moulds and left merged in water. Finally, after 28 days, compressive and flexure strengths of SCC were measured.

4. Results and Discussion

4.1. Fresh properties of concrete

Table 1 shows fresh concrete spread diameter test results of reference and the highest fiber content mixes of 0.125%. It is clear that all mixes are in the range of SCC suggested by the specifications. A decrease of 7.38% in spread diameter was observed when PP fiber was added and just 4.7% decrease when PET employed, this result can be attributed to the high surface area of fiber when added to the mix. On the other hand, the increase of T_{500} value when fiber proves that the cohesion and viscosity of concrete is better which prevents concrete segregation. Table 2 shows the results of J-Ring test of fresh concrete. It is obviously that as the fiber added the passing resistance increases from 5.8 up to 9.2, and this is logic because of the effect of fiber which prevents the material from passing easily.

4.2. Hardened properties concrete

Figure 3 presents the relation between SCC compressive strength and fiber percentage in the mix. It is clear that as the fiber increases concrete compressive increases until percentage of 0.075%. The same results were obtained in the relation between flexure strength and fiber content as shown in Figure 4. However the trend in both tests started going down the percent of 0.1% still higher than the reference mix. However PP fiber resulted in higher concrete strength in both tests the difference is very small and can be neglected. These results agreed with other investigations presented in the introduction for normal concrete. Moreover, since this study was carried out on self compacting concrete, this can be considered a good result because SCC needs high flow which still available even the fiber content reached 0.125%.

4.3. Preparation of Figures and Tables

Table 1: Slump test results of reference and higher fibre content mixes

Mix	Fibre (%)	Diameter(mm)	Specification (mm)	Time T_{500} (sec)	Specification (mm)
Reference	0	745	650-800	1.9	2-5
PP	0.125	690	650-800	2.13	2-5
PET	0.125	710	650-800	2.02	2-5

Table 2: J-Ring test results of reference and higher fibre content mixes

Mix	Fibre (%)	Diameter (mm)	Specification (mm)	Time T_{500} (sec)	Specification (mm)	Value (mm)	Specification (mm)
Ref.	0	710	650-800	2.03	2-5	5.8	0-10

PP	0.125	665	650-800	2.36	2-5	9.2	0-10
PET	0.125	680	650-800	2.17	2-5	9.0	0-10

Figure 1: Preparing of PET from plastic bottles

Figure 2: Comparison between PET (left) and PP (right) fibres

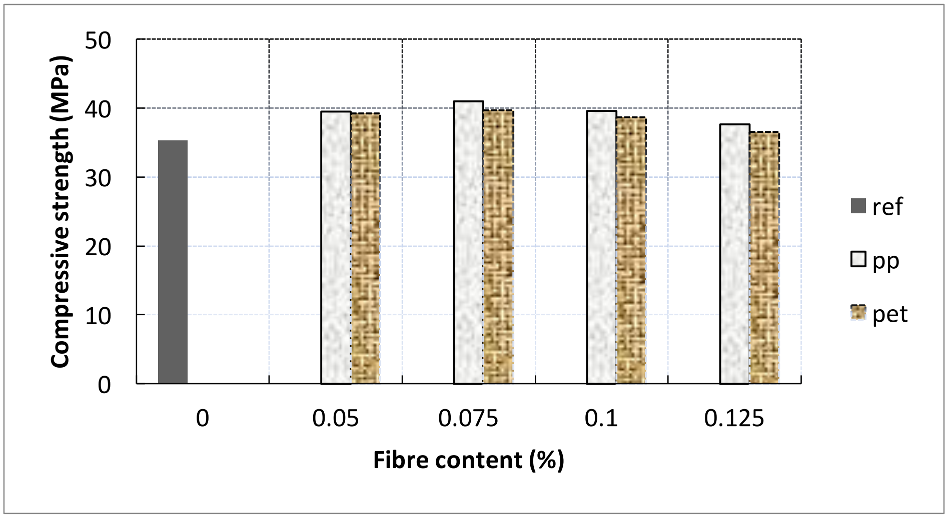

Figure 3: Compressive strength vs. fibre content

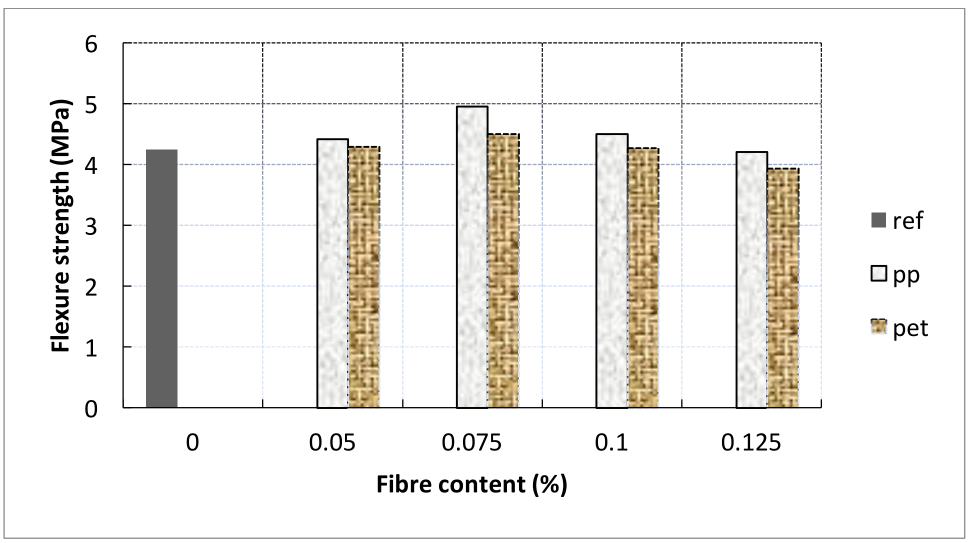

Figure 4: Flexure strength vs. fibre content

5. Conclusions

The main objective from the investigation was achieved, as the fibres excluded from waste drinking water bottles resulted in better concrete properties comparing with that of no fibre. Moreover, waste bottles fibres when compared with manufactured fibres available in the market for building objectives resulted in the same results without losing the advantages of self compacting behaviour of fresh concrete. Moreover, recycle of drinking water bottles will result in many advantages, minimizing concrete cost, land areas needed and pollution as this material is not degradable.

References

[1]. Neville, A. M., "*Properties of Concrete*," *Hand Book, Fifth Edition,* Pearson Education Limited, England, 2011.

[2]. Ahmad, S. ؛Raza, A. ؛ Gupta, H, "*Mechanical Properties of Bamboo Fiber Reinforced Concrete*." 2nd international Conference on Research in Science, Engineering and Technology, Dubai-UAE, March, 2014

[3]. Grunewald, S. "Performance-based design of self-compacting fiber reinforced concrete," *DUP Science*, Netherlands, 2004.

[4]. Wang, C., "Experimental Investigation on Behavior of Steel Fiber Reinforced Concrete (SFRC)" *Master's Thesis in Civil Engineering, the University of Canterbury*, New Zealand, 2006

[5]. Vairagade, L. N. ؛Bhedi, V. M, "Comparison of Strength between Steel Fiber Reinforced Concrete and Conventional Concrete," *International Journal on Recent and Innovation Trends in Computing and Communication*, vol. 3, no. 2, pp. 5-10, 2015

[6]. Gornale, A. ؛ Quadri, S. I. ؛ Quadri, S. M. ؛ Ali, S. M. ؛ Hussaini, S. S. , "Strength Aspects of Glass Fibre Reinforced Concrete.," *International Journal of Scientific & Engineering Research*, vol. 3, no. 7, pp. 1-5, 2012.

[7]. Widodo, S, "Fresh and Hardened Properties of Polypropylene Fiber Added Self-Consolidating Concrete," *International Journal of Civil and Structural Engineering*, vol. 3, no. 1, pp. 85-93, 2012

[8]. Abdelgader A., Shailan D., "Mechanical properties of polymer concrete contain fibers of waste plastic," *Iraqi Journal of Mechanical and Material Engineering*, vol. D, no. 1, pp. 653-664. Iraq, 2009.

[9]. British Standard Institute, BS EN 197-1 "Cement - Part 1: Composition, specifications and conformity criteria for common cements," London, UK, 2011

[10]. Libyan Standard Specification, 294,"Used water in concrete," Tripoli, 1988

[11]. British Standard Institute .BS EN 934-2:2009, "Admixtures for concrete, mortar and grout - Part 2: Concrete admixtures - Definitions, requirements, conformity, marking and labeling," London, UK, 2012.

[12]. British Standard Institute .BS 882:1992, "Specification for aggregates from natural sources for concrete," London, UK, 2002.

[13]. Sika Company, Polypropylene Fibers Data Sheet, 2015

[14]. British Standard Institute .BS EN 12350-8:2010, "Testing fresh concrete - Part 8: Self-compacting concrete - Slump flow test," London, UK,2010.

[15]. British Standard Institute .BS EN 12350-12:2010, "Testing fresh concrete - Part 12: Self-compacting concrete - J-Ring test," London, UK, 2010.

Prediction of Local Concretes Compressive Strength Using The Maturity Method

Mohammed Ali Abdalla Elsageer[1], Wisam Elhmali Mansour[2], Hamad Suliman Abulaaj[3]
[1]drmohammedalsger@gmail.com, [2] wesamelmansour@gmail.com, [3] h_bulaej@yahoo.com
[1]Department of Civil Engineering, Faculty of Engineering, Sirte University, Libya

ABSTRACT

This paper aims to study the maturity method to predict the compressive strength of a local concrete. This method is a non-destructive test of the concrete and can be used to know the time to remove concrete formwork. The method depends on time and the concrete temperature factor on the compressive strength of the concrete by using mathematical equations to predict the value of compressive strength. In the study two Portland Cement concrete mixtures were used, of grades C35 and C45, the compressive strength was tested at 6 hours and 1, 2, 4, 8, 16, 32, 64 days at different curing temperature 20, 30, 40 and 50 °C. The concrete strength was predicted by the maturity based on the Carino and Hansen equations, also the Datum temperatures for each mixture without which the concrete gained no strength was calculated. The laboratory results were compared with the theoretical results obtained from the equations of Carino and Hansen. The value of predicted compressive strength for concretes was accurate at early ages and highest or accurate in the later ages depending on the factors of the equations used.

Keyword— Compressive strength, Maturity, Datum temperatures

1. Introduction

Increasing cost of construction has necessitated use of accelerated construction schedules to achieve economic benefits. Contractors need to know the strength of a structure or roadway in order to meet deadlines for formwork removal, a knowledge of in-situ concrete strength can reduce construction time and cost by efficient movement of forms. Furthermore it also establishes safe time for formwork removal to avoid catastrophic failure of structures with consequent danger to human life.

The strength development of concrete achieved in structural elements will be different from the strength of specimens that cured under standard curing condition, even though they are the same mixture for the following reasons [1]:

- Differences in maturity
- Differences in compaction and curing
- Water and cement migration within the cast element

The differences between the strength of concrete specimens cured under standard curing conditions and that of in-situ strength obtained even though they are the same mix make it difficult to decide whether the quality of concrete supplied to the site was of the required quality. Therefore, it is necessary to determine whether the structural element is adequately strong enough to withstand the intended loading, and allowing the contractor to remove the formwork. The methods listed below are some of the most popular and widely used methods of estimating the early-age concrete strength development during construction for formwork striking purposes [1]:

- Cured Specimens Alongside The Structure, Tables of Formwork Striking Times, Temperature Matching Curing Bath, Maturity Method, Penetration Tests, Break-Off Tests, Pull-Out Tests, Rebound-Hammer Test and Coring Test

1.1. The Maturity Methods

The term 'maturity or maturity index' can be defined as a 'temperature-time factor' that describes the combined effect of temperature and time on the development of concrete strength. The method developed is based on the principle that concretes cast from the same mix that have equal maturity will have equal strength regardless of their actual temperature-time history.

The maturity method is one of the most reliable methods of assessing early-age in-situ concrete strength, particularly for fast-track construction applications. Many methods have been proposed to determine the maturity of concrete empirically [2,3]. In recent years, however, many methods have been developed based on the concept of activation energy and the Arrhenius law[2] on the rate of reaction. This method has a wide variety of applications in the precast concrete industry that include the assessment of strength of prestressed heat accelerated concrete elements[2,3].

Maturity method in determining the time needed for the concrete to achieve adequate strength to permit the release of the pre-stressing force.

The in-situ concrete maturity can be determined using one of the following procedures:

1. Analyzing in-situ temperature recordings using maturity functions.
2. Using electronic maturity meters.
3. Using a commercial maturity probe, which is based on the evaporation of a volatile liquid.

The maturity index is determined from the temperature history of concrete by a maturity function; such as the Nurse-Saul or the Arrhenius formulation proposed by Freiesleben Hansen and Pedersen[2]. Once the maturity index or the equivalent age at a reference temperature, is determined the strength development of concrete cured at other than reference or standard curing temperature can be determined as well.

The index maturity of concrete at standard curing temperature; can then be used to determine the strength of concrete using the strength-maturity correlations of concrete cured at standard temperature. The strength-maturity correlations is developed by statistically analyzing the strength data of cubes, which are cast from the same mix and cured isothermal at the reference temperature. The maturity testing procedure is described in Figure (1).

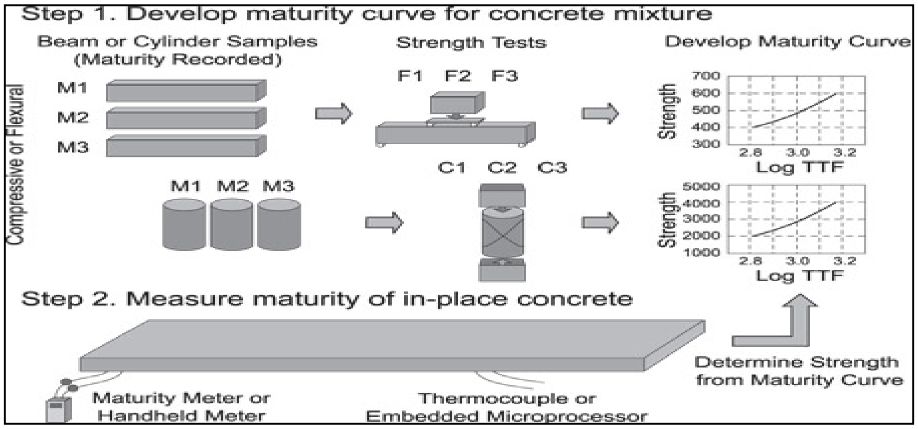

Figure (1): Maturity testing procedure [2]

The Maturity method saves time and money by the accurate prediction of concrete strength to remove formworks, cut and saw timing and open pavement to traffic. This method saves money by reducing the samples required to test. The strength of concrete estimation is also important to the new construction of buildings and roads. Maturity is useful for operating timing of pre-stressed concrete. The method can estimate the strength of concrete at any age.

The negative side of the maturity method is that a complete hydration should continue without ceasing otherwise predictions will be incorrect. This method will not take into account some field actions, like inadequate vibration and insufficient curing. Every mixture has its own unique maturity. So strength maturity curve should be established for every individual mixture[2,3].

The equations used to predict the strength are based on **Nurse-Saul** maturity below:

$$M = \sum_0^t (T - T_0)\Delta t \qquad (1)$$

$\boxed{M = \sum_0^t (T\text{-}T_0)\Delta t}$ Where:

M = Maturity index, °C-hours (or °C-days),

T = Average concrete temperature, °C, during the time interval *Δt*,

T_0 = Datum temperature (usually taken as -10 °C),

t = Elapsed time (concrete age in hours or days),

Δt = Time interval (hours or days).

The Strength-Maturity Relationship Proposed by Carino

Carino›S Strength- Time Relationship

$$S = S_\infty \frac{K_T(t-t_0)}{1+K_T(t-t_0)} \qquad (2)$$

Where:

S_∞ = Limiting strength, N/mm²

t = Age, hours

K_T = Rate constant is equal to Arrhenius equation:

$$K_T = Ae^{\left[\frac{-E}{RT}\right]} \qquad (3)$$

$$\boxed{K_T = Ae^{\left[\frac{-E}{RT}\right]}}$$

Where:

A = A constant

E = Activation energy, J/gmol

R = Universal gas constant, 8.3144 J/gmol-K

t^0 = Age when strength gain begins, hours

The parameters S∞, K_T and t^0 in equation (2) are determined by best-fit curve fitting to strength vs. age data obtained by experiential tests to a concrete cured at different constant temperature. Moreover, the equation is used to determine concrete datum temperature and activation energy[5], which will be discussed in the activation energy section.

In 1982, Knudsen[6] , earlier than Carino, devised a similar equation to represent the degree of hydration of cement rather than concrete strength.

Carino›S Strength- Maturity Relationship:

$$S = S_\infty \frac{K(M-M_0)}{1+K(M-M_0)} \qquad (4)$$

Where:

S_∞ = Limiting strength, N/mm²

M = Maturity, °C-hours

K = A rate constant

M_0 = Maturity when strength gain begins, °C-hours

Freiesleben Hansen and Pedersen Strengh-Maturity Relationship[7, 8]

The equation is a Three Parameter Exponential (TPE) and was proposed in 1985[2], based on the assumption that the strength development should be similar to the curve and relationships of heat of hydration. The Freiesleben Hansen and Pedersen is as follows:

$$S = S_\infty e^{-\left(\frac{\tau}{M}\right)^\alpha} \qquad (5)$$

Where:

S_∞ = Limiting strength, N/mm²

M = Maturity index, °C-hours
τ = Characteristic time constant
α = Shape parameter

Note that changing the value of the time constant preserves the same general shape of the curve while shifting it to the left or right. According to Carino changing the value of the shape parameter alters the shape of the curve in such a way that when α increases then the curve has a more pronounced S shape.
In 1977, Freiesleben Hansen and Pedersen[7] proposed an equivalent age function to compute a maturity index from the recorded temperature history of the concrete based on the well known Arrhenius equation. The earliest mention of the use of the Arrhenius equation, to describe the effects of temperature on the early rate of hydration of cement, was in 1962 by Copland et al[9].

The nonlinear proposed function is as follows:

$$t_e = \sum_0^t e^{\frac{-E}{R}\left[\frac{1}{273+T} - \frac{1}{273+T_r}\right]} \Delta t \qquad (6)$$

Where
t_e = The equivalent age at the reference temperature,
E = Apparent activation energy, J/mol,
R = Universal gas constant, 8.314 J/mol K,
T = Average absolute temperature of the concrete during interval Δt, Kelvin, and
T_r = Absolute reference temperature, Kelvin.

2. Aims and Objectives

The main aim of this paper is to estimate strength development of concrete using the maturity method.

3. Experimental Work

To obtain normal strength concrete of target mean strengths of C35 as classified by European standard BS EN 206-1:2000, the proportions were obtained using the BRE method (mix design of normal concrete)[10]. The mix percentage of the material are shown in Table1.

Table (1): Mix Percentage of The Material to be Used C 35

Cement	Water	sand	Coarse aggregate
1	0.549	1.346	2.617

The strength development under 20, 30, 40 and 50 °C, and were investigated.

4. Materials

All the materials used in all parts of this same study mentioned in detail and will respond as follows:

4.1. Cement

Portland cement type I class 42.5N was used in this study. The cement was supplied by Zliten Factory.

4.2. Aggregate

4.2.1 Coarse Aggregate:

The coarse aggregate used was graded aggregate comprise crushed dolerite stone with a nominal size ranging from 5 to 20 mm. Sieve analyses were carried out in accordance with BS 882:1992[11], in order to check whether the size distributions of the aggregate satisfy the limits required in the standard. The sieve analysis test of aggregates was done on each size alone (20, 10) mm, both sizes of aggregate were mixed (The mixing ratio is 50% for each size) to improve the concrete mix, The sieve analysis test of the mixed aggregates was matching specifications.

4.2.2 Fine Aggregate

Natural sand from Sirte has been used. The sieve analysis test of fine aggregates was done on natural sand and fine aggregate up to 5mm, both sizes of aggregate were mixed to improve the mix although each of them was matching specifications. The mixing ratio is 30% size 5mm fine aggregate & 70% sand. the sieve analysis results was matching specifications.

5. Curing

After casting, the concrete specimens were wrapped in cling film then submerged in water tanks set at 30, 40 and 50 °C curing conditions. Except for 20 °C as the lab temperature was 20 ± 2 °C. The specimens were covered with damp hessian and plastic sheeting, the next day, i.e. 24 hours after casting, the specimens were demoulded and placed back in their initial curing conditions up till the time of testing.

6. Experimental Results and Data Analysis

6.1. Strength Development Concrete at Different Curing Temperatures

The strength development under 20, 30, 40 and 50 °C curing regimes for concretes, with strength error bars based on three replicate samples is shown in Figure (2).

At an early age the strength development of the concrete at high curing temperatures is greater than at low curing temperatures. This is attributed to an increase in the hydration reaction rate. However, at a later age, the strength achieved at high curing temperatures was reduced. The strength development under 20, 30, 40 and 50 °C curing regimes will be used to determine the activation energy and datum temperature of the concrete under investigation according to the ASTM C1074.

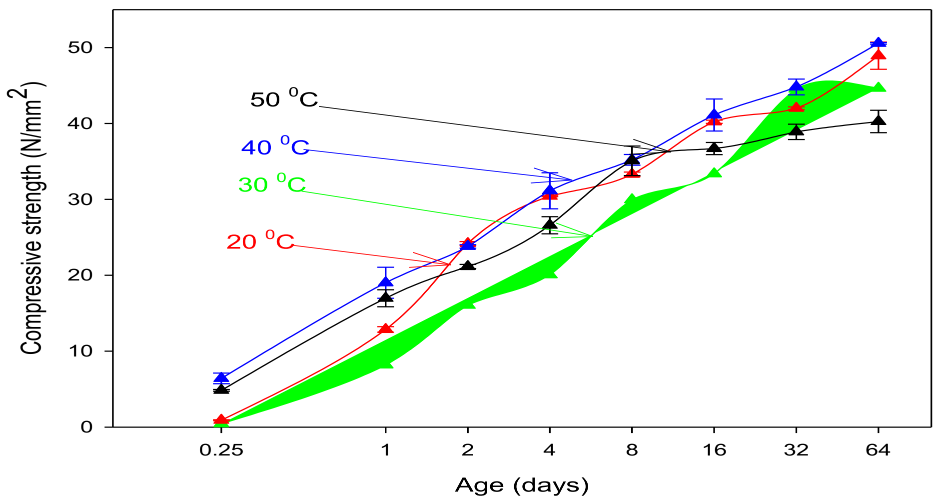

Figure (2): Compressive Strength for C35 Concrete

6.2. Estimation Compressive Strength by The Maturity Method

The maturity method can be used to predict compressive strength of any concrete structural element. In this study slab of grade C35 was cast, the slab size was 35 x 35 x 25 cm and cured outdoors in order to simulate behavior of concrete in-site. The temperature history of the slabs was recorded in order to use to predict the compressive strength by the maturity method. Beside that the actual compressive strength was measured using concrete cubes cured close to slabs, the compressive strength measured from the age of 6 hours up to 64 days.

6.3. Recording The Concrete Temperature

The temperature history of the concrete slab was measured and recorded by a digital thermometer UT321, thermocouple were put inside the concrete in the time of casting and the device was connected to the computer to record the temperature automatically. The recording was to the duration until the slab temperature become the same as the air temperature. Figure (3) shows the temperature history of the slab.

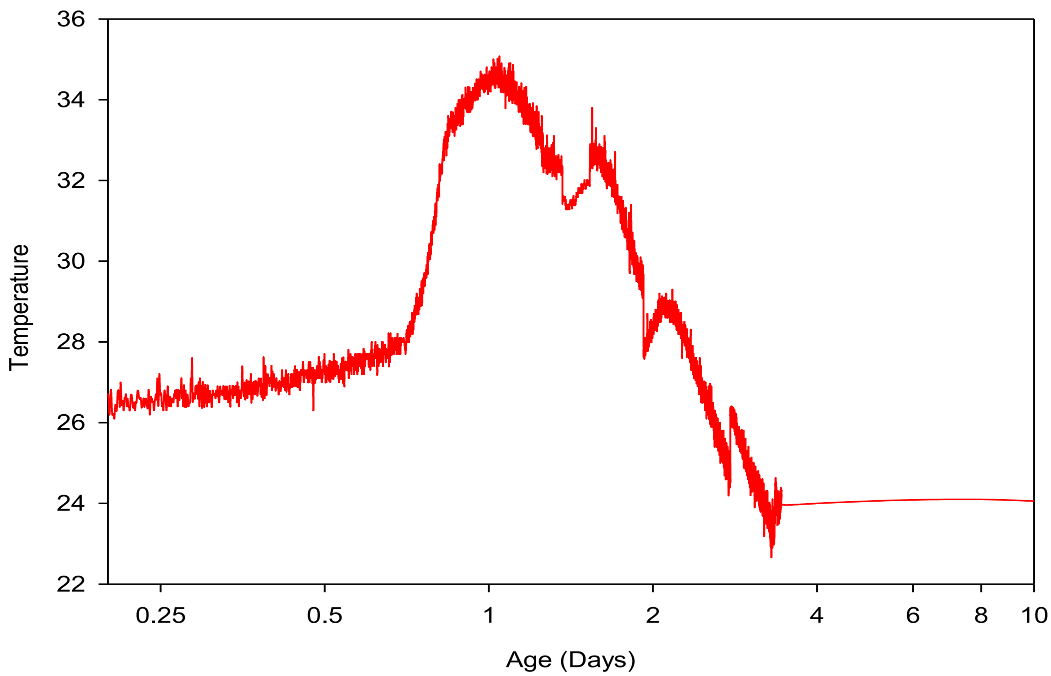

Figure (3): Temperature History of The Slab

6.4. The Use of Maturity Functions to Predict Concrete Strength Development

The temperatures histories were converted into predicted strength development, using Carino equation and the Three Parameter Equation (TPE) suggested by Freiesleben Hansen and Pedersen equation. Predicted strengths were then compared with the actual strength of cubes cured in order to investigate the accuracy of the equations.

A summary of the stages used to predict the strength of the concretes:

- Determine the activation energy and the datum temperature.

- Determination of model parameters for maturity functions, Strength-age parameters based on the Carino's equation and the Freiesleben Hansen and Pedersen equation for concrete cured under standard 20 oC conditions.

The parameters S∞, k and t_0 of Carino's equation and S∞, τ and α of the Three Parameter Equation suggested by Freiesleben Hansen and Pedersen for the Arrhenius equivalent age function, producing the best fit for the experimental data at standard 20 °C, have been calculated. The regression analysis values are listed in Tables (2), and (3) for the concrete grades of 35.

- **Carino Equation :**

Table (2): Parameters Based on Carino Equation (Strength-Age Relationships)

Parameters	20 ^{0}C
S∞ (N/mm2)	44.6443
k (days-1)	0.2000
t^0 (days)	1.4832E-016
R^2	0.9819

- **Hansen Equation :**

Table (3): Parameters Based on Hansen Equation (Strength-Age Relationships)

Parameters	20 ^{0}C
S∞ (N/mm2)	55.5283
τ (days)	3.4769
a	0.5500
R2	0.9931

Note:

o Carino (NS) means that the strength-maturity relationship that has been described by Carino with maturity calculated according to the Nurse-Saul equation is used.

o Carino (Arh) means that the strength-age relationship that has been described by Carino with equivalent age calculated according to expression suggested by Freiesleben Hansen and Pederson using the Arrhenius equation is used.

o Hansen (NS) means that the strength-maturity relationship that has been described by Freiesleben Hansen and Pederson with maturity calculated according to the Nurse-Saul equation is used.

o Hansen (Arh) means that the strength-age relationship that has been described by Freiesleben Hansen and Pederson with equivalent age calculated according to expression suggested by Freiesleben Hansen and Pederson using the Arrhenius equation is used.

The activation energy and datum temperature determined according to the ASTM C1074, the datum temperature value is 5.5 °C and the activation energy values determined from the two methods (ASTM standard and TPE) as in Table 4.

Table (4): Apparent Activation Energy Based on Carino and TPE Methods

Activation energy (kJ/mol) based on	
Carino method	TPE method
15.84	30.06

Figure (4) shows that the only function predict the strength quit well up to age of 8 days is Carino (Arh), at later ages the strength over estimated. The other function predict the strength well up to the age of 1 day only and overestimated the strength for the other ages.

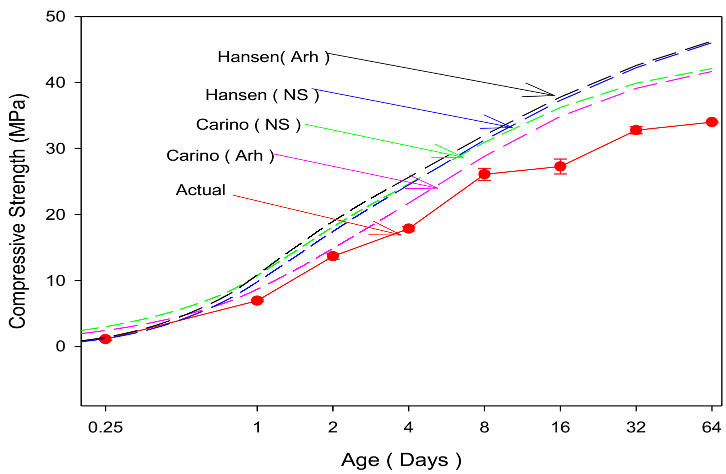

Figure (4): Predicted Compressive Strength Based on The Carino and TPE Equation.

Changing the values of datum temperature in the maturity equation between the determined values 5.5 ^{O}C and recommended values by the standard that -11 ^{O}C, shows that Hansen (NS) function accurately predict the strength up to 8 days. The other equation overestimated the strength at all ages as shown in figure (5).

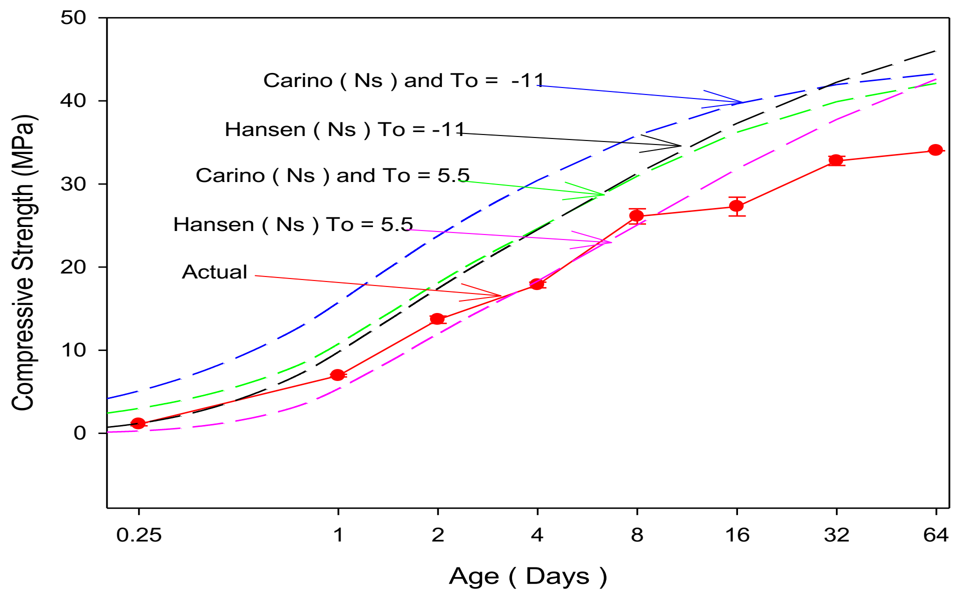

Figure (5): Predicted Compressive Strength Based on The Carino and TPE Equation.

7. Conclusions:

Based on the results of this study, the following conclusions are drawn:

- At early age (1- 4 days) the strength development under 20, 30, 40 and 50°C curing regimes for the concrete cubes increases as the temperature increase. From the age of 8 to 64 days the strength development the strength development decreases as the temperature increase
- The study has shown that Carino (Arh) function is able to predict the compressive strength with sufficient accuracy up to the age of 8 days.
- The study has shown that equation Hansen (NS) considered very accurate to predict the compressive strength using determined datum temperature up to the age of 8 days.

Acknowledgment

First and foremost, we thank Allah. This paper based on undergraduate project during the Academic year 2013/2014 done by the students, Ahmed Mohammed Emsilkh, Ali Nurie Emhlhel, Abdullah Mansour Emhemed and Wisam Elhmali Mansour under the supervision of Dr. Mohammed Ali Abdalla Elsageer. The authors are gratefully and sincerely thank the students for their hard work on the experimental and theoretical parts of the project. Special thanks are due to Mr. Ahmed and Mrs. Haw the technicians in the concrete lab for their assistance with the laboratory work.

References

[1]. Newman, J. B. and Choo, B. S., Advanced Concrete Technology, Volume 2: Concrete Properties 2003: Elsevier Science & Technology.

[2]. Malhotra, V. M. and Carino, N. J., Handbook on nondestructive testing of concrete 2004: ASTM International.

[3]. Carino, N. J. and Lew, H. S., The maturity method: From theory to application. Cement, Concrete, and Aggregates, 1984. 6(2): p. 61-73.

[4]. Association, American Concrete Pavement, Maturity testing of concrete pavements: Applications and benefits. Publication IS257P, 2002.

[5]. ASTM C 1074, Standard Practice for Estimating Concrete Strength by the Maturity Method," Annual Book of ASTM Standards, 2004.

[6]. Geiker M. and Knudsen T., Chemical Shrinkage of Portland cement Pastes. Cement and Concrete Research, 1982. 12(5): p. 603-610.

[7]. Hansen, P. F. and Pedersen, E. J., Maturity computer for controlled curing and hardening of concrete, 1977.

[8]. Hansen, P. F. and Pedersen, E. J., Curing of concrete structures 1984.

[9]. Copeland, L. E., Kantro, D. L., and Verbeck, G. J., Chemistry of hydration of Portland cement 1960: Portland Cement Association, Research and Development Laboratories.

[10]. Teychenne, D., R. Franklin, and H. Erntroy, Design of normal concrete mixes, Vol. 2.1997: BRE (Building Research Establishment UK). 46.

[11]. BSI, BS 882:1992 specification for aggregate from natural sources for concrete 1992, BSI-British Standards Institution.

Design of Vertical Pressure Vessel Using ASME Codes

Najeeb A. Yahya[1], Othman M. Daas[2], Nureddin O. Fahel Alboum[3], Ahmed H. Khalile[4]
[1]nyahya@zu.edu.ly, [2]othmandaas@yahoo.com, [3]fhailboom@yahoo.com, [4]ahmed.hassan.khalile@gmail.com
[1,2,3,4]Department of Mechanical & Industrial, College of Engineering, Zawia University, Libya

ABSTRACT

While preparing this paper many of companies are subjecting to the hazards resulted from the incorrect design and manufacturing of pressure vessels (leakage or Explosion), those used in the storage of dangerous liquids or pressurized fluids. The main objective of using the pressure vessels are used as containers to contain many of materials such as: liquids, air, gases, chemical compounds and fuel, moreover pressure vessels considered as important prop in petroleum and chemical industries especially as storages for oil and chemical components. The main goal of this paper to shed light on the importance processes of the Mechanical Design and Analysis of Vertical Pressure Vessels, also to give scratch to prevent this hazard using. The used model is very close shape to the used vessels in such companies. The design of vertical pressure vessel is carried out using the American Society of Mechanical Engineers (ASME) Codes. ASME section VIII and Division 1 are normally used in design. Various components of the pressure vessel are designed by calculating the appropriate design factors like thickness of the shell, head, stress analysis etc. to validate the design result the pressure vessel is modelled and analyses in Solid works software. The engineering geometrical drawings and Finite Element Analysis (FEA) have been achieved on the targeted model of Vertical Pressure Vessel by using very moderate computer programs to give results agreed and compatible with correct choose of ASME codes. Throughout this paper, the permissible pressures are very considered as well as determination the wall thickness of the vessel is firmed to reach the acceptable maximum stresses. Furthermore, the design of targeted pressure vessel has been achieved under the range of ASME codes and engineering standards to reach the allowable designing boundaries.

Keyword— Pressure vessels; ASME codes; Standards; Maximum stresses; Solid works software.

1. Introduction

Pressure vessels are one of the main equipment those widely used in industrial facilities. The pressure vessels defined as cylindrical or spherical vessels those designed to store or hold pressurized liquids, gases or fluids with a differential pressure between inside and outside.

Usually, the inner pressure is higher than the external pressure, except in some cases. The fluid inside these vessels may undergo a change in state as in the case of steam boiler or may combine with other reagent as in the case of chemical reactor. The reservoirs designed such that no leakage can occur, also deal with operational levels of high pressure and high temperatures[1]. The pressure vessels are differ in terms of capacity, heat and pressure, some of these vessels may contain more the half million barrels of crude oil, the temperatures sometimes more than 200^{o}C specially in asphalt tanks and high viscosity products, the temperatures may slope down to 14^{o}C especially in tanks store hydrocarbons materials such as propane, butane and others, so it is necessary to understand the types of reservoirs and their components as well as the appropriate storage methods[2]. Pressure vessels usually are cylindrical or spherical with semi-spherical covers (domes) and cylindrical tanks. Cylindrical vessels very wide in use and very simple to manufacture and ease in use such as boilers, heat exchangers, refineries …etc. According to the importance of pressure vessels, many of published researches achieved especially in Designing and Analysis of Stresses on the reservoirs as well as the exact use of designing standards, methods of numerical analysis and the mathematical simulation models to identify different collapse occur on reservoirs.

(Apurva R)[3] and friends have used ASME codes to design and analysis of pressure vessel by using maximum permissible pressure to find the factor of safety to obtain the finest design, furthermore, the Finite method element used to study the stresses distribution those deal to reservoir failure. (B. Thakkar and S. Thakka)[4] are designed and constructed in accordance with ASME codes Section VIII, Division 1 by changing internal pressure values of the vessel to obtain the premium design and determination of critical points of collapse in vessel's body. (V. Kumar)[5] used the ANSYS program to design and analyze the loads on the installation fits of horizontal pressure vessel to determine the high stresses concentration between the stiffeners and the wall of the tank, the results were compared with permissible strain of design. (Maharishi J. Bhatt)[6] Studied the design of connecting the nozzle with the tank wall, also to connect this nozzle with upper or lower cover according to ASME codes Section VIII, Division 1. Generally speaking, this paper includes the steps designing calculations to support the nozzle with the tank body and connecting regions.

2. History of ASME Codes for Pressure Vessel

Pressure vessels store energy and as such, have inherent safety risks. Many states began to enact rule and regulations regarding the construction of steam boilers and pressure vessels following several catastrophic accidents that occurred at the turn of the twentieth century that resulted in large Loss of life. By 1911 it was apparent to manufacturers and users of boilers and pressure vessels that the lack of uniformity in these regulations between states made it difficult to construct vessels for Interstate commerce. A group of these interested parties appealed to the Council of the American Society of Mechanical Engineers to assist in the formulation of standard specifications for steam boilers and pressure vessels. (The American Society of Mechanical Engineers was organized in 1880. As an educational and technical society of mechanical engineers.) After years of development and Public comment, the first edition of the Code, ASME Rules of Construction of Stationary Boilers and for Allowable Working Pressures, was published in 1914 and formally adopted in the Spring of 1915. The first Code rules for pressure vessels, entitled Rules for the Construction of Unfired Pressure Vessels, followed in 1925. From this simple beginning the Code has now evolved into the present eleven Section document, with multiple subdivisions, parts, subsections, and Mandatory and non-mandatory appendices.

Almost all pressure vessels used in the process industry in the United States are designed and constructed in accordance with Section VIII, Division 1. A pressure vessel is a closed container designed to hold gases or Liquids at a pressure different from the ambient pressure. The end caps fitted to the cylindrical body is called heads. Pressure vessels are used in a variety of applications. These include the industry and the private sector. Steel pressure vessel in the industrial sector, pressure vessels are designed to operate safely at a specific pressure and temperature, technically referred to as the "Design Pressure" and "Design Temperature". A vessel that is inadequately designed to handle a high pressure constitutes a very significant safety hazard. Because of that, the design and Certification of pressure vessels is governed by design codes such as The ASME Boiler and Pressure Vessel Code in North America, the Pressure Equipment Directive of the EU (PED), Japanese Industrial Standard (JIS), CSA B51 in Canada, AS1210 in Australia and other international standards like Lloyd's, German is cher Lloyd, Det Norske Veritas, Stoomwezen etc. Pressure vessels can theoretically be almost any shape, but shapes made of sections of spheres, cylinders and cones are usually employed. More complicated shapes have historically been much harder to analyse for safe operation and are usually far harder to construct. Theoretically a sphere would be the optimal shape of a pressure vessel.
Unfortunately the sphere shape is difficult to manufacture, therefore more expensive, so most of the pressure vessels are cylindrical shape with 2:1 semi elliptical heads or end caps on each end. Smaller pressure vessels are arranged from a pipe and two covers. Disadvantage of these vessels is the fact that larger diameters make them relatively more expensive. Generally, almost any material with good tensile properties that is chemically stable in the chosen application can be employed. Many pressure vessels are made of steel.

3. Using Method of (ASME Section II & VIII, Div1) Calculation

3.1. Selection of Materials by using (ASME Section II: A,D)

The (Section II: A, D) is used to determine selected materials with full description, it permits to use codes for components with different constructions[3].
The main component of any vessel is metal shells with different dimensions on bottom, top and wall. All these dimensions should be suitable with codes under the authority of the designer himself.

3.2. Design of Vessels by using (ASME Section VIII, Div1)

This code (standard) is used for designing vertical tanks (vessels), according to minimum requirements of design without any failure of tank parts. The specialized code for the vessels those used within range of (0.1 MPa to 20 MPa) and for this range most of vertical vessels are selected [9]. The cylindrical pressure vessel composed of: (Shell – Head – Nozzles – Base support).

3.2.1 Shell Design

he ASME codes presents basic rules while designing shells. It is clear that the thickness of these shells is main consideration, the welding operation on vessels is necessary too. The used thickness equations are:

- In case of circumference stresses (longitudinal welding)

Where: $(p < 0.385\ SE)t_s = \frac{PR}{SE-0.6P}$, $P_s = \frac{SEt_s}{R+0.6t_s}$

- In case of longitudinal stresses (circumference welding)

Where: $(p < 1.25\ SE)$ $t_s = \frac{PR}{2SE+0.4P}$, $P_s = \frac{2SEt_s}{R-0.4t_s}$

Where:

t_s = Shell thickness.

P = Designing pressure.

P_s = Maximum pressure.

R = Internal Radius.

S = Maximum allowable stress.

E = Coefficient of connection of welding.

Note that: E = 1.0 if radiated test is used, meanwhile E = 0.7 is used if non-radiated tests are used

3.2.2 Heads Design

Most of used closing heads are curved to resist pressure, reduce thickness and cost reduction. There are many types of closing heads and mostly used is semi-elliptical head. In this type the base diameter to the high = $\frac{D}{h} = \frac{4}{1}$

The head cover will consist of two main parts are shown in Figure 1:

Spherical radius = (L = 0.9D)

Radius of the neck = (ri = 0.17D)

$t_h = \frac{PD}{2SE-0.2P}$, $P_h = \frac{2SEt}{D+0.2t_h}$

Where:

t_h = head thickness.

P = Designing pressure.

P_h = Maximum pressure.

S = Maximum allowable stress.

D = Internal diameter of tank body.

E = Coefficient of connection of welding.

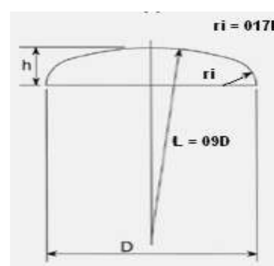

Figure 1. Semi-elliptical Heads

3.2.3 Nozzles Design

During providing the pressure vessels with nozzles, it is important to support these nozzles to avoid or prevent any failure. The type of nozzle is shown in Figure 2

$$t_n = \frac{PR}{(SE-0.6P)}$$

$A_r = d_n * t_s * f$

$A_s = D_n(T_s - t_s) - 2T_n(T_s - t_s)$

$A_n = 2[\, 2.5(T_s) * (T_n - t_n)\,]$

$A_r < (A_s + A_n)$

$d_s = d_n + 2(t_n)$

$x = r_n + T_n \quad , \; y = 2.5 * T_s$

$d_n = D_n - 2\,(T_n + \text{Corrosion Allowance})$

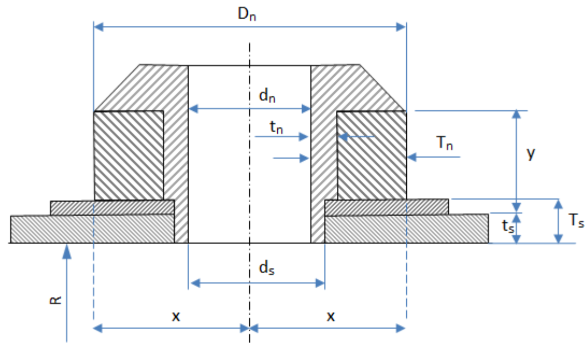

where:

D_n = External nozzle diameter

d_n = Internal nozzle diameter

d_s = Diameter of nozzle on tank wall

f = correction coefficient = 1

t_s = Required thickness of tank

T_s = Actual body thickness

t_n = Required nozzle thickness

T_n = Actual nozzle thickness

r_n = Radius of internal hole

A_r = Area of nozzle hole

A_s = Area of connecting region

A_n = Area of nozzle wall

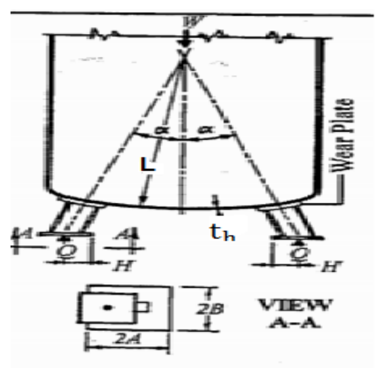

Figure 3. The support

3.2.4 Support Base Design

During designing of high vessels, the support bases, size, volume, weight, wind and earthquake should be taken into consideration. In this work the legs support were used.The support legs are shown in Figure 3. The number of legs depends on the size of the tank and the size of stored material in the tank. The dimensions of the legs and stresses can be calculated as:

- Longitudinal stresses

$$S_L = \frac{Q}{{t_h}^2}\left[\cos\alpha\,(k_1 + 6k_2) + \frac{H}{L}\sqrt{\frac{L}{t_h}}\;\;(K_3 + 6K_4)\right]$$

- Circumference stresses

$$S_c = \frac{Q}{{t_h}^2}\left[\cos\alpha\,(k_5 + 6k_6) + \frac{H}{L}\sqrt{\frac{L}{t_h}}\;\;(K_5 + 6K_6)\right]$$

Note that the longitudinal Stress always positive values (k2, k4, k6, k8) mean while the compressional strain (k1, k3, k5, k7) negative values [11].

4. Design Calculations and Results

The studied vessel with internal pressure not exceeding (1.55 MPa) and internal temperature not exceeding (100 ^{o}C). Table 1 shows the initial material used in vessel.

Table 1: Initial material used in vessel

Part	Material
Tank Shell	SA 515 – Gr 70
Head Cover	SA 515 – Gr 70
Tank Nozzle	SA 106 Gr (B)
Support Base	SA 515 – Gr 70
Support Legs	SA 106 Gr (B)

4.1. Vessel Shell Calculations

Table 2: Properties and dimensions of vessel shell

Internal Pressure	1.55 MPa
Internal Temperature	100 ^{o}C
External Pressure	0.103 MPa
Shell Length (L)	4000 mm
Internal Tank Diameter (Di)	1500 mm
Material Type	SA 515 – Gr 70
Permissible Material Stress	137.9 MPa
Link Efficiency	1.0
Corrosion Permeability	3 mm
Density of Material	/cm^3

4.1.1 Vessel Shell Thickness

Where:

$$P < 0.385 * S * E = 1.55 < 0.385 * 137.9 * 1$$

$$t_s = \frac{PR}{SE - 0.6P} + c.a$$

$$t_s = \frac{1.55 * \left(\frac{1500}{2}\right)}{(137.9 * 1) - (0.6 * 1.55)} + 3 = 11.48\,mm$$

$$(use\ t_s = 12\ mm)$$

4.1.2 Maximum Pressure on Vessel Shell

$$p_s = \frac{SEt}{R + 0.6t_s}$$

$$p_s = \frac{137.9 * 1 * 12}{\left(\frac{1500}{2}\right) + 0.6 * 12} = 2.19\ MPa$$

4.1.3 Vessel Shell Mass

$$Volume = \frac{\pi * \left(D_0^2 - D_i^2\right)}{4} * L$$

$$Volume = 228004.22\ cm^3$$

$$Mass = Volume * Density$$

$$Mass = 228004.22 * 7.73 = 1762.472\ Kg$$

4.1.4 Liquid Mass at Vessel Shell

$$Volume = \frac{\pi * \left(D_i^2\right)}{4} * L$$

$$Volume = 7068583.47\ cm^3$$

$$Mass = Volume * Density$$

Liquid Density=1.00 g/cm^3

$$Mass = 7068.58\ Kg$$

4.2. Head Calculations

Table 3: Properties and dimensions of head cover

Head cover type	Semi-Elliptic
Internal Tank Diameter	1500 mm
Material Type	SA 515 – Gr 70
Permissible Material Stress	137.9 MPa
Link Efficiency	1.0
Corrosion Permeability	3 mm
Internal Spherical Radius	1350 mm
Head High	375 mm

4.2.1 Required Head Thickness

$$t_h = \frac{PD}{2SE - 0.2P} + c.a$$

$$t_h = 11.44\ mm \qquad (use\ t_h = 12\ mm)$$

4.2.2 Maximum Pressure at the Head

$$P_h = \frac{2SEt}{D + 0.2t_h}$$

$$P_h = \frac{2 * 137.9 * 1 * 12}{1500 + 0.2 * 12} = 2.2\ MPa$$

4.2.3 Mass of Head

$$Volume = \frac{2}{3} * \pi(Lo^2\ - Li^2\ ) * h$$

$$Volume = 25559.99\ cm^3$$

$$Mass\ =\ Volume\ * Density$$

$$Mass\ =\ 25559.99 *\ 7.73$$

$$Mass\ =\ 197.58\ kg$$

$$Mass\ of\ two\ heads\ =\ 197.58 * 2 = 395.16\ kg$$

4.2.4 Liquid Mass at Head

$$Volume = \frac{2}{3} * \pi(Li^2\ ) * h$$

$$Volume = \frac{2}{3} * \pi\left(135^2\ \right) * 37.5 = 1431388.153\ cm^{3}$$

$$Mass\ =\ Volume\ * Density$$

Liquid Density=1.00 g/cm^3

$$Mass\ =\ 1431.388\ Kg$$

$$Liqud\ Mass\ of\ two\ heads\ = 2862.776\ kg$$

4.3. Nozzle Calculations

Table 4: Properties and dimensions of tank nozzle

Nozzle Length	200 mm
External Nozzle Diameter	203 mm
Material Type	SA 106 Gr (B)
Permissible Material Stress	117.9 MPa
Link Efficiency	1.0
Corrosion Permeability	3 mm

4.3.1 Required Nozzle Thickness

$$t_n = \frac{PR}{(SE - 0.6P)}$$

$$t_n = \frac{1.55 * (\frac{203}{2})}{(117.9 * 1 - 0.6 * 1.55)} = 1.5\ mm$$

$$(use\ T_n = 10\ mm, ts = 12\ mm\ and\ Ts = 22\ mm$$

4.3.2 Nozzle Reinforcement

$d_n = D_n - 2\ (T_n + Corrosion\ Allowance)$

$d_n = 203 - 2(10+3)$, $d_n = 177\ mm$

$d_s = d_n + 2(t_n)$

$d_s = 177+2(1.5)$, $d_s = 180\ mm$

$A_r = d_n * t_s * f$

$A_r = 177*12*1$, $A_r = 2124\ mm2$

$A_s = D_n\ (T_s - t_s) - 2T_n(T_s - t_s)$

$A_s = 203*(22-12)-2*10*(22-12)$, $A_s = 1830\ mm2$

$A_n = 2[\ 2*1/2(Ts).(T_n - t_n)\ ]$

$A_n = 2[\ 2.5(22).(10 - 1.5)\ ]$, $A_n = 935\ mm2$

$A_r < (A_s + A_n)$

$2124 < (1830+935)$

$x = R_n + T_n$

$x = (177/2) + 10$, $x = 98.5\ mm$

$y = 2.5*T_s$

$y = 2.5*22$, $y = 55\ mm$

4.3.3 Mass of Nozzle

$$Volume = \frac{\pi * (D_n^2 - d_n^2)}{4} * L$$

$$Volume = \frac{\pi * \left(20.3^{\ 2} - 17.7^2\right)}{4} * 20 = 1551.95\ cm^3$$

$$Mass = Volume * Density$$

$$Mass\ =\ 11.99\ kg$$
$$Mass\ of\ two\ nozzles\ =\ 11.99 * 2 = 23.99\ kg$$

4.3.4 Total Mass of Pressure Vessel

Total mass of vessel parts = 130.9+23.99 + 395.16 + 1762.472 = 2312.5 kg

Total liquid mass = 2862.7763+7068.58 = 9931.36 kg

Total mass (T_m)= 9931.36+2312.5 = 12243.9 kg

4.4. Design of Pressure Vessel Support

Table 5: Properties and dimensions of vessel support

Material Type	SA 106 – Gr (B)
Permissible Material Stress on installation sheet	137.9 MPa
Permissible Material Stress on support	117.9 MPa
Link Efficiency (E)	0.6
Number of supporting Legs (n)	4
Spherical Radius (L)	1350 mm
Designed Pressure (P)	55.1 MPa
Lower cover Thickness (th)	12 mm

$$\text{Total mass } = T_m = 12243.9\ kg$$
$$T_{wf} = 12243.9\ * 9.81 = 120112.3\ \text{N}$$
$$\text{Q} = \frac{\text{T}_{\text{wf}}}{\text{n}} = \frac{120112.3}{4}$$
$$\text{Q} = 30028.1\text{N}$$
$$\text{H} = 155\ \text{mm} \quad , \qquad 2\text{A}= 2\text{B} = 300\ \text{mm}$$
$$\cos\alpha = 0.95 \quad , \qquad \text{c} = \sqrt{\text{AB}} = 150$$
$$\text{D}_\text{L} = 1.8\,\frac{\text{C}}{\text{L}}\sqrt{\frac{\text{L}}{\text{t}_\text{h}}} = 1.8 * \frac{150}{1350} * \sqrt{\frac{1350}{12}} = 2.12\ \text{mm}$$

From charts 1,2,3,4 values of K_1 to K_8 can be defined [11].

K_1=0.055 K_2=0.02 K_3= 0.06 K_4=0.02

K_5=0.015 K_6=0.01 K_7=0.02 K_8=0.01

4.4.1 Calculations of supporting leg dimensions

$$Q = 30028.1\ N$$
$$E * S = \frac{Q}{A} = \frac{Q}{\frac{\pi}{4}({D_o}^2 - {D_i}^2)}$$

$$0.6 * 117.9 = \frac{30028.1}{\frac{\pi}{4}({D_o}^2 - 75^2)}$$

$$D_o = 79\ mm$$

5. Finite Element Analyses

The FE analysis starts with an axisymmetric analysis of pressure vessel. Solid works software is used for the three dimensional modeling of solid structures. The element is defined by eight nodes having three degrees of freedom at each node i.e. translations in the nodal x, y, and z directions. The finite element model consists of hemispherical heads, cylindrical shell and legs support. In boundary condition, the vessel is supported at the end corners and internal pressure of 1.55MPa is applied at the inner surface. The boundary condition for hemispherical and end connection pressure vessels are shown in the figure. All parts of vessel have been drawn after finishing all designing calculations. All the drawings drawn by Solid Works Program. The vertical pressure vessel assembly are shown in Figure 4.

Figure 4. Vertical pressure vessel assembly

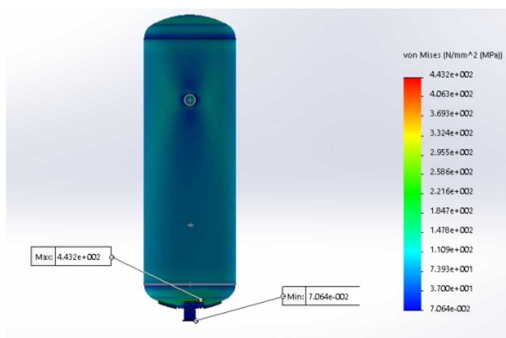

Figure 5. Von-Miss Stresses

The main purpose of simulation is to determine critical points, stresses concentrations resulted by internal pressure and the distributions of stresses at different regions on vertical pressure vessel with four legs support. The results are shown in Figure 5,6 and 7.

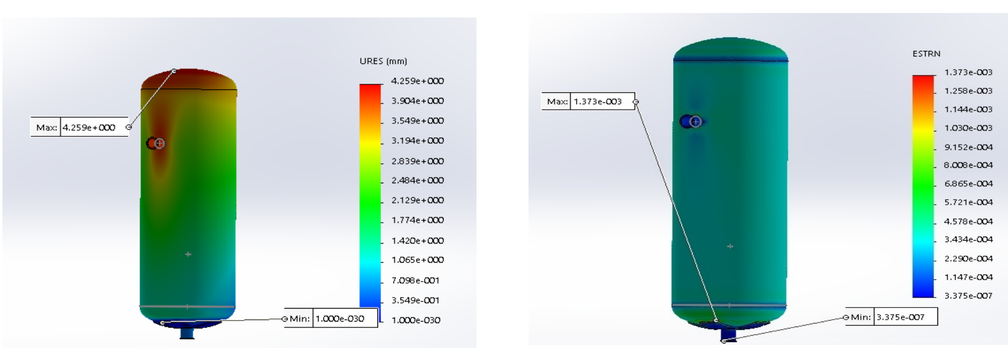

Figure 6. Displacements on vertical pressure vessel

6. Conclusions

It is very clear that the pressure vessels are integrated system in terms of parts and competence. Mechanical design of pressure vessel had been done using Solid Works software. During the designing of Pressure vessels, it is very important to design each part of these vessels individually to obtain more accurate design. All the pressure vessel components are selected on basis of available ASME standards and the manufactures also follow the ASME standards while manufacturing the components. The designing simulation concludes that the stresses concentration regions concentrated on the regions that connect between the bottom of the tank and the fixing base as well as the regions of fixing of the nozzle on the tank body. Also the designing simulation concludes that the most affected regions to displacement by internal pressure are the away regions from fixing points (i.e., farther away from installation points the higher displacement value.)

References

[1]. Eljondi, "Tanks for Petroleum and Control," Books, 2015.

[2]. M. Hassn and A. Eljondi, "Study of allowances External loads at nozzle/shell junctions of petroleum tanks," Journal of Engineering Sciences, First edition, Damusq 2006.

[3]. P. Apurva, "Design and Analysis of Pressure Vessel," International Journal of Innovative Research in Technology & Science, Mumbai 2011.

[4]. Thakkar and S. Thakkar, "Design of Pressure Vessel Using ASME Code, SECTION VIII, DIVISION 1," International Journal of Advanced Engineering Research and Studies, India 2012.

[5]. V. Kumar, N. Kumar, S. Angra and P. Sharma,"Design of Saddle Support for Horizontal Pressure Vessel," International Journal of Mechanical, Aerospace, Industrial, Mechatronic and Manufacturing Engineering, 2014.

[6]. M. Bhatt, A. Gohil, H. Shah and N. Patel. "Design Calculation Of Nozzle Junction Based On ASME Pressure Vessel Design Code," International Journal of Advance Engineering and Research Development, India 2014.

[7]. ASME COMPANY. "ASME Boiler and Pressure Vessel Code, VIII Division 1 ,"New York , 2010.

[8]. E. Kaynejad. "Pressure Vessel Design,fabrication and test ASME section VIII, div. 1 ,"

[9]. M. DENNIS, "PRESSURE VESSEL DESIGN MANUAL," Third edition, USA, 2004.

[10]. V. Patil, "Determination of Safety of Inclined Leg Support for Pressure Vessel Subjected to Arbitrary Wind Load Using FEA," International Journal of Innovations in Engineering and Technology, Vol. 2, 2013

[11]. E. Megyesy "Pressure vessel hand book," , Oklahoma 2001.

Design Methodology for Supply Water Distribution Network; Case Study: Al-Hadeka District, Garaboulli-Libya

Khairi Algrad [1],Abdulghani Ramadan[2]
[1]Kmelgrad@elmergib.edu.ly,[2]amramadan@elmergib.edu.ly
[1]Department of Mechanical Engineering, Faculty of Engineering, Elmergib University, Libya
[2]Department of Mechanical Engineering, Faculty of Engineering, Elmergib University, Libya

ABSTRACT

Pipe network is a hydraulic network containing several or many inter-connected branches where fluid (water) flows through it. This paper presents a design methodology for a supply water pipe network for Al-Hadeka district at Garaboulli-Libya. The proposed network provides water to 150 residential units with an average occupation density of 7 persons per unit. The main objective is to determine the flow rate and pressure head at each individual section of the network in addition to water demand of the region. The governing differential equations were formulated based on the continuity and the energy equations. Hardy Cross Method and EPANET Software were implemented to perform the calculations. Two cases were analyzed and investigated, namely, gravity flow and forced flow. Results of both cases were interpreted and compared. There is a good agreement between the results of both methods, in terms of flow velocities in pipes and pressure heads. These values lie in the allowable range in accordance with the known standards and specifications for water distribution networks. The use of the available software, EPANET, for analysis saves time and effort and gives acceptable results of appropriate precision.

Keyword— Pipe network**,** Hardy Cross, EPANET, Gravity flow, Forced flow.

1. Introduction

Water distribution networks serve many purposes in addition to the provision of water for human consumption. Piped water is used for washing, sanitation, irrigation and fire fighting. Networks are designed to meet peak demands; in parts of the network this creates low-flow conditions that can contribute to the deterioration of microbial and chemical water quality. The purpose of a system of pipes is to supply water at adequate pressure and flow. However, pressure is lost by the action of friction at the pipe wall and pipe accessories and fittings such as valves, elbows…etc. The pressure loss is also dependent on the water demand, pipe length, gradient and diameter. Several established empirical equations describe the pressure–flow relation ship and these have been incorporated into network modelling software packages to facilitate their solution and use. Traditionally, a water distribution network design is based on the proposed street plan and the topography. Various equations have been used in this study as the continuity equation and the energy equation. Hardy Cross Method and EPANET Software was used to perform the calculations required. The hydraulic analysis for the network is applied to two cases, gravity flow and forced flow. Extensive research work on supply water networks has been carried out in literature. For example, studies as shown in references [1], [2], [3], [4]& [5]. Generally, they focused on designing and analyzing supply water pipe networks by Hardy

Cross method and EPANET software. Flow rates and pressure heads at each node and junction in the network are calculated and determined. Comparison of results were also interpreted and discussed.

2. Site Overview

The site is located in Al-Hadeka district at Al-Garaboulli city, with an area of 31125 m² and 150 housing utilities as shown in Figure 1.

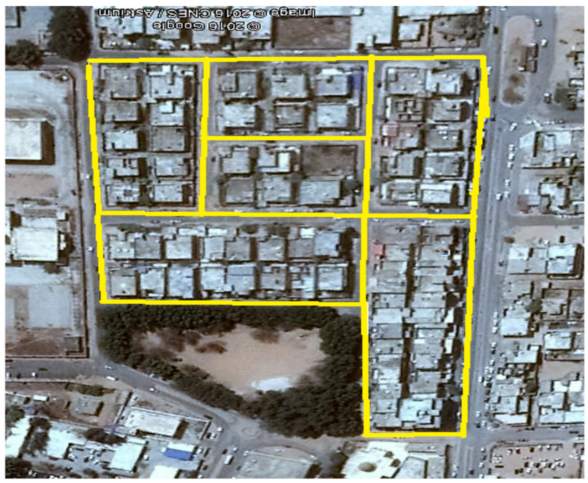

Figure 1: Site Overview for Al-Hadeka district at Al-Garaboulli city.

According to population surveys in Libya , in the year 2014 , it was found that the family member average is 7 persons , this was done with the help of population private data of the previous years , this comprehensive population scanning is done regularly every 10 years, amongst the methods used for future population scanning is the Geometric Method. Accordingly, population of this area is approximated to be 1050 persons and Water consumption rate is 270 Litre/day/person, so that the total water demand is about 284m^3/day [6].

3. Design Methodology

3.1. Hardy Cross Method

Hardy Cross method is an effective method in pipe networks analysis. The Hardy Cross method of analysis is a simplified version of the iteration linear analysis. This method is mainly based on assuming reasonable starting values for water flow rates inside network pipes and their directions according to the proposed loops. Then, the values of flow rates should be adjusted iteratively in order to reach to an optimum and precise approximation. Moreover, the head loss in pipes is evaluated simultaneously. In order to apply this method, the site is divided into many subdivisions and loops as shown in Figure 2.

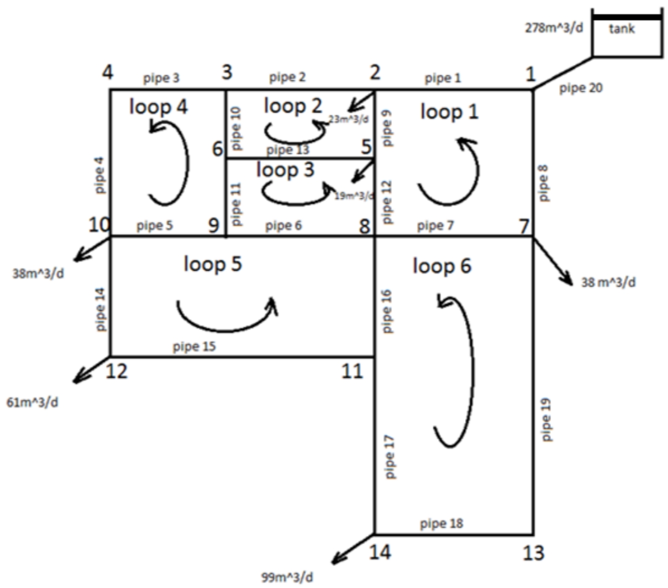

Figure 2: Schematic drawing for pipe network nodes, junctions and loops.

3.2. EPANET Software

EPANET Software, as shown in Figure 3, performs extended period simulation of hydraulics and pipe network analysis. Moreover, it is designed to be applicable also to pressurized pipe networkers. A pipe network consists of pipe, nodes (pipe junctions), pumps, valves and storage tanks or reservoirs. EPANET evaluates the flow rates of the water in each pipe, the pressure at each node. EPANET provides an integration environment for editing network input data, performing hydraulic analysis, and viewing the result in a variety of formats, these include colour- coded network maps, data tables, time series graphs, and contour plots. EPANET was developed by the Water Supply and Water Resources Division of the U.S. Environmental Protection Agency.

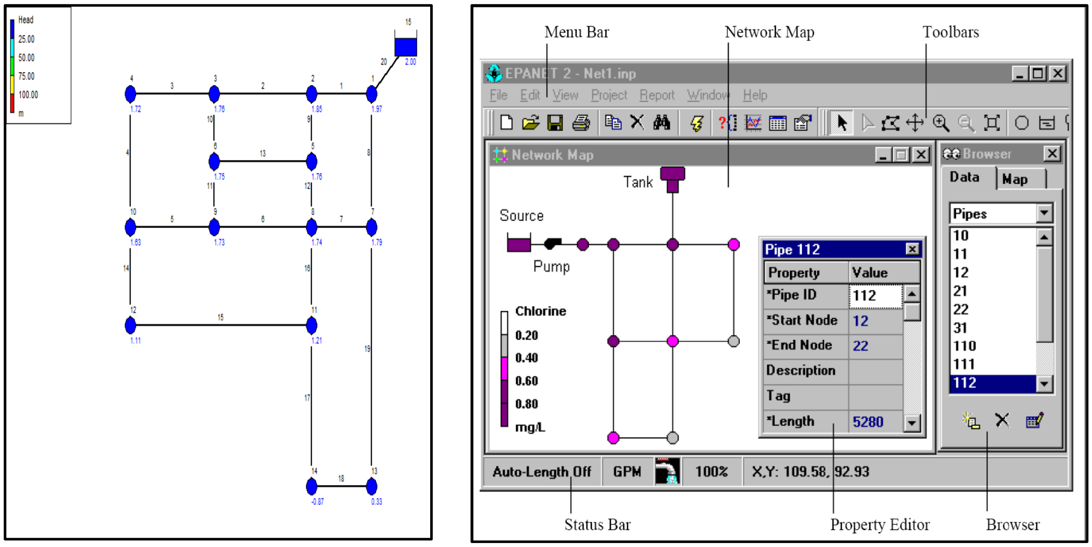

(a) Present study pipe network. (b) EPANET software interface.

Figure 3: Pipe network analysis by EPANET

3.3. Solution Procedure

Following are the steps carried out to model water distribution network using Hardy Cross method and EPANET;

Step 1: Draw a network representation of distribution system.

Step 2: Edit the properties of the objects that make up the system. It includes editing the properties and entering required data in various objects like reservoir, pipes, nodes and junctions.

Step 3: Describe how the system is operated.

Step 4: Select a set of analysis option.

Step 5: Run a hydraulic analysis program/software.

Step 6: View the results of the analysis which can be viewed in various forms i.e. in the form of tables or graphs.

In addition, the pipe network design and operating conditions for this study according to known standards and specifications,[6] are as follows;

- Flow velocity inside pipes ranges from (0.1 to 1.5) m/s.
- The allowable pressure at nodes ranges from (1.5 to 3) bar.
- Pipe diameters range from (32 to 110) mm.
- Pipe material is HDPE can withstand pressure up to 6 bar.

In order to simplify the analysis, some assumptions are also considered as follows;

- Secondary losses inside pipe network fittings and other accessories are assumed to be negligible.

- Pipes are located at the same level inside the study area.

Storage tank capacity of 900 m^3 provides water to site at least for 3 days in case of emergency.

4. Results and Discussion

The hydraulic analysis for the pipe distribution network is applied to two design scenarios, namely, gravity flow case and forced flow case (using a pump).

4.1. Case I: (Gravity Flow)

In the first case the water level on the reservoir is located just 2 meters above ground surface. Results of Hardy Cross method are shown in Table1 and Table 2.

Table1: Output results of water flow rates in pipes.

Link ID	Q (m^3/s)	Q (L/s)	Q (m^3/day)
Pipe 1	0.001808	1.808	156.2112
Pipe 2	0.000726	0.726	62.7264
Pipe 3	0.000572	0.572	49.4208
Pipe 4	0.000572	0.572	49.4208
Pipe 5	0.000483	0.483	41.7312
Pipe 6	0.00011	0.11	9.504
Pipe 7	0.000351	0.351	30.3264
Pipe 8	0.00141	1.41	121.824
Pipe 9	0.000816	0.816	70.5024
Pipe 10	0.000154	0.154	13.3056
Pipe 11	0.000377	0.377	32.5728
Pipe 12	0.000373	0.373	32.2272
Pipe 13	0.000223	0.223	19.2672
Pipe 14	0.000615	0.615	53.136
Pipe 15	9.1E-05	0.091	7.8624
Pipe 16	0.000619	0.619	53.4816
Pipe 17	0.000528	0.528	45.6192
Pipe 18	0.00062	0.62	53.568
Pipe 19	0.00062	0.62	53.568
Pipe 20	0.00322	3.22	278.208

Table 2: Head values at each node.

Node ID.	Head (m)
1	1.97
2	1.85
3	1.76
4	1.72
5	1.76
6	1.75
7	1.79
8	1.74
9	1.73
10	1.63
11	1.21
12	1.11
13	0.33
14	-0.87

Results from EPANET software are shown in Table 3. Flow rates at each pipe, flow velocity, unit head loss and friction factor are determined.

Table 3: EPANET output results for case I.

Link ID	Flow rate (m^3/day)	Velocity (m/s)	Unit Headloss (m/km)	Friction factor
Pipe 1	156.21	0.40	2.87	0.025
Pipe 2	61.95	0.22	1.27	0.030
Pipe 3	48.44	0.27	0.82	0.031
Pipe 4	48.44	0.17	0.82	0.031
Pipe 5	42.61	0.27	2	0.031
Pipe 6	10.49	0.12	0.13	0.034
Pipe 7	30.32	0.19	1.10	0.034
Pipe 8	121.79	0.32	1.83	0.026
Pipe 9	71.26	0.27	1.63	0.029
Pipe 10	13.51	0.12	0.07	0.034
Pipe 11	32.13	0.14	0.40	0.035
Pipe 12	33.64	0.16	0.43	0.034
Pipe13	18.62	0.10	0.16	0.041
Pipe 14	53.05	0.48	8.75	0.029
Pipe 15	7.95	0.12	0.85	0.041
Pipe 16	53.47	0.50	8.88	0.029
Pipe 17	45.52	0.65	19.82	0.029
Pipe 18	53.48	0.77	26.63	0.028
Pipe 19	53.48	0.49	8.88	0.029
Pipe 20	278.00	0.34	1.26	0.024

From above results, Table 2 clearly shows that at node no. 14, the value of pressure head is negative. This means that the pressure at this node is less than atmospheric pressure which in turn implies that water will not reach the node and hence it is clear that the height of the elevated reservoir in case I, is undersized. Therefore, the water reservoir should be located at higher elevation. For this purpose, the tank is elevated at 20 m above ground surface level, this is considered as case II.

4.2. Case II: Gravity Flow using Elevated Tank

Because of the negative pressure in the case I, the tank height will be change to 20 m above ground. The obtained results of both Hardy Cross and EPANET are shown and compared in Table4 and Table 5.

Table 4: Comparison of results for pressure head in case II.

Node ID	Head,H-C (m)	Head, Epanet (m)	Error, %
1	19.98278	19.97	0.06397
2	19.89224	19.85	0.212357
3	19.83574	19.76	0.381859
4	19.81069	19.72	0.457766
5	19.84119	19.76	0.409176
6	19.8304	19.75	0.405418
7	19.86057	19.79	0.355338
8	19.83201	19.74	0.463942
9	19.82799	19.73	0.494182
10	19.76803	19.63	0.698249
11	19.45122	19.21	1.240142
12	19.50449	19.11	2.022568
13	18.81528	18.33	2.579171
14	17.88649	17.13	4.22941

Table 5: Comparison of results for flow rates in case II.

Link ID	Q(m^3/day) H-C	Q(m^3/day) Epanet	Error, %
Pipe 1	156.2112	156.21	0.000768
Pipe 2	62.7264	61.95	1.237756
Pipe 3	49.4208	48.44	1.984589
Pipe 4	49.4208	48.44	1.984589
Pipe 5	41.7312	42.61	2.10586
Pipe 6	9.504	10.49	10.5397
Pipe 7	30.3264	30.32	0.021104
Pipe 8	121.824	121.79	0.027909
Pipe 9	70.5024	71.26	1.07457
Pipe 10	13.3056	13.51	1.5362
Pipe 11	32.5728	32.13	1.359416
Pipe 12	32.2272	33.64	4.38387
Pipe13	19.2672	18.62	3.359077
Pipe 14	53.136	53.05	0.161849
Pipe 15	7.8624	7.95	1.11416
Pipe 16	53.4816	53.47	0.02169
Pipe 17	45.6192	45.52	0.217452
Pipe 18	53.568	53.48	0.164277
Pipe 19	53.568	53.48	0.164277

It should be noted that no negative pressure head values are noticed. The assumption of elevating the water tank to a height of 20 m is reasonable and logic. Moreover, the comparison between the results from Hardy Cross method and EPANET shows a good agreement between results of both methods.

4.3. Case III: Forced flow Using Pump

Another alternative for solving the problem of negative pressure in case I, is based on using a ground water tank equipped with a pump station. In this case, water is forced to flow into the pipe distribution network ensuring suitable water demands and pressure heads values at pipes' nodes. Figure 4 shows the characteristics curve for the chosen pump to be used in the system and analyzed by EPANET Software simulation..

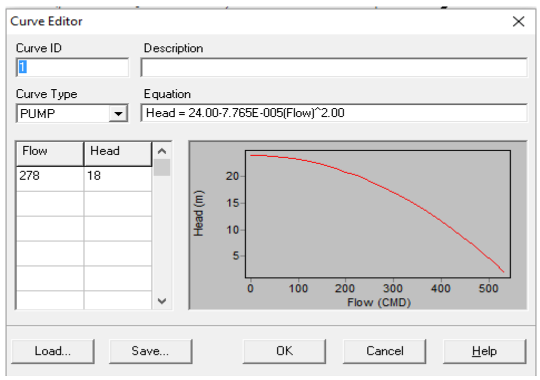

Figure 4: Characteristic curve of the chosen pump.

Table 6 and Table 7 show the results for case III when a pump is considered in the pipeline.

Table 6: Results for demand and pressure head at each node for case III.

Node ID	Demand (m³/day)	Head (m)
1	0	20
2	23	19.87
3	0	19.78
4	0	19.74
5	19	19.79
6	0	19.78
7	38	19.82
8	0	19.77
9	0	19.76
10	38	19.66
11	0	19.24
12	61	19.13
13	0	18.35
14	99	17.15

Table 7: Results for flow rate, velocity, unit head loss and friction factor for case III.

Link ID	Flow rate (m^3/day)	Velocity m/s	Unit Headloss m/km	Friction factor
Pipe 1	156.21	0.40	2.84	0.025
Pipe 2	61.95	0.22	1.28	0.030
Pipe 3	48.44	0.27	0.93	0.031
Pipe 4	48.44	0.17	0.93	0.031
Pipe 5	42.61	0.27	1.73	0.032
Pipe 6	10.49	0.12	0.46	0.038
Pipe 7	30.32	0.19	1.16	0.034
Pipe 8	121.79	0.32	1.86	0.026
Pipe 9	71.26	0.27	1.59	0.029
Pipe 10	13.51	0.12	0.48	0.042
Pipe 11	32.13	0.14	0.57	0.037
Pipe 12	33.64	0.16	0.61	0.033
Pipe13	18.62	0.10	0.49	0.042
Pipe 14	53.05	0.48	8.74	0.029
Pipe 15	7.95	0.12	0.89	0.041
Pipe 16	53.47	0.50	8.94	0.029
Pipe 17	45.52	0.65	19.89	0.029
Pipe 18	53.48	0.77	26.78	0.028
Pipe 19	53.48	0.49	8.92	0.029

In the case of water supply from ground tank using a pump, case III, it is found that the pressure head at the end of each junction (node) and corresponding value of flow rate are acceptable and ensure providing water to consumers. Furthermore, it can be noticed that the velocities at each pipe in Table 7 are within the recommended range stated in the relevant standards.

5. Conclusions

In this paper, Hardy Cross Method and EPANET software were used to perform the required calculations and the hydraulic analysis for the network under study, Al-Hadeka district at Garaboulli city –Libya. Two Scenarios were proposed, gravity flow and forced flow. For gravity flow, Case I, water level in the storage tank is assumed to be 2 meters above the ground. Results show that there is a deficiency in providing the required water quantities at some nodes in the network. In order to correct the situation, storage tank elevation is adjusted to 20 meters above ground, case II. Results indicate that the flow rates and pressure heads among the junctions of the pipe networks are acceptable and lie in the allowable values.

Another alternative is to apply a pump in the network, case III, forced flow. As expected, there is a better output results in terms of flow rates, velocities in pipes and pressure heads at the required points of demand.

The obtained values were found to be within the allowed ranges in accordance with the specifications and standards for water distribution networks. Finally, the use of available software for analysis saves time and effort and gives results of appropriate precision.

References

[1]. **Nwajuaku, Y.M. Wakawa, O.J. Adibeli, "**Analysis of Head-loss Equations under EPANET and Hardy Cross Method," *Saudi Journal of Engineering and Technology*, vol.2, issue 3, pp. 125-134, Mar, 2017.doi:10.21276/sjeat.2017.2.3.1.

[2]. E. Adeniran and M. A. Oyelowo, "An EPANET Analysis of Water Distribution Network of the University of Lagos, Nigeria," *Journal of Engineering Research*, Volume 18, No. 2, June 2013.

[3]. N. Moosavian, M. R. Jaefarzadeh, "Hydraulic Analysis of Water Supply Networks Using a Modified Hardy Cross Method," *International Journal of EngineeringTransactions*, Vol. 27, No. 9, pp 1331-1338, Sep. 2014.

[4]. G. Venkata Ramanaa , V. S. S. Sudheer , B. Rajasekhar, "Network analysis of water distribution system in rural areas using EPANET," *Procedia Engineering*, vol. 119, pp 496-505, 2015.

[5]. R. K. Rai, N.G. Sanap, "Analysis of Hydraulic Network using Hardy Cross Method and EPANET," *International Journal of Innovative Research in Science and Engineering*, vol3, issue 3, pp 516-522, Mar. 2017.

[6]. "Design Standard", *Housing and Infrastructure Board, HIB*, Tajoura, Libya, Aug. 2008.

ESTIMATION OF EMPENNAGE DESIGN WEIGHT IN CONCEPTUAL DESIGN PHASE FOR TACTICAL UAVs

Abdulhakim Muhammad Essari
hakimsari@yahoo.com
Department of Mechanical and Industrial Engineering, Elmergib University, Alkhoms – Libya

ABSTRACT

New formulas for empennage weight estimation and for takeoff weight estimation, in conceptual design phase are derived for a tactical unmanned aerial vehicle (TUAV). Formulas are derived by analyzing existing UAVs of the weighs from 100 to 500 kg, and which have similar characteristics. Based on statistical trends, obtained from analyzed existing UAVs, takeoff weight is estimated from mission specification, and given payload weight. Software tools are developed in Matlab to facilitate takeoff and component weight calculations. The least square method is applied to analyze statistical data in order to develop trend functions which correlate TUAVs empty weight and takeoff weight. Existing formulas, developed for general aviation, for empennage and takeoff weight estimations are applied to TUAV and promising one are selected and adjusted to TUAV conceptual design phase. Empennage weight is related to geometrical parameters, maximum speed, and takeoff weight of the TUAVs

Keyword— TUAV, Empennage, takeoff weight, conceptual design phase.

1. Introduction

The dependence on Unmanned Aerial Vehicles (UAV's) in last decade grow significantly especially for combat missions, and the demand for UAV's is greatly increased. UAV's play an important role in fields like, information superiority, collateral damage, urban area fighting and precision strikes against high payoff targets. UAV's evolved to include size growth of strategic UAV's for carrying more payload weight, and long time endurance, and minimize tactical UAV's size. The most important parameter which dictates all other design parameter is estimation of the UAV's weight. Since there are no enough reliable sources for such estimation, the main goal of this paper is to establish empirical relationships which will lead to reliable empennage weight estimation of the UAV's, with emphasis on tactical UAV's. Only conceptual design phase is considered to be effort of relatively small group of engineers and specialists. This phase is also the cheapest it should provide the answer if the vehicle is possible to design and what characteristics will it have. It is also only paper phase requiring no special equipment and research. Outer geometry of the vehicle is also defined in this phase.[1]

Since conceptual design phase cost least, it is wise to perform it thoroughly and to postpone crucial decisions as late as possible since all subsequent phases are continuation of this phase. This research will contribute to this problem by deriving equations for empennage weight estimation.

2. Materials and Methods

Models of conventional tactical UAVs weights between 100 to 450 kgs are chosen for empennage weight estimation.[2] The parameters values of these UAVs are input into Matlab program to get the results on charts, the results are evaluated for UAV weights 220 kg as takeoff weight to find out the suitable empennage weight.

2.1. Jay Gundlach Method:[1]

The formula used by Gundlach is established for both small and big aircrafts by changing w_a value according to the aircraft type. W_a ranges between 3.5–8 lb/ft2 for supersonic fighters and between 0.8 – 1.2 for small aircrafts. As shown in figure (1).

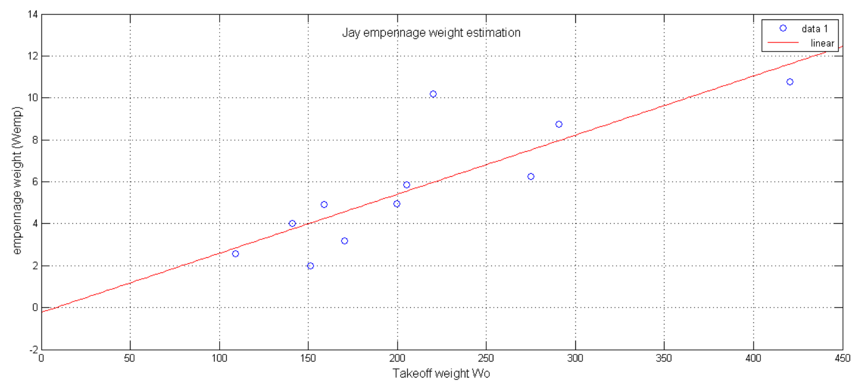

Figure (1) Jay Gundlach empennage weight estimation

$$Wemp = w_a \times (S_h + S_v)\ , \qquad w_a = 0.8{:}\ 1.2\ \text{lb/ft2} \tag{1}$$

W_{emp}, empennage weight, S_H and S_V, surface areas of horizontal and vertical stabilizer.

2.2. Usaf Method:[3]

The equations suggested by United States air force (Usaf) for finding empennage weight estimation should be applied to aircrafts with performance doesn't exceed 300 knots speed.

2.2.1 Horizontal Tail:

$$W_h = 127\times\left(\left(\frac{w_o N_z}{10^5}\right)^{0.87}\times\left(\frac{S_h}{100}\right)^{1.2}\times 0.289\times\left(\frac{l_h}{10}\right)^{0.483}\times\left(\frac{b_h}{t_h}\right)^{0.5}\right)^{0.458} \quad (2)$$

Where, W_o, takeoff weight of UAV, S_H and S_V, surface areas of horizontal and vertical stabilizer, L_H and L_V, horizontal and vertical stabilizer arm (distance between center of gravity and aerodynamic center), b, the wing span, t, tail thickness, N_z, ultimate load factor,

Figure (2) explain the relationship between takeoff weight and horizontal tail weight

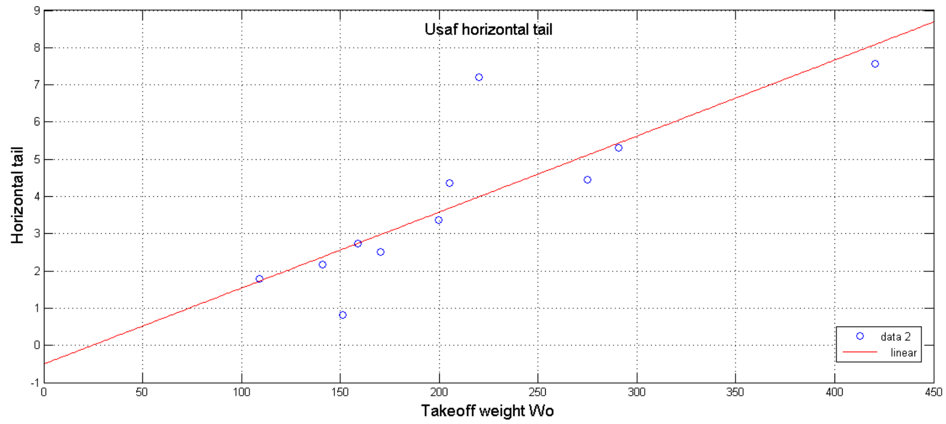

Figure (2) Usaf horizontal tail weight estimation

2.2.2 Vertical Tail:

$$W_v = 98.5\times\left(\left(\frac{w_o N_z}{10^5}\right)^{0.87}\times\left(\frac{S_v}{100}\right)^{1.2}\times 0.289\times\left(\frac{b_v}{t_v}\right)^{0.5}\right)^{0.458} \quad (3)$$

By substitution in equation (3) for V-tail weight estimation we get the results shown in figure (3), figure (4) show the results got for equation (4).

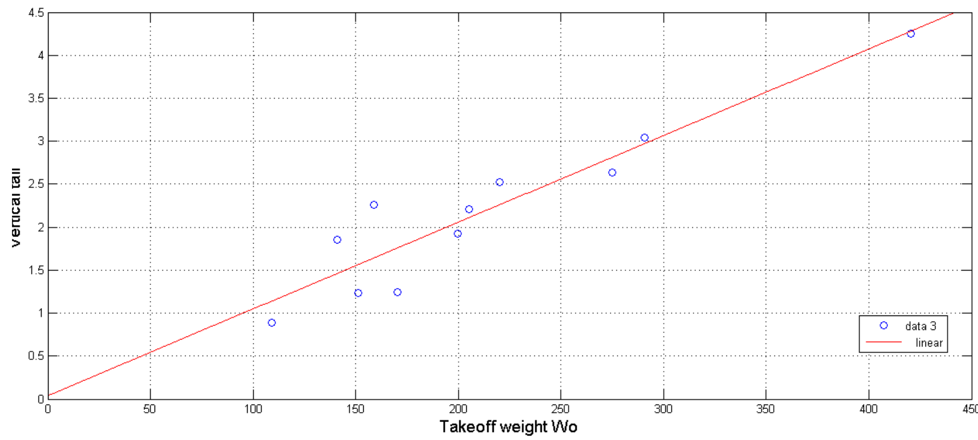

Figure (3) Usaf vertical tail weight estimation

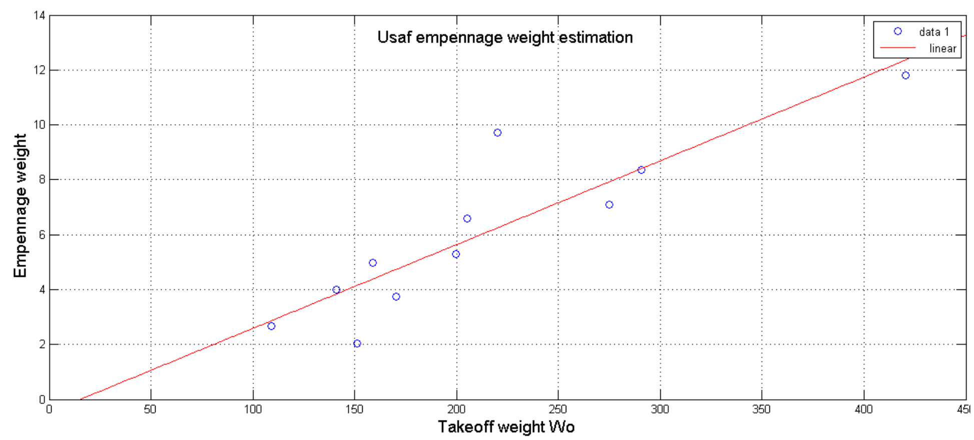

Figure (4) Usaf empennage weight estimation

2.3. Torenbeek Method:[4]

The following equation is applied to light transport aircrafts which has dive speed less than 200 knots.

$$W_{emp} = 0.04\times(N_z\times(S_v + S_h)^2)^{0.75} \quad (4)$$

Where, W_{emp} is empennage weight. S_H and S_V are surface areas of horizontal and vertical stabilizer, and Nz is ultimate load factor.

Torenbeek equation (4), is a simple equation and it is completely depends upon the areas of both horizontal and vertical tails and ultimate load factor.

By substitution in Torenbeek equation (4) we get the results shown in figure (5):

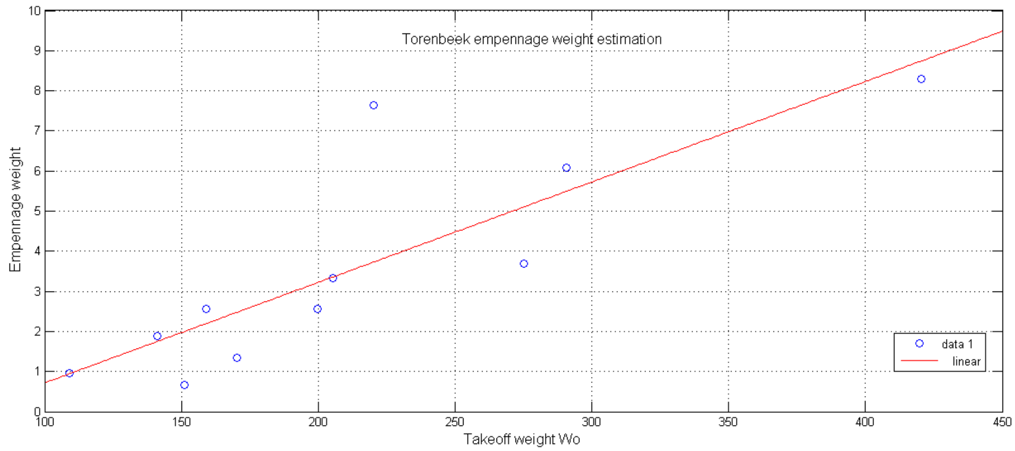

Figure (5) Torenbeek empennage weight estimation

2.4. Raymer Method:[3]

The following equations from Raymer are established for general aviation aircrafts.

2.4.1 Horizontal Tail:

Raymer equation for horizontal tail weight estimation is:

$$W_h = 0.016\times\left(N_z\times W_{dg}\right)^{0.414}\times q^{0.168}\times S_h^{0.896}\times\left(\frac{100\times t/c}{cos\Lambda}\right)^{-0.12} \times\left(\frac{A}{cos^2\Lambda_h}\right)^{0.043}\times\lambda_h^{-0.02} \quad (5)$$

Where, S_H and S_V, surface areas of horizontal and vertical stabilizer, b, the wing span, C is mean aero dynamic chord, V_H, Tail volume coefficient, V_V, Vertical Tail volume coefficient, t, tail thickness, N_z, ultimate load factor, A, aspect ratio, q, dynamic pressure, Λ, sweep angle at 25% MAC, λ, taper ratio.

Figure (6) show the relationship between takeoff weight and horizontal tail weight according to equation (5).

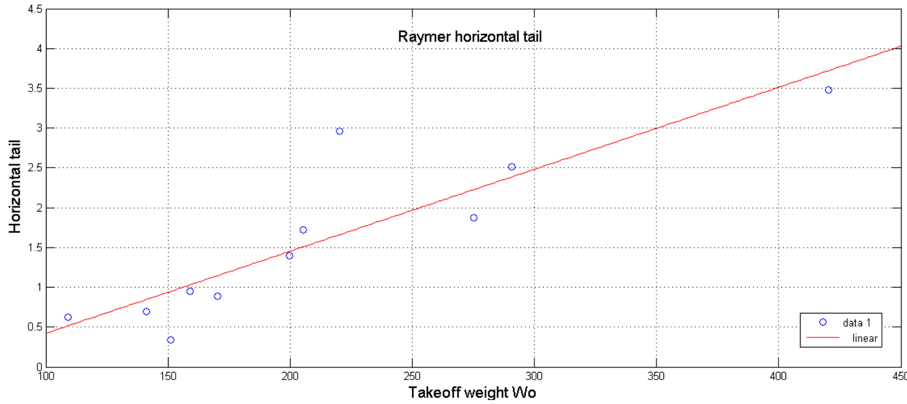

Figure (6) Raymer horizontal tail weight estimation

2.4.2 Vertical Tail:

$$W_h = 0.073\times\left(1 + 0.2\times\frac{H_t}{H_v}\right)\times\left(N_z\times W_{dg}\right)^{0.376}\times q^{0.122}\times S_h^{0.873} \times\left(\frac{100\times t/c}{cos\Lambda}\right)^{-0.49}\times\left(\frac{A}{cos^2\Lambda_h}\right)^{0.357}\times\lambda_h^{0.039} \tag{6}$$

From equation (6) we got the results shown in figure (7),

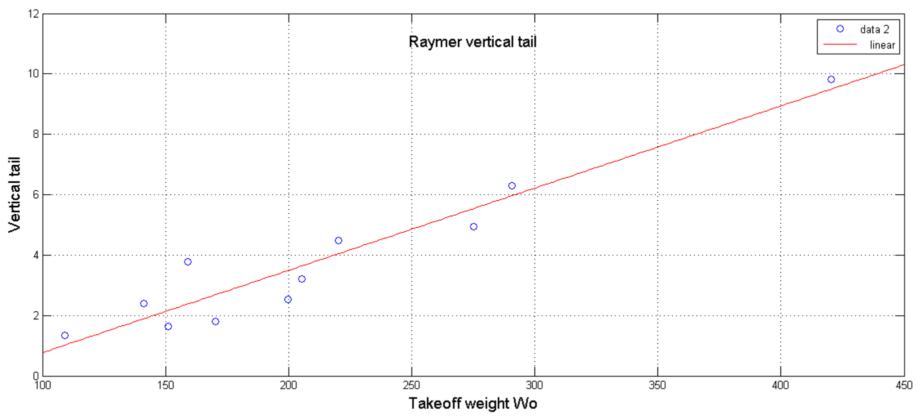

Figure (7) Raymer vertical tail weight estimation

Figure (8) explain the results for empennage group, (horizontal and vertical), weight estimation from Raymer.

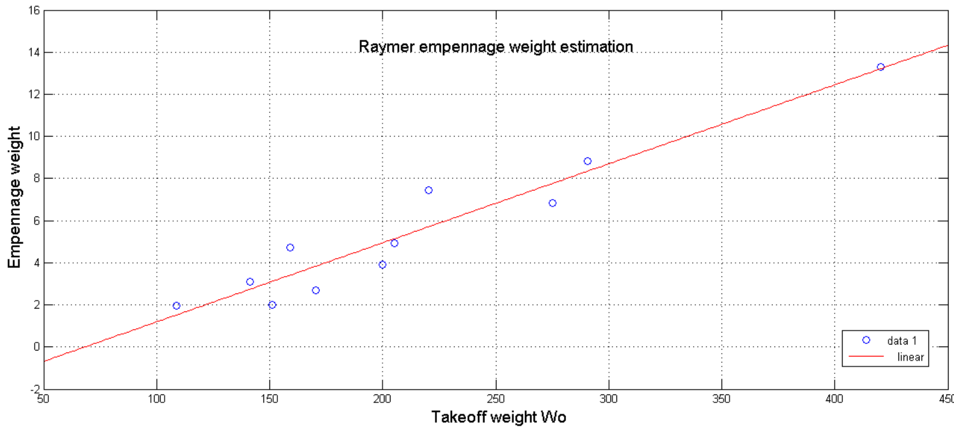

Figure (8) Raymer empennage weight estimation

2.5. Kundu Method:[5]

Horizontal and vertical tails are lifting surfaces. The empennage does not have an engine or undercarriage installation.

Both the horizontal and vertical tails plane mass estimations have a similar form but they differ in the values of constants used.

The equation used here is established for Civil Aircraft.

$$M_{emp} = 0.0213 \times (M_{to} \times N_z)^{0.48} \times S_w^{0.78} \times A \times (1+\lambda)^{0.4} / (cos\Lambda \times t/c^{0.4}) \quad (7)$$

M_{emp}- empennage mass,M_{to} - takeoff weight mass

For nonmetals are used, if there is reduction in mass due to lighter material, then the mass is reduced by that factor. If there is a 10% mass saving, then:

M_E *nonmetal* = 0.9 × M_E *all metal*

Figure (9) show the results got from equations (7) and (8) for empennage weight estimation.

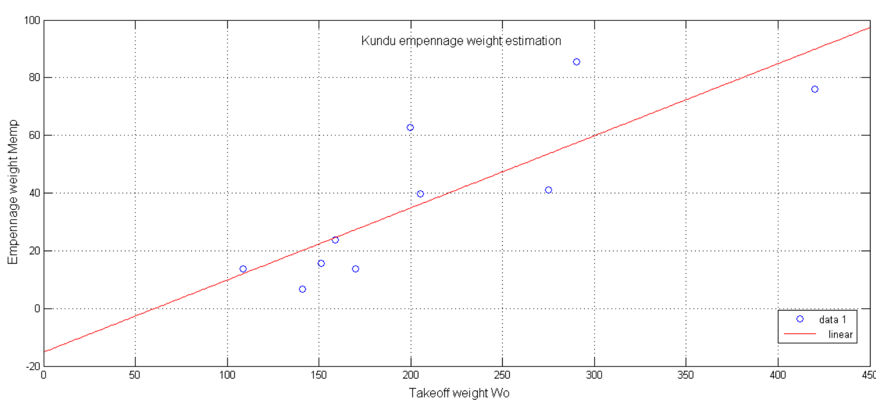

Figure (9) Kundu empennage weight estimation

2.5.1 Horizontal Tail:

$$M_H = 0.02 \times kconf \times (M_{to} \times N_z)^{0.48} \times S_w^{0.78} \times A \times (1+\lambda)^{0.4} / (cos\Lambda \times t/c^{0.4}) \quad (8)$$

2.5.2 Vertical Tail:

$$M_v = 0.0215 \times kconf \times (M_{to} \times N_z)^{0.48} \times S_w^{0.78} \times A \times (1+\lambda)^{0.4} / (cos\Lambda \times t/c^{0.4}) \quad (9)$$

For V-tail configurations, use k_{conf}= 1.1 for a T-tail, 1.05 for a midtail, and 1.0 for a low tail.
Where, W_o, takeoff weight of UAV, W_{emp}, empennage weight, S_H and S_V, surface areas of horizontal and vertical stabilizer, S, wing reference area, L_H and L_V, horizontal and vertical stabilizer arm (distance between center of gravity and aerodynamic center), b, the wing span, C is mean aerodynamic chord, $V_{H,}$ Tail volume coefficient, V_V, Vertical Tail volume coefficient, t, tail thickness, N_z, ultimate load factor, A, aspect ratio, q, dynamic pressure, Λ, sweep angle at 25% MAC, λ, taper ratio.

2.6. Kroo Method:[6]

Kroo introduces two formulas for both horizontal and vertical tails.

2.6.1 Horizontal Tail:

The horizontal tail weight, including elevator, is determined similarly, but the weight index introduces both exposed and gross horizontal tail areas as well as the tail length (distance from airplane c.g. to aerodynamic center of the horizontal tail). The method assumes that the elevator is about 25% of the horizontal tail area.

$$W_h = 5.25 \times S_h + 0.8 \times 10^{-6} \times \frac{\left(N_z \times {b_h}^3 \times W_o \times mac \times S_h^{0.5}\right)}{\left(\left(\frac{t_h}{c_h}\right) \times (\cos \quad)^2 y_h \times l_h \times S_h^{1.5}\right)} \quad (10)$$

Figures (10),(11), and (12) explain the results of equations (10) and (11) for horizontal, vertical, and empennage weight estimation byKroo method.

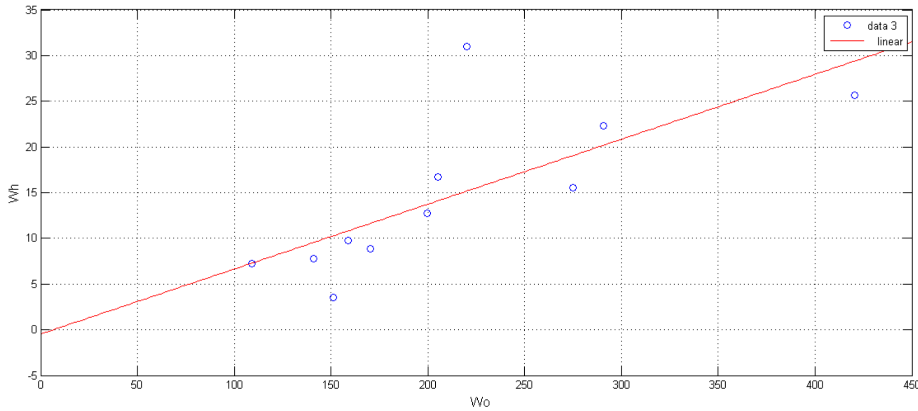

Figure (10) Kroo horizontal tail weight estimation

2.6.2 Vertical Tail:

The rudder itself may be assumed to occupy about 25% of S_V and weighs 60% more per area. The weight of the vertical portion of a T-tail is about 25% greater than that of a conventional tail; a penalty of 5% to 35% is assessed for vertical tails with center engines.

$$W_V = 2.62 \times S_v + 15 \times 10^{-6} \times \frac{\left(N_z \times {b_v}^3 \left(0.8 + 0.44 \times \left(W_o / S_{ref}\right)\right)\ \right)}{\left(\left(\frac{t_h}{c_h}\right) \times (\cos y_h)^2\right)} \tag{11}$$

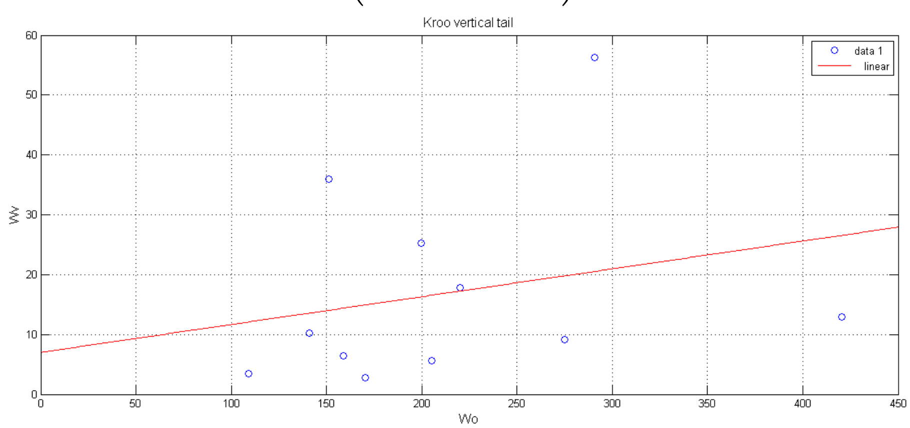

Figure (11) Kroo vertical tail weight estimation

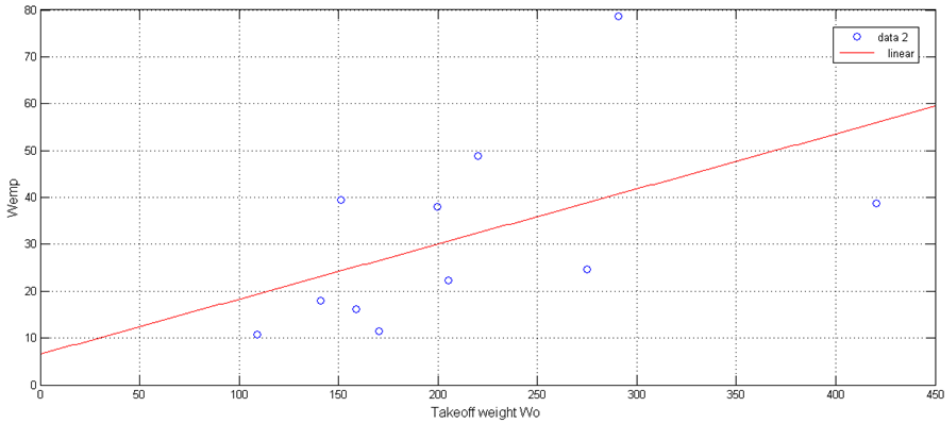

Figure (12) Kroo empennage weight estimation

3. Results and Discussion:

3.1. Empennage Weight Formulas Selection:

For empennage weight estimation many formulas were used for finding the estimated empennage weight, and the results were explained on charts to get the best one. The formulas used for empennage weight mostly were founded for general aviation aircrafts and because of presence a lot of tail group shapes and designs. So in some cases we see unreasonable and extreme results for empennage weight estimation, but in some few cases we got acceptable results such as in Jay Gundlach, Torenbeek and Usaf formulas.
Empennage group has no specific design criteria, because some UAVs have special empennage shapes, some of them have no horizontal tail instead they have delta wing, in some cases the vertical tail is much bigger than the horizontal tail and in some case there are two vertical tails.

3.2. New Formula for Empennage Weight Estimation:

These equations of our work for horizontal and vertical tails weight estimation are modified of Cessna equations. They should be applied to small size and low performance aircrafts which has maximum speed less than 350 km/hr. [7], [8].

3.2.1 Horizontal Tail:

The equation from Cessna for horizontal tail weight estimation, originally established for general aviation aircrafts. The new equation (12) now is valid for UAV's.

$$W_h = \frac{1.46\times(Wo)^{0.887}\times(S_h)^{0.101}\times A_h^{0.138}}{57.5\times t_r^{0.223}}\ lb \qquad (12)$$

Where, W_o is takeoff weight, S_H and S_V, surface areas of horizontal and vertical stabilizer, b, the wing span, C is mean aerodynamic chord, V_H, Tail volume coefficient, V_V, Vertical Tail volume coefficient, t, tail thickness, N_z, ultimate load factor, A, aspect ratio, q, dynamic pressure, Λ, sweep angle at 25% MAC, λ, taper ratio.

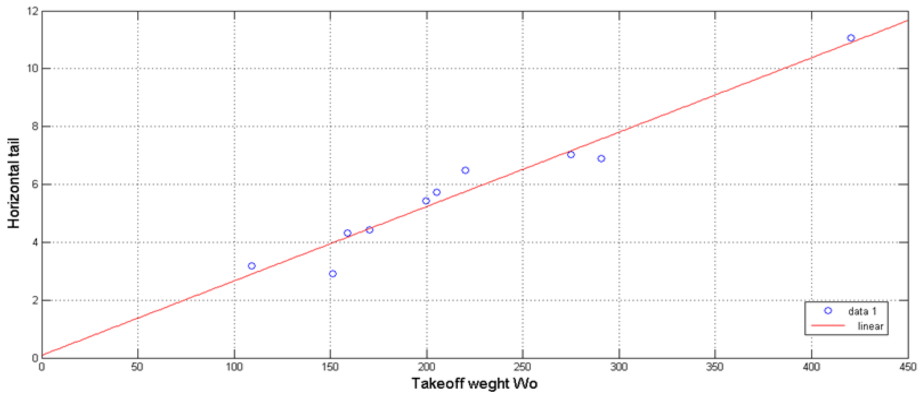

Figure (13) chart for the new equation for horizontal tail weight estimation

3.2.2 Vertical Tail:

The equation from Cessna for vertical tail weight estimation, originally established for general aviation aircrafts. My equation (13) now is valid for UAV's.

$$W_v = \frac{0.039 \times W_o^{0.567} \times S_v^{1.249} \times A_v^{0.482}}{15.6 \times t_r^{0.747} \times \left(cos\Lambda_{1/4}\right)^{0.882}}\ lb \tag{13}$$

Figure (14) show the results from equation (13) for vertical tail weight estimation by the new equation.

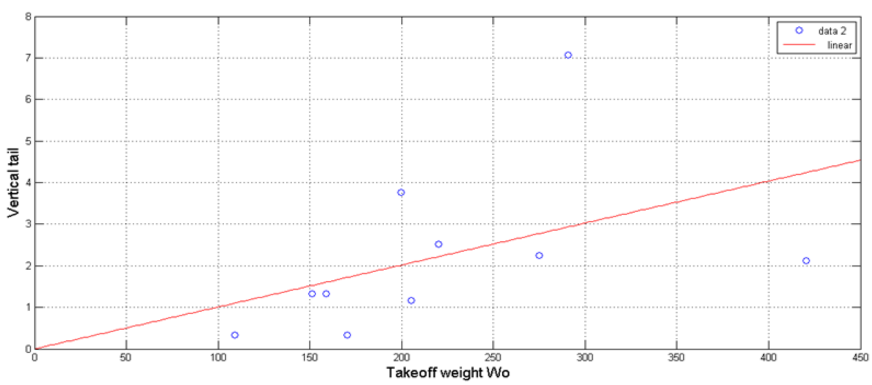

Figure (14) chart for the new equation for vertical tail weight estimation

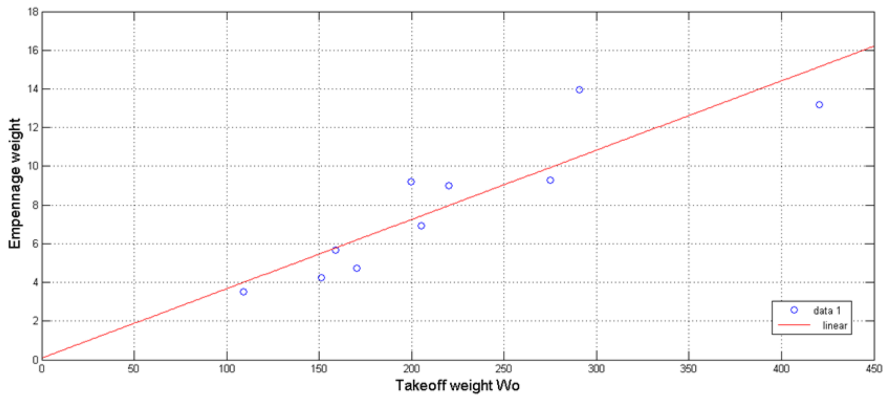

Figure (15) Empennage group

4. Conclusions

Various weight design formulas are applied to estimate empennage weights of UAVs. Since these formulas are developed for manned aircrafts (which are much heavier than tactical UAVs) they sometimes give unacceptable estimations (to high values or to small values than it could be expected by common sense).Modification in coefficients of the available formulas is done in order to get better fit UAV design process. These modified formulas are the main contribution of this paper. Application of these formulas estimates more accurately empennage weight of the UAVs. Two suggested formulas for empennage weight estimation including horizontal and vertical tails are introduced.

References:

[1]. Jay Gundlach. Designing Unmanned Aircraft Systems: A Comprehensive Approach. Published by the American Institute of Aeronautics and Astronautics, Inc. 2012.

[2]. Paul Jackson. Jane's All the World's Aircraft. 2004-2005.

[3]. Daniel P. Raymer. Aircraft Design: A conceptual Approach. Published by the American Institute of Aeronautics and Astronautics, Inc. Second Edition 1992.

[4]. Egbert Torenbeek. Synthesis of subsonic airplane design. Torenbeek1976

[5]. Ajoy Kumar Kundu. Aircraft Design. Published in the United States of America by Cambridge University Press, New York. 2010.

[6]. IlanKroo. Aircraft Design: Synthesis and Analysis. This textbook is copyright by Desktop Aeronautics, Inc. 2001.

[7]. Jan Roskam. Aircraft Design. Part 5. Component Weight Estimation. 1989.

[8]. Mohammad H. Sadraey. Aircraft Design: A system Engineering Approach. A john Wiley & Sons, Ltd Publications. 2012.